

---

# Exploring the End States of Massive Stars using the X-ray Emission of Neutron Stars and Supernova Remnants

Tobias Prinz

---



München 2013



---

# **Exploring the End States of Massive Stars using the X-ray Emission of Neutron Stars and Supernova Remnants**

**Tobias Prinz**

---

Dissertation  
an der Fakultät für Physik  
der Ludwig–Maximilians–Universität  
München

vorgelegt von  
Tobias Prinz  
aus München

München, den 7.11.2013

Erstgutachter: Prof. Dr. Werner Becker  
Zweitgutachter: Prof. Dr. Harald Lesch  
Tag der mündlichen Prüfung: 11.12.2013

# Zusammenfassung

Gegenstand der vorliegenden Arbeit ist die Untersuchung der Endstadien der Sternentwicklung, insbesondere der Röntgenemissionseigenschaften der diffusen und kompakten Überreste von Supernovae.

Der erste Teil dieser Arbeit beschäftigt sich mit der Messung der Eigenbewegung des zentralen Neutronensterns im Supernova-Überrest (SNR) Puppis A. Dies geschah mit dem Ziel Modellparameter, die eine Kernkollaps-Supernova beschreiben, weiter einzuschränken. Der Prozess der zum Kollaps eines massereichen Sterns führt ist zwar gut verstanden, jedoch wird der finale Explosionsmechanismus noch kontrovers diskutiert. Hierfür existieren verschiedene Modelle, die unterschiedliche maximale Eigenbewegungen vorhersagen. Diese Eigenbewegung hängt von der Stärke des Impulses ab, den der Protoneutronenstern während einer asymmetrisch verlaufenden Supernova-Explosion erhält und somit vom finalen Explosionsmechanismus. Bisher konnte die gemessene Eigenbewegung des Neutronensterns RX J0822-4300 in Puppis A von  $1122 \pm 327 \text{ km s}^{-1}$  (68% Konfidenzniveau CL; Hui and Becker, 2006) und  $1570 \pm 240 \text{ km s}^{-1}$  (68% CL; Winkler and Petre, 2007) mit diesen Modellen nicht hinreichend erklärt werden. Im Rahmen dieser Dissertation wurde eine erneute Beobachtung des Neutronensterns durchgeführt. Dadurch konnte der Zeitraum über den sich die verschiedenen Positionsmessungen erstrecken auf 3886 Tage nahezu verdoppelt werden. Zudem ist dies der längste Zeitraum für die Bestimmung der tangentialen Geschwindigkeit eines Neutronensterns im Röntgenbereich. Die Datenauswertung ergab eine Eigenbewegung des Neutronensterns RX J0822-4300 von  $71 \pm 12 \text{ mas yr}^{-1}$  (68% CL) mit einem Positionswinkel von  $244^\circ \pm 11^\circ$  (68% CL). Die Größenordnung und Bewegungsrichtung der Eigenbewegung des Neutronensterns lassen sich auf das optische Expansionszentrum von Puppis A zurückextrapolieren und untermauern daher die Richtigkeit der Messung. Bei einer angenommenen Entfernung zu Puppis A von 2 kpc findet man eine tangentielle Geschwindigkeit von  $670 \pm 120 \text{ km s}^{-1}$  (68% CL). Dieser Wert ist deutlich kleiner als in den zwei vorausgegangenen Untersuchungen. Die Modellierung des finalen Explosionsmechanismus wird hierdurch vereinfacht, da Modelle diesen Wert vorhersagen können. Die neue Messung schließt eine Eigenbewegung von  $900 \text{ km s}^{-1}$  (95% CL) jedoch nicht völlig aus, es bedarf jedoch eines hydrodynamischen Modells mit hochgradig antisymmetrischer Explosion um diese Geschwindigkeit erklären zu können. Zusätzlich konnte aus der tangentialen Geschwindigkeit des Neutronensterns und dem Abstand zwischen der heutigen Position und dem optischen Expansionszentrum des Überrests das Alter von Puppis A auf  $4450 \pm 750$  Jahre (68% CL) eingegrenzt werden.

Im zweiten Teil der Arbeit liegt der Fokus auf der Identifizierung und Untersuchung von

Supernova-Überresten. Ziel war es, die große Diskrepanz zwischen der bekannten und erwarteten Anzahl an Supernova-Überresten in unserer Galaxie zu erklären. Supernova-Überreste kann man typischerweise über  $(6 - 10) \times 10^4$  Jahren beobachten, bevor sie mit der interstellaren Materie verschmelzen. Die Supernova-Rate in unserer Galaxie beträgt  $\approx 2$  pro Jahrhundert. Daher werden ungefähr 1200 Überreste in der Milchstraße vermutet. Von diesen wurden bisher nur 274 entdeckt, die meisten davon im Radiobereich. Diese Gruppe an Überresten ist allerdings nicht repräsentativ, da sie hauptsächlich helle, in der galaktischen Scheibe liegende Überreste beinhaltet. Deshalb wurden in dieser Arbeit die Daten der ersten und bisher einzigen Himmelsdurchmusterung mit einem abbildenden Teleskop im weichen Röntgenband verwendet (ROSAT Himmelsdurchmusterung) um nach weiteren Supernova-Überresten zu suchen. Dazu wurde eine Liste von bisher unidentifizierten, ausgedehnten Röntgenquellen analysiert (Schaudel, 2003). Dies führte zur Identifizierung von zwei zuvor unbekanntem Supernova-Überresten im Rahmen dieser Arbeit. Sie haben die Katalogbezeichnung SNR G308.4–1.4 und SNR G38.7–1.4. Die erste Quelle hat eine kreisförmige Morphologie. Radio-, Infrarot- und Röntgenemission ist jedoch nur im westlichen Bereich der Quelle feststellbar. Das Röntgenspektrum des Überrests weist Absorptionsspuren von interstellarem Gas und Staub mit einer Säulendichte des neutralen Wasserstoffs  $N_{\text{H}}$  von  $(1,02 \pm 0,04) \times 10^{22} \text{ cm}^{-2}$  (68% CL) auf. Es lässt sich mit hinreichender Güte mit dem Modell für ein thermisch strahlendes Plasma, welches sich noch nicht im Ionisationsgleichgewicht befindet, wiedergeben. Das Plasma hat eine Elektronentemperatur von  $6,3_{-0,7}^{+1,2}$  Millionen Kelvin (68% CL). Im Radiobereich wurde nicht-thermische Emission mit einem Spektralindex von  $-0,7 \pm 0,2$  (68% CL) gemessen - ein charakteristischer Wert für junge Überreste. Eine detaillierte Analyse der Röntgendaten unter Verwendung der Sedov-Relation für die adiabatische Ausdehnung einer Explosionswolke legt eine Entfernung zum Überrest von 6 bis 12 kpc nahe, sowie ein Alter von ca. 5000 bis 7500 Jahren. Nahe dem geometrischen Zentrum des Überrests wurden zwei Punktquellen detektiert, die kein Gegenstück in anderen Wellenlängenbereichen haben. Ob eine der Quellen der im Verlaufe der Supernova entstandene Neutronenstern ist, konnte aber noch nicht abschließend geklärt werden. Der zweite in dieser Arbeit identifizierte Supernova-Überrest, G38.7–1.4 besitzt ebenfalls eine kreisförmige Morphologie. Radioemission ist nur im östlichen Teil nachweisbar. Außerdem ist die Quelle durch thermische Röntgenemission im Zentrum gekennzeichnet. Die Identifizierung dieses Überrests basiert zusätzlich auf der Detektion von polarisierter, nicht-thermischer Radioemission mit einem Spektralindex von  $0,65 \pm 0,11$  (68% CL) und von Filamenten in  $\text{H}\alpha$ - und SII-Beobachtungen - charakteristische Merkmale eines Überrests.

Nachdem die Kandidatenliste mit Himmelsdurchmusterungen und Quellkatalogen in anderen Wellenlängenbereichen korreliert worden ist und archivierte Röntgenbeobachtungen der Quellen analysiert worden sind, verbleiben von ursprünglich 205 Quellen 123 Kandidaten als mögliche Supernova-Überreste. Von diesen Kandidaten erfüllen 73 strengere Auswahlkriterien bezüglich der Signifikanz der Quellen und/oder es wurde ein mögliches Gegenstück in einem anderen Wellenlängenbereich detektiert. Letzteres war der Fall bei insgesamt acht Quellen. Diese Quellen sind sehr vielversprechende Kandidaten, da sie mehrere charakteristische Merkmale eines Supernova-Überrests aufweisen. Zudem konnte gezeigt werden, dass alle Supernova-Überreste, die zuerst im Röntgenbereich detektiert worden sind, im Radiobereich entweder eine irreguläre Morphologie aufweisen oder sehr leuchtschwach sind. Vermutlich wird dadurch die

Identifizierung im Radiobereich erheblich erschwert. Die Untersuchungen unterstreichen zudem die Wichtigkeit zusätzlich in anderen Wellenlängenbereichen nach Supernova-Überresten zu suchen. Dadurch und durch die sukzessive Identifizierung der 123 verbleibenden Kandidaten kann die Abweichung zwischen der erwarteten und der bekannten Anzahl an Supernova-Überresten in unserer Galaxie weiter verringert werden.

Zusätzlich zu der Identifikationsstudie und der Suche nach neuen Supernova-Überresten wurde der im RASS detektierte und bereits früher identifizierte Supernova-Überrest SNR G296.7–0.9 im Detail im Röntgenbereich untersucht. Die Morphologie der Quelle ist durch einen hellen Kreisbogen in süd-westlicher Richtung gekennzeichnet, deren Spektrum sich am besten mit dem Modell für ein thermisch strahlendes Plasma, welches sich noch nicht im Ionisationsgleichgewicht befindet, beschreiben lässt. Das Plasma hat eine Elektronentemperatur von  $6,2_{-0,8}^{+0,9}$  Millionen Kelvin (68% CL). Die Emission der Quelle im weichen Röntgenbereich ist teilweise durch interstellares Gas und Staub absorbiert worden, wobei die Säulendichte des neutralen Wasserstoffs  $1,24_{-0,05}^{+0,07} \times 10^{22} \text{ cm}^{-2}$  (68% CL) beträgt. Zusätzlich wurde unter Verwendung der Sedov-Relation ein Alter von 5800 bis 7600 Jahren und eine Entfernung von  $9,8_{-0,7}^{+1,1}$  kpc (68% CL) abgeschätzt. Letzteres weist auf eine räumliche Assoziation mit einer nahegelegenen HII-Region hin. Es wurde kein Hinweis auf die Existenz eines zentralen Neutronensterns gefunden. Somit kann die Art der Supernova, aus der der Überrest hervorgegangen ist, nicht eindeutig bestimmt werden.

Im letzten Teil der Arbeit wird eine systematische Suche nach den Gegenstücken von Radiopulsaren im Röntgenbereich in den Archiven der Röntgenobservatorien XMM-Newton und Chandra durchgeführt. Ziel war es, Aufschluss über den nicht-thermischen Emissionsmechanismus im Hochenergiebereich und über das Verhalten von Materie bei Dichten über der Kerndichte zu erhalten. In dieser Arbeit wurden 18 bisher unbekannte Gegenstücke von Radiopulsaren im Röntgenbereich identifiziert und deren Röntgenflüsse bestimmt. Das Spektrum von sechs dieser Quellen konnte durch ein Schwarzkörperspektrum und/oder ein Potenzgesetz angenähert werden. Im Falle der verbleibenden 12 Röntgenquellen war entweder die Photonenzählrate oder die Energieauflösung des verwendeten Detektors zu gering, so dass eine Spektralanalyse nicht möglich war. Deshalb konnte der Röntgenfluss dieser Quellen nur unter Annahme charakteristischer Spektralparameter für Pulsare annähernd bestimmt werden. Für alle Radiopulsare, die mit den Röntgenobservatorien XMM-Newton und Chandra beobachtet, aber nicht detektiert worden sind, wurden obere Grenzen für deren thermischen und nicht-thermischen Röntgenfluss im Energiebereich von 0,1 bis 2 keV bestimmt. Mithilfe dieser Werte wurde die nicht-thermische Leuchtkraft für 18 und obere Grenzen für 228 Pulsare bestimmt. Die Untersuchung dieser Werte bestätigt die Tendenz, dass mit zunehmender Empfindlichkeit von Röntgenobservatorien immer geringere Röntgeneffizienzen für rotationsgetriebene Pulsare gefunden werden. Die gemessene Schwankung von mehr als drei Größenordnungen in der Röntgeneffizienz muss in der Zukunft in Simulationen von Pulsar-Populationen, die als Eingabe verschiedene Modelle für die Hochenergieemission von Pulsaren haben, reproduziert werden. Dadurch liefern die beobachtungsrelevanten Ergebnisse dieser Arbeit eine weitere Vorgabe für die theoretische Untersuchung des nicht-thermischen Emissionsmechanismus. Zudem wurden für 230 Pulsare obere Temperaturgrenzen bestimmt. Diese oberen Grenzen bewegen sich zwischen  $2,2 \times 10^5 \text{ K}$  für den Pulsar

mit der Katalogbezeichnung PSR J2144–3933 und  $2,7 \times 10^6$  K für PSR J1822–1617. Es wurde gezeigt, dass alle Werte mit aktuellen Kühlungsmodellen für Neutronensterne verträglich sind.

# Summary

This work focuses on the end states of massive stars, more precisely on the X-ray emission properties of the compact and diffuse remnants of supernovae (SNe), i.e., neutron stars and supernova remnants.

The first part of this thesis deals with the measurement of the proper motion of the central neutron star in the supernova remnant Puppis A. The aim of this part was to validate or challenge current core-collapse supernova models. The process by which a star explodes in a core-collapse supernova is reasonably well understood, with the exception of the final explosion mechanism. Several models have been proposed for this last stage. In order to investigate the mechanism in more detail the proper motion of a neutron star was examined. This motion depends on the kick a neutron star gains in the supernova explosion and thus, depends strongly on the final explosion mechanism. Recently, the proper motion of the neutron star RX J0822–4300 in Puppis A was measured to be  $1122 \pm 327 \text{ km s}^{-1}$  (68% confidence level CL; Hui and Becker, 2006) and  $1570 \pm 240 \text{ km s}^{-1}$  (68% CL; Winkler and Petre, 2007). These high velocities can be hard to explain using pulsar-kick models. In order to reduce the error bars of and the discrepancy between, these two measurements a new X-ray observation was obtained, which was analyzed in detail in my thesis. This new observation allowed a proper motion measurement with a total time baseline of 3886 days, which is about twice as long as was available previously. It is the longest baseline used for a proper motion measurement in the X-ray regime so far. Analyzing the data yielded a proper motion of  $71 \pm 12 \text{ mas yr}^{-1}$  (68% CL) at a position angle of  $244^\circ \pm 11^\circ$  (68% CL). Both the magnitude and direction of the proper motion are in agreement with RX J0822–4300 originating near the optical expansion center of the supernova remnant. For an assumed distance of 2 kpc to Puppis A, the proper motion corresponds to a tangential velocity of  $670 \pm 120 \text{ km s}^{-1}$  (68% CL). This velocity is smaller than either of the two previously published numbers and eases most challenges that RX J0822–4300 previously posed to pulsar-kick models. However, the measurement still allows a velocity of  $900 \text{ km s}^{-1}$  (95% CL), which would still require a hydrodynamic kick model with a highly asymmetric explosion. Additionally, the age for the supernova remnant Puppis A of  $4450 \pm 750 \text{ yrs}$  (68% CL) was deduced using the displacement between its birth place and today's position.

In the second part of this thesis, the main focus lies on the identification and investigation of supernova remnants. The aim was to understand the large discrepancy between the number of known and expected supernova remnants in our Galaxy. The latter is about 1200 remnants, given that they are visible for  $\approx (6 - 10) \times 10^4 \text{ yrs}$  until they merge with the surrounding interstellar medium and that the expected supernova rate in our Galaxy is  $\approx 2$  per century. The number

of known supernova remnants is  $\approx 274$ , of which most remnants were detected in the radio band. However, this sample is biased towards selecting mainly large remnants at low galactic latitude. Hence, various attempts have been made to search for them in other wavelengths. Therefore, in this work the first imaging all-sky survey in the soft X-ray regime, the ROSAT All-Sky Survey (RASS) was searched for supernova remnants. This was done by analyzing the candidate list, which Schaudel (2003) obtained in a previous analysis of RASS data. My research lead to the identification of two previously unknown supernova remnants, SNR G308.4–1.4 and SNR G38.7–1.4. The former source was identified using archival data in the radio, infrared and X-ray bands. Its shape is that of a shell-type supernova remnant. X-ray, radio- and infrared emission is only seen in the eastern part of the remnant. The X-ray emission can best be described by an absorbed non-equilibrium collisional plasma model with a hydrogen density of  $N_{\text{H}} = (1.02 \pm 0.04) \times 10^{22} \text{ cm}^{-2}$  (68% CL), a plasma temperature of  $6.3_{-0.7}^{+1.2}$  million Kelvin (68% CL), and an underabundance of iron, neon and magnesium, as well as an overabundance in sulfur with respect to the solar values. The analysis of archival ATCA radio data revealed non-thermal emission from G308.4–1.4 with a radio spectral index of  $-0.7 \pm 0.2$  (68% CL), which is typical for young supernova remnants. A detailed analysis using the Sedov solution for the adiabatic expansion of a blast wave revealed that the remnant is at a distance of 6 to 12 kpc and the progenitor star exploded about 5000 to 7500 years ago. Two faint X-ray point sources located near to the remnant’s geometrical center are detected. Both sources have no counterpart at other wavelengths, leaving them as candidates for the compact remnant of the supernova explosion. Additionally, the second supernova remnant identified in this thesis, SNR G38.7–1.4, was studied in the radio, optical and X-ray bands. Its identification is based on its polarized non-thermal radio emission having a spectral index of  $-0.65 \pm 0.11$  (68% CL), typical for young supernova remnants, as well as on its  $\text{H}\alpha$  and SII filaments matching the radio emission region and on its thermal X-ray emission.

Finally, after correlating the source list with various sky surveys and source catalogs as well as analyzing archival X-ray observations, 123 sources remained as supernova remnant candidates. 73 of these sources fulfill more stringent selection criteria regarding the source significance and/or have a counterpart in other wavelength regimes. A very likely counterpart was detected for eight candidates. This makes them very promising supernova remnant candidates, because they show several characteristic properties of supernova remnants. Furthermore, it seems that all supernova remnants, which were first detected in the X-ray regime, are either faint and/or irregularly shaped in the radio regime. This might hamper the identification of supernova remnants in the radio band where most of all known supernova remnants have been detected so far. Additionally, it underlines the importance of multi-wavelength studies in the field of supernova remnants. With these studies and the gradual identification of the 123 candidates the discrepancy between the expected and measured number of supernova remnants in our Galaxy can be further reduced.

Additionally, the RASS detected and previously identified SNR G296.7–0.9 was studied in more detail in this thesis using data from the X-ray satellite XMM-Newton. A spectro-imaging analysis of this source was performed in order to deduce the basic parameters of the remnant and to search for evidence of an associated young neutron star. In X-rays, the remnant is characterized by a bright arc located in the south-east direction. Its X-ray spectrum can be best described

by an absorbed non-equilibrium collisional plasma model with a hydrogen column density of  $N_{\text{H}} = 1.24^{+0.07}_{-0.05} \times 10^{22} \text{ cm}^{-2}$  (68% CL) and a plasma temperature of  $6.2^{+0.9}_{-0.8}$  million Kelvin (68% CL). The Sedov solution indicates a remnant age of 5800 to 7600 years and a distance of  $9.8^{+1.1}_{-0.7}$  kpc (68% CL), implying a spatial association with a close-by HII region. No evidence was found for the existence of a young neutron star associated with the remnant. Thus, the type of the SN in which this supernova remnant was formed is still unconstrained.

In the last part of this work, a systematic search for the X-ray counterparts of radio pulsars in the public archives of the XMM-Newton and Chandra X-ray observatories is presented. The aim was to further shed light on the non-thermal high energy emission mechanism of pulsars and to infer the composition of matter at supernuclear densities. In addition to the 185 rotation-powered pulsars known to emit in X-rays, 18 previously unknown X-ray counterparts of radio pulsars were detected. For 6 of them a fit to the energy spectrum with one- or two-component models was possible. In all other cases the counting rates were too low or the used detector had a poor intrinsic energy resolution. Therefore, the energy flux and X-ray luminosity were estimated by assuming a non-thermal spectrum and an estimate for the hydrogen column density, which was based on the radio dispersion measure. For pulsars observed by the XMM-Newton and Chandra X-ray observatories, for which no source could be detected, upper limits on the non-thermal and thermal X-ray flux have been derived in the 0.1 to 2 keV band. Thus, the non-thermal X-ray luminosity for 18 and its upper limit for 228 pulsars were obtained in this thesis and used to further study the scatter in the relation of non-thermal X-ray luminosity to spin-down power. The investigation confirms the trend for finding smaller X-ray efficiencies with increasing sample size and higher sensitivity of X-ray observatories. It was shown that the X-ray efficiency differs by more than three orders of magnitude among all X-ray detected rotation-powered pulsars. In the future this large scatter has to be reproduced by a simulated pulsar population for which a certain high energy emission model was assumed. Hence, the results of the study presented in this work provides further input for the theoretical modeling of the high energy emission mechanism of pulsars. Additionally, 230 upper limits on the blackbody temperature were derived in this thesis, ranging from  $2.2 \times 10^5 \text{ K}$  (PSR J2144–3933) to  $2.7 \times 10^6 \text{ K}$  (PSR J1822–1617). All measured temperature upper limits are compatible with current cooling models.



# Contents

<b>Zusammenfassung</b>	<b>v</b>
<b>Summary</b>	<b>ix</b>
<b>1 Introduction</b>	<b>1</b>
1.1 Brief history . . . . .	1
1.2 Supernova remnants . . . . .	3
1.3 Neutron stars and pulsars . . . . .	5
<b>2 Scientific background</b>	<b>7</b>
2.1 Modeling supernova explosions . . . . .	10
2.1.1 Thermonuclear supernovae . . . . .	10
2.1.2 Core-collapse supernovae . . . . .	11
2.1.3 Supernova rates . . . . .	13
2.2 Supernova remnants . . . . .	14
2.2.1 Classification . . . . .	14
2.2.2 Evolutionary states . . . . .	14
2.2.3 High energy emission . . . . .	17
2.3 Neutron stars and pulsars . . . . .	19
2.3.1 Composition and cooling of neutron stars . . . . .	19
2.3.2 High energy emission of pulsars . . . . .	25
<b>3 The supernova remnant Puppis A</b>	<b>29</b>
3.1 Introduction . . . . .	29
3.2 Observations and data analysis . . . . .	31
3.2.1 Chandra . . . . .	31
3.2.2 XMM-Newton . . . . .	36
3.2.3 Optical . . . . .	37
3.3 Results . . . . .	37
3.3.1 The proper motion of RX J0822–4300 . . . . .	37
3.3.2 Is there a second supernova remnant in Puppis A? . . . . .	37
3.4 Summary . . . . .	42

<b>4</b>	<b>Supernova remnant candidates in the ROSAT All-Sky Survey</b>	<b>43</b>
4.1	Introduction . . . . .	43
4.2	X-ray observations and data analysis . . . . .	45
4.3	Results and discussion . . . . .	47
4.3.1	Correlation with archival observations and catalogs . . . . .	47
4.3.2	Final list of candidates . . . . .	55
4.3.3	Candidates of special interest . . . . .	56
4.3.4	Identified candidates . . . . .	59
4.4	Conclusion and future prospects . . . . .	65
<b>5</b>	<b>Exploring the supernova remnant G308.4–1.4</b>	<b>67</b>
5.1	Introduction . . . . .	67
5.2	X-ray observations and data analysis . . . . .	68
5.2.1	Spatial analysis . . . . .	69
5.2.2	Spectral analysis of G308.4–1.4 . . . . .	70
5.2.3	The central sources . . . . .	74
5.3	Radio observation and data analysis . . . . .	77
5.4	Observations in other wavelength regimes . . . . .	79
5.5	Discussion and conclusion . . . . .	80
5.5.1	Distance . . . . .	81
5.5.2	Age . . . . .	83
5.5.3	The central sources . . . . .	84
5.6	Summary . . . . .	86
<b>6</b>	<b>Supernova remnant G296.7–0.9 in X-rays</b>	<b>87</b>
6.1	Introduction . . . . .	87
6.2	X-ray observation and data reduction . . . . .	88
6.2.1	Spatial analysis . . . . .	89
6.2.2	Spectral analysis . . . . .	90
6.3	Discussion . . . . .	92
6.3.1	Comparison with the ROSAT results . . . . .	92
6.3.2	Distance and age . . . . .	92
6.3.3	Central neutron star . . . . .	94
6.4	Conclusion and summary . . . . .	94
<b>7</b>	<b>A search for X-ray counterparts of radio pulsars</b>	<b>95</b>
7.1	Introduction . . . . .	95
7.2	Observations and data reduction . . . . .	97
7.2.1	Spatial analysis . . . . .	98
7.2.2	Spectral analysis . . . . .	99
7.2.3	Timing analysis . . . . .	100
7.2.4	Upper limits . . . . .	100
7.3	Results . . . . .	102

---

7.3.1	Detections . . . . .	102
7.3.2	Upper limits . . . . .	111
7.4	Summary and future prospects . . . . .	116
<b>8</b>	<b>Discussion and future prospects</b>	<b>119</b>
8.1	Modeling supernova explosions . . . . .	119
8.2	Supernova remnants . . . . .	121
8.2.1	Is there a second supernova remnant in Puppis A? . . . . .	121
8.2.2	Supernova remnant candidates in the ROSAT All-Sky Survey . . . . .	122
8.2.3	G308.4-1.4 . . . . .	122
8.2.4	G296.7-0-9 . . . . .	125
8.2.5	Concluding remarks on supernova remnants . . . . .	126
8.3	Neutron stars and pulsars . . . . .	127
8.4	Future prospects . . . . .	129
8.4.1	Future X-ray missions . . . . .	131
8.4.2	Occultations . . . . .	133
<b>A</b>	<b>Supernova remnant candidates in the ROSAT All-Sky Survey</b>	<b>135</b>
A.1	Source catalogue of high significant sources . . . . .	135
A.2	Source catalogue of low significant sources . . . . .	136
A.3	RASS images of all SNR candidates . . . . .	137
A.3.1	High significant candidates with an extent of less than 30 arcmin . . . . .	138
A.3.2	Low significant candidates with an extent of less than 30 arcmin . . . . .	144
A.3.3	Candidates with an extent between 30 and 60 arcmin . . . . .	150
A.3.4	Candidates with an extent between 60 and 120 arcmin . . . . .	152
A.3.5	Candidates with an extent of more than 120 arcmin . . . . .	152
<b>B</b>	<b>A search for X-ray counterparts of radio pulsars</b>	<b>155</b>
B.1	List of pulsars detected at high energies . . . . .	155
B.2	Used observations . . . . .	159
B.3	Upper limits . . . . .	170
	<b>Danksagung</b>	<b>211</b>



# List of Figures

<b>2</b>	<b>Scientific background</b>	
2.1	Stellar evolution of stars I . . . . .	8
2.2	Stellar evolution of stars II . . . . .	9
2.3	Classification of SNRs . . . . .	15
2.4	Phase diagram of ultra dense matter . . . . .	20
2.5	A cross-section of the interior of a neutron star . . . . .	21
2.6	Mass-radius diagram for neutron stars . . . . .	22
2.7	Cooling curve with and without nucleon paring . . . . .	24
2.8	Pulsars magnetosphere . . . . .	27
2.9	Pulsars slot gap . . . . .	28
<b>3</b>	<b>The supernova remnant Puppis A</b>	
3.1	X-ray image of SNR Puppis A . . . . .	30
3.2	The 2010 epoch Chandra HRC-I image of RX J0822–4300 . . . . .	33
3.3	An enlargement of the immediate region of RX J0822–4300 . . . . .	38
3.4	The four positions of RX J0822–4300 measured over a baseline of 3886 days . . . . .	38
3.5	X-ray image and spectra of the western part of the Puppis A SNR . . . . .	39
3.6	EW images for O Ly $\alpha$ , Fe L, Ne He $\alpha$ , Mg He $\alpha$ , Si He $\alpha$ , and S He $\alpha$ . . . . .	40
3.7	The western part of Puppis A in H $\alpha$ + [NII], [SII], and [OIII] . . . . .	41
<b>4</b>	<b>Supernova remnant candidates in the ROSAT All-Sky Survey</b>	
4.1	Cumulative photon count profile for G337.2+13.0 and G38.7–1.4 . . . . .	46
4.2	XMM-Newton MOS1/2 exposure-corrected image of G309.8–2.5 . . . . .	50
4.3	RASS images of selected remnant candidates with radio contours . . . . .	51
4.4	RASS images of selected SNR candidates with infrared contours . . . . .	52
4.5	H $\alpha$ + [NII] and [SII] images of five SNR candidates . . . . .	54
4.6	The distribution of the RASS SNR candidates across the sky . . . . .	55
4.7	Radio image of SNR G38.7–1.4 . . . . .	57
4.8	XMM-Newton MOS1/2 exposure-corrected image and spectrum of G332.5+6.3 . . . . .	64
<b>5</b>	<b>Exploring the supernova remnant G308.4–1.4</b>	
5.1	ROSAT RASS image of G308.4–1.4 . . . . .	69
5.2	Chandra ACIS-I color image of G308.4–1.4 . . . . .	70

5.3	Spectrum and fitted model of the X-ray emission of the whole SNR G308.4–1.4 . . . . .	72
5.4	Spectrum and fitted model of the X-ray emission of G308.4–1.4 in various regions . . . . .	73
5.5	Dependence of the blackbody-emitting radius on the distance to the compact central object candidate in G308.4–1.4 . . . . .	75
5.6	Spectrum of the compact central object candidate in SNR G308.4–1.4 . . . . .	75
5.7	Flux variation of the compact central object candidate in the Chandra observation . . . . .	77
5.8	Gray-scale image of SNR G308.4–1.4 at 1.4 GHz and 2.5 GHz . . . . .	78
5.9	Chandra image of G308.4–1.4 overlaid with the ATCA data at 1.4 GHz . . . . .	79
5.10	WISE image of the region around G308.4–1.4 at 22 micron . . . . .	80
5.11	HI spectrum on- and off-source in the direction of SNR G308.4–1.4 . . . . .	83
<b>6</b>	<b>Supernova remnant G296.7–0.9 in X-rays</b>	
6.1	XMM-Newton MOS1/2 color image of G296.7–0.9 . . . . .	89
6.2	Spectrum of SNR G296.7–0.9 . . . . .	91
<b>7</b>	<b>A search for X-ray counterparts of radio pulsars</b>	
7.1	X-ray images of all radio pulsars with newly detected X-ray counterparts . . . . .	103
7.2	Radial intensity distribution around PSR J1112–6103 . . . . .	107
7.3	X-ray spectrum of PSR J1112–6103 . . . . .	107
7.4	Distribution of pulsars in a $P-\dot{P}$ diagram . . . . .	112
7.5	Spin-down luminosity plotted against the isotropic X-ray luminosity . . . . .	113
7.6	Comparison of the derived temperature and bolometric luminosity upper limits with minimal cooling models . . . . .	114
<b>8</b>	<b>Discussion and future prospects</b>	
8.1	Simulated occultation profile . . . . .	134

# List of Tables

<b>3</b>	<b>The supernova remnant Puppis A</b>	
3.1	Chandra observations of the neutron star in Puppis A . . . . .	31
3.2	Position, proper motion and angular distance of astrometric reference stars . . . . .	32
3.3	Properties of the astrometric reference stars . . . . .	32
3.4	Positions of RX J0822–4300 . . . . .	36
3.5	Spectral parameters for different regions in the western part of Puppis A . . . . .	40
<b>4</b>	<b>Supernova remnant candidates in the ROSAT All-Sky Survey</b>	
4.1	Summary of the used sky surveys and observatories . . . . .	47
4.2	Used archival pointed observations. . . . .	49
4.3	Spatial analysis of the candidates with archival pointed observations . . . . .	49
4.4	Results of the spectral analysis of selected SNR candidates. . . . .	49
4.5	List of identified SNR candidates . . . . .	60
<b>5</b>	<b>Exploring the supernova remnant G308.4–1.4</b>	
5.1	Detected sources around G308.4–1.4 . . . . .	71
5.2	Spectral parameters of the best-fit model for different parts of SNR G308.4–1.4. . . . .	73
5.3	Spectral fit results of the central compact object candidate in G308.4–1.4 . . . . .	76
5.4	Fundamental parameters of SNR G308.4–1.4. . . . .	86
<b>6</b>	<b>Supernova remnant G296.7–0.9 in X-rays</b>	
6.1	Detected X-ray sources in the region around G308.4–1.4 . . . . .	89
6.2	Spectral parameters of the best-fit models for SNR G296.7–0.9 . . . . .	91
<b>7</b>	<b>A search for X-ray counterparts of radio pulsars</b>	
7.1	Pulsar parameters of detected radio pulsars. . . . .	102
7.2	Spectral parameters of detected pulsars with more than 70 source counts . . . . .	104
7.3	Pulsar parameters of radio pulsars which have a counterpart in the X-ray band. . . . .	104
7.4	The pulsars with the lowest X-ray efficiency upper limit . . . . .	111
7.5	The pulsars with the lowest $3\sigma$ temperature upper limit . . . . .	116
<b>8</b>	<b>Discussion and future prospects</b>	
8.1	SNRs discovered in the ROSAT All-Sky Survey . . . . .	126

**A Supernova remnant candidates in the ROSAT All-Sky Survey**

A.1	Source catalogue of the SNR candidates. . . . .	135
A.2	Source catalogue of the SNR candidates. . . . .	136
B.1	List of all detected pulsars in X-rays and/or $\gamma$ -rays . . . . .	155
B.2	Used observations . . . . .	159
B.3	Pulsar parameters of radio pulsars which were not detected in the X-ray band . . .	170

# Chapter 1

## Introduction

The field of neutron star and supernova remnant research brings together all disciplines in physics. Here the length scales range from femtometers to parsecs and the density ranges from several times the nuclear density to 1 particle per  $\text{cm}^3$ , in the core of a neutron star and over the extend of a supernova remnant, respectively. Therefore, detailed knowledge of nuclear, particle and condensed matter physics are required for understanding the reactions and composition occurring in the interior of neutron stars and at the shock front of supernova remnants. Additionally, gravity must be considered, because masses of more than  $1 M_{\odot}$  interact within the small volume of neutron stars and supernova remnants.

The outline of this thesis is the following: Firstly, in the next section a short historical review of neutron star and supernova research is presented. Additionally, open questions in this field of research related to this work are discussed in this chapter together with possible solutions. Next, in Chapter 2 the scientific background on neutron stars and supernova remnants is summarized. This is then followed by the results of my work. In Chapter 3 the findings of the investigation of the proper motion of the neutron star in the SNR Puppis A and the western part of the SNR in the X-ray regime are presented. In Chapter 4 a search for supernova remnant candidates in the ROSAT All-Sky Survey is presented, in Chapter 5 the identification of SNR G308.4–1.4 as supernova remnant is shown and in Chapter 6 the exploration of SNR G296.7–0.9 in the X-ray regime is given. In Chapter 7 the outcome of a search for X-ray counterparts of radio pulsars is presented. Finally, this thesis is concluded with a discussion of all my results and an outlook.

### 1.1 Brief history

The existence of a star composed entirely of neutrons was first proposed by Baade and Zwicky (1934), motivated by the discovery of the neutron two years before by Chadwick (1932). In addition, Baade and Zwicky (1934) predicted that such a “neutron star” would be formed in a supernova (SN). Shortly after that, Tolman (1939) and Oppenheimer and Volkoff (1939) calculated the first models of neutron star structure based on Einsteins field equation. They could show that neutron stars are in a stable equilibrium with a density below nuclear density and have a radius on the order of 10 kilometers. However, observing these small bodies seemed beyond

any possibility at that time, because neutron stars have small emitting areas. Hence, their residual thermal luminosity would be too low to be observable at astronomical distances with the instruments available at that time (Shapiro and Teukolsky, 1983). Therefore, neutron star research was not paid much attention until the 1960s, when several discoveries were made that verified the existence and observability of neutron stars.

In 1962 the first Galactic X-ray source outside the solar system was detected by Giacconi et al. (1962). Several theorists proposed that this source, designated Sco X-1, could be a hot neutron star. Hence, they began investigating the thermal evolution of such an object (Shapiro and Teukolsky, 1983). The source was later identified as a low mass X-ray binary, a system composed of an X-ray emitting neutron star and an evolved star (van der Klis et al., 1996). However, in the early 1960s the idea of neutron stars as X-ray source was not taken seriously by astrophysicists. This picture changed soon after the first pulsating radio source was discovered by Hewish et al. (1968), which was later associated with a rapidly spinning neutron star (Pacini, 1968; Gold, 1968). Additionally, shortly before this detection, it was argued that a fast rotating and highly magnetized neutron star at the center of the Crab nebula might be its source of energy (Pacini, 1967), which was detected only one year later (Staelin and Reifenstein, 1968; Lyne and Graham-Smith, 2005). These discoveries initiate intensive theoretical work on their properties and large surveys in the radio regime to find more pulsating radio sources, i.e., pulsars. To date, more than 2250 pulsars are known (Manchester et al., 2005) and their number increased steadily in the past decades, because of large efforts in building even larger telescopes and more sensitive detectors. More than 185 of these objects were detected in the X-ray regime (see Table B.1), a number which has increased by an order of magnitude in the last 15 years with the increasing sensitivity of X-ray observatories.

Supernova and supernova remnant research started much earlier. For example, as early as in 185 A.D. a “guest star” was observed by Chinese astronomers (Green and Stephenson, 2003). As we know now it was a supernova and its remnant, supernova remnant (SNR) RCW 86, is still visible today (Williams et al., 2011). After that event only six other Galactic supernovae have been recorded in historical records in the past two thousand years - SN 386 (G11.2–0.3), SN 1006, SN 1181 (3C58), Crab SN, Tycho SN, and the Kepler SN. Several other records of “guest stars” by ancient Chinese astronomers exist. However, no solid identification with a known supernova remnant has been possible so far for most of them (Green and Stephenson, 2003). Furthermore, the first extragalactic supernova was observed on the 31st August 1885 (Müller et al., 1922) and was followed by large optical surveys to detect such time-variable sources. With the advances made in radio astronomy in the early 1950s, ten years before the first detection of a neutron star, various extended sources were detected within our Galaxy which had a non-thermal, power law shaped radio spectrum. These sources were proposed to be the remnants of undetected supernovae and their spectral shape was explained by synchrotron emission of relativistic charged particles (Reynolds, 2008, and references therein). This was first confirmed by the identification of the Crab nebula as an SNR and followed by the association of several of these extended radio sources with historical supernovae (Baade and Minkowski, 1954). Later, it was recognized by several authors (e.g., Blandford and Ostriker, 1978) that the acceleration of charged particles in SNRs may be the main source of cosmic rays (Reynolds, 2008). To date, more than 274 SNRs have been detected, most of them by their steep radio spectrum (Green, 2009).

## 1.2 Supernova remnants

Supernovae can occur in two ways, either by the thermonuclear disruption of a white dwarf or by the core-collapse of a massive star. The former case is also called SN of type Ia. It is assumed that the explosion occurs when a massive white dwarf accretes matter from a companion and the mass exceeds the Chandrasekhar mass limit. Here the explosion mechanism is reasonably well understood. Because in most cases the white dwarf explodes with the same physical conditions their light curves are very similar. Hence, SNe of type Ia can be used as distance indicators and Perlmutter et al. (1999) used them to confirm the detection of the accelerated expansion of the universe. Thus, understanding the processes responsible for an SN of type Ia is very crucial to put better constraints on cosmological parameters. However, it is still unclear in what kind of progenitor system such an SN can explode. No progenitor systems of thermonuclear SNe have been observed so far, because white dwarfs are faint sources and thus, white dwarfs are only observable in the solar neighborhood. Nevertheless, various progenitor systems have been proposed, which are more or less supported by observations of the remnants of these SNe type (see Section 2.1.1 for more details).

As mentioned in the first section, only 7 galactic SNe have been observed directly within the last 2000 years (Green and Stephenson, 2003). Additionally, the SN of the brightest SNR in the radio sky, Cassiopeia A, as well as the SN of the youngest Galactic SN (SNR G1.9+0.3; Reynolds et al., 2008) were missed by optical observers, probably due to visible-band interstellar dust extinction. The only SN observed with modern telescopes was the SN 1987A in the Large Magellanic Cloud. Therefore, the only way to study SNe in detail with a sufficiently large sample is by investigating their remnants, because SNRs are observable for up to  $10^5$  yrs (Frail et al., 1994) and let one draw conclusions on the underlying SN explosion mechanism.

However, a small sample size is also the main problem in investigating the remnants of thermonuclear SNe, because only four SNRs are known in our Galaxy for which clear evidence exists that their progenitor star exploded in an SN of type Ia. Furthermore, in the nearby dwarf galaxies Small and Large Magellanic Cloud (SMC and LMC) only 13 SNRs are identified as the remnants of an SN of type Ia (Reynolds, 2008). Thus, finding more SNRs which can be identified as the diffuse remnant of this kind of SN event is essential, because it will allow us to pinpoint the binary companion of most SN Ia. For that, an extensive study of and search for SNRs is needed to infer the type of SN and thus, increase the sample of remnants of SN Ia. For this reason an identification campaign of SNRs in the ROSAT All-Sky Survey (RASS) was performed based on the candidate list of Schaudel (2003). Moreover, deep spectro-imaging of a known (SNR G296.7–0.9; Section 6) and candidate (RASS SNR candidate G308–1.4; Section 5) was performed to reveal their nature.

The second case in which a star can end its evolution is by the collapse of the iron core of a massive star. Here the process is reasonably well understood with the exception of the final explosion mechanism. Several models have been proposed for this last stage. In order to understand the mechanism in more detail various observational methods have been proposed. For example, the proper motion of a neutron star (NS) can be investigated, because it depends on the kick a neutron star gains in the SN where they are formed. Therefore, the proper motion strongly depends on the final explosion mechanism. The proper motion measurement of the neutron star

RX J0822–4300 in Puppis A by Hui and Becker (2006) and Winkler and Petre (2007) can be hard to explain with these explosion models (see Section 2.1.2 for more details). In order to reduce the error bars of and the discrepancy between these two measurements a new X-ray observation was analyzed (see Chapter 3.3.1). With this additional data it will be possible to validate current core-collapse SN models or challenge them even further.

Another motivation to examine the X-ray emission of SNRs is to understand the formation of stars, because SNe feed the interstellar medium with energy and enrich it with heavy elements like Iron. The first stars were metal-poor. The elemental abundance measured in the solar system indicates an SN explosion as trigger for the formation of the sun and the planets (Gritschneider et al., 2012). Hence, increasing our knowledge of the interaction of the diffuse remnant of an SN with its environment is crucial to understand the formation of the solar system.

Furthermore, SNR shocks are collisionless plasmas<sup>1</sup>, which are not yet well understood (Vink, 2006), but are thought to be excellent particle accelerators (Reynolds, 2008). Thus investigating and understanding the origin of the thermal and non-thermal part of their spectrum can help to explain the interaction of a shock wave with the tenuous interstellar medium (ISM) and to confirm that SNRs are responsible for the Galactic contribution to the measured cosmic ray spectrum (Reynolds, 2008). Both emission mechanisms will be explained in Section 2.2.3.

Finally, current estimates for the Galactic SN rate are given by various approaches and yield rate estimates between 0.8 and 2.8 SNe per century (see Section 2.1.3). Furthermore, Keane and Kramer (2008) showed that the NS birth rate exceeds the SN rate, which would indicate that the Galactic SN rate currently found in the literature is on the upper side of the range. Therefore, assuming this is true and using an average SNR life time of  $\approx 60$  kyrs (Frail et al., 1994), more than 1000 SNRs can be found in the Galaxy. By 2009, 274 known SNRs were published (Green, 2009, and references therein). Thus, a large number of SNRs are not detected so far, mostly due to difficulties in finding very faint objects. Some remnants will never be observable, because they are hidden behind dust, in particular remnants located behind the Galactic Center will never be seen from Earth. Most SNRs were detected in the radio band, but this sample is biased towards selecting mainly large remnants at low galactic latitude (Green, 2004). Only three SNRs of the 274 remnants listed in Green (2009) have a diameter of  $< 3'$  and five supernova remnants are at a galactic attitude  $|b| > 7^\circ$ . Hence, various attempts have been made to search for SNRs in other wavelengths, e.g., Sabin et al. (2013) in an optical  $H_\alpha$  survey and Helfand et al. (2006) in the infrared regime. What is more, Bußer (1998) and Schaudel (2003) made use of the first imaging all-sky survey in the soft X-ray regime, the ROSAT All-Sky Survey (RASS) and pinpointed several SNR candidates. In Chapter 4 the candidate list of Schaudel (2003) will be used and the candidates will be cross-correlated with current catalogues in various wavelengths to identify their origin and to reduce the discrepancy between the number of expected and already identified remnants.

---

<sup>1</sup>The interstellar medium has such a low density ( $\approx 1 \text{ cm}^{-3}$ ) that two-body interactions are rare, hence SNR shocks are called collisionless

## 1.3 Neutron stars and pulsars

Neutron stars are the most dense objects directly observable in the universe. Their density can reach values of more than 10 times the nuclear density. The main goal in this field of research is to explore the composition of matter at a density two times above the nuclear density, where the composition of a neutron star is no longer constrained by theoretical modeling of nuclear matter and particle physics experiments: Is the neutron star core composed out of normal nucleon matter or is “exotic” matter needed to explain observations? One way to address this question is to study the mass-radius relation, which depends strongly on the assumed equation of state and the composition of the neutron star core. However, no radius has been measured with high-accuracy and more importantly, no radius has been inferred for any NS with a very accurate mass measurement. Hence, only weak restrictions can be put on matter at high densities. Another very promising approach is the investigation of the thermal evolution (cooling) of neutron stars, which is heavily affected by the behavior of matter at high densities (see Section 2.3.1 for more detail on the composition and cooling of a neutron star).

For constraining the equation of state through the investigation of the cooling of neutron stars the temperature and the age of a large sample of neutron stars is needed. Even upper limits on the thermal emissivity can help to put more significant constraints on cooling models and the assumptions made in them. However, only a few neutron stars are known with measured temperatures and they have large uncertainties, both in age and bolometric luminosity. Furthermore, only for a few pulsars deep upper limits on the temperature have been obtained. Therefore, it is important to increase the sample of known thermal-emitting neutron stars and in the case of a non-detection of thermal emission from a neutron star to infer upper limits on the temperature. In Chapter 7 this was done by using the archives of the X-ray observatories XMM-Newton and Chandra. Here the minimal cooling paradigm was further tested by searching for neutron stars whose temperature deviates from the predicted cooling curve.

In recent years a lot of progress has been made in identifying the non-thermal high energy emission mechanism of pulsars (see 2.3.2 for more details on the proposed high energy emission mechanisms and the advances made in recent years). However, it is still not fully understood which physical processes are responsible for the single-particle emission of pulsars at high energies. A more detailed study will be possible in the future with the ongoing search for pulsars with the Fermi satellite. Furthermore, studying the high energy emission properties in other wavelengths will be of importance. For example, studying the dependence of the emitted energy in one wavelength regime on the total emitted power, as done in Chapter 7, can help to understand the high energy emission even further, because the scatter has to be reproduced by a simulated pulsar population for which a certain high energy emission model was assumed

Furthermore, neutron stars manifest themselves in a number of different ways: rotation-powered pulsars, magnetars, central compact objects in SNRs, rotating radio transients, X-ray dim isolated neutron stars, and the recently discovered intermittent pulsars (reviews of the different classes of neutron stars can be found in Becker (2009), Hurley (2009), de Luca (2008), McLaughlin (2009), Turolla (2009), and Lyne (2009), respectively). The fact that the NS birth rate exceeds the SN rate (Keane and Kramer, 2008) could also be a hint that there is an evolution of the type of NSs with time. It might be that, for example, rotation-powered pulsars, rotating

radio transients and X-ray dim isolated neutron stars are different manifestations of the same type of neutron star (Keane and Kramer, 2008). However, it still needs to be proven whether such an evolution exists in nature and even if it exists it is still not clear what physical parameters are necessary so that a neutron star is born or evolves in one of these classes. Also how core collapse SNe influence the birth properties of neutron stars, e.g., the magnetic field strength of the compact remnant, needs to be elucidated.

To sum up, although about 185 pulsars are detected in the X-ray band and more than 274 SNRs are known so far, it is clear from what has been said above that it is important to continue the search for so far undetected neutron stars and SNRs. Nonetheless, probably the best reason is studying the unknown, because every new detection might contribute new insights in neutron star and supernova remnant science. For example, a newly detected source might be the missing link to explain which properties are responsible for the different manifestation of neutron stars. The success of such an ongoing search can be demonstrated in the case of SNR G1.9+0.3, the youngest SNR in our Galaxy which was found by Chandra (Reynolds et al. 2008), or the detection of intermittent pulsars (e.g., Kramer et al., 2006), which seem like ordinary radio and X-ray pulsars, but can switch their radio emission off quasi-periodically with different spin-down rates at time scales from months to years. The continuation of the search for X-ray pulsars and SNRs, as done for this thesis, will therefore be of uttermost importance to discover previously unknown phenomena in this field of research.

## Chapter 2

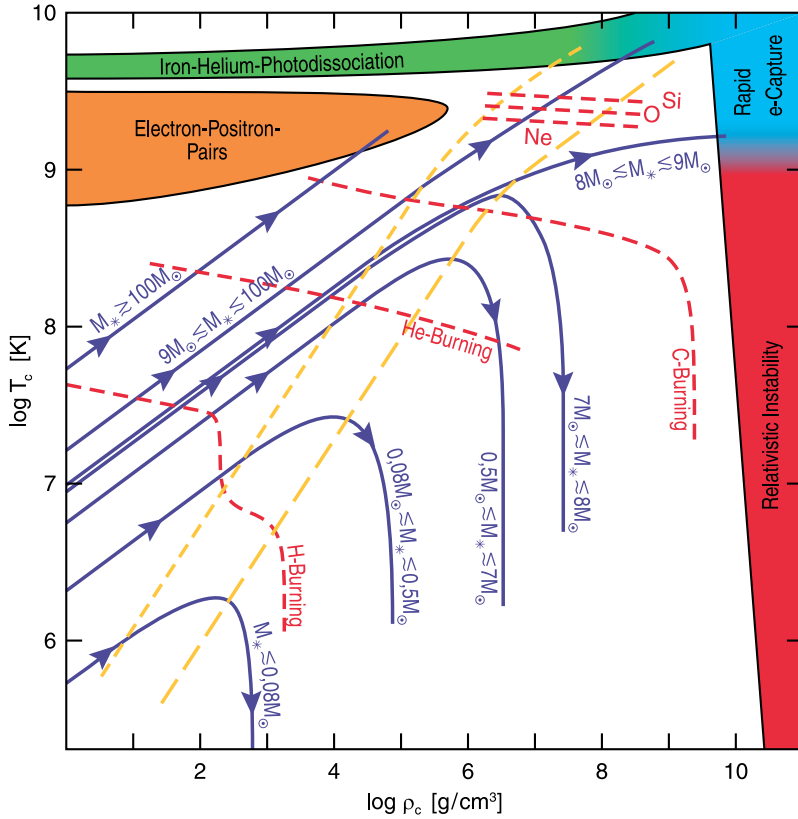
# Scientific background

A star is born, undergoes different periods of evolutionary states and has to die at the end. Its ashes enriches the environment and helps to create new stars. This work focuses on the end states of massive stars, more precisely on the X-ray emission properties of neutron stars (NSs) and supernova remnants (SNRs). In the following, the life and death of stars will be outlined briefly. In the Sections 2.2 and Section 2.3 our knowledge about formation, properties and evolution of NSs and SNRs will be described in detail.

Stars are formed in dense gas or dust clouds in the ISM. For example, in our Galaxy star formation takes place mainly in the spiral arms. These clouds are stable as long as their internal pressure compensates the gravitational force. When two clouds are merging or an external force is acting on the cloud (e.g., occurrence of a close-by supernova explosion) the cloud collapses and fragments into smaller units. During the collapse the fragmented cloud is heated up to  $(5 - 10) \times 10^3$  K where it reaches a thermostatic equilibrium and becomes optically thick. When the temperature of the cloud is high enough to stop matter from falling into the central region, the star reaches hydrostatic equilibrium. This collapse takes about  $10^5 - 10^6$  yrs for a star with  $1 M_{\odot}$ . After the star reaches the so-called Hayashi line the gravitational energy produced by the still ongoing contraction of the inner region of the star will be carried to the envelope by convection or radiation for low-mass or high-mass stars, respectively. The contraction remains until the core temperature of the protostar is high enough to start the first thermonuclear reaction - burning the less abundant Deuterium. Finally the so-called protostar reaches the zero age main sequence (ZAMS), where all stars with a mass larger than  $0.08 M_{\odot}$  start burning their Hydrogen (H) core.

From now on, in general the evolution of stars is the following: The star burns the most abundant elements in its core until it is almost depleted there, first H, Helium (He) until Nickel (Ni) is burned to Iron (Fe). After about 99% of the nuclei at the center are fused to heavier elements the burning stops and starts in an outer shell. Before that, at the time when about 95% of the central fuel is burned the core contracts until the central temperature is high enough to start the fusion of the next heavier element in the core, because until that reaction starts the gravitation is not balanced by radiation pressure. Additionally, the envelope expands and cools down. These steps are repeated with small variation and smaller timescales until the core is entirely made up

**Figure 2.1:** Stellar evolution of stars on the basis of their core density  $\rho_c$  and temperature  $T_c$  for different  $M_{ZAMS}$  in blue. The red lines show the critical temperature for different burning stages and the colored region indicate the stages where the stars get unstable and undergo a gravitative collapse. (Figure taken from Janka (2012))



of Fe, the element with the highest nuclear binding energy per nucleon and thus, further fusion is energetically unfavorable. Exceptions of this are stars with a mass at the zero age main sequence  $M_{ZAMS}$  of less than  $9 M_{\odot}$ . Here the collapse of the central region is stopped by the Fermi pressure of degenerated electrons before the critical temperature for fusion of He ( $0.08 M_{\odot} \lesssim M_{ZAMS} \lesssim 0.5 M_{\odot}$ ), Carbon ( $0.5 M_{\odot} \lesssim M_{ZAMS} \lesssim 7 M_{\odot}$ ) or Neon ( $7 M_{\odot} \lesssim M_{ZAMS} \lesssim 8 M_{\odot}$ ) is reached (see Figure 2.1). In these cases the remaining star is called a white dwarf (WD) and is the final state with a typical mass of  $\sim 0.6 M_{\odot}$ , a maximal mass of  $1.4 M_{\odot}$  (the Chandrasekhar limit for non rotating WD), and a radius of  $\sim 10^4$  km. Thereafter the white dwarf cools down, if no mass transfer from a companion occurs (see Section 2.1.1).

The core temperature and density of stars in the mass range  $8 M_{\odot} \lesssim M_{ZAMS} \lesssim 9 M_{\odot}$  is high enough that atoms capture electrons before the neon burning temperature is reached and emit neutrinos, which leave the star instantaneously. This leads to a sudden decrease in pressure (see Figure 2.1). Finally, this ends the life of such a star in a core-collapse supernova (SN). For stars with  $M_{ZAMS} \gtrsim 9 M_{\odot}$  a similar process happens after Neon, Oxygen and Silicon is burned and the core is composed entirely of  $^{56}\text{Fe}$ . At this stage the temperature in the core is high enough to photodisintegrate Iron into Helium nuclei and the subsequently emitted neutrinos cause an instantaneous loss of pressure and a core-collapse SN (see Figure 2.1). Stars with  $M \gtrsim 100 M_{\odot}$  are even hotter and become unstable because of electron-positron pair creation after the central C burning (Woosley et al., 2002), but also explode in a core-collapse SN. All these SNe are defined as SN of type Ib, Ic or II, depending on the existence or lack of H, He and Si lines

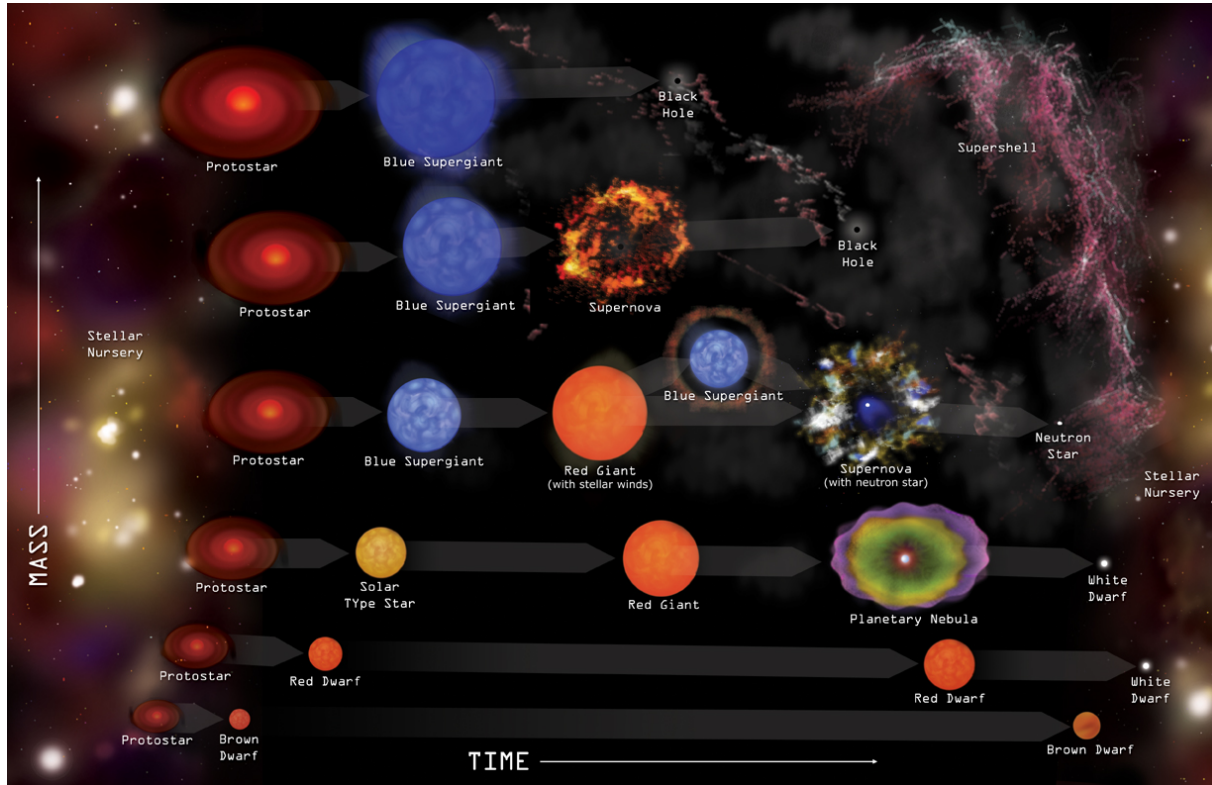


**Figure 2.2:** Stellar evolution of stars with different masses The evolution shown here starts at the zero age main sequence and ends with their final state as white dwarf, neutron star or black hole. (Image courtesy: NASA CXC Photo album)

in their early spectra (Vink, 2012). The current theoretical understanding of SNe is summarized in Section 2.1 and the evolutionary track for various masses, as discussed above, are depicted in Figure 2.2.

Stars lose mass during their evolution due to stellar winds. Thus, their  $M_{ZAMS}$  is larger than the mass at their death. For massive stars these winds are driven by radiation with mass loss rates  $\dot{M} \lesssim 10^4 M_{\odot}/\text{yr}$  (van Loon et al., 2005) that sum up to 50% mass loss in their entire life. During the He burning in the core or in the shell (at the asymptotic giant branch)  $\dot{M} \lesssim 10^6 M_{\odot}/\text{yr}$ , e.g., a  $5 M_{\odot}$  star can lose up to 80% of its mass by winds. These matter outflows are especially important when investigating SNRs, because the SN shock wave is sweeping up this matter and is responsible for the shape and size of the remnant (see below).

Furthermore, about 80% of all stars are in systems with one or more companions and therefore, the WD stadium does not have to be the death of a star. If a carbon-oxygen WD has a mass close to the Chandrasekhar limit and accretes mass from a binary star it explodes in a thermonuclear runaway (SN of type Ia). The current understanding of thermonuclear SNe will be discussed in Section 2.1 as far as it is relevant for this work.

## 2.1 Modeling supernova explosions

As mentioned above there are in general two different mechanisms that lead to the explosion of an SN: The thermonuclear explosion of C/O WD (SN type Ia) and the core-collapse of an evolved star (SN types Ib, Ic, II). In the following the current understanding of the explosion mechanisms are summarized including current estimates of their rates.

### 2.1.1 Thermonuclear supernovae

In a thermonuclear SNe the energy comes from explosive nuclear burning rather than from the released energy of the gravitational collapse in a core-collapse SN. Hence, it is called a thermonuclear SN. It is assumed that the explosion occurs when a massive WD accretes matter from a companion and the mass exceeds the Chandrasekhar mass limit.<sup>1</sup> Thus, almost all progenitors of SNe Ia must have similar evolution tracks with only some small variations in the peak brightness of the explosion and they can occur in almost all stellar environments, because WD can be found in young and old stellar populations. These conclusions are observationally confirmed: 85% of all SN Ia have very similar peak luminosities, light curves, and spectra. Moreover, SN Ia are also observed in elliptical galaxies, which are thought to be old and have very little star formation (Hakobyan et al., 2011). In the case of core-collapse SN almost all events are observed in spiral galaxies (Hakobyan et al., 2011). In addition, the amount of energy produced in the conversion of  $1.4 M_{\odot}$  of C,O into Fe is in the same order as the observed energy of an SN Ia explosion of  $\sim 10^{51}$  erg (Thielemann et al., 2004). Because their light curves are very similar these SNe can be used as distance indicators.<sup>2</sup> This finding led to the detection of the accelerated expansion of the universe (Perlmutter et al., 1999).

Currently, the models that explain the measured properties of an SN Ia are the deflagration-detonation transitions models (see Hillebrandt and Niemeyer (2000) for a review). In these models the WD ignites near the center; in the beginning the convective thermonuclear wave moves through the star subsonically (deflagration) and the star is expanding. At a certain point the remaining star detonates and the nuclei are mostly fused to intermediate mass elements, e.g., Silicon (Vink, 2012). This completely disrupts the WD and no compact remnant is left behind.

The deflagration-detonation transition model is reasonably well supported by observations, because it can very accurately reproduce SN Ia spectra and light curves which are dominated by the radioactive decay of  $^{56}\text{Ni}$  into  $^{56}\text{Co}$  and finally into  $^{56}\text{Fe}$ . Additionally, the resulting nucleosynthesis abundances with respect to the solar values are in good agreement with observations (Hillebrandt and Niemeyer, 2000, and references therein).

However, it is still unclear in what kind of progenitor system an SN Ia can explode, because WD are faint sources and thus, no progenitor system of an SN Ia has been observed so far. As mentioned before, a WD must accrete matter in a close binary system. But this still allows several possibilities for the mass donor star: A second WD (double degenerate system) or a

<sup>1</sup>Models with sub-Chandrasekhar masses for the WD have problems explaining observations but could be responsible for low luminosity SN Ia (Hillebrandt and Niemeyer, 2000)

<sup>2</sup>An empirical relation has been found by Phillips (1993), which relates the peak brightness of an SN event with its post peak decline time, which allows a calibration of the peak brightness.

single degenerate system with either a main sequence or an evolved star. To accrete matter onto the WD it is crucial that the mass transfer rate is in a certain range, because a higher rate would lead to a common envelope phase which results in an unstable mass transfer and a lower rate would lead to novae in which accreted matter is blown off the WD. Various channels that lead to type Ia SNe are reviewed in Wang and Han (2012). An example for a stable mass transfer is given by Hachisu et al. (1999). They could demonstrate that a WD that undergoes rapid mass accretion can produce a thermonuclear SN, if it is stabilized by a strong, optically thick wind.

With the advances made in X-ray spectroscopy it is now possible to identify SNRs of SN Ia in our Galaxy or the close-by dwarf galaxies (SMC and LMC) at different stages of their evolution (a summary table of known SNR of SN Ia is given in Vink (2012)). The basic criteria to distinguish between the SNR of a thermonuclear or core-collapse SN is the asymmetry of the remnant (Lopez et al., 2009), the existence of a neutron star associated with the SNR and the yield of the most abundant elements in the spectrum of the SNR. Furthermore, with the detection of light echoes of historical SNRs, e.g., the Tycho SNR of the SN observed in the year 1572, a clear evidence for the type of the SN has been found, because these light echoes preserve some of the spectra of the SN and it can be restored with difference imaging in the optical wavelength regime (Krause et al., 2008; Rest et al., 2005, 2008).

As aforesaid, stars lose some of their mass at several stages during their life time: at the main sequence, as red giant, at the asymptotic giant branch or from a WD itself (van Loon et al., 2005; Kato, 1997). The companion candidates can have very different wind properties which shape their circumstellar medium (CSM) and leave imprints in it. By studying the CSM and its interaction with a remnant of an SN Ia it is therefore possible to rule out some progenitor systems. Many optically observed remnants have so-called Balmer-dominated shocks that are only observable if the fraction of neutral gas is high (Heng, 2010). Hence, a companion which ionizes its surrounding can be excluded. Such sources are the so-called supersoft sources.<sup>3</sup> White dwarfs can be observed as supersoft sources, if they accrete hydrogen-rich matter onto their surface and burn it there (Kahabka and van den Heuvel, 1997). In addition, investigation of the X-ray spectra of various SNRs by Badenes et al. (2007) and Borkowski et al. (2006) led to the rejection of the model of Hachisu et al. (1999) which was mentioned above, because no signs for the large winds predicted by this model were found in these remnants. Furthermore, a detailed examination of the Kepler SNR led to the conclusion that the progenitor system was composed of a C/O WD with a star located at the asymptotic giant branch (Chiotellis et al., 2012). Nevertheless, it is not clear whether the Kepler SN was a very particular event or the prototype of an SN Ia, because of the unusual morphology of the SNR.

### 2.1.2 Core-collapse supernovae

As explained in the first section of this chapter a star with a mass  $M_{\text{ZAMS}} \gtrsim 8 M_{\odot}$  ends its life in a core-collapse SN. The gravitative collapse releases an energy of the order of  $10^{53}$  erg and is finally stopped when the core density reaches nuclear density. At this density a proto-neutron star

---

<sup>3</sup>Supersoft sources are identified by their very soft X-ray spectra and their high luminosities, which range from  $10^{36}$  to  $10^{38}$  ergs<sup>-1</sup>.

or for the most massive stars ( $M_{\text{ZAMS}} \gtrsim 25 M_{\odot}$ ) a black hole is formed (Janka, 2012). Only  $\sim 1\%$  of the gravitational energy is used for the explosion, the remaining 99% leave the star in the form of neutrinos, which only interact with neutron star matter in the first 10 s when the proto-neutron star is still very hot and dense (Mazure and Basa, 2009). 13 neutrinos from SN 1987A in the LMC (Hirata et al., 1987; Bionta et al., 1987), the closest SN observed with modern telescopes support this theoretical prediction.

According to theory, matter from the outer stellar layers are pulled inward, bounce back from the proto-neutron star and create a radially propagating shock wave after the collapse in the center has stopped. However, in numerical simulations this shock wave is stopped by the outer layers and cannot produce the observed SN. How a massive star finally explodes is still an open question and a field of intense research. Several mechanisms have been proposed by which a massive star explodes in a core-collapse SN. A good review on the current status of modeling core-collapse SN can be found in Janka (2012). In the following the most promising models and how they can be tested by current instruments are summarized.

A mechanism that is studied in detail is the neutrino heating. Here the main idea is that energy is deposited in an accretion layer at a radius close to the proto-neutron star by absorption of neutrinos leaving the proto-neutron star. This leads to a global runaway instability that finally triggers the SN. For example, this assumption was implemented by Blondin et al. (2003) in the so-called non-spherically symmetric standing accretion shock model. It can explain neutron star kicks with velocities up to 1000 km/s (Wongwathanarat et al., 2013, and will be discussed below in more detail), the asymmetries in the SNRs mentioned in Section 2.1.1 and the high-velocity clumps of inner-core elements in the outer layers of the exploding star, as seen in the SN 1987A (Hammer et al., 2010). Furthermore, simulations show that in this framework spin periods between 100 ms and several seconds can be achieved (Wongwathanarat et al., 2013) and, if rotation of the collapsing core is assumed, even the estimated NS spin periods at birth of  $\sim 10$  ms may be reachable (Ott et al., 2006). However, the observed spin-kick alignment is not reproducible in any simulation so far and the maximal explosion energy and Nickel mass obtained in this model is less than  $\sim 2 \times 10^{51}$  erg and below  $0.1 M_{\odot}$ , much less than observed in high luminosity SNe (Janka, 2012).

Other mechanisms, which can successfully explode a star are the magnetohydrodynamic and the acoustic mechanism. The former is based on the assumption that compressional amplification of the non-radial magnetic field strength during collapse and secondary amplifications lead to the explosive runaway (Wheeler et al., 2002) that can explain the observed population of high luminosity SNe. The acoustic mechanism is based on a secondary shock which is initiated by gravity-mode oscillations of the proto-neutron star core with amplitudes on the order of kilometers that finally leads to a disruption (Burrows et al., 2006).

For core-collapse SNe it is more difficult to compare simulated light curves and spectra with observations, because of the diversity of observed SNe. However, there are some diagnostics. As mentioned before the most abundant elements in type I SNe are intermediate mass elements. In contrast, yields in core-collapse SNe are dominated by the elements produced in the stellar burning phases, e.g., Carbon, Oxygen. Thus, element yields in simulations have to match the abundances measured for a core-collapse SN.

To date, other validation of core-collapse SN models can come from studying Oxygen-rich

SNR or the youngest near-by core-collapse SN 1987A (details are given in Vink (2012) and references therein). Another way to rule out unrealistic core-collapse SN models is by investigating the proper motion of neutron stars. The average proper motion in three dimensions of non-recycled NSs are  $\sim 400 \text{ km s}^{-1}$  (Hobbs et al., 2005), which cannot be explained by a binary breakup (Janka, 2012). Additionally, a turbulent transfer of momentum between proto-neutron star and shock shortly after the onset of the SN explosion can be ruled out, because the maximal velocity of an NS in this case is  $\sim 200 \text{ km s}^{-1}$  (Janka and Mueller, 1994). For electro-magnetically driven kicks, where the NS is accelerated along its spin axis by radiation from an off-centered rotating magnetic dipole a proper motion of  $1000 \text{ km s}^{-1}$  can be achieved (Lai, 2001). However, it requires a period of the NS of  $\sim$  milliseconds (Lai, 2001), which is not observed in young NSs. In the framework of the neutrino-magnetic field driven kick model it is assumed that a large magnetic field introduces an asymmetry in the neutrino emission (Lai, 2001). This model can only explain velocities of the order of  $250 \text{ km s}^{-1}$  when a magnetic field greater than  $10^{15} \text{ G}$  is assumed (Lai et al., 2001). However, this magnetic field strength is much higher than the measured values for most NSs. Another kick mechanism relies on anisotropic neutrino emission, which could in general accelerate the NS to velocities of  $\sim 300 \text{ km s}^{-1}$ , if the neutrino emissivity is stable. This is not the case and the maximal effect on the velocity is on the order of  $10 \text{ km s}^{-1}$  (Janka, 2012, and references therein).

A more realistic calculation was presented by Burrows et al. (2007) where they assume that the NS kick is produced by strong anisotropic winds. Their model prediction for the NS kick velocity  $v_k$  is

$$v_k \sim 1000 \frac{E}{10^{51} \text{ erg}} \cdot \sin(\alpha) \text{ km s}^{-1}, \quad (2.1)$$

with the explosion energy  $E$  in erg,  $\alpha$  a parameterization of the explosion anisotropy. Here it was assumed that the wind speed can be approximated by the sound speed. In this model measured proper motions of  $\sim 1000 \text{ km s}^{-1}$  can be explained with a large anisotropy in the explosion.

Furthermore, Wongwathanarat et al. (2013) shows that the kick is introduced by a long-lasting, anisotropic gravitational pull on the NS and the velocity is given in the following form:

$$v_k \sim 540 \frac{\Delta_{-3}}{r_{i,7} \cdot v_{s,5000}} \text{ km s}^{-1}, \quad (2.2)$$

where  $\Delta_{-3}$  is a mass defect in units of  $10^{-3} M_\odot$  that is moving with a velocity  $v_{s,5000}$  in units of  $5000 \text{ km s}^{-1}$  away from the NS with an initial radius of  $r_{i,7}$  in units of  $10^7 \text{ cm}$ . Thus, a slowly moving shell with  $v_s \approx 3000 \text{ km s}^{-1}$  can accelerate the NS to a velocity of  $\approx 900 \text{ km s}^{-1}$ .

### 2.1.3 Supernova rates

Current estimates for the SN rate are given by various approaches and yield following rate estimates:

- Using the observed SN rate in Milky Way like nearby spiral galaxies (Sbc galaxies) and scale it to the size of the Milky Way results in an SN rate  $\beta_{\text{SN}}$  of  $2.8 \pm 0.6 \text{ century}^{-1}$

with a systematic error of factor 2 (Li et al., 2011). For core-collapse SN they calculated  $\beta_{\text{CC}} = 2.3 \pm 0.5 \text{ century}^{-1}$ .

- Measuring the abundance of the radioactive element  $^{26}\text{Al}$  from massive stars in our Galaxy (Diehl et al., 2006) leads to  $\beta_{\text{CC}} = 1.9 \pm 1.1 \text{ century}^{-1}$ .
- Keane and Kramer (2008) found  $\beta_{\text{CC}} = 1.1 \pm 0.9$  and  $\beta_{\text{CC}} = 0.8 \pm 0.4$  depending on the used initial mass function<sup>4</sup>. They also showed that the NS birth rate exceeds the SN rate and therefore, it is possible that their Galactic SN rate is too low.

## 2.2 Supernova remnants

In the following sections, first the classification scheme of SNRs will be described and then the current understanding of the evolution and the high energy emission mechanisms will be summarized, in which the latter is crucial for the identification as SNR and inferring fundamental parameters of the SNR.

### 2.2.1 Classification

For only a few SNRs a clear distinction can be made between their parent SN, core-collapse or thermonuclear. Therefore, in literature SNRs are grouped by their morphology into shell-type SNRs, plerions, composite and thermal-composite SNRs (see Figure 2.3 for examples of the different morphologies). A shell-like structure is created when the shock wave propagates through the ISM and heats the plasma. Hence, an SNR that shows such a structure is named shell-type SNR and this group includes most know remnants. A plerion is a non-thermal wind of relativistic electrons and positrons, accelerated to ultra-relativistic energies by a rapidly rotating neutron star (pulsar), also referred to as pulsar wind nebula (PWN; see Kargaltsev et al. (2013) for a review and a listing of known PWN). Remnants with a PWN surrounded by a shell are designated as composite SNRs, but only a few of this kind have been detected so far. The thermal-composite SNRs show a shell-like structure in the radio band and thermal X-ray emission from the center of the remnant.

### 2.2.2 Evolutionary states

The evolution of SNRs is divided into four states (Woltjer, 1972), where  $M_{\text{ej}}$  is the mass ejected with a velocity  $V_0$  and total energy  $\varepsilon$ ,  $M_{\text{sw}} = 4\pi\rho_0 R^3/3$  the swept-up mass with  $R$  the radius of the shock front,  $\rho_0$  the density of the ISM and  $d\varepsilon/dt_{\text{rad}}$  the energy loss per time:

**Phase I: Ejecta dominated phase**  $M_{\text{ej}} \gg M_{\text{sw}}$ . The ejecta, with a characteristic initial explosion velocity of  $5 \times 10^3 \text{ km/s}$  (core-collapse SN) to  $10 \times 10^3 \text{ km/s}$  (thermonuclear SN; Reynolds, 2008), forms a blast wave. The matter behind it is expanding almost free and

<sup>4</sup>The initial mass function is the probability distribution that a star at the zero age main sequence has an initial mass in the range of  $m + dm$ .

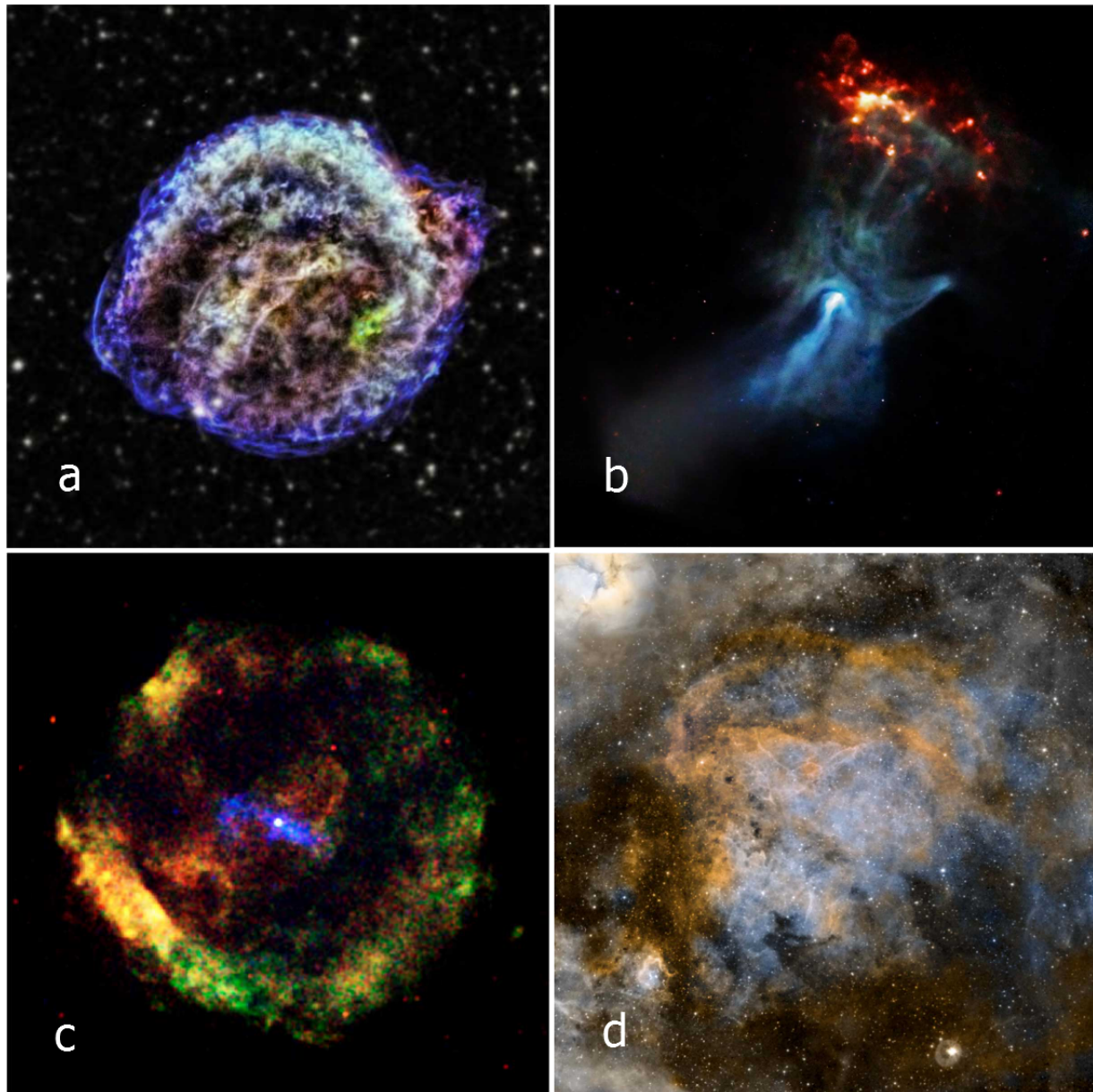


**Figure 2.3:** The classification of SNRs by means of their morphology. *Upper left:* The Kepler SNR (SN 1604) is a shell-type SNR with a size of  $3'$  (Burkey et al., 2013). *Upper right:* Here the plerion or PWN around PSR B1509–58 is shown. *Lower left:* The SN from 386 A.D. (SNR G11.2–0.3) consists of a shell and a PWN, thus it belongs to the group of composite SNR (Roberts et al., 2003). *Lower right:* The remnant W28 is an example for a thermal-composite SNR. All images are false-color images with red indicating a low energy, green a medium energy and blue a high energy. In the case of *d* the optical image is overlaid in gray and the radio image in orange. (Image courtesy: NASA CXC Photo album)

is therefore cooling down adiabatically. Later, it is reheated by the reverse shock. A contact discontinuity is formed between the shock-heated ISM or CSM and the ejected matter. This two-shock structure exists until  $M_{\text{ej}} \approx M_{\text{sw}}$ . At this point all ejecta are shocked and the SNR will reach the next phase. Phase I lasts for hundreds to thousand years depending on the density of the ambient medium and on the ejected mass (Truelove and McKee, 1999). The shock wave radius  $R$  in this phase can be approximated by  $R \propto t^m$  (Chevalier, 1982), with  $t$  the age of the remnant and  $m = (n - 3)/(n - s)$  the so-called deceleration parameter.  $m$  can be measured by comparing the SNR radius of two or more epochs and shed light on the medium surrounding the SNR indicated by  $n$  and the type of SNR itself ( $s$ ). It is expected that  $n = 10 - 12$  for core-collapse SNe and  $n = 7$  for thermonuclear SN. Furthermore,  $s = 0$  for a constant medium around the SNR and  $s = 2$  for a medium shaped by the progenitor's stellar wind (Patnaude and Fesen, 2009). For example, the core-collapse SN 1993J has  $m = 0.845 \pm 0.005$  (Marcaide et al., 2009) in agreement with  $n = 9$  for a core-collapse SN and  $s = 2$  for a circumstellar wind. In the case of the young SNR Cassiopeia A  $m = 0.65 \pm 0.02$  (Patnaude and Fesen, 2009), indicating a remnant between phase I and II (see below) and  $s = 2$ . Thus, studying the expansion or the proper motion of filaments of young remnants provides an insight into the ambient medium and the SN itself.

**Phase II: Sedov phase**  $M_{\text{ej}} \ll M_{\text{sw}}$  and  $\int d\varepsilon/dt_{\text{rad}}dt \ll \varepsilon$ . After several times the ejected mass has been swept up, the evolution can be estimated by the Sedov self-similar solution (Sedov, 1959). Here it is assumed that the explosion is adiabatic, evolves in a uniform medium with homogeneous density and radiative losses are negligible. The radius can be expressed as  $R \propto t^{2/(5-s)}$  (Culhane, 1977; Vink, 2012). Thus  $m = 2/5$  for  $s = 0$  and if a remnant is crossing from phase I to II it should have a deceleration parameter close to 0.4 and  $2/3$ , depending on the ambient medium as seen in Cassiopeia A. In the Sedov formalism various fundamental parameters of the SNR can be estimated, like expansion velocity, age of the remnant and distance (see set of equations in Section 5.5 and Section 6.3.2). This phase lasts for up to tens of thousand of years, depending on the initial explosion energy and the density of the ISM/CSM (Blondin et al., 1998).

**Phase III: Momentum conservation phase** At a certain time in the evolution of an SNR the cooling time of the shock-heated plasma is less than the age of the remnant and radiative losses cannot be neglected any more. This is due to fast cooling of matter located behind the shock front, e.g., oxygen line emission (Vink, 2012). The evolution of the system is then dominated by momentum conservation instead of energy conservation; pressure forces can be neglected. At the transition between Phase II and III the post-shock temperature is about  $10^5$  K, the expansion velocity is less than 200 km/s and the deceleration parameter  $m \approx 1/4$  (Vink, 2012).

**Phase IV: Merging phase** When the shock velocity becomes comparable to the random motions of the ISM ( $\approx 10$  km/s) and the temperature behind the shock is close to the temperature of the ISM the remnant merges with the ISM.

These discrete phases are an oversimplification and in reality an SNR cannot always be so easily assign a phase. Furthermore, different parts of an SNR may have swept up different

amounts of mass due to inhomogeneities in the surrounding medium and the explosion itself. Therefore, it seems that some regions of the remnant may be in different phases, even though all regions have the same age. For example, the SNR RCS 86, the probable remnant of the SN in 185 A.D., has an emission region in the southwest that seems to be in phase III and one in the north that is in phase I (Williams et al., 2011).

### 2.2.3 High energy emission

The observed high energy emission of SNR is due to thermal and non-thermal emission. Understanding the observed emission provides insights in properties of the remnant (see Section 2.2.2), properties of the ambient medium, into shock physics and cosmic-ray acceleration. In the following, the physical background and basic concept of modeling the X-ray radiation of SNRs and how it can be used to broaden the insight into the aforementioned topics are summarized.

#### Thermal X-ray emission

The shock wave of an SN is observable as hot, X-ray emitting plasma, which is in a first-order approximation optically thin. Furthermore, the plasma in young SNR is mostly not in equilibrium as it did not have enough time to reach it.

The observed thermal X-ray spectra of SNR consists of absorbed thermal continuum emission by bremsstrahlung, recombination, two-photon processes and line-emission from collision excitation of ions (Vink, 2012). In order to show how to extract important properties of an SNR these processes are summarized in the following, based on the reviews of Mewe (1999) and Kaastra et al. (2008):

- Bremsstrahlung or free-free (ff) emission is caused by the collision of an ion with a free electron and the emissivity  $\varepsilon_{\text{ff}}$  is given by

$$\varepsilon_{\text{ff}} = EM \cdot g_{\text{ff}}(T_e) T_e^{-1/2} \exp\left(-\frac{h\nu}{kT_e}\right) \quad (2.3)$$

with the gaunt factor  $g_{\text{ff}} \approx 1$ , the electron temperature  $T_e$  and a normalization constant called emission measure  $EM$  that depends on the electron  $n_e$  and ion densities  $n_i$  and the ion charge  $Z_i$ . For abundances on the order of solar abundances or below,  $EM$  is dominated by electrons colliding with hydrogen (H) or helium (He) ions. Thus,  $EM \propto n_e \sum_i n_i Z_i^2 \approx n_e n_{\text{H}}$ . For young, and hence hot, SNRs this does not have to be the case and the continuum contribution of heavier elements must be taken into account. Moreover, in X-ray astronomy the integral over the plasma volume  $V$  is measured in a spectral fit. Hence,  $EM \propto \int_V n_e n_{\text{H}} dV / (4\pi d^2)$ , with  $d$  the distance to convert to flux units.

- Recombination or free-bound (fb) emission occurs when a free electron is captured by an ion and a photon is emitted (the reverse process of photoionisation). It dominates the continuum emission in some cases, e.g., for temperatures  $k_{\text{B}}T_e = 0.1$  keV it dominates the spectrum at  $E > 1$  keV.

- Two-photon emission is caused by excitation of the metastable 2s level and emission of two photons when decaying into the 1s ground state. A normal decay from 2s to 1s is forbidden by quantum-mechanical selection rules. The total energy of the two photons is equal to the difference in energy between state 2s and 1s and a symmetric spectrum around this energy difference is measurable. This is in particular important for H and He ions and for a temperature  $0.5 \text{ keV} < k_B T_e < 5 \text{ keV}$ . This process can only happen when the density is low enough that no collisional excitation in a higher state occurs before the decay (Mewe et al., 1986).
- Line emission is caused when an excited ion in state  $j$  decays back into a lower state  $i$  and emits a photon with an energy  $E = E_j - E_i$ . In SNRs the dominant process is collisional excitation, in most cases electron-ion collisions.

All these emission processes have to be modeled when fitting a spectrum of an SNR. As mentioned before, in some cases SNRs have not reached collisional equilibrium. In young SNRs, for example, after the shock wave changed its temperature very rapidly, the plasma did not have enough time to reach ionization balance again. This non-equilibrium ionization (NEI) implicates that the change per unit time of the ion concentration  $n_Z$  with charge  $Z$  is given by the ionization and recombination rate of ions with  $Z - 1$  and  $Z + 1$ , respectively. These coupled differential equations have to be solved numerically and the solution has to be included when fitting the spectrum. The time evolution of a plasma in NEI can be described by the so-called ionization age of the plasma  $n_e t$ , where  $t$  is the age of the SNR. Nevertheless, it should be kept in mind that the temperature measured in spectral fitting of NEI plasmas is the electron temperature and is in general not equal to the ion temperature. After a plasma reaches equilibrium<sup>5</sup> it is called collisional ionization equilibrium (CIE) and can, for example, be observed in clusters of galaxies (see Böhringer and Werner, 2010, for a review) and in evolved SNRs. For typical SNR temperatures ( $0.5 \text{ keV} < k_B T_e < 4 \text{ keV}$ ) the time a plasma needs to reach CIE and thus, ion and electron temperature balance, is  $n_e t \approx 10^{12} \text{ cm}^{-3} \text{ s}$ .

### Non-thermal X-ray emission

SNRs have typical magnetic fields of 10 to 500  $\mu\text{G}$  (Hinton and Hofmann, 2009) and thus, emit non-thermal X-ray emission by synchrotron radiation of gyrating relativistic electrons (Ginzburg and Syrovatskii, 1965). With this magnetic field strength the relativistic electrons have energies of 10 to 100 TeV and thus, SNRs can be detected at these energies (Nolan et al., 2012). The non-thermal contribution to the X-ray spectrum of an SNR can best be described by a power law  $I \propto E^\Gamma$ , with the photo index  $\Gamma$ .

Zirakashvili and Aharonian (2007) showed that high shock velocities ( $v > 2000 \text{ km s}^{-1}$ ) are necessary for SNRs to emit synchrotron radiation in X-rays and hence, this process can only be observed in young remnants. Finding more SNRs that show a power law spectrum can help to

---

<sup>5</sup>Ionization equilibrium means that the net charge after ionization and recombination of an ion concentration  $n_Z$  with charge  $Z$  is zero

further constrain the emission mechanism in SNRs and explain the reason why some SNRs are only synchrotron radiators and show no or only very faint thermal emission.

As aforementioned, SNRs are considered to be the main source of cosmic rays up to the “knee”<sup>6</sup>. Using the galactic cosmic ray density of  $\sim 1.8 \text{ eV/cm}^3$  (Webber, 1998) and the average time the cosmic rays spend in the Galaxy, a total power of  $\sim 10^{41} \text{ erg/s}$  is required (Ginzburg and Syrovatskij, 1967). The only known Galactic sources that can be responsible for such energetic particles are SNRs. With a rate of  $\approx 2$  per century (see Section 2.2) they produce  $\sim 10^{42} \text{ erg/s}$ . Thus, about 10% of their total explosion energy may account for accelerating cosmic rays.

Cosmic rays are thought to be produced by the so-called first-order Fermi process or diffuse shock acceleration (Bell, 1978). In this framework charged particles, which have high enough energies to pass the shock front, are repeatedly scattered elastically when crossing the shock front. This is because of the presence of a turbulent magnetic field. Each time a particle crosses the shock front its energy increases due to different plasma velocities upstream and downstream (Bell, 1978; Vink, 2012). More information can be found in the review of Vink (2012) and references therein.

## 2.3 Neutron stars and pulsars

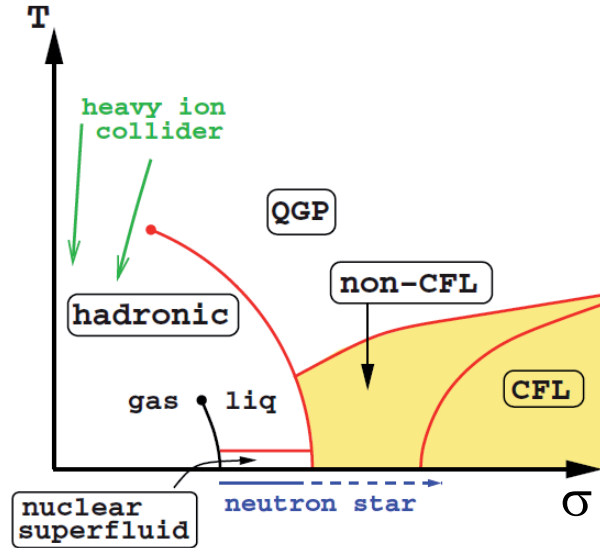
### 2.3.1 Composition and cooling of neutron stars

Neutron stars are the most dense objects directly observable in the universe. Their densities can reach values of more than 10 times the nuclear density  $\rho_0 = 2.8 \times 10^{14} \text{ g/cm}^3$  (Tsuruta, 2009). Matter at these densities is stable against the gravitational force because of the Fermi pressure of the highly degenerated neutrons and protons (Yakovlev and Pethick, 2004).<sup>7</sup> In addition, the relative low temperature in addition to the nuclear density in neutron stars cannot be reached in laboratories. This can be illustrated in a phase diagram, where density is plotted against temperature (see Figure 2.4). The experiments at the Large Hadron Collider (LHC) at Cern reach comparable energy densities, but at very high temperatures and thus, low matter densities. Currently at the GSI Helmholtzzentrum für Schwerionenforschung and the Facility for Antiproton and Ion Research (FAIR) in Darmstadt a heavy-ion experiment is built up, which will explore matter at higher densities as at Cern but with lower temperatures (Friese, 2006). A detailed review of other experiments to study the structure of dense matter can be found in Lattimer and Prakash (2007). Therefore, matter at low temperature and several times nuclear density can only be studied in neutron stars.

<sup>6</sup>At an energy of  $\sim 3 \times 10^{15} \text{ eV}$  the cosmic ray spectrum changes its slope from a power law with index  $-2.7$  to an index of  $-3.1$ . This spectral feature is called “knee”.

<sup>7</sup>A neutron star mainly consists of neutrons and only a few percent of protons, hence the name neutron star

**Figure 2.4:** Schematic view of the phase diagram of matter at high densities  $\sigma$  and temperatures  $T$  (taken from Alford et al. (2008)), where QGP is the abbreviation for quark-gluon plasma and CFL for color-flavor locked quark matter (for details see Alford et al. (2008)).



## Composition

The composition of a typical neutron star is shown in Figure 2.5 and is reviewed in Haensel et al. (2007) and Yakovlev and Pethick (2004): It is expected that a thin atmosphere exists at the surface of the star, which is made up of a plasma composed of Hydrogen, Helium and Iron nuclei. This is the last scattering surface of photons coming from inside the star and thus, determine the observed spectrum and temperature, which is of high importance for exploring NSs, especially if the cooling of these kind of objects with time is studied. This is a major part of this work (Section 7) and will be explained in detail in the next section.

Below that layer four regions can be distinguished, which in literature are referred to as outer and inner crust and outer and inner core. The matter in the outer crust consists of ions and a highly degenerated electron gas, which becomes relativistic at  $\rho > 10^6 \text{ g/cm}^3$ . With increasing density the nuclei can capture neutrons and become neutron rich. This layer has a thickness of  $\sim 100 \text{ m}$  and at the boundary between inner and outer crust the density is  $\rho_{\text{ND}} \approx 4 \times 10^{11} \text{ g/cm}^3$ . When the density exceeds  $\rho_{\text{ND}}$  neutrons begin to drop out of the nucleons and thus, the inner crust contains free neutrons in addition to a relativistic electron gas and neutron rich atomic nuclei. Here, protons are in all probability a superconductor of type II and neutrons in a superfluid phase. The density at the base of the crust is about  $0.5 \rho_0$ , the density where nuclei are disintegrated. This layer is about one kilometer thick.

In the outer core, where the density is  $0.5\rho_0 < \rho < 2\rho_0$ , matter is in the so called n-p-e- $\mu$  composition, that is a composition of mainly neutrons and in addition several percent protons, electrons and possibly muons. All particles are strongly degenerated (Yakovlev and Pethick, 2004). This layer is several kilometers thick and if the star has a low mass the outer core reaches to the center of the star. The discrimination in outer and inner core has no physical interpretation, it is only given by the fact that below  $2\rho_0$  the composition of a neutron star is reasonably well constrained by theoretical modeling of nuclear matter and particle physics experiments. Above  $2\rho_0$  there are many suggestions for the constituents in the inner core and it is one of the main

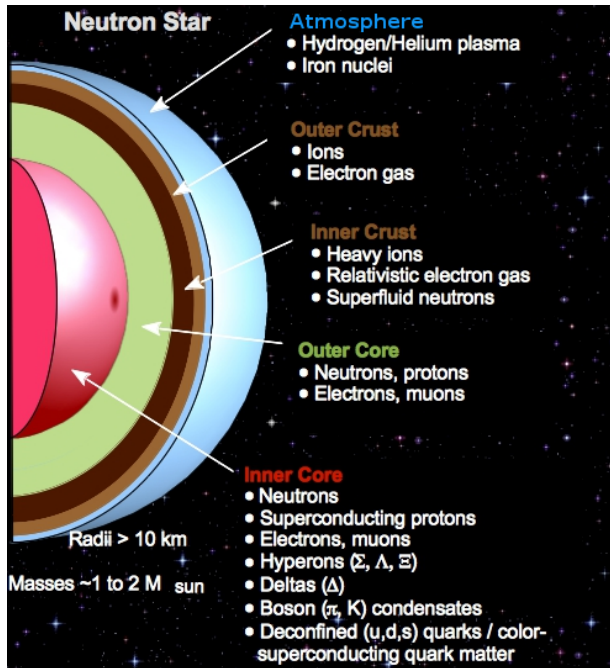


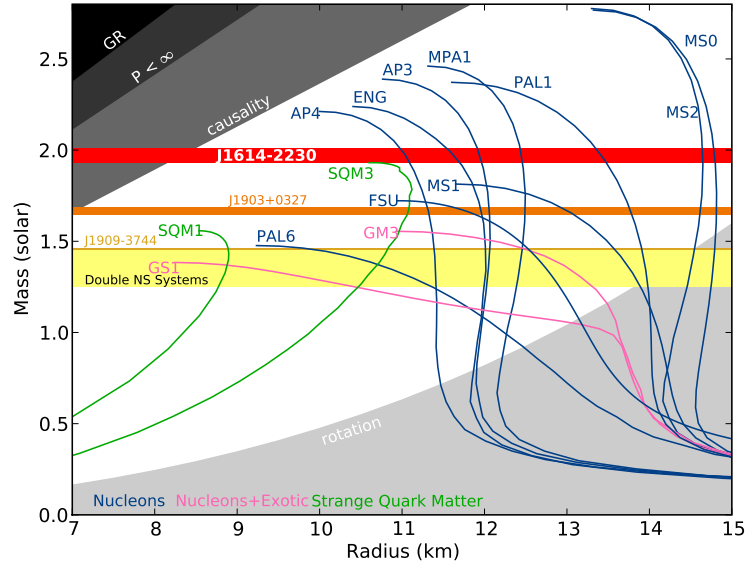
**Figure 2.5:** A cross-section of the interior of a neutron star showing the layer composition. (taken from Weber et al. (2013b))

goals to rule out models, which describe the composition of the inner core. The main four hypotheses are:

1. *Nucleon matter:* No inner core as in the case of low-mass stars.
2. *Hyperons:* At higher densities the chemical potential can be high enough to create hyperons, e.g.,  $\Lambda$  and  $\Sigma^-$  which are the lightest hyperons.
3. *Pion or Kaon condensate:* At this matter densities a Bose-Einstein condensate of pions ( $\pi$ ) or kaons ( $K$ ) could be possible. Both particles are mesons.
4. *Quark confinement:* In some theories it is predicted that above several times nuclear density a phase transition occurs and matter consists of deconfined up and down quarks and some percentage of strange quarks (Weber et al., 2009). At these densities the neutron and proton chemical potential exceeds the mass of up, down and strange quarks and thus, neutron and protons may be broken up into their quark constituents.

Here points 2-4 are called “exotic” matter. The question is, how is it possible to determine the actual composition of neutron stars and whether exotic matter is needed to explain the observations? Even if one massive star shows some indications of, for example Quark confinement, this does not rule out the possibility that the core of a less massive star is just made up of hadronic matter. Many efforts have been made in the last decades to exclude some of the possibilities mentioned above and to combine observations with theoretical models. In all these attempts the starting point is the equation of state (EOS) of dense matter, because in nature only one EOS of dense matter is realized. The EOS describes the dependence of the pressure  $p$  on the energy

**Figure 2.6:** Diagram of the non-rotating mass versus physical radius taken from Demorest et al. (2010). In addition the M-R relation is plotted for several EOSs (Lattimer and Prakash, 2001), where the blue curves are EOSs assuming only nucleon matter, pink nucleon and exotic matter and green strange quark matter. The horizontal bands show some measured masses of neutron stars and the gray shaded regions of the diagram are excluded by theoretical or experimental proofs (see Lattimer and Prakash (2007) for a detailed description).



density  $\varepsilon$  and strongly depends on the constituents assumed in the core of an NS. As aforementioned, for  $\rho \lesssim \rho_0$  the EOS has been calculated reasonable well, however at densities above nuclear density the EOS cannot be tested in laboratories and has to be modeled theoretically. Thus, many different EOSs can be found in the literature (some are shown in Figure 2.6) assuming different compositions and different particle interactions. In addition, the Einstein field equation for a spherical symmetric system has to be solved to obtain the global structure of an NS, because of the strong gravitational field introduced by an NS. This calculation results in the Tolman-Oppenheimer-Volkoff equation (TOV, Tolman, 1939; Oppenheimer and Volkoff, 1939).

Providing an EOS and assuming energy conservation, the TOV can be solved and a relation between the mass  $M$  and the radius  $R$  can be obtained for the given EOS. Thus, using these two most basic measurable quantities of neutron stars it is possible to rule out unrealistic EOSs.

The most precise mass determination is obtained by timing binary pulsars and measuring of at least two relativistic effects. These effects are reviewed in Lattimer (2012) and include the advance of the periastron of the binary orbit, the orbital period decay due to the emission of gravitational waves and the Shapiro delay, caused by the gravitational field of the companion. With this method more than 30 precise mass measurement were possible (Lattimer, 2012), including the recently discovered, two most massive NSs, PSR J1614-2230 with  $1.97 \pm 0.04 M_\odot$  (Demorest et al., 2010) and PSR J0348+0432 with  $2.01 \pm 0.04 M_\odot$  (Antoniadis et al., 2013). These two neutron stars can rule out many soft EOSs, which cannot explain such massive stars (see Figure 2.6) and set strong limits on the maximally compact EOS (Prakash, 2013). However, Quark matter in neutron stars cannot be ruled out as stated by Lattimer (2012). For example, the simplified MIT bag model EOS (Chodos et al., 1974) can be excluded, but more detailed studies show that a hybrid star, where a first order phase transition between quark and nuclear matter is possible, can produce a  $2 M_\odot$  star (Alford et al., 2013).

Even if a lot of progress has been made in constraining the EOS, no high-accuracy radius measurement is available. And what is more important, no radius has been inferred for any NS with a very accurate mass measurement. Most observational methods to determine the radius of

a neutron star are summarized in Lattimer (2012). For example, the radius can be inferred from the thermal X-ray flux of isolated neutron stars, where the normalization of the fitted blackbody spectrum to such a star is  $\propto R^2/D^2$ , where  $D$  is the distance to the source. However, the distances have in most cases large uncertainties and the emission could come from a hotter or colder region of the NS surface. Only for a few sources the radius could be obtained with high confidence (see the caption of Figure 7.6 for a summary of known thermal emitting NSs).

### Cooling

Therefore, many other ways to look for signatures of “exotic” matter have been proposed. One very promising way is to study the thermal evolution (cooling) of neutron stars, that is the change of the temperature  $T$  with time  $t$  (see Figure 2.7). The main advantage of this method is that the temperature of an NS is easily extracted from the X-ray spectrum of an NS and even upper limits on the temperature can help to constrain the cooling (Becker et al., 1993b; Becker, 1995). In addition, the age  $\tau$  of NSs, which are observable as rotation-powered pulsars, can be estimated from their spin-down rates:

$$\tau = P/2\dot{P}, \quad (2.4)$$

where  $P$  is the rotational period of the star and  $\dot{P}$  its first time derivative. For some NSs even kinematic information is available, e.g., association of an NS with an SNR with historical age. The basic principle of NS cooling, expressed by the decrease of temperature with time  $dT/dt$ , can be explained by the energy balance equation in the Newtonian limit:

$$\frac{dE_{\text{th}}}{dt} = C_V \frac{dT_s}{dt} = -L_V - L_\gamma + H. \quad (2.5)$$

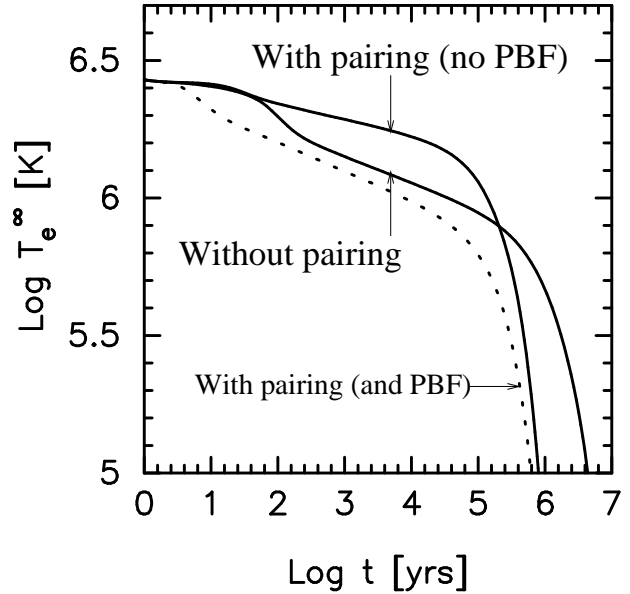
This equation states that the luminosity emitted by neutrinos from the whole star  $L_V$  and photons from the surface  $L_\gamma = 4\pi\sigma_B R^2 T_s^4$  ( $\sigma_B$  is the Stefan-Boltzmann constant and  $T_s$  the temperature on the surface) must be balanced by a change in the thermal energy content  $E_{\text{th}}$  of the star and by some heating mechanism  $H$  taking place in the star (reviewed in Page et al. (2006)).  $E_{\text{th}}$  is given by the product of the specific heat  $C_V = \sum_i C_{V,i}$  and the temperature  $T_s$ , where the index  $i$  of the sum denotes all constituent particles (electrons, muons, neutrons, protons, ...). To obtain a cooling curve, the  $M$  vs  $R$  relation has to be inferred first, as explained before. However, for the cooling further input parameters have to be considered: Besides the EOS and the constitute particles, the most important factor that determines the cooling is the neutrino emissivity  $q_V = q_V^{\text{fast}} + q_V^{\text{slow}}$  (see Table 1 in Page et al. (2006) for a summary of neutrino emitting processes and their time scales). The neutrino processes with the highest  $L_V$  is the so called direct URCA (dURCA) process:

$$B_1 \rightarrow B_2 + \ell + \bar{\nu}_\ell, \quad (2.6)$$

$$B_2 + \ell \rightarrow B_1 + \nu_\ell. \quad (2.7)$$

Here  $B_i$  are baryons (neutron, proton) and  $\ell$  is a lepton (electron or muon). Including this process in cooling models shows that the thermal evolution of such stars is not consistent with data (Tsuruta, 1998, Figure 15). Moreover, for  $B_1 = \text{neutron}$  the dURCA process is only allowed

**Figure 2.7:** Cooling curve with and without nucleon pairing. In addition, the effect of the Cooper pair braking and formation (PBF) process is shown. (taken from Page et al. (2004))



at high enough densities (Lattimer et al., 1991), otherwise the Pauli Exclusion Principle prohibits it (Tsuruta, 2009). In this case the dURCA process needs to be modified and a bystander baryon has to be included in the process to ensure energy and momentum conservation. This is the so called modified URCA (mURCA) process and reduces the emissivity by more than six orders of magnitude, letting the star cool more slowly. However, if some of the exotic matter listed above is present dURCA processes are possible, but with a smaller impact on the cooling (Lattimer and Prakash, 2007). Another very important aspect for the cooling is the pairing effect of a degenerated system of fermions, including the neutrino emission from Cooper pair braking and formation. This is discussed in detail by Page et al. (2004, 2009). In general, the pairing reduces the cooling by neutrinos, because the pairing is energetically favorable and an energy gap is formed. Hence, less fermions contribute to  $L_\nu$  by process 2.6 and 2.7. However, when the temperature is close to a critical temperature Cooper pair braking and formation occurs and neutrinos are emitted by the following process:



where  $[nn]$  denotes the formation of a Cooper pair. Thus, taking all this neutrino sources into account and model the various layers in a consisted way is difficult.

The envelope of the neutron star is reasonable well modeled and the models can be taken from literature (Gudmundsson et al., 1982; Potekhin et al., 1997). However, the interior has to be solved numerically<sup>8</sup>, adjusted to be continuous when reaching the envelope and after the star is built has to satisfy the relativistic form of equation 2.5. A cooling scenario, termed minimal cooling (Page et al., 2004, 2009) can reasonably well match observational data (see Figure 7.6). This scenario does not allow any dURCA processes from baryons, but the Cooper pair braking

<sup>8</sup>A cooling code, written by Dany Page taking into account most of the physics presented in this section, is available at <http://www.astroscu.unam.mx/neutrones/>.

and formation process and all slow neutrino processes. It also includes effects on the cooling due to uncertainties in the composition of the envelope and due to the large magnetic field of NSs (see below). In the former only a small fraction of heavy elements can significantly increase  $T_s$  (Page et al., 2004).

### Mass

In the framework of the minimal cooling scenario, the effect of the NS mass on the cooling is negligible, because all processes included in this model have no energy or density threshold (Page et al., 2004). This picture drastically changes if neutrino emission via the direct URCA channel is allowed. As mentioned before dURCA processes are only possible above a critical density (Lattimer et al., 1991) and thus, its occurrence depends on mass. Above a critical mass neutrinos are emitted by the dURCA process and hence, the NS is cooling down very fast (Tsuruta, 2009). Below that mass limit the NS is evolving like in the case of the minimal cooling scenario.

### Magnetic field and rotation

For a complete modeling of an NS the strong magnetic field  $B$ , up to  $10^{15}$  G and the rotation  $f$  of up to 700 Hz has to be taken into account. In 2D simulations the impact of  $B$  on the cooling was investigated by Aguilera et al. (2008) and they showed that for  $B \sim 10^{14}$  G the cooling is significantly affected and has to be taken into account when modeling such a star. However, the magnetic field has no effect on the composition (Lattimer and Prakash, 2007). Rotation significantly affects the composition, and thus the cooling, but only for frequencies above 50% the Kepler frequency<sup>9</sup> (Weber et al., 2013a). The Kepler frequency depends on mass and is  $\sim 1000$  Hz. Therefore, only a few known pulsars will show a change of composition by their rotation.

The understanding of cooling neutron stars has been brought a big step forward with the rapidly cooling of the central compact object in the SNR Cassiopeia A (Ho and Heinke, 2009). In a later publication, Shternin et al. (2011) found a decline of the temperature from 2.12 million Kelvin to 2.02 million Kelvin in the time span from January 2000 to November 2010. They could also show that this decline can be explained by the fact that neutrons recently become superfluid, a result which was confirmed by Page et al. (2011) and Blaschke et al. (2012). However, Elshamouty et al. (2013) claims that the error in the temperature measurement is underestimated because of the complexity of the bright and varying SNR background and thus the decline with time is not significant. Therefore, more observations are needed to decide if the decline is real or just a statistical fluctuation.

### 2.3.2 High energy emission of pulsars

On the one hand neutron stars are hot objects with a temperature on the order of million degrees as shown in the last section. Thus, their thermal emission can be detected in the soft X-ray band. On the other hand neutron stars are fast rotators with periods from milliseconds to seconds and

<sup>9</sup>The Kepler frequency is the maximal frequency at which a star can rotate before it is disrupted

have large magnetic fields from  $10^9$  G to  $10^{15}$  G, which accelerates electrons to ultra relativistic velocities. Thus, synchrotron and curvature radiation is emitted by the gyrating electrons. This emission is the reason that neutron stars can be observed as pulsars and as non-thermal X-ray sources. The first magnetosphere model was proposed by Goldreich and Julian (1969), shortly after the first detection of a radio pulsar by Hewish et al. (1968) and was improved ever since. To date, over 2200 pulsars are known<sup>10</sup> (Manchester et al., 2005). However, the origin of the non-thermal emission is still not fully understood and several models have been proposed to explain the observed radiation. In the following the current understanding of particle acceleration in the pulsar magnetosphere and what observational proof there is in favor of a model is summarized.

If the rotational and magnetic field axis are aligned, the Lorentz force on the charged particles is larger than the gravitational force by more than 10 orders of magnitude, because of the strong magnetic field (Lorimer and Kramer, 2004).<sup>11</sup> Therefore, charges are pulled from the surface and the neutron star cannot be surrounded by a vacuum (Goldreich and Julian, 1969). This is also predicted for a non-aligned rotator (Mestel, 1971).

The ambient plasma rotates at the same angular velocity  $\Omega$  as the star, because it experiences the same field as the interior of the star. However, at the so-called light cylinder radius  $R_{LC} = \Omega/c$  of the neutron star the magnetic field lines break-up, because a co-rotation above this radius would imply  $\Omega > c$ , where  $c$  is the speed of light (see Figure 2.8). In the region with closed field lines no particle emission is possible, because this region is in a force-free state. Thus, all non-thermal emission models of pulsars have focused on the open field lines. Two zones in the magnetosphere of the neutron star were identified in which the force-free state is locally violated and hence, particles could be accelerated and photons are emitted. These two zones are located in the inner and outer magnetosphere, where a depletion of plasma is expected. Furthermore, three different models can be found in literature. These theories will be explained in the following, based on the reviews of Harding (2009) and Lorimer and Kramer (2004). They only differ in the location where the particles are accelerated, but they all assume that the emission comes from curvature radiation. The curvature radiation can be seen as a generalization of synchrotron radiation, where the motion of the extremely relativistic particles follows the curved field lines. The electron (or positron) will be accelerated transverse to the curved magnetic field lines and photons are emitted under a pitch angle<sup>12</sup> close to zero (Lyne and Graham-Smith, 2005). Here the curvature radius depends only on the geometry of the magnetic field and the emission spectrum  $dE/dt$ .

**Polar cap** The open field lines on the surface of the neutron star define the polar cap. In the polar cap model an accelerating gap just above this polar cap with a large residual electric field is predicted, where a dense electron-positron pair plasma is required (Sturrock, 1971). Therefore, charged particles are accelerated in the gap to relativistic velocities along the curved magnetic field lines and emit  $\gamma$ -photons, either by curvature radiation (Ruderman and Sutherland, 1975) or inverse Compton scattering (Daugherty and Harding,

<sup>10</sup>A listing of all known pulsars can be found at <http://www.atnf.csiro.au/people/pulsar/psrcat/>

<sup>11</sup>The gravitational force  $F_{\text{grav}}$  on an electron at the surface is  $F_{\text{grav}} \sim 10^{-18}$  N and the electric force  $F_{\text{el}} \sim 10^{-6} \sqrt{(P/s)^{-1} \cdot \dot{P}/10^{-15}}$  N

<sup>12</sup>The pitch angle is the angle between velocity vector and magnetic field.

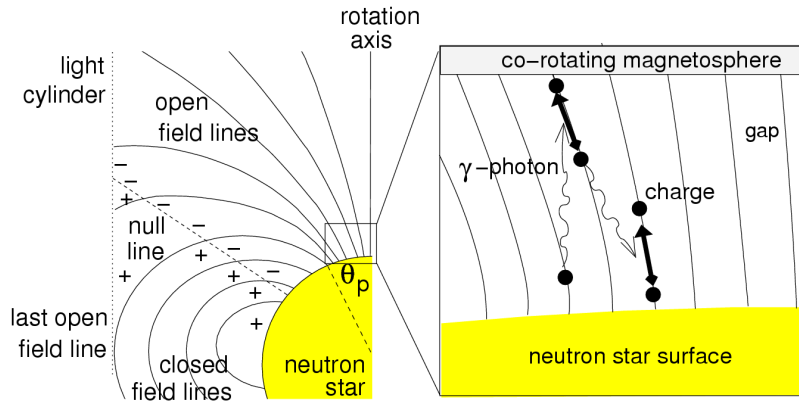


**Figure 2.8:** Model of the magnetosphere of a pulsar. (taken from Lorimer and Kramer (2004))

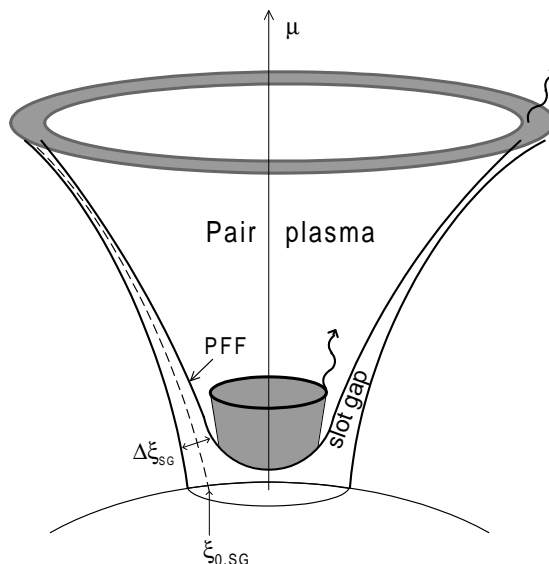
1986). If the energy of a created photon exceeds twice the rest mass of an electron, electron-positron pairs are created in the strong magnetic field at the pair formation front (see Figure 2.9), leading to further production of photons and particles (see right side of Figure 2.8) and an increase of the initial plasma density by one to three orders of magnitude (Arendt and Eilek, 2002). It is thought that this secondary pair plasma is responsible for the observed coherent radio emission and that its resonant inverse Compton scattering with infrared photons may explain the incoherent high energy emission (Lorimer and Kramer, 2004). Therefore, a lack of such cascades can hamper the radio emission and a pulsar would be radio quiet. In addition, these secondary processes may be quenched by magnetic fields above a critical value  $B_{\text{crit}} \approx 4.4 \times 10^{13}$  G (Baier and Katkov, 2007), which could explain the lack of radio emission of magnetars<sup>13</sup>.

**Slot gap** Here the acceleration occurs also in the polar cap region with similar electromagnetic pair cascades. However, in any polar cap model a slot gap is a characteristic feature which cannot be avoided (Muslimov and Harding, 2003). The slot gap is a high-altitude acceleration region near the rim of the polar cap where the pair formation front approaches asymptotically the last open field line and the parallel electric field  $E_{\parallel} \rightarrow 0$  (see Figure 2.9). Thus, the electrons may be accelerated over longer distances and radiate  $\gamma$ -rays into the outer magnetosphere, resulting in a beam, which is much broader and less collimated as in the polar cap model (Pierbattista et al., 2012). It should be noted that Dyks and Rudak (2003) developed a model (called the two-pole caustic model) which is based only on geometric considerations and on the slot gap theory to explain light curves of pulsars at high energy.

**Outer gap** This particle acceleration region is a vacuum gap located at the outer magnetosphere at the so-called null line where  $\vec{\Omega} \cdot \vec{B} = 0$ , which separates particles with different charges. This can be seen on the left side of Figure 2.8 where the outer gap is close to the light cylinder. Because the charges change sign at the null line an out-flowing charge would not be replaced and thus, an extended gap occurs (Hollow, 1973; Lorimer and Kramer, 2004).

<sup>13</sup>Neutron stars with strong magnetic fields above  $B_{\text{crit}}$  are called magnetars and can be observed as anomalous X-ray pulsars (AXPs) and soft gamma repeaters (SGRs). See Rea and Esposito (2011) for a review.

**Figure 2.9:** Illustration of the slot gap in the pulsars magnetosphere. The figure shows the high-altitude acceleration gap near the rim of the polar cap where  $E_{\parallel} \rightarrow 0$  and the pair formation front approaches asymptotically the last open field line at high altitude.  $\Delta\xi_{\text{SG}}$  indicates the slot gap thickness,  $\xi_{0,\text{SG}}$  the colatitude at the center of the slot gap and  $\mu$  the magnetic field axis. (taken from Muslimov and Harding (2003))



The resulting electric field accelerates electron-positron pairs downwards to the surface, which then radiates  $\gamma$ -rays tangential to the magnetic field lines by curvature radiation and synchrotron emission (Lorimer and Kramer, 2004). No radio emission is expected to come from outer gap models (Lorimer and Kramer, 2004). An exception might be the Crab pulsar (Lorimer and Kramer, 2004). The relevant processes are different than for polar cap models and the most important factor here is the local magnetic field, which is much weaker than on the surface. Thus, higher Lorentz factors  $\gamma$  are needed to emit photons.

Furthermore, in the pulsars magnetosphere the energy of emitted  $\gamma$ -rays are limited, due to pair creation when the magnetic field reaches high values. The maximal energy of a photon  $E_{\text{max}} \propto 1/B$ , with  $B$  the magnetic field. Thus, the highest energies can be found furthest out in the gap. For example, this can be seen in the Crab pulsar, where the main pulse in  $\gamma$ -rays comes before the optical main pulse (Abdo et al., 2010a). Hence, studying the difference in the pulse arrival time can help to distinguish between the three models described above.

Additionally, the outer gap spectrum should extend to higher energies and thus, a simple discrimination between polar cap and outer gap is possible by studying pulsar at GeV energies. In the last years a large progress was made in this energy regime with the Large Area Telescope (LAT) on-board of the Fermi satellite (Atwood et al., 2009). After three years of scanning the whole sky in the energy range 20 MeV to 300 GeV, about 123 gamma-ray pulsars were detected above 0.1 GeV (see Table B.1). This large sample allows for population synthesis by comparing their global properties with model predictions. Pierbattista et al. (2012) used the three models polar cap, slot gap and outer gap to created a simulated pulsar population and compared it with the Fermi LAT data. Their finding was that the outer gap model best describes the  $\gamma$ -ray pulsar population, because the predicted luminosity and beam size can easily explain the observed pulsars, whereas in the case of the slot gap and polar cap model they cannot. Nevertheless, all models fail to explain the number of Fermi detected pulsars with high spin-down luminosity  $\dot{E}$ .

## Chapter 3

# The supernova remnant Puppis A

The content of this chapter is adopted from the referred paper entitled “The Proper Motion of the Central Compact Object RX J0822-4300 in the Supernova Remnant Puppis A” published in *The Astrophysical Journal* (Becker et al., 2012) to which I contributed the data analysis and the drafting. In addition, this chapter contains a draft of the X-ray and optical study of the western part of this remnant, which will be submitted to *Astronomy & Astrophysics*.

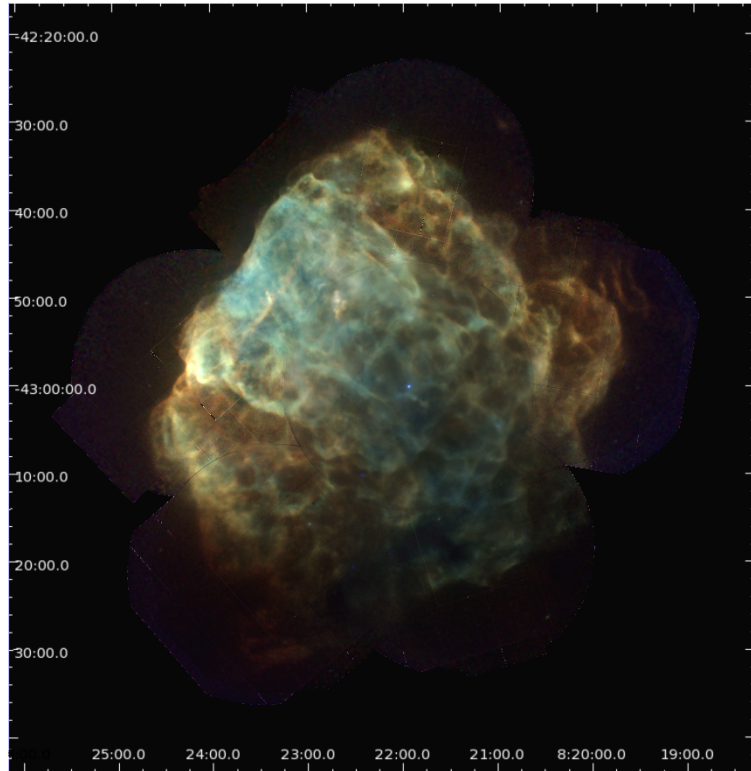
In this chapter I address the proper motion of the central compact object RX J0822-4300 in the supernova remnant Puppis A. Furthermore, I will answer the question, is there a second supernova remnant overlapping Puppis A? The detailed discussion of the results is presented in Chapter 8.

### 3.1 Introduction

There has long been broad consensus that core-collapse supernovae - the explosions of massive progenitors that produce Types II, Ib, and Ic events at least - leave behind a compact stellar remnant: either a neutron star or a black hole. Numerous central compact objects (CCOs) have been found within supernova remnant (SNR) shells (cf. Becker (2009) for a review), including near the centers of all three of the “oxygen-rich” SNRs (those with optical filaments dominated by ejecta that stem only from core-collapse supernovae) in the Galaxy: Cas A (Tanaka et al., 1999; Chakrabarty et al., 2001), Puppis A (Petre et al., 1996, see Figure 3.1), and G292.0+1.8 (Hughes et al., 2001; Camilo et al., 2002b).

Observations of proper motions for these CCOs, and of the ejecta-dominated filaments, provide the opportunity to investigate the dynamics of core-collapse explosions, as imprinted on the compact remnant and the ejecta. Anisotropies and/or bipolar jets appear typical of the ejecta distribution from core-collapse explosions. These are predicted from two- and three-dimensional models for core-collapse SNe (e.g., Burrows et al., 1995; Scheck et al., 2004, 2006; Wongwathanarat et al., 2010), and have been observed in all three of the Galactic oxygen-rich remnants. Asymmetries in the ejecta distribution are closely linked to the recoil of a CCO through conservation of momentum: if the explosion expels ejecta preferentially in one direction, the CCO must recoil in the opposite direction. One expects this recoil to be particularly apparent in

**Figure 3.1:** X-ray image of SNR Puppis A. Here all observations with XMM-Newton and Chandra have been combined. The red, green, and blue component of the image corresponds to the 0.3–0.7 keV, 0.7–1.0 keV and 1.0–8.0 keV band, respectively. The data are Gaussian-smoothed to an angular resolution of 10 arcsec and the intensity scale is square root. The blue dot in the center is the CCO RX J0822–4300. (taken from Dubner et al. (2013))



Puppis A, where Winkler et al. (1988) found that all the visible ejecta knots are moving generally toward the north and east.

Following the discovery of RX J0822–4300 near the center of Puppis A (Petre et al., 1996), measuring its proper motion and recoil velocity was of obvious interest, and observations with this goal were carried out early in the Chandra mission. We have previously done two independent studies of the proper motion of RX J0822–4300 in a pair of papers: Hui and Becker (2006), henceforth HB06, and Winkler and Petre (2007), henceforth WP07. Both these papers were based on the same three epochs of data from the Chandra HRI over the 5.3-year period 1999 December–2005 April, and both measured a motion to the southwest, as expected, but with surprisingly high velocity: HB06 measured  $\mu = 107 \pm 34 \text{ mas yr}^{-1}$ , while WP07 found  $165 \pm 25 \text{ mas yr}^{-1}$ , corresponding to a transverse velocity of  $1122 \pm 327 \text{ km s}^{-1}$ , or  $1570 \pm 240 \text{ km s}^{-1}$ , respectively, if we take Puppis A’s distance as 2 kpc. Both these values are large compared with the typical birth velocities for pulsars of  $\sim 500 \text{ km s}^{-1}$  (Caraveo, 1993; Frail et al., 1994; Hobbs et al., 2005). Furthermore, a recoil velocity much larger than  $1000 \text{ km s}^{-1}$  challenges models for producing pulsar kicks. Therefore, we have undertaken this joint follow-up study, taking advantage of Chandra’s unique spatial resolution with a time baseline twice as long as for our previous measurements (see Section 3.3.1).

Furthermore, the Puppis A supernova remnant is one of the most studied SNRs, because of its apparent large size of  $60 \times 50 \text{ arcmin}$ , its distance of  $\approx 2 \text{ kpc}$  (Reynoso et al., 2003) and its brightness in the radio and X-ray band. It is located in a very peculiar region for supernova

remnant research, where, in addition to Puppis A, two more supernova remnants are seen to be located in a  $\sim 10$  degree small part of the sky. All three remnants, interestingly, are believed to be physically unrelated, partly overlapping each other just by chance along the line of sight. There is no other place in our Galaxy where this is seen. It seems therefore to be a big surprise that there might be even a forth remnant located at the edge of the Puppis A remnant.

Dubner et al. (2013) studied the Puppis A SNR in detail in the X-ray regime with XMM-Newton and Chandra (see Figure 3.1). They confirm that the irregular structure of the remnant is due to the evolution of it in an inhomogeneous interstellar medium and that a broad band with crosses the remnant from northeast to southwest is caused by absorption of foreground gas.

However, Dubner et al. (2013) did not discuss a emission region located at the western side of the remnant. This almost perfectly circular shaped emission feature was already noticed in archival ROSAT HRI data. It is reminiscent of a shell-type supernova remnant which is laying by coincidence on the edge of the Puppis A SNR. The location of this circular structure at this position does not fit to the overall shape of the remnant at its western side. This brings up the question what has caused this peculiar feature. Is it the imprint of shock/cloud interactions as suggested by Dubner et al. (2013) for a southwestern feature or is it indeed a second SNR which is just by coincidence close to Puppis A. In Section 3.3.2 these questions will be answered with the help of an archival X-ray observation with XMM-Newton, images of all-sky surveys in the radio and infrared wavelength regime and deep optical observation taken with the 2.2 m MPG/ESO telescope in La Silla, Chile.

## 3.2 Observations and data analysis

### 3.2.1 Chandra

During the course of the Chandra mission, RX J0822–4300 has been observed on four occasions with the High Resolution Camera (HRC), the first of these in 1999 December. The first three observations have been already archived for several years. Because of the importance of RX J0822–4300 and the somewhat discrepant results found by HB06 and WP07, a new observation was proposed and carried out 2010 August, 10-11. The new observation was carried out as two consecutive ObsIDs, with exposure times of  $\sim 40$  and  $\sim 38$  ks, with no intervening repointing, so they we have merged the event data for these in our analysis, for a total exposure of 78.9 ks. All observations are summarized in Table 3.1.

**Table 3.1:** Chandra observations of the neutron star in Puppis A

Instrument	ObsId	Date (MJD)	ONTIME (sec)	Exposure Time (sec)
HRC-I	749	21/22 Dec 1999 (51533)	18014	9907
HRC-S	1859	25 Jan 2001 (51934)	19667	19524
HRC-I	4612	25 Apr 2005 (53485)	40165	21410
HRC-I	11819	10/11 Aug 2010 (55418)	33681	15509
HRC-I	12201	11 Aug 2010 (55419)	38680	17855

We downloaded fresh copies of the archived observations, and have reprocessed the events using the `chandra_repro` script. This and all subsequent analysis has been carried out using CIAO 4.4, and CALDB 4.4.8 to ensure that the latest corrections have been applied uniformly.

At the  $\sim 2$  kpc distance of Puppis A, a  $1000 \text{ km s}^{-1}$  transverse velocity of RX J0822–4300 would result in a proper motion of only  $\sim 0.1'' \text{ yr}^{-1}$ . Even for Chandra, whose absolute aspect resolution<sup>1</sup> is  $\sim 0.''6$ , the measurement of such a small proper motion is a challenge. Fortunately, there are three nearby X-ray sources whose positions are very well determined, since all correspond to optical stars in the UCAC3 (Zacharias et al., 2009) and 2MASS (Cutri et al., 2003) catalogs. Both HB06 and WP07 used these stars for astrometric correction in their analysis of the 1999 – 2005 data. We summarize their properties in Table 3.2 using the same nomenclature as in HB06. All three sources are detected with high significance in the 2010 observation. Using `wavedetect` we determined their position and count rates, including those of RX J0822–4300, as listed in Table 3.3. An image depicting their locations relative to RX J0822–4300 is shown in Fig. 3.2.

**Table 3.2:** Position, proper motion and angular distance of astrometric reference stars near to RX J0822–4300 as listed in the UCAC3 catalog (Zacharias et al., 2009).

Designation	3UCAC	Position (J2000.0)		Proper Motion		$\delta d$ arcmin
		R.A. (h m s)	DEC (d m s)	$\mu_{RA}$ mas yr <sup>-1</sup>	$\mu_{Decl}$ mas yr <sup>-1</sup>	
A	094-058669	08 21 46.292(1)	-43 02 03.64(5)	$-14.3 \pm 2.0$	$-3.6 \pm 5.5$	2.8
B	095-060051	08 22 24.003(3)	-42 57 59.37(2)	$0.0 \pm 4.0$	$10.2 \pm 2.0$	5.3

**Table 3.3:** Properties of the astrometric reference stars

ObsID	Epoch	Source	X-ray <sup>α</sup>		Counts	Rate cts/ks	Optical <sup>α</sup>	
			R.A. (h m s)	DEC (d m s)			R.A. (h m s)	DEC (d m s)
749	1999.97	NS	08 21 57.411(01)	-43 00 16.63(01)	2544	257.0		
		A	08 21 46.295(10)	-43 02 03.26(17)	46	4.6	08 21 46.292(01)	-43 02 03.64(02)
		B	08 22 24.008(25)	-42 57 59.58(17)	46	4.7	08 22 24.003(03)	-42 57 59.37(04)
		C	08 21 48.874(18)	-43 01 28.13(26)	13	1.3	08 21 48.876(06)	-43 01 28.33(09)
1851	2001.07	NS	08 21 57.390(01)	-43 00 16.91(01)	5005	256.5		
		A	08 21 46.316(09)	-43 02 03.77(11)	70	3.6	08 21 46.291(01)	-43 02 03.64(02)
		B	08 22 23.930(21)	-42 57 59.38(20)	139	7.1	08 22 24.003(03)	-42 57 59.36(04)
		C	08 21 48.880(17)	-43 01 28.62(28)	11	0.5	08 21 48.870(07)	-43 01 28.33(09)
4612	2005.31	NS	08 21 57.374(01)	-43 00 17.07(01)	5596	261.6		
		A	08 21 46.297(08)	-43 02 03.70(08)	91	4.3	08 21 46.285(02)	-43 02 03.66(05)
		B	08 22 24.006(11)	-42 57 59.60(23)	57	2.7	08 22 24.003(04)	-42 57 59.31(05)
		C	08 21 48.881(22)	-43 01 28.40(26)	7	0.3	08 21 48.849(10)	-43 01 28.32(11)
11819/12201	2010.61	NS	08 21 57.329(01)	-43 00 17.38(01)	9152	274.7		
		A	08 21 46.268(08)	-43 02 03.93(07)	132	4.0	08 21 46.279(03)	-43 02 03.68(08)
		B	08 22 23.979(13)	-42 57 59.60(23)	96	2.9	08 22 24.003(07)	-42 57 59.26(06)
		C	08 21 48.853(22)	-43 01 28.68(17)	21	0.6	08 21 48.822(14)	-43 01 28.31(15)

**Notes.** <sup>(α)</sup>  $1\sigma$  uncertainty of the last two digits in parentheses.

<sup>1</sup><http://cxc.harvard.edu/cal/ASPECT/celmon/>

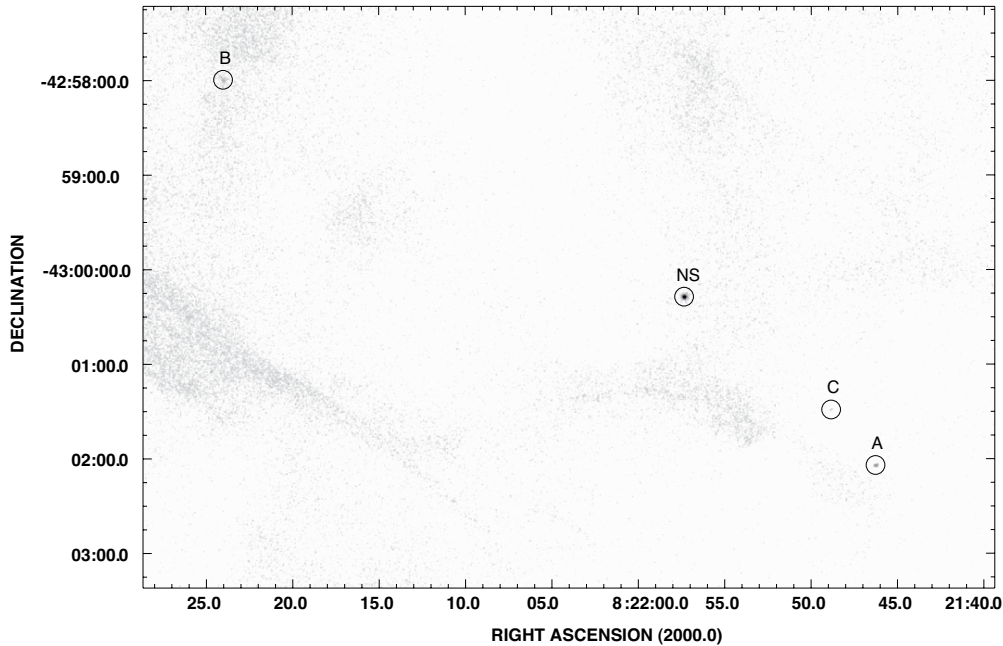


**Figure 3.2:** The 2010 epoch Chandra HRC-I image with reference sources and RX J0822–4300 marked by circles. NS marks the position of RX J0822–4300; A, B and C that of the fiducial stars used as local calibrators for absolute astrometry. The field measures 6 by 9 arcmin and is oriented north up, east left.

In order to achieve the highest accuracy in measuring the proper motion of RX J0822–4300, we followed the method described in §3.4 of WP07 with some improvements: we first measured the X-ray positions of RX J0822–4300 and the reference stars A, B, and C in each of the three archival datasets and in the 2010 observation (§3.2.1). The X-ray and optical positions of the stars were then used to transform the respective images of each observation to an absolute reference frame (§3.2.1). This procedure is necessary in order to include the HRC-S observation into our analysis, as there are small systematic effects and offsets in the rotation between the HRC-I and HRC-S detectors (WP07). The transformation coefficients determined this way were then used to derive the position of the neutron star at the corresponding epoch. We calculate the error budget exactly, rather than use the approximate method of WP07, which leads to somewhat larger errors for the corrected X-ray positions of RX J0822–4300 in the 1999 – 2005 data when compared to their work.

### Spatial analysis

In order to determine the position of the three reference stars and RX J0822–4300 we first generated a point-spread function (PSF) for every source in each of the four observations. This is required as the PSF broadens for sources at larger off-axis angles, leading to a larger position uncertainty when using the `wavedetect` tool. These positions were then used as input to

*ChaRT*,<sup>2</sup> which computed the PSF for a point source at any off-axis angle. The computations were performed by generating 10 rays  $\text{mm}^{-2}$  for a peak energy of either 1.5 keV (WB & TP, the same as used by HB06) or 1.0 keV (FW, as in WP07); the resulting PSFs are virtually identical. The rays were then projected onto the HRC detector using *Marx*<sup>3</sup> to create an image of the PSF.

We obtained best-fit positions for all three reference stars and for RX J0822–4300 at each of the epochs using *Sherpa*, Chandra’s modeling and fitting package.<sup>4</sup> We followed the *Sherpa* thread “Accounting for PSF Effects in 2D Image Fitting”, in which a simulated PSF is convolved with an assumed source model to produce the best fit to the actual observational data. For each of the sources, we used a 2-D Gaussian model whose width was fixed at a small value—in most cases equal to the bin size used in the images—so that small intrinsic fluctuations in different PSFs and in the data did not lead to divergence. In our independent analyses, we used binnings of  $0.5 \times 0.5$  and  $1 \times 1$  pixel for RX J0822–4300, and  $1 \times 1$  and  $2 \times 2$  pixels for stars A, B, and C. In each case a PSF was constructed with *Marx* to match the bin size for the data. Because of the relatively low count rates for the three reference stars, we used the C-statistic to measure the goodness of fit. To obtain uncertainties, we used the *Sherpa* procedure `reg_proj` to map out  $1\sigma$ , 90%-confidence, and  $2\sigma$  contours in  $(x, y)$  detector coordinates. In every case, the best fits obtained with different binning choices were consistent, but smaller bin sizes generally gave somewhat smaller uncertainties.

Early in our data analysis we found a subtle software bug in the *Sherpa* package for CIAO version 4.3. By default *Sherpa* was using the brightest pixel in the PSF-image as the reference point for the convolution, regardless of the PSF-input-position specified to the task at the command line. For near on-axis sources, the brightest pixel is always very close to the nominal PSF center, but there can be significant displacements for a source that is a few arcminutes off-axis, with direction differences that depend on roll angle. This bug appears to be a long-standing one, and was apparently at work in the analysis reported in WP07, for two of us (WB & TP) were able to approximately reproduce those results for the 1999-2005 data. (HB06 used a different approach that did not involve PSF fits, so the result they reported was not affected.)

The Chandra Help Desk was able to identify this bug and eventually provided us with a workaround,<sup>5</sup> which WB & TP have then used for all subsequent analysis. This workaround has been incorporated into CIAO version 4.4, which PFW has used to give essentially identical results. There are other differences between both the 2006-07 analyses and the present one that relate to the data themselves. Subsequent to the earlier analyses, there has been a complete reprocessing of all the Chandra data. Differences include use of improved aspect files and updated values for the degap corrections, detector gain, and the telescope effective focal length. As noted earlier, the present analysis has incorporated all the current wisdom regarding telescope and instrument performance.

The fitted X-ray positions of RX J0822–4300 (labeled as NS) and that of the three fiducial reference stars are listed for each of the four observations in Table 3.3, along the respective HRC counting rates.

<sup>2</sup>Chandra Ray Tracer, <http://cxc.harvard.edu/chart/index.html>

<sup>3</sup><http://space.mit.edu/CXC/MARX/>

<sup>4</sup><http://cxc.harvard.edu/sherpa/>

<sup>5</sup>see <http://cxc.harvard.edu/sherpa/bugs/psf.html>

### Transformation to the world coordinate system (WCS)

In order to determine the position of RX J0822–4300 relative to the three reference stars we assume a linear transformation with four free parameters: translations in Right Ascension,  $t_{RA}$ , and in Declination,  $t_{Decl}$ , a scale factor  $r$ , and a rotation of the detector  $\theta$ . The transformation can be expressed in the following way:

$$\begin{pmatrix} x_A & -y_A & 1 & 0 \\ y_A & x_A & 0 & 1 \\ x_B & -y_B & 1 & 0 \\ y_B & x_B & 0 & 1 \end{pmatrix} \begin{pmatrix} r \cos \theta \\ r \sin \theta \\ t_{RA} \\ t_{Decl} \end{pmatrix} = \begin{pmatrix} x'_A \\ y'_A \\ x'_B \\ y'_B \end{pmatrix}, \quad (3.1)$$

where  $x_i, y_i$  is the x-, and y-position of star  $i$  in the HRC image at epoch  $T$  and  $x'_A, y'_A$  are the corresponding optical coordinates of star  $i$ . These coordinates are given by the UCAC3 catalog and are corrected for proper motion (see Table 3.2 and Table 3.3). We used stars A and B to calculate the transformation and star C to verify the resulting parameters. Multiplying equation 3.1 with the inverse of the matrix leads to the missing parameters  $t_x, t_y, r$  and  $\theta$ . The position of RX J0822–4300 at epoch  $T$  can then be calculated straightforwardly by the following equation:

$$\begin{pmatrix} x'_{NS} \\ y'_{NS} \end{pmatrix} = \begin{pmatrix} r \cos \theta & -r \sin \theta \\ r \sin \theta & r \cos \theta \end{pmatrix} \begin{pmatrix} x_{NS} \\ y_{NS} \end{pmatrix} + \begin{pmatrix} t_{RA} \\ t_{Decl} \end{pmatrix}. \quad (3.2)$$

Calculating the transformation gives a rotation angle  $\theta$  of  $-0.061(31)^\circ$ ,  $0.076(28)^\circ$ ,  $-0.018(27)^\circ$  and  $0.000(29)^\circ$  and a scale factor  $r$  of 1.00059(60), 1.00182(52), 1.00044(40) and 1.00033(45) for the epochs 1999.97 (HRC-I), 2001.07 (HRC-S), 2005.31 (HRC-I) and 2010.61 (HRC-I), respectively (numbers in parentheses represent the uncertainty in the final digits). The values of  $r$  and  $\theta$  for the HRC-I observations match within the  $1\sigma$  error and are significantly smaller than these for the HRC-S observation.  $t_{RA}$  and  $t_{Decl}$  used in the translations of the position of RX J0822–4300 from the image- to the world coordinate system are all below  $0.5''$ . Indeed, the largest shift is  $0.29''$  for the y-coordinate in the 2010 HRC-I observation. The positions of the neutron star in the four epochs are listed in Table 3.4.

To estimate the error in the coordinates of RX J0822–4300, we used the Gaussian elimination algorithm to solve equation 3.1 for  $t_x, t_y, r$  and  $\theta$ . We then inserted these parameters into equation 3.2. This results in equations for  $x'_{NS}$  and  $y'_{NS}$  that depend only on values with known errors:  $x_A, y_A, x_B, y_B, x'_A, y'_A, x'_B, y'_B, x_{NS}$  and  $y_{NS}$ . The uncertainties in these two neutron star coordinates at each epoch can then be derived through straightforward error propagation:

$$\sigma_{x'_{NS}} = \sqrt{\left(\frac{\partial x'_{NS}}{\partial x_A}\right)^2 \sigma_{x_A}^2 + \left(\frac{\partial x'_{NS}}{\partial y_A}\right)^2 \sigma_{y_A}^2 + \dots + \left(\frac{\partial x'_{NS}}{\partial y_{NS}}\right)^2 \sigma_{y_{NS}}^2} \quad (3.3)$$

The same formula is applicable for  $\sigma_{y'_{NS}}$ . The corresponding values are listed in parentheses in Table 3.4.

To check the robustness of our results we applied several cross-checks. We first repeated the transformation using the fiducial points B & C rather than A & B. The positions of RX J0822–4300 obtained this way are also listed in Table 3.4 for comparison. As can be seen, they have

**Table 3.4:** Positions of RX J0822–4300

Epoch	Ref. Stars	R.A. <sup>α</sup> (h m s)	DEC <sup>α</sup> (d m s)
1999.97	A & B	08 21 57.403(11)	-43 00 16.80(13)
	B & C	08 21 57.409(16)	-43 00 16.72(21)
2001.07	A & B	08 21 57.398(10)	-43 00 16.74(10)
	B & C	08 21 57.403(15)	-43 00 16.65(22)
2005.31	A & B	08 21 57.363(08)	-43 00 16.93(10)
	B & C	08 21 57.349(19)	-43 00 16.92(22)
2010.61	A & B	08 21 57.343(08)	-43 00 17.08(11)
	B & C	08 21 57.312(21)	-43 00 16.99(18)

**Notes.** <sup>(α)</sup>  $1\sigma$  uncertainty of the last two digits in parentheses.

larger errors than using the reference stars A & B (because star C has only a few counts at each epoch) but match the other positions within the  $1\sigma$  uncertainty range. Using the combination of stars A & C rather than A & B leads to large errors, as A and C are located quite close to one another and are in approximately the same direction relative to RX J0822–4300. In a third test we calculated the position of RX J0822–4300 by applying only a two-dimensional translation of the four images. We weighted the shifts of the three reference stars inversely as the variance and calculated their mean for every epoch. The results for the position of RX J0822–4300 differ for the HRC-I observations by at most 0.4 pixel from the ones calculated according to equation 3.1. For the HRC-S image the difference in x is  $\approx 1$  pixel, though this is mainly due to systematic offsets between the HRC-S and HRC-I detectors. This is also seen if we compare the scale factors and rotation angles which we computed for the HRC-I and HRC-S observations.

### 3.2.2 XMM-Newton

The western part of the Puppis A SNR was observed with the EPIC cameras (Strüder et al., 2001) on board of the X-ray observatory XMM-Newton (Obs.ID 0303530101) for 38.2 ksec. The two MOS and the PN camera were operated in full-frame mode using the thin filter. We used the XMM SAS version 12.0.1 to reprocess and reduce the data. The observation was affected by high particle background radiation. Therefore, times of high background activity were identified by inspecting the light curves of the MOS1/2 and PN data at energies above 10 keV. After removing these times, the net exposures of the PN, and MOS1/2 cameras were 6.9 ksec, and 10.6 ksec, respectively.

For the spectral fitting, we used the X-Ray Spectral Fitting Package (XSPEC) version 12.7.0u. Single and double events were selected from the PN data and single to quadruple events from the MOS data sets. Below 0.4 keV, the detector and telescope response is not well established and hence, we excluded this range from the spectrum.

### 3.2.3 Optical

The western part of Puppis A was observed with the Wide Field Imager (WFI) at the 2.2 m MPG/ESO telescope at La Silla, Chile on March 2012, 14-15. The exposures were taken with the  $H_\alpha$  + [NII], [SII], and [OIII] filters for 10800 s, 3600 s, and 3600 s. In addition, the same region was observed with the broadband filters for the visual and red band with an exposure time of 300 s.

For the reduction of the data we made use of the Theli package<sup>6</sup> (Erben et al., 2005). All frames were bias-subtracted and flat-field-corrected using a set of flat-field taken in twilight. Furthermore, a superflat was generated and a collapse-correction was applied. All observations were taken in photometric nights with a seeing between 0.''7 and 0.''9.

All given uncertainties represent the  $1\sigma$  confidence range for one parameter of interest, unless stated otherwise.

## 3.3 Results

### 3.3.1 The proper motion of RX J0822–4300

To measure the proper motion of RX J0822–4300 over a baseline of 3886 days we used all four positions obtained from the observations between 1999.97 and 2010.61 and fitted a linear function to  $x'_{NS}(T)$  and  $y'_{NS}(T)$  separately:

$$x'_{NS}(T) = \mu_x T + const_x, \quad (3.4)$$

$$y'_{NS}(T) = \mu_y T + const_y. \quad (3.5)$$

In these fits the projected proper motion coordinates  $\mu_x$  and  $\mu_y$  were taken as free parameters for which we find  $\mu_{RA} = -63.6 \pm 11.9 \text{ mas yr}^{-1}$  and  $\mu_{Decl} = -31.2 \pm 13.2 \text{ mas yr}^{-1}$ , implying a total proper motion of  $\mu_{tot} = 71 \pm 12 \text{ mas yr}^{-1}$ . For the position angle we find  $244 \pm 11$  degrees, in excellent agreement with the position angle of 243 degrees as implied by the location of the optical expansion center (Winkler et al., 1988). The corresponding transverse space velocity for RX J0822–4300 is  $(672 \pm 115)d_2 \text{ kms}^{-1}$ , scaled relative to a distance of  $d_2 = d/2$  kpc.

Figure 3.3 shows the actual data for RX J0822–4300 at the three HRC-I epochs, after alignment to a common coordinate system, and Figure 3.4 shows the progression of RX J0822–4300 and the linear fit to its positions as measured by Chandra.

### 3.3.2 Is there a second supernova remnant in Puppis A?

#### X-ray emission

Five regions were selected for spectral analysis: Region 1 and 5 were used for extracting the spectrum of the peculiar feature, region 2 and 4 for the spectrum of Puppis A and region 3 for the spectrum of the central bright emission region. This is illustrated in Figure 3.5. All spectra were

<sup>6</sup>See <http://www.astro.uni-bonn.de/theli/>.

**Figure 3.3:** This enlargement of the immediate region of RX J0822–4300 shows the data from all three HRC-I epochs (after alignment to a common coordinate system) in different colors. The neutron star’s motion is apparent.

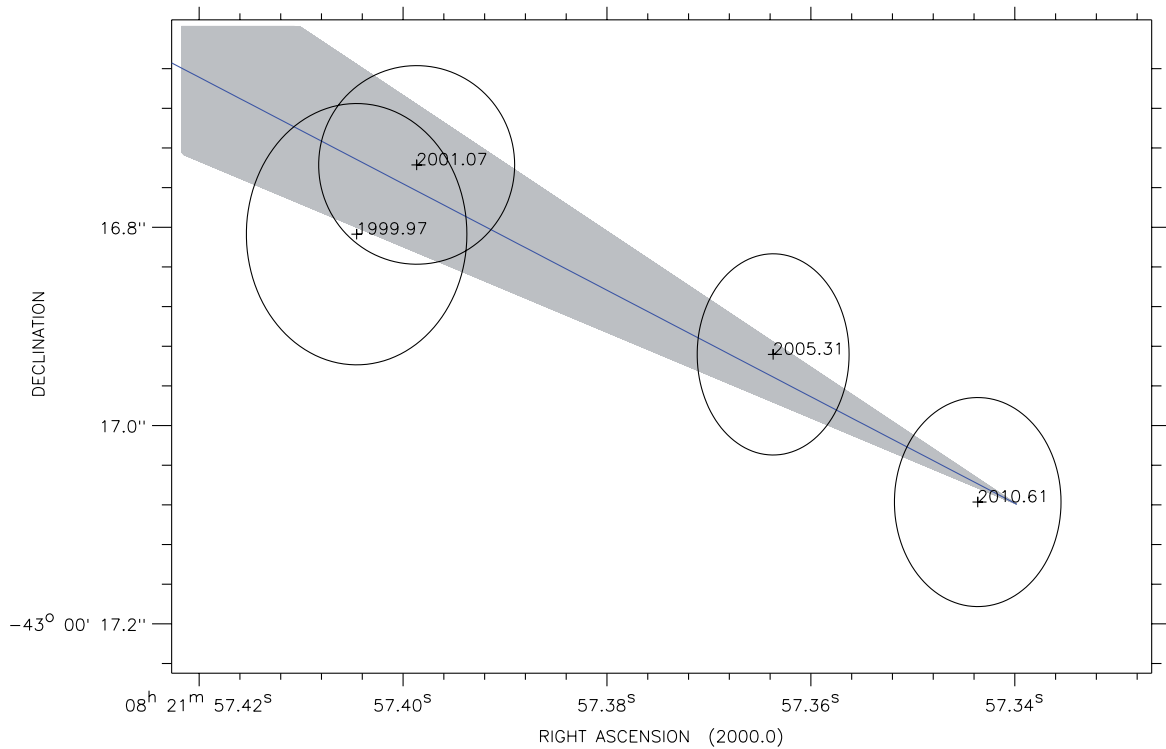
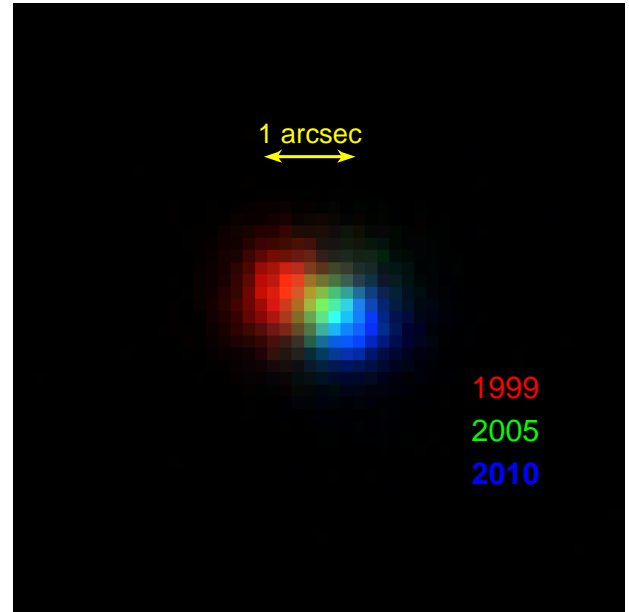


**Figure 3.4:** Four positions of RX J0822–4300 measured over a baseline of 3886 days. Their  $1\sigma$  position uncertainty is indicated. Observation dates are labeled. The gray shaded bar depicts the direction to the remnant’s optical expansion center, i.e. to the birth place of RX J0822–4300. The straight blue line indicates the CCO’s proper motion path as fitted from the four positions. The proper motion direction is from the upper left to the lower right.

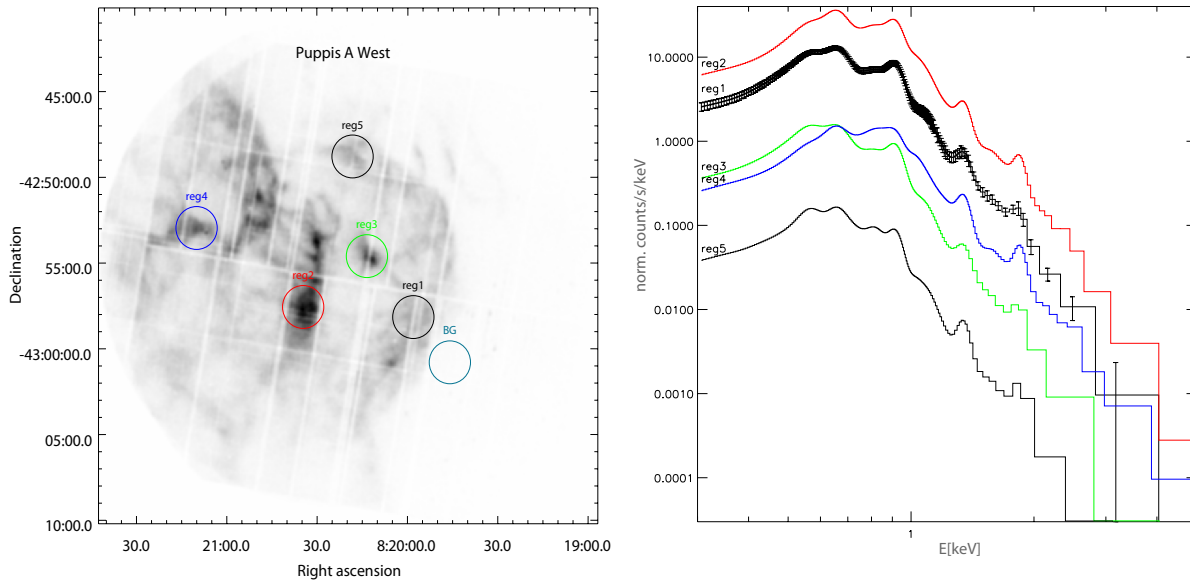


**Figure 3.5:** Left: X-ray image of the western part of SNR Puppis A. The regions for spectral analysis and the background region are indicated by circles. Right: Model spectra of the five selected regions. To show the difference between the spectral shapes the spectra of region 2 to 5 were scaled by an arbitrary factor. In addition, for the spectrum of region 1 the error bars of the data are indicated. The colors used here correspond to the colors of the circles on the left.

fitted with a constant temperature, plane-parallel shock plasma model (in XSPEC VPSHOCK) as used by Katsuda (2003) when studying the X-ray emission of Puppis A. The results are listed in Table 3.5.

The element abundance was studied in detail to find clear differences in the emission properties between the regions of interest and the Puppis A SNR. For that reason emission-line equivalent width (EW) images were created by following the method described in Hwang et al. (2000) and Park et al. (2002). The resulting images in the lines of O Ly $\alpha$ , Fe L, Ne He $\alpha$ , Mg He $\alpha$ , Si He $\alpha$ , and S He $\alpha$  are shown in Figure 3.6. For the image generation the same energy bands for the selected lines and the underlying continuum are used as in Katsuda (2003). All images are binned with 20'' and smoothed by a Gaussian kernel with  $\sigma = 60''$ .

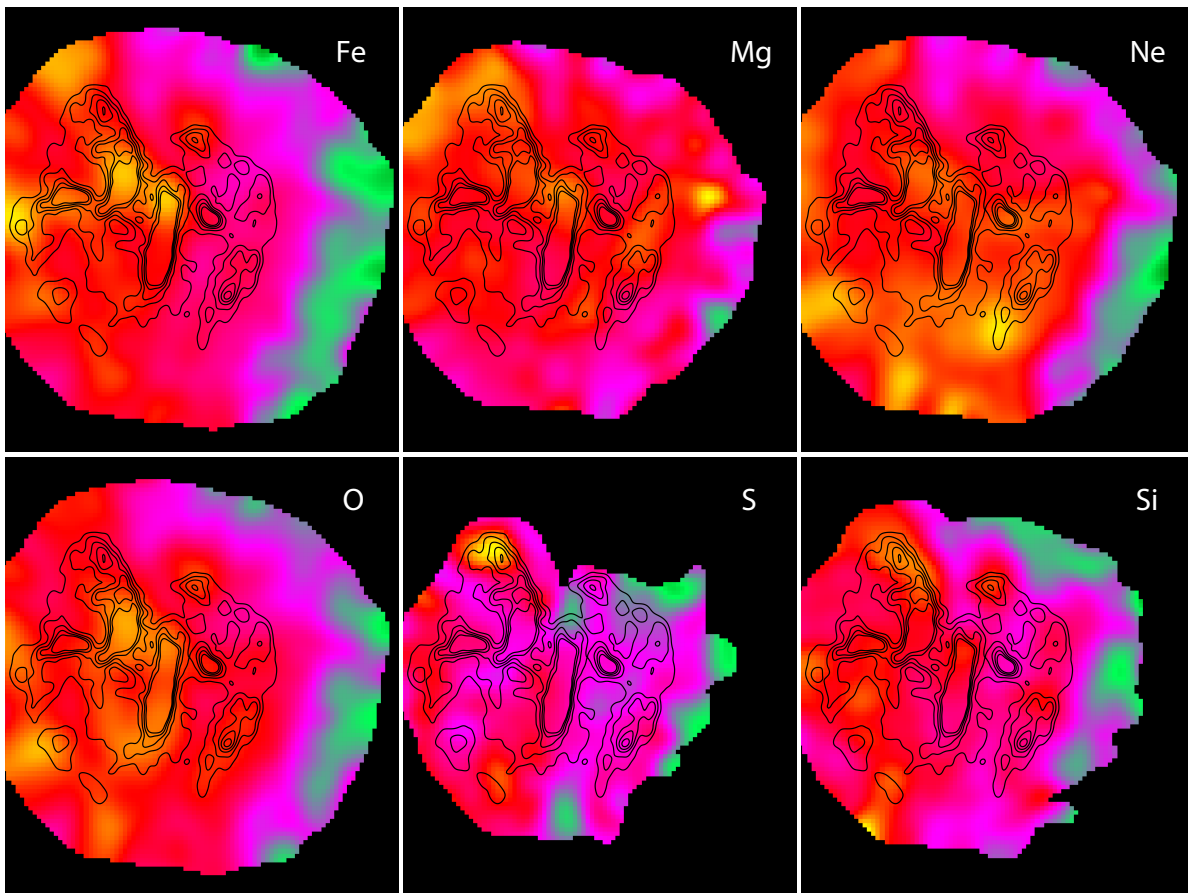
### Optical emission

Figure 3.7 shows images of the western part of Puppis A taken with the H $\alpha$  + [NII], [SII], and [OIII] filters. Here the continuum emission was subtracted following the method described in Waller (1990) in order to allow a clear detection of the filament structure. In all three images no difference in the strength and size of the filaments between the region of interest and the optical bright region in the south-east of the image can be seen.

**Table 3.5:** Spectral parameters of the best-fit models for different regions in the western part of Puppis A.

#	$N_{\text{H}}$ [ $10^{22}\text{cm}^{-2}$ ]	$k_{\text{B}}T$ [keV]	$\tau^{\alpha}$ [ $10^{11}\text{s/cm}^3$ ]	C/N/O/Ne/Mg/Si/Fe $^{\beta}$	Norm $^{\gamma}$ [ $10^{-2}\text{cm}^{-5}$ ]	$\chi^2/\text{d.o.f.}$
1	$0.47 \pm 0.01$	$0.34 \pm 0.01$	$0.9 \pm 0.1$	3.1(5)/1.4(1)/1.0(-)/1.0(-)/0.4(1)/0.5(1)/0.4(1)	$4.1 \pm 0.4$	645/350
2	$0.34 \pm 0.01$	$0.43 \pm 0.01$	$1.3 \pm 0.1$	1.0(-)/0.3(1)/0.5(1)/0.8(1)/0.4(1)/0.4(1)/0.3(1)	$5.7 \pm 0.4$	1307/457
3	$0.35 \pm 0.01$	$0.28 \pm 0.01$	$2.2 \pm 0.3$	1.7(3)/0.9(1)/0.7(1)/1.0(-)/0.4(1)/0.8(1)/0.4(1)	$3.6 \pm 0.5$	594/334
4	$0.28 \pm 0.01$	$0.55 \pm 0.01$	$1.4 \pm 0.1$	1.0(-)/0.2(1)/0.4(1)/0.7(1)/0.5(1)/0.6(1)/0.4(1)	$2.3 \pm 0.2$	787/443
5	$0.38 \pm 0.01$	$0.31 \pm 0.01$	$1.2 \pm 0.2$	4.2(5)/1.1(1)/1.0(-)/1.0(-)/0.5(1)/0.7(1)/0.7(1)	$2.7 \pm 0.3$	434/258

**Notes.**  $(^{\alpha})$  ionization timescale  $(^{\beta})$  Abundance with respect to the solar value, truncated to the first decimal digit. A – indicates that no deviation from solar abundance was inferred.  $(^{\gamma})$  Norm =  $\frac{10^{-14}}{4\pi[D_{\text{A}}(1+z)]^2} \int n_{\text{e}}n_{\text{H}}dV$ , where  $D_{\text{A}}$  is the angular diameter distance to the source in cm and  $n_{\text{e}}$  and  $n_{\text{H}}$  are the post-shock electron and hydrogen densities in  $\text{cm}^{-3}$ , respectively.

**Figure 3.6:** EW images for O Ly $\alpha$ , Fe L, Ne He $\alpha$ , Mg He $\alpha$ , Si He $\alpha$ , and S He $\alpha$  scaled with increasing intensity from green to yellow. All images are overlaid with the XMM-Newton X-ray contours.

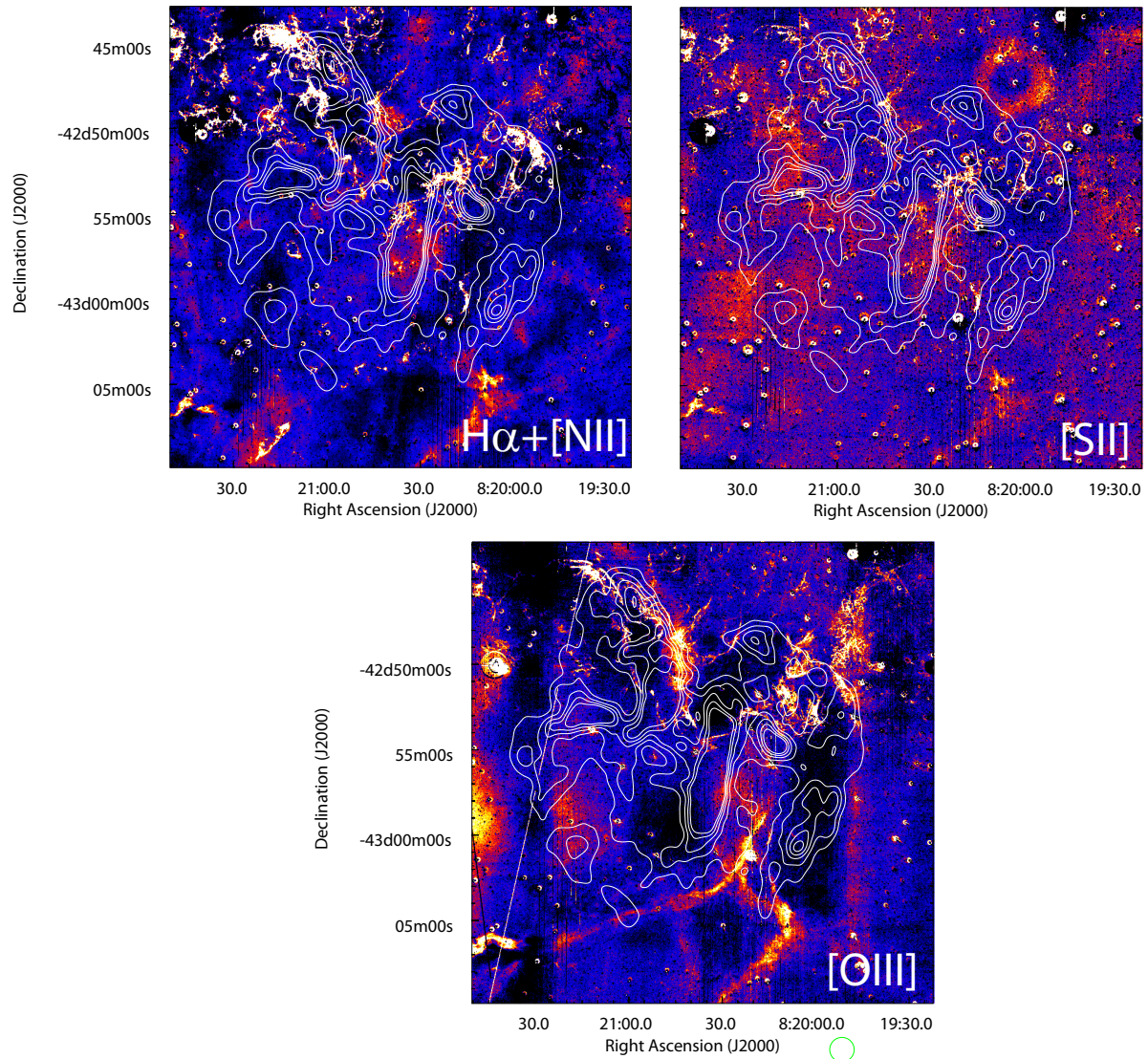


**Figure 3.7:** The western part of Puppis A observed at a wavelength around the  $H\alpha + [NII]$ ,  $[SII]$ , and  $[OIII]$  emission line. The filaments are shown in yellow. All images are overlaid with the XMM-Newton X-ray contours.

### Radio, infrared and $\gamma$ -ray emission

Using data from the Sydney University Molonglo Sky Survey (SUMSS, Bock et al., 1999) at 843 MHz we found an arc matching the southern feature. However, no difference to the emission from the whole remnant is observable. In addition, data from the Wide-field Infrared Survey Explorer (WISE, Wright et al., 2010) was used to investigate the region in the infrared regime at  $22 \mu\text{m}$ . The infrared and X-ray emission region of the western edge have a perfect match and no difference is noticeable. Furthermore, the Puppis A SNR can be seen in  $\gamma$ -rays with the Fermi Large Area telescope (Hewitt et al., 2012). Therefore, we inspected the Fermi archive, but no emission in this region can be seen.

## 3.4 Summary

Two previous proper motion measurements of RX J0822–4300, incorporating the same Chandra HRC data sets, produced discrepant results. HB06 found a proper motion of  $104 \pm 35 \text{ mas yr}^{-1}$  at a position angle of  $240^\circ \pm 28^\circ$ . WP07, using a different analysis approach, found a considerably higher value of  $165 \pm 25 \text{ mas yr}^{-1}$  at a position angle of  $248^\circ \pm 14^\circ$ . A combined analysis, incorporating a new deep observation and a total time baseline twice as long as available previously, yields an improved value that is smaller than either of the two published numbers, but at a position angle consistent with both. We now find with high confidence a value for the proper motion of  $71 \pm 12 \text{ mas yr}^{-1}$  at a position angle of  $244^\circ \pm 11^\circ$ . For an assumed distance to Puppis A of 2 kpc, the proper motion corresponds to a tangential velocity of  $672 \pm 115 \text{ km s}^{-1}$ . This smaller velocity eases most challenges that RX J0822–4300 previously posed to pulsar-kick models, but still requires a hydrodynamic kick model in a highly asymmetric explosion. Considering the proper motion based age estimate as a second and independent measurement to the one inferred from the motion of optical filaments, it can be averaged to  $4450 \pm 750 \text{ yrs}$  which implies that Puppis A is slightly older than the generally accepted 3700 yrs.

Furthermore, after studying the western part of the Puppis A SNR in the radio, infrared, optical, X-ray, and  $\gamma$ -ray regime there is no single evidence that the western sphere-like structure is different to the Puppis A SNR. This feature belongs to the Puppis A SNR and the sphere-like shape is probably evolving in a bubble in the highly inhomogeneous medium surrounding the remnant.

The detailed discussion of the results is presented in Chapter 8.

## Chapter 4

# Supernova remnant candidates in the ROSAT All-Sky Survey

This chapter is adopted from a paper draft, which will be submitted to *Astronomy & Astrophysics*.

### 4.1 Introduction

Supernovae (SNe) mark the end of stellar evolution of massive stars as well as the beginning of stellar evolution by enrichment and decompression of the interstellar medium. Our solar system showing imprints in metal abundance of an SN is a very good example for this process (Gritschneider et al., 2012). Thus, it is crucial to understand the processes happening in such cataclysmic events.

However, only seven Galactic supernovae have been observed with historical records in the past two millennia – SN 185 (RCW 86), SN 386 (G11.2–0.3), SN 1006, SN 1181 (3C58), Crab SN, Tycho SN, and the Kepler SN. Ancient Chinese astronomers recorded several other guest stars, but for most of them no solid identification with a known supernova remnant has been possible so far (Green and Stephenson, 2003). Moreover, in the last 400 years no SN has been directly observed in our Galaxy (Green and Stephenson, 2003). A reason for that is the interstellar dust which leads to visible-band extinction of the supernova. For example, the supernova Cassiopeia A (Cas A) which exploded about 300 years ago may belong to this group. No widespread reports of Cas A exist in the literature of the 17th century (cf. Hartmann et al., 1997). A more recent example is the youngest supernova known in our Galaxy, G1.9+0.3, which was totally missed by optical observatories about 100 years ago (Reynolds et al., 2008).

Therefore, the best possibility to study SN is to observe their remnants which are detectable for more than  $10^4$  years (e.g., SNR W28 has an age of  $\approx 3.6 \times 10^4$  yrs and is detected in X-rays (Rho and Borkowski, 2002)) over a large range of the electromagnetic band: First, from the emission of the remnant in the radio band which is mostly caused by synchrotron radiation to the emission in the infrared band by, for example, stochastically or thermally heated dust (Pinheiro Gonçalves et al., 2011). Second, from optical emission due to the cooling of shocked

interstellar cloud material in the case of evolved remnants (Fesen et al., 1985) to ultraviolet and X-ray emission which arises from thermal radiation (Blair et al., 2006). And finally emission in the high energy regime up to 1 TeV (see Reynolds (2008) for more details about the different emission mechanism). Up to now 274 supernova remnants in our Galaxy are known. However, the majority of supernova remnants that have been identified so far were found in radio surveys in which the observations are unhampered by interstellar dust (Green, 2009, and references therein).

However, the expected rate of SN in our Galaxy is 1 to 3 per century (Keane and Kramer, 2008). Assuming that the lifetime of an SNR in which it is bright enough to be detected is a few 10 to 100 kyrs there is a discrepancy by a factor of 2 to 5 between observed and expected SNRs. As the SNR rate is well established the discrepancy is probably explained by the fact that the radio sample of SNR is not complete. Physical reasons which may prevent a remnant from being radio bright and hence being missed in radio surveys are for example:

- An SN-shock wave, which expands within the hot phase of the ISM and reaches a very large diameter until it has swept up sufficient mass from the low density gas to form a radio shell. In this case density inhomogeneities in such a large volume will cause distortions in the shell and make the identification as an SNR rather difficult, in particular in the presence of confusing unrelated emission from the same area.
- An SN-shock wave, which expands in a very dense medium would result in a rather short SNR life-time, because material is quickly swept up and decelerated. Such an environment is likely to be relevant, e.g., for massive star members of OB-associations that are surrounded by dense molecular clouds and warm gas. Even during their short lifetime such events are difficult to identify within the strong thermal radio emission from those regions.

Given these selection effects in radio surveys and the detection of previous unknown SNR in the X-ray band (e.g., Pfeffermann and Aschenbach, 1996; Busser et al., 1996; Asaoka and Aschenbach, 1994; Asaoka et al., 1996; Egger et al., 1996; Folgheraiter et al., 1996) it was an obvious task to start searching for SNR and SNR candidates in the X-ray band by using the ROSAT All-Sky survey. It was the first all-sky survey performed with an imaging X-ray telescope. Bußer (1998) found  $\approx 400$  SNR candidates in the RASS data, which Schaudel et al. (2002) reduced to 210 candidates after a re-processing of the RASS data and a correlation with various multi-wavelength source catalogs. The RASS re-processing with more stringent parameters removed many spurious sources from the data and thus provided a clearing of the candidate list (Voges et al., 1999). From their candidate list several sources have meanwhile been confirmed as SNR (Jackson et al., 2008; Prinz and Becker, 2013; Roberts and Brogan, 2008; Stupar et al., 2007; Tian et al., 2010; Prinz and Becker, 2012; Brogan et al., 2006). Moreover, Schaudel (2003) claimed the identification of another SNR designated with G38.7-1.4 in the RASS data with the help of a deep radio observation with the Effelsberg 100 m telescope.

In the last ten years new sky surveys in various wavelength regimes were conducted and X-ray telescopes with better spatial and spectral resolution were launched. Therefore, we re-analyzed the candidate list of Schaudel et al. (2002) in this work. In Section 4.2 we describe the used observations and data reduction. In Section 4.3 we present a detailed analysis of selected

candidates with archival pointed X-ray observations and the correlation of the remnant candidates with catalogs and images in the radio, infrared, optical,  $H_\alpha$ , UV and  $\gamma$ -ray band. In the same section the final candidate list and a detailed description of promising and identified candidates is given. In Section 4.4 we conclude by focusing on the future prospects of this project.

## 4.2 X-ray observations and data analysis

The X-ray data used in this paper originate from the ROSAT All Sky Survey, observed with the Position Sensitive Proportional Counter (PSPC, Briel and Pfeffermann, 1986). The PSPC provided a moderate energy resolution of 0.43 keV at 0.93 keV, a field-of-view of  $2^\circ$  and a spatial resolution of  $\sim 25''$  in pointing mode (Briel and Pfeffermann, 1986). The detector was sensitive to incoming photons with an energy of 0.1 to 2.4 keV, best suited for the search for new SNR, because the expected temperature of these objects ranges from several million Kelvin for evolved remnants to  $\sim 10^7$  K for young SNRs.

The RASS was the first all-sky with an imaging telescope in the soft X-ray band. The main part of the survey was carried out in 1990 and 1991. The exposure times varied between  $\sim 400$  and 40 000 s in the ecliptic plane and the poles (Voges et al., 1999). Furthermore, the average spatial resolution expressed in form of FWHM (full width at half maximum) in the scan mode was approximately  $90''$  (Boese, 2000). We used the archival RASS data reprocessed with the Standard Analysis Software System III (SASS III) version 8.2.0.<sup>1</sup>

To identify the supernova remnant candidates in the RASS images we first created a list of extended (with a diameter  $d \geq 5'$ ) and unidentified X-ray sources which are at low Galactic latitude ( $|b| \leq 15^\circ$ ) based on the analysis of Bußer (1998) and Schaudel (2003). In addition, this list contains the objects, which Schaudel (2003) claimed to be no SNRs. The net counting rate for the SNR candidates were obtained by subtracting the background events from the events extracted in an ellipse around the source position and dividing by the effective exposure time. In some cases we had to adjust the position of Schaudel (2003) because the morphology of some sources changed slightly in the SASS III processing. The background contribution was calculated by averaging the counts of six regions around the source position which had the same area as the region used for extracting the source counts and had no other sources in it.

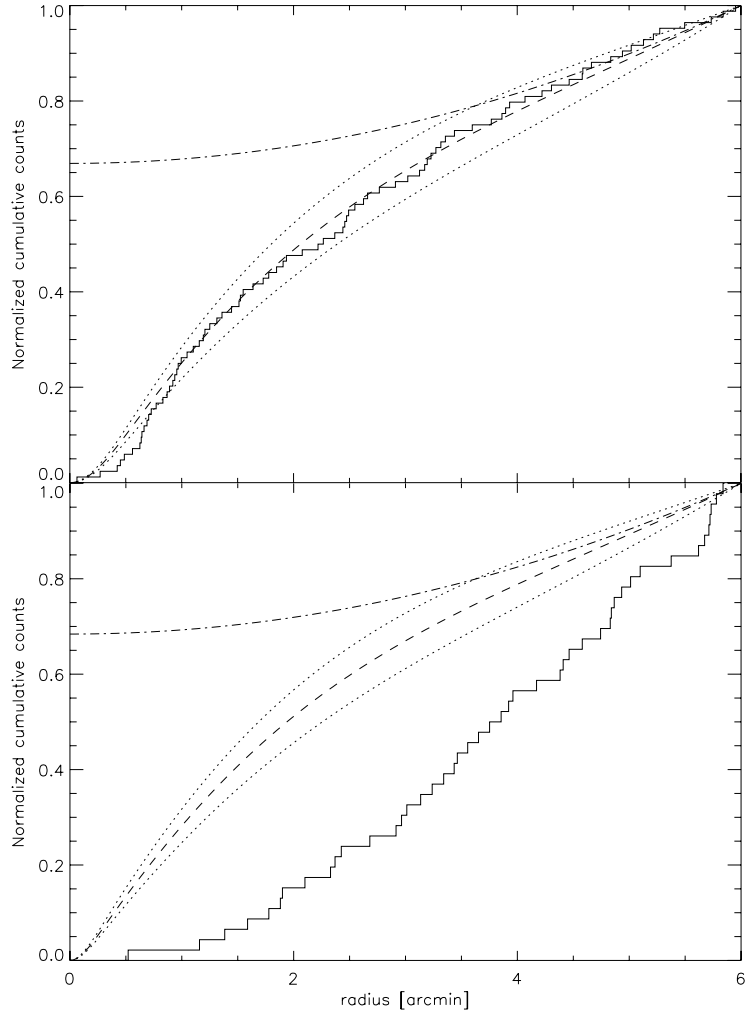
The relative low exposure of a few hundred seconds for most parts of the Galactic disc and the poor spatial resolution of the RASS data do not allow for a qualitative spectral analysis of these sources in order to identify them as SNR by their X-ray morphology and spectral source properties. Therefore, only a quantitative study could be performed to discriminate between e.g., Galactic and extragalactic background sources.

First, we determined if the sources are indeed extended or seemingly extended spherical sources in the RASS. For that we applied the growth curve analysis (GCA) of Böhringer et al. (2000) which was designed to characterize Galaxy Clusters (GCs) in the RASS. The GCA method determines the probability of a source to be extended. This is done by comparing

---

<sup>1</sup>Access to various public archives of X-ray observatories under <http://heasarc.gsfc.nasa.gov/cgi-bin/W3Browse/w3browse.pl>

**Figure 4.1:** Comparison of the cumulative photon count profile for G337.2+13.0 (*upper panel*) and G38.7–1.4 (*lower panel*) with the expected profile for a point source including the background contribution (dashed line). The dotted lines indicate the expected profile with a variation of the background of  $\pm 30\%$  and the dashed dotted line shows the background contribution. All profiles are normalized to 1 at the outer radius of  $\delta'$



the expected cumulative count profile for a point source including the background contribution with the cumulative and unbinned photon count profile of the source with the help of the Kolmogorov-Smirnov (K-S) test. The expected profile of the ROSAT RASS point-spread-function was taken from Boese (2000). The probability of the source extend  $P_{\text{ext}}$  is then defined as  $P_{\text{ext}} = -\log_{10}(\text{K-S probability})$  and the energy band with the highest signal-to-noise ratio was used for the calculation. Only those sources with  $P_{\text{ext}} > 2$  were kept in the list of SNR candidates. This criterion was used for RASS selected GCIs and results in a misclassification rate of about 5% (Böhringer et al., 2000). Two examples are shown in Figure 4.1. In the upper diagram the X-ray count profile of 2MASS J15472911–3754587 is plotted, which was listed in Schaudel (2003) as SNR candidate G337.2+13.0 and identified as point source with an archival ROSAT HRI observation. In the lower panel the profile of G38.7–1.4 can be seen, which is a very promising candidate (Schaudel et al., 2002). The probability of the source extend is  $P_{\text{ext}} = 0.3$  for G337.2+13.0 and  $P_{\text{ext}} = 6.9$  for G38.7–1.4 in the soft and hard ROSAT band, respectively.

Second, we accepted all sources with a net count rate at a signal-to-noise ratio ( $S/N$ ) greater than  $5 \sigma_G$  in the soft, hard or broad ROSAT band. The variable  $\sigma_G$  is defined as  $\sigma_G = 1 +$

$\sqrt{c_{\text{bg}} + 0.75}$ , where  $c_{\text{bg}}$  are the background counts. This criterion ensures that no background feature is included by chance. The candidates, which have  $S/N < 5\sigma_G$  and a counterpart in other wavelengths are also included in the list.

In the next section the cross-correlation of all candidates with catalogs and archival observations in the radio, infrared, optical, ultraviolet, X-ray and  $\gamma$ -ray band is explained. The reason for this correlation is to remove already identified sources from the final list. For example, HII regions or GCIs would be extended sources in the RASS, but would have one or more counterparts in other wavelengths which may be already identified. In this work we put more emphasis on correlating the X-ray contours of the SNR candidates with images in other wavelengths to ensure that the X-ray contours match the position of the presumable counterpart in other wavelengths.

## 4.3 Results and discussion

### 4.3.1 Correlation with archival observations and catalogs

Table 4.1 gives an overview of the sky surveys and instruments used in this work. These surveys and instruments will be described in more detail in the following sections.

**Table 4.1:** Summary of the used sky surveys and observatories in the radio, infrared, optical, UV, X-ray and  $\gamma$ -ray regime.

Survey/Telescope	band	sky coverage	Ref.
SUMSS	radio (0.843 GHz)	$b < -30^\circ$	1
NVSS	radio (1.4 GHz)	$b > -40^\circ$	2
Effelsberg Survey	radio (2.695 GHz)	$b > -40^\circ$	3
PMN	radio (4.85 GHz)	$b < +10^\circ$	4
87GB	radio (4.85 GHz)	$0^\circ < b < 70^\circ$	5
Effelsberg 100 m	radio (4.85 GHz)	-	-
WISE	IR (12 and 22 $\mu\text{m}$ )	$> 99\%$ of sky	6
ESO DSS2red	optical (650 $\pm$ 80 nm)	98% of sky	-
SuperCOSMOS	H $\alpha$ (659.0 $\pm$ 2.5 nm)	$-75^\circ < \delta < +2.5^\circ$ $ b  < 10^\circ$	7
SHASSA	H $\alpha$ (656.3 nm)	$-90^\circ < \delta < +15^\circ$	8
GALEX	UV (154 and 232 nm)	$\sim 30000 \text{ deg}^2$	9
ROSAT	X-ray (0.1-2.4 keV)	-	10
XMM-Newton	X-ray (0.15-15 keV)	-	11
Fermi LAT	$\gamma$ -ray (0.02 - 300 GeV)	whole sky	12

**References.** (1) Bock et al. (1999); (2) Condon et al. (1998); (3) Reich et al. (1984);(4) Griffith and Wright (1993); (5) Condon et al. (1989); (6) Wright et al. (2010); (7) Parker et al. (2005); (8) Gaustad et al. (2001); (9) Morrissey et al. (2007); (10) Briel and Pfeffermann (1986); (11) Strüder et al. (2001); (12) Atwood et al. (2009)

### Pointed X-ray observations

Using the NASA web-tool HEASARC Browse<sup>1</sup> we searched the archives of the Chandra X-ray observatory, ROSAT, Suzaku, Swift, XMM-Newton, ASCA and BeppoSAX for pointed observations of the SNR candidates. A sample of 5 of the 73 detected sources have been observed with longer exposures. These observations of the X-ray observatories XMM-Newton and ROSAT were analyzed in addition to the RASS data as they provide spectral information with better signal-to-noise ratios and higher spatial resolution.

In the final list (Table A.1 and Table A.2) all remnants with archival X-ray observations are flagged with a pointing flag of 1. A pointing flag of 2 is given if archival observations exist where the source is at the edge of the detector. All other sources have a pointing flag of 3.

In addition, Table 4.2 lists all used data sets and Table 4.3 summarizes the results of the spatial analysis of these observations. With the exception of G309.8–2.5 all used data are taken with the ROSAT PSPC. The FWHM of the PSPCB PSF in pointing mode is  $12''/50''/95''/140''/190''$  at an off-axis angle of  $0'/24'/36'/48'/57'$  (Boese, 2000). We verified if the candidates observed with ROSAT are extended by applying the GCA method (see Section 4.2). The resulting probability is also given in Table 4.3. The ROSAT data was reduced with the HEASOFT software package, version 6.11.

After extraction of the source and background counts the resulting spectra were binned to have about 10 to 15 spectral bins in order to oversample the five ROSAT PSPC spectral channels at most by a factor of three. The spectral fitting was done with the X-Ray Spectral Fitting Package (XSPEC) version 12.7.0u. Only for one candidate we had enough counts for a detailed spectral analysis (G265.8–7.1). Additionally, we analyzed the spectra of G38.7–1.4 and G309.8–2.5 because Schaudel (2003) claimed that G38.7–1.4 is indeed a SNR and G309.8–2.5 is listed as SNR candidate in Duncan et al. (1997) where it is designated with G309.8–2.6. In this cases we fitted various absorbed spectral models to the energy distribution: A blackbody spectrum, a power law model, a model of a collisional plasma which is in non-equilibrium and allows a temperature evolution (GNEI, Borkowski et al., 2001), a hot diffuse gas model (MEKAL), a model for a collisionally-ionized diffuse gas (APEC) and a thermal bremsstrahlung model. The results for all fits with an reduced  $\chi^2$  less than two and reasonable fit parameters are listed in Table 4.4. Here we added the information on the integrated hydrogen column density  $N_{\text{H}}$  toward the sources derived by Kalberla et al. (2005) which indicates if the candidate is of Galactic origin. The derived values for  $N_{\text{H}}$  are based on HI emission line measurements at 21 cm and refer to the entire hydrogen column density in the line of sight.

In the case of G309.8–2.5, the SNR candidate in Duncan et al. (1997), two XMM-Newton and one Chandra observations are available. All three had the pulsar PSR J1357-6429 as target. First, we checked if the X-ray emission of the pulsar is responsible for the X-ray emission seen in the RASS. We used the spectral parameters derived by Lemoine-Goumard et al. (2011) and converted it to a PSPC count rate using the web-interface of the Portable, Interactive Multi-Mission Simulator (WebPIMMS), version 4.1b.<sup>1</sup> This resulted in a count rate of  $\approx 0.02$ , whereas the count rate in the RASS hard band is  $0.12 \pm 0.03$ . Therefore, we started with the analysis of the

<sup>1</sup>Accessible under <http://heasarc.gsfc.nasa.gov/Tools/w3pimms.html>

**Table 4.2:** Used archival pointed observations.

candidate	Detector	Obs.ID	$t_{exp}/t_{eff}^{\alpha}$ ksec/ksec	offset $^{\beta}$ '
G35.9+6.0	ROSAT/PSPCB	rp400266n00	12.4/7.8	40
G38.7-1.4	ROSAT/PSPCB	rp400271a01	20.1/9.5	49
	ROSAT/HRI	rh500509n00	11.9/-	2
G176.0-11.8	ROSAT/PSPCB	rp400271n00	2.8/1.3	49
	ROSAT/PSPCB	rp201015n00	10.1/5.7	43
G265.8-7.1	ROSAT/PSPCB	rp300289n00	27.0/16.4	30
	ROSAT/PSPCB	rp300289m01	6.7/4.4	32
G309.8-2.5	XMM-Newton	0603280101	84.9/-	3
	Chandra/ACIS-I	10880	60.0/-	4
	XMM-Newton	0306910101	14.9/-	4

**Notes.**  $(\alpha)$  Exposure time on-axis  $t_{exp}$  and on source  $t_{eff}$   $(\beta)$  Off-axis angle between source position and pointing of telescope.

**Table 4.3:** Results of the spatial analysis of the SNR-candidates with archival pointed observations listed in Table 4.2.

candidate	R.A. (J2000)	DEC (J2000)	extent arcmin <sup>2</sup>	count rate 10 <sup>-2</sup> cts/s	$P_{ext}$
G38.7-1.4	19:07:05	+04:30:35	15 × 11	5.0(6)	11.4 $^{\alpha}$
G35.9+6.0 $^{\beta}$	18:35:15	+05:24:23	9 × 8	4.3(4)	10.7
G176.0-11.8 $^{\beta}$	04:51:38	+25:28:04	11 × 7	3.9(6)	8.3 $^{\alpha}$
G265.8-7.1	08:22:11	-49:30:29	15 × 12	15.3(5)	> 40

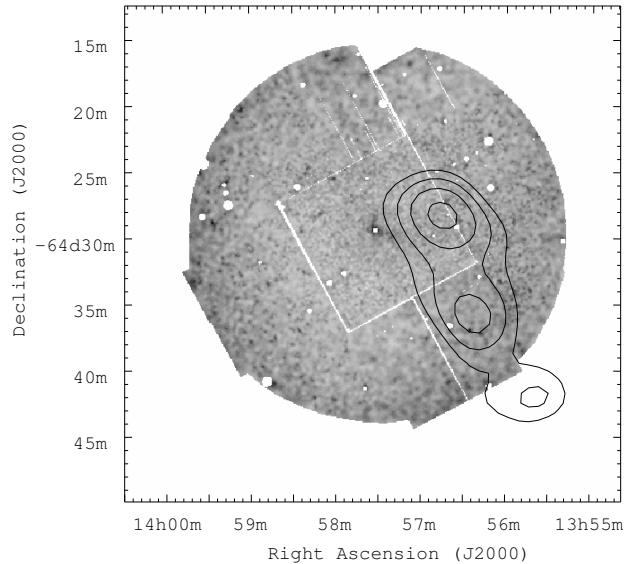
**Notes.**  $(\alpha)$  calculated in the ROSAT hard band.  $(\beta)$  not enough counts for spectral analysis.

**Table 4.4:** Results of the spectral analysis of selected SNR candidates.

SNR candidate	Model	$N_H$ 10 <sup>22</sup> cm <sup>-2</sup>	$T_1/\Gamma$ keV/-	$\chi^2$ (d.o.f.)	$f_{0.1-2.4}$ ergs cm <sup>-2</sup> s <sup>-1</sup>
G38.7-1.4 $^{\alpha}$ $N_H^{LAB} = 9.1 \times 10^{21}$ cm <sup>-2</sup>	bb	0.4 $^{0.3}_{-0.2}$	0.19 $^{+0.07}_{-0.05}$	15.16(11)	7.6 × 10 <sup>-12</sup>
	gnei	0.2 $^{0.5}_{-0.1}$	0.2 $^{+0.3}_{-0.1}$	13.9(9)	6.8 × 10 <sup>-12</sup>
	Raymond	0.01 $^{0.07}_{-0.01}$	1.3 ± 0.2	15.6(11)	2.6 × 10 <sup>-12</sup>
	brems	0.6 $^{0.3}_{-0.2}$	0.3 $^{+0.3}_{-0.1}$	15.2(11)	6.4 × 10 <sup>-11</sup>
G265.8-7.1 $^{\alpha}$ $N_H^{LAB} = 4.1 \times 10^{21}$ cm <sup>-2</sup>	bb	0.2 ± 0.1	0.13 $^{+0.02}_{-0.01}$	13.0(11)	2.1 × 10 <sup>-11</sup>
	MEKAL	0.67 $^{0.10}_{-0.06}$	0.14 $^{+0.02}_{-0.03}$	16.2(11)	7.0 × 10 <sup>-10</sup>
	gnei	0.5 $^{0.3}_{-0.4}$	0.14 $^{+0.04}_{-0.02}$	12.7(9)	1.9 × 10 <sup>-10</sup>
	brems	0.44 $^{0.13}_{-0.11}$	0.17 ± 0.03	13.3(11)	4.4 × 10 <sup>-10</sup>

**Notes.**  $(\alpha)$  energy range restricted to 0.44-2.04 keV

**Figure 4.2:** XMM-Newton MOS1/2 exposure-corrected image of G309.8–2.5 in the 0.1–9 keV range overlaid with the RASS image. The XMM-Newton image shows the result if all point-like sources are removed. The image is binned with  $\sim 3''$  per pixel and smoothed by a adaptive filter.



archival data. However, the first observation with XMM-Newton is contaminated by soft proton flares and the Chandra observation has a much lower sensitivity than the XMM-Newton observation. Analyzing the second XMM-Newton data set (obs.ID 0603280101) with the help of the XMM-Newton SAS and the XMM-Newton Extended Source Analysis Software (XMM-ESAS), both in version 11.0 and removing all point sources we found no excess emission surrounding PSR J1357-6429 which matches the RASS contours (see Figure 4.2).

### Radio band

For the comparison of the X-ray emission regions with radio images we used the NRAO VLA Sky Survey (NVSS, Condon et al., 1998) for source with a declination  $\delta$  above  $-40^\circ$ . For sources with  $\delta < -40^\circ$  we made use of the Sydney University Molonglo Sky Survey (SUMSS, Bock et al., 1999). Both surveys had a resolution of  $45''$ . In most cases this data was sufficient to search for correlations. However, for remnants with an extent larger than  $1^\circ$  and to look for faint radio emission we compared the X-ray contours with the data taken in the Parkes-MIT-NRAO surveys (PMN, Griffith and Wright, 1993) and the 4.85 GHz sky survey (87GB, Condon et al., 1989). These surveys have a resolution of  $3.5'$  (FWHM) and have the advantage of a lower noise level. For extended sources, which have an extend of several times the resolution of the survey or are faint close to the noise level this is more important than having images with high spatial resolution.

To describe the presence or absence of radio emission coming from the candidates in the final list we use the following classification scheme: (1) good positional match between the radio and X-ray contours, (2) extended radio emission within or close to the X-ray position of the SNR candidate, (3) no radio emission and (4) only point-like sources within the extent of the X-ray emission. These radio flags for every candidate is listed in Table A.1 and Table A.2.

In five cases we detected contours in the radio band which have a good match with the X-ray

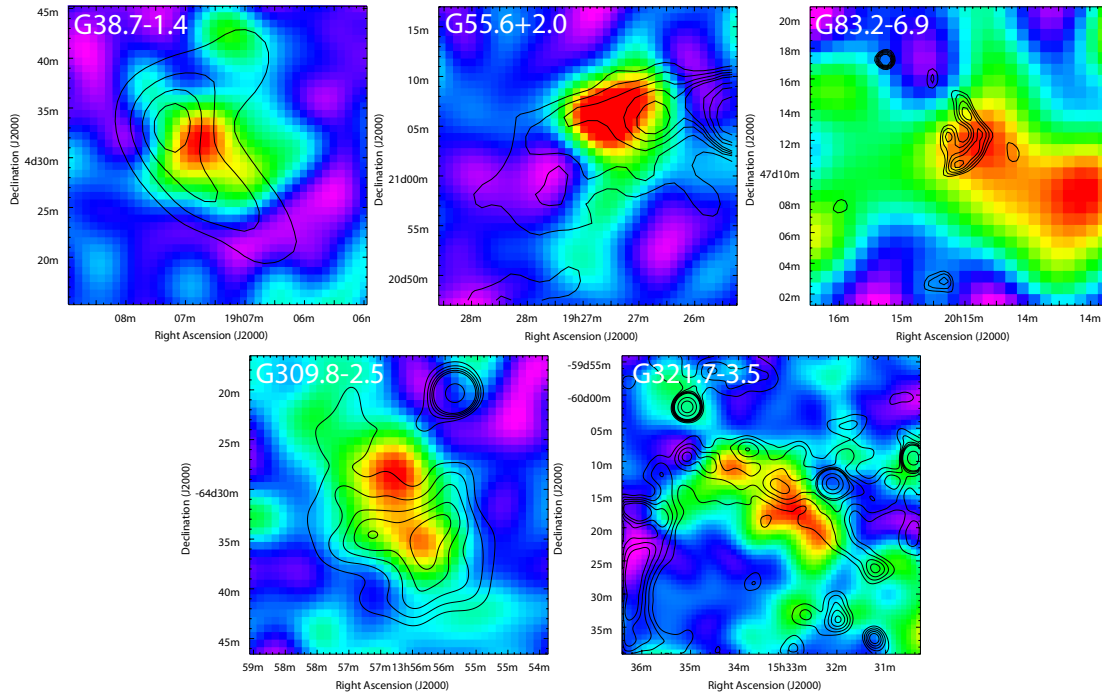


**Figure 4.3:** RASS images of the remnant candidates which have a good positional match between its radio and X-ray contours: *Upper left:* G38.7–1.4 with Effelsberg 4.85 GHz contour lines at 80, 110, 140, 170, and 200 mJy; *Upper center:* G55.6+2.0 overlaid with PMN 4.85 GHz contour lines at 5, 10, 15, 20, 25, 50, 75 and 150 mJy; *Upper right:* G83.2+6.9 with NVSS 1.4 GHz contour lines at 0.7, 0.8, 1.0, 1.1, and 1.3 mJy.; *Lower left:* G309.8–2.5 with radio contours of the SUMSS 0.843 GHz survey at 0.5, 1.25, 2, 2.75, 3.5, and 10 mJy; *Lower right:* G321.7–3.5 overlaid with SUMSS 0.843 GHz radio contours at 0.1, 0.6, 1.0, 1.5, 2, 5, and 8 mJy.

emission region: G38.7–1.4, G55.6+2.0, G83.2+6.9, G309.8–2.5 and G321.7–3.5. Their X-ray images with the radio contours as overlay are displayed in Figure 4.3.

Additionally, for G38.7–1.4 and G83.2+6.9 we found two archival Effelsberg observations. Both sources were observed in July 2001 for 1.8 hrs and 1 hr with the Effelsberg 100 m telescope at a frequency of 4.85 GHz. These data sets were analyzed as described in Schaudel (2003).

### Infrared

The correlation in the infrared regime was done with the help of the public available images of the Wide-Field Infrared Survey Explorer (WISE, Wright et al., 2010) where the whole sky was observed at 3.4, 4.6, 12, and 22  $\mu\text{m}$  with an angular resolution of  $6''1$ ,  $6''4$ ,  $6''5$ , and  $12''0$ , respectively.

The presence of infrared emission is described similar to that of the radio emission. The infrared levels listed in Table A.1 and Table A.2 have the following meaning: (1) good positional match between the infrared and X-ray contours, (2) extended infrared emission within or close to the X-ray position of the SNR candidate which could be related to the candidate, (3) no infrared

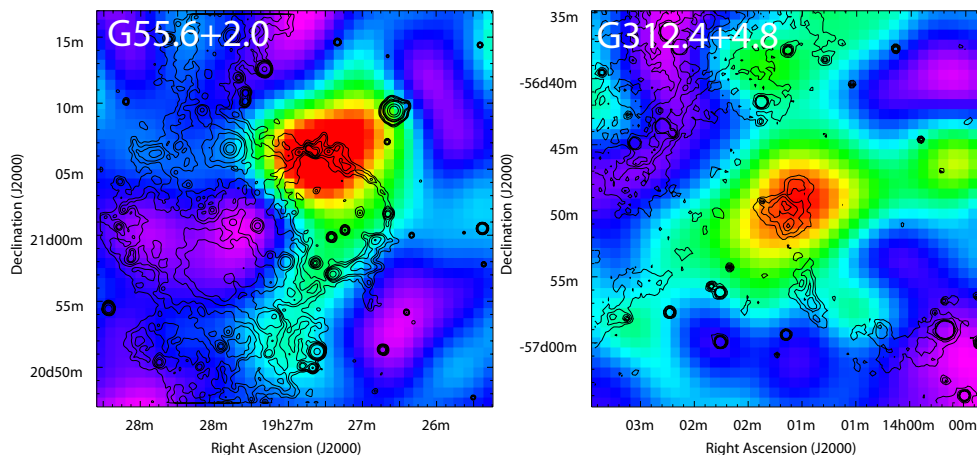


**Figure 4.4:** RASS images of the SNR candidates which have a good positional match between its infrared and X-ray contours. Both images are overlaid with the WISE infrared contours.

emission or infrared emission which belongs to a larger emission region and is very likely not related to the SNR candidate.

Two candidates have a level 1 match between the X-ray and infrared contours: G55.6+2.0 and G312.4+4.8. Their X-ray images with the infrared contours overlaid are displayed in Figure 4.4.

### Optical band and $H_\alpha$

The  $1\sigma_{\text{RASS}}$  positional accuracy of the RASS sources is  $\approx 13'$  and the maximal extent of bright sources in the RASS is  $2'.5$  (Voges et al., 1999). However, there is still the possibility of having a point-like source, e.g. a young star, producing an extended source in the RASS. To exclude this possibility we correlated the position of the SNR candidates which had an extent of less than  $30'$  with the SIMBAD database<sup>2</sup> and the ESO DSS2red images and searched for bright sources with a visual magnitude  $V$  of less than 12 within a box of length  $3\sigma_{\text{RASS}}$ .

Moreover, in the course of analyzing the candidate list of Schaudel (2003) we found several candidates which seem to be extended in the RASS but are just several point-like sources when using high-resolution images of archival X-ray observations. For example, this is the case for the massive star-forming complex NGC 6357 (Wang et al., 2007b) which was denoted with G353.2+0.9 in Schaudel (2003).

Therefore, we added an optical flag in the resulting candidate lists to indicate if two or more point-like sources with a visual magnitude less than 12 are within the X-ray bright region. This is indicated with a level 2 flag. Level 1 corresponds to no more than one optical sources with  $V < 12^{\text{mag}}$  and no source with  $V < 10^{\text{mag}}$  within the X-ray contours. A level 3 flag was given for candidates with an extent greater than  $30'$  that had a good positional match between bright emission region in the DSS2red images and the X-ray contours.

<sup>2</sup><http://simbad.u-strasbg.fr/simbad/>

In addition, we investigated the existence of filament structures using the  $H_\alpha$ , SII, and OIII emission lines. In March 2012 and Mai 2013 some of the southern sources were observed with the Wide Field Imager (WFI) at the 2.2 m MPG/ESO telescope at La Silla, Chile. The exposures were taken with the  $H_\alpha$  + [NII], [SII], and [OIII] filters with an exposure time of 3600 s. In addition, the broadband filters for the visual and red band were used with an exposure time of 300 s. However, a source was only observed with the [SII], and [OIII] filter if filamentary structures were seen with the  $H_\alpha$  + [NII] filter. For the reduction of the data we made use of the Theli package<sup>3</sup> (Erben et al., 2005). All frames were bias-subtracted and flat-field-corrected using a set of flat-field taken in twilight. Furthermore, a superflat was generated and a collapse-correction was applied. Finally, the continuum emission was subtracted following the method described in Waller (1990) in order to allow a clear detection of the filament structure.

For the remaining southern sources we made use of the publicly available AAO/UKST SuperCOSMOS  $H_\alpha$  survey (Parker et al., 2005) at a wavelength of  $659.0 \pm 2.5$  nm. This survey covered the sky at  $-75^\circ < \delta < +2.5^\circ$  and Galactic latitude of  $|b| < 10^\circ$  with a resolution of  $\sim 1''$ . For all other sources located south of  $\delta < 15^\circ$  we correlated the X-ray contours with the Southern H-Alpha Sky Survey Atlas (SHASSA, Gaustad et al., 2001). This survey covers the sky between  $+15^\circ < \delta < -90^\circ$  at an angular resolution of  $\approx 0.8$ . In the case of the other remaining sources we made use of a full-sky  $H_\alpha$  map (Finkbeiner, 2003). However, with its  $6'$  (FWHM) resolution we were not able to search for filamentary structure associated with an SNR.

Using the WFI images and these surveys we detected five SNR candidates, which shows some filamentary structure around the X-ray contours (see Figure 4.5): G38.7–1.4, G290.4–1.9, G295.4–3.0, G312.4+4.8, and G319.8–2.0. However, for the SNR candidates G290.4–1.9, G295.4–3.0, and G319.8–2.0 the correlation between the region of X-ray emission and filaments is only weak.

## UV

To search for correlations between the candidates and sources in the ultraviolet (UV) we used the Galaxy Evolution Explorer (GALEX, Morrissey et al., 2007). This survey covered about 30000 deg<sup>2</sup> of the sky in the far UV at 1350-1780 and near UV at 1770-2730 with a spatial resolution of  $4.3''$  and  $5.3''$ . No extended source was detected in the images matching the X-ray contours of the SNR candidates. In addition, we did not find any bright UV source matching the X-ray position.

## $\gamma$ -rays

To find matches between the SNR candidates and  $\gamma$ -ray sources we used the Fermi Large Area Telescope (LAT) Second Source Catalog (Nolan et al., 2012). This catalog contains all sources detected in the first 24 months of the LAT science mission.

The LAT is sensitive to photons with energies from 20 MeV to 300 GeV and monitors the whole sky approximately every three hours. It has an energy dependent PSF with a FWHM of  $\sim 1^\circ$  at 1 GeV. Therefore, the position of LAT sources is only known with a high uncertainty of

<sup>3</sup>See <http://www.astro.uni-bonn.de/theli/>.

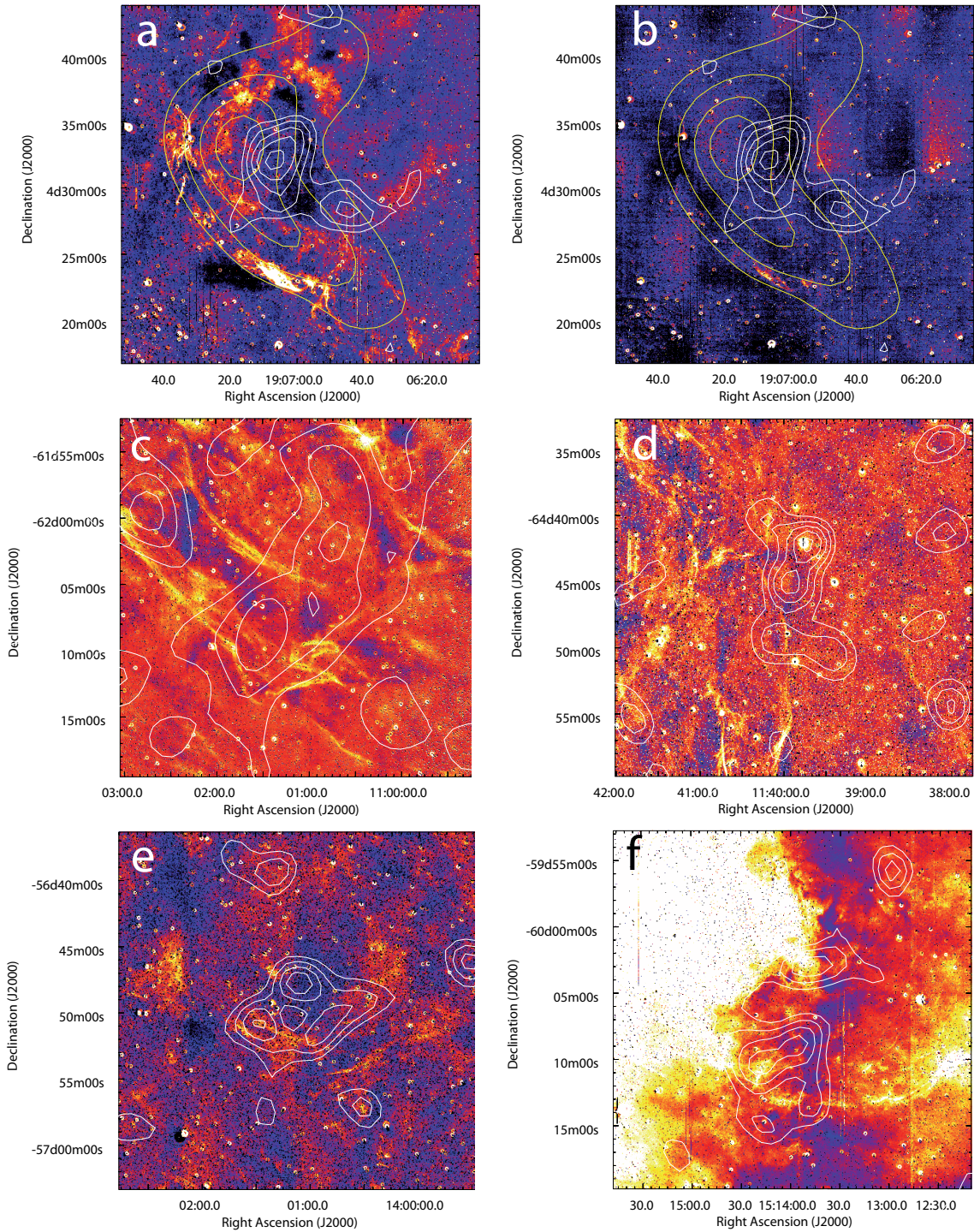


**Figure 4.5:** WFI  $H_\alpha + [NII]$  images of G38.7-1.4 (a), G290.4-1.9 (c), G295.4-3.0 (d), G312.4+4.8 (e), and G319.8-2.0 (f) overlaid with the contours of the RASS X-ray emission in white. Additionally, SNR candidate G38.7-1.4 is shown in  $[SII]$  (b) and for this source the Effelsberg radio contours are added in yellow.

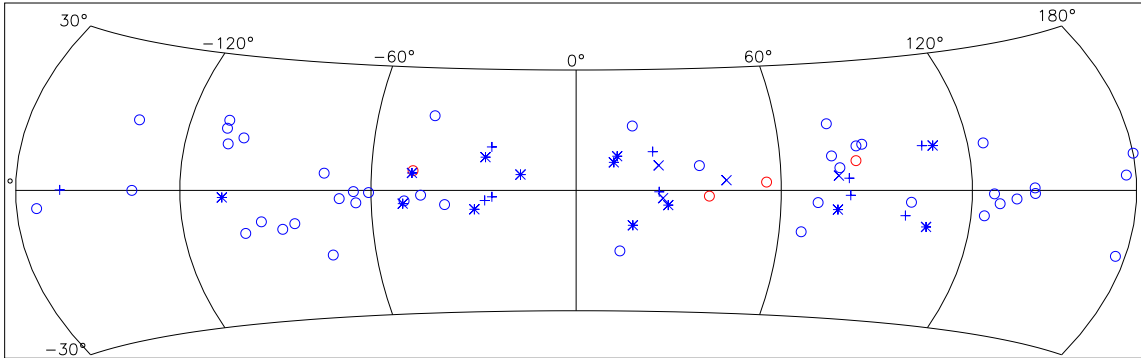


**Figure 4.6:** The distribution of the 73 RASS SNR candidates across the sky. The sources with an extent of less than  $30'$  are indicated by circles. Here the red circles show candidates, which had a signal-to-noise ratio less than  $5 \sigma_G$ , but have counterparts in other wavelength regimes with high probability. Candidates with an extent of  $30'$  to  $60'$ ,  $60'$  to  $120'$ , and greater than  $120'$  are presented by plus, cross and star signs. The image shows an Aitoff-Hammer projection in Galactic coordinates.

the order of several arcminutes. We searched for sources in the catalog whose position is less than 3 times the positional uncertainty in the  $\gamma$ -ray coordinates away from a remnant candidate of our list. We found one match, G309.8-2.5. However, this  $\gamma$ -ray source designated with 2FGL J1356.0-6436 is associated with the pulsar PSR J1357-6429 (Lemoine-Goumard et al., 2011).

The lack of  $\gamma$ -ray emission from the SNR candidates can be explained by the poor spatial resolution of the Fermi-LAT telescope which makes it hard to distinguish faint extended sources from the diffuse emission of the Galactic plane. From the 274 known SNRs only 7 have been detected by Fermi-LAT so far (Nolan et al., 2012).

### 4.3.2 Final list of candidates

After the correlation we were left with 123 SNR candidates. However, after applying the selection criteria introduced in section 4.2 regarding the extent, the signal-to-noise ratio of the sources and having a counterpart in other wavelengths a total of 73 remnant candidates remained, which we will discuss in the following section.

Figure 4.6 depicts the distribution of the remaining RASS SNR candidates, plotted according to their position in Galactic coordinates. Table A.1 and Table A.2 list the coordinates, count rates, hardness ratios and flags of all remaining SNR candidates after correlation with archival observations and catalogs. The list is sorted by the Galactic latitude of the source. Table A.1 contains 73 high significant SNR candidates, whereof 46, 10, 4, and 13 are sources with a diameter  $d < 30'$ ,  $30' < d < 60'$ ,  $60' < d < 120'$  and  $d > 120'$ , respectively. 50 candidates do not fulfill the criteria established in Section 4.2 and are listed separately in Table A.2.

The standard ROSAT hardness ratios  $HR1$  and  $HR2$  are defined the following way:

$$HR1 = \frac{B-A}{B+A}, \quad HR2 = \frac{D-C}{D+C}, \quad (4.1)$$

where  $A, B, C$  and  $D$  represents all counts in the ROSAT PSPC channels 11-41, 52-201, 52-90, and 91-201, respectively. For bright sources these values can give hints on the origin and the temperature of the source. For example, a source with two positive hardness ratios  $HR1$  and  $HR2$  is strongly absorbed and/or has a high temperature of several million Kelvin.

### 4.3.3 Candidates of special interest

We found five diffuse emission regions in the radio and three in the infrared band matching the X-ray contours as well as five candidates with optical filaments in  $H\alpha$ , which will be discussed in detail in the following.

**G38.7–1.4:** This candidate was first mentioned by Schaudel et al. (2002) and claimed to be an SNR by Schaudel (2003). Moreover, based on its emission in the  $H\alpha$  wavelength regime it is listed as an SNR candidate in Sabin et al. (2013), where it is designated with G038.7–1.3. It shows X-ray emission in the RASS with an extent of  $13' \times 10'$ . Based on the fits to the two ROSAT PSPC data sets (see Section 4.3.1) we conclude that the origin of the X-ray emission is thermal. The inferred  $N_H$  places the source within our Galaxy. In the infrared regime extended emission can be seen in the direction of the remnant candidate which does not correlate with the X-ray bright region.

In both, the Effelsberg Galactic Plane 11 cm-survey and the pointed Effelsberg 6 cm data, we detected the incomplete radio shell (see upper and middle panel in Figure 4.7), which matches the X-ray emission region. The total flux in the Effelsberg Galactic Plane survey at 2.695 GHz is  $1.7 \pm 0.3$  Jy. For the calculation of the spectral index  $\alpha$  we used the T-T plot method (Turtle et al., 1962) and the definition  $S_\nu = S_0 \nu^{-\alpha}$ , where  $S_\nu$  is the flux density at frequency  $\nu$ . Using the T-T plot method has the advantage that a different offset in the two wavelengths is taken into account. In this method  $\alpha$  is determined by plotting the flux density  $S_\nu$  of all map pixels in a given spatial region for the two frequencies  $\nu_1$  and  $\nu_2$  against each other. Both images were convolved with the same beam. The slope  $a$  of a linear regression fit to the data yields the mean spectral index  $\alpha = \frac{\log(a)}{\log(\nu_1/\nu_2)}$  of the selected region. In order to deduce the error in  $\alpha$  we used the following method (Leahy et al., 1998): First, we fitted both,  $S_{\nu_1}$  against  $S_{\nu_2}$  and vice versa. The average spectral index was then taken as the best estimate for  $\alpha$  and one half of the difference in the two slopes as the error of  $\alpha$ , because it is larger than the statistical error. This is displayed in the lower panel of Figure 4.7. The fits resulted in  $\alpha = -0.65 \pm 0.11$ , indicating that the candidate is a young to middle-aged SNR (Dickel, 1991).

In the pointed Effelsberg observation at 4.85 GHz the Stokes parameter  $Q$  and  $U$  were recorded. Hence, we were able to create a linear polarization  $I_p = \sqrt{Q^2 + U^2}$  image and to deduce the polarization vectors. The polarization is mostly parallel to the shell which is displayed in the upper panel of Figure 4.7. Only the bright central part of the shell shows a different orientation, tilted by  $45^\circ$ . In this region two compact sources can be detected in the NVSS survey at 1.4 GHz. Using the T-T plot method the spectral index in this part is  $-1.2 \pm 0.4$ , indicating a source of extragalactic origin.

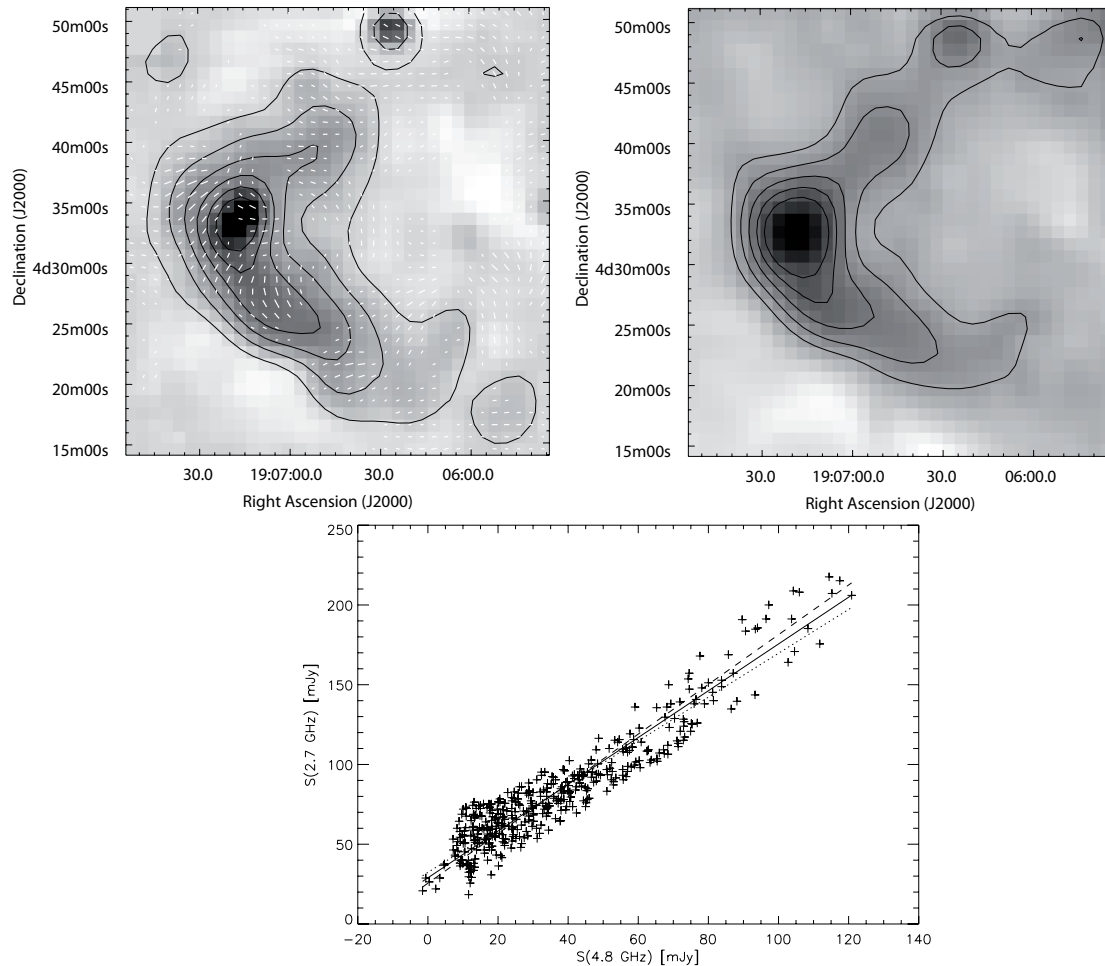


**Figure 4.7:** *Upper left:* Radio image of SNR G38.7–1.4 at 4.85 GHz taken with the Effelsberg 100 m telescope, overlaid with contour lines from 2 to 38 mJy/beam in steps of 6 mJy/beam and polarization vectors. The vectors point in the direction of the electric field and the strength is given relative to 6 mJy/pixel; *Upper right:* Radio image of SNR G38.7–1.4 at 2.695 GHz from the Effelsberg 11 cm survey (Reich et al., 1984), overlaid with contour lines at 60 to 140 mJy/beam in steps of 20 mJy/beam; *Lower:* T-T plot for the determination of the spectral index of the remnant. The two different fits to the data are indicated by dashed and dotted lines and the straight line shows the mean slope.

The polarized, non-thermal radio emission and the thermal X-ray emission directly points towards an SNR interpretation. However, deeper radio and X-ray observations are needed to derive fundamental parameters of this SNR, such as age and distance and to search for a possible neutron star associated with the remnant.

**G55.6+2.0** This source is remarkable because it has a match in both infrared and radio. The infrared image shows a perfect semi circle which matches the X-ray contours. Moreover, in the PMN 4.85 GHz radio survey a bright source is detected in the north of G55.6+2.0 which diffuses towards the south. Thus, this source is a very promising SNR candidate and needs deeper observations, both in the X-rays and in the radio band to uncover its origin.

**G83.2+6.9** The small X-ray source with an extent of about  $6' \times 6'$  is surrounded by an incomplete radio shell in the NVSS data at 1.4 GHz (Fig. 4.3 lower right). A faint radio point source is located very close to the central brightened X-ray source. The radio and X-ray flux of G83.2+6.9 is marginally above the noise level in the NVSS and RASS data. Additionally, Schaudel (2003) reported on radio data obtained at 4.85 GHz with the Effelsberg 100 m telescope. Using the NVSS and the Effelsberg data sets he inferred that the spectral index is about -0.9 with high uncertainty due to small flux values. In addition, no significant amount of polarization was found. The WISE image at 22 micron shows a extended source which is probably not connected to the SNR candidate. Although non-thermal radio emission was detected, the nature of G83.2+6.9 is still unclear and needs to be investigated in more detail.

**G265.8–7.1** The SNR candidate consists of a bright X-ray shell which is slightly elongated in south-north direction. The spectral analysis of this source revealed thermal emission from an extended source with a temperature of 1.5 to 2 million Kelvin. The fitted hydrogen column density does not allow a clear conclusion if it is of Galactic or extragalactic origin. No radio emission from G265.8–7.1 is detected in the SUMSS survey and only two bright spots can be seen in the X-ray bright region of the candidate, which could be connected to the source. Therefore, the nature of this source is still unclear and needs further exploration.

**G290.4–1.9 and G295.4–3.0** In the  $H_\alpha$  images of these sources some filamentary structure is detectable. However, it does not match the X-ray contours very well and in the radio and infrared regime no diffuse emission is detectable. Thus, we have no proof for a connection between the filaments and the bright X-ray sources.

**G309.8–2.5** This SNR candidate consists of a bright radio shell in the east and a smaller embedded X-ray emission region. G309.8–2.5 is listed as an SNR candidate in Duncan et al. (1997) where it is designated with G309.8–2.6. The absence of X-ray emission in the long XMM-Newton exposure can be explained by the fact that the PSPCB detector had a low noise level and was more sensitive to soft X-ray emission. In the case of XMM-Newton the soft X-ray emission was blocked by the medium filter used in the observation and the remaining soft X-ray emission was dominated by the particle background.

The infrared image shows extended emission close to the X-ray position of the SNR candidate, which cannot be clearly associated with the remnant candidate. Thus, more information about the radio emission must be obtained to draw a final conclusion about the origin of this source.

**G312.4+4.8** For this source an infrared counterpart was detected. However, the extent of the infrared source is  $6' \times 5'$ , a factor 2 to 3 smaller than the X-ray source. Furthermore, faint filaments can be seen in  $H\alpha$ , perfectly matching the X-ray contours. No extended counterpart is detected in the radio band. Therefore, it shows signs of an SNR origin, but further studies are needed to claim an identification as SNR.

**G319.8–2.0** The  $H\alpha$  image of this candidate shows some filamentary structure on the southwestern edge matching the X-ray contours. However, this optical emission could be related to a larger emission region, as can be seen in Figure 4.5. Furthermore, no diffuse emission is detectable in the radio and infrared regime. Thus, we have no proof for a connection between the filaments and the bright X-ray source.

**G321.7–3.5** This remnant candidate consists of an incomplete X-ray shell matching very well with the region of radio emission in the north (see figure 4.3). No infrared emission connected with this sources can be seen. Thus, more information about the X-ray and radio emission must be obtained to draw some conclusion about the origin of this source.

#### 4.3.4 Identified candidates

Schaudel (2003) lists 210 SNR candidates. From these candidates 27 can be found in the literature and are listed in Table 4.5. Here the type of the source and the references is given. In the following details to all other identification are given, which cannot be found in literature and could be identified by archival X-ray observations, using the GCA method mentioned above, and/or cross-correlation with multi-wavelength catalogs.

**G1.1-0.8** In several observations this former candidate turns out to be part of a larger emission region.

**G1.85-2.52** This candidate is part of the Galactic bulge.

**G7.6+2.0** After the latest reprocessing of the RASS data no source can be detected any more. Furthermore, in a Suzaku observation (Obs.ID 507065010) no source can be seen.

**G7.9–6.4** In two pointed ROSAT PSPC observations (rp201546n00, rp300050n00) no source is detectable, thus it is very likely a background feature.

**G11.61+3.96** This source cannot be distinguished from other nearby emitting regions.

**G17.03–3.48** Here several SNRs can be seen within the region defined by Schaudel (2003) and thus, are responsible for the emission seen in the RASS.

**Table 4.5:** List of identified SNR candidates which can be found in literature.

Source	Identification <sup>(<math>\alpha</math>)</sup>	Reference
G7.48–1.51	SNR G7.5–1.7	Roberts and Brogan (2008)
G26.6+1.8	Herbig Stars AS 310	Stelzer et al. (2009)
G31.9–1.1	X-ray point source (AX J1853.3–0128)	Muno et al. (2008)
G33.7+7.6	Star (1RXS J182549.2+040925)	Fuhrmeister and Schmitt (2003)
G67.4+10.7	CIG (CIZA J1916.1+3525)	Kocevski et al. (2007)
G69.45+1.19	SNR G69.4+1.2	Yoshita et al. (2000)
G85.4+0.8	SNR G85.4+0.7	Jackson et al. (2008)
G151.9+11.7	CIG (CIZA J0515.3+5845)	Ebeling et al. (2002)
G178.9+16.0	QSO (NVSS J065039.9+374256)	Flesch (2010)
G207.73+1.55	part of Monogem Ring	Plucinsky et al. (1996)
G229.2–17.2	CIG (CIZA J0616.3–2156)	Kocevski et al. (2007)
G256.7–6.7	Seyfert 2 Galaxy (IGR J07565–4139)	de Rosa et al. (2008)
G286.8–0.1	part of Eta Carinae surrounding nebula	Seward et al. (1979)
G287.6–0.8	Eta Carinae and surrounding nebula	Seward et al. (1979)
G288.1–0.1	part of Eta Carinae surrounding nebula	Seward et al. (1979)
G296.7–0.9	SNR G296.7–0.9	Robbins et al. (2012)
G307.5+5.0	CIG (CIZA J1324.6–5736)	Mullis et al. (2005)
G308.3–1.4	SNR G308.4–1.4	Prinz and Becker (2012) and Chapter 5
G314.6+13.6	CIG (CIZA J1358.9–4750)	Kocevski et al. (2007)
G320.47–1.67	SNR G320.6–1.6	Milne et al. (1993)
G328.1+15.8	Probably extragalactic origin	Kaplan et al. (2006)
G332.5–5.6	SNR G332.5–5.6	Stupar et al. (2007)
G337.51+12.70	Lupus star forming region	Krautter et al. (1997)
G342.4–1.9	XTE J1704–445	Markwardt et al. (2007)
G349.1+13.0	CIZA J1627.9–2952	Kocevski et al. (2007)
G353.2+0.9	massive star-forming region (NGC 6357)	Wang et al. (2007b)
G353.6–0.8	SNR G353.6–0.7	Tian et al. (2010)

**Notes.** <sup>( $\alpha$ )</sup> SNR: Supernova remnant; GCl: Galaxy cluster; QSO: Quasar

**G17.8–12.9** This former candidate consists of two point sources, which were identified by analyzing different spectral bands. One source is vanishing in the soft band. And the other is probably the X-ray counterpart of the star HD 179024 ( $V = 8.2^{\text{mag}}$ ).

**G27.48–0.25** In its center the SNR Kes 73 can be found. Furthermore, this region cannot be separated from a larger emission region, which is probably the galactic plane.

**G31.4–0.4** In a SWIFT observation (Obs.ID 00044524001) of the region around this source only a point-like source can be detected. A likely counterpart for that source is 2MASS J18495543–0134087, a star with  $K = 8.8^{\text{mag}}$ .

**G35.2+17.1** Applying the GCA method yielded  $P_{\text{ext}} = 1.0$  and using the brightest pixel of the source as center  $P_{\text{ext}} = 0.1$ . For this source two archival ROSAT PSPC observations were analyzed with a net exposure of 5.4 ksec. The source is detected with a count rate of  $12.1 \pm 0.6$  cts/ksec. However, the probability of having an extended source in this pointed observations are  $P_{\text{ext}} = 1.4$  and  $P_{\text{ext}} = 1.9$ . Therefore, this source is not extended and is probably the X-ray counterpart of TYC 1011–976–1, a star with an optical magnitude  $V = 11.1^{\text{mag}}$ .

**G38.3+10.6** This source is not extended ( $P_{\text{ext}} = 1.4$ ) in the ROSAT hard X-ray band. It has

probably an optical counterpart with TYC 1014–1444–1, a star with  $V = 10.8^{\text{mag}}$ .

**G46.7–12.7** is probably a point-like source, because of its small extend in the RASS. Furthermore, a radio source is at the center of the X-ray emission region.

**G56.3–2.3** Using an archival SWIFT observation (Obs.ID 00036931001) this source could be identified as point-like source. It is the X-ray counterpart of the bright star HD 350379 ( $V = 9.2^{\text{mag}}$ ).

**G57.0+4.3** Using two ROSAT PSPC pointings (rp200052a01, rp200052n00) this source could be identified as point-like X-ray source.

**G57.4+6.1** With the help of a ROSAT PSPC pointing (rp300337n00) this former candidate was identified as point-like source and can be associated with the star HD 343989 ( $V = 9.3^{\text{mag}}$ ).

**G63.4+0.4** Three ROSAT PSPC observations of the region around this source can be found in the ROSAT archive (rp500086n00, rp500083n00, and rp500087n00). A bright star (HD 187614,  $V = 9.3^{\text{mag}}$ ) matches the position of the X-ray source in the merged PSPC image very well. Furthermore, the spectral analysis of this data indicates a close by source, because of a small  $N_{\text{H}}$  in the best-fit.

**G70.5+1.6** In an archival ROSAT PSPC observation (rp500124n00) a point-like source is detectable within the X-ray emission region of this former candidate. This is likely the counterpart of the star TYC 2674–5404–1 ( $V = 11.0^{\text{mag}}$ ).

**G73.1+5.5** In a SWIFT observation (Obs.ID 00039881001) only a point-like source is detectable, which is denoted with 1RXS J195225.7+380014 in Voges et al. (1999).

**G73.2–15.9** No extended source can be detected in a SWIFT observation (Obs.ID 00035783001) of this region. Therefore, the X-ray emission seen in the RASS is probably from the X-ray source seen in the SWIFT image, which was also detected in the XMM-Newton slew survey where it is designated with XMMSL1 J211420.7+252419.

**G74.1+0.3** Four observations with the ROSAT PSPC detector (rp200564n00, rp500247n00, rp500248a01, rp500248n00) are available for this source. Merging the images two point-like sources are clearly detectable. Both are very likely stars, TYC 2674–5404–1 ( $K = 7.6^{\text{mag}}$ ) and HD 193093 ( $V = 8.3^{\text{mag}}$ ).

**G75.43–0.22** The region covered by this remnant contains the pulsar wind nebula G75.2+0.1 of PSR J2021+3651 and is probably responsible for the X-ray emission seen in the RASS.

**G76.3+0.4** The source region was covered two times with ROSAT PSPC (rp900158a00, rp900158a01) and only a point-like source can be detected in the merged image. However, it has no counterpart in other wavelengths, as already noted by Mukherjee et al. (2000).

**G77.88–4.63** In an archival SWIFT pointing (Obs.ID 00039892001) only two point-like sources and no extended emission can be seen.

- G79.43–4.89** In a ROSAT PSPC pointing (rp400138n00) only point sources and no extended emission is detectable.
- G84.6–0.1** Observations with SWIFT, ROSAT HRC and ROSAT PSPC cover the X-ray emission region of this source. All show only X-ray emission of point-like sources.
- G88.6+6.0** This former candidate was observed with SWIFT (Obs.ID 00031798001) and ROSAT PSPC (rp500224n00). In both images a point-like source can be seen at the western edge of the emission region defined by Schaudel (2003). It has a counterpart in the optical regime, the binary star HD 235299 ( $K = 7.8^{\text{mag}}$ )
- G94.8–4.9** In a deep ROSAT PSPC observation (rp201522n00) only two point-like sources at the southern edge of the emission region defined by Schaudel (2003) and no extended emission can be seen.
- G103.5–8.8** The source region was observed twice with the SWIFT satellite (Obs.ID 00040190001 and 00040190002) and shows only a point-like source designated with 1RXS J225010.6+492609 in Voges et al. (1999).
- G105.6+13.6** In a deep observation with XMM-Newton (Obs.ID 0673540901) several point sources and no extended emission is detectable within the source region. Thus, the X-ray emission in the RASS is due to the point-like sources.
- G110.9+2.8** The source region was covered in an archival ROSAT PSPC observation (rp500322n00) and indicates that the extended X-ray emission is due to several point sources. These sources probably belong to Cep OB3, a young association of O and B stars (Naylor and Fabian, 1999).
- G127.4-0.7** In an archival SWIFT observation only one point-like X-ray source was detected in the RASS emission region (1RXS J012944.6+614756).
- G148.3–13.1** Three galaxies are detectable within the X-ray emitting area and the central galaxy is a radio galaxy. Therefore, this candidate is very likely a galaxy cluster.
- G153.3+3.8** In the latest reprocessing of the RASS data only a point-like source can be seen with a positional discrepancy to the coordinates given in Schaudel (2003). This new position is in agreement with a bright flaring star HD 232979 ( $V = 8.6^{\text{mag}}$ ).
- G173.9+0.3** This source is likely the X-ray counterpart of the HII regions S237.
- G187.7+0.4** Analyzing an archival ROSAT PSPC observation (rp201225n00) an X-ray source is detected close to the RASS position, which is point-like and has a counterpart with the star V\* V391 Gem ( $K = 8.9^{\text{mag}}$ ).
- G193.0+12.4** The former candidate consists of two point-like sources, the radio galaxy 2MASX J07012902+2313260 and an X-ray point source.

- G198.7+4.0** The source is a point-like source and has an optical counterpart TYC 758–2255–1 with  $K = 9.3^{\text{mag}}$ .
- G203.4+9.0** The extended X-ray emission of this source is coming from three point-like sources, as can be seen in an archival SWIFT observation (Obs.ID 00038566001). None of the three sources have a counterpart in other wavelength regimes.
- G218.6–15.7** In two SWIFT observations (Obs.ID 00038647001 and Obs.ID 00046979001) this source is still extended. However, spectral analysis revealed a hot plasma with a temperature of  $3.5 \pm 1.2$  keV and an  $N_{\text{H}} = 3 \pm 2 \times 10^{21}$  cm $^{-2}$ . All other plasma models either produce similar results for the temperature and  $N_{\text{H}}$  or are unreasonable. Therefore, G218.6–15.7 is a galaxy cluster.
- G226.0+0.5** This source was already identified by Schaudel (2003) as galaxy, but was still listed as an SNR candidate.
- G238.5–6.4** This former candidate is probably a galaxy cluster, because five 2MASS galaxies are detected within  $3'$  around the center of it.
- G258.3+1.5** The X-ray emission of this source is probably coming from a bright star (TYC 7662–2949–1,  $K = 8.0^{\text{mag}}$ ) and several other point sources, which can be seen in the radio band.
- G262.8–9.1** Two ROSAT observations cover the region of this source (rh201688n00, rp400158n00), but only two point-like sources are detectable.
- G271.6+2.8** In a ROSAT PSPC observation (rp900377n00) only a point-like source is detectable, which is probably the counterpart of the bright star TYC 8171–980–1 ( $V = 10.5^{\text{mag}}$ ).
- G290.9–1.1** Four archival ROSAT observations cover the region of this former candidate (rp200699n00, rp500307a01, rp500307n00, rp900526n00) and only a point-like source is detectable in the merged image. This is likely the X-ray counterpart of the binary star HD 306131 ( $V = 9.3^{\text{mag}}$ ).
- G292.3+0.6** No extended source can be seen in an archival ASCA (Obs.ID 43025000) and ROSAT PSPC (rp900165n00) observation. It could be some residual emission from the bright high mass X-ray binary Cen X–3.
- G294.9–1.6** In a PSPC pointing (rp200706n00) covering the region of this source several point sources can be detected. Two of them are eclipsing binary stars ( $V^*$  V1051 Cen with  $V = 7.2^{\text{mag}}$  and  $V^*$  V871 Cen with  $V = 6.5^{\text{mag}}$ ).
- G299.3–0.6** In a pointed Suzaku observation (Obs.ID 507064010) only a point-like source and no extended emission is detectable.

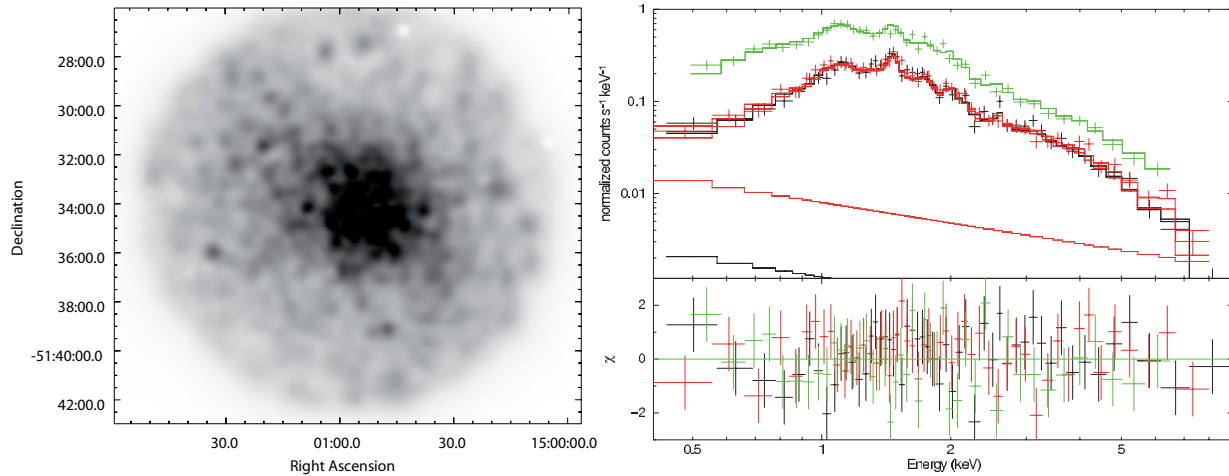


**Figure 4.8:** XMM-Newton MOS1/2 exposure-corrected image (*left*) and spectrum (*right*) of G332.5+6.3. The XMM-Newton image shows the result after removal of all point-like sources. The image is binned with  $\sim 3''$  per pixel and smoothed by an adaptive filter. The spectrum was fitted with MEKAL for the source and a power law for every detector to model the residual soft-proton contamination.

**G305.5–1.9** One SWIFT (Obs.ID 00020064001) and two ROSAT PSPC pointings (rp190243n00, rp190600n00) are available for this candidate. The SWIFT observation shows several point sources and in the ROSAT pointing no extended emission can be seen.

**G322.5+6.3** This candidate was observed with XMM-Newton (Obs.ID 0204710201) for 6.9 ksec. The data reduction was performed with the Extended Source Analysis Software (XMM-ESAS) package (Snowden et al., 2008). The resulting spectrum was fitted with an emission spectrum from a hot diffuse gas (MEKAL) and yielded a  $\chi^2 = 131.7$  for 138 d.o.f., a hydrogen column density  $N_{\text{H}} = 2.8 \pm 0.1 \times 10^{21} \text{ cm}^{-2}$ , and a temperature of  $k_{\text{B}}T = 3.7 \pm 0.3 \text{ keV}$ . The hydrogen column density is in the same order as the integrated hydrogen column  $N_{\text{H}}$  density toward the sources derived by Kalberla et al. (2005). In addition the temperature is one order of magnitude larger than what is expected for evolved SNRs. Thus, the remnant candidate is very likely a galaxy cluster. Figure 4.8 shows the X-ray image and spectrum of this source.

**G332.9+1.9** On the northern edge of this former candidate a HII region (GAL 333.04+02.02) and on the southern edge a bright star (HD 144918,  $V = 9.9^{\text{mag}}$ ) can be found.

**G334.44–3.19** In all RASS bands no source can be found which is matching the region defined by Schaudel (2003). Therefore, it is assumed that this is a background feature.

**G337.2+13.0** Analyzing an archival ROSAT HRI observations (rh201941n00) only a point source could be detected. It is probably the counterpart of the bright star HD 140901 ( $V = 6.0^{\text{mag}}$ ). In addition, this region was observed with Chandra (Obs.ID 13769) and also no extended source can be seen.

**G338.3+15.3** Several ROSAT PSPC pointings are available for this source. However only a point source is detected in the merged image. With high probability this is the X-ray counterpart of the TTauri star 2MASS J15443529–3521492 ( $K = 8.8^{\text{mag}}$ ).

**G351.17+6.64** In three archival SWIFT observation (Obs.ID 00030890005, Obs.ID 00090247001, and Obs.ID 00030890006), which cover most of the SNR candidate, only three bright point-like sources can be seen. Two are probably the X-ray counterparts of TYC 7364–1316–1 and HD 152805, stars with a visual magnitude of 10.7 and 7.5. The third source is the X-ray point source 1RXS J65633.7–322513. There is no sign of an extended emission around these sources.

**G353.7+16.0** In an archival XMM-Newton observation this candidate consists of three point-like sources: the TTauri stars 2MASS J16312012–2430052 with  $K = 6.7^{\text{mag}}$ , 2MASS J16311574–2434022 with  $K = 7.1^{\text{mag}}$ , and 2MASS J16311501–2432436 with  $K = 8.7^{\text{mag}}$ .

**G353.7+17.7** Using a pointed ROSAT PSPC observation (rp900362n00) three point-like sources were identified. These sources are probably two stars in double systems, HD 147932 ( $V = 7.3^{\text{mag}}$ ) and HR 6112 ( $V = 5.1^{\text{mag}}$ ), and an X-ray point-like source.

**G355.7+10.6** The extended source seen in RASS consists of three point-like sources, two of them seem to have a counterpart in the radio band.

**G358.2+6.5** In an archival ROSAT PSPC observation only a point-like source can be detected. Its position is close to the star CD–26 12037, which has a visual magnitude of 11.5.

**G359.8–14.1** A bright binary star (HR 7029,  $V = 4.8^{\text{mag}}$ ) is within the X-ray emission region and is responsible for the X-ray emission with high probability.

## 4.4 Conclusion and future prospects

In this chapter the re-analysis of the RASS SNR candidates list of Schaudel (2003) was presented. After correlating the source list with various sky surveys and source catalogs as well as analyzing archival X-ray observations 123 sources remained as SNR candidates. 73 of these sources fulfill the criteria that the source significance is  $> 5\sigma_G$  and/or have a counterpart in other wavelengths. Therefore, these sources are no fluctuations in the X-ray background. In addition, the possibility that these SNR candidates are point sources can be ruled out, because it was shown that all spherical symmetric sources are extended (95% CL). However, the remaining 50 candidates do not fulfill one or more of the selection criteria. Thus, it cannot be excluded that some of these sources are indeed fluctuations in the X-ray background.

Nevertheless, it is still possible that some of these 123 sources are of extragalactic origin. For example, galaxy clusters are extended sources and have temperatures of a few times  $10^7$  K (Böhringer and Werner, 2010). Hence, they can be seen in the RASS and can be confused with SNRs. With the RASS data it is not possible to decide whether the source emission originates from inside or outside the Galaxy, because in the RASS the temperature or the hydrogen column

density cannot be measured, because of the short exposures and the poor spectral resolution. The only indication of their origin is the hardness ratio. Galaxy clusters, for example, have hardness ratios  $HR1$  and  $HR2$  roughly in the range from 0 to +1, because of their high temperature (Böhringer et al., 2000). Supernova remnants have lower temperatures and higher absorption by the interstellar medium. Therefore, the hardness ratio  $HR1$  is in the same order as galaxy clusters, but  $HR2$  should be  $\lesssim 0$  (Voges et al., 1999; Schaudel, 2003). This is the case for more than 80% of the remnant candidates.

In addition, the conclusion of Schaudel (2003) that candidate G38.7–1.7 is an SNR could be confirmed. This source shows non-thermal polarized radio emission, filaments in  $H\alpha$  and thermal X-ray emission. In addition, the fitted hydrogen column density places this source within our Galaxy. All these are clear indicators that G38.7–1.4 is an SNR. Furthermore, the SNR candidate G265.8–7.1 shows emission from a thermally emitting plasma in the X-ray regime, four candidates have counterparts in the radio band (G55.6+2.0, G83.2+6.9, G309.8–2.5, and G321.7–3.5), two X-ray sources show related emission in the infrared regime (G55.6+2.0 and G312.4+4.8), and four objects show some filamentary structure around the X-ray emission region in  $H\alpha$  (G290.4–1.9, G295.4–3.0, G312.4+4.8, and G319.8–2.0). In addition, for three SNR candidates archival X-ray observations were analyzed and indicate X-ray emission from an extended source. These candidates are of special interest, because they show several properties typical for SNRs.

The origin of the remaining SNR candidates is still unclear. However, they are promising remnant candidates, because they are extended and bright in the soft X-ray regime.

Assuming that the remaining 123 SNR candidates mentioned above are indeed SNRs and adding them to the  $\approx 280$  SNRs known (including the two remnants identified in this work - G38.7–1.4 and G308.4–1.4) the discrepancy between the expected and measured SN rate in our Galaxy can be explained to some extent. Nevertheless, searching for SNRs in the RASS survey yielded a large number of additional SNRs and by gradually identifying the 123 candidates, the discrepancy between the expected and measured number of supernova remnants in our Galaxy can be further reduced.

In the future, the most promising SNR candidates will be followed-up in the radio, optical ( $H\alpha$ ) and X-ray band by using the candidate list (Table A.1). This will help to pinpoint the origin of the detected X-ray emission.

Additionally, by the end of 2015 eROSITA, the successor of the ROSAT mission, will start to image the whole X-ray sky with an increased sensitivity and with a higher spatial and spectral resolution. The eROSITA telescopes on board of the Russian Spektrum-Roentgen-Gamma mission will be approximately 20 times more sensitive than the RASS mission and will have a resolution of  $25''$  to  $30''$  in survey mode. The average exposure will be  $\approx 3$  ks (Predehl et al., 2010). Therefore, we will be able to study the candidates in much more detail. The longer and deeper exposures will enable us to perform a spectro-imaging analysis of the candidates. Particularly the remnant candidates with a large extent can only be studied in detail with eROSITA because the current X-ray observatories have a field of view of  $\sim 30'$  and need several pointings to cover the larger remnants.

## Chapter 5

# Exploring the supernova remnant G308.4–1.4

The content of this chapter is adopted from Prinz and Becker (2012) published in *Astronomy & Astrophysics*.

### 5.1 Introduction

Supernovae (SNe), the core-collapse of massive stars or the thermonuclear disruption of white dwarfs, are rare events, occurring on average every 50 years in the Galaxy (Keane and Kramer, 2008). However, only seven Galactic SNe have been observed with historical records in the past two thousand years – SN 185 (RCW 86), SN 386 (G11.2–0.3), SN 1006, SN 1181 (3C58), Crab SN, Tycho SN, and the Kepler SN. Several other records of guest stars by ancient Chinese astronomers exist. However, no solid identification with a known supernova remnant (SNR) has been possible for most of them so far (Green and Stephenson, 2003). Most Galactic SNe go unobserved owing to visible-band extinction by interstellar dust. For example, SN Cas A may belong to this group. No widespread reports of Cas A exist in the literature of the 17th century (cf. Hartmann et al., 1997). A more recent example is the youngest supernova known in our Galaxy, G1.9+0.3, which was totally missed by optical observatories about 100 years ago (Reynolds et al., 2008). The majority of supernova remnants that have been identified so far were found in radio surveys in which the observations are unhampered by interstellar dust (Green, 2009, and references therein). Nevertheless, the radio band is not free of selection effects. Supernova remnants with a diameter of  $< 3'$  are difficult to identify. Only three of the 274 remnants listed in the Green catalog fall into this category. In addition, most searches for SNRs focus on the Galactic plane, leaving remnants located at a higher galactic latitude underrepresented. Only five supernova remnants with  $|b| > 7^\circ$  are listed in Green's catalog. Hence, small remnants at high latitude are easily missed in radio surveys.

Most SNRs emit thermal radiation when the SN blast wave expands into the surrounding interstellar medium (ISM), forms a shock wave at the shock front, which then ionizes the atoms,

and increases the temperature to  $10^6 - 10^7$  K. Therefore, the successful completion of the ROSAT All-Sky Survey (RASS) in the X-ray regime provided a new window for finding SNRs and the compact objects that may reside within them. The seven X-ray detected and radio-quiet central compact objects that were associated with SNRs (see Gotthelf and Halpern, 2008a, for a review) are a good example for the impact on pulsar and SN science of X-ray observatories. Additionally, X-ray observations of SNRs at moderate spectral resolution can determine remnant properties such as shock velocities, post-shock gas densities and temperature as well as swept-up shell mass and overall morphology.

The ROSAT All-Sky survey has demonstrated the potential power for finding new SNRs (Pfeffermann and Aschenbach, 1996; Busser et al., 1996; Asaoka and Aschenbach, 1994; Asaoka et al., 1996; Egger et al., 1996; Folgheraiter et al., 1996). This has motivated Bußer (1998) and Schaudel et al. (2002) to investigate the all-sky survey data more systematically to search for unidentified supernova remnants. They analyzed RASS data in a systematic search for extended ( $\geq 5'$ ) X-ray sources at Galactic latitudes ( $b \leq \pm 15^\circ$ ) by correlating them with databases such as SIMBAD, NED, NVSS, SUMSS, DSSII, NRAO, ATNF, Parkes, and the Effelsberg radio survey data. From their candidate list several sources have meanwhile been confirmed as SNR (e.g., Jackson et al., 2008; Robbins et al., 2012; Roberts and Brogan, 2008; Stupar et al., 2007; Tian et al., 2010). These identifications suggest that many of their SNR candidates are indeed radio-under-luminous, explaining why past radio surveys could not detect or identify them before.

In Schaudel (2003) nine sources are listed that appear to be very promising SNR candidates. One of them is G308.4–1.4 designated with G308.3–1.4 in Schaudel et al. (2002) and Schaudel (2003). Since the RASS had only an average exposure time of  $\sim 400$ s for sources in the Galactic plane the available ROSAT data do not support a detailed spectral and spatial analysis of these sources. However, G308.4–1.4 appears in the RASS data as a spherical center-filled X-ray source, whereas in the Sydney University Molonglo Sky Survey (SUMSS) two radio arcs have been detected that partly overlap with the RASS data (see Fig. 5.1). Moreover, G308.4–1.4 is listed in the MOST supernovae remnant catalog as a possible SNR candidate (Whiteoak and Green, 1996).

In this paper we report on the identification of G308.4–1.4 as an SNR using archival data from the Chandra, SWIFT, ATCA, and WISE observatories. The results of the spatial and spectral analysis of the X-ray and radio data are presented in Sect. 5.2 and 5.3, respectively. In Sect. 5.4 we report on data of G308.4–1.4 in other wavelength regimes. A concluding discussion about the identification of G308.4–1.4 and its central sources is given in Sect. 5.5. Furthermore, in the same section we use the inferred spectral parameters of the SNR to derive an estimate for the age, the radius, the expansion velocity and the distance to the remnant. Section 5.6 provides a summary.

## 5.2 X-ray observations and data analysis

The SNR candidate G308.4–1.4 was observed with the Advanced CCD Imaging Spectrometer (ACIS-I) on board the Chandra X-ray observatory on 26 and 27 June 2010 (obs.ID. 11249) for

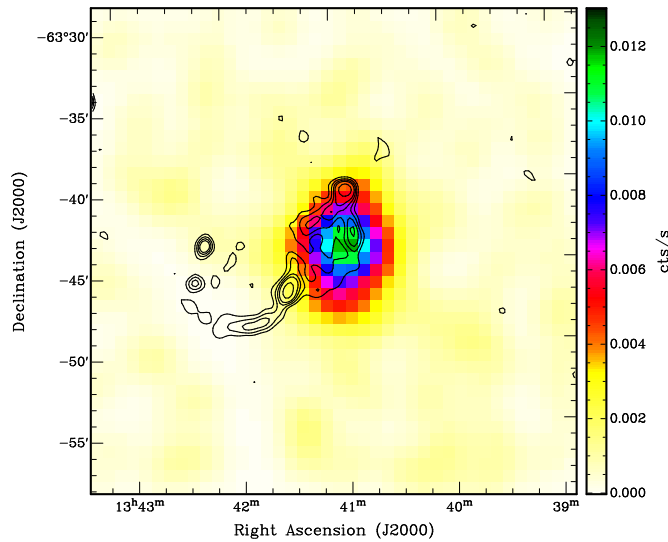


**Figure 5.1:** ROSAT RASS  $30' \times 30'$  image of G308.4–1.4 (0.1–2.4 keV) overlaid with the SUMSS image at 843 MHz (contour lines at 4, 8, 12, 16, and 25 mJy). The half-power beam-width of the telescope is  $43''$ . The RASS image is binned with  $0.75'$  per pixel and smoothed by a Gaussian kernel of  $\sigma \approx 2'$ .

$\approx 15.1$  ks. All data were uncontaminated by soft proton flares. After dead-time correction 14.9 ks of good data remained. Standard processed data were used with up-to-date calibration applied. The data were reduced with the Chandra Interactive Analysis software CIAO, version 4.3. For the spectral fitting we used the X-Ray Spectral Fitting Package (XSPEC) developed by NASA, version 12.7.0.

In addition to Chandra, we used the SWIFT observatory to analyze X-ray point sources detected in the central region of the remnant. G308.4–1.4 was observed three times with the Swift X-ray Telescope (XRT) on 17 June 2011 (obs.ID 00032030001), 7 (obs.ID 00032030002) and 11 August 2011 (obs.ID 00032030003) for 3.5 ks, 4.2 ks and 1.3 ks, respectively. These data were reduced with the HEASOFT software package, version 6.11. For the spatial and spectral analysis we used the high-resolution Chandra data because they contain five times more counts of G308.4–1.4.

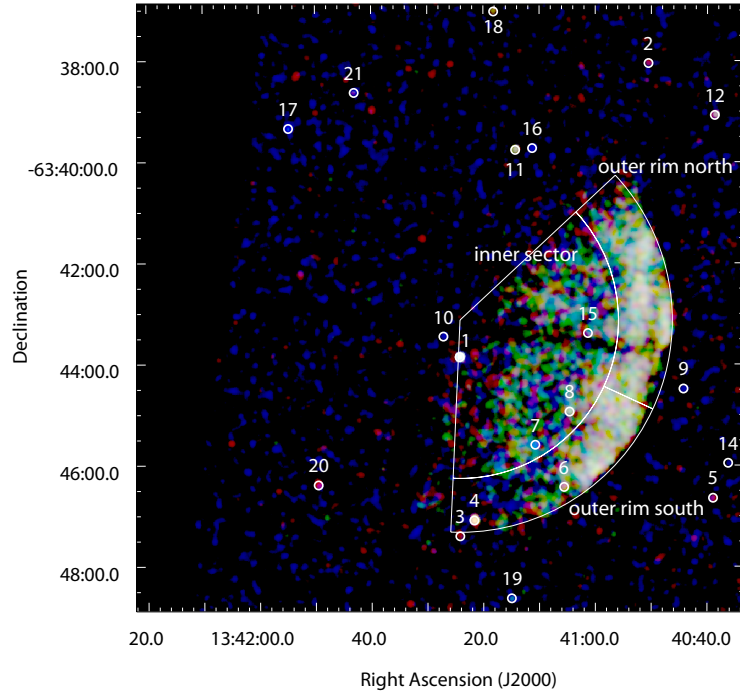
To calculate the error in the X-ray flux we used a publicly available XSPEC tool<sup>1</sup>. For the spectral analysis of the extended source emission we restricted the energy range to 0.5 – 4.0 keV because the count rate detected at higher energies is too sparse for a meaningful spectral analysis. Below 0.5 keV the detector and telescope response is not well established. In all other cases the energy range was restricted to 0.1–5 keV. All errors in this publication represent the  $1\sigma$  confidence range for one parameter of interest, unless stated otherwise.

### 5.2.1 Spatial analysis

Inspecting Fig.5.2, the X-ray image of G308.4–1.4 shows strong emission in the eastern part. This region has a circular shape with a diameter of  $\sim 8.4'$ . The radiation is fading toward the geometrical center of the source. The coordinate of the circle center is  $RA_c = 13^h 41^m 23.9^s \pm 0.7^s$ ,  $DEC_c = -63^\circ 43' 08'' \pm 04''$ , which was obtained by fitting an annulus to the outer skirts of

<sup>1</sup>fluxerror.tcl, see <http://heasarc.nasa.gov/xanadu/xspec/fluxerror.html>

**Figure 5.2:** Chandra ACIS-I color image of G308.4–1.4 (red 0.1–1.0 keV, green 1–1.5 keV and blue 1.5–5 keV). The images are binned with  $1''$  per pixel and smoothed by a Gaussian kernel of  $\sigma = 3''$ . 20 point sources were detected in the  $12' \times 12'$  area around the center of G308.4–1.4 (c.f. Table 5.1).



the extended emission.

Searching for point sources in a  $12' \times 12'$  box around G308.4–1.4 using a wavelet source detection algorithm (CIAO-tool `wavdetect`) yielded a list of 21 sources. Their position, positional error and signal-to-noise ratio are listed in Table 5.1. The sources themselves are marked in Fig. 5.2. Cross-correlating the sources with the help of the VizieR online tool<sup>2</sup> we found seven matches. They are included with their positional error in Table 5.1.

Eight of the detected sources are located within the extended emission of G308.4–1.4 and two of them (# 1 and # 10) are within  $\approx 1$  arcmin of the geometrical center of the SNR candidate. Source 1 is the brightest among all detected point sources and its designation is CXOU J134124.22–634352.0. Its position is coincident with 2MASS J13412422–6343520. In the optical source catalogs this source has no information about its proper motion. Hence we cannot put better constraints on the positional coincidence of source # 1 and the 2MASS object. Source 10 has no optical counterpart and is designated with CXOU J134127.12–634327.7.

## 5.2.2 Spectral analysis of G308.4–1.4

To extract the spectra of the SNR candidate we first removed all point-like sources and then selected all photons in a circular sector with a radius of  $4.2'$  and opening angle of  $\approx 136^\circ$  (see Fig. 5.2). The background spectrum was derived from all photons in an annular sector with the same opening angle as the circular one but with the radii  $5.5'$  and  $7.2'$ . After subtracting the background contribution (0.054 cts/pix) 11 752 counts for the spectral analysis of the whole remnant-candidate remained. Additionally, the emission region of G308.4–1.4 was divided into

<sup>2</sup><http://vizier.u-strasbg.fr/viz-bin/VizieR>

**Table 5.1:** Detected sources in a  $12' \times 12'$  box around G308.4–1.4. The sources are denoted as in Fig. 5.2.

Source	RA (J2000) h:m:s	DEC (J2000) d:m:s	$\delta$ RA arcsec	$\delta$ DEC arcsec	$S/N$ $\sigma_G^{(\alpha)}$	optical counterpart (positional discrepancy)
1	13:41:24.217	-63:43:52.04	0.41	0.40	63.0	2MASS J13412422–6343520 (0.07')
2	13:40:50.534	-63:38:03.12	0.45	0.42	2.7	
3	13:41:24.203	-63:47:24.47	0.70	0.42	3.1	
4	13:41:21.634	-63:47:05.63	0.44	0.43	25.5	2MASS J13412162–6347053 (0.27')
5	13:40:38.921	-63:46:38.83	0.54	0.45	3.3	2MASS 13403887–6346384 (0.48')
6	13:41:05.585	-63:46:25.89	0.47	0.42	4.9	
7	13:41:10.742	-63:45:36.11	0.52	0.42	4.9	
8	13:41:04.580	-63:44:56.66	0.52	0.42	6.7	
9	13:40:44.230	-63:44:29.50	0.65	0.41	2.4	
10	13:41:27.121	-63:43:27.72	0.56	0.44	3.8	
11	13:41:14.267	-63:39:45.91	0.57	0.43	9.7	3UC 053–222814 (0.02')
12	13:40:38.666	-63:39:04.77	0.61	0.43	9.0	2MASS J13403862–6339044 (0.41')
13	13:41:02.437	-63:38:00.00	0.56	0.44	0.8	
14	13:40:36.217	-63:45:57.41	0.47	0.44	2.0	
15	13:41:01.308	-63:43:23.50	0.40	0.40	2.9	
16	13:41:11.249	-63:39:44.07	0.76	0.44	4.7	
17	13:41:54.767	-63:39:20.68	0.91	0.67	6.7	2MASS J13415473–6339207 (0.22')
18	13:41:18.147	-63:37:01.87	1.31	0.53	3.8	
19	13:41:14.934	-63:48:38.00	0.67	0.54	3.2	
20	13:41:49.497	-63:46:23.59	1.06	0.65	4.1	
21	13:41:43.058	-63:38:38.10	1.24	0.50	5.4	2MASS J13414304–6338371 (0.93')

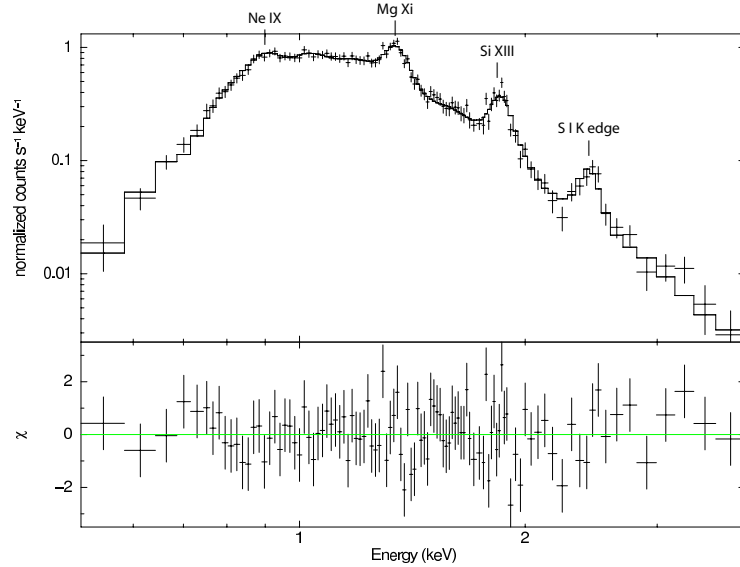
**Notes.**  $(\alpha)$   $\sigma_G = 1 + \sqrt{c_{bg} + 0.75}$ , where  $c_{bg}$  are the background counts.

four separate regions, which are illustrated in Fig. 5.2. The net counts are 4095 for the inner sector and 7658 for the outer shell, and 4499 for the northern part of the outer shell and 3158 for the southern part. The spectrum of every single region was binned with at least 50 counts per bin. Only the spectra of the southern and northern parts of the outer rim were binned with at least 75 counts per bin.

To fit the X-ray spectrum of G308.4–1.4 we tried various one- and two-component spectral models. However, only a model of an absorbed collisional plasma that is in non-equilibrium and allows a temperature evolution (Borkowski et al., 2001) reproduces the energy distribution of the extended source. In XSPEC this model is implemented as VGNEI. To improve the goodness of the fit and to obtain the abundance of metals in the plasma, we thawed the parameter of every single metal and monitored the improvement of the fit statistic.

The analysis results in a best-fit model with a reduced  $\chi^2$  of 1.03 for 95 degrees of freedom (d.o.f.) and a hydrogen column density  $n_H = 1.02 \pm 0.04 \times 10^{22} \text{ cm}^{-2}$ . The value for  $n_H$  is lower than the integrated hydrogen column density toward G308.4–1.4, which is  $1.31 \times 10^{22} \text{ cm}^{-2}$  (Kalberla et al., 2005) and  $1.45 \times 10^{22} \text{ cm}^{-2}$  (Dickey and Lockman, 1990). These values are based on HI emission line measurements at 21 cm and therefore refer to the entire hydrogen column density in the line of sight. The temperature of the plasma is found to be  $6.3_{-0.7}^{+1.2}$  million Kelvin. The best fit was obtained when thawing the abundance in neon, magnesium, sulfur and iron, which differ significantly from the solar values:  $\text{Ne} = (0.72 \pm 0.14) \text{ Ne}_\odot$ ,  $\text{Mg} = 0.70_{-0.08}^{+0.09} \text{ Mg}_\odot$ ,  $\text{S} = 2.3_{-0.8}^{+0.7} \text{ S}_\odot$ , and  $\text{Fe} = 0.70_{-0.12}^{+0.14} \text{ Fe}_\odot$ . The ionization timescale  $\tau_0 = t_0 N_e$  ( $t_0$  is the

**Figure 5.3:** Spectrum and fitted model of the X-ray emission of the whole remnant.



remnant's age and  $N_e$  the post-shock electron number density) is  $2.7 \times 10^{10}$  s/cm<sup>3</sup> and the ionization timescale-averaged temperature  $\langle kT \rangle = \int_{t_s}^{t_0} T(t) N_e(t) dt / \tau = 1.2_{-0.4}^{+2.2}$  keV ( $t_s$  is the age of the shock). Thus, the unabsorbed flux of G308.4–1.4 in the energy band 0.5 – 4.0 keV is  $f_X = 1.61_{-0.23}^{+0.15} \times 10^{-10}$  ergs cm<sup>-2</sup>s<sup>-1</sup>. The model fit and the raw spectrum are shown in Fig. 5.3. The fitted parameters are listed in Table 5.2.

Adding a second plasma component that is in non-equilibrium results in  $\chi_{red}^2 = 1.06$  for 91 d.o.f. and hence is no improvement over a single component model. The other models that we fitted to the spectral distribution are a hot diffuse gas model (VMEKAL,  $\chi_{red}^2 = 2.92$  for 96 d.o.f.), a model for a collisionally ionized diffuse gas (VAPEC,  $\chi_{red}^2 = 2.34$  for 96 d.o.f.) and a thermal bremsstrahlung model ( $\chi_{red}^2 = 7.7$  for 101 d.o.f.). None of these models can reproduce the spectrum of G308.4–1.4. However, all three model fits result in  $n_H \approx 1 \times 10^{22}$  cm<sup>-2</sup> and a plasma temperature of  $\sim 0.5$  keV.

### The inner sector and the outer rim

As mentioned in Sect. 5.2.2, the extended source was divided into four regions. This was done to investigate the spatial variation of the hot plasma. To extract the background spectra of the inner sector and the outer rim we used the same area on the detector as for the whole remnant. The northern and southern region of the outer rim were analyzed separately. For the background we used only the part of this annular sector that has the same opening angle as the source region.

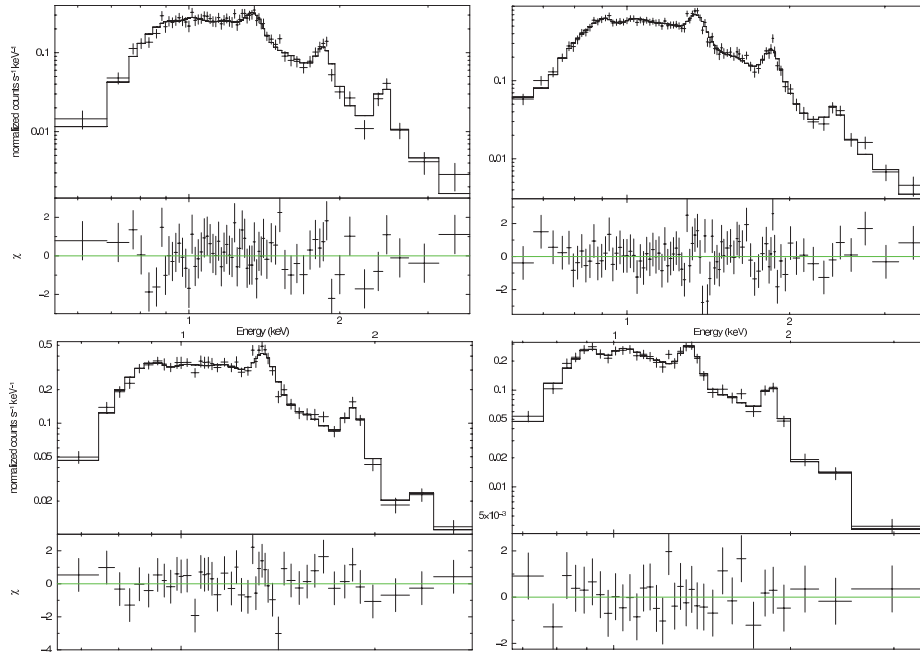
First we fitted the plasma model with free  $n_H$ . In every one of the four spectral fits we found a hydrogen column density that agrees well with the  $n_H$  of the whole remnant. Second, we fitted the spectra with an  $n_H$  fixed to the value of the whole remnant. The fitted value for  $n_H$  and the results of the fits with a fixed column density are summarized in Table 5.2. The spectra with the respective fits are shown in Fig. 5.4.

Within the statistical uncertainties, all regions turned out to have a similar temperature. Only the ionization timescale-averaged temperature was varying. The large statistical uncertainty also

**Table 5.2:** Spectral parameters of the best-fit model for different parts of SNR G308.4–1.4.

	Whole remnant	Inner rim	Outer rim	Outer rim north	Outer rim south
$n_{\text{H}}$ [ $10^{22} \text{cm}^{-2}$ ]	$1.02 \pm 0.04$	$1.05^{+0.11}_{-0.09}$	$1.00 \pm 0.05$	$1.02 \pm 0.09$	$0.99 \pm 0.09$
$k_{\text{B}}T$ [keV]	$0.54^{+0.10}_{-0.06}$	$0.55^{+0.08}_{-0.10}$	$0.54^{+0.08}_{-0.05}$	$0.50^{+0.12}_{-0.06}$	$0.57 \pm 0.08$
$\text{Ne}^{\alpha}$ [ $\text{Ne}_{\odot}$ ]	$0.72 \pm 0.14$	$0.7 \pm 0.3$	$0.73^{+0.15}_{-0.14}$	$0.5 \pm 0.2$	$0.8 \pm 0.2$
$\text{Mg}^{\alpha}$ [ $\text{Mg}_{\odot}$ ]	$0.70^{+0.09}_{-0.08}$	$0.80^{+0.20}_{-0.17}$	$0.67^{+0.10}_{-0.09}$	$0.83^{+0.14}_{-0.13}$	$0.62^{+0.14}_{-0.12}$
$\text{S}^{\alpha}$ [ $\text{S}_{\odot}$ ]	$2.3^{+0.7}_{-0.8}$	$3.0^{+1.9}_{-1.0}$	$1.7^{+0.8}_{-0.7}$	$2.4^{+1.3}_{-1.0}$	–
$\text{Fe}^{\alpha}$ [ $\text{Fe}_{\odot}$ ]	$0.70^{+0.14}_{-0.12}$	$0.9 \pm 0.3$	$0.64^{+0.14}_{-0.12}$	–	$0.45^{+0.19}_{-0.15}$
$\tau^{\beta}$ [ $10^{10} \text{s/cm}^3$ ]	2.7	8.1	2.1	5.2	2.0
$\langle kT \rangle^{\gamma}$ [keV]	$1.2^{+2.2}_{-0.4}$	$0.72^{+0.75}_{-0.12}$	$1.4^{+1.6}_{-0.5}$	$0.81^{+0.76}_{-0.15}$	$1.1^{+1.4}_{-0.4}$
$\text{Norm}^{\delta}$ [ $10^{-2} \text{cm}^{-5}$ ]	$3.3 \pm 0.9$	$0.9^{+0.5}_{-0.2}$	$2.4 \pm 0.5$	$1.4 \pm 0.4$	$1.0 \pm 0.3$
$\chi^2$	98.19	57.54	76.81	38.74	18.55
d.o.f.	95	57	77	38	27
$f_{\text{X}}^{\epsilon}$ [ $10^{-10} \text{ergs cm}^{-2} \text{s}^{-1}$ ]	$1.61^{+0.15}_{-0.23}$	$0.30^{+0.01}_{-0.02}$	$1.25^{+0.08}_{-0.09}$	$0.55^{+0.02}_{-0.04}$	$0.56^{+0.07}_{-0.06}$

**Notes.**  $(\alpha)$  abundance with respect to solar value  $(\beta)$  ionization timescale  $(\gamma)$  ionization timescale-averaged temperature  $(\delta)$   $\text{Norm} = \frac{10^{-14}}{4\pi[D_{\text{A}}(1+z)]^2} \int N_{\text{e}}N_{\text{H}}dV$ , where  $D_{\text{A}}$  is the angular diameter distance to the source in cm,  $N_{\text{e}}$  and  $N_{\text{H}}$  are the post-shock electron and hydrogen densities in  $\text{cm}^{-3}$ , respectively.  $(\epsilon)$  X-ray flux in the energy range 0.5 to 4.0 keV

**Figure 5.4:** Spectrum and fitted model of the X-ray emission of the various regions. *Upper left:* inner part of the remnant, *upper right:* outer rim, *lower left:* outer rim north and *lower right:* outer rim south.

prevents us from concluding on a temperature evolution with the distance to the expected center of the remnant. No variation of the neon and magnesium abundance over the surface of the remnant is detectable. The only noticeable change in abundance is in sulfur and iron in the outer rim. The spectrum in the northern rim shows an abundance in iron comparable with the solar value. In the southern rim no significant deviation from the solar value was found in the abundance of sulfur. Furthermore, the ionization timescale varies with distance from the remnant's center and the direction of the expanding shock wave into the ISM. The highest values for  $\tau$  were found for the inner sector ( $8.1 \times 10^{10}$  s/cm<sup>3</sup>) and the lower one in the southern part of the rim ( $2.0 \times 10^{10}$  s/cm<sup>3</sup>), which implies a different post-shock electron number density in the inner and outer regions of the SNR candidate.

### 5.2.3 The central sources

As mentioned above, two point sources were detected close to the presumed center of the remnant, source # 1 (CXOU J134124.22–634352.0) and # 10 (CXOU J134127.12–634327.7). For the spectral analysis of source # 1 we used all photons within a circular region of radius 10 arcsec centered on the source position. The background was extracted from an annulus with radii 15'' and 20''. After background correction 195 source counts in the energy band between 0.5 and 10.0 keV remained. We used the CIAO tool `psextract` to compute the response matrices necessary to compensate for the changing spectral response of the CCD and the telescope with energy and off-axis angle. The spectrum was binned with at least 20 counts per bin.

A single absorbed blackbody or a single absorbed power law model for fitting the spectral distribution gives poor results. In the case of a blackbody spectrum the reduced  $\chi^2 = 2.67$  for 6 degrees of freedom is unacceptably large. The power law model fit results in a reduced  $\chi^2$  of 0.94 (6 d.o.f.). However, the post-fit residuals show systematic derivations between the data points and the fitted model. Therefore, we used a two-component absorbed blackbody model that resulted in  $\chi^2 = 1.62$  (4 d.o.f.) and a  $n_H = 1.34^{+1.80}_{-1.31} \times 10^{22}$  cm<sup>-2</sup>. To better constrain the spectral parameters we fixed  $n_H$  to the hydrogen column density obtained from fits to G308.4–1.4. This yielded a reasonable fit with  $\chi^2 = 1.96$  for 5 d.o.f. (see Fig. 5.6). The temperatures of the two blackbodies are  $T_1 = 1.3^{+0.3}_{-0.2} \times 10^6$  K and  $T_2 = 6.4^{+2.8}_{-1.4} \times 10^6$  K. The normalization factors of the two blackbodies are  $K_1 = 7^{+21}_{-5} \times 10^{-5}$  and  $K_2 = (1.3 \pm 0.4) \times 10^{-6}$ . Using these values and the distance to the source  $D_{10}$  in units of 10 kpc we estimated the emitting source radius  $R$  as follows:

$$R_i = \sqrt{\frac{K_i \cdot D_{10}^2 \times 10^{39} \text{ erg/s}}{4\pi\sigma_B T^4}} \text{ m}, \quad (5.1)$$

where  $\sigma_B$  is the Stefan-Boltzmann constant. Because we do not know the distance to G308.4–1.4 we considered the emitting radius as a function of the distance to the source. This is illustrated in Fig. 5.5. The result for the second blackbody is  $R_2 = 340^{+302}_{-158} D_{10}^{-1}$  m. The unabsorbed flux in the energy band 0.5 to 10 keV is  $f_X = 2.2^{+0.5}_{-1.9} \times 10^{-12}$  ergs cm<sup>-2</sup>s<sup>-1</sup> and in the energy band 0.3 to 3.5  $f_X = (4 \pm 2) \times 10^{-12}$  ergs cm<sup>-2</sup>s<sup>-1</sup>.

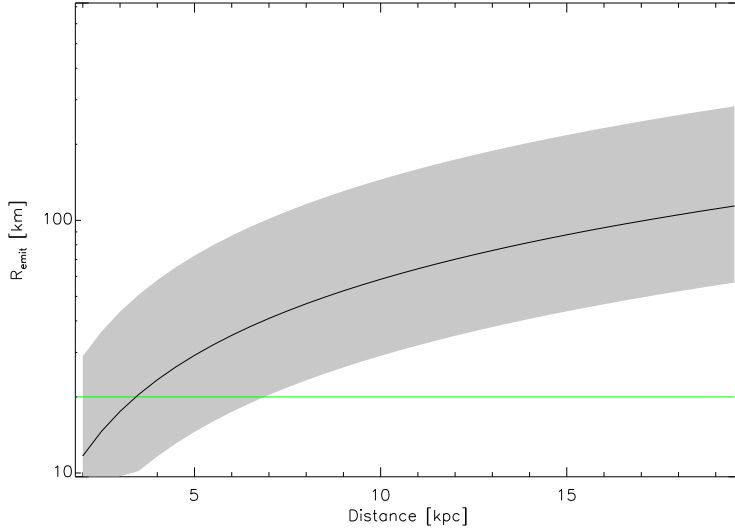


**Figure 5.5:** Dependence of the blackbody-emitting radius  $R_1$  of the first blackbody in the double blackbody spectral fit on the distance to source # 1 in kpc (equation 5.1). The error range is gray shaded and the green line indicates the upper limit on the radius of a neutron star.

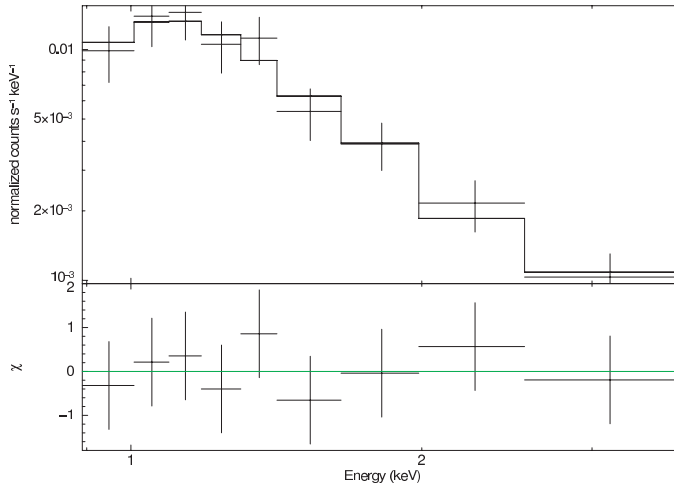


**Figure 5.6:** Spectrum of source # 1 fitted with a double blackbody spectrum.

Additionally, we tried a model composed of a blackbody and a power law with the same fixed  $n_H$  as before. This gives a reasonable fit with  $\chi^2 = 2.17$  (5 d.o.f.). The photon index is  $2.4^{+1.0}_{-1.2}$  and the blackbody temperature is  $(1.3 \pm 0.3) \times 10^6$  K. With the normalization of  $K_1 = 9^{+53}_{-7} \times 10^{-5}$  the emitting radius is  $73^{+216}_{-45} D_{10}^{-1}$  km. The unabsorbed flux in the energy band 0.5 to 10 keV is  $f_X = 2.5^{+0.5}_{-2.3} \times 10^{-12}$  ergs  $\text{cm}^{-2} \text{s}^{-1}$ .

As mentioned in section 5.2.1, the position of source # 1 is consistent with 2MASS J13412422–6343520, a star with a magnitude of  $B = 19.7$ ,  $R = 19.6$ ,  $J = 14.0$ ,  $H = 13.3$  and  $K = 13.1$ . This implies an X-ray-to-visual flux ratio of  $\log(f_X/f_V) = \log(f_X) + V/2.5 + 5.37 = 1.55$  (Maccacaro et al., 1988). Here  $f_X$  is the X-ray flux in the 0.3 – 3.5 keV band in ergs  $\text{cm}^{-2} \text{s}^{-1}$ ,  $V$  is the visual magnitude; we assumed that  $V \approx R$ .

In addition we tried to fit various plasma models to the source spectrum. The only reasonable fit was found when using a collisionally ionized diffuse gas model (APEC). The goodness of fit that we found for 6 d.o.f. was  $\chi_{red}^2 = 0.78$  for the following spectral parameters:  $n_H < 0.47 \times 10^{22}$

**Table 5.3:** Spectral fit results of the central source # 1.

Model	$\chi^2/\text{d.o.f.}$	$n_{\text{H}}$ $10^{22} \text{ cm}^{-2}$	$\Gamma/kT_1$ -/keV	$K_1$	$kT_2$ keV	$K_2$	$f_X^{0.5-10}/f_X^{0.3-3.5}$ $10^{-12} \text{ ergs cm}^{-2} \text{ s}^{-1}$
BB $^{\alpha,\delta}$	16.00/6	$1.2 \times 10^{-4}$	0.44	$9.9 \times 10^{-7}$	–	–	–/–
PL $^{\alpha,\gamma}$	5.62/6	< 0.33	$2.2^{+0.9}_{-0.4}$	$3.9^{+4.3}_{-0.9} \times 10^{-5}$	–	–	$0.16^{+0.03}_{-0.02}/0.16^{+0.04}_{-0.03}$
BB+BB $^{\beta}$	1.96/5	$1.34^{+1.80}_{-1.31}$	$0.11^{+0.03}_{-0.02}$	$7^{+21}_{-5} \times 10^{-5}$	$0.55^{+0.24}_{-0.12}$	$(1.3 \pm 0.4) \times 10^{-6}$	$2.2^{+0.5}_{-1.9}/4 \pm 2$
PL+BB $^{\beta,\gamma}$	2.74/5	< 3.8	$2.4^{+1.0}_{-1.2}$	$7^{+11}_{-5} \times 10^{-5}$	$0.11 \pm 0.03$	$9^{+53}_{-7} \times 10^{-5}$	$2.5^{+0.5}_{-2.3}/5^{+3}_{-4}$
APEC	4.66/6	< 0.47	$2.7^{+1.5}_{-1.2}$	$9.0^{+3.0}_{-1.5} \times 10^{-5}$	–	–	$0.13^{+0.03}_{-0.02}/0.11^{+0.04}_{-0.03}$
BREMS $^{\alpha,\delta}$	6.98/6	$1.8 \times 10^{-9}$	$2.1^{+2.1}_{-0.8}$	$5.1^{+2.3}_{-1.3} \times 10^{-5}$	–	–	–/–
RAYMOND $^{\alpha}$	5.70/6	< 0.21	$2.8^{+2.0}_{-1.1}$	$8.9^{+1.8}_{-0.8} \times 10^{-5}$	–	–	$0.13 \pm 0.02/0.11^{+0.02}_{-0.01}$

**Notes.**  $^{(\alpha)}$  fit shows systematic derivations between the data points and the fitted model.  $^{(\beta)}$  the spectral parameters are calculated with  $n_{\text{H}}$  fixed to the value obtained in the fit to the spectrum of G308.4–1.4.  $^{(\gamma)}$  Power law norm in photons  $\text{keV}^{-1} \text{cm}^{-2} \text{s}^{-1}$  at 1 keV.  $^{(\delta)}$  some errors could not be calculated.

$\text{cm}^{-2}$ ,  $T = 3.1^{+1.7}_{-1.4} \times 10^7$  K. For this model the flux in the 0.3 to 3.5 keV range is  $f_X = 1.1^{+0.2}_{-0.1} \times 10^{13} \text{ ergs cm}^{-2} \text{s}^{-1}$ . Thus, the X-ray-to-visual flux ratio is  $\log(f_X/f_V) = 0.25$ . Again no variation in the spectral parameters between the flaring and quiescence epoch are detectable. All fitted models and their inferred spectral parameters are listed in Table 5.3.

### Temporal analysis of source # 1

To search for any temporal variability we binned the photon time of arrivals with 400 s per bin (see Fig. 5.7). The data clearly show a flare in the first kilo-seconds of the observation. The spectral parameter of the double blackbody in the flaring and quiescence epoch match the overall spectrum within the error bars. Varying only the normalizations of the two blackbodies, the flux in the quiescence epoch is with  $f_X^{0.5-10} = (1.9 \pm 0.3) \times 10^{-12} \text{ ergs cm}^{-2} \text{s}^{-1}$  slightly lower than the flux in the total exposure. However, the flux in the time interval when the source was flaring is  $f_X^{0.5-10} = (5.2 \pm 1.5) \times 10^{-12} \text{ ergs cm}^{-2} \text{s}^{-1}$ , three times the quiescence flux. However, the sparse photon statistics lead to large uncertainties in the derived errors of the quiescence and flaring fluxes and thus they are only rough estimates. Merging the SWIFT observations we cannot detect a source at the position of source # 1. In the merged image a total of four counts were recorded within a circle with radius 15 arcsec (equals an encircled energy of 70 %) centered on the position of source # 1. The total exposure time of the source was 8344 s. Hence, the  $3\sigma$  upper limit for the counting rate is approximately  $8.6 \times 10^{-4} \text{ cts/s}$ . Using the mission count rate simulator for X-ray observatories WebPIMMS<sup>3</sup> with the SWIFT response and the spectral parameters derived for a double blackbody spectrum, the upper limit on the flux is  $\approx 5.3 \times 10^{-13} \text{ ergs cm}^{-2} \text{s}^{-1}$ . For the APEC model the upper limit is  $\approx 2.3 \times 10^{-14} \text{ ergs cm}^{-2} \text{s}^{-1}$ . These limits are less than 25 % of the average flux in the Chandra observation, clearly indicating that the source flux is variable on time scales of at least several hours to weeks.

<sup>3</sup><http://heasarc.nasa.gov/Tools/w3pimms.html>

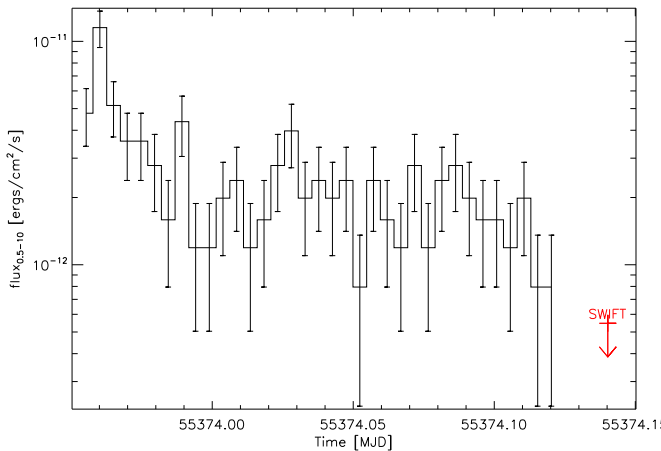


**Figure 5.7:** Flux variation of source # 1 in the Chandra observation binned with 400 s per bin and scaled with the mean flux in the whole exposure. The red arrow indicates the  $3\sigma$  upper limit derived with the SWIFT observations.

### Extent of source # 1

With the help of a one-dimensional distribution of the counts per  $0.5''$  bin along a vertical line in the Chandra image around source # 1 we checked if the source is extended. The resulting diagram was obtained by integrating all counts within  $5'' \times 0.5''$  rectangular apertures moving along the western direction with  $0.5''$  steps. We compared this with the count distribution of a point source simulated with MARX<sup>4</sup>. However, no excess emission of point source # 1 could be detected.

For source # 10, the other source located close to the center of the remnant, we detected only eight net counts. Hence, the count rate is  $(5.1 \pm 1.9) \times 10^{-4}$  cts/s, but no spectral analysis is possible because of the limited statistics.

## 5.3 Radio observation and data analysis

The source G308.4–1.4 was observed for 11.25 hours with the Australia Telescope Compact Array, a synthesis telescope near Narrabri, New South Wales on 11 January 2002 at 1.432 and 2.448 GHz with 13 channels per band. The single-pointing continuum observations of the source G308.4–1.4 were carried out with the array configuration 0.75C (maximum baseline length is 750 m). All four Stokes parameters have been recorded.

The flux density calibration was performed through observations of PKS B1934–638, which is the standard primary calibrator for ATCA observations. Phases were calibrated using observations of secondary calibrating sources PKS 1329–665. Since the primary beam response is frequency-dependent, we did not merge the data from two observing bands before imaging and cleaning. Every single observing run and each of the two observing bands were calibrated separately following the standard procedures for ATCA observations.

<sup>4</sup>MARX is a software that can be used to simulate the performance of the Chandra X-ray observatory; see <http://space.mit.edu/cxc/marx/>

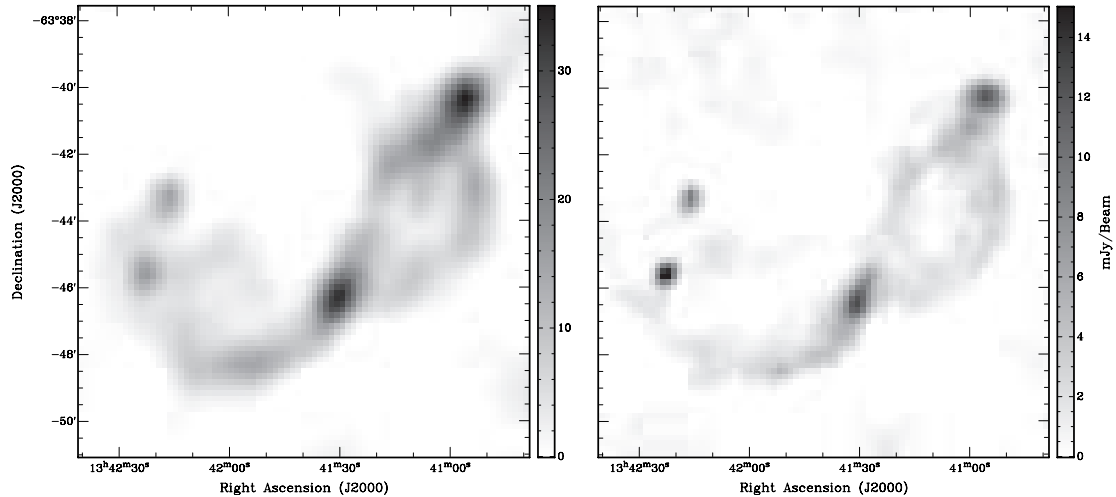


**Figure 5.8:** Gray-scale image of SNR G308.4–1.4. The left image displays the SNR at 1.4 GHz and on the right the same region at 2.5 GHz. The 1.4 GHz image is smoothed with a beam of  $63.6'' \times 53.2''$  and the 2.5 GHz with a beam of  $35.2'' \times 29.3''$ .

The reduction was carried out using the ATNF release of the Multichannel Image Reconstruction, Image Analysis and Display (MIRIAD, Sault et al., 1995). A number of steps in the reduction process (i.e. “flagging”) were performed interactively.

Because of the poor phase stability during the observation, the scalar averaging of gains over the interval of 5 min (the length of secondary calibrator scan) was performed. Then, a total-intensity continuum image square region was formed using multi-frequency synthesis, uniform weighting and a cell size of 10 arcsec. At the stage of the dirty map production all correlations with 6th baseline were excluded to obtain images with better signal-to-noise ratio. The next step was to de-convolved both images using the standard CLEAN algorithm (Clark, 1980) with 10 000 iterations. The resulting images were restored and corrected for the mean primary beam response of the ATCA antennas. The final images have synthesized beam sizes of  $63.6'' \times 53.2''$  and  $35.2'' \times 29.3''$  for the 1.384 GHz and 2.496 GHz band, respectively.

In both frequency bands the images show two radio arcs (see Fig. 5.8). The eastern arc matches the X-ray emission region. For the western arc no counterpart is visible in the X-ray regime. There are also two radio-bright knots within the arcs that have neither a counterpart in X-rays (see Fig. 5.9) nor in the optical band (dss2red). No difference can be seen to the morphology of the extended source in the SUMSS 843 MHz map.

The flux densities of G308.4–1.4 without the two bright knots are 235, 174, and 110 mJy at 843, 1384, and 2496 MHz, respectively. These values were obtained by integrating the emission within multiple polygons enclosing the remnant. The 843 MHz flux density was deduced from the SUMSS image. The bright southern knot has a flux density of 110, 75, and 70 mJy at 843, 1384, and 2496 MHz, whereas for the northern knot we measured a flux density of 96, 76, and 56 mJy at 843, 1384, and 2496 MHz. In all cases we assumed a conservative error of 20% in the flux density.

The rms noise levels are  $0.28 \text{ mJy beam}^{-1}$  and  $0.05 \text{ mJy beam}^{-1}$  for the 1.384 GHz and

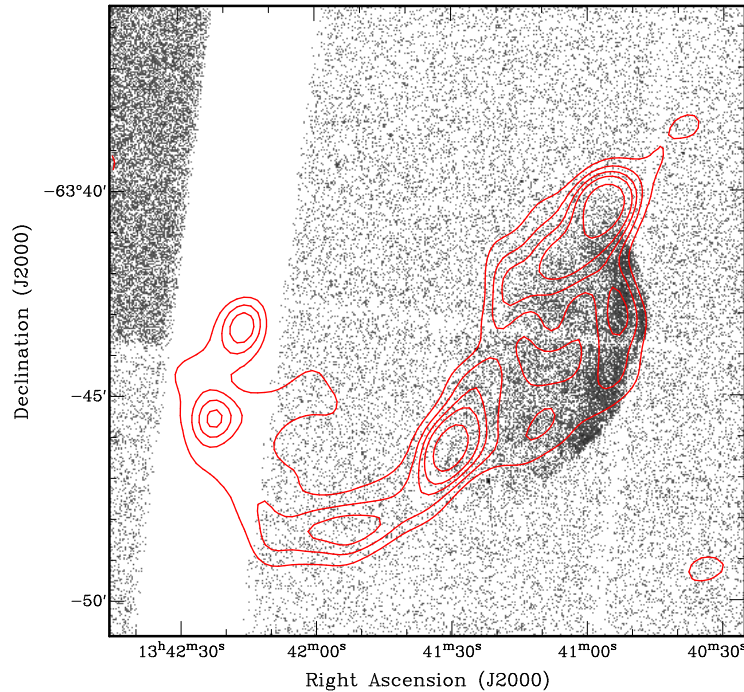


**Figure 5.9:** Chandra  $15' \times 15'$  image of G308.4–1.4 overlaid with the ATCA data at 1.4 GHz. The contour levels are 4, 8, 12, 16, and 24  $\text{mJy beam}^{-1}$ . The radio image has a full width at half maximum (FWHM) of  $63.6'' \times 53.2''$  and the X-ray image is binned with  $1''$  per pixel.

2.496 GHz image. The levels were measured by integrating over nearby source-free regions. The spectral indices were computed using the total flux density measurements in all available frequencies (0.843, 1.384, and 2.496 GHz). Fitting the data with a power law  $S_\nu \propto \nu^\alpha$ , we obtained a spectral index for the northern knot  $\alpha = -0.50 \pm 0.14$  and for the southern knot  $\alpha = -0.49 \pm 0.16$ , respectively. The radio emission of the two arcs, however, have a spectral index  $\alpha = -0.7 \pm 0.2$ . No significant polarized radio emission could be detected.

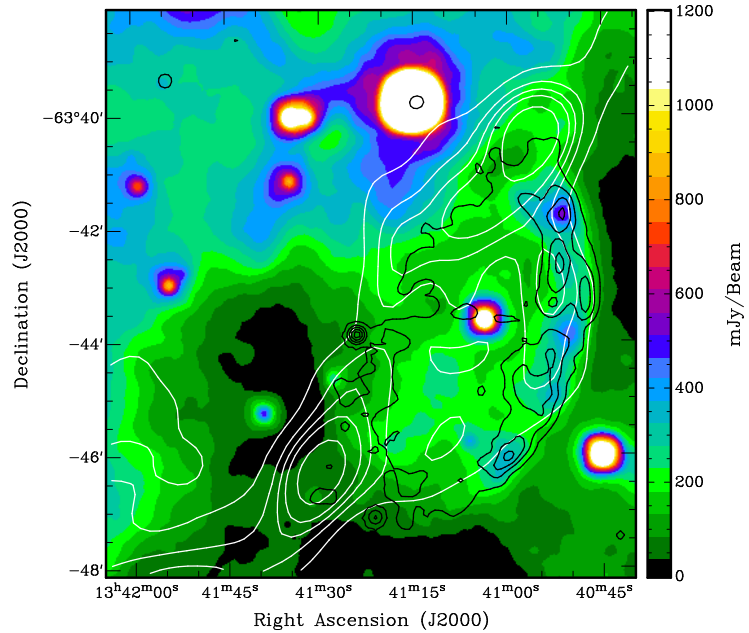
## 5.4 Observations in other wavelength regimes

The region around G308.4–1.4 was observed in the four infrared bands 3, 5, 12, and  $22 \mu\text{m}$  during the Wide-field Infrared Survey (WISE, Wright et al., 2010). With the  $22 \mu\text{m}$  filter an extended infrared emission is detectable that overlaps with the radio and X-ray emission regions (see Fig. 5.10). After subtracting the background contribution the intensity image in the  $22 \mu\text{m}$  band was converted into a flux image using the explanatory supplement to the WISE All-Sky Data Release Products<sup>5</sup>. We did not apply color correction because the emission mechanism in the infrared regime is uncertain. In addition, the integrated flux was not corrected for extinction. To compare the infrared with the 1.4 GHz image the flux density in the  $22 \mu\text{m}$  observation was scaled to  $\text{Jy/beam}$ , where the beam is  $63.6 \times 53.2 \text{ arcsec}^2$ . Using the region of infrared emission that is clearly associated with the remnant, the integrated flux of G308.4–1.4 in the  $22 \mu\text{m}$  band is  $\approx 1.7 \text{ Jy}$ .

The shock wave of an SN that is running into the interstellar medium can interact with ad-

<sup>5</sup>[http://wise2.ipac.caltech.edu/docs/release/allsky/expsup/sec2\\_3f.html](http://wise2.ipac.caltech.edu/docs/release/allsky/expsup/sec2_3f.html)

**Figure 5.10:**  $10' \times 10'$  WISE image of the region around G308.4–1.4 at 22 micron with the radio contour lines in white at 3, 8, 12, 16, and 24 mJy and the X-ray contours in black.



adjacent molecular clouds and produce  $\gamma$ -rays via decays of  $\pi^0$  (Abdo et al., 2011). We therefore checked the archive of the Fermi Large-Area Telescope for a  $\gamma$ -ray source at the position of G308.4–1.4. The Fermi  $\gamma$ -ray satellite monitors the sky continuously since August 2008. However, no source has been detected close to G308.4–1.4 in the Fermi-LAT Second Source Catalog (Nolan et al., 2012) and investigating the images ourselves we found no  $\gamma$ -ray emission matching the X-ray morphology.

## 5.5 Discussion and conclusion

Comparing the fitted  $n_{\text{H}}$  with the integrated hydrogen column density toward the source of Kalberla et al. (2005) and Dickey and Lockman (1990) places G308.4–1.4 within our Galaxy.

The plasma model we used to fit the energy spectrum of G308.4–1.4 was especially designed to improve the modeling of X-ray spectra of SNR. Other plasma models assume ionization equilibrium and are therefore not able to reproduce the spectra of young SNRs that are not evolved enough to reach ionization equilibrium (Borkowski et al., 2001). Furthermore, the temperature of the plasma of approximately 6 million Kelvin is in the typical range for SNRs (McKee, 1987).

The analysis of the archival ATCA radio data revealed non-thermal emission with a spectral index of  $\approx -0.7$ , which is typical for young to middle-aged SNRs (Dickel, 1991). The spectral index has a large error due to the noise in the 2.5 GHz observation but still agrees with the expected value of 0.4 to 0.5 for middle-aged SNR.

Infrared radiation from SNRs is expected to come either from thermal emission of dust grains in the hot plasma that are heated through collision, or from the forbidden lines of elements such as neon, oxygen, and iron (Seok et al., 2008). Several authors were able to show that by comparing the infrared and radio emission it is possible to distinguish between SNRs and HII-

regions (Fürst et al., 1987; Broadbent et al., 1989; Pinheiro Gonçalves et al., 2011). Moreover, in the work by Pinheiro Gonçalves et al. (2011) the ratio between the flux density in the MIPS GAL 24- $\mu\text{m}$  (Carey et al., 2009) and the 1.4-GHz band was used. These authors found that the ratio is  $\leq 10$  for SNR and higher than 30 for HII-regions. For SNR G308.4–1.4 the 22  $\mu\text{m}$  band was observed, which covers roughly the wavelength range from 20  $\mu\text{m}$  to 27  $\mu\text{m}$ . Thus, the band is comparable with the MIPS GAL 24  $\mu\text{m}$  band, which is sensitive for infrared emission in the range from 20  $\mu\text{m}$  to 30  $\mu\text{m}$  (Pinheiro Gonçalves et al., 2011). The 22- $\mu\text{m}$  to 1.4-GHz ratio for G308.4–1.4 is  $\approx 10$ . Hence, the infrared emission matching the radio and X-ray morphology and the measured 22- $\mu\text{m}$  to 1.4-GHz ratio additionally supports that G308.4–1.4 is an SNR.

The lack of  $\gamma$ -ray emission from G308.4–1.4 can be explained by the poor spatial resolution of the Fermi-LAT telescope ( $\sim 1^\circ$  at 1 GeV), which makes it hard to distinguish faint extended sources from the diffuse emission of the Galactic plane. Of the 274 known SNRs only seven have been detected by Fermi-LAT so far (Nolan et al., 2012).

There are various physical scenarios to show what might cause a plasma to emit X-rays. However, the two emission models for hot diffuse (MEKAL, Mewe et al., 1986) and collisionally ionized diffuse gas (APEC, Smith et al., 2001), which are often used to describe the X-ray emission of Galaxy Clusters (ClGs), cannot reproduce the spectrum of G308.4–1.4. Moreover, the temperature of ClGs is typically several  $10^7$  K (Böhringer and Werner, 2010), one order of magnitude higher than the fitted value. Thus, we can conclude that G308.4–1.4 is not a ClG. In addition, we can exclude that G308.4–1.4 is a planetary nebula (PN) because its X-ray flux is three orders of magnitude higher than the flux of the brightest PN detected in X-rays, which is at a distance of  $\approx 1$  kpc (Guerrero et al., 2006) and because of the low 22- $\mu\text{m}$  to 1.4-GHz flux ratio. Furthermore, the temperature of G308.4–1.4 is a factor of two higher than the highest measured temperature of the hotter, type 2 PNe (Guerrero et al., 2000).

Based on these results we conclude that G308.4–1.4 is indeed a supernova remnant. Only the eastern part of the remnant can be seen in the radio-, infrared- and X-ray regime, which is not unusual for SNRs (e.g., Castro et al., 2011). A reason for that could be that its shock wave is expanding in more dense ISM in the east or the emission in the western part is absorbed by ISM that is in front of the SNR. Figure 5.10 shows an extended and infrared-bright region in the northwestern part of the SNR, whose emission is not correlated with the SNR.

Using the inferred spectral parameters we can estimate fundamental characteristics of the remnant, such as the distance from Earth and its age.

### 5.5.1 Distance

To derive a rough estimate for the distance to SNR G308.4–1.4 we used a method described by various authors (Sun et al., 1999; Safi-Harb et al., 2001; Gonzalez and Safi-Harb, 2003): From the distribution of mean color excess  $\langle E_{B-V} \rangle$  per kiloparsec derived by Lucke (1978) we found  $\langle E_{B-V} \rangle = (0.3 \pm 0.1) \text{ mag kpc}^{-1}$ . Using the fitted hydrogen column density for the whole remnant  $n_{\text{H}} = (1.02 \pm 0.04) \times 10^{22} \text{ cm}^{-2}$ , the relation between the hydrogen column density  $n_{\text{H}}$  and the visual extinction  $A_{\text{V}}$  of Predehl and Schmitt (1995)  $n_{\text{H}} = (1.79 \pm 0.03) \times 10^{21} \text{ cm}^{-2} A_{\text{V}}$  and adopting the relation between  $A_{\text{V}}$  and the color excess  $A_{\text{V}} / \langle E_{B-V} \rangle = (3.2 \pm 0.2)$  (Zombeck, 2007), the distance to G308.4–1.4 is  $d = 5.9 \pm 2.0 \text{ kpc}$ . We note that this distance is a lower

boundary of the real distance. This is because the mean color excess  $\langle E_{B-V} \rangle$  we used was derived for reddening layer up to 2 kpc. For distance estimates for Galactic PNe the reddening inferred distances are mostly significantly shorter than distances derived with other methods (Phillips, 2006). This leads us to assume that  $d \approx 6$  kpc is the lower boundary limit for the distance to SNR G308.4–1.4.

Another approach to determine the distance to G308.4–1.4 uses the fact that the radius of the remnant  $R_s$  can be determined in two ways, where  $R_s$  depends on the distance  $d$  with different exponents. The first equation is a result of the Sedov analysis discussed in the next section (equation 5.4) and depends on  $d^{1/6}$ . The second equation to determine  $d$  is simply the comparison of the radius of the remnant in pc ( $R_s$ ) and in arcmin ( $\theta$ ),  $d = R_s/\theta$ , which depends linearly on the distance unit  $d$ . Using these dependencies we derive

$$d = 7420 \cdot (\theta [\text{arcmin}])^{-3/5} \left( \frac{E_{51}}{T_s [\text{K}]} \right)^{2/5} \left( \frac{f}{\text{Norm}} \right)^{1/5} = 9.8_{-0.7}^{+0.9} \text{ kpc}, \quad (5.2)$$

where  $T_s$  is the post-shock temperature and  $E_{51}$  the SN explosion released kinetic energy in units of  $10^{51}$  ergs.

Furthermore, with the help of the ATCA radio observations and the publicly available HI data from the Southern Galactic Plane Survey (SGPS; McClure-Griffiths et al., 2005), it is possible to constrain the distance using the Galactic rotation model of Fich et al. (1989). For the region around G308.4–1.4 the SGPS archive provides ATCA data observed with a beam size of  $130'' \times 130''$  and a  $1\sigma$  sensitivity of  $\sim 1.6$  K. However, the data cover only the northern part of the remnant. The SGPS archive also holds Parkes data that cover the region around the SNR, but with an angular resolution of  $15'$ . This beam is twice the size of the remnant's diameter. Therefore, we chose to use the ATCA data for the subsequent analysis.

First, we convolved the radio continuum image at 1.4 GHz to the same beam size as the SGPS data. We assumed that the emission of the remnant does not vary significantly across the emission region. Second, the convolved image was used to generate an on-source spectrum of SNR G308.4–1.4 by averaging the HI emission for every velocity bin in the HI data cube at which the radio continuum emission was higher than 5 mJy. The off-source spectrum was computed by taking the average of the emission in the surrounding of the on-source region of the remnant. These two profiles and the difference plot between these two profiles are shown in Fig. 5.11. The difference profile is dominated by drifts in the zero level. This is because the source is at the border of the image and as we are using public data, the pointing is not perfect for the method applied. In addition to the drifts, we detect one absorption feature with a significance of  $> 3\sigma$  at  $V_r \sim 30$  km/s. With the standard IAU parameter for the distance to the center of the Galaxy  $R_0 = 8.5$  kpc and the solar orbit velocity of  $V_0 = 220$  km/s derived by Kerr and Lynden-Bell (1986) and the already mentioned Galactic rotation model we deduce a distance to G308.4–1.4 of  $2.0 \pm 0.6$  kpc and  $12.5 \pm 0.7$  kpc. For the error estimate we assumed an uncertainty in the velocity-to-distance conversion of 7 km/s as suggested by various authors (e.g., Clifton et al., 1988) and used the FWHM of the feature as the uncertainty in the velocity determination. Based on the calculated lower limit for the distance of the remnant we can rule out the lower value as unreasonable. The low significance of the absorption feature leads to the

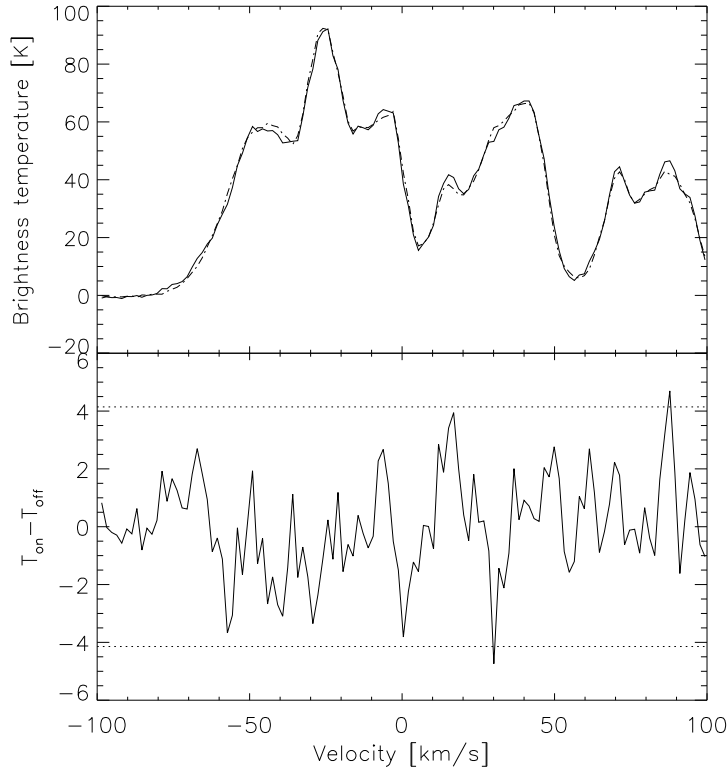


**Figure 5.11:** Top: HI spectrum on- and off-source (continuous and dotted line, respectively) in the direction of SNR G308.4–1.4. Bottom: Difference profile with the  $3\sigma$  level indicated by a dotted vertical line.

conclusion that the Sedov-analysis-based distance approximation is the more reliable estimate for the distance to SNR G308.4–1.4. Thus, in the following all important quantities are given in units of  $d_{9.8} = d/9.8$  kpc. Using the flux values deduced for G308.4–1.4 we compute its X-ray luminosity to be  $L_X^{0.5-4} = 1.8_{-0.2}^{+0.3} \times 10^{36} d_{9.8}^{-2}$  erg/s.

### 5.5.2 Age

First we deduced the post-shock hydrogen density  $N_H$ . Using the normalization constant derived in the model fit of a collisional plasma that is in non-equilibrium (VGNEI) and assuming that the hydrogen and electron densities are constant over the volume  $V$  of the emission region, we derived the following relation:  $N_e N_H = Norm \cdot \frac{\pi D_A^2}{10^{-14} V} \text{ cm}^{-6}$ .  $V$  can be approximated by a sphere with radius  $r \approx \frac{4.2' \pi}{180} \cdot D$  of which only a fraction of  $\sim \frac{136}{360}$  is sufficiently bright to be detected in the X-ray regime. Therefore, the volume is  $V = 1.14 \times 10^{54} (r[\text{arcmin}])^3 d_{kpc}^3 \text{ cm}^3 = 7.98 \times 10^{58} d_{9.8}^3 \text{ cm}^3$ . Here  $d_{kpc}$  is the distance to G308.4–1.4 in kpc. For a fully ionized plasma with cosmic abundances ( $\approx 10\%$  He) the ratio between hydrogen and electron density can be estimated by  $N_H/N_e \approx 0.8$ . Thus, the post-shock hydrogen density  $N_H = (0.77 \pm 0.11) d_{9.8}^{-1/2} \text{ cm}^{-3}$  and the corresponding swept-up mass  $M = 1.4 N_H m_H V \sim 71.7 d_{9.8}^{5/2} M_\odot$  (Slane et al., 2002).

The age of the remnant can be approximated by (McKee, 1987)

$$t = 2.71 \times 10^9 \left( \frac{E_{51}}{N_H} \right)^{\frac{1}{3}} T_s^{-\frac{6}{5}} d_{9.8}^{\frac{1}{6}} \text{ yr.} \quad (5.3)$$

Assuming that the explosion energy is equal to the canonical value of  $10^{51}$  ergs and the fitted temperature is approximately  $T_s$ , the derived value for the hydrogen density suggests an age of  $\approx 5000 - 7500$  years for SNR G308.4–1.4. Using this result we can calculate the theoretical radius of the remnant (Culhane, 1977)

$$R_s = 0.34 \left( \frac{E_{51}}{N_H} \right)^{\frac{1}{5}} t^{\frac{2}{5}} \text{ pc} = 11.9_{-1.8}^{+1.9} d_{9.8}^{\frac{1}{6}} \text{ pc} \quad (5.4)$$

and the shock velocity (Sedov, 1959)

$$v_s = \frac{2 R_s}{5 t} = 730_{-160}^{+190} \text{ km/s,} \quad (5.5)$$

which is independent of the assumed distance. The age for the transition from the Sedov-phase into the radiative phase is about 29 kyr (Blondin et al., 1998). The fact that G308.4–1.4 is much younger than the transition time scale suggests that G308.4–1.4 is in the Sedov-phase. Furthermore, the energy spectrum of the remnant supports that G308.4–1.4 is in the Sedov-phase.

However, the derived parameters should only be seen as rough estimates because we were unable to determine whether a full temperature equilibrium is already established. If this is not the case, a generally higher ion temperature, which determines the SNR dynamics, would lead to a higher shock velocity and subsequently to, e.g., an overestimation of the remnant's age.

### 5.5.3 The central sources CXOU J134124.22–634352.0 and CXOU J134127.12–634327.7

No radio counterpart for CXOU J134124.22–634352.0 has been detected in the ATCA and SUMSS observations of G308.4–1.4. An explanation could be that the variable source is also variable in the radio band and therefore the source was missed in all previous observations of this region. To decide if this is the case new observations are needed.

Additionally, CXOU J134124.22–634352.0 has no compact/extended X-ray emission as seen in other young and powerful pulsars. Its best-fit spectral model consists of two blackbodies. Thus, source # 1 shows some properties that have been also seen in central compact objects (CCO, see Gotthelf and Halpern, 2008a, for a review). These CCOs are young neutron stars that are located in SNRs with an age of less than 10 kyr. They have X-ray luminosities between  $10^{32}$  and  $10^{33}$  erg/s in the energy range 0.5–10 keV. No CCO has a detected counterpart in the radio and optical band so far. For one member of the CCO group, 1E 161348–5055 in RCW 103, flares have been detected in which the flux varies between 0.8 and  $60 \times 10^{-12}$  ergs  $\text{cm}^{-2} \text{ s}^{-1}$ . This is comparable to source # 1 whose maximum flux is  $\approx 10^{-11}$  ergs  $\text{cm}^{-2} \text{ s}^{-1}$  and the upper limit derived from the SWIFT observations is  $\approx 5 \times 10^{-13}$  ergs  $\text{cm}^{-2} \text{ s}^{-1}$ .

Using the distance derived in Sect. 5.5.1 the luminosity of CXOU J134124.22–634352.0 is  $L_X^{0.5-10} = 2.5_{-0.6}^{+1.2} \times 10^{34} d_{9.8}^{-2}$  erg/s. This is slightly higher than the derived luminosity for the normal population of CCO (Becker, 2009, p.121), only the flaring CCO in RCW 103 has a comparable luminosity of  $0.1 - 8 \times 10^{34}$  erg/s (de Luca, 2008).

Krautter et al. (1999) found for all X-ray-bright stars with an optical counterpart a ratio of  $\log(f_X/f_V) = -2.46 \pm 1.27$  in the ROSAT All-Sky Survey. Therefore, the X-ray-to-visual flux ratio of 1.55 and the fitted  $n_H$ , which is on the order of what has been observed for G308.4–1.4, suggest a CCO interpretation for source # 1.

Assuming that the source is indeed the compact remnant, we can derive the proper motion of the object  $\mu = \sqrt{(RA_c - RA_{\#1})^2 + (DEC_c - DEC_{\#1})^2}/t = (45 \pm 4)''/t$  using the inferred center and the age of the SNR. We deduce the proper motion to be  $\mu = 7 \pm 2$  mas/yr =  $320 \pm 100$  km/s. The upper limit on  $\mu$  is higher than the mean two-dimensional proper motion of pulsars in SNRs of  $\sim 227$  km/s (Hobbs et al., 2005), but would not be an exception. For example, the CCO RX J0822-4300 in the SNR Puppis A has a 2d proper motion of  $672 \pm 115$  km/s (Becker et al., 2012).

Nevertheless, the lower limit of the inferred emitting radius of the blackbody in the double blackbody or the power law-blackbody spectral fit is on the order of the expected value for the neutron star radius of 10 to 20 km only if the source is at a distance of at least 7 kpc (see Fig. 5.5). Moreover, we found an infrared and optical source whose position is consistent with source # 1. The spectral distribution of the source allows us to fit a collisionally ionized diffuse gas model (APEC), which Osten et al. (2005) used to model the energy distribution in the X-ray band of the M dwarf flare star EV Lacertae. In addition, the fitted hydrogen column density is consistent with that of a nearby star and the X-ray-to-visual flux ratio is 0.25, only  $2\sigma$  higher than the value for stars derived by Krautter et al. (1999).

Using the stellar density in the direction of G308.4–1.4 we can derive the chance association of the observed 2MASS source with the compact remnant candidate. The chance association is given by  $P_{coin} = \frac{N}{l_{RA}l_{Decl.}} \pi \delta RA \delta DEC$ , where  $N$  is the number of sources detected within a rectangular region of length  $l_{RA}$  and width  $l_{Decl.}$  and  $\delta RA$ ,  $\delta DEC$  are the errors in the position of the source. The 2MASS catalog contains 2206 point-like sources in a box with side length of 5 arcmin around the center of the remnant and the chance association is 1.3%. Thus, the possibility of a false association between the X-ray and the 2MASS source cannot be excluded.

Until now, we did not discuss the western radio arc, which has no counterpart in the X-ray and infrared image. The arc could be interpreted as a relativistic radio jet of a source at the geometrical center of the SNR. If that is the case, the central source is either a black hole of stellar mass or a neutron star in a binary system (Mirabel and Rodríguez, 1999, and reference therein). Especially the possibility that the central source is a black hole is an interesting speculation which, if proven, would mean that G308.4–1.4 is the remnant of a type II core-collapse SN. Thus, would be the first one known that left a black hole.

To obtain a rough estimate of the source flux of the other source in the center of the remnant, source # 10, we assumed that the source is a CCO, should have at least a spectrum with a blackbody of temperature 2.6 million Kelvin as the CCO in Puppis-A (cf. Table 6.4, Becker, 2009). Using the WebPIMMS tool with the source count rate and the fitted  $n_H$  of the SNR the flux in the 0.3 – 3.5 keV range is  $f_X \approx 2.2 \times 10^{-14}$  ergs  $\text{cm}^{-2}\text{s}^{-1}$  and in the 0.5 – 10 keV range

**Table 5.4:** Fundamental parameters of SNR G308.4–1.4.

SNR	
distance	$9.8^{+0.9}_{-0.7}$ kpc
age	5000 – 7500 yrs
radius	$\sim 4.2/11.9^{+1.9}_{-1.8}d_{9.8}^{1/6}$ pc
expansion velocity	$730^{+190}_{-160}$ km/s

is  $f_X \approx 1.9 \times 10^{-14}$  ergs cm<sup>-2</sup>s<sup>-1</sup>. The normalization of a blackbody with this flux, temperature and  $n_H$  is  $2.5 \times 10^{-5}$ , which corresponds to an emitting radius of the source of  $\approx 9d_{9.8}^{-1}$  km. This value perfectly agrees with the expected value for the neutron star radius. The corresponding luminosity in the energy band 0.5 – 10 keV is  $L_X^{0.5-10} = 2.1 \times 10^{32} d_{9.8}^{-2}$  erg/s, a typical value for CCOs. Furthermore, the X-ray-to-visual flux ratio is  $\log(f_X/f_V) > 0.11$  taking into account that no optical source was detected in the USNO-B1.0 catalog and the limiting magnitude of this catalog is 21 (Monet et al., 2003). Thus, no clear evidence for the origin of the emission of source # 10 could be found.

Finally we mention that the detector support structure of Chandra covers the central part of G308.4–1.4 (see Fig. 5.2). It is therefore not excluded from our observations that other faint X-ray point sources are located at this position. However, the non-detection of a source in the SWIFT data at the assumed position of the remnant’s expansion center sets a strict upper limit of  $5 \times 10^{-13}$  ergs cm<sup>-2</sup> s<sup>-1</sup> on the flux of such an object.

## 5.6 Summary

The high-resolution imaging and spectroscopic capability of Chandra revealed that the X-ray emission of the source is an extended plasma and G308.4–1.4 is indeed a supernova remnant. The emission region is spherically symmetric with a diameter of 8.4 arc-minutes and an excess emission toward the east.

The radio morphology at 0.843, 1.384 and 2.496 GHz is characterized by two arcs. The eastern arc matches the X-ray and infrared contours. The second arc, which is bending in the west and shows a decreasing brightness toward the center of G308.4–1.4, has no counterpart in other wavelengths. The remnant without the two bright knots has a spectral index of  $\alpha = -0.7 \pm 0.2$ .

The Sedov analysis lead to the conclusion that the SNR is about 6200 years old and is expanding with a velocity on the order of  $\approx 730$  km/s. All fundamental parameters of the SNR are summarized in Table 5.4.

The X-ray point-like source CXOU J134124.22–634352.0, located close to the geometrical center of the SNR G308.4–1.4, is seen to exhibit variable and flaring X-ray emission. However, no certain conclusion on the origin of this source and the other central source CXOU J134127.12–634327.7 could be drawn. Deeper observations of the central part of SNR G308.4–1.4 are needed to resolve the obvious ambiguities.

# Chapter 6

## Supernova remnant G296.7–0.9 in X-rays

This chapter is adopted from Prinz and Becker (2013) published in *Astronomy & Astrophysics*.

### 6.1 Introduction

Every year, several hundred supernova (SN) events are observed, representing the end state of stellar evolution in which a core-collapse of a massive star or the thermonuclear disruption of a white dwarf takes place. SNe are the most energetic events that can be observed in the universe. They are often as bright as a whole galaxy, and their extreme brightness allows them to be seen up to distances of Gpc (Rodney et al., 2011). On this scale, though, the only information obtainable from them is the characteristic rising and fading of their light as a function of time, i.e., their photometric light curve, and their spectral evolution, both of which are important for their classification (Sako et al., 2008). Most of these events are discovered in the optical band by comparing observations taken at different epochs.

In our own Galaxy, the rate of observed SNe is small. For core-collapse SNe, it averages only about two per century. This estimate is suggested by the  $\gamma$ -ray radiation from  $^{26}\text{Al}$  in the Galaxy (Diehl et al., 2006), in which a certain yield is expected to be formed in each core-collapse SN. Many SNe, though, remain unobserved due to optical light extinction. The last recorded SN in our Galaxy, the Kepler SN, was observed in AD 1604, and only six other SNe have been detected in the Galaxy in the past two thousand years (Green and Stephenson, 2003). The optical light from the two youngest Galactic SNe, G1.9+0.3 and Cas A, was not observed about 100 and 350 years ago, respectively (Reynolds et al., 2008; Green and Stephenson, 2003).

If there is no direct light from an SN observed, then we at least have the opportunity to study the light of the remnants of several nearby SNe because the light of these supernova remnants (SNRs) remain visible in various spectral bands for up to  $10^5$  years. Although the light echo from the SN Cas A was found recently (Rest et al., 2008), it is one of the few cases so far where the SN light could be studied a few hundred years after the SN. Thus, the most promising way

to learn about the evolution of an SN shock front and the feedback on the evolution of their host galaxy is to study the diffuse emission of SNRs.

In the last few years, several new SNRs have been detected thanks to the increasing sensitivity of modern X-ray observatories. One of those remnants is G296.7–0.9, which was first detected in X-rays by Schaudel et al. (2002) and later identified to be an SNR by Schaudel (2003) and Robbins et al. (2012). It is a shell-like SNR in which X-ray and radio emissions have been detected. In addition, filaments in the infrared and  $H_\alpha$  band were detected in near the source (Robbins et al., 2012). Whether they are associated with the remnant still remains to be shown.

A first detailed study of the SNR G296.7–0.9 was presented by Robbins et al. (2012) using ROSAT PSPC data. As this detector had roughly five independent energy channels in the range 0.1–2 keV, the spectral results of their analysis were very limited. They suggested that the X-rays were emitted from a thermal plasma. Robbins et al. (2012) were therefore not able to put any constraints with high confidence on the derived spectral parameters. The ROSAT data did not allow them to deduce parameters such as the age or the expansion velocity of the remnant.

In this work we report on an XMM-Newton observation that was targeted on SNR G296.7–0.9. The results of the spatial and spectral analysis of this data are presented in Section 6.2. In the discussion in Section 6.3, we use the inferred spectral parameters of G296.7–0.9 to derive an estimate for its age, radius, expansion velocity, and distance. Section 6.4 provides the concluding summary.

## 6.2 X-ray observation and data reduction

G296.7–0.9 was observed for 13.6 ksec on 28 June 2011 with EPIC cameras (Strüder et al., 2001) on board the X-ray observatory XMM-Newton (ObsID 0675070101). The two MOS and the PN cameras were operated in full-frame mode using the medium filter. Part of the observation was taken with the filter wheel in closed position because the observation was strongly affected by particle background radiation. Therefore, the performed duration was only 4.4 ksec and 5.5 ksec for the PN and MOS1/2 detectors, respectively.

We used the XMM SAS version 11.0.0 to reprocess and reduce the data. Times of high background activity were identified by inspecting the light curves of the MOS1/2 and PN data at energies above 10 keV. After removing these times, the effective exposures of the PN, MOS1, and MOS2 cameras were 3.7 ksec, 5.1 ksec, and 5.3 ksec, respectively. We extracted images and exposure maps in the five standard bands of XMM-Newton using all EPIC instruments. Single and double events were selected from the PN data and single to quadruple events from the MOS data sets.

For the spectral fitting, we used the X-Ray Spectral Fitting Package (XSPEC) version 12.7.0u. The energy range was restricted to 0.4 – 6.0 keV because the count rate detected at higher energies was too sparse for a meaningful spectral analysis. Below 0.4 keV, the detector and telescope response is not well established. All given uncertainties represent the  $1\sigma$  confidence range for one parameter of interest, unless stated otherwise.

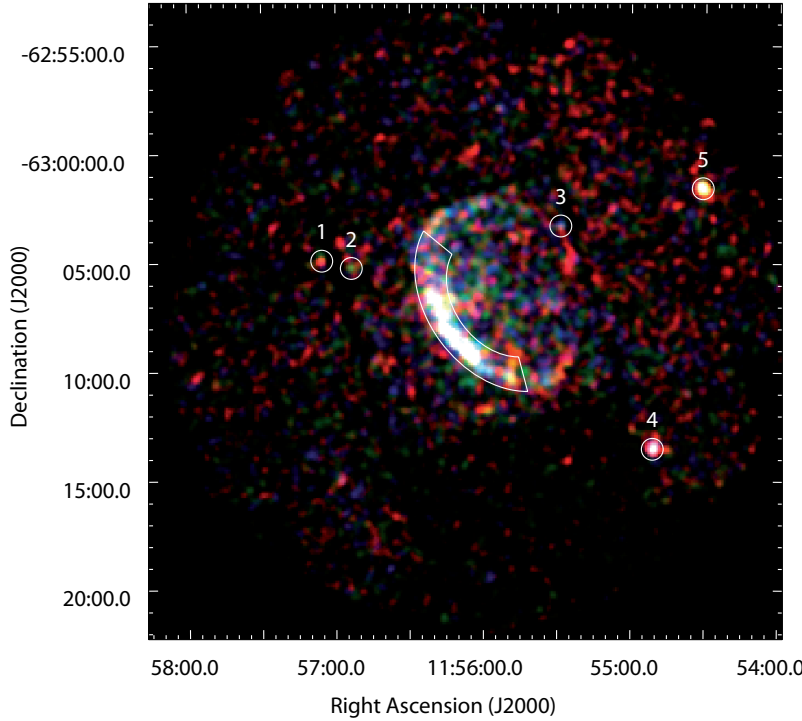


**Figure 6.1:**  $30' \times 30'$  XMM-Newton MOS1/2 color image of G296.7–0.9 (red 0.5–0.9 keV, green 0.9–1.3 keV, and blue 1.3–2 keV). The superimposed images are binned with  $6''$  per pixel and smoothed by a Gaussian kernel of  $\sigma = 30''$  to enhance the visibility of the diffuse emission. The photons detected in the annular sector shown in white were used for spectral analysis of the SNR.

### 6.2.1 Spatial analysis

Figure 6.1 shows the X-ray color image of SNR G296.7–0.9. A bright arc that appears to lie along an elliptical shell is clearly detected in the south-east. Its center is at  $RA_c = 11^{\text{h}}55^{\text{m}}52^{\text{s}}.3 \pm 0^{\text{s}}.7$ ,  $DEC_c = -63^{\circ}06'29'' \pm 3''$  with a semimajor axis of  $5'$  and a semiminor axis of  $3'.75$ .

We searched for point sources with a signal-to-noise ratio (S/N) of at least  $3\sigma$  in the five standard bands using a sliding box source detection algorithm (SAS tool `edetect_chain`). Five point sources were detected (see Fig. 6.1), which all have an  $S/N \geq 7\sigma_G$  ( $\sigma_G = 1 + \sqrt{c_{\text{bg}} + 0.75}$ , where  $c_{\text{bg}}$  are the background counts). Their position, positional error, S/N, and count rate in the merged image are listed in Table 6.1.

In order to search for optical counterparts, we cross-correlated the position of each X-ray

**Table 6.1:** Detected sources in XMM-Newton observation 0675070101. The sources are denoted as in Fig. 6.1.

No.	RA (J2000) h:m:s	DEC (J2000) d:m:s	S/N $\sigma_G$	Rate cts/ksec
1	$11 : 57 : 05.7 \pm 0.3$	$-63 : 04 : 53 \pm 2$	7.7	5.2
2	$11 : 56 : 53.9 \pm 0.3$	$-63 : 05 : 13 \pm 2$	8.5	5.7
3	$11 : 55 : 28.6 \pm 0.3$	$-63 : 03 : 18 \pm 2$	7.0	4.1
4	$11 : 54 : 51.2 \pm 0.3$	$-63 : 13 : 31 \pm 2$	34.1	26.4
5	$11 : 54 : 31.1 \pm 0.3$	$-63 : 01 : 33 \pm 2$	22.2	16.4

source with the various online catalogs provided by the VizieR service<sup>1</sup>. We found a candidate counterpart for source #5, HD 103442 (Høg et al., 2000), which is an A3/4IV star with an optical magnitude  $V = 8.8$ . Its angular separation from source #5 is  $4''.0$ , corresponding to twice the observatory’s absolute astrometric accuracy<sup>2</sup>. The source density  $\rho$  in this region of the Galactic plane using the Tycho-2 catalog is  $\rho \approx 0.09 \text{ arcmin}^{-2}$ . The probability of a chance association computes then like  $P_{\text{coin}} = \rho \cdot \delta^2$ , where  $\delta$  is the angular separation between the optical and X-ray source. For the optical counterpart of source #5, we compute a chance probability of  $4 \times 10^{-4}$  for a mis-identification. Its X-ray flux within the 0.3 to 3.5 keV band is  $1.2 \times 10^{-12} \text{ erg cm}^{-2} \text{ s}^{-1}$ , yielding an X-ray-to-visual flux ratio of  $\log(f_X/f_V) = -3.1$ . This is in the allowed range of  $-3.86 \pm 0.79$  for A-type stars (Maccacaro et al., 1988; Agüeros et al., 2009), which further strengthens the association between source #5 and its candidate optical counterpart.

No source has been detected close to the geometrical center of the SNR. Using the merged MOS1/2 data, we determined a  $3\sigma$  upper limit on the count rate of a hypothetical central X-ray source of  $4.3 \times 10^{-3} \text{ cts/s}$  in the energy range 0.2 to 12 keV.

## 6.2.2 Spectral analysis

The energy spectrum of G296.7–0.9 was extracted from an elliptical annular sector with the center at  $\text{RA}_c$  and  $\text{DEC}_c$ , semimajor axes of  $5'$  and  $2'.9$ , semiminor axes of  $3'.75$  and  $2'.2$ , and an opening angle of  $140^\circ$ . The background spectrum was derived from a nearby region placed on the same MOS1/2 chip with the same size as the source region. The background contribution was found to be  $\approx 50\%$  in the two MOS cameras and  $\approx 71\%$  in the PN data. After subtracting the background, 1232, 1236, and 3077 source counts remained in the MOS1, MOS2, and PN data. For the spectral analysis of the remnant, these counts were binned to have at least 75 counts per bin in the case of the MOS1/2 observations and 150 counts per bin for the PN data.

We checked whether the spectral fitting results would change if we model the instrumental background according to the suggestions made by Kuntz and Snowden (2008). They proposed to add a Gaussian at the fluorescence line of Al  $K\alpha$  at  $E = 1.49 \text{ keV}$  with zero width and a power law for modeling the remaining soft proton contamination, which is not convolved with the instrumental response. From this analysis, however, the model fits were not significantly better than without adding these components using the standard F-test. Thus, the following results were obtained without modeling the instrumental background separately.

We fitted the spectrum of G296.7–0.9 with various models: A hot diffuse gas model (MEKAL), a model for a collisionally ionized diffuse gas (APEC), a power law model, a thermal bremsstrahlung model, a Raymond-Smith diffuse gas model, a non-equilibrium collisional plasma that allows a temperature evolution (GNEI) or has a constant temperature (NEI, see Figure 6.2), a plane-parallel shock plasma model (PSHOCK), an ionization equilibrium collisional plasma model (EQUIL), and a Sedov model with separate ion and electron temperatures. For spectral models with  $\chi_{\text{red}}^2 < 1.4$ , all fit parameters are listed in Table 6.2.

In the following, we will use the best-fit results of the NEI model to derive related SNR

<sup>1</sup><http://vizier.u-strasbg.fr/viz-bin/VizieR>

<sup>2</sup>[xmm.vilspa.esa.es/docs/documents/CAL-TN-0018.pdf](http://xmm.vilspa.esa.es/docs/documents/CAL-TN-0018.pdf).

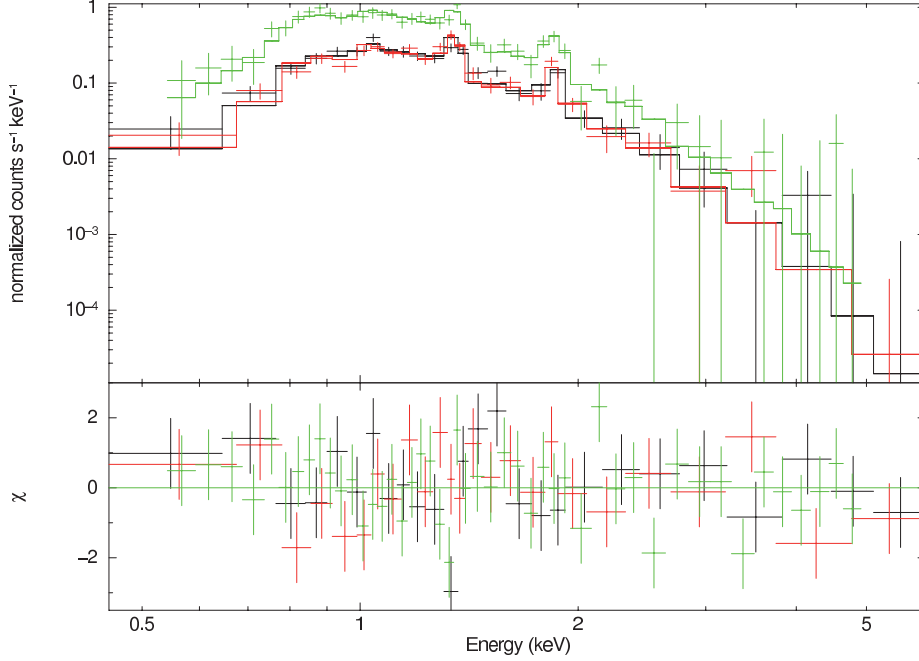


**Figure 6.2:** Spectrum and fitted model (NEI) of the X-ray emission of SNR G296.7–0.9. The black colored line indicates the MOS1 data, the red the MOS2, and the green the PN data.

**Table 6.2:** Spectral parameters of the best-fit models for SNR G296.7–0.9.

model	$N_{\text{H}}$ [ $10^{22}\text{cm}^{-2}$ ]	$k_{\text{B}}T$ [keV]	$\tau^{\alpha}$	$k_{\text{B}}T_{\text{e}}^{\beta} / \langle kT \rangle^{\gamma}$ [keV]	Norm $^{\delta}$	$\chi^2/\text{d.o.f.}$	$f_{\text{X}}^{\epsilon}$
NEI	$1.24^{+0.07}_{-0.05}$	$0.53^{+0.08}_{-0.07}$	$1.2^{+0.8}_{-0.4}$	-/-	$1.3^{+0.6}_{-0.3}$	89.3/94	$5.2^{+1.1}_{-0.9}$
PSHOCK	$1.16^{+0.14}_{-0.06}$	$0.54^{+0.08}_{-0.06}$	$8^{+15}_{-7}$	-/-	$1.1^{+0.6}_{-0.2}$	87.5/94	$3.5^{+0.5}_{-0.3}$
SEDOV	$1.27^{+0.10}_{-0.09}$	$0.35^{+0.19}_{-0.08}$	$6^{+7}_{-4}$	$< 0.54/-$	$2.3^{+2.1}_{-0.9}$	89.4/93	$8 \pm 3$
GNEI	$1.27 \pm 0.08$	$0.49^{+0.11}_{-0.08}$	$1.0^{+0.8}_{-0.5}$	$-/0.55^{+0.11}_{-0.08}$	$1.5^{+0.9}_{-0.6}$	88.6/93	$6.0^{+1.0}_{-1.5}$
EQUIL	$1.10 \pm 0.04$	$0.52 \pm 0.04$	-	-/-	$1.09^{+0.21}_{-0.15}$	96.8/95	$2.5 \pm 0.2$
APEC	$1.23 \pm 0.05$	$0.38^{+0.10}_{-0.03}$	-	-/-	$2.0^{+0.6}_{-0.5}$	107.0/95	$4.6^{+0.6}_{-0.5}$

**Notes.**  $(\alpha)$  ionization timescale in units of  $10^{11}$  s/cm $^3$   $(\beta)$  electron temperature immediately behind the shock front  $(\gamma)$  ionization timescale-averaged temperature  $\langle kT \rangle = \int_{t_s}^{t_0} T(t)n_e(t)dt/\tau$   $(\delta)$  Norm= $\frac{10^{-14}}{4\pi[D_{\text{A}}(1+z)]^2} \int n_e n_{\text{H}} dV$  in units of  $10^{-2}$  cm $^{-5}$ , where  $D_{\text{A}}$  is the angular diameter distance to the source in cm and  $n_e$  and  $n_{\text{H}}$  are the post-shock electron and hydrogen densities in cm $^{-3}$ , respectively.  $(\epsilon)$  X-ray flux in the energy range 0.5 to 4.0 keV in  $10^{-11}$  erg cm $^{-2}$ s $^{-1}$ .

parameters. For all models with a non-equilibrium equation of state, we measure an ionization timescale value  $\tau = t_0 n_e < 10^{12} \text{ s cm}^{-3}$  ( $t_0$  is the age of the remnant and  $n_e$  the post-shock electron number density), which is smaller than the expected timescale at which collisional ionization equilibrium is reached (Borkowski et al., 2001). Therefore, the APEC and EQUIL models are unlikely to apply. For the GNEI model, the temperature and the ionization timescale-averaged temperature are almost the same, which is no improvement over the NEI model. Additionally, we will not use the results of the SEDOV model any further, because the determination of the post-shock temperature  $T_e$  in that model is only possible at energies above 3 to 4 keV (Borkowski et al., 2001), where the spectrum of G296.7–0.9 is not well constrained.

The value for  $N_H$  in the NEI model fit is slightly lower than the average integrated hydrogen column density toward SNR G296.7–0.9, which is  $N_H^{LAB} = 1.39 \times 10^{22} \text{ cm}^{-2}$  (Kalberla et al., 2005). This value is based on HI emission line measurements at a radio frequency of 21 cm and refers to the entire hydrogen column density along the line of sight. The temperature of the plasma is  $6.2_{-0.8}^{+0.9} \times 10^6 \text{ K}$ . No improvement in the best-fit statistic was observed when we allowed the abundances to differ from the solar values. Using the derived parameters of the NEI model fit, the flux in the 0.5 to 4 keV band is  $5.2_{-0.9}^{+1.1} \times 10^{-11} \text{ erg/cm}^2/\text{s}$ .

In addition, we investigated the spatial variation of the spectral parameters by extracting all photons in the northern and southern part of the remnant. However, no difference was found within the derived errors.

## 6.3 Discussion

### 6.3.1 Comparison with the ROSAT results

Schaudel (2003) and Robbins et al. (2012) independently analyzed two pointed ROSAT PSPCB observations. These data were taken between 1 and 8 February 1993 and 19 and 21 February 1998. Both authors found that the temperatures of the X-ray emitting gas and the hydrogen column density  $N_H$  are lower by at least a factor of two when compared with the results deduced in our work. Only Schaudel (2003) found a  $N_H$  that is comparable with our value listed in Table 2 by fitting the Raymond-Smith model, though his value had a much higher uncertainty. As mentioned in the introduction, the PSPCB had about five independent energy channels, which limits the conclusions drawn from their spectral fits, especially when 70 spectral bins were used as in the work of Robbins et al. (2012). The latter corresponds to an oversampling of about 15 times the spectral resolution of the detector!

### 6.3.2 Distance and age

Using the deduced spectral parameters from the NEI fit, we can derive basic properties of the remnant, such as the distance  $d$ , post-shock hydrogen density  $n_H$ , swept-up mass  $M$ , the age of the remnant  $t$ , the radius in pc  $R_s$ , and the shock velocity  $v_s$ . We used the following set of

equations, which is described in detail in Prinz and Becker (2012) and references therein:

$$\begin{aligned}
d_{\text{Sedov}} &= 7420 \cdot \theta^{-3/5} \left( \frac{E_{51}}{T_s} \right)^{2/5} \left( \frac{f}{\text{Norm}} \right)^{1/5} \text{ [kpc]} \\
d_{\text{Reddening}} &= N_H / (N_H/A_V \cdot A_V/E_{B-V} \cdot E_{B-V}/\text{kpc}) \text{ [kpc]} \\
V_{\text{emit}} &= 3.029 \times 10^{54} \cdot f \cdot \theta^3 \cdot (d_{\text{Sedov}}[\text{kpc}])^3 \text{ [cm}^3\text{]} \\
n_H &= 70.27 \sqrt{\frac{\text{Norm}}{d_{\text{Sedov}} \cdot f \cdot \theta^3}} \text{ [cm}^{-3}\text{]} \\
M &= 1.4 \cdot n_H \cdot m_H \cdot V \text{ [kg]} \\
t &= 2.71 \times 10^9 \left( \frac{E_{51}}{n_H} \right)^{1/3} T_s^{-6/5} \text{ [yr]} \\
R_s &= 0.34 \left( \frac{E_{51}}{n_H} \right)^{1/5} t^{2/5} \text{ [pc]} \\
v_s &= 0.4 \cdot R_s/t \text{ [km/s]}.
\end{aligned}$$

Here  $\theta = \sqrt{\text{major} \times \text{minor axis}}$  is the reduced radius of the remnant in arcmin,  $E_{51}$  the explosion energy in units of  $10^{51}$  erg,  $T_s$  the fitted plasma temperature,  $f$  the filling factor to correct for the morphology of the SNR, Norm the normalization of the spectral fit,  $N_H$  the fitted column density,  $V_{\text{emit}}$  the X-ray emitting volume, and  $m_H$  the mass of a hydrogen atom. The errors listed with the numbers deduced from these equations are statistical errors. The systematic errors might be larger but are unknown.

The Sedov-analysis-based distance is  $d_{\text{Sedov}} = 9.8_{-0.7}^{+1.1}$  kpc. In the following, we give all important quantities in units of  $d_{9.8} = d/9.8$  kpc because  $d_{\text{Sedov}}$  has a smaller uncertainty than other distance estimates. From Figure 6.1 we infer that only  $f = 15\%$  of the remnant is bright enough to be used for spectral analysis. Therefore, the post-shock hydrogen density  $N_H$  is  $0.73_{-0.10}^{+0.18}$  and the swept-up mass is  $M = 29M_{\odot} d_{9.8}^{5/2}$ . Assuming that the explosion energy  $E$  is equal to the canonical value of  $10^{51}$  erg, the age of the remnant is 5800 to 7600 years and the radius is  $R_s = 12.2_{-0.8}^{+1.2} d_{9.8}^{1/6}$  pc. We derive a shock velocity  $v_s$  of  $720_{-100}^{+130}$  km/s. Using the flux values deduced in Section 6.2 we compute its luminosity to be  $L_X^{0.5-4} = 6.0_{-1.4}^{+1.8} \times 10^{35} d_{9.8}^2$  erg/s.

Independently of the Sedov analysis, another method that allows us to estimate the remnant's distance makes use of a relation between the visible extinction  $A_V$  and the color excess  $A_V/E_{B-V} = 3.2 \pm 0.2$ . The remnant's color excess was not known, so we used the distribution of the mean color excess  $E_{B-V}$  per kiloparsec derived by Lucke (1978). In the direction of the remnant, we find  $E_{B-V}/\text{kpc} = 0.25 \pm 0.10$ . In addition, we used the relation between  $N_H$  and the visual extinction  $A_V$  of Predehl and Schmitt (1995)  $N_H/A_V = (1.79 \pm 0.03) \times 10^{21} \text{ cm}^{-2}$ . This leads to a distance of  $d_{\text{Reddening}} = 9 \pm 4$  kpc, which is in agreement with the distance deduced from the Sedov analysis. However, the mean color excess  $\langle E_{B-V} \rangle$  that we used to calculate  $d_{\text{Reddening}}$  was derived for a reddening layer up to 2 kpc and thus is just a rough estimate.

### 6.3.3 Central neutron star

To obtain a rough estimate of the flux upper limit for a hypothetical compact source in the center of the remnant, we assumed that the source has properties similar to a central compact object (CCO), because no compact source or radio pulsar has been detected in G296.7–0.9 so far (Robbins et al., 2012). Like other CCOs, e.g., the one in the SNR Puppis A, we assume that the spectrum is dominated by blackbody emission with a temperature of  $\approx 2.6 \times 10^6$  Kelvin and a luminosity in the 0.5–10 keV band of at least  $10^{32}$  erg/s (see Becker (2009) for a review). This corresponds to a flux in this energy range of  $\approx 9 \times 10^{-15}$  erg cm $^{-2}$ s $^{-1}$ . Using the WebPIMMS tool with the fitted  $N_{\text{H}}$  of the SNR, the count rate in the 0.2–12 keV range is  $> 2 \times 10^{-4}$  cts/s for the merged MOS1 and MOS2 observations, an order of magnitude lower than the derived  $3\sigma$  upper limit for a point-like source at the center of the remnant. That we do not detect emission from a CCO in G296.7–0.9 does therefore not mean that there is none. The observation might not be deep enough to detect it. The type of the supernova is also unconstrained.

## 6.4 Conclusion and summary

The remnant is characterized by a bright arc in the south-east direction and by diffuse emission with low surface brightness in its western part. We showed that the X-ray emission of G296.7–0.9 is in agreement with coming from a collisionally heated plasma that has not yet reached equilibrium. The Sedov analysis leads to the conclusion that the SNR is about 6600 years old and expanding with a velocity on the order of  $\approx 720$  km/s.

The close-by HII region G296.593–0.975 has a velocity of  $+25 \pm 1$  km s $^{-1}$ , based on measured hydrogen recombination lines (Caswell and Haynes, 1987). With the standard IAU parameter for the distance to the center of our Galaxy  $R_0 = 8.5$  kpc and the solar orbit velocity of  $V_0 = 220$  km/s (Kerr and Lynden-Bell, 1986) and the Galactic rotation model of Fich et al. (1989), we deduce a distance to the HII region of  $9.3 \pm 0.6$  kpc. For the error estimate, we assumed an uncertainty in the velocity-to-distance conversion of 7 km/s (e.g., Clifton et al., 1988).

The deduced distance  $d_{\text{Sedov}}$  is in good agreement with the distance of the close-by HII region G296.593–0.975. This is a strong indicator for a spatial association between the SNR and the HII region, as already suggested by Robbins et al. (2012).

The observation used in this analysis was strongly affected by particle background radiation, which led to a net observation time that was shorter by a factor of three than the approved exposure time. Therefore, only limited statements can be made about the existence of a compact source located near the center of the SNR. Deeper observations might help to clarify this question and shed light on the type of the SN.

# Chapter 7

## A search for X-ray counterparts of radio pulsars

This chapter is adopted from a paper draft, which will be submitted to *Astronomy & Astrophysics*. The detailed discussion of the results is presented in Chapter 8.

### 7.1 Introduction

Neutron stars (NSs) are the most dense objects observable in the universe and thus a powerful laboratory to study dense matter. In laboratories nuclear physicists are currently investigating the equation of state (EOS) of dense matter with comparable or even higher energy densities of  $\geq 170 \text{ MeV fm}^{-3}$  (Hands, 2001), but much lower baryonic densities than in neutron stars. This is done for example by studying the isospin diffusion in heavy-ion collisions (Tsang et al., 2009) and the electric dipole polarizability of  $^{208}\text{Pb}$  (Piekarewicz et al., 2012). These and other experimental data show a remarkable agreement with modeling of astrophysical observations (see Lattimer (2012) for a review). However, the parameters determined in nuclear experiments have large uncertainties when applied to neutron rich matter. Therefore, one needs other observational constraints on the dense matter EOS, which help to understand the internal composition of neutron stars.

In recent years, a large step forward in constraining the EOS of dense matter was made by the discovery of two neutron stars with high masses: PSR J1614-2230 with  $1.97 \pm 0.04 M_{\odot}$  (Demorest et al., 2010) and PSR J0348+0432 with  $2.01 \pm 0.04 M_{\odot}$  (Antoniadis et al., 2013). These are the first neutron stars with such high masses and small uncertainties in the mass determination. All high mass NSs detected so far have large uncertainties and were used with caution (see Lattimer (2012) for a summary of neutron star mass measurements). The  $2 M_{\odot}$  NS measurement alone can rule out all EOS that do not allow such a massive neutron star (e.g., Demorest et al., 2010, Figure 3). In this case most EOSs that assume exotic matter to be present in the central part of the star at densities a few times the nuclear density can be ruled out. In the literature, charged mesons,  $K^{-}$  or  $\pi^{-}$  condensates, hyperons and deconfined quarks are denoted

as exotic matter. However, their existence in neutron star interiors cannot be excluded. Thus, finding neutron stars that show signs for exotic matter in its interior is one of the main goals of studying neutron stars.

Another very promising approach to rule out EOSs of dense matter is to look at the evolution of the thermal radiation from neutron stars with time and compare it with models. Furthermore, this attempt gives insight into the complex composition of the interior of a neutron star. NSs are hot, around  $10^6$  K at the surface, and are thus observable in the soft X-ray regime. Several attempts have been made to learn more about the interior by comparing observed surface temperatures of neutron stars with theoretical predictions, in which a certain composition in the interior of the star is assumed (Becker et al., 1993b; Becker, 1995; Tsuruta, 1998; Yakovlev and Pethick, 2004; Page et al., 2004, 2009). However, only in the last decade the number of neutron stars that clearly showed thermal emission from the whole surface and cover a large range of ages increased by a factor of four. Using that sample, a reasonable study could be performed, e.g., Page et al. (2009). Page et al. (2004) introduced the minimal cooling paradigm, which includes the cooling by Cooper-pair breaking and formation in addition to the standard cooling scenario (Tsuruta, 1998). This scenario could well explain the observed temperatures of neutron stars within the uncertainties, but not within one single model and composition of the envelope. Nevertheless, only about 18 isolated neutron stars show thermal emission from the whole surface (Page et al., 2004, 2009; Özel, 2013; Zhu et al., 2011), whereof five have no distance estimate and therefore, are not easily compared among each other (Tsuruta, 2009). Using the ROSAT All-Sky Survey Becker et al. (1993b) derived  $2\sigma$  upper limits on the temperature for several other pulsars. However, with some exceptions the measured temperature upper limits were all above  $10^6$  K for neutron star ages above  $10^4$  years, too high and too old to challenge up-to-date cooling models.

Apart from this the high energy emission of pulsars is still poorly understood. However, in recent years several attempts have been made to connect measured X-ray quantities with fundamental properties of a radio pulsar. Since the first imaging telescope with focusing optics, the Einstein X-ray observatory (Giacconi et al., 1979), was launched various authors analyzed the existence of a correlation between the X-ray luminosity  $L_X$  and the spin-down energy loss  $\dot{E}$  in different energy bands, e.g., Seward and Wang (1988) used Einstein observations and found  $L_X(0.2 - 4 \text{ keV}) \approx 10^{1.39} \dot{E}$ , Becker and Trümper (1997) fitted  $L_X(0.1 - 2.4 \text{ keV}) \approx 10^{1.03} \dot{E}$  with ROSAT data, and at harder X-rays Possenti et al. (2002) derived with the help of ASCA, RXTE, BeppoSAX, Chandra, and XMM-Newton data  $L_X(2 - 10 \text{ keV}) \approx 10^{1.34} \dot{E}$ . In addition, Li et al. (2008) fitted  $L_X(2 - 10 \text{ keV}) \approx 10^{0.92} \dot{E}$  and Becker (2009)  $L_X(0.1 - 2 \text{ keV}) \approx 10^{0.997} \dot{E}$ , both deduced with XMM-Newton and Chandra observations. The large spread in the fitted quantities can be explained by the fact that different approaches were applied and in some samples the thermal emission was included. However, in all these a large scatter in the derived values for  $L_X$  is detectable and Possenti et al. (2002) already showed that the fit is not acceptable in terms of the  $\chi^2$  statistic.

Furthermore, with the increasing sensitivity and angular resolution of the currently flying X-ray satellites the sample of rotation-powered pulsars that are detected in X-rays is steadily increasing, to  $\approx 185$  by September 2013 (see Table B.1). This enables us to reduce the bias in the current sample, which represents mainly the luminous X-ray pulsars and allows to search

for underluminous ones. This increases the dispersion in the  $L_X - \dot{E}$  correlation even more, e.g. PSR J2022+3842 has an X-ray efficiency  $\mu_X = L_X/\dot{E} = 6 \times 10^{-5}$  in the 2–10 keV range (Arzoumanian et al., 2011) and Kargaltsev et al. (2012) found that  $\mu_X$  of PSR J0940–5428 and PSR J1913+1011 is below  $4.0 \times 10^{-6}$  and  $3.3 \times 10^{-6}$  in the 0.5–8 keV energy range, respectively. Kargaltsev et al. (2012) concluded that the scatter in the X-ray efficiency cannot only be explained by incorrectly derived distances and missing beaming corrections of the radiation coming from the pulsars magnetosphere. This indicates that the X-ray luminosity does not only depend on the spin-down luminosity. However, another parameter that determines how luminous a pulsar is at high energies is still unknown.

To sum up, it is crucial to enlarge the sample of known X-ray pulsars that would help to follow the cooling of neutron stars over a larger range of ages and reduce the bias to the brightest sources in the  $L_X - \dot{E}$  correlation even more. Even upper limits on the thermal and non-thermal emission can help to put more significant constraints on these curves.

Hence, we searched for undetected X-ray counterparts of radio pulsars in the archives of XMM-Newton and Chandra using the coordinates of all known pulsars. The data were taken from the ATNF Pulsar Catalogue (Manchester et al., 2005)<sup>1</sup>, which currently lists 2267 pulsars. In Section 7.2 we describe the used observations and provide the details of the data processing and data filtering of the XMM-Newton and Chandra observations. Furthermore, we explain the criteria that have to be met for a positive detection and how fluxes and upper limits were derived. The results of the spatial and spectral analysis of the detected and the upper-limits for the not-detected pulsars are given in Section 7.3. In Section 7.4 we give a concluding summary about the findings and in Section 8.3 the results are discussed in detail.

## 7.2 Observations and data reduction

We made use of all public data from the archives of the two X-ray observatories XMM-Newton<sup>2</sup> and Chandra<sup>3</sup> available by September 2013 and searched for X-ray counterparts of all known isolated radio pulsars and millisecond pulsars in our Galaxy, listed in the ATNF Pulsar Catalogue (Manchester et al., 2005). The two observatories used here are ideal for the search, because of their large collecting power compared to other missions and good sky coverage after 14 years of observation: The XMM-Newton observatory covered 504 deg<sup>2</sup> by 2009 (Watson et al., 2009) and the Chandra X-ray satellite 310 deg<sup>2</sup> by 2007 (Evans et al., 2010)). We found 164 observations taken with XMM-Newton and 188 taken with Chandra where the field-of-view (FOV) covers the position of a radio pulsar, summing up to a total of 7.8 Msec observation time. In total 255 pulsars were observed. A summary of the used observations, used instruments, filters, and exposure times is given in Table B.2.

For the reduction of XMM-Newton data we used the XMM-Newton Science Analysis Software (SAS), version 12.0.1. In case of the Chandra data we used standard processed level-2 data and the Chandra Interactive Analysis of Observations (CIAO) software, version 4.4. In

<sup>1</sup><http://www.atnf.csiro.au/research/pulsar/psrcat/>

<sup>2</sup><http://xmm.esac.esa.int/xsa/index.shtml>

<sup>3</sup><http://cda.harvard.edu/chaser/>

both cases we had to remove flares from the observation. As for XMM-Newton these flares are mostly coming from soft protons hitting the detector. To remove these time intervals of high particle background we inspected the light curves of the MOS1/2 and PN event files at energies above 10 keV. We created a light curve with a bin size of 100 s and detected flares in almost all XMM-Newton data sets. Therefore, we rejected time intervals in which the count rate per bin was  $3\sigma$  higher than the mean count rate without flares. Regarding Chandra observations we made use of the CIAO `deflare` script, which applies the criterion mentioned above automatically.

The effective exposure time  $t(\theta)$  was obtained by generating an exposure map with the SAS-tool `eexpmap` or the CIAO-tool `fluximage` after correcting for times with high background and dead time correction. In both cases the task takes into account the vignetting of the telescope at an off-axis angle  $\theta$ . The net exposure on the source  $t(\theta)$  and on the background region  $t_{\text{BG}}(\theta)$  was then calculated by averaging the exposure map over the source and background region, respectively. This has to be done to include the effect of the CCD gaps on the exposure time. The on-axis exposure  $t_{\text{on-axis}}$  and  $t(\theta)$  are listed in Table B.2.

### 7.2.1 Spatial analysis

In order to search for a possible X-ray counterpart in the available datasets where a pulsar was observed we applied a sliding box source detection algorithm for XMM-Newton data (SAS-tool `edetect_chain`) using the five standard bands (0.2 – 0.5 keV, 0.5 – 2 keV, 2 – 4.5 keV, 4.5 – 7.5 keV, and 7.5 – 12 keV) or a wavelet source detection algorithm for observations with Chandra (CIAO-tool `wavdetect`) in the energy range 0.1–10 keV. The derived source positions were then compared with the radio timing position of the corresponding pulsar. The uncertainties in right ascension  $\delta RA$  and declination  $\delta DEC$  were determined by combining the statistical errors of the X-ray source position and the absolute astrometric accuracy of the corresponding X-ray observatory squared. For Chandra ACIS-S, ACIS-I and HRC-S data the 68 % confidence level is  $\approx 0.21''$ ,  $\approx 0.4''$  and  $\approx 0.36''$ , respectively.<sup>4</sup> The absolute astrometric accuracy for XMM-Newton data is  $\approx 2''$  (r.m.s.).<sup>5</sup>

We claim a possible detection, if the distance  $\Delta$  between the X-ray position ( $RA_X$ ,  $DEC_X$ ) and the radio timing position ( $RA_R$ ,  $DEC_R$ )

$$\Delta = \sqrt{(RA_R - RA_X)^2 + (DEC_R - DEC_X)^2} \leq 3\sigma. \quad (7.1)$$

The uncertainty  $\sigma$  in this equation was obtained by deducing the error in  $\Delta$ .

To exclude the possibility that an X-ray source is by chance at the position of the neutron star, we calculate the probability of a coincidence  $P_{\text{coin}}$  as follows:

$$P_{\text{coin}} = \frac{N_X}{l_{\text{RA}} l_{\text{Decl.}}} \pi \delta RA \delta DEC, \quad (7.2)$$

<sup>4</sup>See <http://cxc.harvard.edu/cal/ASPECT/celmon/> for more details about Chandra absolute astrometric accuracy.

<sup>5</sup>More information can be found at [xmm.vilspa.esa.es/docs/documents/CAL-TN-0018.pdf](http://xmm.vilspa.esa.es/docs/documents/CAL-TN-0018.pdf).

where  $N_X$  is the number of sources detected within the FOV of the observation with length  $l_{RA}$  and width  $l_{Decl.}$ .  $P_{\text{coin}}$  should be below  $10^{-3}$  to exclude a by-chance detection of an X-ray source as the X-ray counterpart of a radio pulsar.

Additionally, we correlated the positions of the X-ray sources with the USNO-B Catalog, which covers the whole sky and is thought to be complete down to a visible magnitude of  $V = 21$  (Monet et al., 2003). The correlation was done using the online tool VizieR<sup>6</sup>. This data allowed us to put constraints on the X-ray-to-visual flux ratio (Maccacaro et al., 1988)

$$\log(f_X/f_V) = \log(f_X) + V/2.5 + 5.37. \quad (7.3)$$

Here  $f_X$  is the X-ray flux in the 0.3–3.5 keV band in  $\text{erg cm}^{-2} \text{s}^{-1}$ . If no optical source could be detected within an error box of side length  $3\sigma$  around the source, we took the limiting magnitude of the USNO-B Catalog as an estimate for  $V$ . For stars, the ratio  $\log(f_X/f_V)$  should be in the range  $\log(f_X/f_V) = -2.46 \pm 1.27$  (Krautter et al., 1999). Therefore,  $\log(f_X/f_V)$  should be greater than  $-1.19$  to exclude a false detection as a star. The resulting detection will be described in the next section.

### 7.2.2 Spectral analysis

All used focal instruments are CCDs and thus provide spectral information for the detected X-ray counterparts. The only exceptions are the HRC detectors of the Chandra X-ray observatory, which are microchannel plate instruments and have a spectral resolution of  $\Delta E/E \approx 1$  at 1 keV.<sup>7</sup> However, the quality of spectral fits and the constraints on the parameters of the spectral model are strongly dependent on the photon statistics and thus vary among the detected counterparts.

For data obtained with XMM-Newton the corresponding response and effective area of the pulsar and the background were extracted using the SAS-script `especget`. For the PN camera we used only those events with a detection pattern between 1 and 4 (single and double events). For the MOS camera we included triple events as well, which have a pattern between 5 and 12. The pattern value indicates which neighboring pixels on the detector are hit by a single photon. In case of Chandra observations we extracted the source and background spectra as well as the corresponding response and effective area files with the CIAO-script `specextract`. Both scripts execute all the steps necessary for spectral fitting, including the binning of the resulting spectrum.

Furthermore, if we detected a possible X-ray counterpart of a radio pulsar with more than 70 source counts a power law and blackbody model spectra were fitted to the extracted energy distribution. This was done by using the software package XSPEC, version 12.7.0u. Additionally, the sparse photon statistics for most detected radio pulsars requires to fix the hydrogen column densities  $N_H$ . We estimated  $N_H$  by using the dispersion measure  $DM$  of the radio timing solution and assumed a 10 % ionization degree of the interstellar medium along the line of sight towards the pulsar. The values for the dispersion measure are taken from the ATNF Pulsar Catalogue (Manchester et al., 2005). If the calculated  $N_H$  is higher than the average integrated hydrogen

<sup>6</sup><http://vizier.u-strasbg.fr/viz-bin/VizieR>

<sup>7</sup>See “The Chandra Proposers’ Observatory Guide”

[http://cxc.harvard.edu/proposer/POG/pog\\_pdf.html](http://cxc.harvard.edu/proposer/POG/pog_pdf.html).

column density  $N_{\text{H}}^{\text{LAB}}$  towards the source of the LAB Survey of Galactic HI (Kalberla et al., 2005) then this value is adopted.  $N_{\text{H}}^{\text{LAB}}$  is based on HI emission line measurements at a radio frequency of 21 cm and refers to the entire hydrogen column density along the line of sight.

As mentioned before, for sources observed with the HRC cameras no spectral information can be obtained from the pulsar. The only information we have is the counting rate in the energy range of the camera where it is sensitive to incoming photons. In this case and in the case of observations with less than 70 source counts we obtained constraints on the X-ray flux and luminosity by converting the pulsar counting rate into an equivalent flux. First, we obtained the net counting rate for these pulsar counterparts by dividing the source counts derived with the source detection software by the effective exposure time  $t(\theta)$ . The X-ray flux was then deduced for a typical pulsar spectrum using the method described in Section 7.2.4. As a typical pulsar spectrum we assumed a power law model with photon index 1.7 (Becker, 2009) and a hydrogen column density based on the dispersion measure as mentioned in the last paragraph.

The used  $DM$  and  $N_{\text{H}}$  for the possible X-ray counterparts are listed in Table 7.3. Additionally,  $N_{\text{H}}$  and  $N_{\text{H}}^{\text{LAB}}$  are given in Table B.3 for all analyzed pulsars.

### 7.2.3 Timing analysis

The timing resolution of the ACIS and the EPIC-MOS camera ( $\sim 1$  s) was insufficient to study the pulsed emission of the pulsars. Additionally, the time resolution of the EPIC-PN CCDs depends on the used observation mode. For all observations that had a high enough time resolution to study the temporal properties of a rotating neutron star we converted the event time tags to the Barycentric Dynamical Time using the SAS-tool `barycen` with the radio timing position. After folding the events with the pulsar's rotation frequency given by the ATNF Pulsar Catalogue (Manchester et al., 2005) we searched for a periodic signal by applying the H-test (de Jager et al., 1989). However, for none of the detected counterparts a pulsed emission could be found with high significance (95% confidence level).

### 7.2.4 Upper limits

For all observations where no source close to the radio position was detected we derived an upper limit on the count rate as follows: First, we extracted the counts  $N_i$  including the background contribution for every single data set from XMM-Newton or Chandra within a circle of radius  $r = 30''$  or  $r = 2''$  about the radio position in the energy band  $E_{\text{min}}$  to  $E_{\text{max}} = 4.5$  keV.  $E_{\text{min}}$  is 0.2 keV for XMM-Newton and 0.1 keV for Chandra events. For Chandra data sets where the pulsar was observed far off-axis the radius had to be adjusted, because above  $\approx 4'$  the point-spread-function broadens significantly. Hence, for an off-axis angle  $4' < \theta \leq 8'$  the applied radius  $r = 5''$  and for  $\theta > 8'$  the radius  $r = 10''$ . The background counts  $B_i$  were extracted from an annulus of inner radius  $r_{\text{inner}} = 1.5r$  and outer radius  $r_{\text{outer}} = 2.5r$ . To obtain the background counts in the source region, we had to normalize these counts to the source region by the fraction  $c_1$  between source region area and annulus area and by the fraction  $c_2$  between  $t(\theta)$  and  $t_{\text{BG}}(\theta)$ . Because we used a finite region, we had to correct for the missing flux in the unselected wings

of the point-spread function. This encircled energy fraction ( $EEF_i$ ) was calculated with the help of the `eregonanalyse`- (XMM-Newton) and `psf-tool` (Chandra).

If  $\sum_i^n N_i > 20$  counts, where  $n$  is the number of X-ray observations of a single pulsar, we derived the  $x \cdot \sigma$  upper limit on the count rate with the following equation:

$$UL(x \cdot \sigma) = \frac{\max\left(\sum_i^n \frac{N_i - c_1 c_2 \cdot B_i}{EEF_i}, 0\right) + x \cdot \sum_i^n \frac{\sqrt{N_i + c_1^2 c_2^2 B_i}}{EEF_i}}{\sum_i^n t_i(\theta_i)}. \quad (7.4)$$

Otherwise, the upper limit was derived using the Bayesian approach introduced by Kraft et al. (1991).

Assuming a pure blackbody (BB) spectrum and neglecting the influence of the magnetic field and the neutron star atmosphere we can deduce the  $3\sigma$  upper limit on the effective temperature  $T_e = T_\infty(1+z)$  ( $T_\infty$  is the temperature measured by a distant observer) by minimizing the difference  $UL(3\sigma) - UL_{\text{BB}}(T_e)$  (Becker et al., 1993b; Becker, 1995), where

$$UL_{\text{BB}}(T_e) = \text{const.} \cdot \int_{E_{\text{min}}}^{E_{\text{max}}} \frac{E^2 A_{\text{eff}}(E) \cdot \exp(-\sigma(E) \cdot N_{\text{H}}^{\text{ul}})}{\exp(E(1+z)/k_{\text{B}} T_e)} dE. \quad (7.5)$$

Here  $\text{const.} = \frac{2\pi(1+z)^2 R_0^2}{h^3 c^2 d_{\text{ul}}^2}$  with  $z$  the gravitational red shift for a neutron star with radius  $R_0 = 11.43$  km and mass  $M = 1.4M_\odot$ ,  $h$  the Planck constant,  $c$  the speed of light and  $d_{\text{ul}}$  the upper limit of the distance to the pulsar. Furthermore,  $\sigma(E)$  is the interstellar photoelectric absorption cross section (Morrison and McCammon, 1983),  $N_{\text{H}}^{\text{ul}}$  the upper limit of the hydrogen column density,  $k_{\text{B}}$  is the Boltzmann constant and  $A_{\text{eff}}$  is the weighted effective area of all used instruments with which a certain source was observed:

$$A_{\text{eff}}(E) = \frac{\sum_i^n A_i(E) t_i(\theta_i)}{\sum_i^n t_i(\theta_i)}, \quad (7.6)$$

where  $A_i$  is the on-axis effective area of the instrument used in the  $i$ th observation of the pulsar. Because the count rate is already vignetting corrected we used the on-axis effective area obtained with the SAS-task `calview` for the XMM-Newton EPIC cameras with different filters. The Chandra ACIS and HRC effective area were taken from the Portable, Interactive Multi-Mission Simulator (WebPIMMS), version 4.6.<sup>8</sup>  $N_{\text{H}}^{\text{ul}}$  is calculated as described in Section 7.2.2, except that we add the error of  $DM$  to obtain the upper limit of  $N_{\text{H}}$ .

The distance estimate is based on the work by Verbiest et al. (2012), where they present a detailed analysis of all measured distances to pulsars. For all other sources we used the NE2001 model of Cordes and Lazio (2002) to transform the measured  $DM$  to a distance. We apply a distance error of 20 % to 120 % depending on their Galactic coordinates. This large difference in the used uncertainties is because the error in  $d$  is larger for a pulsar in a region of small electron density than in a region with higher density (Cordes and Lazio, 2002).

To estimate the  $2\sigma$  upper limit of the non-thermal X-ray efficiency we derived an expression for  $UL_{\text{model}}$  in a similar way as for the blackbody spectrum, except that we inserted a power law

<sup>8</sup>See <http://heasarc.nasa.gov/docs/software/tools/pimms.html>

**Table 7.1:** Pulsar parameters of detected radio pulsars.

PSR	RA hh:mm:ss	DEC dd:mm:ss	$\Delta$ arcsec	S/N $\sigma_G^{(\alpha)}$	$P_{\text{coin}}$	$\log(f_x/f_v)$
J0117+5914	01 : 17 : 38.5 ± 0.3	+59 : 14 : 38 ± 2	1.6 ± 2.1	16.9	1.3 × 10 <sup>-4</sup>	> 0.2
J0543+2329	05 : 43 : 09.5 ± 0.2	+23 : 29 : 07 ± 2	3.4 ± 4.8	5.9	2.8 × 10 <sup>-4</sup>	> -0.4
J0907-5157	09 : 07 : 15.6 ± 0.2	-51 : 58 : 01 ± 2	3.4 ± 2.3	6.3	4.1 × 10 <sup>-4</sup>	> -0.5
J0922+0638	09 : 22 : 14.16 ± 0.14	+06 : 38 : 24 ± 2	2.4 ± 2.1	17.8	6.3 × 10 <sup>-4</sup>	> -0.7
J1105-6107	11 : 05 : 26.03 ± 0.07	-61 : 07 : 50.4 ± 0.3	1.4 ± 0.5	4.4	3.2 × 10 <sup>-4</sup>	> -0.4
J1112-6103	11 : 12 : 14.87 ± 0.03	-61 : 03 : 30.7 ± 0.2	0.6 ± 0.5	43.0	4.1 × 10 <sup>-4</sup>	> 0.0
J1224-6407	12 : 24 : 21.8 ± 0.3	-64 : 07 : 55 ± 2	2.9 ± 2.3	6.1	2.3 × 10 <sup>-4</sup>	> -0.3
J1301-6310	13 : 01 : 28.2 ± 0.3	-63 : 10 : 42 ± 2	1.9 ± 2.3	10.4	2.0 × 10 <sup>-4</sup>	> -0.2
J1341-6220	13 : 41 : 43.1 ± 0.3	-62 : 20 : 18 ± 2	4.2 ± 2.4	6.4	3.4 × 10 <sup>-3</sup>	> -0.8
J1600-3053	16 : 00 : 51.8 ± 0.2	-30 : 53 : 49 ± 2	0.8 ± 2.4	5.8	3.0 × 10 <sup>-5</sup>	> -0.6
J1658-5324	16 : 58 : 39.35 ± 0.05	-53 : 24 : 06.8 ± 0.3	0.2 ± 0.3	9.6	6.2 × 10 <sup>-6</sup>	> -0.1
J1730-2304	17 : 30 : 21.5 ± 0.2	-23 : 04 : 30 ± 2	2.7 ± 2.1	24.4	5.5 × 10 <sup>-4</sup>	> -0.2
J1825-0935	18 : 25 : 30.7 ± 0.2	-09 : 35 : 23 ± 2	1.5 ± 2.3	6.7	2.4 × 10 <sup>-5</sup>	> -1.1
J1843-1113	18 : 43 : 41.25 ± 0.02	-11 : 13 : 30.6 ± 0.4	0.5 ± 0.4	2.8	5.2 × 10 <sup>-6</sup>	> -0.6
J1911-1114	19 : 11 : 49.5 ± 0.2	-11 : 14 : 23 ± 2	3.1 ± 2.8	6.5	8.7 × 10 <sup>-4</sup>	> -0.8
J1933-6211	19 : 33 : 32.49 ± 0.05	-62 : 11 : 46.3 ± 0.4	0.7 ± 0.4	3.7	1.6 × 10 <sup>-5</sup>	> -0.6
J2017+0603	20 : 17 : 22.70 ± 0.01	+06 : 03 : 05.4 ± 0.2	0.2 ± 0.2	8.7	3.6 × 10 <sup>-6</sup>	> -0.3
J2222-0137	22 : 22 : 05.95 ± 0.01	-01 : 37 : 15.7 ± 0.2	0.1 ± 0.2	8.9	2.0 × 10 <sup>-5</sup>	> -0.7

**Notes.**  $^{(\alpha)} \sigma_G = 1 + \sqrt{c_{\text{bg}} + 0.75}$ , where  $c_{\text{bg}}$  are the background counts.

model (PL) with photon index  $\Gamma = 1.7$  (Becker, 2009) and minimizing  $UL(2\sigma) - UL_{\text{PL}}(K)$  with

$$UL_{\text{PL}}(K) = K \int_{E_{\text{min}}}^{E_{\text{max}}} E^{-\Gamma} \exp(-\sigma(E) \cdot N_{\text{H}}^{\text{ul}}) \cdot A_{\text{eff}}(E) dE. \quad (7.7)$$

Using the resulting value for the normalization constant  $K$  and the assumed photon index we can derive the flux upper limit in a certain energy range by integrating the power law model with the derived normalization over this energy band.

In the following, all given uncertainties represent the  $1\sigma$  confidence range for one parameter of interest, unless stated otherwise.

## 7.3 Results

### 7.3.1 Detections

In addition to the already known pulsars, we found 18 X-ray sources close to the corresponding radio timing positions. Their X-ray images are displayed in Figure 7.1. The coordinates of the X-ray counterparts, the discrepancy between X-ray and radio position  $\Delta$ , the chance probability  $P_{\text{coin}}$  and the X-ray to visual flux ratio are summarized in Table 7.1. For six neutron stars a detailed spectral analysis was possible. The results of this analysis are shown in Table 7.2. In Table 7.3 all fundamental parameters of the detected pulsars are listed, including the flux, the luminosity and the X-ray efficiency  $\mu_{0.1-2 \text{ keV}}$  in the 0.1–2 keV range.

In the following paragraphs we will give a short overview of the detected counterparts of radio pulsars and if applicable, give detailed information about the spectral analysis.

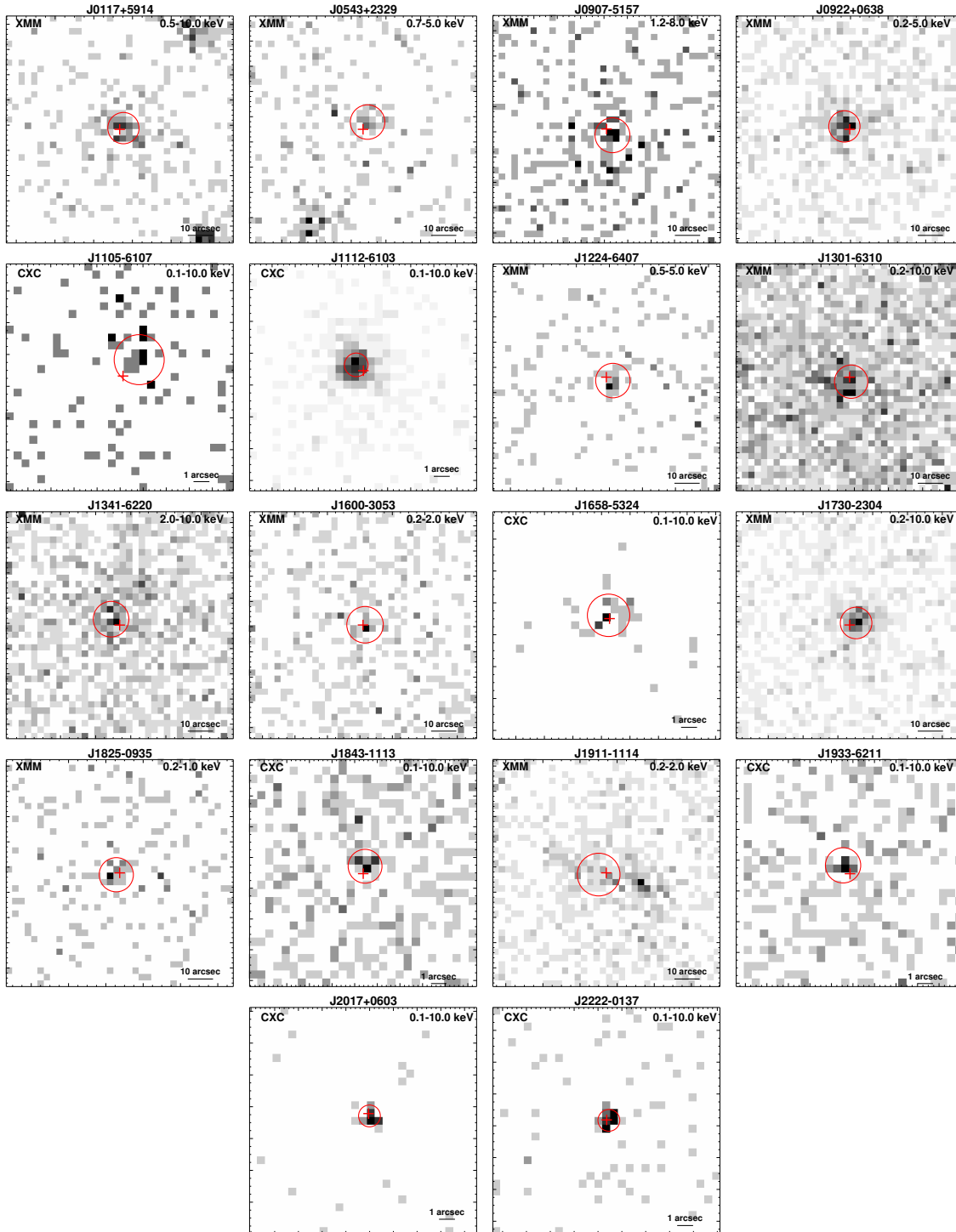


**Figure 7.1:** X-ray images of the region around all radio pulsars where an X-ray counterpart was detected. Each panel has a size of  $1'.5 \times 1'.5$  for XMM-Newton observations and  $15'' \times 15''$  for Chandra observations. North is up and east is to the left. The cross marks the radio position of the pulsar and the red circle indicates the  $3\sigma$  uncertainty in the measured X-ray position.

**Table 7.2:** Spectral parameters of detected pulsars with more than 70 source counts.

PSR	model	$\chi^2/\text{d.o.f.}$	$N_{\text{H}}$ $10^{22} \text{ cm}^{-2}$	$\Gamma/T_{\text{emit}}$ -/keV	Norm $^{\beta}$	$R_{\text{emit}}$ km
J0117+5914	BB $^{\alpha}$	12.2/13	< 0.48	$0.18^{+0.04}_{-0.03}$	$3.7^{+1.3}_{-1.1} \times 10^{-7}$	$0.4 \pm 0.2$
	PL $^{\alpha}$	13.2/13	$0.5^{+0.7}_{-0.5}$	$3.3 \pm 0.5$	$(8 \pm 2) \times 10^{-6}$	-
J0922+0638	PL	4.0/8	< 0.12	$2.3^{+0.8}_{-0.4}$	$1.9^{+0.9}_{-0.4} \times 10^{-6}$	-
J1112-6103	PL	9.7/11	$1.2^{+1.1}_{-1.0}$	$1.5 \pm 0.7$	$1.3^{+2.3}_{-0.8} \times 10^{-5}$	-
J1301-6310	BB $^{\alpha}$	23.8/16	< 0.09	$0.25^{+0.08}_{-0.07}$	$9^{+4}_{-2} \times 10^{-8}$	$0.08^{+0.04}_{-0.03}$
	PL $^{\alpha}$	16.4/16	< 0.39	$3.4^{+0.8}_{-0.6}$	$(3.2 \pm 0.7) \times 10^{-6}$	-
J1341-6220	PL $^{\alpha}$	13.6/23	$4 \pm 3$	$1.1 \pm 0.7$	$1.5^{+2.1}_{-1.0} \times 10^{-6}$	-
J1730-2304	BB $^{\alpha}$	12.2/18	< 0.53	$0.26^{+0.06}_{-0.21}$	$1.5^{+0.4}_{-0.7} \times 10^{-7}$	$0.026^{+0.009}_{-0.023}$
	PL $^{\alpha}$	17.0/17	< 0.47	$2.7^{+0.9}_{-0.5}$	$3.3^{+0.9}_{-1.2} \times 10^{-6}$	-

**Notes.**  $^{\alpha}$  Spectral parameters were obtained with  $N_{\text{H}}$  fixed to DM based value  $^{\beta}$  PL: photons  $\text{keV}^{-1} \text{ cm}^{-2} \text{ s}^{-1}$  at 1 keV; BB:  $L[10^{39} \text{ erg/s}]/(D[10 \text{ kpc}])^2$ , where  $L$  is the source luminosity and  $D$  the distance to the source.

**Table 7.3:** Pulsar parameters of radio pulsars which have a counterpart in the X-ray band.

PSR	DM $\text{pc cm}^{-3}$	P ms	$\log(\text{Age})$ yrs	$\log(\dot{E})$ $\text{erg s}^{-1}$	$n_{\text{H}}$ $10^{21} \text{ cm}^{-2}$	d kpc	model	$f_{0.1-2 \text{ keV}}$ $\text{erg s}^{-1} \text{ cm}^{-2}$	$L_{0.1-2 \text{ keV}}$ $\text{erg s}^{-1}$	$\mu_{0.1-2 \text{ keV}}$
J0117+5914	49.423	101	5.4	35.3	1.5	2.2	BB	$(3.1 \pm 0.6) \times 10^{-14}$	$(1.8 \pm 0.4) \times 10^{31}$	$(8 \pm 2) \times 10^{-5}$
							PL	$1.8^{+1.4}_{-0.8} \times 10^{-13}$	$1.1^{+0.9}_{-0.4} \times 10^{32}$	$(5 \pm 2) \times 10^{-4}$
J0543+2329	77.7115	245	5.4	34.6	2.4	2.1	PL $^{\alpha}$	$(8 \pm 2) \times 10^{-15}$	$(4.1 \pm 1.1) \times 10^{30}$	$(10 \pm 3) \times 10^{-5}$
J0907-5157	103.72	253	6.3	33.6	3.2	0.9	PL $^{\alpha}$	$(7 \pm 2) \times 10^{-15}$	$(7 \pm 2) \times 10^{29}$	$(1.5 \pm 0.4) \times 10^{-4}$
J0922+0638	27.271	430	5.7	33.8	0.8	1.1	PL	$1.2^{+1.4}_{-0.6} \times 10^{-14}$	$1.7^{+2.0}_{-0.9} \times 10^{30}$	$(2.6 \pm 1.4) \times 10^{-4}$
J1224-6407	97.47	216	5.8	34.3	3.0	4.0	PL $^{\alpha}$	$(10 \pm 3) \times 10^{-15}$	$(1.9 \pm 0.5) \times 10^{31}$	$(10 \pm 3) \times 10^{-4}$
J1301-6310	86.1	663	5.3	33.9	2.7	1.9	BB	$(7.4 \pm 1.4) \times 10^{-15}$	$(3.0 \pm 0.6) \times 10^{30}$	$(4.0 \pm 0.8) \times 10^{-4}$
							PL	$9^{+7}_{-4} \times 10^{-14}$	$3^{+3}_{-2} \times 10^{31}$	$(5 \pm 2) \times 10^{-3}$
J1341-6220	717.3	193	4.1	36.1	22.1	11.1	PL	$5^{+4}_{-3} \times 10^{-15}$	$7^{+6}_{-4} \times 10^{31}$	$(5 \pm 3) \times 10^{-5}$
J1600-3053	52.3262	3	9.8	33.9	1.6	2.4	PL $^{\alpha}$	$(6 \pm 2) \times 10^{-15}$	$(4.1 \pm 1.1) \times 10^{30}$	$(5.1 \pm 1.3) \times 10^{-4}$
J1730-2304	9.617	8	9.8	33.2	0.3	0.5	BB	$1.4^{+0.1}_{-0.2} \times 10^{-14}$	$4.9^{+0.4}_{-0.6} \times 10^{29}$	$(3.3 \pm 0.4) \times 10^{-4}$
							PL	$3.5^{+1.8}_{-1.1} \times 10^{-14}$	$1.2^{+0.6}_{-0.4} \times 10^{30}$	$(8 \pm 2) \times 10^{-4}$
J1825-0935	19.38	769	5.4	33.7	0.6	0.9	PL $^{\alpha}$	$(1.7 \pm 0.4) \times 10^{-14}$	$(1.6 \pm 0.4) \times 10^{30}$	$(3.4 \pm 0.8) \times 10^{-4}$
J1911-1114	30.9750	3	9.6	34.1	1.0	1.2	PL $^{\alpha}$	$3.7^{+0.9}_{-0.8} \times 10^{-15}$	$6.5^{+1.6}_{-1.5} \times 10^{29}$	$(5.6 \pm 1.3) \times 10^{-5}$
J1105-6107	271.01	63	4.8	36.4	8.4	5.0	PL $^{\alpha}$	$(1.0 \pm 0.3) \times 10^{-14}$	$3.0^{+0.8}_{-0.9} \times 10^{31}$	$(1.2 \pm 0.4) \times 10^{-5}$
J1112-6103	599.1	64	4.5	36.7	18.5	12.3	PL	$4^{+3}_{-2} \times 10^{-14}$	$6^{+5}_{-4} \times 10^{32}$	$(1.4 \pm 0.9) \times 10^{-4}$
J1658-5324	30.8	2	9.5	34.5	1.0	0.9	PL $^{\alpha}$	$(1.6 \pm 0.3) \times 10^{-14}$	$(1.7 \pm 0.3) \times 10^{30}$	$(5.6 \pm 1.1) \times 10^{-5}$
J1843-1113	59.96	1	9.5	34.8	1.9	1.7	PL $^{\alpha}$	$(7 \pm 3) \times 10^{-15}$	$(2.5 \pm 1.0) \times 10^{30}$	$(4 \pm 2) \times 10^{-5}$
J1933-6211	11.499	3	10.2	33.5	0.4	0.5	PL $^{\alpha}$	$(6 \pm 2) \times 10^{-15}$	$(2.0 \pm 0.7) \times 10^{29}$	$(6 \pm 2) \times 10^{-5}$
J2017+0603	23.918	2	9.7	34.1	0.7	1.6	PL $^{\alpha}$	$(1.1 \pm 0.3) \times 10^{-14}$	$(3.3 \pm 0.8) \times 10^{30}$	$(2.4 \pm 0.6) \times 10^{-4}$
J2222-0137	3.27511	32	10.0	31.7	0.10	0.3	PL $^{\alpha}$	$4.5^{+1.0}_{-0.9} \times 10^{-15}$	$(5.2 \pm 1.1) \times 10^{28}$	$(10 \pm 2) \times 10^{-4}$

**Notes.**  $^{\alpha}$  Flux derived using PIMMS with a power law model and a photon index of 1.7.

### PSR B0114+58

The pulsar PSR B0114+58 (PSR J0117+5914) was first detected in the Princeton-NRAO pulsar survey (Stokes et al., 1985). We made use of an archival XMM-Newton observation (see Table B.2) and extracted the counts in a circle of radius  $20''$  about the pulsars X-ray position. The background spectra were extracted from an annulus with inner and outer radius of  $45''$  and  $75''$ . The extracted counts were binned with at least 8 counts/bin in case of the PN data and 5 counts/bin for the two MOS data sets.

First, we fitted the energy spectra with an absorbed power law and free varying  $N_{\text{H}}$ . This resulted in  $\chi^2 = 12.1$  for 12 d.o.f. and  $N_{\text{H}} = 0.5^{+0.7}_{-0.5} \times 10^{22} \text{ cm}^{-2}$  in agreement with the  $DM$  based estimate of  $N_{\text{H}} = 0.15 \times 10^{22} \text{ cm}^{-2}$ . To put better constraints on the remaining parameter we fixed  $N_{\text{H}}$  to the  $DM$ -based value. This gave an acceptable result ( $\chi^2 = 13.2$ , 13 d.o.f.) with a photon index  $\Gamma = 3.3 \pm 0.5$ . Using a blackbody model gave also an acceptable fit with  $\chi^2 = 12.2$  (13 d.o.f.). The resulting blackbody temperature is  $2.1^{+0.4}_{-0.3} \times 10^6 \text{ K}$  with a normalization factor  $K = 3.7^{+1.3}_{-1.1} \times 10^{-7}$ . Using the normalization factor  $K = L_{39}/D_{10}^2$  ( $L_{39} = L/10^{39} \text{ erg/s}$  and  $D_{10} = d/10 \text{ kpc}$ ) we can estimate the emitting source radius  $R$  as follows:

$$R = \sqrt{\frac{K \cdot D_{10}^2 \times 10^{39} \text{ erg/s}}{4\pi\sigma_B T^4}} = (0.4 \pm 0.2) \text{ km}, \quad (7.8)$$

where  $\sigma_B$  is the Stefan-Boltzmann constant.

### PSR B0540+23

The 246 ms pulsar B0540+23 (PSR J0543+2329) was first detected by Davies et al. (1972). In an archival X-ray observation with XMM-Newton we found a very faint source with  $17 \pm 4$  source counts close to the radio position. Taking the exposure times listed in Table B.2 into account, we derive a count rate of  $(0.9 \pm 0.4) \text{ cts/ksec}$  in the energy range 0.2 to 12 keV. Thus, the X-ray flux in the 0.1 to 2 keV range, applying Equation 7.7, is  $F_{\text{X}}^{0.1-2 \text{ keV}} = (8 \pm 2) \times 10^{-15} \text{ erg s}^{-1} \text{ cm}^{-2}$ .

### PSR B0905–51

B0905–51 (PSR J0907–5157) is an old pulsar and was detected by Manchester et al. (1978). Analyzing an archival XMM-Newton and two Chandra ACIS-I observations of the SNR G272.2–3.2 we detected two faint sources close to the radio position. However, only in the XMM-Newton data the second source is detectable with a good signal-to-noise ratio ( $S/N > 6$ ) and it dominates over the other source only above 1 keV. In addition, this source is closer to the radio position of PSR B0905–51 with a discrepancy of  $3.4 \pm 2.3 \text{ arcsec}$ . We measured  $48 \pm 12$  counts after background subtraction and hence, an X-ray flux of  $7 \pm 2 \times 10^{-15} \text{ erg s}^{-1} \text{ cm}^{-2}$  in the 0.1–2 keV band.

The other source is more than 15 arcsec displaced to the south and thus, cannot be the counterpart of PSR B0905–51.

### PSR B0919+06

The pulsed radio emission of the middle-aged pulsar PSR B0919+06 (PSR J0922+0638) was first recorded in the second Molonglo pulsar survey (Manchester et al., 1978). Verbiest et al. (2012) found the distance to PSR B0919+06 to be  $1.1 \pm 0.2$  kpc by measuring the parallax of this pulsar.

The pulsars energy spectrum was extracted from the PN and MOS1/2 data (see Table B.2) by selecting all events detected in a circle of radius  $15''$  centered on the pulsar's X-ray position. The background spectrum was extracted from an annulus around the pulsar with the same radii as for PSR B0114+58. The spectral data were binned to have at least 20 counts/bin and 10 counts/bin for data obtained at the PN and MOS CCDs, respectively. Fitting a power law model gave a  $\chi^2 = 4.0$  for 8 d.o.f. and an  $N_{\text{H}} < 1.2 \times 10^{21} \text{ cm}^{-2}$ . This is in agreement with the dispersion-based value of  $8.42 \times 10^{20} \text{ cm}^{-2}$ . The fitted photon index  $\Gamma$  is  $2.3^{+0.8}_{-0.4}$ . A single blackbody fit showed systematic deviation between data point and model and did not result in an acceptable fit ( $\chi^2 = 15.9$ , 8 d.o.f.).

### PSR J1112–6103

PSR J1112–6103 was discovered by the Parkes multibeam pulsar survey (Manchester et al., 2001). Two observations with Chandra are covering the radio position of the pulsar (see Table B.2).

With the CIAO-tool `srcextent` we found that the source is extended at a 90 % confidential level. To proof the existence of a PWN around PSR J1112–6103 we produced radial profiles centered on the deduced X-ray position (see Table 7.1) for both ACIS observations. The profiles were obtained by integrating all counts in 12 concentric, equally-spaced annuli with a minimum radius of  $0''5$  and maximum radius  $6''$  and dividing by the respective areas. This profiles were then compared with the profile of a point source at the same off-axis angle, simulated with MARX<sup>9</sup> and convolved with a Gaussian with a full width at half maximum (FWHM) of  $1''$  as used by Romani and Ng (2003) to detect a faint PWN surrounding PSR J0538+2817. Figure 7.2 shows the resulting diagram obtained for obs.ID 6706. No extension of the X-ray source is visible with a significance of  $3\sigma$ . Therefore, we see no evidence for a PWN surrounding J1112–6103.

The counts within an aperture of  $3''$  about the X-ray position were extracted for spectral fitting of the pulsar. These counts were binned to have at least 20 cts/bin. We fitted an absorbed power law on the energy distribution of the pulsar, which resulted in  $\chi^2 = 17.6$  and 27 degrees of freedom (see Figure 7.3). Furthermore, a blackbody model fit resulted in an acceptable fit ( $\chi^2 = 26.0$  for 29 d.o.f.), but with a blackbody temperature of  $T = (1.4 \pm 0.2) \times 10^7$  K, a factor of 10 higher than the highest temperature of all known neutron stars with thermal emission. Thus, the spectral energy distribution cannot be described by a single blackbody spectrum.

The fitted column density  $N_{\text{H}} = 1.2^{+1.1}_{-1.0} \times 10^{22} \text{ cm}^{-2}$  is in agreement with the results of the LAB Survey of Galactic HI (Kalberla et al., 2005), where the  $N_{\text{H}}$  in the direction of PSR J1112-6103 is between  $1.0 \times 10^{22} \text{ cm}^{-2}$  and  $1.3 \times 10^{22} \text{ cm}^{-2}$  and with the *DM* based estimate of  $N_{\text{H}} = 1.8 \times 10^{22} \text{ cm}^{-2}$ .

<sup>9</sup>See <http://space.mit.edu/cxc/marx/>

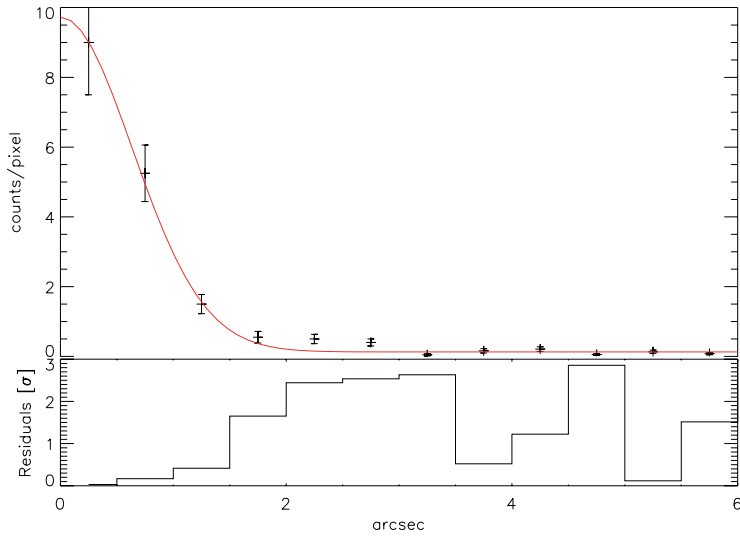


**Figure 7.2:** *Top:* Radial intensity distribution around PSR J1112–6103 in obs.ID 6706. The red line shows the simulated distribution for a point source convolved with a Gaussian with a FWHM=1". *Bottom:* Difference between this two profiles, expressed in terms of the  $1\sigma$  uncertainty in the derived counts per annulus.

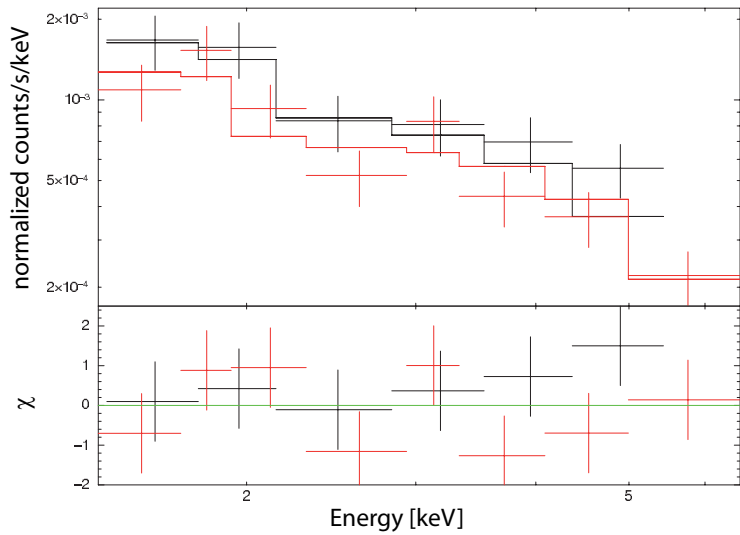


**Figure 7.3:** X-ray spectrum of PSR J1112–6103 fitted with a power law model. The  $\chi^2$  statistic is shown for comparison.

**PSR J1105–6107**

The young pulsar PSR J1105–6107 was discovered by Kaspi et al. (1997) and an association with the supernova remnant G290.1-0.8 (MSH 11-61A) was suggested for this source (Kaspi et al., 1997). After merging two Chandra observations we detected a faint source close to the radio position with  $19 \pm 5$  source counts after background subtraction. With the deduced exposure times (see Table B.2) the count rate in the energy range 0.1–10 keV is  $(0.8 \pm 0.2)$  cts/ksec. The X-ray flux in the 0.1 to 2 keV range is  $F_X^{0.1-2 \text{ keV}} = (1.0 \pm 0.3) \times 10^{-14} \text{ erg s}^{-1} \text{ cm}^{-2}$  (Equation 7.7).

**PSR B1221–63**

The radio emission from PSR B1221–63 (PSR J1224–6407) was first detected by Komesaroff et al. (1973). The distance to this source is  $(4 \pm 2)$  kpc (Verbiest et al., 2012). An archival XMM-Newton observation was found for this source (see Table B.2). In the merged XMM-Newton image  $(30 \pm 8)$  cts were detected from the possible X-ray counterpart of this pulsar. These counts are already corrected for the encircled energy fraction. Using the net exposure time on this source of 3.9 and 6.4 ksec for the PN and the two MOS cameras the count rate is  $(1.8 \pm 0.5)$  cts/ksec in the merged image in the energy band 0.2–12 keV. Using Equation 7.7 the X-ray flux in the 0.1 to 2 keV range is  $F_X^{0.1-2 \text{ keV}} = (1.0 \pm 0.3) \times 10^{-14} \text{ erg s}^{-1} \text{ cm}^{-2}$ .

**PSR J1301–6310**

The middle-aged pulsar PSR J1301–6310 was discovered in the Parkes multibeam pulsar survey (Kramer et al., 2003a). For the spectral analysis we had to exclude the observation with the MOS1 CCDs in obsID 0303440101, because the pulsar could not be detected in this observation. We extracted the events within a circle of  $20''$  radius and binned the extracted counts with at least 20 cts/bin for the PN camera and 10 cts/bin for the MOS cameras.

Using both, a power law and a blackbody spectrum gave similar findings. The fit of a power law results in  $\chi^2 = 15.2$  for 15 d.o.f. and an  $N_H < 3.9 \times 10^{21} \text{ cm}^{-2}$ . Using a blackbody spectrum leads to  $\chi^2 = 17.0$  for 15 d.o.f.,  $N_H \leq 9 \times 10^{20} \text{ cm}^{-2}$ . After fixing  $N_H$  to the *DM* based value of  $2.6 \times 10^{21} \text{ cm}^{-2}$  both fits are still reasonable (see Table 7.2). The normalization factor is  $K = 9_{-2}^{+4} \times 10^{-8}$  and thus, the emitting source radius is  $R = 0.09 \pm 0.03 \text{ km}$ .

**PSR B1338–62**

PSR B1338–62 (PSR J1341-6220) is a young, Vela-like pulsar discovered in 1985 at the Parkes radio telescope (Manchester et al., 1985). The pulsar is associated with the supernova remnant G308.8–0.1 (Kaspi et al., 1992) and according to Wang et al. (2000) among the most actively glitching pulsars known. Two X-ray sources were found close to the radio position in the merged PN and MOS observations (see Table B.2):  $S_1$  with the coordinates  $\text{RA} = 13^{\text{h}}41^{\text{m}}43.1^{\text{s}} \pm 0.3^{\text{s}}$ ,  $\text{DEC} = -62^{\circ}20^{\text{m}}18^{\text{s}} \pm 2^{\text{s}}$  and  $S_2$  with  $\text{RA} = 13^{\text{h}}41^{\text{m}}43.3^{\text{s}} \pm 0.3^{\text{s}}$ ,  $\text{DEC} = -62^{\circ}20^{\text{m}}06^{\text{s}} \pm 2^{\text{s}}$ .

Correlating both sources with the 2MASS All-Sky Catalog of Point Sources (Cutri et al., 2003) gave a match for  $S_2$ , 2MASS J13414307-6220063 with a positional discrepancy of  $1''.5 \pm$

2''2. Source  $S_1$  is close to the pulsar radio timing position, the difference is  $4''2 \pm 2''4$ . This source is only distinguishable from  $S_2$  at energies above  $\sim 2$  keV (see Figure 7.1).

In order to fit the energy distribution of the detected X-ray source we extracted the counts within a radius of  $12''5$  about  $S_1$  in obs.ID 0301740101 and excluded the region around  $S_2$ . The background spectra were extracted from a region close to the source. The other two observations are highly contaminated by particle background radiation. Therefore, the effective exposures are too short for a spectral analysis. The resulting background subtracted count rates are listed in Table B.2. The counts were binned with at least 10 counts per bin for the PN-camera and 5 cts/bin for MOS1/2. Using a power law to fit the energy spectra gave a good result ( $\chi^2 = 3.1$  for 8 d.o.f.) with  $N_H = 4 \pm 3 \times 10^{22} \text{ cm}^{-2}$ . This is in agreement with the  $DM$  based value of  $2.2 \times 10^{22} \text{ cm}^{-2}$ . After fixing  $N_H$  to the  $DM$  based value the fit was still good with  $\chi^2 = 3.2$  (9 d.o.f.) and a photon index  $\Gamma = 1.1 \pm 0.7$ . A blackbody model fit gave  $\chi^2 = 2.8$  for 7 d.o.f. with fixed  $N_H$ , but the resulting value for the temperature  $kT = 1.2_{-0.4}^{+1.6} \text{ K}$  is too high to be consistent with emission coming from the neutron star surface or a hot spot.

### PSR J1600–3053

The high Galactic latitude binary pulsar J1600–3053 was detected by Jacoby et al. (2007). A very faint source was found close to the radio position in an archival XMM-Newton observation (see Table B.2). With the help of the XMM-Newton source detection software we detected a source with  $37 \pm 10$  source counts close to the radio position. With the net exposure of 24.5 ksec and 23.5 ksec for the MOS1 and MOS2 cameras the count rate is  $(8 \pm 2)$  cts/ksec in the merged MOS1/2 image in the 0.2–12 keV band. Further, the PN camera was operated in timing mode, therefore no imaging with this instrument was possible.

### PSR J1658–5324

This pulsar was detected in a survey of unidentified Fermi LAT sources with the Parkes radio telescope (Kerr et al., 2012). Using the coordinates given in the Second Fermi Large Area Telescope Catalog of Gamma-ray Pulsars (Abdo et al., 2013) we detected a source with  $25.9 \pm 5.3$  counts close to the radio position. The positional discrepancy is  $0.22 \pm 0.28$  arcsec.

### PSR J1730–2304

The solitary millisecond pulsar J1730–2304 was discovered by Lorimer et al. (1995). In an XMM-Newton observation (see Table B.2) the source spectrum was extracted from a circle of radius  $20''$  around the X-ray source, which was detected  $2''7$  off the radio position of PSR J1730–2304. These counts were binned with at least 20 cts/bin and 10 cts/bin for the PN and MOS camera, respectively.

Fitting a single power law or blackbody spectrum yielded model spectra with large deviations from the recorded ones at an energy of  $\approx 1.4$  keV. Adding a Gaussian line profile at this energy results in a  $\chi^2 = 17.0$  for 16 d.o.f. in case of the power law. As for the blackbody model fit the

model still shows systematic deviations from the data points. The line center is at  $1.36_{-0.1}^{+0.08}$  keV. However, the origin of the line is unclear and could be instrumental.

### PSR B1822-09

The middle-aged pulsar B1822-09 (PSR J1825–0935) was first mentioned in the literature by Davies et al. (1972). In an XMM-Newton observation with a net exposure time of 1.3, 3.8 and 4.3 ksec for the PN, MOS1, and MOS2 camera, the observation was not deep enough to study this neutron star in the X-ray regime in detail. Nevertheless, we found an X-ray source only  $1.5''$  off the radio coordinates. The X-ray source has  $46 \pm 11$  source counts and thus, a count rate of  $(4.9 \pm 1.2)$  cts/ksec.

### PSR J1843–1113

The solitary millisecond pulsar PSR J1843–1113 was discovered in the Parkes multibeam pulsar survey (Hobbs et al., 2004). In an archival Chandra HRC-S observation we found a source with  $6.8 \pm 2.8$  net source counts only  $0''.5 \pm 0''.4$  off the radio timing position. With the effective exposure time of 19.9 ksec the counting rate is  $(0.34 \pm 0.14)$  cts/ksec in the 0.1–10 keV band.

### PSR J1911–1114

PSR J1911–1114 was discovered by Lorimer et al. (1996) and is a binary millisecond pulsar. Because the PN camera of the pointed XMM-Newton observation of this pulsar was taken in timing mode, only the MOS1 and MOS2 camera can be used for spatial analysis. Close to the radio position of the pulsar a source was detected with  $54 \pm 13$  source counts, observed in the merged MOS1 and MOS2 image with 51.5 ksec (MOS1) and 48.7 ksec (MOS2) exposure time. Therefore, the count rate is  $(0.54 \pm 0.13)$  cts/ksec.

### PSR J1933–6211

The binary pulsar PSR J1933–6211 has a period of 3.4 ms and a companion with a minimum mass of  $0.32 M_{\odot}$ . It was discovered with four other recycled pulsars, including J1600–3053 in a high Galactic latitude survey by Jacoby et al. (2007). In a Chandra HRC-S observation (obs. ID 9115) we found a source with  $10.0 \pm 3.5$  source counts and a distance to the radio timing position of  $0''.7 \pm 0''.4$ . With the effective exposure time of 19.9 ks the counting rate is  $(0.5 \pm 0.2)$  cts/ksec in the 0.1–10 keV band.

### PSR J2017+0603

PSR J2017+0603 is a millisecond pulsar in a binary system and was first detected by its pulsed emission with the Fermi satellite in the  $\gamma$ -ray regime (Cognard et al., 2011). In the discovery paper they derived an upper limit on the X-ray flux in the 0.5–8 keV band of  $F_X^{0.5-8 \text{ keV}} < 6 \times 10^{-14} \text{ erg s}^{-1} \text{ cm}^{-2}$ . Using an archival Chandra ACIS-S observation we detected an X-ray source with  $19 \pm 5$  source counts with a discrepancy to the radio coordinates of  $0''.2$ . With the exposure

**Table 7.4:** The pulsars with the lowest X-ray efficiency upper limit.

PSR	$\frac{\dot{E}}{4\pi d^2}$ erg s <sup>-1</sup> cm <sup>-2</sup>	$\dot{E}$ erg s <sup>-1</sup>	$\mu_{0.1-2 \text{ keV}}^{\text{PL}}$	$d$ kpc	$\log(\tau)$ yrs	$B_{\text{surf}}$ G
J0940–5428	$1.9 \times 10^{-09}$	$1.9 \times 10^{+36}$	$2.2 \times 10^{-6}$	3.0	4.6	$1.7 \times 10^{+12}$
J1913+1011	$1.1 \times 10^{-09}$	$2.9 \times 10^{+36}$	$6.9 \times 10^{-6}$	4.8	5.2	$3.5 \times 10^{+11}$
J1730–3350	$8.2 \times 10^{-10}$	$1.2 \times 10^{+36}$	$9.7 \times 10^{-6}$	3.5	4.4	$3.5 \times 10^{+12}$
J2129–5721	$8.3 \times 10^{-10}$	$1.6 \times 10^{+34}$	$2.1 \times 10^{-5}$	0.4	9.5	$2.8 \times 10^{+08}$
J1928+1746	$3.9 \times 10^{-10}$	$1.6 \times 10^{+36}$	$2.1 \times 10^{-5}$	5.8	4.9	$9.6 \times 10^{+11}$
J1835–1106	$1.9 \times 10^{-10}$	$1.8 \times 10^{+35}$	$3.5 \times 10^{-5}$	2.8	5.1	$1.9 \times 10^{+12}$
J1702–4310	$2.0 \times 10^{-10}$	$6.3 \times 10^{+35}$	$4.5 \times 10^{-5}$	5.2	4.2	$7.4 \times 10^{+12}$
J1906+0746	$7.7 \times 10^{-11}$	$2.7 \times 10^{+35}$	$4.5 \times 10^{-5}$	5.4	5.1	$1.7 \times 10^{+12}$
J1739–3023	$3.0 \times 10^{-10}$	$3.0 \times 10^{+35}$	$5.7 \times 10^{-5}$	2.9	5.2	$1.2 \times 10^{+12}$
J1828–1101	$3.0 \times 10^{-10}$	$1.6 \times 10^{+36}$	$6.3 \times 10^{-5}$	6.6	4.9	$1.0 \times 10^{+12}$

time of 9.9 ksec this corresponds to a count rate of  $(1.9 \pm 0.5)$  cts/ksec and a flux of  $F_X^{0.1-10 \text{ keV}} = (1.1 \pm 0.3) \times 10^{-14}$  erg s<sup>-1</sup>cm<sup>-2</sup> (Equation 7.7) in the 0.1–10 keV energy band.

### PSR J2222–0137

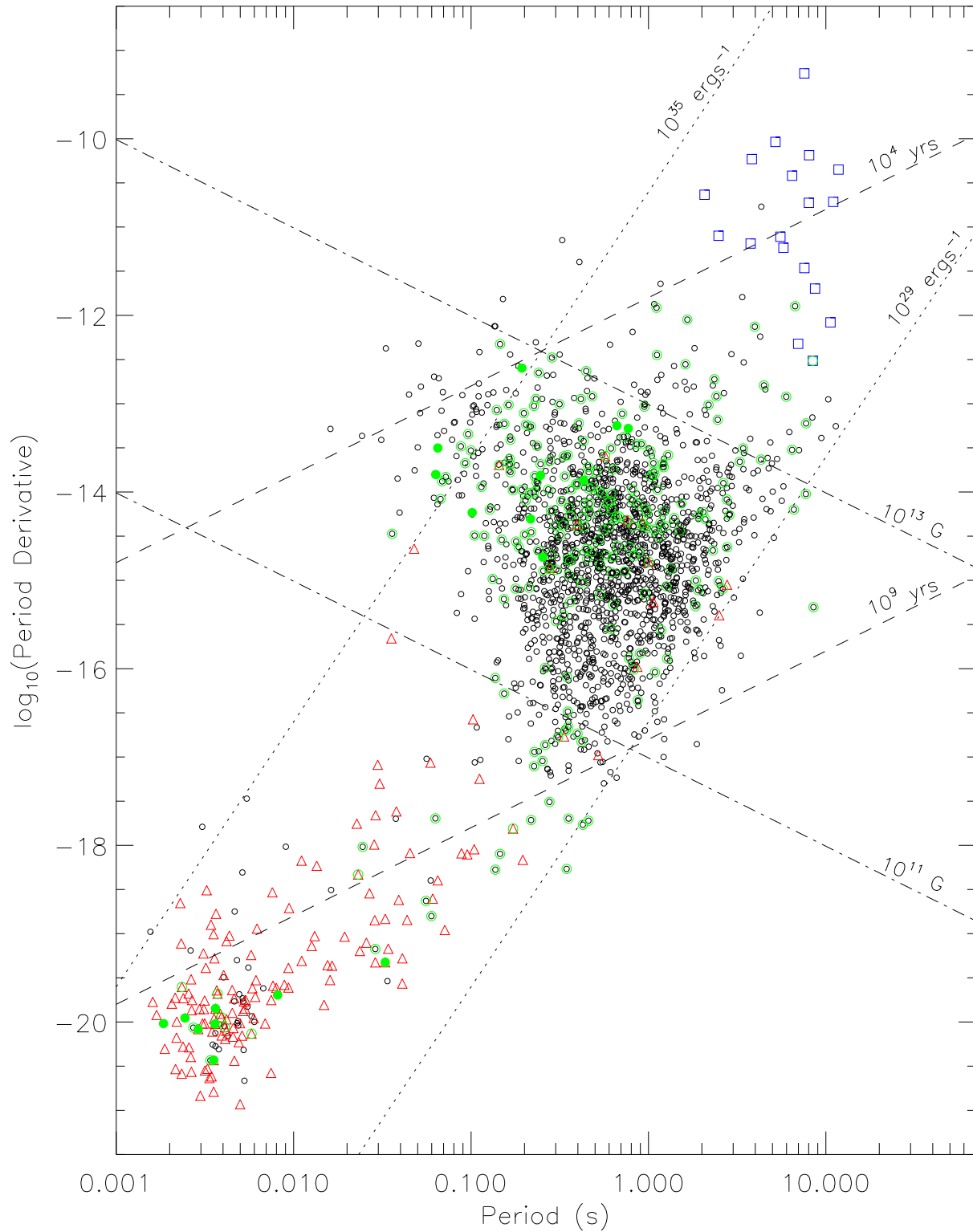
The recently discovered millisecond pulsar PSR J2222–0137 is a mildly recycled binary pulsar (Boyles et al., 2013). It was observed with the ACIS-S camera on board the Chandra X-ray observatory with a net exposure of 27.4 ksec. We found a source with  $26 \pm 5$  source counts, leading to a count rate of  $(1.0 \pm 0.2)$  cts/ksec in the 0.1–10 keV energy band.

### 7.3.2 Upper limits

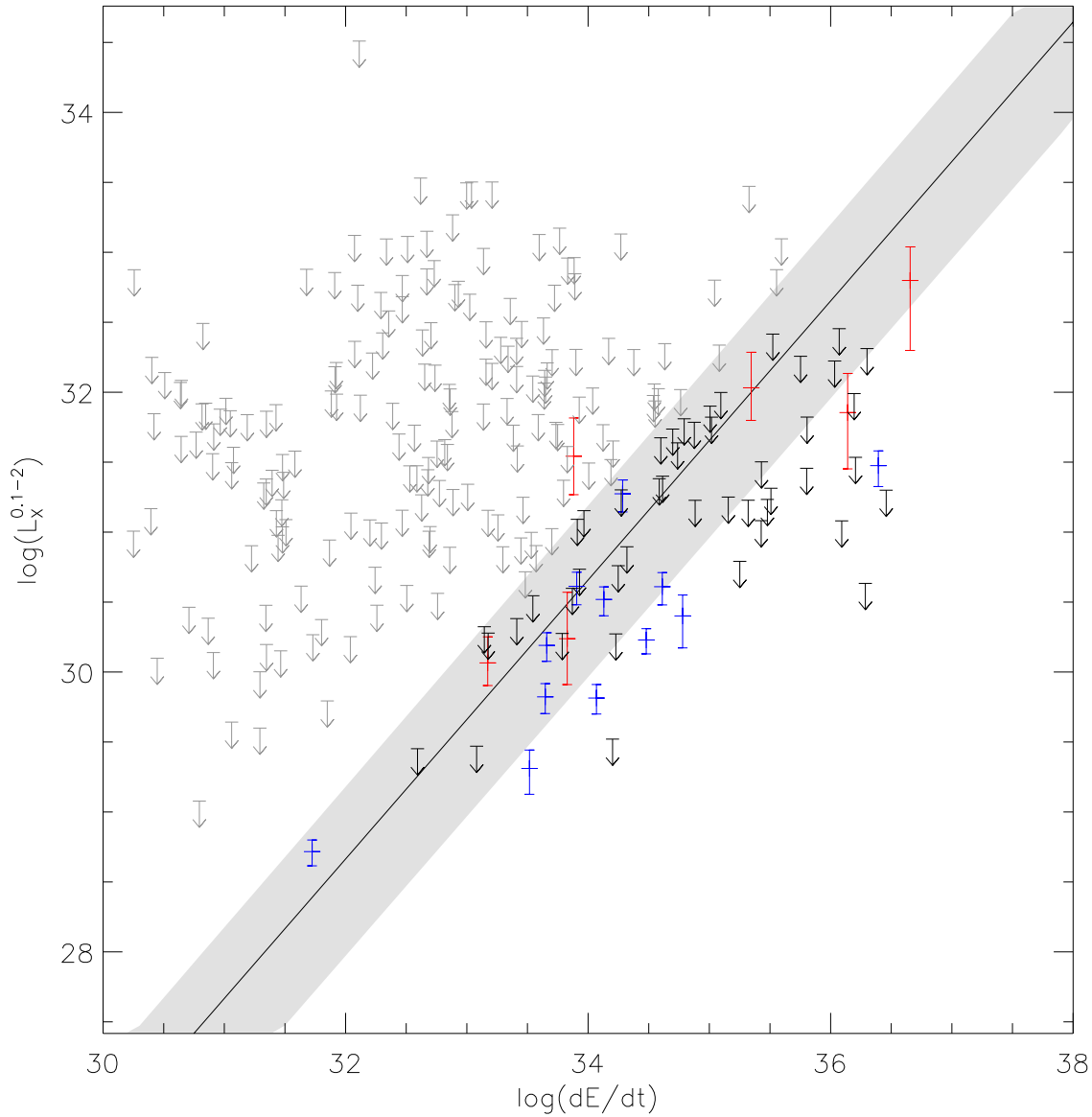
In Table B.3 the results for the non-thermal flux  $F_{0.1-2 \text{ keV}}^{\text{PL}}$  and the upper limit on the blackbody temperature  $T_\infty$  as measured by a distant observer are listed (see also Figure 7.4 for an overview of these sources including the 18 detected PSRs in a  $P$ - $\dot{P}$  diagram). Furthermore, the non-thermal luminosity  $L_{0.1-2 \text{ keV}}^{\text{PL}} = 4\pi d_{\text{UL}}^2 F_{0.1-2 \text{ keV}}^{\text{PL}}$  and the X-ray efficiency  $\mu_{0.1-2 \text{ keV}}^{\text{PL}} = L_{0.1-2 \text{ keV}}^{\text{PL}}/\dot{E}$  are added, where  $\dot{E} = -4\pi^2 I \dot{P} P^{-3}$  is the spin-down luminosity and  $I \approx 10^{45}$  g cm<sup>2</sup> the moment of inertia. In Table 7.4 the pulsars with the lowest X-ray efficiency in the energy band 0.1 – 2 keV of all non-detected sources can be found.

Figure 7.5 displays the dependence of the isotropic X-ray luminosity  $L_X^{0.1-2}$  in the 0.1–2 keV band on the spin-down luminosity  $\dot{E}$ . We added the X-ray luminosity for all detected X-ray pulsar candidates for which we were able to fit a spectrum in red and for which we had to assume the spectral shape in blue. Furthermore, we added the  $2\sigma$  upper limit on the non-thermal X-ray luminosity for all pulsars, for which at least a dispersion measure dependent distance estimate and the rotation period  $P$  and period derivative  $\dot{P}$  are known. The gray shaded region in this graph shows the correlation between  $L_X^{0.1-2}$  and  $\dot{E}$  found by Becker (2009):

$$L_X^{0.1-2} = 10^{-3.24 + 0.26 \log \dot{E} - 0.997 + 0.008 \log \dot{E}} \quad (7.9)$$



**Figure 7.4:** Distribution of pulsars in a  $P-\dot{P}$  diagram. The 18 newly detected X-ray pulsars and the pulsars for which upper limits were calculated are indicated by green dots and circles, respectively.



**Figure 7.5:** Spin-down luminosity  $dE/dt = \dot{E}$  plotted against the isotropic X-ray luminosity  $L_x^{0.1-2}$  in the 0.1–2 keV band of the newly detected pulsars. The red error bars are used for pulsars where a spectral analysis was possible. For the remaining detected pulsars blue error bars were used. In case of the non-detected pulsars the  $2\sigma$  upper limit is indicated with an arrow. The straight line represent the relation found by Becker (2009) with the error range indicated by the gray shaded region.

For this fit he used  $\approx 80$  rotation-powered pulsars for which spectral information was obtained in XMM-Newton and Chandra observations.

In Figure 7.6 we plot the derived  $3\sigma$  temperature upper limits at infinity  $T_\infty$  against the age of the pulsar. If no association with a hosting supernova remnant is possible the only way to estimate the age of a pulsar is by its spin-down age  $\tau = 2P/\dot{P}$ . The uncertainty in  $\tau$  is not known by now and therefore,  $\tau$  should be used with caution. In Figure 7.6 we show an error bar in the

$x$ -direction only if kinematic informations are available, i.e., the age is known with accurately determined errors.

To compare the data with actual cooling models we used the cooling curves of Page et al. (2009). For the computation of the curves they used a  $1.4 M_{\odot}$  neutron star with the equation of state (EOS) of Akmal et al. (1998), different neutron  $^1S_0$ , proton  $^1S_0$ , and neutron  $^3P_2$  gap models taken from Page et al. (2004). They showed that the cooling of a neutron star in the minimal cooling paradigm is only slightly dependent on the neutron star mass and the used neutron and proton  $^1S_0$  gap model. The main uncertainty in the minimal cooling paradigm are a possible time evolution of the chemical composition of the envelope and the number of different gap models that are allowed by current measurements. Therefore, we compare our data with the allowed range given by the sum of all uncertainties mentioned before in Figure 7.6.

In Figure 7.6 we also plot the bolometric luminosity against the age and add the neutron stars for which thermal emission from the surface has been detected or upper limits on the temperature have been derived. These data are taken from Page et al. (2004, 2009), Özel (2013), and Zhu et al. (2011). Additionally, for the central compact object in Puppis-A we adopted the new age estimate of Becker et al. (2012). By using the bolometric luminosity we are able to compare all derived luminosities with each other and with model predictions, because these values are independent of the assumed radius for an upper limit and of the used spectral model to derive a temperature.

---

**Figure 7.6 (following page):** Comparison of the derived upper limits on the temperature (*upper panel*) and bolometric luminosity (*lower panel*) of the radio pulsars with minimal cooling models taken from Page et al. (2009). The upper limits are indicated by arrows. All models are computed for a  $1.4 M_{\odot}$  star with the equation of state (EOS) of Akmal et al. (1998), different neutron  $^1S_0$ , proton  $^1S_0$ , and neutron  $^3P_2$  gap models as introduced by Page et al. (2004): The area in dark and light gray contain models computed with heavy- and light-element dominated envelope, respectively. The error bar indicate the error range in temperature or bolometric luminosity of all pulsars with detected thermal emission. (1) Cas A: Shternin et al. (2011); Fesen et al. (2006); (2) J0822–4300: Zavlin et al. (1999); Becker et al. (2012); (3) J1210–5226: Zavlin et al. (1998); Roger et al. (1988); (4) B0833–45: Pavlov et al. (2001); Aschenbach et al. (1995); (5) B1706–44: McGowan et al. (2004); Koribalski et al. (1995); (6) B0656+14: Marshall and Schulz (2002); Brisken et al. (2003); (7) J0633+1748: Halpern and Wang (1997); Caraveo et al. (2001); (8) B1055–52: De Luca et al. (2005); Kramer et al. (2003a); (9) J1856–3754: Burwitz et al. (2003); Mignani et al. (2013); (10) J0720–3125: Kaplan et al. (2003); Tetzlaff et al. (2011); (11) J0538+2817: Zavlin and Pavlov (2004b); Kramer et al. (2003b); (12) B2334+61: McGowan et al. (2006); Yar-Uyaniker et al. (2004); (13) J1119–6127: Safi-Harb and Kumar (2008); Kumar et al. (2012). In addition, all pulsars with derived temperature upper limit are indicated by a red arrow. (a) Crab: Weisskopf et al. (2011); (b) J0205+6449: Slane et al. (2004a); Fesen et al. (2008); (c) J1124–5916: Hughes et al. (2003); Camilo et al. (2002b); (d) RX J0007.0+7302: Halpern et al. (2004); Slane et al. (2004b); (e) B2224+65: Gonzalez et al. (2004); (f) B1929+10: Hui and Becker (2007b); (g) B0950+08: Becker et al. (2006); Chatterjee et al. (2004); (h) B0628–28: Zavlin and Pavlov (2004a); Brisken et al. (2002); (i) B0823+26: Becker et al. (2005); (k) J2043+2740: Becker et al. (2004); Brisken et al. (2002). We added the error in the age for pulsars with known kinematic age.

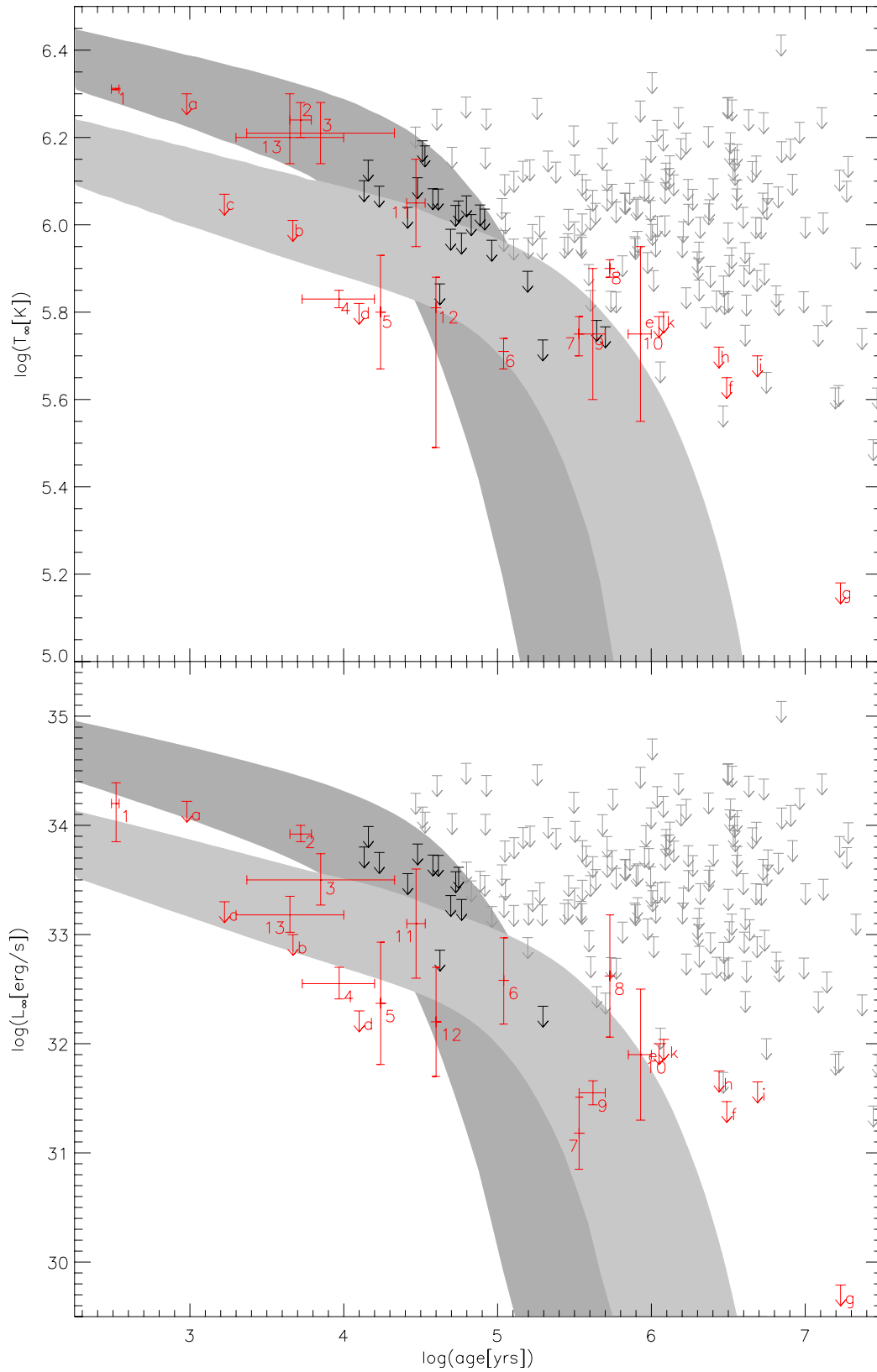


**Table 7.5:** The pulsars with the lowest  $3\sigma$  temperature upper limit (indicated by a black arrow in the upper panel of Figure 7.6). *Left:* Young neutron stars with  $\tau \leq 5 \times 10^4$  yrs. *Right:* Neutron stars with  $\tau > 5 \times 10^4$  yrs.

PSR	log(age) yrs	$T_\infty$ $10^5$ K	PSR	log(age) yrs	$T_\infty$ $10^5$ K
J0940–5428	4.63	7.3	J0157+6212	5.29	5.5
J1524–5706	4.70	9.8	J1457–5902	5.70	5.8
J1730–3350	4.42	11.0	J1846–0257	5.65	6.0
J1637–4642	4.62	12.1	J0742–2822	5.20	7.8
J1907+0918	4.58	12.1	J1913+0446	4.96	9.2
J1702–4310	4.23	12.3	J1801–2304	4.77	9.6
J1413–6141	4.13	12.6	J1850–0026	4.83	10.6
J1841–0524	4.48	12.8	J1928+1746	4.92	10.9
J1726–3530	4.16	14.1	J1055–6028	4.73	11.1
J1837–0604	4.53	15.2	J1828–1101	4.89	11.1
J1646–4346	4.51	15.6	J1841–0345	4.75	11.3
			J1806–2125	4.80	11.7

In Table 7.5 we summarize the neutron stars with the lowest  $3\sigma$  upper limit on the surface temperature in our sample, which are indicated by a black arrow in the upper panel of Figure 7.6.

For some pulsars either no distance or period derivative can be determined, because of missing values for  $\dot{P}$  and/or  $DM$  in the literature. Nevertheless, these objects are added in the resulting list (Table B.3).

## 7.4 Summary and future prospects

In a systematical search within the archives of the X-ray observatories Chandra and XMM-Newton we detected 18 previously unknown X-ray counterparts of radio pulsars. For 6 of them we were able to fit the X-ray spectrum of the pulsar and derive the X-ray flux and luminosity. In all other cases the counting rates were too low or the used detector had a poor intrinsic energy resolution. Therefore, the energy flux and X-ray luminosity were estimated by assuming a non-thermal spectrum and an estimate for the hydrogen column density, which was based on the radio dispersion measure. For pulsars observed in the X-ray band, for which no source could be detected upper limits on the non-thermal and thermal X-ray flux have been derived. We have confirmed the trend for finding smaller X-ray efficiencies with increasing sample size and higher sensitivity of X-ray observatories. Moreover, we have summarized possible explanations for the large dispersion in this relationship and concluded that they are not sufficient to explain the observed data points. Regarding the thermal emission we found that all our measurements are compatible with a neutron star composed only of nucleonic matter. No enhanced cooling mechanism, nor exotic matter has to be included to explain the obtained temperature upper limits. However, it does not rule out the possibility that “exotic” matter is present in the core of neutron stars, because only upper limits were used for this comparison.

The sources in Table 7.5 and Table 7.4 are of particular interest, because investigating them in more detail could help us to put better constraints on the cooling of neutron stars or the models that explain the non-thermal emission of pulsars. Detecting, for example, a neutron star with a surface temperature lower than the expectations from the minimal cooling paradigm, one has to include enhanced cooling mechanism in the modeling of the interior of a neutron star.

In 2015 eROSITA, the successor of the ROSAT mission, will start to image the whole X-ray sky with increased sensitivity (Merloni et al., 2012). This will enable us to study all  $\approx 2250$  known pulsars in the X-ray band with three times better resolution and 20 times larger sensitivity than in the ROSAT All-Sky Survey. Thus, the eROSITA survey will add data to the analysis done here with a larger and even less biased sample. The pulsars in the eROSITA sample will have equal exposures and will cover the whole galactic plane. However, the exposure will be only 3 ksec. The average exposure in the sample studied with XMM-Newton in this chapter was ten times higher. In the case of a non-detection a upper limit on the thermal and non-thermal flux can be calculated, which will then be in general lower than the already derived limits. Nevertheless, it will further constrain the cooling of neutron stars and the dependence of the non-thermal X-ray luminosity and the spin-down energy loss.

The detailed discussion of the results is presented in Chapter 8.



# Chapter 8

## Discussion and future prospects

In this chapter I will summarize and discuss the results obtained in my thesis. Finally, future prospects in this field of research are presented.

### 8.1 Modeling supernova explosions

By measuring the proper motion of a neutron star it is possible to validate current core-collapse SN models. Two previous proper motion measurements of the Central Compact Object RX J0822–4300 in the SNR Puppis A seemed to challenge models for producing neutron star kicks. In these measurements the same Chandra HRC data sets were used, but produced discrepant results. Hui and Becker (2006) found a proper motion of  $(104 \pm 35)$  mas yr<sup>-1</sup> at a position angle of  $240^\circ \pm 28^\circ$ . Winkler and Petre (2007), using a different analysis approach, found a considerably higher value of  $(165 \pm 25)$  mas yr<sup>-1</sup> at a position angle of  $248^\circ \pm 14^\circ$ . In Chapter 3.3.1 a combined analysis, incorporating a new deep observation and a total time baseline twice as long as was available previously, yields an improved value that is smaller than either of the two published numbers, but at a position angle consistent with both. The proper motion was measured with high confidence and yielded a value of  $(71 \pm 12)$  mas yr<sup>-1</sup> at a position angle of  $244^\circ \pm 11^\circ$ . The much smaller value compared to the result of Winkler and Petre (2007) is due to a bug in the PSF fitting routine, which I found in the Chandra software by redoing their analysis. Furthermore, the 68% confidence levels of the proper motion measured by Hui and Becker (2006) and in this thesis are in agreement. For an assumed distance to Puppis A of 2 kpc the proper motion corresponds to a tangential velocity of  $(670 \pm 120)$  km s<sup>-1</sup>.

Even though RX J0822–4300 is not moving as fast as previously thought, its association with a supernova remnant of well-constrained age and reasonably well-localized explosion center (Winkler et al., 1988) makes it worthwhile to reexamine the implications of the revised velocity on explosion kinematics and dynamics. The reduced tangential velocity of the neutron star means a proportionately smaller momentum. Assuming a typical neutron star mass of  $1.4 M_\odot$ , its momentum is  $\sim 2 \times 10^{41}$  g cm s<sup>-1</sup>, roughly a factor of two smaller than the estimate in Winkler and Petre (2007). Their paper compared the momentum of the neutron star with that of the optical filaments moving in the opposite direction at approximately 1500 km s<sup>-1</sup>. Assuming

a typical knot mass of  $0.04 M_{\odot}$  (Winkler et al., 1988), the momentum per knot in the direction opposite to the neutron star is  $\sim 1.2 \times 10^{41} \text{ g cm s}^{-1}$ . The momentum of the neutron star would thus be balanced by about 16 such knots, which roughly corresponds to the known number. Thus, to the degree of accuracy to which the filament mass can be inferred, a momentum balance is still feasible.

More drastic is the reduction of the estimate of the kinetic energy carried by the stellar remnant:  $6.5 \times 10^{48}$  ergs, which is a quarter of that estimated in Winkler and Petre (2007). This corresponds to only 0.6 percent of the nominal  $10^{51}$  ergs produced in a canonical core-collapse supernova explosion. This reduced value undoubtedly poses less of a challenge for supernova models. In fact, a potential discrepancy, as pointed out in Winkler and Petre (2007), is resolved. Using the prediction for the kick velocity from the explosion model of Burrows et al. (2007); Scheck et al. (2004, 2006); Wongwathanarat et al. (2010) given in Equation 2.1 and the previous tangential velocity value, even for the most extreme values of anisotropy, corresponding to  $\sin \alpha \sim 1$ , the explosion energy needed to be higher than the canonical  $10^{51}$  ergs. With the new, reduced tangential velocity, a range of values of  $\sin \alpha = 0.6$  to  $0.8$  is consistent with an explosion having an energy of  $10^{51}$  ergs. Interestingly, this range of  $\sin \alpha$  indicates a highly asymmetric explosion.

Additionally, the revised proper motion has mild implications regarding the age of Puppis A. The proper motions of the optical filaments point back to a common location at RA (2000.) =  $08^{\text{h}}22^{\text{m}}27.^{\text{s}}5$ ; Decl (2000.) =  $-42^{\circ}57'29''$ ; presumably the site of the explosion (Winkler et al. 1988). If no deceleration is assumed, the remnant age inferred from the filament motion is  $3700 \pm 300$  years. The path of the neutron star, projected backward in time, passes directly through the elliptical region in which the explosion is likely to have occurred. The distance between the current neutron star location and the nominal explosion center is  $371 \pm 31$  arc seconds. Using the new proper motion measurement of  $71 \pm 12 \text{ mas yr}^{-1}$  and assuming that the neutron star was born within the optically-defined explosion location its age should be  $(5.2 \pm 1.0) \times 10^3$  years. The age inferred from the neutron star and filament motions can be considered as two independent measurements of the same quantity. They average to  $4450 \pm 750$  yrs for the age of Puppis A, slightly older than the generally accepted 3700 yrs.

While the tangential velocity of RX J0822–4300 is not as extreme as previously thought, it is still high, though more consistent with other fast moving neutron stars (e.g., Hobbs et al., 2005). In light of this new proper motion measurement the implications for kick mechanisms are briefly reconsidered. As discussed in Winkler and Petre (2007), electromagnetically driven or neutrino/magnetic field driven mechanisms are generally not capable of providing a kick velocity in excess of  $500 \text{ km s}^{-1}$ . Even with the lower velocity, these mechanisms are thus unlikely to be applicable to RX J0822–4300: hydrodynamic recoil mechanisms are the only ones capable of providing a sufficient kick. In fact, recent studies (e.g., Nordhaus et al., 2012) suggest that kick velocities as high as  $\sim 600 \text{ km s}^{-1}$  are easily induced by hydrodynamically driven mechanisms after about 1 second of post-bounce evolution during core collapse. In the models of Nordhaus et al. (2012) the gravitational pull of slowly moving ejecta in front of the nascent neutron star can continue to accelerate it to considerably higher velocities.

Strong independent evidence supporting a hydrodynamic kick mechanism for RX J0822–4300 comes from the implications associated with the discovery and the modeling of its pulsa-

tions. Gotthelf and Halpern (2009a) discovered a period of 112 ms in RX J0822–4300. This periodicity had been missed by prior investigators because of an abrupt 180-degree phase change of the pulse profile at about 1.2 keV. The period and the very small period derivative imply a surface magnetic field strength of  $\lesssim 9.8 \times 10^{11}$  G and a spin-down age of larger than  $2.2 \times 10^5$  yrs. The very low magnetic field gives rise to the attribution of “antimagnetar” to this object. Energy- and pulse-phase resolved spectroscopy led to a model that reproduces the observed properties. The model consists of two antipodal hot spots, modeled by blackbodies whose crossover in flux corresponds to the energy at which the phase reverses. The angles from the hot spot to the pole and from the line of sight to the rotation axis are degenerate; one has a value of  $86^\circ$ , the other a value of  $6^\circ$  (Gotthelf et al., 2010b). Interestingly, the model degeneracy allows either for the spin axis to be parallel with the direction of motion, or for the spin and kick directions to be maximally misaligned.

The two most constraining aspects of these results on possible kick models are the low magnetic field and the initial spin period. Models invoking magnetic processes require the nascent neutron star to have a high magnetic field and/or high initial spin periods (Lai, 2001). As pointed out in Gotthelf and Halpern (2009a), the only current models satisfying these new constraints are the hydrodynamical ones that potentially produce very high velocities. Thus, despite the less restrictive, lower inferred space velocity of RX J0822–4300, the conclusion of Winkler and Petre (2007) regarding likely ejection mechanisms still holds.

The solution that favors spin-kick alignment is supported circumstantially by the fact that such alignment is observed in a number of neutron stars (e.g., Figure 5 in Wang et al., 2007a). More specific support from within Puppis A comes from the alignment of HI cavities, which presumably represent the path of jets from the initial explosion, along the direction of motion of the neutron star (Reynoso et al., 2003). Further, the comparison of numerical simulations with the distribution of pulsars with known spin-kick angles suggests that the observed spin-kick distribution requires the initial spin period to be shorter than the kick timescale (Wang et al., 2007a). Since the hydrodynamic recoil time scale ( $\gtrsim 1$  s) is considerably longer than the 112 ms pulsation period, one might reasonably expect spin-kick alignment in RX J0822–4300.

## 8.2 Supernova remnants

### 8.2.1 Is there a second supernova remnant in Puppis A?

In Chapter 3.3.2 the question was investigated, whether the emission from an almost perfectly circular region located at the western side of Puppis A is a second SNR that is just by coincidence close to Puppis A or whether it is the imprint of shock/cloud interactions of Puppis A with the surrounding medium. After studying the western part of Puppis A in radio, infrared, optical, X-ray, and  $\gamma$ -ray there is no single evidence that the western sphere-like structure is different to Puppis A. Therefore, we conclude that this feature belongs to Puppis A and that this sphere-like shape is probably evolving in a bubble in the highly inhomogeneous medium surrounding the remnant. However, how this feature evolved into a nearly perfect circular shape is still unclear and has to be further investigated, e.g., with a deeper Chandra observation.

## 8.2.2 Supernova remnant candidates in the ROSAT All-Sky Survey

In Chapter 4 the re-analysis of the RASS SNR candidate list of Schaudel (2003) was presented. After correlating the source list with various sky surveys and source catalogs as well as analyzing archival X-ray observations 123 sources remained as SNR candidates. 73 of these sources fulfill the criteria that the source significance is  $> 5\sigma_G$  and/or have a counterpart in other wavelengths. Therefore, these sources are no fluctuations in the X-ray background. In addition, the possibility that these SNR candidates are point sources can be ruled out, because it was shown that all spherical symmetric sources are extended (95% CL). However, the remaining 50 candidates do not fulfill one or more of the selection criteria. Thus, it cannot be excluded that some of these sources are indeed fluctuations in the X-ray background.

Nevertheless, it is still possible that some of these 123 sources are of extragalactic origin. For example, galaxy clusters are extended sources and have temperatures of a few times  $10^7$  K (Böhringer and Werner, 2010). Hence, they can be seen in the RASS and can be confused with SNRs. With the RASS data it is not possible to decide whether the source emission originates from inside or outside the Galaxy, because in the RASS neither the temperature nor the hydrogen column density can be measured, because of the short exposures and the poor spectral resolution. The only indication of their origin is the hardness ratio. Galaxy clusters, for example, have hardness ratios  $HR1$  and  $HR2$  roughly in the range from 0 to +1, because of their high temperature (Böhringer et al., 2000). Supernova remnants have lower temperatures and higher absorption by the interstellar medium. Therefore, their hardness ratio  $HR1$  is in the same order as for galaxy clusters, but  $HR2$  should be  $\leq 0$  (Voges et al., 1999; Schaudel, 2003). This is the case for more than 80% of the remnant candidates.

In addition, the conclusion of Schaudel (2003) that candidate G38.7–1.7 is an SNR could be confirmed. This source shows non-thermal polarized radio emission, filaments in  $H\alpha$  and thermal X-ray emission. In addition, the fitted hydrogen column density places this source within our Galaxy. All these are clear indicators that G38.7–1.4 is an SNR. Furthermore, the SNR candidate G265.8–7.1 shows emission from a thermally emitting plasma in the X-ray regime, four candidates have counterparts in the radio band (G55.6+2.0, G83.2+6.9, G309.8–2.5, and G321.7–3.5), two X-ray sources show related emission in the infrared regime (G55.6+2.0 and G312.4+4.8), and four objects show some filamentary structure around the X-ray emission region in  $H\alpha$  (G290.4–1.9, G295.4–3.0, G312.4+4.8, and G319.8–2.0). In addition, for three SNR candidates archival X-ray observations were analyzed and indicate X-ray emission from an extended source. All these candidates are of special interest, because they show several properties typical for SNRs.

The origin of the remaining SNR candidates is still unclear. However, they are promising remnant candidates, because they are extended and bright in the soft X-ray regime.

## 8.2.3 G308.4-1.4

In Chapter 5 the RASS SNR candidate G308.4–1.4 was examined in detail and the following arguments are in favor of an SNR interpretation: First, comparing the fitted  $N_H$  with the integrated hydrogen column density toward G308.4–1.4 (Kalberla et al., 2005; Dickey and Lockman, 1990)

places the source within our Galaxy. In addition, the plasma model used to fit the energy spectrum of G308.4–1.4 was especially designed to improve the modeling of X-ray spectra of SNR. Other plasma models assume ionization equilibrium and are therefore not able to reproduce the spectra of young SNRs that are not evolved enough to reach ionization equilibrium (Borkowski et al., 2001). Second, the temperature of the plasma of approximately 6 million Kelvin is in the typical range for SNRs (McKee, 1987). Third, the analysis of the archival ATCA radio data revealed non-thermal emission with a spectral index of  $-0.7 \pm 0.2$ , which is typical for young to middle-aged SNRs (Dickel, 1991). The spectral index has a large error due to the noise in the 2.5 GHz observation but still agrees with the expected value of -0.4 to -0.5 for middle-aged SNRs. Fourth, the 22- $\mu\text{m}$  to 1.4-GHz flux ratio for G308.4–1.4 is  $\approx 10$ , the upper limit for SNRs (Carey et al., 2009; Pinheiro Gonçalves et al., 2011). Hence, the infrared emission matching the radio and X-ray morphology and the measured 22- $\mu\text{m}$  to 1.4-GHz flux ratio additionally supports that G308.4–1.4 is an SNR. Next, the lack of  $\gamma$ -ray emission from G308.4–1.4 can be explained by the poor spatial resolution of the Fermi-LAT telescope ( $\sim 1^\circ$  at 1 GeV), which makes it hard to distinguish faint extended sources from the diffuse emission of the Galactic plane. Of the 274 known SNRs only seven have been detected by Fermi-LAT so far (Nolan et al., 2012). Finally, G308.4–1.4 is neither a galaxy cluster, nor a planetary nebula. There are various physical scenarios to show what might cause a plasma to emit X-rays. However, the two emission models for hot diffuse (MEKAL, Mewe et al., 1986) and collisionally ionized diffuse gas (APEC, Smith et al., 2001), which are often used to describe the X-ray emission of galaxy clusters, cannot reproduce the spectrum of G308.4–1.4. Moreover, the temperature of galaxy clusters is typically several  $10^7$  K (Böhringer and Werner, 2010), one order of magnitude higher than the fitted value. In addition, G308.4–1.4 cannot be a planetary nebula because its X-ray flux is three orders of magnitude higher than the flux of the brightest planetary nebula detected in X-rays, which is at a distance of  $\approx 1$  kpc (Guerrero et al., 2006) and because of the low 22- $\mu\text{m}$  to 1.4-GHz flux ratio. Furthermore, the temperature of G308.4–1.4 is a factor of two higher than the highest measured temperature of the hotter, type 2 planetary nebulae (Guerrero et al., 2000).

Based on these results it was concluded in this thesis that G308.4–1.4 is indeed a supernova remnant. Only the eastern part of the remnant can be seen in the radio-, infrared- and X-ray regime, which is not unusual for SNRs (e.g., Castro et al., 2011). A possible explanation could be that its shock wave is expanding in more dense ISM in the east or the emission in the western part is absorbed by ISM that is in front of the SNR. In the infrared a bright and extended region can be seen in the northwestern part of the SNR, whose emission is not correlated with the SNR. The radio morphology of the remnant at 0.843, 1.384 and 2.496 GHz is characterized by two arcs. The eastern arc matches the X-ray and infrared contours. The second arc, which is bending in the west and shows a decreasing brightness toward the center of G308.4–1.4, has no counterpart in other wavelengths. Its nature is not clear by now and has to be studied in more detail.

A Sedov analysis suggests that the SNR is about 6200 years old and is expanding with a velocity on the order of  $\approx 730$  km/s. All fundamental parameters of the SNR are summarized in Table 5.4.

The X-ray point-like source CXOU J134124.22–634352.0 (source # 1), located close to the geometrical center of the SNR G308.4–1.4, is seen to exhibit variable and flaring X-ray emission. It has no extended X-ray emission as seen in other young and powerful pulsars. Its best-fit

spectral model consists of two blackbodies. Thus, source # 1 shows some properties that have been also seen in central compact objects (CCO, see Gotthelf and Halpern, 2008a, for a review). No CCO has a detected counterpart in the radio and optical band so far. For one member of the CCO group, 1E 161348–5055 in RCW 103, flares have been detected in which the flux varies between 0.8 and  $60 \times 10^{-12}$  ergs cm<sup>-2</sup> s<sup>-1</sup>. This is comparable to source # 1 whose maximum flux is  $\approx 10^{-11}$  ergs cm<sup>-2</sup> s<sup>-1</sup> and the upper limit derived from the SWIFT observations is  $\approx 5 \times 10^{-13}$  ergs cm<sup>-2</sup> s<sup>-1</sup>. The luminosity of source # 1 is  $L_X^{0.5-10} = 2.5_{-0.6}^{+1.2} \times 10^{34} d_{9.8}^{-2}$  erg/s. This is slightly higher than the derived luminosity for the normal population of CCO (Becker, 2009, p.121), only the flaring CCO in RCW 103 has a comparable luminosity of  $0.1 - 8 \times 10^{34}$  erg/s (de Luca, 2008). Krautter et al. (1999) found for all X-ray-bright stars with an optical counterpart a ratio of  $\log(f_X/f_V) = -2.46 \pm 1.27$  in the ROSAT All-Sky Survey. Therefore, the X-ray-to-visual flux ratio of 1.55 and the fitted  $N_H$ , which is on the order of what has been observed for G308.4–1.4, suggest a CCO interpretation for source # 1.

Assuming that the source is indeed the compact remnant, we can derive the proper motion of the object  $\mu = \sqrt{(RA_c - RA_{\#1})^2 + (DEC_c - DEC_{\#1})^2}/t = (45 \pm 4)''/t$  using the inferred center and the age of the SNR. We deduce the proper motion to be  $\mu = 7 \pm 2$  mas/yr =  $320 \pm 100$  km/s. The upper limit on  $\mu$  is higher than the mean two-dimensional proper motion of pulsars in SNRs of  $\sim 227$  km/s (Hobbs et al., 2005), but would not be an exception. For example, the CCO RX J0822–4300 in the SNR Puppis A has a 2d proper motion of  $670 \pm 120$  km/s (Becker et al., 2012).

Nevertheless, the lower limit of the inferred emitting radius of the blackbody in the double blackbody or the power law-blackbody spectral fit is on the order of the expected value for the neutron star radius of 10 to 20 km only if the source is at a distance of at least 7 kpc (see Fig. 5.5). Moreover, we found an infrared and optical source whose position is consistent with source # 1. The spectral distribution of the source allows us to fit a collisionally ionized diffuse gas model (APEC), which Osten et al. (2005) used to model the energy distribution in the X-ray band of the M dwarf flare star EV Lacertae. In addition, the fitted hydrogen column density is consistent with that of a nearby star and the X-ray-to-visual flux ratio is 0.25, only  $2\sigma$  higher than the value for stars derived by Krautter et al. (1999). Therefore, no certain conclusion on the origin of this source could be drawn.

Using the stellar density in the direction of G308.4–1.4 we can derive the chance association of the observed 2MASS source with the compact remnant candidate. The chance association is given by  $P_{\text{coin}} = \frac{N}{l_{RA}l_{Dec}} \pi \delta RA \delta DEC$ , where  $N$  is the number of sources detected within a rectangular region of length  $l_{RA}$  and width  $l_{Dec}$ . and  $\delta RA$ ,  $\delta DEC$  are the errors in the position of the source. The 2MASS catalog contains 2206 point-like sources in a box with side length of 5 arcmin around the center of the remnant and the chance association is 1.3%. Thus, the possibility of a false association between the X-ray and the 2MASS source cannot be excluded.

Until now, we did not discuss the western radio arc, which has no counterpart in the X-ray and infrared image. The arc could be interpreted as a relativistic radio jet of a source at the geometrical center of the SNR. If that is the case, the central source is either a black hole of stellar mass or a neutron star in a binary system (Mirabel and Rodríguez, 1999, and reference therein). Especially the possibility that the central source is a black hole is an interesting speculation which, if proven, would mean that G308.4–1.4 is the remnant of a type II core-collapse SN.

Thus, would be the first one known that left a black hole.

To obtain a rough estimate of the source flux of the other source in the center of the remnant, source # 10, we assumed that the source is a CCO, should have at least a spectrum with a blackbody of temperature 2.6 million Kelvin as the CCO in Puppis-A (cf. Table 6.4, Becker, 2009). Using the WebPIMMS tool with the source count rate and the fitted  $n_{\text{H}}$  of the SNR the flux in the 0.3 – 3.5 keV range is  $f_X \approx 2.2 \times 10^{-14}$  ergs cm $^{-2}$ s $^{-1}$  and in the 0.5 – 10 keV range is  $f_X \approx 1.9 \times 10^{-14}$  ergs cm $^{-2}$ s $^{-1}$ . The normalization of a blackbody with this flux, temperature and  $n_{\text{H}}$  is  $2.5 \times 10^{-5}$ , which corresponds to an emitting radius of the source of  $\approx 9d_{9.8}^{-1}$  km. This value perfectly agrees with the expected value for the neutron star radius. The corresponding luminosity in the energy band 0.5 – 10 keV is  $L_X^{0.5-10} = 2.1 \times 10^{32} d_{9.8}^{-2}$  erg/s, a typical value for CCOs. Furthermore, the X-ray-to-visual flux ratio is  $\log(f_X/f_V) > 0.11$  taking into account that no optical source was detected in the USNO-B1.0 catalog and the limiting magnitude of this catalog is 21 (Monet et al., 2003). Thus, no clear evidence for the origin of the emission of source # 10 could be found.

Finally, it should be mentioned that the detector support structure of Chandra covers the central part of G308.4–1.4 (see Fig. 5.2). It is therefore not excluded from our observations that other faint X-ray point sources are located at this position. However, the non-detection of a source in the SWIFT data at the assumed position of the remnant’s expansion center sets a strict upper limit of  $5 \times 10^{-13}$  ergs cm $^{-2}$  s $^{-1}$  on the flux of such an object. Deeper observations of the central part of SNR G308.4–1.4 are needed to resolve the obvious ambiguities.

### 8.2.4 G296.7-0-9

In Chapter 6 the X-ray emission of the RASS selected SNR candidate G296.7-0-9 was studied in detail. This candidate was already identified as SNR by Robbins et al. (2012). However, they only investigated the radio emission of G296.7-0-9. In X-rays the remnant is characterized by a bright arc in the south-west direction and by diffuse emission with low surface brightness in its western part. It could be shown that the X-ray emission of G296.7–0.9 is in agreement with coming from a collisionally heated plasma that has not yet reached equilibrium. The Sedov analysis leads to the conclusion that the SNR is about 6600 years old and expanding with a velocity on the order of  $\approx 720$  km/s.

The deduced distance  $d_{\text{Sedov}} = 9.8_{-0.7}^{+1.1}$  kpc is in good agreement with the distance of the close-by HII region G296.593–0.975. This is a strong indicator for a spatial association between the SNR and the HII region, as already suggested by Robbins et al. (2012).

The observation used in this analysis was strongly affected by particle background radiation, which led to a net observation time that was shorter by a factor of three than the approved exposure time. Therefore, only limited statements can be made about the existence of a compact source located near the center of the SNR. That no emission from a CCO in G296.7–0.9 was detected does therefore not mean that there is none. The observation might not be deep enough to detect it. Thus, the type of the supernova is unconstrained. Deeper observations might help to clarify this question and shed more light on the type of the SN.

**Table 8.1:** SNRs discovered in the ROSAT All-Sky Survey

SNR	radio	X-ray	reference
G7.5–1.7	part of rim	centrally brightened	Roberts and Brogan (2008)
G13.3–1.3	amorphous emission	elongated emission	Seward et al. (1995)
G28.8+1.5	part of rim	centrally brightened	Schwentker (1994)
G32.1–0.9	possible faint shell	diffuse, with clumps	Folgheraiter et al. (1996)
G38.7–1.4	bright arc	centrally brightened	this work
G69.4+1.2	single arc	elongated emission	Asaoka et al. (1996), Yoshita et al. (2000)
G85.4+0.7	faint, incomplete shell	centrally brightened	Jackson et al. (2008)
G156.2+5.7	faint shell	filamentary ring	Pfeffermann et al. (1991)
G189.6+3.3	single arc	complete shell	Asaoka and Aschenbach (1994)
G272.2–3.2	diffuse shell	centrally brightened	Egger et al. (1996)
G296.7–0.9	bilateral	part of shell	Robbins et al. (2012) and this work
G299.2–2.9	faint source	centrally brightened	Busser et al. (1996)
G308.4–1.4	two bright arcs	diffuse, brighter to west	this work
G320.6–1.6	faint shell	part of shell	Milne et al. (1993)
G332.5–5.6	bipolar shell, central emission	centrally brightened	Stupar et al. (2007)
G347.3–0.5	faint emission	non-thermal	Pfeffermann and Aschenbach (1996)
G353.6–0.7	shell	shell	Tian et al. (2010)

## 8.2.5 Concluding remarks on supernova remnants

Bußer (1998) predicted the number of X-ray SNRs detectable in the RASS to be  $215 \pm 5$  SNRs. To obtain this number he simulated the theoretical distribution of SNe in our Galaxy and the RASS count rate of their remnants. He included only simulated remnants with a signal-to-noise ratio of  $\geq 2\sigma$  and a diameter  $\geq 15$  arcmin as well as smaller SNRs with more than 1000 counts. Correlating the list of known SNRs with the RASS images a counterpart for about 80 SNRs was detected in the X-ray regime, which fulfill the criteria aforementioned. Therefore,  $135 \pm 5$  unidentified SNRs are expected to be detectable in the RASS, which is in agreement with the number of 123 RASS SNR candidates found in my work.

Assuming that the remaining 123 SNR candidates mentioned above are indeed SNRs and adding them to the  $\approx 280$  SNRs known (including the two remnants identified in this work - G38.7–1.4 and G308.4–1.4) the discrepancy between the expected and measured SN rate in our Galaxy can be explained to some extent. Nevertheless, searching for SNRs in the RASS survey yielded a large number of additional SNRs and by gradually identifying the 123 candidates, the discrepancy between the expected and measured number of supernova remnants in our Galaxy can be further reduced.

All 17 SNRs listed in Table 8.1, including the three SNRs studied in this work, were first detected in the RASS survey and their identification was mostly based on the X-ray emission. In some cases the candidates were subsequently observed and identified in the radio band with deep pointed observations. As can be seen, all X-ray selected SNRs are faint and/or irregularly shaped in the radio regime. This likely hampers the identification of SNRs in the radio band and supports the view that it is important to search for SNRs in various wavelengths and not to rely on radio surveys alone. Furthermore, with the exception of a few sources, most RASS SNR

candidates show only very faint or no radio emission. If they are indeed SNRs the lack of radio emission can be explained by, e.g., a weak magnetic field (see the introduction of Chapter 4 for more reasons for the non-detection of radio emission). Therefore, the lack of an identification of the RASS selected SNR candidates in the radio band is no criterion to exclude these X-ray objects from being SNRs.

### 8.3 Neutron stars and pulsars

In Chapter 7 a systematic search for the X-ray counterparts of radio pulsars in the archives of the Chandra and XMM-Newton X-ray observatories is presented. With the exception of J1341–6220, which will be discussed in the next paragraph, all 18 detected X-ray counterparts of radio pulsars fulfill the following criteria (see also Section 7.2): The discrepancy between the radio and X-ray source position is less than  $3\sigma$ , the possibility that an X-ray source is by-chance at the pulsar’s position is below  $10^{-3}$  and the X-ray-to-visual flux ratio is greater than  $-1.2$ . Furthermore, the non-thermal X-ray efficiency of all sources is in agreement with the predictions made by Becker (2009). Only a small scatter is noticeable, which is probably due to the normal scattering (e.g. Becker et al., 2010, figure 18) and to the uncertainties introduced by assuming the spectral parameters for the pulsars with less than 70 detected counts. The uncertainties that can cause the scatter in equation 7.9 will be discussed in the next section.

Further, four of the 18 sources were mentioned in the literature. J1341–6220 is listed as radio pulsar with X-ray counterpart in Kaplan et al. (2004) and Smith et al. (2008), but no detailed analysis of the X-ray properties of PSR J1341–6220 was presented by the authors. For this source the probability of a by-chance detection is not negligible. Nevertheless, all other criteria are fulfilled by this pulsar. For the radio pulsars PSR J1112–6103 and PSR J2222–0137 a detection is claimed by Townsley et al. (2011) and Boyles et al. (2011), respectively. However, they did not investigate the X-ray data in detail. For the detection of an X-ray counterpart of the radio pulsar PSR J1105–6107 two contradicting references can be found. Gotthelf and Kaspi (1998) used data taken with the ASCA observatory and claimed a detection. On the other hand Kargaltsev et al. (2012) listed this source as non-detected in a Chandra observation. The analysis presented in this work is based on two Chandra ACIS-S observations and clearly shows an X-ray source close to the radio timing position. Hence, it confirms the detection claimed by Gotthelf and Kaspi (1998). Nevertheless, the parameters deduced by Gotthelf and Kaspi (1998) cannot be confirmed. Their spectral parameters for PSR J1105–6107 lead to a count rate for the Chandra ACIS-S detector of 0.04 cts/s, two orders of magnitude higher than the rate measured in the merged Chandra ACIS-S image. For all pulsars that were observed with a temporal resolution of at least five times the pulsars period (PSR J0922+0638, PSR J1301–6310, and PSR J1825–0935) the non-detection of a pulsed signal can be explained by the low count number.

Therefore, the detection of the 18 X-ray counterparts of radio pulsars listed in Table 7.1 is claimed. To date, more than 200 pulsars are detected in the X-ray band (see Table B.1). This, in addition to the calculated upper limits, enables a more detailed study of the non-thermal X-ray emission of pulsars, which is presented in the next section.

## Non-thermal X-ray emission

First, the reliability of the measured upper limits on the non-thermal X-ray emission was verified, by comparing the values derived in Section 7.2.4 with upper limits found in the literature. The limits on  $\mu_X$  of Kargaltsev et al. (2012) were confirmed, even though a different energy band and a larger confidential level of 95.4 % was used in this work. Only in the case of PSR J1837–0604 our derived upper limit on the flux is three times higher. However, this can be explained by the fact that in Kargaltsev et al. (2012) the counts were not corrected for the encircled energy fraction.

Thereafter, the non-thermal X-ray luminosity for 18 and the upper limit on it for 228 pulsars was used to further study the scatter in the relation of the non-thermal X-ray luminosity to the spin-down power. Eleven sources were found with upper limits on  $\mu_{0.1-2 \text{ keV}}$  below  $10^{-4}$  and one detected source with  $\mu_{0.1-2 \text{ keV}} = (1.2 \pm 0.4) \times 10^{-5}$  (PSR J1105–6107), also lower than  $10^{-4}$ . The investigation confirms the trend for finding smaller X-ray efficiencies with increasing sample size and higher sensitivity of X-ray observatories. The X-ray efficiency can be as high as  $1.9 \times 10^{-3}$ , e.g., for the Crab pulsar (Becker, 2009), but also be below  $3.1 \times 10^{-6}$ .

It should be noted that young pulsars with  $\dot{E} > \dot{E}_c \approx 4 \times 10^{36}$  erg/s could manifest a distinct pulsar wind nebula (PWN, Gotthelf, 2004). If such a PWN exists and/or thermal emission from the pulsar's surface is hot enough to contribute to the X-ray emission, the non-thermal X-ray efficiency of several pulsars is much lower than the determined upper limit.

Theory predicts a distinct relation between the X-ray efficiency and the spin-down power. The detected large scatter contradicts such a tight relation and favors the interpretation of Becker (2009) that it represents an average approximation to the X-ray efficiency rather than a fixed correlation. A reason for the large dispersion could be unfavorable viewing angles (Possenti et al., 2002, and references therein). Because the orientation of the pulsar's magnetic axes with respect to the observer's line of sight might not have been optimal and no beaming correction can be applied to the observed luminosity, the X-ray efficiency of these pulsars appears to be smaller than that of pulsars with optimal geometry. However, Kargaltsev and Pavlov (2010) reviewed all known PWNe and investigated their X-ray efficiency. They found a smaller but still large scatter in the measured luminosities, despite of the fact that PWN emission is thought to be un-beamed (Gaensler and Slane, 2006). Therefore, the beaming angle can contribute only a small scatter in  $\mu_X$  for most pulsars, although in some extreme cases the effect could be 1 to 2 orders of magnitude, e.g. the Vela pulsar (Possenti et al., 2002).

Additionally, wrongly determined distances can contribute to another uncertainty in the derived X-ray luminosities. Although the errors in the distance measurement were included in the calculations, most distances used in this work are based on the dispersion measure and large fluctuations in  $DM$  are not included in the model calculations. This could introduce a scatter of roughly one order of magnitude in the derived X-ray luminosity for a few sources.

Another reason for the large scatter could be a wrongly determined spin-down luminosity. In the last years several intermittent pulsars have been discovered (e.g., Kramer et al., 2006; Camilo et al., 2012; Lorimer et al., 2012), which seemed like ordinary radio pulsars, but switch their radio emission off quasi-periodically with different spin-down rates at time scales from months to years. In the so called on-state the spin-down rate increases by a factor of 2 to 3

compared to the off-state. Because the spin-down luminosity is proportional to the spin-down rate and for some radio pulsars only a few observations exist it is possible that some sources have a lower  $\dot{E}$  than calculated with the period and period derivative taken from literature.

Taking all these sources of uncertainty into account it is still unclear where the large scatter in  $\mu_X$  of three orders of magnitude is coming from. However, in the future high energy emission models have to reproduce this large scatter in the measured relation.

### Thermal X-ray emission

As for the non-thermal X-ray emission, the reliability of the measured upper limits were tested. Temperature upper limits for eight pulsars can be found in the literature (Gonzalez et al., 2004; Kaplan et al., 2009; Olausen et al., 2013; Keane et al., 2013), including the coolest pulsar in the sample presented in this work, PSR J2144–3933. For six pulsars similar values for the temperature upper limit were found, with a minor deviation of  $\pm 10\%$ . This small discrepancy may be due to the fact that Olausen et al. (2013) did not include the distance error in their calculations. Additionally, it is difficult to compare the results in detail because all aforementioned authors used slightly different methods to calculate the upper limits and no detailed information is given in Olausen et al. (2013) about the effective exposure time and extracted region for PSRs J1814–1744 and J1847–0130. However, the method used in this work makes use of all archival observations of one pulsar and, thus, derives in general deeper upper limits. In case of PSR B1845–19 (Olausen et al., 2013) and PSR J0157+6212 (Gonzalez et al., 2004) a much lower temperature upper limit was found in this work. For PSR B1845–19 it is because two archived XMM-Newton observations were used instead of one (Olausen et al., 2013). In the case of PSR J0157+6212 the difference is partly due to using different values for  $N_H$ , but a large, and yet unexplained, difference remains between the measured upper limit here and the work by Gonzalez et al. (2004).

In total, 230  $3\sigma$  upper limits on the blackbody temperature were derived, ranging from 18.8 eV (PSR J2144–3933) to 218.6 eV (PSR J1822–1617). All measured temperature upper limits are in agreement with current cooling models, which assume only nuclear matter in the core of a neutron star and Cooper-pair breaking and formation as the main source of neutrino emission. These models include the uncertainties regarding the allowed amounts of light elements in the envelope of the star and the different possible neutron  $^3P_2$  gap models. A comparison of the data presented in this work with other cooling curves (e.g. Tsuruta, 1998; Yakovlev and Pethick, 2004; Tsuruta, 2009) confirms the conclusion that for all measured data points in this work standard cooling with Cooper-pair breaking and formation is sufficient to explain the temperature upper limits.

## 8.4 Future prospects

Chapter 3 showed that it is possible to measure the proper motion of a neutron star in the X-ray regime with high precision. For this analysis only two reference sources with known proper motion are needed and even observations taken with different instruments can be used. At the

moment, I am searching the archive of the Chandra X-ray observatory for observations of pulsars which are appropriate for a proper motion measurement. For that a pulsar should have been observed at least two times and the observations should lie more than one year apart. These data will then be analyzed as described in Chapter 3.3.1 to calculate the proper motion of these sources. For pulsars with known proper motion in other wavelengths the analysis will indicate how accurate it can be measured in the X-ray regime. In case of the remaining pulsars the proper motion or an upper limit on it will be measured for the first time. This is important in particular for sources which are radio quiet or whose position cannot be measured with high accuracy in the radio regime because of timing noise. Hence, with the exception of a few nearby pulsars, which can be seen in the infrared, using Chandra X-ray observations is the only way to measure this important parameter.

Currently, I am analyzing an archival XMM-Newton observation of the SNR G38.7–1.4, which will help to shed light on the age and distance to this source. Furthermore, another XMM-Newton observation of SNR G308.4–1.4 will become available soon and it may help to reveal the origin of the central compact object, which remained an open question in Chapter 5.

In the future, the most promising SNR candidates will be followed-up in the radio, optical ( $H\alpha$ ) and X-ray band by using the candidate list (Table A.1). This will help to pinpoint the origin of the detected X-ray emission.

Additionally, tests of different thermonuclear and core-collapse SN models will be obtained in the future by, for example, measuring the electron neutrinos, muon neutrinos and tau neutrinos coming from a close-by SN and comparing it with model predictions, as well as the gravitational wave signal of an SN, which can be even extragalactic. The large distance range for gravitational waves is due to the fact that here the amplitude is measured, which decreases with  $\sim 1/r$ , whereas for neutrinos the intensity of the emission is measured, which decreases with  $\sim 1/r^2$ . Furthermore, gravitational waves are not subject to absorption and a signal could be observed even through highly absorbing objects, like dark clouds. The measured gravitational wave signal depends strongly on the progenitor system and the explosion mechanism. Thus, a detected SN signal will immediately rule out most explosion models. Furthermore, observing gravitational waves from binaries with two neutron stars or a neutron star with a black hole would yield the masses of the two gravitating bodies as well as the radius of the NS (Lattimer and Prakash, 2007). In addition, the gravitational wave pattern depends on the interior of the NS (Lattimer and Prakash, 2007) and thus, after the first gravitational wave detections of NS binaries it will be possible to find the true nature of matter at supernuclear densities. Nevertheless, until now only indirect measurements of gravitational waves have been reported. These were obtained by measuring the orbital decay of two neutron stars in a binary system (Weisberg et al., 2010). In the next years the advanced LIGO<sup>1</sup> should start its operation and it is assumed that it can observe 40 NSs per year which are spiraling in (Harry and LIGO Scientific Collaboration, 2010).

Furthermore, it would be very important to study the pulsars, which have a very low temperature or non-thermal flux upper limit and are young and energetic (see Table 7.4 and Table 7.5), because these objects could help to put better constraints on the cooling of neutron stars or the

<sup>1</sup>Laser Interferometer Gravitational-wave Observatory

models that explain the non-thermal emission of pulsars. If one detects, for example, a neutron star with a surface temperature lower than the expectations from the minimal cooling paradigm, one has to include enhanced cooling mechanisms in the modeling of the interior of a neutron star.

### 8.4.1 Future X-ray missions

By the end of 2015 eROSITA, the successor of the ROSAT mission, will start to image the entire X-ray sky with a surpassing sensitivity and a higher spatial and spectral resolution than ROSAT. It will be composed of seven identical telescopes which all have a CCD in its focus. The eROSITA telescopes on board of the Russian Spektrum-Roentgen-Gamma mission will be approximately 20 times more sensitive in the soft X-ray band than the RASS. Furthermore, in the hard X-ray regime (2-10 keV) it will survey the sky for the first time with an imaging telescope (Merloni et al., 2012). It will have a resolution of 25 arcsec to 30 arcsec in survey mode, the average exposure in the galactic plane will be about 3 ksec (Predehl et al., 2010).

Therefore, it will be possible to study the SNR candidates presented in Chapter 4 in much more detail: The higher resolution will allow a spatial investigation of the sources. This will reveal whether the RASS emission of the candidates is coming from one extended source or from two or more point sources. In addition, the deeper exposure times and the higher spectral resolution will provide data for a spectral analysis of the candidates to rule out an extragalactic origin. Additionally, if the candidates show emission from a thermal plasma it will be possible to calculate fundamental parameters for the remnant, e.g., age and distance. In particular, the remnant candidates with a large extent can be studied in detail with eROSITA, because the current X-ray observatories have a field of view of only  $\sim 30'$  and need several pointings to cover the larger remnants. The prospects of X-ray all-sky surveys for large SNRs was impressively shown with the HEAO-1 survey and RASS, where a large, close-by and old SNR with a diameter of approximately 25 degrees was detected, the Monogem Ring (Plucinsky et al., 1996). With current telescopes, e.g., XMM-Newton, more than 1000 pointings would be necessary to cover the remnant and in a single observation the remnant would only be recorded as high X-ray background.

It should be mentioned that some of the candidates may be missed. The ROSAT PSPC detector used for the RASS had the major advantage of very low detector noise and a spectral response down to 0.1 keV provided perfect conditions to search for SNRs (Voges et al., 1999). This is because extended sources can be strongly affected by the background and SNRs emit mostly in the soft X-ray band. On the other hand, the eROSITA detectors are CCDs, which are only sensitive to incoming photons in the energy range 0.3-10 keV, and have a higher background, comparable with the EPIC cameras on-board of XMM-Newton (Merloni et al., 2012). Thus, faint extended sources will be harder to detect, as in the RASS. This was already shown for the SNR candidate G309.8–2.5 in Chapter 4, where a bright source is detected in RASS, but a deep observation with XMM-Newton of this region did not show any extended source emission.

For all 274 known SNRs which emit X-rays, a detailed analysis will be possible and for the remaining sources X-ray counterparts can be searched for. In particular, the remnants G38.7–1.4, G296.7–0.9 and G308.4–1.4, which were explored in this work can be studied in more detail. In the case of G308.4–1.4 a deep spectro-imaging analysis was already done, but the origin of the

central compact objects is still not solved. It could be the compact remnant belonging to the SNR.

The identification of previously unknown SNR with eROSITA will allow a search for neutron stars residing within the diffuse remnants. This could be a central neutron star without a counterpart in other wavelength regimes. Only seven members of this class of neutron stars are known to date and finding more of these sources may help to understand how this manifestation of neutron stars is related to other classes and which parameters decided that a neutron star can be observed as central compact object.

Further, the eROSITA survey will add data to the analysis done in Chapter 7 with a larger and even less biased sample. In the eROSITA survey a detailed search for X-ray counterparts of all known pulsars without detected X-ray counterpart can be conducted. The pulsars in the eROSITA sample will have equal exposures and will cover the whole galactic plane. However, the exposure will be only 3 ksec. The average exposure in the sample studied with XMM-Newton in Chapter 7 was ten times higher. In the case of a non-detection a upper limit on the thermal and non-thermal flux can be calculated, which will be in general lower than the already derived limits. Nevertheless, it will further constrain the cooling of neutron stars and the dependence of the non-thermal X-ray luminosity and the spin-down energy loss, because of the ten times larger sample of observed neutron stars.

Because microcalorimeters are now operating in space (e.g., NuSTAR; Harrison et al., 2013) it will be possible to study the emission of X-ray sources in much more detail. These detectors will have a typical spectral resolution of 2.5 eV at 5 keV, 60 times better than current observatories (Nandra et al., 2013). However, the energy range of the microcalorimeter operating on the NuSTAR satellite, which was launched in June 2012, is not suitable for studying SNRs. Therefore, one has to wait for future missions, like Athena+ (Nandra et al., 2013), the next large X-ray mission that is proposed to be launched after 2028. It will probably have an effective area of 2 m<sup>2</sup> at 1 keV and an angular resolution on-axis of 5 arcsec (Nandra et al., 2013). Two detectors are planned, a CCD camera and an X-ray microcalorimeter. The latter will have a spectral resolution of 2.5 eV at 6 keV and hence, will allow investigations of SNRs by different spectral line diagnostics, which are hardly possible to date. In addition, the large collection power will make it possible to study neutron stars in much more detail. For example, it might enable a investigation of the cooling of a very young NS in the SN 1987A, which has to be found yet (Manchester, 2007).

Not only in the X-ray band new larger telescopes are planned. For example in the radio band the square kilometer array will start to observe the radio sky with 10 to 100 times higher sensitivity using single telescopes build all around the world. These telescopes will have a total collecting power of nearly one million square meters (Smits et al., 2009) and will lead to the detection of many new pulsars and supernova remnants. Additionally, the sample of neutron stars with accurate mass and radius measurement will increase even further. Finally, it could help to identify the 123 SNR candidates presented in Chapter 4.

### 8.4.2 Occultations

The X-ray emission of neutron stars can also be used to investigate small objects in the solar system, namely Kuiper Belt objects, main-belt asteroids and trans-Neptunian objects. These objects can be investigated through stellar occultation of a bright background source and most detections of such objects have been made in the optical. However, small objects with a diameter of less than a few kilometers are only detectable because of the broadening of their shadow by diffraction (see Roques and Moncuquet, 2000, for more details). The characteristic scale  $d$  of this effect, the so-called Fresnel diffraction effect, is  $d \approx \sqrt{\lambda D/2} = \sqrt{92 \cdot D[\text{AU}]/E[\text{keV}]}$  m, where  $\lambda$  is the wavelength,  $E$  the energy of the photons and  $D$  the distance to the occulting objects. Therefore, the occultation of an object with a diameter of  $\sim 100$  m at a distance of 40 AU has the largest shadow broadening at an energy of  $\sim$  keV, hence the X-ray regime. Only a few of these small objects have been detected so far (Chang et al., 2006) with low significance and therefore, the density of such objects is poorly known. However, this information is important for understanding the formation of planets (Roques and Moncuquet, 2000).

In X-rays accreting neutron stars like Scorpius X-1, the brightest X-ray source outside the solar system can be used to search for occultations. This was already done by Chang et al. (2006) using Scorpius X-1 observations of the Rossi X-ray Timing Explorer (RXTE). However, they claimed some detections, which could not be verified (Chang et al., 2013). In the future large X-ray telescopes will be launched and finding occultations of small solar system bodies will help to increase our knowledge of these objects regarding their occurrence and will finally tell us more about the formation of the solar system. To investigate if this is possible, the effect of occultations was studied assuming a telescope with an effective area on the order of square meters, like it is expected for Athena+ (Nandra et al., 2013) and using the theory of Roques et al. (1987) and Roques and Moncuquet (2000). It could be shown that an occultation can be detected easily (see Figure 8.1), if the temporal resolution of the detector is in the order of milliseconds and the behavior of it at this high count rates can be understood in detail. The latter was the main problem with the RXTE detectors, because random fluctuations in the measured source flux by high-energy photons or protons were wrongly identified as occultations (Chang et al., 2013). Furthermore, with this large collecting power, not only Scorpius X-1 can be used as a bright background source, but also several other bright X-ray sources may be used (Chang et al., 2013).

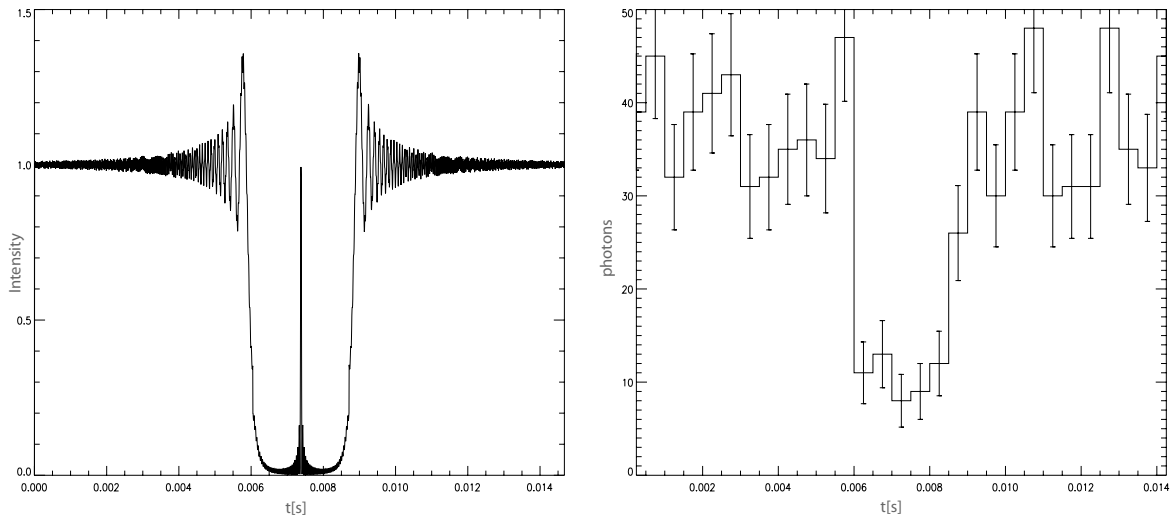


**Figure 8.1:** *Left:* Occultation profile with diffraction for a point source as background source and a spherical object as foreground source with a diameter of 80 m at a distance of 40 AU. *Right:* Simulated occultation profile as seen by a X-ray telescope with an effective area on the order of square meters. Here the X-ray flux of the Low Mass X-ray Binary GX 17+2 was used for simulating the background source and a time resolution of 0.5 ms was assumed.

# Appendix A

## Supernova remnant candidates in the ROSAT All-Sky Survey

### A.1 Source catalogue of high significant sources

Table A.1: Source catalogue of the SNR candidates.

No.	Source	R.A. (J2000)	DEC (J2000)	extend arcmin	count rate cts/s	S/N $\sigma_G$	HR1	HR2	type/ $P_{\text{ext}}^{(\alpha)}$	pointing	IR	Radio	optical( $H_\alpha$ )
		hh:mm:ss	dd:mm:ss						flag/-	flag	flag	flag	flag
1	G11.0+6.9	17:44:38	-16:00:27	290x270	19.67 ± 0.72	41	+1.00	-0.20	-	3	3	3	1
2	G12.0+8.4	17:41:22	-14:22:41	250x250	18.00 ± 0.62 $^\beta$	44	+1.00	-0.15	-	3	3	3	1
3	G13.0-14.9	19:11:21	-24:15:27	15x13	0.19 ± 0.05	6	+0.84	-0.00	s/5.8	3	3	3	2
4	G16.5-8.6	18:52:49	-18:26:30	180x160	6.67 ± 0.45	23	+0.55	-0.51	-	3	3	3	1
5	G16.7+15.9	17:25:01	-06:33:25	20x10	0.16 ± 0.03	8	+0.41	-0.02	-	3	3	4	1
6	G22.4+9.5	17:58:14	-04:53:46	40x35	0.31 ± 0.06 $^\beta$	8	+0.71	-0.04	-	3	3	3	1
7	G24.0+6.1	18:13:15	-05:05:08	120x120	2.34 ± 0.18 $^\beta$	22	+0.63	-0.09	-	3	3	3	1
8	G24.1-0.3	18:36:24	-08:02:36	35x20	0.28 ± 0.05	8	+0.79	+0.65	-	2	3	2	1
9	G25.2-1.9	18:44:05	-07:44:22	80x65	1.47 ± 0.17 $^\beta$	13	+1.00	-0.14	-	3	3	3	1
10	G26.7-3.6	18:53:01	-07:09:45	180x180	5.70 ± 0.33	24	+0.98	-0.28	-	3	3	3	1
11	G35.9+6.0	18:35:21	+05:24:23	14x10	0.11 ± 0.03	6	+0.45	+0.13	-	1	3	3	1
12	G38.7-1.4	19:06:59	+04:30:15	13x10	0.09 ± 0.03 $^\beta$	5	+0.99	+0.32	s/6.9	1	2	1	1(1)
13	G43.8+2.5	19:02:30	+10:46:13	110x50	0.54 ± 0.09 $^\beta$	11	+0.95	+0.41	-	3	3	2	1
14	G55.6+2.0	19:27:10	+21:02:02	13x12	0.07 ± 0.03 $^\beta$	4	+1.00	+0.85	s/10.3	3	1	1	2
15	G66.7-9.8	20:35:51	+24:13:33	13x11	0.08 ± 0.02 $^\beta$	5	+0.89	+0.05	s/3.9	2	3	4	1
16	G71.2-2.9	20:21:45	+31:49:14	18x10	0.10 ± 0.02	7	+0.07	+0.16	-	3	2	4	1
17	G72.1+9.2	19:33:35	+38:54:53	18x9	0.09 ± 0.03	5	+0.72	+0.14	-	3	3	3	2
18	G75.8+8.0	19:47:52	+41:30:52	13x9	0.11 ± 0.02 $^\beta$	7	+0.70	+0.03	s/5.5	3	2	3	1
19	G75.8+15.6	19:10:51	+44:55:59	16x9	0.11 ± 0.03 $^\beta$	7	+0.83	-0.06	s/6.0	3	3	4	1
20	G77.3-4.5	20:45:33	+35:49:06	170x105	2.06 ± 0.22	14	+0.84	-0.19	-	3	3	3	1
21	G77.6+3.4	20:13:41	+40:38:42	90x90	5.82 ± 0.17	54	+0.56	+0.02	-	1	3	2	1
22	G78.0+5.3	20:06:45	+42:00:25	12x8	0.07 ± 0.02 $^\beta$	6	+0.86	-0.05	s/3.9	3	2	3	1
23	G80.7+2.8	20:25:55	+42:54:08	40x35	0.51 ± 0.07	11	+0.92	-0.08	-	3	3	2	1
24	G81.1-1.1	20:44:10	+40:49:29	40x40	0.48 ± 0.06 $^\beta$	11	+0.89	+0.18	-	3	2	2	3
25	G83.2+6.9	20:14:48	+47:11:23	6x6	0.01 ± 0.01 $^\beta$	2	+0.33	-0.43	-	3	2	1	1
26	G83.8+10.3	19:59:17	+49:29:14	25x20	0.10 ± 0.02 $^\beta$	8	+0.37	+0.16	-	3	3	3	2
27	G85.7+10.6	20:03:16	+51:16:34	16x11	0.11 ± 0.02	9	+0.64	+0.38	s/18.5	3	3	4	2
28	G98.6-5.7	22:14:11	+49:36:58	35x35	0.20 ± 0.06 $^\beta$	5	+0.79	+0.06	-	3	3	3	1
29	G100.2-2.7	22:11:40	+53:00:39	24x14	0.14 ± 0.03	8	+0.71	+0.23	-	3	2	3	2
30	G104.7+9.9	21:38:00	+65:41:54	45x30	0.34 ± 0.05 $^\beta$	10	+0.87	-0.44	-	3	3	3	1
31	G105.7-8.1	23:00:06	+51:01:26	160x160	4.38 ± 0.30 $^\beta$	22	-0.18	-0.36	-	3	2	3	1
32	G108.3+9.9	22:05:52	+67:53:59	350x210	4.54 ± 0.23 $^\beta$	29	+1.00	-0.30	-	3	3	3	1
33	G124.5-5.4	01:02:54	+57:28:04	12x8	0.14 ± 0.03	7	-0.07	-0.22	s/4.7	3	3	4	1
34	G125.3+10.0	01:23:32	+72:44:22	14x13	0.10 ± 0.02 $^\beta$	8	+0.91	+0.71	s/10.6	3	3	3	1
35	G129.5-2.8	01:43:08	+59:26:08	30x18	0.09 ± 0.03 $^\beta$	6	+1.00	+0.14	-	3	3	3	1
36	G135.2-1.8	02:28:15	+58:47:11	23x16	0.06 ± 0.02 $^\beta$	6	+0.97	+0.36	-	3	3	3	2
37	G141.5+0.5	03:19:02	+57:56:29	16x10	0.08 ± 0.02	5	+0.45	+1.00	s/5.4	3	3	4	1
38	G141.6-0.6	03:15:24	+56:55:37	20x9	0.09 ± 0.02	6	-0.41	+0.07	-	3	3	3	2

Continued on next page

Table A.1 – continued from previous page

No.	Source	R.A. (J2000)	DEC (J2000)	extend	count rate	$S/N$	HR1	HR2	type/ $P_{\text{ext}}^{(\alpha)}$	pointing	IR	Radio	optical( $H_{\alpha}$ )
39	G176.0-11.8	04:51:48	+25:31:13	15x10	$0.10 \pm 0.03^{\beta}$	6	+1.00	+0.36	-	1	3	2	1
40	G176.0+2.7	05:46:51	+33:43:59	16x11	$0.08 \pm 0.02^{\beta}$	8	+1.00	+0.21	-	3	2	3	1
41	G180.0+6.5	06:11:46	+32:10:52	16x8	$0.10 \pm 0.03^{\beta}$	6	+0.85	-0.08	s/8.7	3	3	3	2
42	G188.1-3.3	05:51:38	+20:16:39	11x6	$0.07 \pm 0.02$	6	+0.54	+0.13	-	3	3	3	1
43	G197.4+0.1	06:22:51	+13:49:48	50x40	$0.24 \pm 0.05^{\beta}$	7	+1.00	+0.17	-	3	3	3	1
44	G222.0+14.4	07:59:17	-01:19:02	13x11	$0.18 \pm 0.04^{\beta}$	7	+0.42	+0.07	s/10.4	3	3	3	1
45	G223.7+0.0	07:11:12	-09:32:28	15x12	$0.10 \pm 0.03^{\beta}$	5	+0.23	+0.69	s/3.9	3	3	4	1
46	G253.0+15.5	09:12:14	-25:26:10	25x21	$0.18 \pm 0.04$	7	+0.46	-0.15	-	3	3	3	2
47	G253.0+13.7	09:06:14	-26:36:07	12x12	$0.11 \pm 0.02^{\beta}$	7	+0.17	+0.13	s/7.8	3	3	4	1
48	G253.8-1.6	08:11:03	-36:27:46	240x200	$5.00 \pm 0.44$	19	-0.53	-0.51	-	3	2	2	1
49	G254.4+10.3	08:58:21	-29:53:10	15x11	$0.11 \pm 0.03^{\beta}$	6	+0.27	+0.70	s/6.3	3	2	4	1
50	G259.1+11.7	09:17:43	-32:24:36	13x10	$0.09 \pm 0.02^{\beta}$	6	+0.45	+0.26	s/2.5	3	3	4	1
51	G260.3-9.6	07:52:18	-46:11:37	15x10	$0.11 \pm 0.03$	6	+0.50	+0.20	-	3	3	2	1
52	G265.8-7.1	08:22:21	-49:32:07	17x13	$0.18 \pm 0.03$	11	+0.92	-0.17	s/22.2	1	2	3	1
53	G272.2-8.9	08:36:45	-55:46:06	16x12	$0.11 \pm 0.03$	6	+0.95	+0.19	-	3	3	3	1
54	G276.2-7.7	09:01:58	-58:05:56	18x14	$0.18 \pm 0.04$	6	+0.54	-0.14	s/7.5	3	3	3	1
55	G285.7+4.0	10:48:39	-54:41:42	11x9	$0.15 \pm 0.04^{\beta}$	5	+0.22	+0.07	s/2.9	3	3	3	2
56	G286.6-15.2	09:10:49	-70:39:31	18x12	$0.11 \pm 0.03$	6	+0.55	-0.13	-	3	3	4	1
57	G290.4-1.9	11:01:06	-62:06:05	20x10	$0.16 \pm 0.05$	5	+0.67	+0.26	-	3	3	3	2(1)
58	G294.7-0.3	11:40:34	-62:01:34	11x9	$0.13 \pm 0.03$	8	+0.23	-0.22	s/4.0	3	2	3	1
59	G295.4-3.0	11:39:53	-64:46:16	13x7	$0.10 \pm 0.03^{\beta}$	6	+0.51	-0.15	-	3	2	3	2(1)
60	G309.4-3.2	13:53:52	-65:16:08	220x180	$6.29 \pm 0.39^{\beta}$	25	+0.86	+0.10	-	3	3	3	1
61	G309.8-2.5	13:56:13	-64:31:37	19x12	$0.12 \pm 0.03^{\beta}$	6	+0.83	+0.75	-	1	2	1	1
62	G312.1+4.2	14:00:04	-57:26:48	240x140	$9.13 \pm 0.46^{\beta}$	30	+0.49	-0.26	-	3	3	3	1
63	G312.4+4.8	14:01:07	-56:49:53	17x12	$0.10 \pm 0.03^{\beta}$	4	+0.67	+0.52	-	3	1	4	1(1)
64	G314.7-1.2	14:33:30	-61:40:18	25x20	$0.21 \pm 0.05$	6	+0.57	+0.56	-	3	2	3	1
65	G317.4+18.2	14:06:34	-42:35:39	20x20	$0.43 \pm 0.09$	7	+0.30	+0.22	-	3	3	4	1
66	G319.8-2.0	15:13:59	-60:06:18	20x14	$0.12 \pm 0.04$	5	+0.52	-0.05	-	3	2	3	1(1)
67	G321.7-3.5	15:33:18	-60:16:28	27x18	$0.25 \pm 0.06$	6	+0.60	-0.43	-	3	3	1	1
68	G330.4-4.6	16:28:24	-55:27:08	230x110	$13.56 \pm 0.49$	44	-0.40	-0.47	-	3	3	3	1
69	G333.5-2.5	16:31:57	-51:46:01	37x37	$0.42 \pm 0.11^{\beta}$	6	+0.57	-0.40	-	3	3	2	1
70	G333.5+8.1	15:49:05	-43:55:29	180x180	$3.73 \pm 0.43$	12	+0.85	-0.46	-	3	3	2	1
71	G335.3+10.7	15:47:41	-40:53:47	55x50	$0.94 \pm 0.14^{\beta}$	10	+0.41	-0.25	-	3	3	3	1
72	G335.6-1.6	16:36:45	-49:35:50	60x52	$0.91 \pm 0.14$	10	+0.29	+0.01	-	3	3	3	1
73	G343.9+3.9	16:44:35	-39:46:58	290x210	$8.08 \pm 0.42^{\beta}$	29	+1.00	-0.24	-	3	3	2	1

Notes.  $(\alpha)$  morphology of SNR candidate and if spherical (s) than the probability  $P_{\text{ext}}$  is added (see Section 4.2 for details).  $(\beta)$  count rate and image in ROSAT hard band.

## A.2 Source catalogue of low significant sources

Table A.2: Source catalogue of the SNR candidates.

No.	Source	R.A. (J2000)	DEC (J2000)	extend	count rate	$S/N$	HR1	HR2	type/ $P_{\text{ext}}^{(\alpha)}$	pointing	IR	Radio	optical( $H_{\alpha}$ )
		hh:mm:ss	dd:mm:ss	arcmin	cts/s	$\sigma_G$			flag/-	flag	flag	flag	flag
1	G0.4-7.9	18:18:28	-32:27:47	14x10	$0.09 \pm 0.06^{\beta}$	1.7	+1.00	+0.52	s/1.3	2	3	4	2
2	G13.1+6.3	17:51:19	-14:30:47	24x21	$0.12 \pm 0.05^{\beta}$	3.7	+1.00	-0.53	-	3	2	3	1
3	G15.9-3.9	18:34:06	-16:55:40	27x24	$0.16 \pm 0.07^{\beta}$	3.1	+1.00	+0.23	-	3	2	3	1
4	G17.8-12.5	19:10:05	-19:03:06	11x9	$0.07 \pm 0.03^{\beta}$	3.4	+0.98	+0.20	s/3.1	2	2	4	1
5	G23.6-4.2	18:49:23	-10:13:33	13x9	$0.07 \pm 0.03^{\beta}$	3.4	+1.00	-0.06	-	3	3	3	1
6	G26.3-9.8	19:14:42	-10:15:26	15x15	$0.07 \pm 0.04^{\beta}$	2.5	+1.00	+0.51	-	3	3	2	1
7	G34.5-12.0	19:37:07	-04:02:51	12x9	$0.08 \pm 0.03^{\beta}$	4.7	+0.84	+0.56	s/2.4	3	2	4	2
8	G35.6-5.8	19:16:52	-00:15:10	16x9	$0.09 \pm 0.03^{\beta}$	4.2	+0.94	+0.15	-	3	3	4	1
9	G38.5+7.3	18:35:14	+08:13:50	15x15	$0.08 \pm 0.03^{\beta}$	4.0	+1.00	-0.05	-	3	2	3	1
10	G42.0-11.4	19:48:40	+02:42:27	15x15	$0.09 \pm 0.04^{\beta}$	3.1	+0.78	+0.15	-	3	3	3	1
11	G46.8-2.2	19:24:55	+11:17:09	10x10	$0.03 \pm 0.01$	3.7	+1.00	+0.56	s/2.0	3	3	2	1
12	G56.2+8.2	19:04:34	+24:23:46	19x17	$0.06 \pm 0.02^{\beta}$	4.9	+1.00	+0.35	-	3	3	3	1
13	G64.0-0.1	19:53:13	+27:17:03	14x10	$0.05 \pm 0.02^{\beta}$	3.1	+1.00	+1.00	s/3.2	3	2	2	1
14	G66.8-1.3	20:04:34	+29:04:15	18x12	$0.05 \pm 0.02^{\beta}$	3.9	+1.00	+0.06	-	3	3	3	1
15	G80.8+6.7	20:08:08	+45:10:31	11x11	$0.05 \pm 0.02$	3.8	+0.20	-0.24	s/3.4	3	2	3	2
16	G83.9+12.4	19:47:53	+50:35:32	12x9	$0.04 \pm 0.02^{\beta}$	3.8	+0.74	-0.21	s/4.7	3	3	4	2
17	G95.4-3.8	21:51:31	+49:14:38	10x9	$0.05 \pm 0.02$	4.1	+0.26	+0.17	s/1.0	3	3	4	1
18	G106.0+13.2	21:23:26	+68:55:06	13x13	$0.05 \pm 0.02$	4.1	-0.05	+0.23	s/4.9	3	3	4	1
19	G107.9-1.3	22:53:58	+58:03:01	23x16	$0.06 \pm 0.03^{\beta}$	2.4	+1.00	+0.96	s/5.3	3	2	3	2
20	G117.1-0.9	00:02:10	+61:23:12	27x12	$0.07 \pm 0.03$	3.2	+0.02	+0.17	-	3	2	3	2
21	G118.8-11.5	00:25:21	+51:07:25	12x10	$0.03 \pm 0.02$	2.3	+0.92	+0.48	-	3	2	3	1
22	G118.9-15.3	00:28:20	+47:21:06	17x9	$0.06 \pm 0.02^{\beta}$	3.8	+1.00	-0.53	-	3	3	3	1
23	G128.2+2.6	01:41:55	+64:58:39	7x7	$0.02 \pm 0.01$	2.4	+0.13	+0.44	s/2.3	3	3	3	1
24	G138.8-12.5	02:24:46	+47:29:10	10x10	$0.06 \pm 0.02^{\beta}$	4.5	+0.45	-0.02	s/3.4	3	2	3	2

Continued on next page

Table A.2 – continued from previous page

No.	Source	R.A. (J2000)	DEC (J2000)	extend	count rate	$S/N$	HR1	HR2	type/ $P_{\text{ext}}^{(\alpha)}$	pointing	IR	Radio	optical( $H_{\alpha}$ )
25	G141.6+2.0	03:26:05	+59:11:08	14x9	$0.05 \pm 0.02^{\beta}$	3.8	+0.30	+0.07	s/3.5	3	3	3	2
26	G142.7+8.9	04:09:31	+63:54:21	11x11	$0.04 \pm 0.01^{\beta}$	4.1	+0.92	+0.36	s/2.1	3	3	4	1
27	G142.7-8.3	02:56:31	+49:44:36	20x13	$0.05 \pm 0.02^{\beta}$	3.0	+1.00	+0.31	-	3	3	3	1
28	G146.0+12.0	04:49:58	+63:34:43	15x8	$0.07 \pm 0.02^{\beta}$	4.5	+0.19	+0.27	s/1.6	3	3	3	1
29	G149.2+15.1	05:27:38	+62:47:43	16x12	$0.04 \pm 0.02^{\beta}$	3.3	+1.00	+0.20	-	3	3	3	2
30	G162.9+13.9	06:05:57	+50:30:17	16x10	$0.07 \pm 0.03$	3.5	+0.52	+0.27	s/2.8	3	3	2	2
31	G173.1-0.1	05:27:49	+34:42:02	17x12	$0.07 \pm 0.02$	4.1	+0.89	+0.60	-	3	2	2	2
32	G178.3-3.3	05:28:36	+28:38:09	8x8	$0.04 \pm 0.01^{\beta}$	4.2	+0.74	-0.36	s/0.5	3	2	4	1
33	G219.4-14.6	06:10:21	-12:14:43	15x10	$0.05 \pm 0.02$	3.5	+0.59	+0.70	s/1.9	3	3	3	1
34	G221.7+1.5	07:12:50	-07:07:43	18x10	$0.07 \pm 0.03^{\beta}$	3.8	+0.72	+0.30	-	3	3	3	1
35	G253.8-3.0	08:05:09	-37:16:57	24x20	$0.08 \pm 0.02^{\beta}$	4.9	+0.43	-0.17	-	3	3	3	1
36	G254.8-7.1	07:49:50	-40:11:34	19x10	$0.11 \pm 0.04^{\beta}$	4.6	+0.57	-0.56	-	3	3	4	1
37	G255.5+10.8	09:03:31	-30:22:08	9x9	$0.05 \pm 0.02$	3.1	+0.49	+0.50	s/0.8	3	3	3	1
38	G258.3-7.5	07:57:29	-43:27:02	12x8	$0.08 \pm 0.03$	4.5	+0.84	-0.04	-	2	3	3	2
39	G259.4+10.9	09:15:49	-33:12:09	28x28	$0.12 \pm 0.05$	3.5	+0.28	+0.11	-	3	3	2	1
40	G261.6+15.6	09:38:30	-31:23:04	15x11	$0.04 \pm 0.02$	2.8	-0.08	-0.96	-	3	3	3	1
41	G265.2+8.1	09:25:32	-39:13:01	12x8	$0.06 \pm 0.02^{\beta}$	4.3	+0.58	+0.08	s/3.3	3	3	3	1
42	G266.1+9.7	09:34:18	-38:43:20	14x10	$0.05 \pm 0.02$	4.0	+0.90	-0.33	s/1.3	3	3	4	2
43	G266.4+9.7	09:35:53	-38:53:53	12x8	$0.08 \pm 0.03^{\beta}$	4.3	+0.94	+0.35	s/4.6	3	3	4	1
44	G278.0+12.4	10:32:51	-43:41:59	20x11	$0.14 \pm 0.04^{\beta}$	4.5	+0.04	+0.35	-	3	3	3	2
45	G310.8-1.2	14:01:60	-62:58:46	10x8	$0.05 \pm 0.02^{\beta}$	4.8	+1.00	-0.12	s/3.2	3	3	3	2
46	G315.5+0.4	14:34:23	-59:54:42	20x13	$0.11 \pm 0.04$	3.6	+0.18	+0.76	-	3	2	3	2
47	G334.1-8.9	17:08:20	-55:21:03	21x17	$0.15 \pm 0.07^{\beta}$	3.2	+0.28	-0.19	-	3	4	2	1
48	G334.5-9.3	17:12:03	-55:16:20	13x10	$0.07 \pm 0.04$	2.3	+1.00	+0.07	s/2.0	3	3	4	1
49	G335.9-4.4	16:51:31	-51:10:53	19x12	$0.10 \pm 0.05^{\beta}$	2.9	+0.83	+0.13	-	3	3	3	1
50	G355.8-7.1	18:04:54	-36:07:23	15x15	$0.21 \pm 0.08$	3.4	+1.00	+0.12	-	3	2	3	1

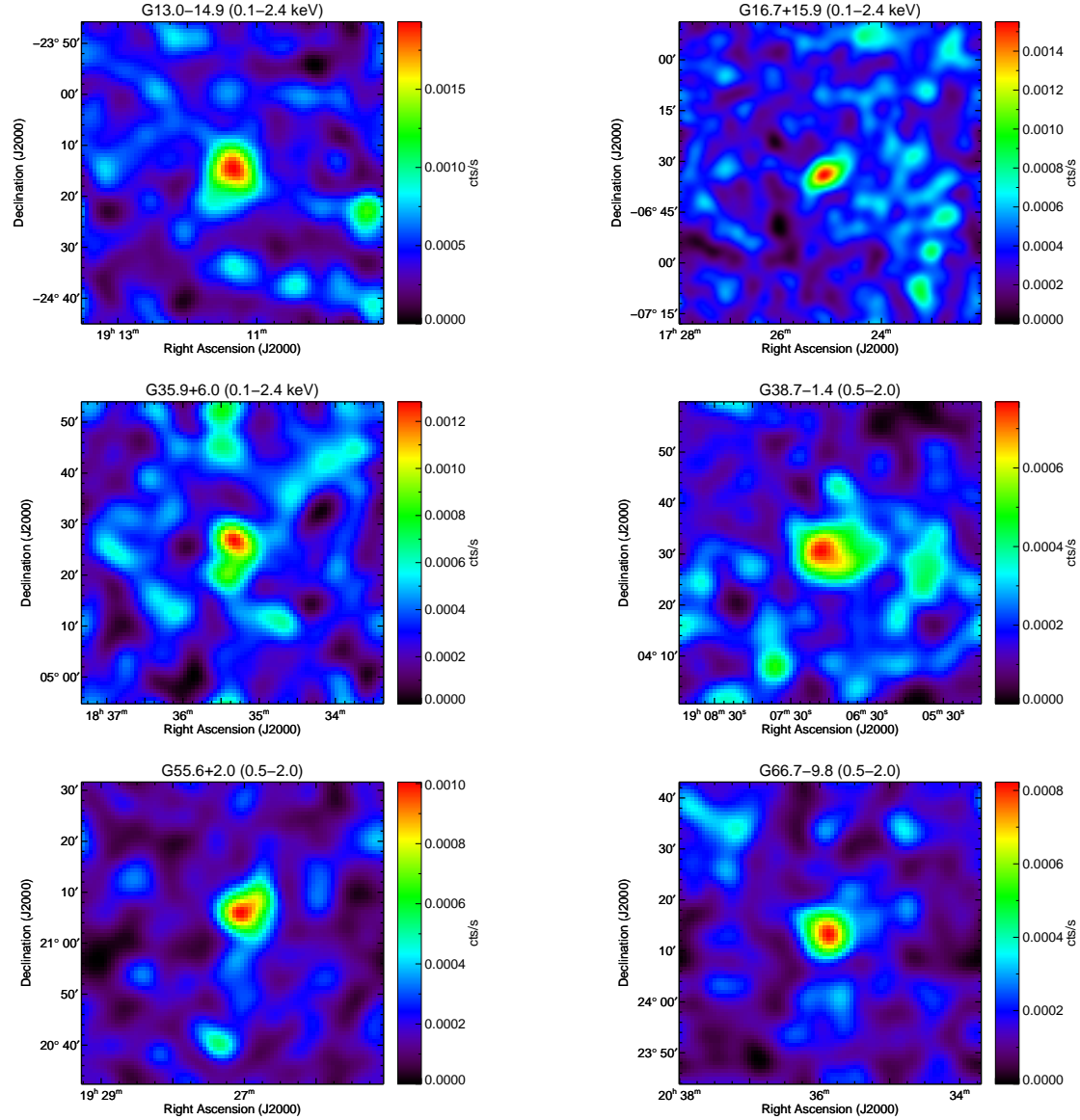
Notes.  $(\alpha)$  morphology of SNR candidate and if spherical (s) than the probability  $P_{\text{ext}}$  is added (see Section 4.2 for details).  $(\beta)$  count rate and image in ROSAT hard band.

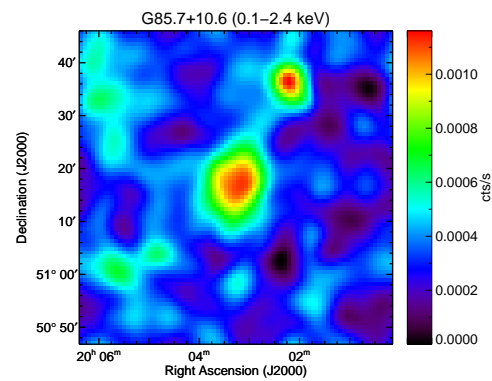
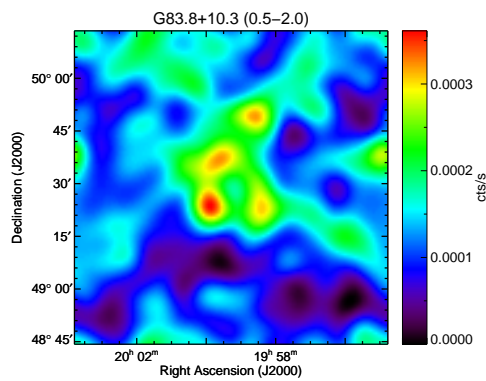
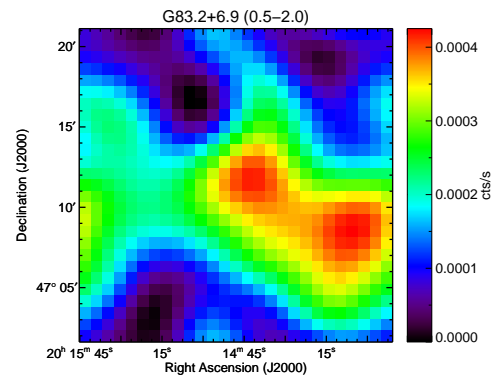
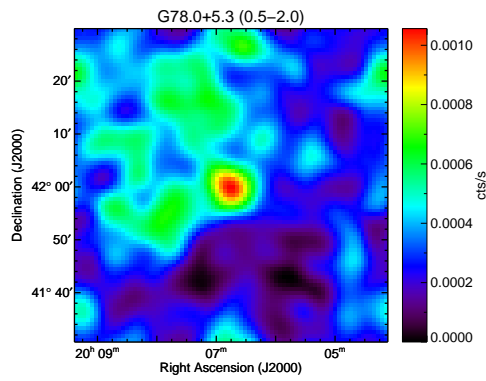
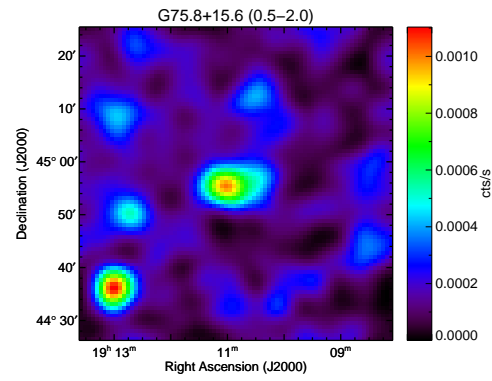
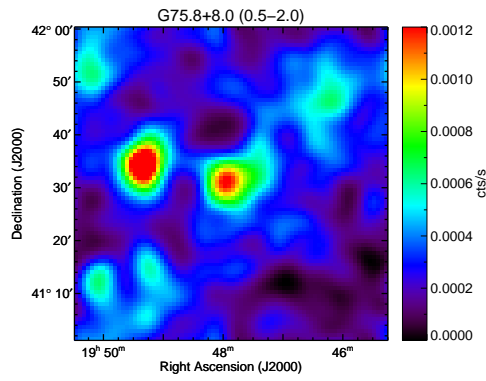
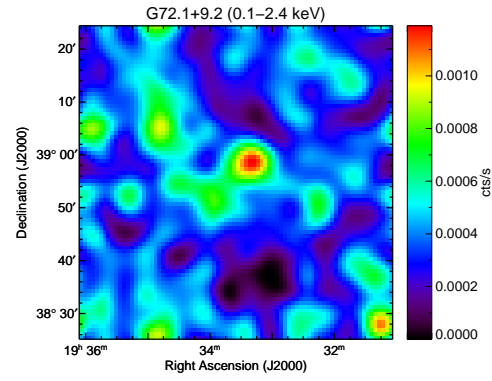
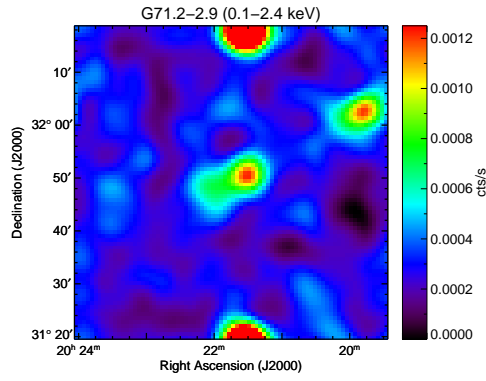
### A.3 RASS images of all SNR candidates

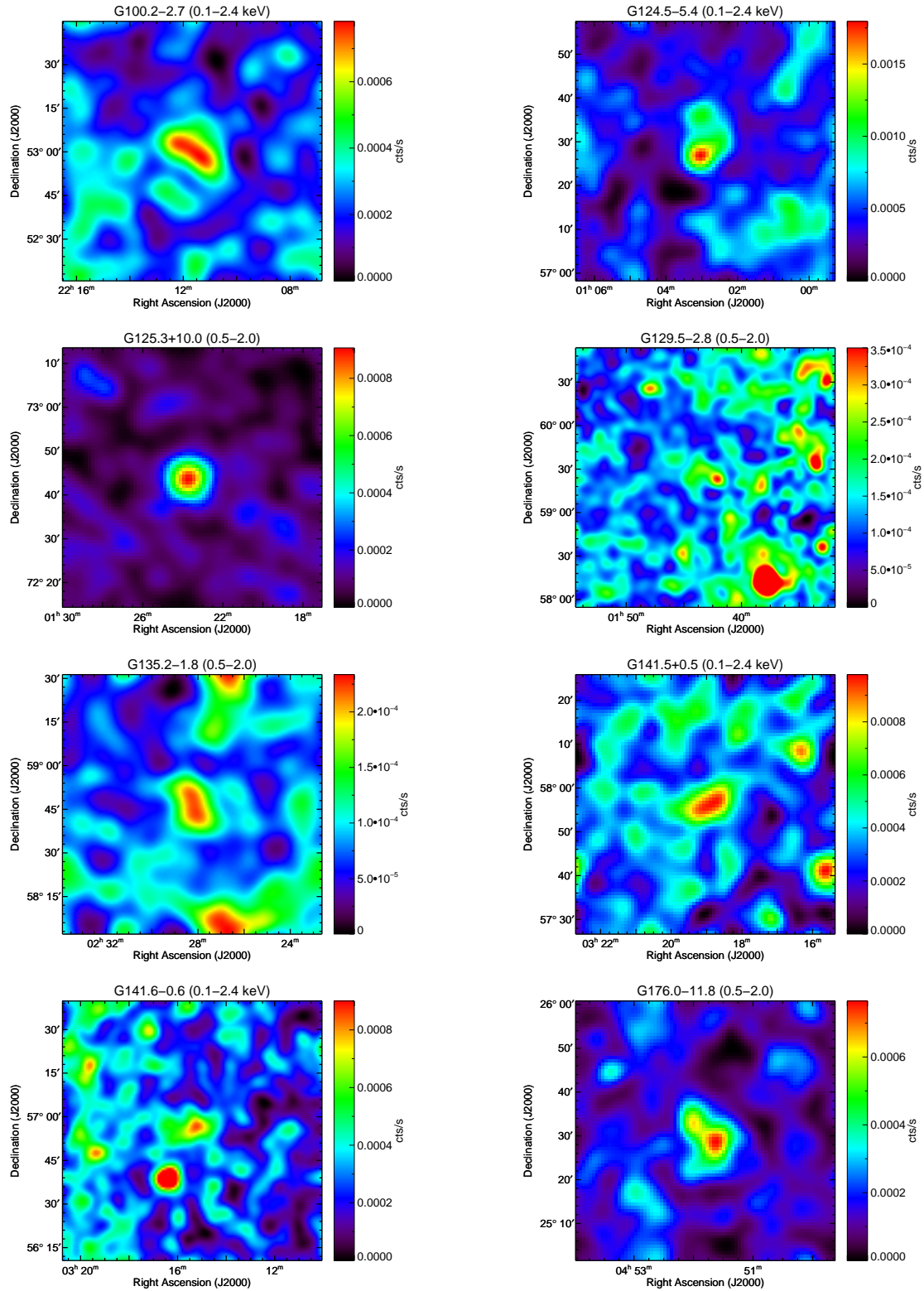
In the following the RASS images of all remaining supernova remnant candidates are shown in the same order as in Table A.1. They are divided in five groups depending on their extent and signal-to-noise ratio ( $S/N$ ). All RASS images have been exposure corrected, were binned with  $0'.75$  per pixel and smoothed by a Gaussian kernel of  $\sigma = 4'.5$  in order to reduce the noise and to keep a moderate resolution.

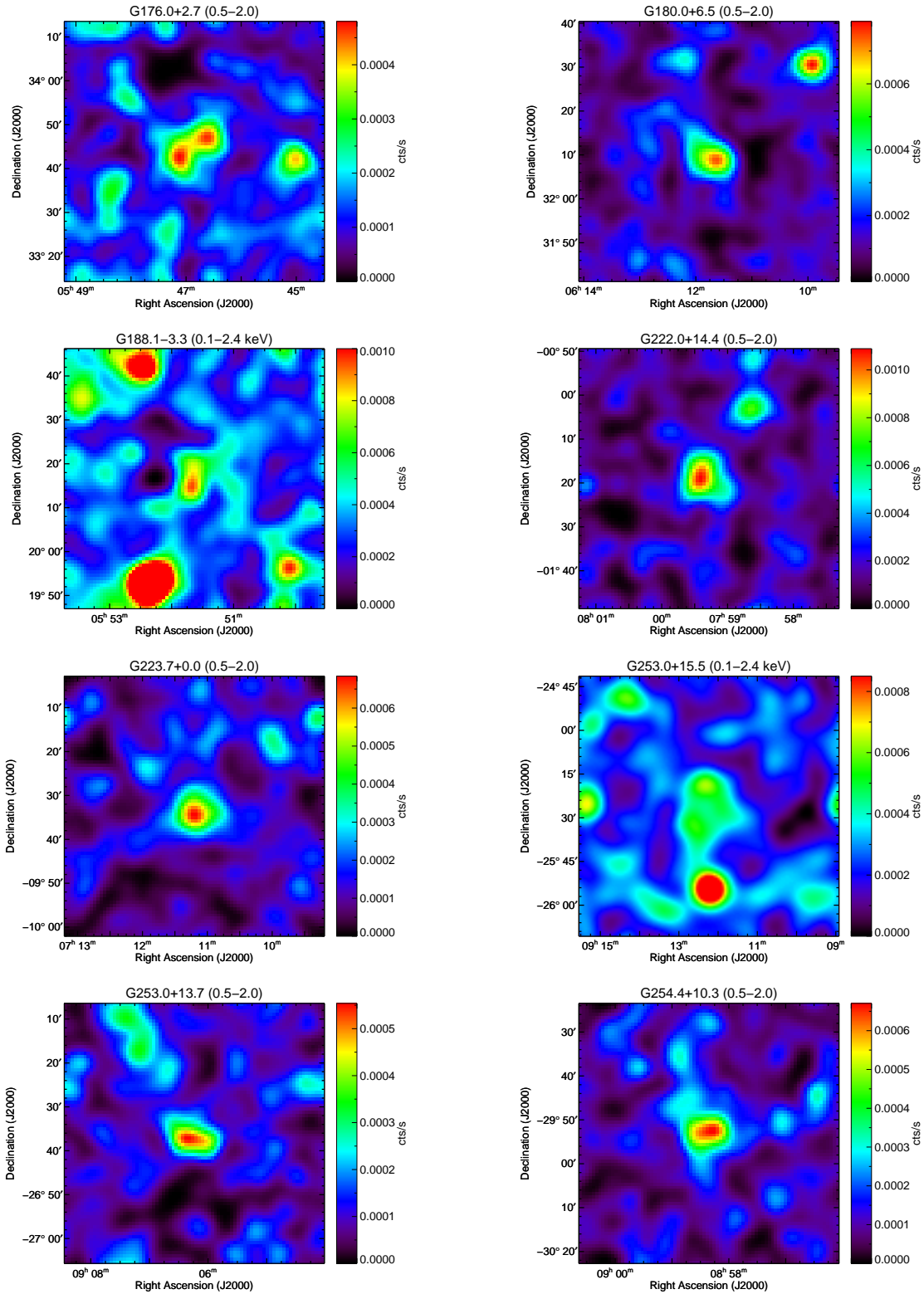
The displayed images have a size of  $1^{\circ} \times 1^{\circ}$ ,  $1.5^{\circ} \times 1.5^{\circ}$ ,  $3^{\circ} \times 3^{\circ}$ ,  $6^{\circ} \times 6^{\circ}$ ,  $9^{\circ} \times 9^{\circ}$ ,  $15^{\circ} \times 15^{\circ}$  for SNR candidates with a semi-major axis of less than  $20'$ ,  $30'$ ,  $1^{\circ}$ ,  $2^{\circ}$ ,  $3^{\circ}$  and  $5^{\circ}$ , respectively. For sources with a semi-major axis greater than  $5^{\circ}$  the image has a size of  $17.5^{\circ} \times 17.5^{\circ}$ . The only exception is the SNR candidate G83.2+6.9 with an image size of  $20' \times 20'$ .

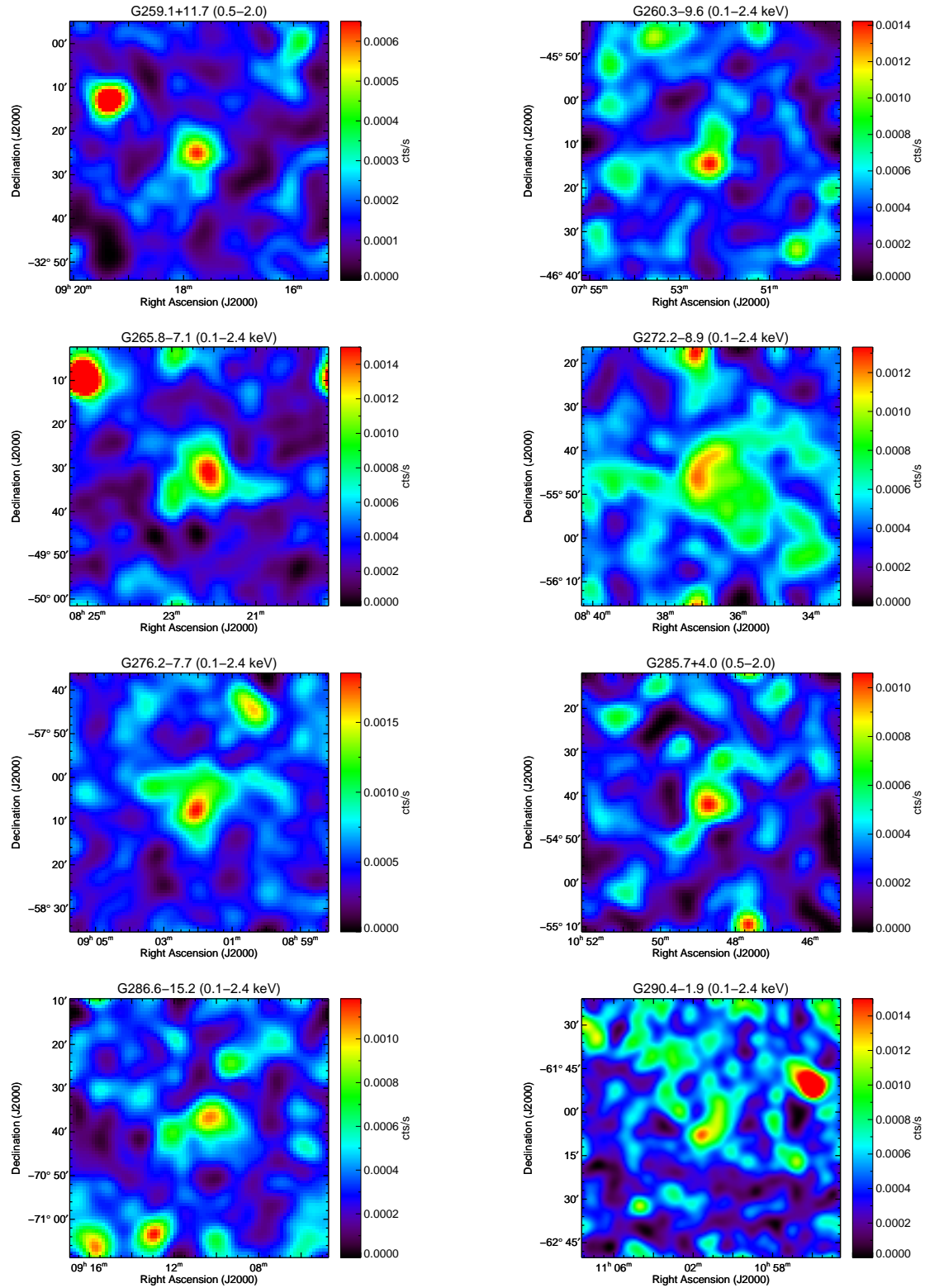
### A.3.1 High significant candidates with an extent of less than 30 arcmin

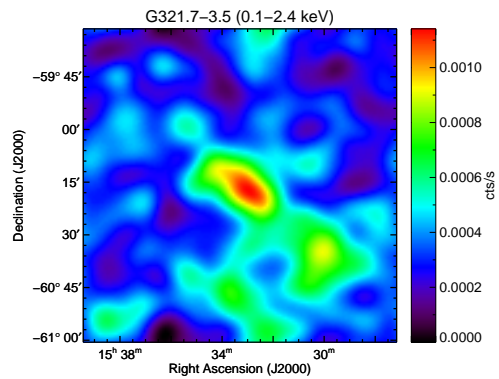
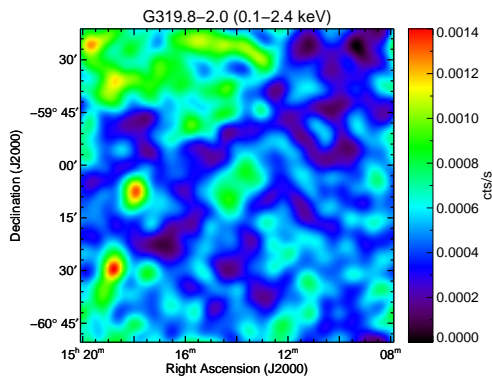
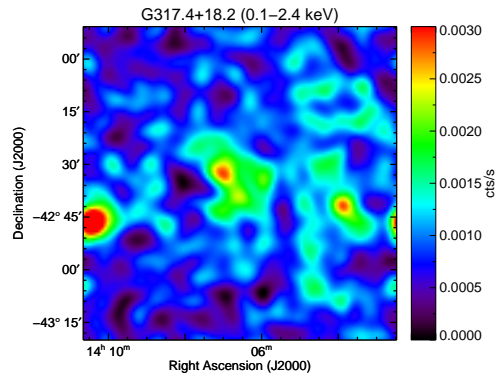
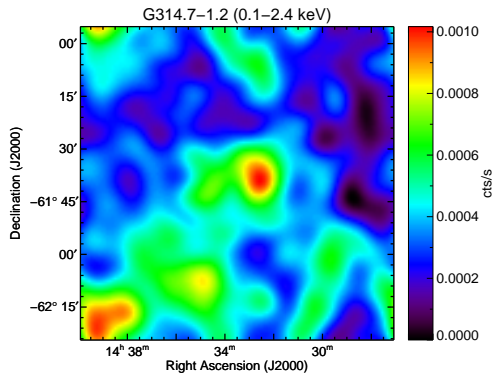
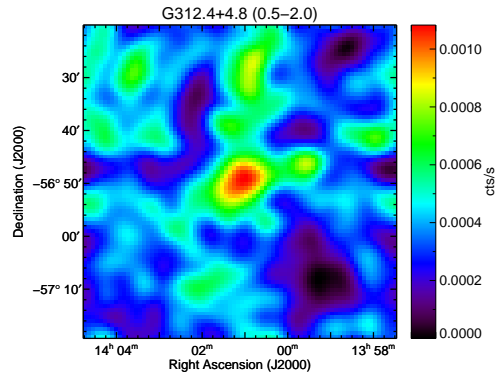
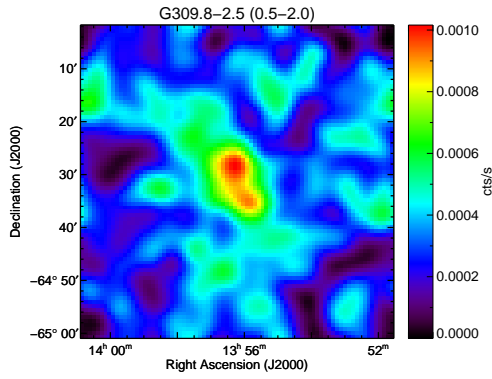
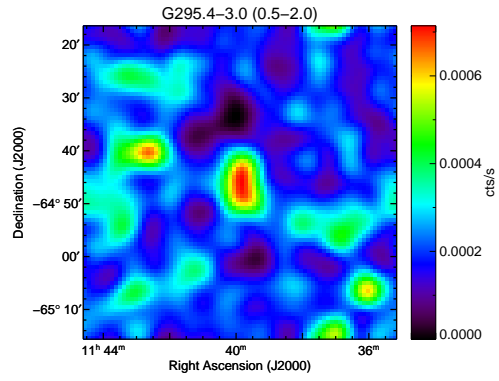
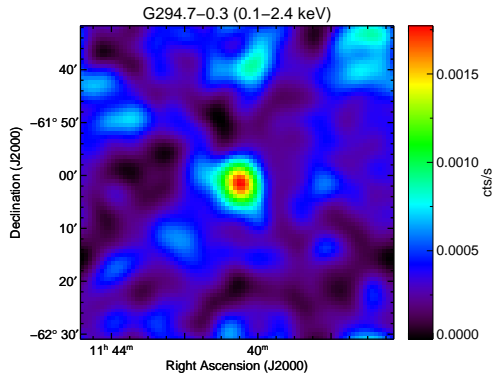




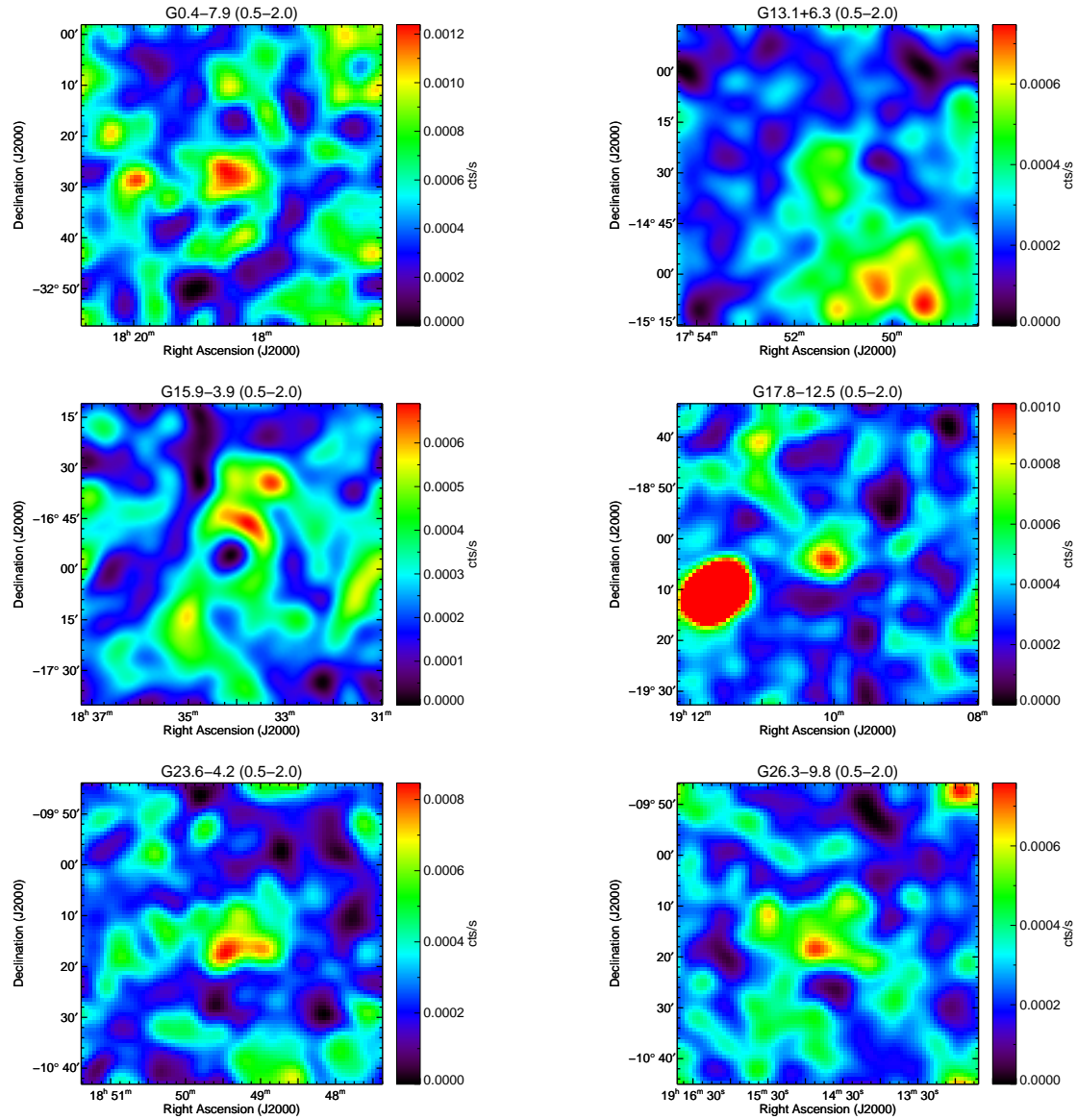


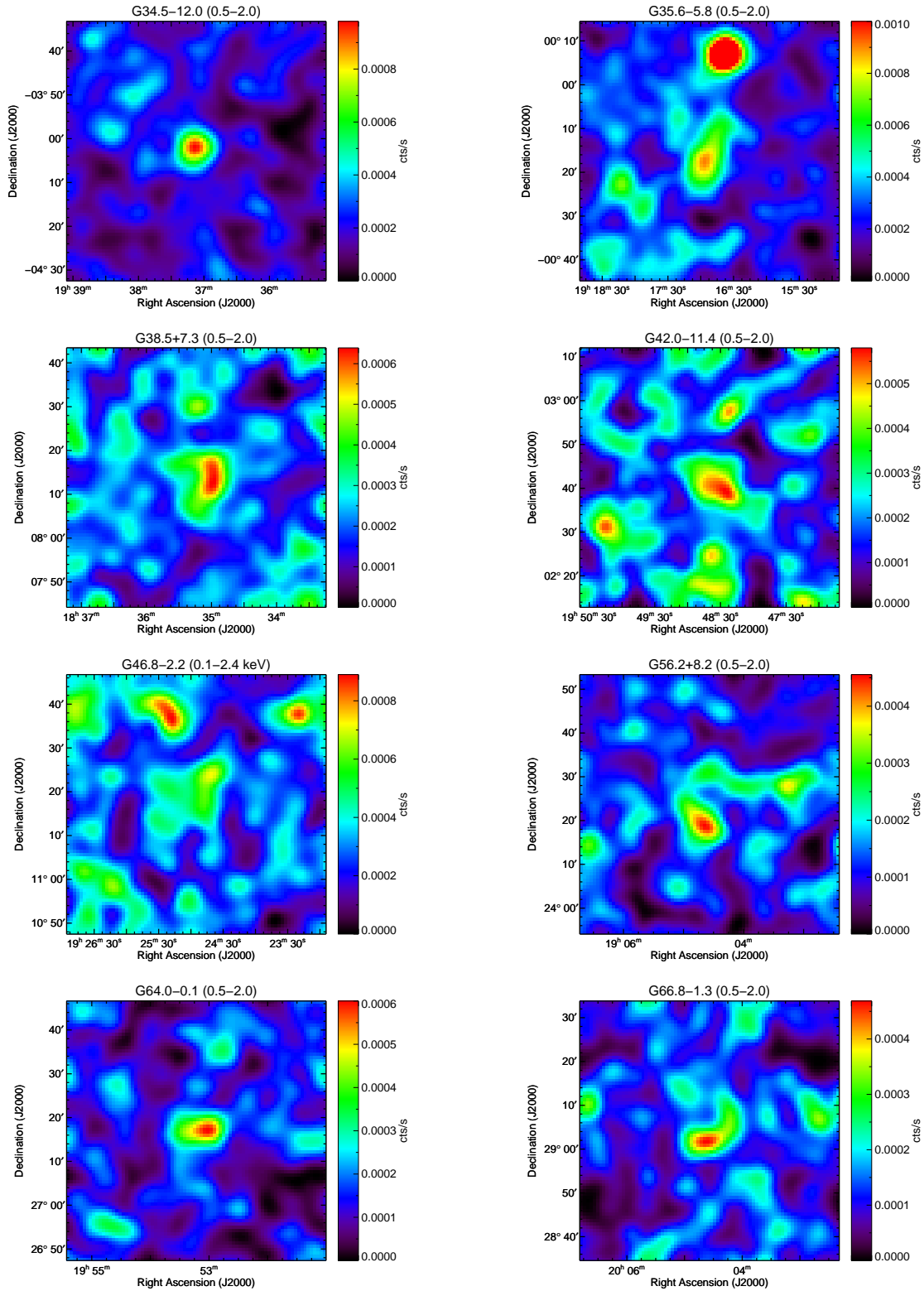


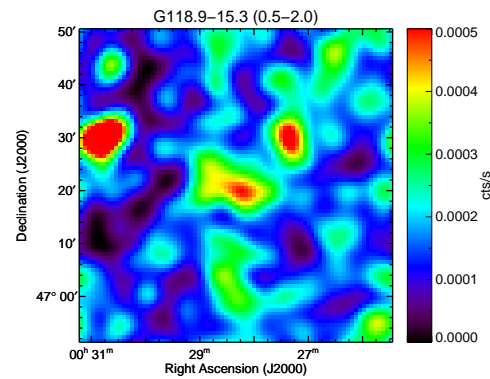
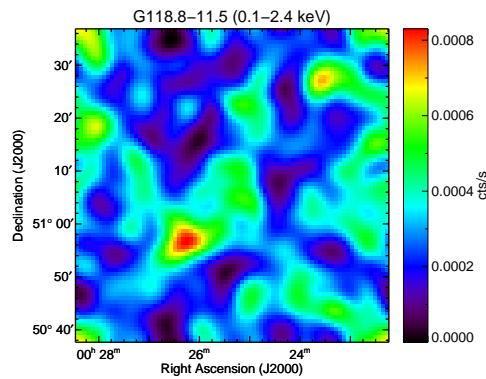
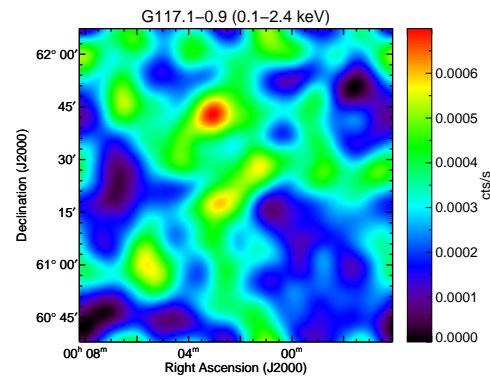
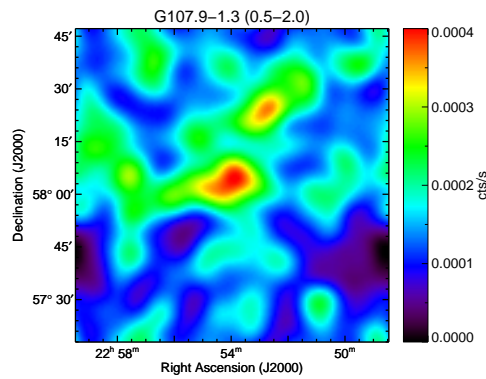
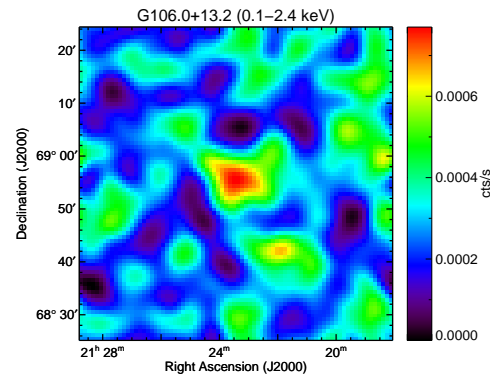
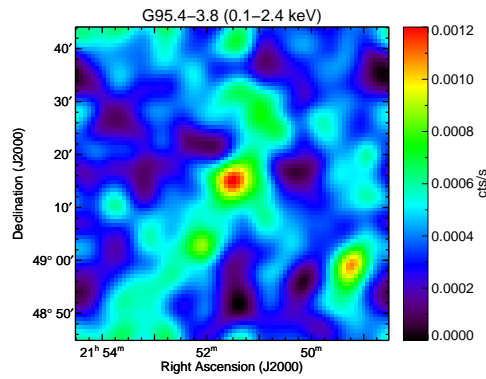
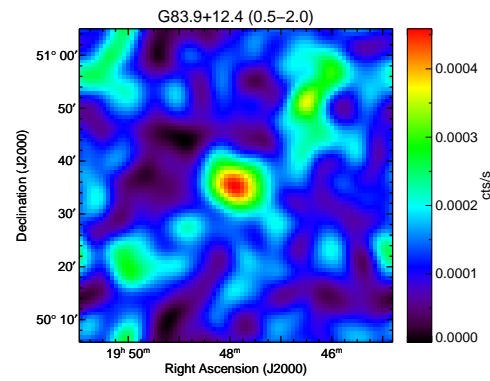
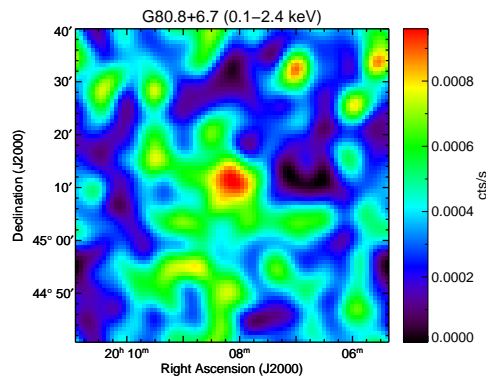


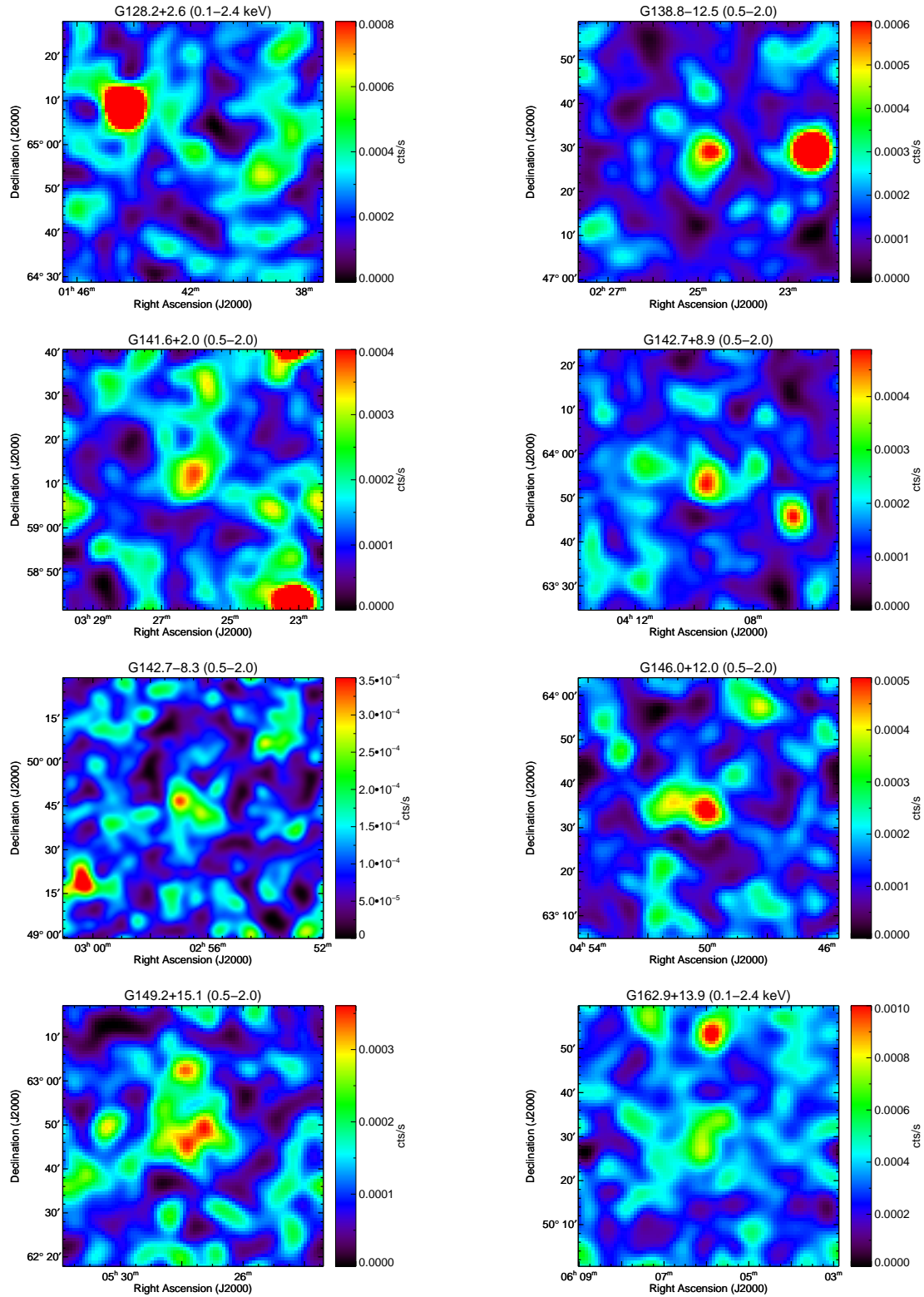


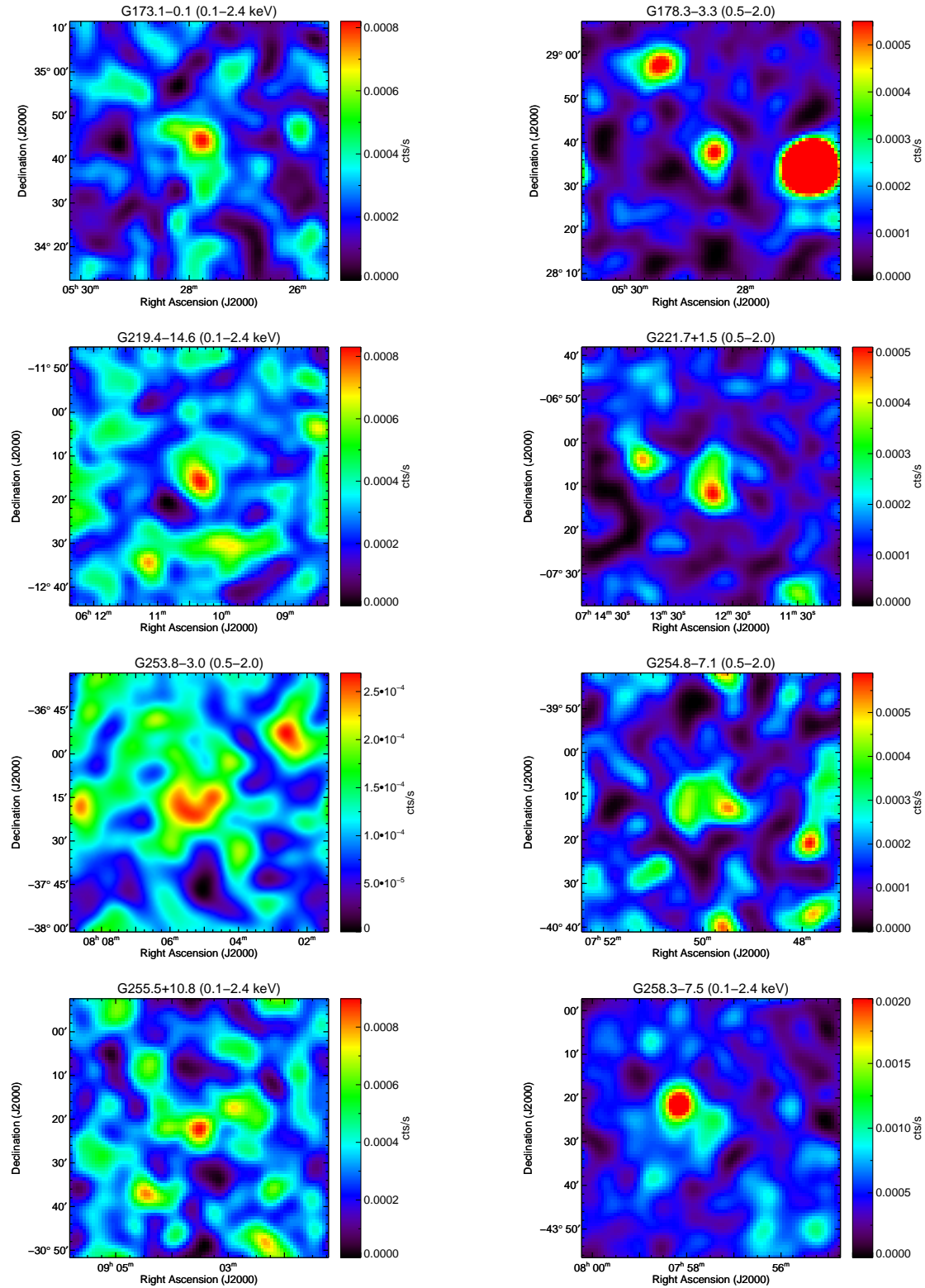
### A.3.2 Low significant candidates with an extent of less than 30 arcmin

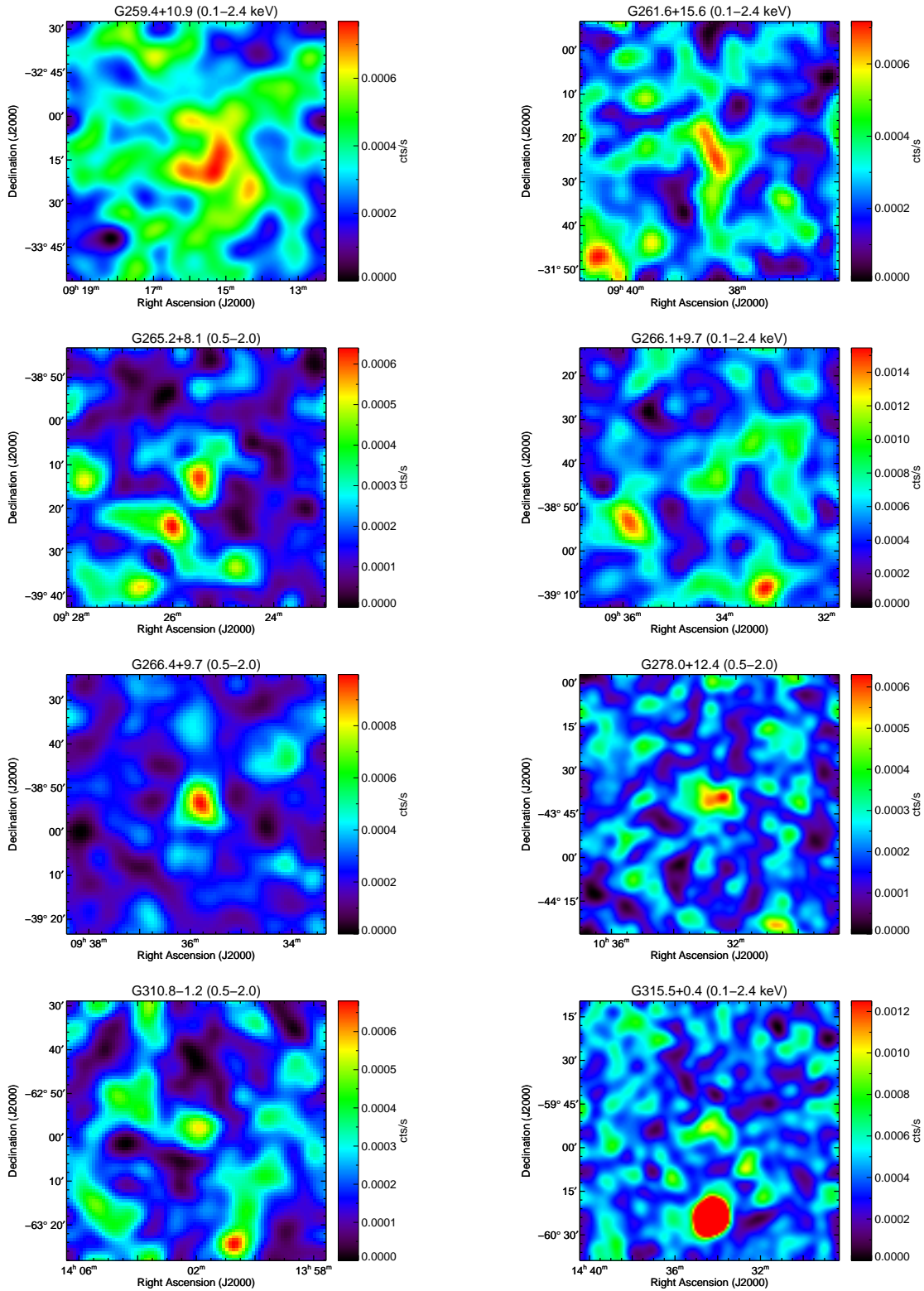


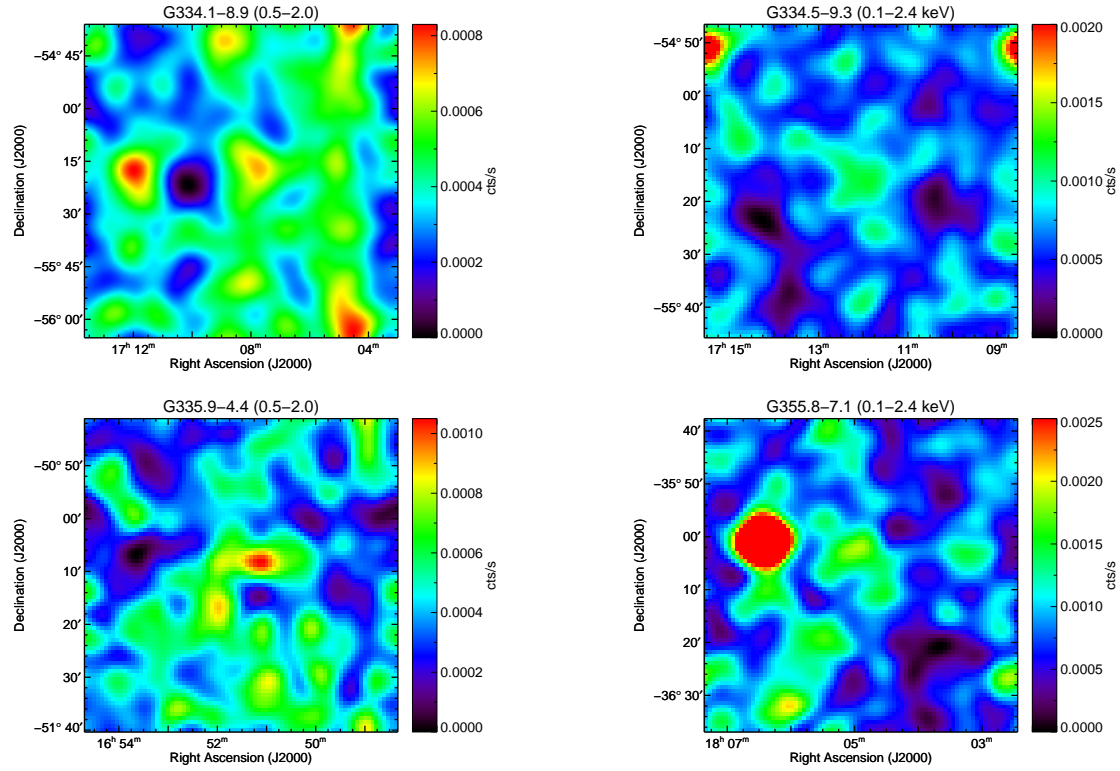




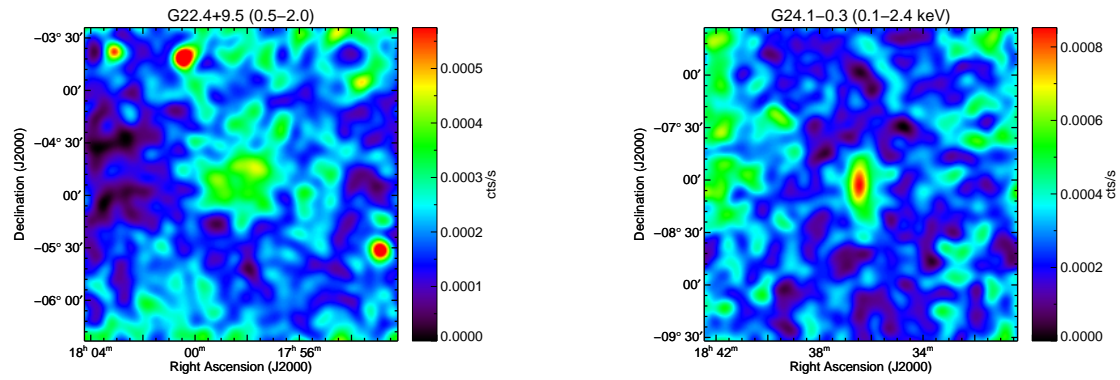


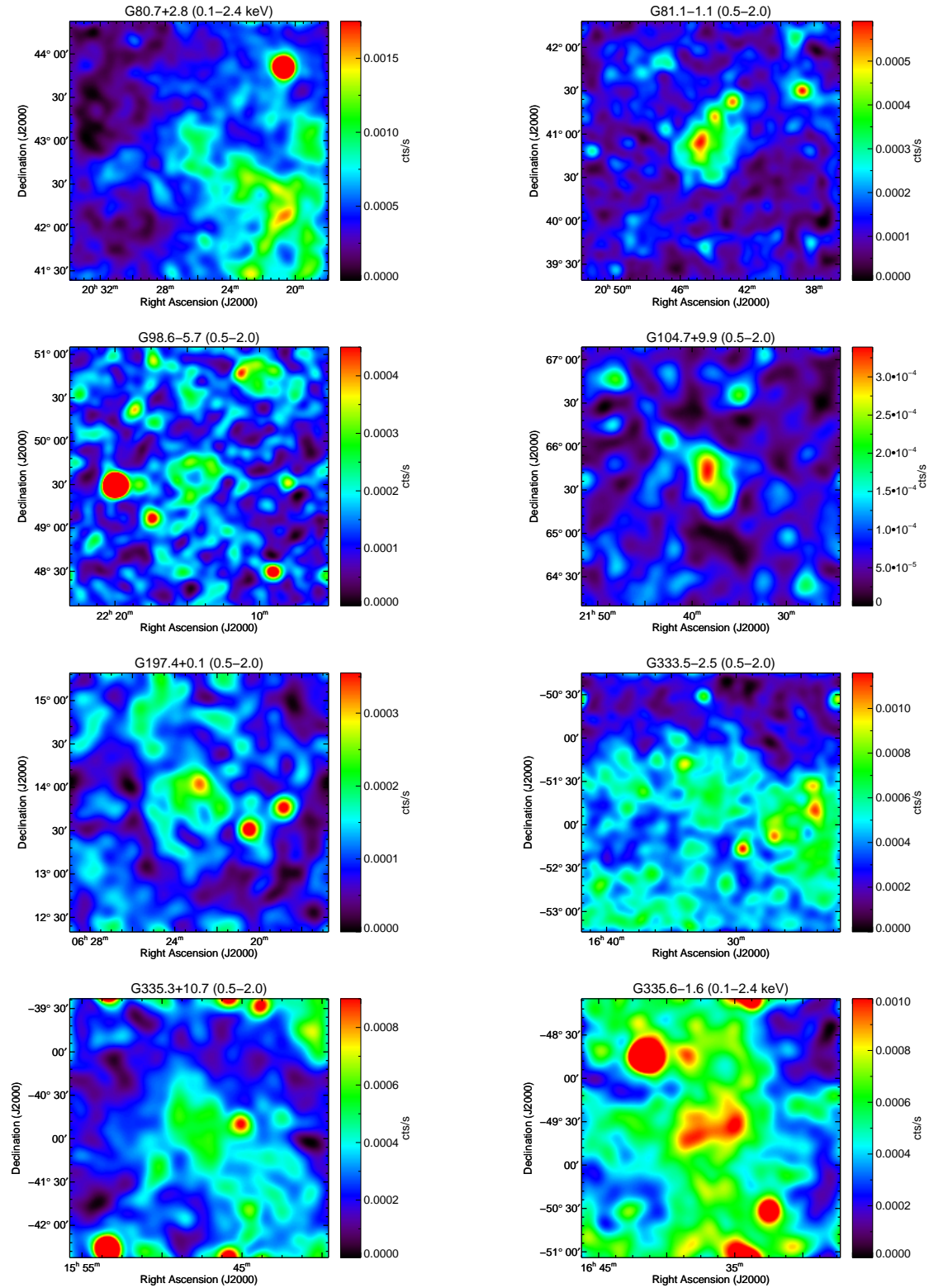




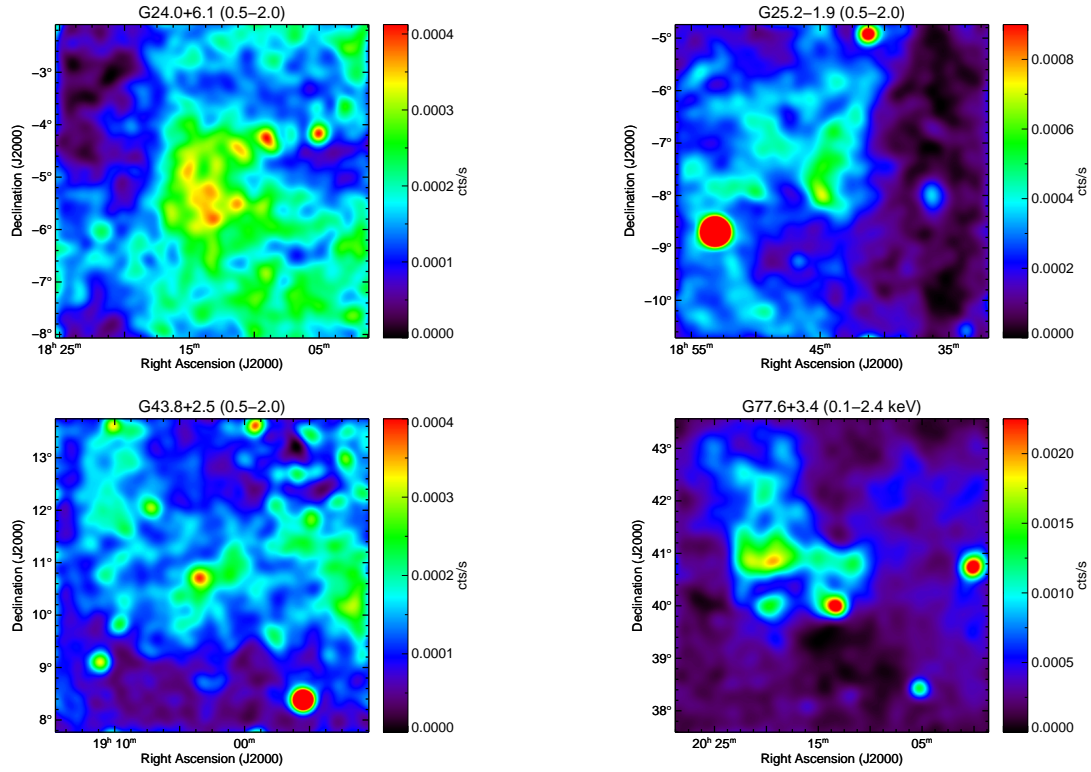


### A.3.3 Candidates with an extent between 30 and 60 arcmin

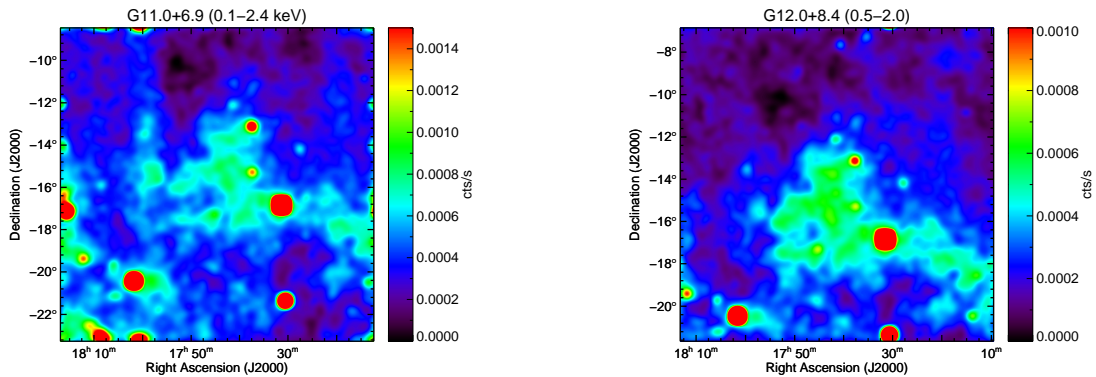


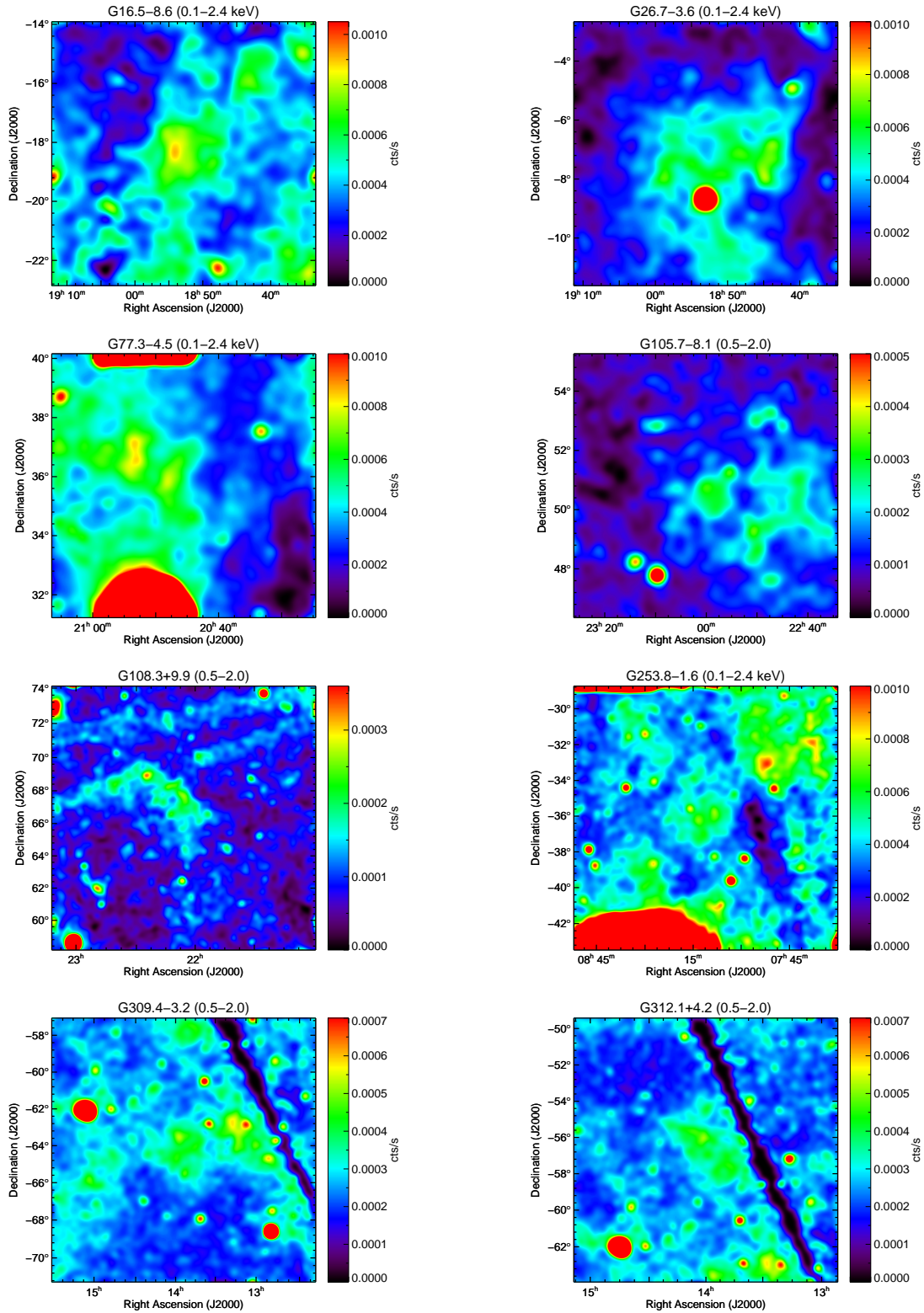


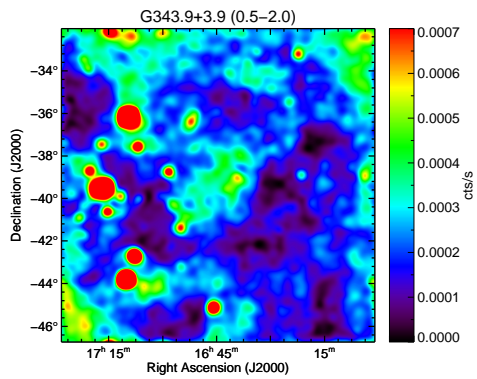
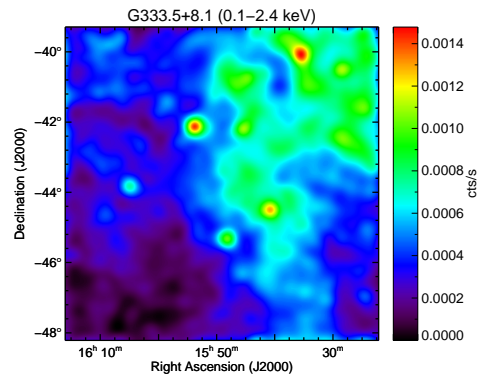
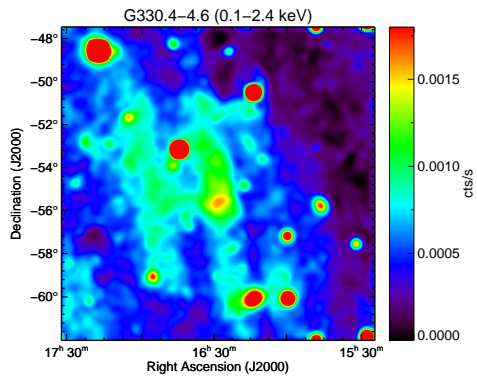
### A.3.4 Candidates with an extent between 60 and 120 arcmin



### A.3.5 Candidates with an extent of more than 120 arcmin







# Appendix B

## A search for X-ray counterparts of radio pulsars

### B.1 List of pulsars detected at high energies

**Table B.1:** List of all detected pulsars in X-rays and/or  $\gamma$ -rays

	PSR	X-ray	Type	X-ray reference	$\gamma$ -ray	$\gamma$ -ray reference
1	J0007+7303	p	Vela-like	Caraveo et al. (2010)	p	Abdo et al. (2013)
2	J0023+0923	d	MSP	Gentile et al. (2013)	p	Abdo et al. (2013)
3	B0021-72C	d	MSP	Cameron et al. (2007)	-	-
4	B0021-72D	p	MSP	Cameron et al. (2007)	-	-
5	B0021-72E	d	MSP	Cameron et al. (2007)	-	-
6	B0021-72F	d	MSP	Cameron et al. (2007)	-	-
7	B0021-72G	d	MSP	Cameron et al. (2007)	-	-
8	B0021-72H	d	MSP	Cameron et al. (2007)	-	-
9	B0021-72I	d	MSP	Cameron et al. (2007)	-	-
10	B0021-72J	d	MSP	Cameron et al. (2007)	-	-
11	B0021-72L	d	MSP	Cameron et al. (2007)	-	-
12	B0021-72M	d	MSP	Cameron et al. (2007)	-	-
13	B0021-72N	d	MSP	Cameron et al. (2007)	-	-
14	J0024-7204O	p	MSP	Cameron et al. (2007)	-	-
15	J0024-7204Q	d	MSP	Cameron et al. (2007)	-	-
16	J0024-7204R	p	MSP	Cameron et al. (2007)	-	-
17	J0024-7204S	d	MSP	Cameron et al. (2007)	-	-
18	J0024-7204T	d	MSP	Cameron et al. (2007)	-	-
19	J0024-7204U	d	MSP	Cameron et al. (2007)	-	-
20	J0024-7204W	d	MSP	Cameron et al. (2007)	-	-
21	J0024-7204Y	d	MSP	Cameron et al. (2007)	-	-
22	J0030+0451	p	MSP	Bogdanov and Grindlay (2009)	p	Abdo et al. (2013)
23	J0034-0534	d	MSP	Zavlin (2006)	p	Abdo et al. (2013)
24	CXOU J010043.1-721134	d	AXP	McGarry et al. (2005)	-	-
25	J0101-6422	-	MSP	-	p	Abdo et al. (2013)
26	J0102+4839	-	MSP	-	p	Abdo et al. (2013)
27	J0106+4855	-	Old	-	p	Abdo et al. (2013)
28	J0108-1431	p	MSP	Pavlov et al. (2009)	-	-
29	4U 0142+614	p	AXP	Hellier (1994)	-	-
30	J0205+6449	p	Crab-like	Murray et al. (2002)	p	Abdo et al. (2013)
31	J0218+4232	p	MSP	Kuiper et al. (2002)	p	Abdo et al. (2013)
32	J0248+6021	-	Vela-like	-	p	Abdo et al. (2013)
33	J0307+7443	-	MSP	-	p	Ray et al. (2012)
34	J0340+4130	-	MSP	-	p	Abdo et al. (2013)
35	J0357+3205	d	Cooling	De Luca et al. (2011)	p	Abdo et al. (2013)
36	B0355+54	d	Cooling	McGowan et al. (2007)	-	-
37	SGR 0418+5729	p	AXP	van der Horst et al. (2009)	-	-
38	RX J0420.0-5022	p	XINS	Haberl et al. (1999)	-	-
39	J0437-4715	p	MSP	Becker et al. (1993a)	p	Abdo et al. (2013)
40	SGR 0501+4516	p	AXP	Göğüş et al. (2010b)	-	-
41	SGR 0526-66	d	AXP	Danner et al. (1998)	-	-
42	B0531+21	p	Crab-like	Massaro et al. (2000)	p	Abdo et al. (2013)

Continued on next page

Table B.1 – continued from previous page

	PSR	X-ray	Type	X-ray reference	$\gamma$ -ray	$\gamma$ -ray reference
43	J0537-6910	p	Crab-like	Chen et al. (2006)	-	-
44	J0538+2817	p	Cooling	McGowan et al. (2003)	-	-
45	B0540-69	p	Crab-like	Kaaret et al. (2001)	-	-
46	J0610-2100	-	MSP	-	p	Abdo et al. (2013)
47	J0613-0200	d	MSP	Marelli et al. (2011)	p	Abdo et al. (2013)
48	J0614-3329	d	MSP	Ransom et al. (2011)	p	Abdo et al. (2013)
49	J0622+3749	-	Cooling	-	p	Abdo et al. (2013)
50	B0628-28	p	Old	Becker et al. (2005)	-	-
51	J0631+1036	d	Vela-like	Torii et al. (2001)	p	Abdo et al. (2013)
52	J0633+0632	d	Vela-like	Ray et al. (2011)	p	Abdo et al. (2013)
53	J0633+1746	p	Cooling	De Luca et al. (2005)	p	Abdo et al. (2013)
54	B0656+14	p	Cooling	De Luca et al. (2005)	p	Abdo et al. (2013)
55	RX J0720-3125	p	XINS	Kaplan et al. (2003)	-	-
56	J0726-2612	p	Cooling	Speagle et al. (2011)	-	-
57	J0729-1448	d	Vela-like	Kargaltsev et al. (2012)	p	Abdo et al. (2013)
58	J0734-1559	-	Cooling	-	p	Abdo et al. (2013)
59	J0737-3039A	p	MSP	Pellizzoni et al. (2008)	p	Guillemot et al. (2013)
60	B0740-28	-	Cooling	-	p	Abdo et al. (2013)
61	J0751+1807	d	MSP	Webb et al. (2004)	p	Abdo et al. (2013)
62	RX J0806.4-4123	p	XINS	Haberl and Zavlin (2002)	-	-
63	RX J0822-4300	p	CCO	Gotthelf and Halpern (2009a)	-	-
64	B0823+26	d	Old	Becker et al. (2004)	-	-
65	B0833-45	p	Vela-like	Manzali et al. (2007)	p	Abdo et al. (2013)
66	B0834+06	d	Old	Gil et al. (2008)	-	-
67	CXOU J085201.4-461753	d	CCO	Kargaltsev et al. (2002)	-	-
68	J0855-4644	d	Cooling	Acero et al. (2013)	-	-
69	B0906-49	d	Cooling	Kargaltsev et al. (2012)	p	Abdo et al. (2013)
70	J0940-5428	-	Vela-like	-	p	Abdo et al. (2013)
71	B0943+10	d	Old	Zhang et al. (2005)	-	-
72	B0950+08	p	Old	Becker et al. (2004)	-	-
73	J1012+5307	d	MSP	Webb et al. (2004)	-	-
74	J1016-5857	d	Vela-like	Camilo et al. (2001)	p	Abdo et al. (2013)
75	J1019-5749	-	Cooling	-	p	Abdo et al. (2013)
76	J1023+0038	p	MSP	Bogdanov et al. (2011)	-	-
77	J1023-5746	d	Crab-like	Kargaltsev et al. (2012)	p	Abdo et al. (2013)
78	J1024-0719	p	MSP	Zavlin (2006)	p	Abdo et al. (2013)
79	J1028-5819	d	Vela-like	Abdo et al. (2009)	p	Abdo et al. (2013)
80	J1044-5737	-	Vela-like	-	p	Abdo et al. (2013)
81	B1046-58	d	Vela-like	Gonzalez et al. (2006)	p	Abdo et al. (2013)
82	1E 1048.1-5937	p	AXP	Tiengo et al. (2002)	-	-
83	B1055-52	p	Cooling	De Luca et al. (2005)	p	Abdo et al. (2013)
84	J1105-6107	d	Vela-like	Gotthelf and Kaspi (1999)	p	Abdo et al. (2013)
85	J1112-6103	-	Vela-like	-	p	Abdo et al. (2013)
86	J1119-6127	p	Crab-like	Gonzalez et al. (2005)	p	Abdo et al. (2013)
87	J1124-3653	d	MSP	Gentile et al. (2013)	p	Abdo et al. (2013)
88	J1124-5916	p	Crab-like	Camilo et al. (2002b)	p	Abdo et al. (2013)
89	J1125-5825	-	MSP	-	p	Abdo et al. (2013)
90	J1135-6055	-	Vela-like	-	p	Abdo et al. (2013)
91	B1133+16	d	Old	Kargaltsev et al. (2006b)	-	-
92	1E 1207.4-5209	p	CCO	Gotthelf and Halpern (2007)	-	-
93	J1231-1411	d	MSP	Ransom et al. (2011)	p	Abdo et al. (2013)
94	B1257+12	d	MSP	Pavlov et al. (2007)	-	-
95	J1301-6305	d	Vela-like	H.E.S.S. Collaboration et al. (2012)	-	-
96	B1259-63	d	Cooling	Chernyakova et al. (2006)	-	-
97	RX J1308.6+2127	p	XINS	Kaplan and van Kerkwijk (2005)	-	-
98	J1311-3430	d	MSP	Ray et al. (2013)	p	Pletsch et al. (2012)
99	J1357-6429	p	Crab-like	Zavlin (2007)	p	Abdo et al. (2013)
100	J1400-6325	p	Vela-like	Renaud et al. (2010)	-	-
101	J1410-6132	-	Vela-like	-	p	Abdo et al. (2013)
102	RXS J141256.0+792204	p	MSP	Zane et al. (2011)	-	-
103	J1413-6205	d	Vela-like	Kargaltsev et al. (2012)	p	Abdo et al. (2013)
104	J1418-6058	d	Vela-like	Marelli et al. (2011)	p	Abdo et al. (2013)
105	J1420-6048	p	Vela-like	Roberts et al. (2001)	p	Abdo et al. (2013)
106	J1429-5911	-	Vela-like	-	p	Abdo et al. (2013)
107	J1446-4701	-	MSP	-	p	Abdo et al. (2013)
108	B1451-68	d	Old	Posselt et al. (2011)	-	-
109	J1459-6053	p	Vela-like	Pancrazi et al. (2012)	p	Abdo et al. (2013)
110	J1509-5850	d	Cooling	Hui and Becker (2007a)	p	Abdo et al. (2013)
111	B1509-58	p	Crab-like	Cusumano et al. (2001)	p	Abdo et al. (2013)
112	J1514-4946	-	MSP	-	p	Abdo et al. (2013)
113	J1524-5625	d	Vela-like	Kargaltsev et al. (2012)	-	-
114	J1531-5610	d	Vela-like	Kargaltsev et al. (2012)	p	Abdo et al. (2013)
115	B1534+12	d	MSP	Kargaltsev et al. (2006a)	-	-
116	1E 1547.0-5408	d	AXP	Gelfand and Gaensler (2007)	-	-
117	J1600-3053	-	MSP	-	p	Abdo et al. (2013)
118	CXOU J160103.1-513353	d	CCO	Park et al. (2009)	-	-
119	RX J1605.3+3249	d	XINS	van Kerkwijk et al. (2004)	-	-
120	J1614-2230	p	MSP	Pancrazi et al. (2012)	p	Abdo et al. (2013)
121	B1610-50	d	Crab-like	Pivovarov et al. (2000)	-	-
122	J1617-5055	p	Crab-like	Becker and Aschenbach (2002)	-	-
123	J1620-4927	-	Cooling	-	p	Abdo et al. (2013)
124	J1622-4950	d	Crab-like	Levin et al. (2010)	-	-
125	B1620-26	d	MSP	Pavlov et al. (2007)	-	-
126	SGR 1627-41	d	AXP	Wachter et al. (2004)	-	-

Continued on next page

Table B.1 – continued from previous page

	PSR	X-ray	Type	X-ray reference	$\gamma$ -ray	$\gamma$ -ray reference
127	CXOU J164710.2-455216	p	AXP	An et al. (2013)	-	-
128	J1648-4611	-	Cooling	-	p	Abdo et al. (2013)
129	J1658-5324	-	MSP	-	p	Abdo et al. (2013)
130	J1701-3006B	d	MSP	Becker et al. (2010)	-	-
131	J1701-3006C	d	MSP	Becker et al. (2010)	-	-
132	J1702-4128	d	Vela-like	Chang et al. (2008)	p	Abdo et al. (2013)
133	1RXS J170849.0-400910	p	AXP	den Hartog et al. (2008)	-	-
134	B1706-44	p	Vela-like	McGowan et al. (2004)	p	Abdo et al. (2013)
135	J1713+0747	-	MSP	-	p	Abdo et al. (2013)
136	1WGA J1713.4-3949	d	CCO	Lazendic et al. (2003)	-	-
137	J1714-3810	p	Crab-like	Sato et al. (2010)	-	-
138	J1718-3718	d	Vela-like	Kaspi and McLaughlin (2005)	-	-
139	J1718-3825	d	Vela-like	Hinton et al. (2007)	p	Abdo et al. (2013)
140	B1719-37	d	Cooling	Oosterbroek et al. (2004)	-	-
141	B1727-33	-	Vela-like	-	p	Abdo et al. (2013)
142	J1732-3131	d	Cooling	Ray et al. (2011)	p	Abdo et al. (2013)
143	J1734-3333	d	Crab-like	Olansen et al. (2010)	-	-
144	J1740+1000	p	Cooling	Kargaltsev et al. (2008)	-	-
145	J1740-5340A	d	MSP	Bogdanov et al. (2010)	-	-
146	J1741+1351	-	MSP	-	p	Abdo et al. (2013)
147	J1741-2054	d	Cooling	Camilo et al. (2009b)	p	Abdo et al. (2013)
148	J1744-1134	d	MSP	Becker and Trümper (1999)	p	Abdo et al. (2013)
149	J1745+1017	-	MSP	-	p	Barr et al. (2013)
150	J1746-3239	-	Cooling	-	p	Abdo et al. (2013)
151	J1747-2809	d	Crab-like	Camilo et al. (2009a)	-	-
152	J1747-2958	d	Vela-like	Gaensler et al. (2004)	p	Abdo et al. (2013)
153	J1747-4036	-	MSP	-	p	Abdo et al. (2013)
154	J1748-2021B	d	Crab-like	Becker et al. (2010)	-	-
155	B1744-24A	d	Crab-like	Becker et al. (2010)	-	-
156	B1757-24	d	Vela-like	Kaspi et al. (2001)	p	Abdo et al. (2013)
157	B1800-21	d	Vela-like	Kargaltsev et al. (2007)	-	-
158	J1803-2149	-	Vela-like	-	p	Abdo et al. (2013)
159	SGR 1806-20	p	AXP	Mereghetti et al. (2005)	-	-
160	J1809-1917	d	Vela-like	Kargaltsev and Pavlov (2007)	-	-
161	XTE 1810-197	p	AXP	Levin et al. (2010)	-	-
162	J1809-2332	d	Vela-like	Van Eten et al. (2012)	p	Abdo et al. (2013)
163	J1810+1744	d	MSP	Gentile et al. (2013)	p	Abdo et al. (2013)
164	J1811-1925	p	Vela-like	Roberts et al. (2003)	-	-
165	J1813-1246	d	Vela-like	Ray et al. (2011)	p	Abdo et al. (2013)
166	J1813-1749	p	Crab-like	Gotthelf and Halpern (2009b)	-	-
167	J1816+4510	-	MSP	-	p	Kaplan et al. (2012)
168	J1819-1458	p	RRAT	McLaughlin et al. (2007)	-	-
169	B1820-30A	-	MSP	-	p	Abdo et al. (2013)
170	B1821-24A	p	MSP	Becker et al. (2010)	-	-
171	J1824-2452G	d	MSP	Becker et al. (2010)	-	-
172	J1824-2452H	d	MSP	Becker et al. (2010)	-	-
173	J1826-1256	d	Vela-like	Marelli et al. (2011)	p	Abdo et al. (2013)
174	B1823-13	d	Vela-like	Gaensler et al. (2003)	-	-
175	SGR J1833-0832	p	AXP	Göğüş et al. (2010a)	-	-
176	J1833-1034	d	Crab-like	Matheson and Safi-Harb (2010)	p	Abdo et al. (2013)
177	J1834-0845	d	AXP	Esposito et al. (2013)	-	-
178	J1835-1106	-	Cooling	-	p	Abdo et al. (2013)
179	RX J1836.2+5925	d	XINS	Halpern et al. (2007a)	p	Abdo et al. (2013)
180	J1838-0537	-	Crab-like	-	p	Abdo et al. (2013)
181	J1838-0655	p	Vela-like	Gotthelf and Halpern (2008b)	-	-
182	1E 1841-045	p	AXP	Gotthelf et al. (2002)	-	-
183	J1846+0919	-	Cooling	-	p	Abdo et al. (2013)
184	J1846-0258	p	Crab-like	Kumar and Safi-Harb (2008)	-	-
185	J1849-0001	p	Vela-like	Gotthelf et al. (2010a)	-	-
186	CXOU J185238.6+004020	p	CCO	Halpern et al. (2007b)	-	-
187	B1853+01	d	Vela-like	Petre et al. (2002)	-	-
188	J1856+0245	d	Vela-like	Nice et al. (2013)	-	-
189	RX J1856.5-3754	p	XINS	Mereghetti et al. (2012)	-	-
190	J1858-2216	-	MSP	-	p	Abdo et al. (2013)
191	J1902-5105	-	MSP	-	p	Abdo et al. (2013)
192	J1907+0602	d	Vela-like	Abdo et al. (2010b)	p	Abdo et al. (2013)
193	SGR 1900+14	p	AXP	Göğüş et al. (2011)	-	-
194	J1909-3744	d	MSP	Kargaltsev et al. (2012)	-	-
195	J1910-5959B	d	MSP	Becker et al. (2010)	-	-
196	J1910-5959C	d	MSP	Becker et al. (2010)	-	-
197	J1910-5959D	d	MSP	Becker et al. (2010)	-	-
198	B1916+14	d	Vela-like	Zhu et al. (2009)	-	-
199	J1930+1852	p	Crab-like	Camilo et al. (2002a)	-	-
200	B1929+10	p	Old	Becker et al. (2006)	-	-
201	B1937+21	p	MSP	Nicastro et al. (2004)	p	Abdo et al. (2013)
202	B1951+32	d	Cooling	Li et al. (2005)	p	Abdo et al. (2013)
203	J1953+1846A	d	MSP	Becker et al. (2010)	-	-
204	J1954+2836	-	Vela-like	-	p	Abdo et al. (2013)
205	J1957+5033	-	Cooling	-	p	Abdo et al. (2013)
206	J1958+2846	d	Vela-like	Marelli et al. (2011)	p	Abdo et al. (2013)
207	B1957+20	d	MSP	Huang and Becker (2007)	p	Abdo et al. (2013)
208	J2017+0603	-	MSP	-	p	Abdo et al. (2013)
209	J2021+3651	p	Vela-like	Hessels et al. (2004)	p	Abdo et al. (2013)
210	J2021+4026	p	Vela-like	Lin et al. (2013)	p	Abdo et al. (2013)

Continued on next page

Table B.1 – continued from previous page

	PSR	X-ray	Type	X-ray reference	$\gamma$ -ray	$\gamma$ -ray reference
211	J2022+3842	p	Crab-like	Arzoumanian et al. (2011)	-	-
212	J2028+3332	-	Cooling	-	p	Abdo et al. (2013)
213	J2030+3641	-	Cooling	-	p	Abdo et al. (2013)
214	J2030+4415	-	Cooling	-	p	Abdo et al. (2013)
215	J2032+4127	d	Cooling	Camilo et al. (2009b)	p	Abdo et al. (2013)
216	J2043+1711	-	MSP	-	p	Abdo et al. (2013)
217	J2043+2740	d	Old	Becker et al. (2004)	p	Abdo et al. (2013)
218	J2047+1053	-	MSP	-	p	Abdo et al. (2013)
219	J2051-0827	d	MSP	Wu et al. (2012)	p	Abdo et al. (2013)
220	J2055+2539	d	Old	Marelli et al. (2011)	p	Abdo et al. (2013)
221	J2111+4606	-	Vela-like	-	p	Abdo et al. (2013)
222	J2124-3358	p	MSP	Zavlin (2006)	p	Abdo et al. (2013)
223	J2139+4716	-	Old	-	p	Abdo et al. (2013)
224	J2214+3000	d	MSP	Ransom et al. (2011)	p	Abdo et al. (2013)
225	J2215+5135	d	MSP	Gentile et al. (2013)	p	Abdo et al. (2013)
226	B2224+65	d	Old	Hui and Becker (2007b)	-	-
227	J2229+6114	p	Vela-like	Halpern et al. (2001)	p	Abdo et al. (2013)
228	J2238+5903	-	Vela-like	-	p	Abdo et al. (2013)
229	J2240+5832	-	Cooling	-	p	Abdo et al. (2013)
230	J2241-5236	d	MSP	Keith et al. (2011)	p	Abdo et al. (2013)
231	J2256-1024	d	MSP	Gentile et al. (2013)	p	Gentile et al. (2013)
232	1E 2259+586	p	AXP	İçdem et al. (2012)	-	-
233	J2302+4442	d	MSP	Cognard et al. (2011)	p	Abdo et al. (2013)
234	CXOU J232327.9+584842	d	CCO	Page et al. (2011)	-	-
235	B2334+61	d	Vela-like	McGowan et al. (2006)	-	-

**Notes.** In total 185 NSs are detected in X-rays and 123 in the  $\gamma$ -ray regime, whereas 73 are detected in both regimes. Of the X-ray pulsars 17 are Anomalous X-ray Pulsars (AXPs) or Soft Gamma-ray Repeaters (SGRs), 7 Central Compact Objects (CCOs), 22 Crab-like pulsars ( $\tau \leq 10^4$  yrs), 41 Vela-like pulsars ( $10^4$  yrs  $< \tau \leq 10^5$  yrs), 17 cooling NSs ( $10^5$  yrs  $< \tau \leq 10^6$  yrs), 11 old NSs ( $10^6$  yrs  $< \tau \leq 10^8$  yrs), and 62 millisecond pulsars (MSPs,  $\tau > 10^8$  yrs and  $P < 20$  ms). In the  $\gamma$ -ray regime 46 MSPs, 9 Crab-like pulsars, 39 Vela-like pulsars, 24 cooling NSs, and 4 old NSs are detected so far.

## B.2 Used observations

Table B.2

PSR	satellite <sup>(<math>\alpha</math>)</sup>	obsID	date	instrument <sup>(<math>\beta</math>)</sup>	filter	$t_{\text{on-axis}}$ ksec	$t(\theta)$ ksec	$\theta$ <sup>(<math>\gamma</math>)</sup> arcmin	count rate <sup>(<math>\delta</math>)</sup> cts/ksec	flag <sup>(<math>\delta</math>)</sup>
J0117+5914	X	0112200201	2002-07-09	PN/FF	Medium	5.8	5.1	1.7	18.71	d
	X	0112200201	2002-07-09	MOS1	Medium	7.9	7.7	1.7	3.23	d
	X	0112200201	2002-07-09	MOS2	Medium	8.1	7.9	1.7	3.84	d
J0134-2937	X	0654800501	2010-12-30	PN/FF	Medium	30.4	11.8	11.4	3.44	ul
	X	0654800501	2010-12-30	MOS1	Medium	39.0	2.1	11.4	1.44	ul
	X	0654800501	2010-12-30	MOS2	Medium	39.5	19.1	11.4	1.55	ul
J0139+5814	X	0103262501	2003-01-16	PN/FF	Medium	2.7	2.4	1.7	2.86	ul
	X	0103262501	2003-01-16	MOS1	Medium	4.4	4.3	1.7	1.95	ul
	X	0103262501	2003-01-16	MOS2	Medium	4.4	4.2	1.7	0.74	ul
J0157+6212	X	0150820201	2003-03-06	PN/SW	Thin	12.1	8.4	1.8	4.06	ul
	X	0150820201	2003-03-06	MOS1	Medium	12.8	12.6	1.8	0.94	ul
	X	0150820201	2003-03-06	MOS2	Medium	13.3	11.4	1.8	1.23	ul
J0248+6021	C	13289	2012-09-25	ACIS-I	-	9.3	8.6	0.3	1.15	ul
J0543+2329	X	0103262801	2003-10-09	PN/FF	Medium	5.5	4.9	1.7	5.89	d
	X	0103262801	2003-10-09	MOS1	Medium	7.6	7.5	1.7	0.41	d
	X	0103262801	2003-10-09	MOS2	Medium	7.5	7.1	1.7	3.00	d
J0609+2130	C	12687	2011-04-14	ACIS-S	-	5.1	5.0	0.3	0.62	ul
J0622+3749	C	12842	2011-01-29	ACIS-I	-	2.1	1.9	2.2	1.56	ul
J0742-2822	X	0103262401	2002-10-11	PN/FF	Medium	2.7	2.4	1.7	14.54	ul
	X	0103262401	2002-10-11	MOS1	Medium	5.1	5.0	1.7	3.54	ul
	X	0103262401	2002-10-11	MOS2	Medium	5.7	5.5	1.7	2.22	ul
J0828-3417	X	0400020101	2006-11-13	PN/FF	Thin	35.4	30.6	1.7	1.34	ul
	X	0400020101	2006-11-13	MOS1	Thin	41.5	40.7	1.7	0.58	ul
	X	0400020101	2006-11-13	MOS2	Thin	42.3	40.8	1.7	0.54	ul
J0847-4316	C	7626	2007-02-08	ACIS-I	-	10.8	8.6	1.1	0.54	ul
J0907-5157	X	0112930101	2001-12-11	PN/FF	Thin	12.1	5.5	9.0	8.10	d
	X	0112930101	2001-12-10	MOS1	Thin	23.0	11.2	9.0	2.91	d
	X	0112930101	2001-12-10	MOS2	Thin	23.8	13.2	9.0	3.77	d
	C	9147	2008-08-26	ACIS-I	-	42.2	20.7	9.3	1.44	d
	C	10572	2008-08-27	ACIS-I	-	23.1	11.1	9.3	1.45	d
J0922+0638	X	0502920101	2007-11-09	PN/LW	Thin	15.5	14.2	1.7	9.50	d
	X	0502920101	2007-11-09	MOS1	Thin	25.2	24.7	1.7	1.83	d
	X	0502920101	2007-11-09	MOS2	Thin	24.9	23.5	1.7	2.64	d
J0940-5428	C	9077	2008-08-20	ACIS-I	-	10.2	9.1	0.8	0.34	ul
J0943+1631	X	0046940201	2001-05-07	MOS1	Medium	5.2	1.8	11.6	1.72	ul
	X	0046940201	2001-05-07	MOS2	Medium	4.9	2.0	11.6	1.54	ul
	X	0046940401	2001-11-02	MOS1	Medium	14.9	5.3	14.7	0.58	ul
	X	0046940401	2001-11-02	MOS2	Medium	14.7	4.4	14.7	0.71	ul
J1001-5939	C	12561	2011-10-08	ACIS-S	-	19.0	17.2	0.2	0.24	ul
J1038+0032	C	13801	2012-01-18	ACIS-S	-	3.5	3.5	0.2	0.89	ul
J1055-6022	X	0600030101	2010-01-21	PN/FF	Medium	16.5	10.5	4.4	3.56	ul
	X	0600030101	2010-01-21	MOS1	Medium	18.9	9.2	4.4	1.90	ul
	X	0600030101	2010-01-21	MOS2	Medium	20.0	11.8	4.4	1.33	ul
J1055-6028	X	0600030101	2010-01-21	PN/FF	Medium	16.5	10.8	5.5	3.52	ul
	X	0600030101	2010-01-21	MOS1	Medium	18.9	14.6	5.5	1.48	ul
	X	0600030101	2010-01-21	MOS2	Medium	20.0	14.6	5.5	1.36	ul
J1103-5403	C	12538	2011-09-08	ACIS-S	-	10.0	9.9	0.2	0.80	ul
J1104-6103	C	4380	2002-10-01	ACIS-S	-	11.9	8.0	7.6	1.55	ul
	C	2780	2002-09-29	ACIS-S	-	11.8	7.9	7.6	0.30	ul
J1105-6107	C	4380	2002-10-01	ACIS-S	-	11.9	11.5	2.0	1.15	d
	C	2780	2002-09-29	ACIS-S	-	11.8	11.4	2.0	0.53	d
J1107-5907	C	12688	2011-03-31	ACIS-S	-	5.1	5.0	0.3	1.67	ul
J1112-6103	C	6706	2006-09-16	ACIS-S	-	34.6	33.3	0.1	3.54	d
	C	8905	2007-11-10	ACIS-I	-	59.1	53.0	2.4	2.82	d

Continued on next page

Table B.2 – continued from previous page

PSR	satellite <sup>(<math>\alpha</math>)</sup>	obsID	date	instrument <sup>(<math>\beta</math>)</sup>	filter	$t_{\text{on-axis}}$	$t(\theta)$	$\theta$ <sup>(<math>\gamma</math>)</sup>	count rate <sup>(<math>\delta</math>)</sup>	flag <sup>(<math>\delta</math>)</sup>
J1157–6224	X	0503780301	2008-02-16	PN/FF	Medium	15.9	4.5	12.8	12.20	ul
	X	0503780301	2008-02-16	MOS1	Medium	18.8	5.3	12.8	3.80	ul
	X	0503780301	2008-02-16	MOS2	Medium	17.6	5.2	12.8	2.99	ul
	X	0550170101	2008-08-16	MOS1	Medium	45.3	15.0	14.2	2.51	ul
J1159–7910	X	0550170101	2008-08-16	MOS2	Medium	45.9	18.8	14.2	1.58	ul
	X	0550120601	2009-03-16	PN/FF	Medium	2.9	0.6	11.7	15.38	ul
	X	0550120601	2009-03-16	MOS1	Medium	9.7	3.0	11.7	4.30	ul
J1224–6407	X	0550120601	2009-03-16	MOS2	Medium	9.2	1.1	11.7	8.11	ul
	X	0103260901	2002-08-10	PN/FF	Medium	4.3	3.9	1.7	8.45	d
	X	0103260901	2002-08-10	MOS1	Medium	6.6	6.4	1.7	4.42	d
J1225–6408	X	0103260901	2002-08-10	MOS2	Medium	6.6	6.4	1.7	1.57	d
	X	0103260901	2002-08-10	MOS1	Medium	6.6	3.2	9.2	0.95	ul
	X	0103260901	2002-08-10	MOS2	Medium	6.6	2.7	9.2	3.64	ul
	X	0653030501	2010-08-08	MOS2	Thick	17.7	7.7	5.7	0.40	ul
J1301–6310	X	0653030601	2010-08-14	MOS1	Medium	18.5	2.4	5.7	1.28	ul
	X	0653030601	2010-08-14	MOS2	Thick	18.6	8.7	5.7	2.14	ul
	X	0653030701	2010-08-16	MOS1	Medium	18.3	4.7	5.8	3.19	ul
	X	0653030701	2010-08-16	MOS2	Thick	18.6	8.5	5.8	1.32	ul
	X	0303440101	2005-07-12	PN/LW	Thin	27.1	24.9	1.8	4.76	d
	X	0303440101	2005-07-12	MOS1	Medium	29.8	27.3	1.8	1.06	d
	X	0303440101	2005-07-12	MOS2	Medium	29.7	28.5	1.8	2.71	d
J1302–6313	X	0302340101	2005-07-14	PN/FF	Medium	24.2	11.4	11.3	3.83	d
	X	0302340101	2005-07-14	MOS1	Medium	30.1	15.0	11.3	2.72	d
	X	0302340101	2005-07-14	MOS2	Medium	30.5	16.3	11.3	2.84	d
	X	0302340101	2005-07-14	MOS1	Medium	30.0	25.6	5.2	0.74	ul
	X	0302340101	2005-07-14	MOS2	Medium	30.7	26.0	5.2	1.35	ul
	X	0303440101	2005-07-12	MOS1	Medium	29.8	19.7	5.3	0.90	ul
	X	0303440101	2005-07-12	MOS2	Medium	29.7	20.0	5.3	1.26	ul
J1303–6305	C	6098	2004-09-25	ACIS-I	-	4.7	3.8	3.9	0.76	ul
	X	0302340101	2005-07-14	MOS1	Medium	30.3	19.2	8.5	1.40	ul
	X	0302340101	2005-07-14	MOS2	Medium	30.6	17.6	8.5	1.24	ul
	X	0303440101	2005-07-12	MOS1	Medium	29.8	10.4	12.3	1.44	ul
	X	0303440101	2005-07-12	MOS2	Medium	29.8	10.5	12.3	1.59	ul
J1305–6256	C	6098	2004-09-25	ACIS-I	-	4.7	3.6	6.2	1.30	ul
J1306–6242	X	0303100201	2005-08-25	PN/FF	Medium	5.1	1.4	13.1	45.55	ul
J1309–6526	X	0303100201	2005-08-25	PN/FF	Medium	8.1	4.6	6.9	6.12	ul
	X	0303100201	2005-08-25	MOS1	Medium	7.3	4.9	6.9	2.78	ul
	X	0303100201	2005-08-25	MOS2	Medium	10.7	7.0	6.9	2.14	ul
J1317–5759	X	0090030201	2004-07-20	PN/FF	Thick	75.7	33.8	8.1	1.31	ul
	X	0090030201	2004-07-20	MOS1	Thick	84.9	39.8	8.1	0.98	ul
	X	0090030201	2004-07-20	MOS2	Thick	90.4	36.2	8.1	0.95	ul
	X	0605670201	2009-07-19	PN/FF	Thick	52.3	22.5	8.1	1.74	ul
	X	0605670201	2009-07-19	MOS1	Thick	53.7	25.0	8.1	1.11	ul
	X	0605670201	2009-07-19	MOS2	Thick	53.2	20.9	8.1	1.27	ul
	X	0406450101	2006-07-16	PN/SW	Thin	25.1	17.3	1.8	3.80	ul
J1317–6302	X	0406450101	2006-07-16	MOS1	Thin	29.7	28.7	1.8	1.36	ul
	X	0406450101	2006-07-16	MOS2	Thin	30.6	28.9	1.8	1.03	ul
	C	9049	2008-09-11	ACIS-I	-	5.1	4.1	7.9	0.69	ul
J1320–3512	C	13797	2012-03-20	ACIS-S	-	3.5	3.4	0.2	0.90	ul
J1324–6302	C	1913	2001-09-10	ACIS-S	-	5.1	3.2	11.4	2.09	ul
J1333–4449	C	13800	2012-03-28	ACIS-S	-	3.5	3.4	0.2	0.85	ul
J1339–4712	C	13799	2012-05-13	ACIS-S	-	3.5	3.4	0.2	0.85	ul
J1341–6220	X	0301740101	2005-07-26	PN/LW	Thick	35.5	32.6	1.7	3.98	d
	X	0301740101	2005-07-26	MOS1	Thick	37.3	34.1	1.7	1.98	d
	X	0301740101	2005-07-26	MOS2	Thick	36.9	35.8	1.7	1.26	d
	X	0143400201	2003-07-17	PN/LW	Thick	6.2	5.7	1.7	5.44	d
	X	0143400201	2003-07-17	MOS1	Thick	6.6	6.5	1.7	4.57	d
	X	0143400201	2003-07-17	MOS2	Thick	6.5	6.3	1.7	2.45	d
	X	0143400101	2003-02-11	PN/LW	Thick	5.3	4.9	1.7	9.78	d
	X	0143400101	2003-02-11	MOS1	Thick	4.9	4.8	1.7	2.52	d
	X	0143400101	2003-02-11	MOS2	Thick	5.3	5.0	1.7	4.29	d

Continued on next page

Table B.2 – continued from previous page

PSR	satellite <sup>(<math>\alpha</math>)</sup>	obsID	date	instrument <sup>(<math>\beta</math>)</sup>	filter	$t_{\text{on-axis}}$	$t(\theta)$	$\theta$ <sup>(<math>\gamma</math>)</sup>	count rate <sup>(<math>\delta</math>)</sup>	flag <sup>(<math>\delta</math>)</sup>
J1355–5925	X	0007422301	2001-02-08	PN/FF	Medium	12.1	3.1	12.5	7.56	ul
	X	0007422301	2001-02-08	MOS1	Medium	14.8	4.7	12.5	0.66	ul
	X	0007422301	2001-02-08	MOS2	Medium	14.6	4.6	12.5	3.21	ul
J1355–6206	C	13806	2012-05-28	ACIS-S	-	3.5	3.4	0.2	0.85	ul
J1359–6038	X	0007421101	2002-02-13	MOS1	Medium	10.3	3.4	14.6	0.90	ul
	X	0007421101	2002-02-13	MOS2	Medium	10.5	3.7	14.6	0.83	ul
J1412–6145	C	1985	2001-07-26	ACIS-I	-	9.4	8.5	0.3	0.36	ul
J1413–6141	C	1985	2001-07-26	ACIS-I	-	9.4	6.9	8.7	0.81	ul
J1425–5723	C	12686	2011-06-02	ACIS-S	-	5.1	5.0	0.3	0.62	ul
J1432–5032	X	0690210101	2012-08-10	PN/FF	Thick	11.5	7.7	3.8	2.32	ul
	X	0690210101	2012-08-10	MOS1	Thick	13.1	8.8	3.8	1.39	ul
	X	0690210101	2012-08-10	MOS2	Thick	13.1	10.4	3.8	1.68	ul
J1444–5941	C	8235	2007-10-19	ACIS-S	-	1.8	0.9	9.6	3.35	ul
J1453–6413	X	0103261001	2001-02-28	PN/SW	Medium	4.8	3.3	1.8	5.82	ul
	X	0103261001	2001-02-28	MOS1	Medium	5.7	5.6	1.8	2.35	ul
	X	0103261001	2001-02-28	MOS2	Medium	5.6	4.9	1.8	0.63	ul
J1457–5900	C	11880	2010-05-05	ACIS-S	-	10.2	9.9	0.6	0.31	ul
J1457–5902	C	11880	2010-05-05	ACIS-S	-	10.2	10.0	1.0	0.31	ul
J1507–6640	X	0551430301	2009-02-02	PN/FF	Medium	26.3	7.6	11.2	5.41	ul
	X	0551430301	2009-02-02	MOS1	Medium	30.6	9.4	11.2	2.08	ul
	X	0551430301	2009-02-02	MOS2	Medium	30.9	10.7	11.2	2.00	ul
J1511–5835	C	11881	2010-06-14	ACIS-S	-	10.0	6.7	13.0	0.46	ul
J1514–5925	X	0207050101	2004-09-14	PN/FF	Medium	4.7	0.9	9.9	35.44	ul
	X	0207050101	2004-09-14	MOS1	Medium	10.5	4.1	9.9	10.17	ul
	X	0207050101	2004-09-14	MOS2	Medium	10.6	4.6	9.9	8.28	ul
	X	0302730101	2005-08-07	PN/FF	Medium	15.9	4.7	10.1	19.55	ul
	X	0302730101	2005-08-07	MOS2	Medium	13.9	6.5	10.1	5.93	ul
J1517–4636	X	0204710901	2004-08-03	PN/FF	Medium	6.4	2.2	11.3	18.10	ul
	X	0204710901	2004-08-03	MOS1	Medium	14.1	6.6	11.3	10.31	ul
	X	0204710901	2004-08-03	MOS2	Medium	15.5	8.1	11.3	3.41	ul
J1524–5706	C	2784	2002-07-16	ACIS-I	-	28.2	21.2	8.8	0.15	ul
J1529–5611	C	12417	2011-06-22	ACIS-I	-	5.2	3.6	2.8	0.80	ul
J1535–4114	X	0652610201	2011-02-25	PN/FF	Thick	72.4	33.6	6.1	1.59	ul
	X	0652610201	2011-02-25	MOS1	Thick	102.3	80.3	6.1	0.62	ul
	X	0652610201	2011-02-25	MOS2	Thick	80.9	64.3	6.1	0.60	ul
J1538–5551	C	10509	2009-01-24	ACIS-S	-	4.6	2.8	8.8	1.12	ul
	C	9600	2008-05-24	HRC-I	-	1.2	0.9	10.6	10.56	ul
J1542–5034	C	12429	2011-10-09	ACIS-I	-	5.1	4.8	13.0	1.49	ul
J1548–4821	C	13805	2012-07-28	ACIS-S	-	3.5	3.4	0.2	0.85	ul
J1549+2113	X	0136040101	2002-02-18	PN/FF	Thin	15.6	4.4	14.2	5.82	ul
	X	0136040101	2002-02-18	MOS1	Thin	17.7	6.5	14.2	1.83	ul
	X	0136040101	2002-02-18	MOS2	Thin	17.8	5.5	14.2	2.10	ul
J1553–5456	C	1955	2001-07-15	ACIS-I	-	49.9	40.4	7.1	0.08	ul
J1554–5512	C	13767	2012-05-24	ACIS-I	-	143.5	120.8	7.1	0.03	ul
	C	13768	2012-05-22	ACIS-I	-	161.5	135.9	7.1	0.02	ul
	C	14430	2012-05-27	ACIS-I	-	37.1	31.5	7.1	0.18	ul
J1555–2341	X	0112380101	2000-08-26	PN/FF	Medium	34.8	13.8	12.6	2.21	ul
	X	0112380101	2000-08-26	MOS1	Medium	37.8	17.1	12.6	1.22	ul
	X	0112380101	2000-08-26	MOS2	Medium	39.4	12.6	12.6	1.23	ul
J1600–3053	X	0503190401	2008-02-17	MOS1	Medium	25.0	24.5	1.7	1.59	d
	X	0503190401	2008-02-17	MOS2	Medium	25.3	23.5	1.7	1.66	d
J1611–5847	C	13802	2012-05-21	ACIS-S	-	3.5	3.4	0.2	0.91	ul
J1613–5211	X	0555660101	2008-08-15	PN/FF	Medium	21.6	18.1	2.9	3.78	ul
	X	0555660101	2008-08-15	MOS1	Medium	32.3	29.1	2.9	1.20	ul
	X	0555660101	2008-08-15	MOS2	Medium	31.7	30.0	2.9	1.08	ul
J1614–5144	X	0406650101	2006-08-15	PN/EFF	Medium	19.7	14.8	3.3	2.61	ul
	X	0406650101	2006-08-15	MOS1	Medium	30.9	27.8	3.3	0.97	ul
	X	0406650101	2006-08-15	MOS2	Thin	30.7	28.2	3.3	1.04	ul
	X	0406550101	2007-02-13	PN/FF	Medium	7.7	2.9	4.5	7.73	ul
	X	0406550101	2007-02-13	MOS1	Medium	12.0	10.0	4.5	6.55	ul
	X	0406550101	2007-02-13	MOS2	Medium	11.7	10.1	4.5	1.86	ul

Continued on next page

Table B.2 – continued from previous page

PSR	satellite <sup>(<math>\alpha</math>)</sup>	obsID	date	instrument <sup>(<math>\beta</math>)</sup>	filter	$t_{\text{on-axis}}$	$t(\theta)$	$\theta$ <sup>(<math>\gamma</math>)</sup>	count rate <sup>(<math>\delta</math>)</sup>	flag <sup>(<math>\delta</math>)</sup>
J1616–5109	X	0302390101	2005-08-23	MOS1	Medium	60.8	25.7	12.3	1.45	ul
	X	0302390101	2005-08-23	MOS2	Medium	60.1	28.3	12.3	1.72	ul
J1616–5208	C	2546	2002-10-23	ACIS-S	-	41.4	30.5	11.7	0.70	ul
J1620–4927	X	0406750201	2007-02-25	PN/FF	Medium	6.0	1.3	11.5	13.71	ul
	X	0406750201	2007-02-25	MOS1	Medium	7.6	2.4	11.5	3.92	ul
	X	0406750201	2007-02-25	MOS2	Medium	3.7	0.7	11.5	11.14	ul
J1622–4944	C	10929	2009-07-10	ACIS-I	-	20.1	15.8	6.1	0.20	ul
	C	8161	2007-06-13	ACIS-S	-	2.9	2.5	3.0	1.23	ul
J1623–4949	X	0654110101	2011-02-22	MOS1	Thin	55.6	25.1	12.3	2.99	ul
	X	0654110101	2011-02-22	MOS2	Thin	55.6	27.1	12.3	1.56	ul
	C	8161	2007-06-13	ACIS-S	-	2.9	1.3	10.9	3.12	ul
J1625–4904	X	0403280201	2007-02-14	MOS1	Medium	15.2	5.3	10.2	7.59	ul
	X	0403280201	2007-02-14	MOS2	Medium	15.6	5.8	10.2	4.78	ul
J1625–4913	X	0403280201	2007-02-14	PN/FF	Medium	7.6	2.7	10.7	8.39	ul
	X	0403280201	2007-02-14	MOS1	Medium	15.2	5.8	10.7	4.49	ul
	X	0403280201	2007-02-14	MOS2	Medium	17.7	6.4	10.7	3.50	ul
J1632–4757	X	0128531101	2003-03-04	PN/LW	Medium	4.8	3.0	8.9	5.03	ul
	X	0128531101	2003-03-04	MOS2	Medium	5.0	2.8	8.9	3.61	ul
	X	0201700301	2004-08-19	PN/FF	Thin	35.2	22.8	4.0	1.92	ul
	X	0556140101	2008-08-14	PN/FF	Thin	5.5	3.6	4.0	4.86	ul
	X	0556140101	2008-08-14	MOS1	Thin	9.4	6.3	4.0	1.93	ul
	X	0556140101	2008-08-14	MOS2	Thin	9.1	6.9	4.0	1.82	ul
	X	0556140201	2008-08-16	PN/FF	Thin	2.5	1.7	3.9	11.80	ul
	X	0556140201	2008-08-16	MOS1	Thin	3.5	2.4	3.9	1.30	ul
	X	0556140201	2008-08-16	MOS2	Thin	3.5	2.8	3.9	2.08	ul
	X	0556140301	2008-08-18	PN/FF	Thin	5.0	3.3	4.0	8.47	ul
	X	0556140301	2008-08-18	MOS1	Thin	6.7	4.5	4.0	2.69	ul
	X	0556140301	2008-08-18	MOS2	Thin	6.1	4.8	4.0	4.00	ul
	X	0556140401	2008-08-20	PN/FF	Thin	8.3	5.1	4.0	3.87	ul
	X	0556140401	2008-08-20	MOS1	Thin	12.5	8.5	4.0	1.63	ul
	X	0556140401	2008-08-20	MOS2	Thin	12.5	9.9	4.0	1.48	ul
	X	0556140501	2008-08-21	PN/FF	Thin	2.0	1.3	4.0	10.54	ul
	X	0556140501	2008-08-21	MOS1	Thin	4.9	3.4	4.0	0.92	ul
	X	0556140501	2008-08-21	MOS2	Thin	4.3	3.4	4.0	0.91	ul
	X	0556140601	2008-08-22	PN/FF	Thin	10.7	5.7	4.1	3.17	ul
	X	0556140601	2008-08-22	MOS1	Thin	14.0	9.5	4.1	1.55	ul
	X	0556140601	2008-08-22	MOS2	Thin	13.4	10.4	4.1	1.49	ul
	X	0556140701	2008-08-24	PN/FF	Thin	6.2	3.3	3.9	10.42	ul
	X	0556140701	2008-08-24	MOS1	Thin	10.0	6.9	3.9	1.71	ul
	X	0556140701	2008-08-24	MOS2	Thin	9.8	7.7	3.9	1.73	ul
	X	0556140801	2008-08-26	PN/FF	Thin	8.9	4.5	4.0	3.94	ul
	X	0556140801	2008-08-26	MOS1	Thin	11.1	7.7	4.0	1.77	ul
	X	0556140801	2008-08-26	MOS2	Thin	11.2	8.8	4.0	1.56	ul
	X	0556141001	2008-09-17	PN/FF	Thin	4.2	2.5	4.0	5.02	ul
	X	0556141001	2008-09-17	MOS1	Thin	7.0	4.9	4.0	2.68	ul
	X	0556141001	2008-09-17	MOS2	Thin	6.4	5.0	4.0	0.62	ul
	C	10088	2009-06-22	ACIS-I	-	9.8	7.0	8.3	0.44	ul
	C	8155	2007-10-23	HRC-I	-	2.7	1.9	12.7	1.65	ul
J1633–4805	C	10982	2010-06-05	ACIS-S	-	100.0	65.1	8.2	0.25	ul
J1636–4803	C	9007	2008-05-27	HRC-I	-	1.2	0.9	14.3	3.57	ul
J1637–4553	X	0103261101	2002-02-23	PN/FF	Medium	4.0	3.5	1.8	14.91	ul
	X	0103261101	2002-02-23	MOS1	Medium	5.3	5.2	1.8	3.97	ul
	X	0103261101	2002-02-23	MOS2	Medium	6.2	5.8	1.8	3.88	ul
J1637–4642	C	12518	2011-06-11	ACIS-I	-	19.8	15.1	8.6	0.93	ul
J1637–4721	X	0204500201	2004-02-16	MOS1	Thin	18.1	6.6	14.4	2.18	ul
	X	0204500201	2004-02-16	MOS2	Thin	18.0	7.1	14.4	2.42	ul
	X	0204500301	2004-09-04	PN/FF	Thin	28.7	7.8	13.9	3.42	ul
	X	0204500301	2004-09-04	MOS1	Thin	32.2	5.5	13.9	4.61	ul
	X	0307170201	2005-08-19	PN/FF	Medium	42.2	18.0	12.8	2.34	ul
	X	0307170201	2005-08-19	MOS1	Medium	63.8	28.8	12.8	1.96	ul
	X	0307170201	2005-08-19	MOS2	Medium	69.9	32.0	12.8	0.91	ul

Continued on next page

Table B.2 – continued from previous page

PSR	satellite <sup>(<math>\alpha</math>)</sup>	obsID	date	instrument <sup>(<math>\beta</math>)</sup>	filter	$t_{\text{on-axis}}$	$t(\theta)$	$\theta$ <sup>(<math>\gamma</math>)</sup>	count rate <sup>(<math>\delta</math>)</sup>	flag <sup>(<math>\delta</math>)</sup>
	C	12525	2011-06-14	ACIS-I	-	19.8	18.5	13.1	1.00	ul
	C	12522	2011-06-13	ACIS-I	-	19.3	15.8	5.4	0.20	ul
	C	12523	2011-06-14	ACIS-I	-	19.3	16.0	6.6	0.19	ul
	C	12503	2011-02-05	HRC-I	-	1.2	0.8	13.8	3.64	ul
J1638–4725	C	12522	2011-06-13	ACIS-I	-	19.3	16.1	6.4	0.19	ul
J1640–4648	C	6261	2005-05-04	ACIS-S	-	10.2	9.9	0.6	0.42	ul
	C	12510	2011-06-09	ACIS-I	-	20.2	17.9	0.7	0.28	ul
	C	12513	2011-06-27	ACIS-I	-	20.4	19.2	12.7	0.88	ul
J1646–4346	X	0553110201	2009-03-09	PN/FF	Medium	2.7	1.5	2.2	21.27	ul
	X	0553110201	2009-03-09	MOS1	Medium	3.1	3.0	2.2	9.41	ul
	X	0553110201	2009-03-09	MOS2	Medium	2.8	2.7	2.2	21.95	ul
J1648–4458	X	0512180101	2008-03-21	MOS2	Medium	27.2	10.0	12.3	1.91	ul
J1648–4611	C	11836	2010-01-24	ACIS-I	-	10.2	8.7	4.9	0.35	ul
J1649–4349	C	6270	2005-10-21	HRC-I	-	4.2	4.1	0.2	0.75	ul
J1650–4341	C	13777	2012-06-22	ACIS-S	-	8.1	7.9	0.2	0.39	ul
J1652–4406	C	8145	2007-10-25	ACIS-S	-	2.2	1.0	11.2	3.13	ul
J1653–4315	C	13774	2012-07-07	ACIS-S	-	5.1	5.0	0.2	0.62	ul
J1654–4140	X	0109490101	2001-09-05	PN/FF	Thick	29.8	12.1	10.7	3.05	ul
	X	0109490101	2001-09-05	MOS1	Thick	32.9	16.4	10.7	1.01	ul
	X	0109490101	2001-09-05	MOS2	Thick	32.5	15.6	10.7	1.61	ul
	X	0109490201	2001-09-06	PN/FF	Thick	16.4	6.9	10.7	5.14	ul
	X	0109490201	2001-09-06	MOS1	Thick	19.3	9.6	10.7	1.79	ul
	X	0109490201	2001-09-06	MOS2	Thick	19.4	9.3	10.7	1.49	ul
	X	0109490301	2001-09-07	PN/FF	Thick	28.7	12.5	10.8	2.46	ul
	X	0109490301	2001-09-07	MOS1	Thick	33.2	16.6	10.8	1.24	ul
	X	0109490301	2001-09-07	MOS2	Thick	34.0	16.3	10.8	1.23	ul
	X	0109490401	2001-09-08	PN/FF	Thick	11.8	5.3	10.7	3.86	ul
	X	0109490401	2001-09-08	MOS1	Thick	19.7	10.0	10.7	2.30	ul
	X	0109490401	2001-09-08	MOS2	Thick	19.4	9.3	10.7	2.83	ul
	X	0109490501	2001-09-09	PN/FF	Thick	24.9	11.1	10.8	2.50	ul
	X	0109490501	2001-09-09	MOS1	Thick	30.9	15.5	10.8	1.46	ul
	X	0109490501	2001-09-09	MOS2	Thick	30.9	14.8	10.8	1.32	ul
	X	0109490601	2001-09-10	PN/FF	Thick	30.3	13.4	10.8	3.22	ul
	X	0109490601	2001-09-10	MOS1	Thick	32.8	16.4	10.8	1.30	ul
	X	0109490601	2001-09-10	MOS2	Thick	32.8	15.7	10.8	1.80	ul
J1658–5324	C	5372	2005-07-03	ACIS-I	-	77.2	58.6	9.6	0.22	ul
	C	12535	2011-01-25	ACIS-S	-	10.0	9.4	4.4	3.84	d
J1702–4217	C	13776	2012-06-24	ACIS-S	-	8.7	8.5	0.2	0.57	ul
J1702–4306	C	9083	2009-01-30	ACIS-I	-	9.8	9.4	3.2	0.33	ul
J1702–4310	C	9083	2009-01-30	ACIS-I	-	9.8	9.6	0.8	0.32	ul
J1703–4851	C	4446	2004-02-04	ACIS-S	-	29.8	18.2	11.9	0.57	ul
J1705–1906	X	0112200501	2002-03-14	PN/FF	Medium	3.6	3.2	1.7	9.64	ul
	X	0112200501	2002-03-14	MOS1	Medium	6.0	5.9	1.7	3.67	ul
	X	0112200501	2002-03-14	MOS2	Medium	6.2	5.7	1.7	2.76	ul
J1705–4108	X	0406750301	2007-02-25	PN/FF	Medium	5.9	5.2	2.3	2.54	ul
	X	0406750301	2007-02-25	MOS1	Medium	7.6	7.0	2.3	1.40	ul
	X	0406750301	2007-02-25	MOS2	Medium	7.4	6.4	2.3	0.48	ul
J1706–4310	C	3791	2003-06-19	HRC-I	-	1.0	0.9	8.1	3.60	ul
J1707–4053	X	0144080101	2002-09-27	PN/FF	Medium	10.9	9.6	0.9	1.94	ul
	X	0144080101	2002-09-27	MOS1	Medium	17.0	16.5	0.9	0.89	ul
	X	0144080101	2002-09-27	MOS2	Medium	17.0	16.0	0.9	1.94	ul
J1709–3626	C	12505	2011-03-06	HRC-I	-	1.1	1.0	7.7	6.23	ul
J1709–4401	X	0105470201	2000-09-11	MOS1	Medium	13.4	5.9	9.9	3.89	ul
	X	0105470201	2000-09-11	MOS2	Medium	13.4	4.8	9.9	8.16	ul
	X	0105470501	2001-08-28	MOS1	Medium	6.0	2.5	9.8	9.93	ul
	X	0105470501	2001-08-28	MOS2	Medium	6.8	2.2	9.8	10.93	ul
J1711–3826	C	13621	2012-06-30	ACIS-I	-	49.8	35.3	8.3	0.32	ul
J1712–2715	X	0206610101	2004-08-29	PN/EFF	Thin	43.3	9.6	14.1	3.30	ul
	X	0206610101	2004-08-29	MOS1	Thin	47.9	15.5	14.1	1.30	ul
	X	0206610101	2004-08-29	MOS2	Thin	47.8	15.9	14.1	1.26	ul
J1715–3859	C	8976	2008-09-22	ACIS-I	-	1.2	0.9	6.4	3.52	ul

Continued on next page

Table B.2 – continued from previous page

PSR	satellite <sup>(<math>\alpha</math>)</sup>	obsID	date	instrument <sup>(<math>\beta</math>)</sup>	filter	$t_{\text{on-axis}}$	$t(\theta)$	$\theta$ <sup>(<math>\gamma</math>)</sup>	count rate <sup>(<math>\delta</math>)</sup>	flag <sup>(<math>\delta</math>)</sup>
J1716–3720	C	9607	2008-09-20	ACIS-S	-	1.4	0.8	12.8	4.11	ul
J1717–3737	C	2785	2002-05-13	ACIS-S	-	56.5	18.0	15.2	1.15	ul
J1717–4043	C	7536	2007-10-23	HRC-I	-	1.2	1.1	4.8	4.19	ul
J1717–40433	C	7536	2007-10-23	HRC-I	-	1.2	1.1	5.0	3.56	ul
J1718–3714	C	2785	2002-05-13	ACIS-S	-	56.5	43.0	11.8	0.37	ul
	C	10768	2009-10-23	ACIS-S	-	37.7	32.5	5.0	0.10	ul
J1718–4539	X	0200680201	2004-09-22	MOS1	Medium	14.0	5.3	14.4	2.73	ul
	X	0200680201	2004-09-22	MOS2	Thick	22.6	9.1	14.4	1.59	ul
J1719–1438	X	0674950201	2012-02-20	PN/FF	Thin	3.3	2.9	1.7	5.99	ul
	X	0674950201	2012-02-20	MOS1	Thin	3.9	3.8	1.7	0.80	ul
	X	0674950201	2012-02-20	MOS2	Thin	3.9	3.5	1.7	0.87	ul
J1720–3659	C	10525	2009-02-08	ACIS-S	-	7.8	4.7	8.8	0.66	ul
J1721–1936	C	9957	2009-07-10	ACIS-S	-	16.0	6.7	2.5	0.46	ul
J1723–3659	X	0103261201	2002-02-24	MOS1	Medium	6.4	2.4	11.7	6.51	ul
	X	0103261201	2002-02-24	MOS2	Medium	6.1	2.7	11.7	3.35	ul
J1725–3546	C	10514	2009-02-06	ACIS-S	-	5.5	3.3	12.9	0.94	ul
	C	8222	2007-10-23	HRC-I	-	1.2	0.9	13.2	14.82	ul
J1726–3530	C	8154	2007-10-26	ACIS-S	-	2.3	1.5	13.3	2.01	ul
	C	10514	2009-02-06	ACIS-S	-	5.5	3.9	5.0	0.75	ul
J1730–2304	X	0650140101	2011-03-29	PN/FF	Thin	9.1	7.8	1.7	12.52	d
	X	0650140101	2011-03-29	MOS1	Thin	22.6	20.7	1.7	3.32	d
	X	0650140101	2011-03-29	MOS2	Thin	22.6	21.1	1.7	5.53	d
J1730–3350	C	9080	2008-10-27	ACIS-I	-	10.1	9.8	0.8	0.31	ul
J1730–3353	C	9080	2008-10-27	ACIS-I	-	10.1	9.0	5.5	0.82	ul
J1731–1847	X	0694710101	2012-09-01	PN/FF	Thin	21.5	18.9	1.7	5.30	ul
	X	0694710101	2012-08-31	MOS1	Medium	36.5	33.4	1.7	1.67	ul
	X	0694710101	2012-08-31	MOS2	Medium	38.3	37.2	1.7	1.75	ul
J1732–3426	X	0405680201	2007-03-21	MOS2	Medium	24.6	7.9	12.1	5.95	ul
J1733–3030	C	8686	2008-05-22	ACIS-I	-	2.2	2.0	14.1	6.54	ul
J1733–3322	X	0553850101	2009-03-09	MOS1	Medium	10.5	1.3	11.5	2.38	ul
	X	0553850101	2009-03-09	MOS2	Medium	10.6	3.8	11.5	8.10	ul
	X	0653320101	2011-03-11	MOS2	Medium	39.7	14.5	11.4	1.69	ul
	C	674	2000-08-02	HRC-I	-	15.1	13.1	6.8	0.70	ul
J1733–3716	C	12683	2011-05-06	ACIS-S	-	2.0	1.3	8.5	2.36	ul
J1735–3258	X	0654190101	2011-03-06	PN/FF	Medium	18.0	11.8	8.1	3.06	ul
	X	0654190101	2011-03-06	MOS1	Medium	21.4	15.4	8.1	1.22	ul
	X	0654190101	2011-03-06	MOS2	Medium	21.3	13.9	8.1	1.39	ul
	C	9050	2009-02-06	ACIS-I	-	4.8	3.9	8.1	0.79	ul
J1736–2843	C	9993	2009-02-03	ACIS-I	-	2.2	2.0	4.9	1.56	ul
J1739–2903	X	0304220101	2005-09-29	MOS1	Medium	6.8	3.6	10.5	0.86	ul
	X	0304220101	2005-09-29	MOS2	Medium	6.4	3.6	10.5	0.85	ul
	C	8678	2008-05-18	ACIS-I	-	2.2	1.8	7.1	1.71	ul
	C	8679	2008-05-18	ACIS-I	-	2.2	1.6	7.7	1.80	ul
J1739–3023	X	0554720101	2008-10-01	PN/LW	Medium	32.8	14.7	5.3	5.24	ul
	X	0554720101	2008-10-01	MOS1	Medium	39.3	25.1	5.3	0.96	ul
	X	0561580101	2009-03-11	MOS1	Thin	34.0	24.4	8.1	1.85	ul
	X	0561580101	2009-03-11	MOS2	Thin	33.2	21.7	8.1	1.12	ul
J1739–3049	C	2687	2002-05-07	ACIS-I	-	21.0	14.2	13.9	0.22	ul
J1739–3951	C	12685	2011-02-01	ACIS-S	-	5.1	5.0	0.3	0.62	ul
J1740–3052	X	0301730101	2006-03-05	PN/FF	Thick	55.6	25.2	10.7	1.61	ul
	X	0301730101	2006-03-05	MOS1	Thick	61.3	31.7	10.7	0.84	ul
	X	0301730101	2006-03-05	MOS2	Thick	60.7	32.9	10.7	0.95	ul
	C	11837	2010-07-24	ACIS-I	-	10.0	8.1	7.5	0.38	ul
J1741–2719	C	8667	2008-05-17	ACIS-I	-	2.2	1.7	5.9	1.83	ul
J1741–2733	C	8666	2008-05-18	ACIS-I	-	2.2	0.8	4.9	3.49	ul
J1743–3150	C	13573	2011-11-02	ACIS-I	-	2.0	0.4	9.5	7.90	ul
	C	13576	2011-11-02	ACIS-I	-	2.0	1.8	6.1	1.64	ul
J1743–3153	C	13576	2011-11-02	ACIS-I	-	2.0	1.9	0.9	1.51	ul
J1744–3130	C	8751	2008-05-15	ACIS-I	-	2.2	1.9	3.3	1.52	ul
J1744–3922	X	0304960301	2006-02-28	PN/SW	Medium	3.8	2.6	1.7	11.88	ul
	X	0304960301	2006-02-28	MOS2	Medium	4.5	4.3	1.7	2.69	ul

Continued on next page

Table B.2 – continued from previous page

PSR	satellite <sup>(<math>\alpha</math>)</sup>	obsID	date	instrument <sup>(<math>\beta</math>)</sup>	filter	$t_{\text{on-axis}}$	$t(\theta)$	$\theta$ <sup>(<math>\gamma</math>)</sup>	count rate <sup>(<math>\delta</math>)</sup>	flag <sup>(<math>\delta</math>)</sup>
J1745–3040	X	0103261301	2001-03-21	PN/FF	Medium	4.3	3.8	1.7	3.57	ul
	X	0103261301	2001-03-21	MOS1	Medium	7.3	7.2	1.7	1.69	ul
	X	0103261301	2001-03-21	MOS2	Medium	7.4	6.7	1.7	1.75	ul
J1747–2802	C	1036	2000-10-27	ACIS-S	-	35.5	22.3	9.0	0.53	ul
	C	2274	2001-07-16	ACIS-I	-	10.6	10.0	12.5	0.31	ul
J1748–3009	C	8756	2008-05-13	ACIS-I	-	2.2	1.5	10.0	1.91	ul
	C	8755	2008-05-13	ACIS-I	-	2.2	2.0	13.0	3.20	ul
	C	8744	2008-05-15	ACIS-I	-	2.2	1.9	4.0	1.49	ul
J1749–3002	C	8755	2008-05-13	ACIS-I	-	2.2	1.9	3.6	1.53	ul
J1751–2857	X	0603850201	2010-04-07	MOS1	Medium	18.6	10.0	12.1	2.96	ul
	X	0603850201	2010-04-07	MOS2	Medium	19.1	8.6	12.1	4.01	ul
	C	7562	2008-02-05	ACIS-S	-	4.8	3.0	11.2	4.39	ul
	C	8722	2008-05-13	ACIS-I	-	2.2	2.0	12.9	1.51	ul
	C	8710	2008-05-13	ACIS-I	-	2.2	1.6	1.9	3.07	ul
J1753–1914	C	13803	2012-07-18	ACIS-S	-	3.5	3.4	0.2	0.85	ul
J1754–3443	X	0300690101	2006-04-02	PN/FF	Thick	38.3	19.1	10.1	2.50	ul
	X	0300690101	2006-04-02	MOS1	Thick	42.0	23.8	10.1	1.18	ul
	X	0300690101	2006-04-02	MOS2	Thick	41.8	22.8	10.1	1.18	ul
J1755–2725	C	8717	2008-05-14	ACIS-I	-	2.2	1.5	8.7	2.00	ul
	C	8718	2008-05-14	ACIS-I	-	2.2	1.9	6.1	1.66	ul
J1757–2421	X	0112201501	2002-09-09	PN/FF	Medium	4.2	1.8	3.9	9.20	ul
	X	0112201501	2002-09-09	MOS1	Medium	5.8	5.6	3.9	2.08	ul
	X	0112201501	2002-09-09	MOS2	Medium	5.7	5.1	3.9	3.13	ul
J1759–2205	C	7471	2007-10-23	HRC-I	-	1.2	1.1	6.6	2.89	ul
	C	12506	2011-02-20	HRC-I	-	1.1	1.0	6.6	3.12	ul
J1759–2302	X	0135742301	2003-03-20	PN/FF	Medium	2.9	1.1	3.8	2.73	ul
	X	0135742301	2003-03-20	MOS1	Medium	4.0	3.7	3.8	2.42	ul
	X	0135742301	2003-03-20	MOS2	Medium	4.2	3.9	3.8	0.79	ul
J1759–2307	X	0135742301	2003-03-20	PN/FF	Medium	2.9	1.9	5.7	6.33	ul
	X	0135742301	2003-03-20	MOS1	Medium	4.0	3.2	5.7	0.96	ul
	X	0135742301	2003-03-20	MOS2	Medium	4.2	3.0	5.7	1.02	ul
J1759–3107	C	10083	2009-08-05	HRC-I	-	1.2	0.7	14.4	32.44	ul
J1801–2304	X	0135742501	2003-03-20	PN/FF	Medium	2.3	1.8	5.5	11.30	ul
	X	0135742501	2003-03-20	MOS1	Medium	3.3	2.8	5.5	1.09	ul
	X	0135742501	2003-03-20	MOS2	Medium	3.2	2.6	5.5	1.19	ul
J1804–0735	C	8949	2008-10-31	ACIS-S	-	15.2	15.0	0.2	0.37	ul
J1805–1504	X	0405390301	2007-03-03	MOS1	Medium	13.1	7.2	11.5	2.28	ul
	C	7275	2006-03-28	HRC-I	-	1.1	0.9	10.0	4.10	ul
J1806–2125	X	0405750201	2007-03-02	PN/FF	Medium	10.7	4.9	11.3	5.09	ul
	X	0405750201	2007-03-02	MOS1	Medium	14.9	8.5	11.3	3.99	ul
	X	0405750201	2007-03-02	MOS2	Medium	15.4	6.5	11.3	2.49	ul
J1808–2701	X	0692210101	2012-09-15	PN/FF	Thin	4.8	4.2	1.7	4.48	ul
	X	0692210101	2012-09-15	MOS1	Medium	16.5	15.1	1.7	1.60	ul
	X	0692210101	2012-09-15	MOS2	Medium	16.7	16.1	1.7	1.93	ul
J1809–1850	X	0152835701	2003-10-09	PN/FF	Medium	7.3	2.3	11.4	10.88	ul
	X	0152835701	2003-10-09	MOS1	Medium	9.2	4.3	11.4	4.79	ul
	X	0152835701	2003-10-09	MOS2	Medium	9.9	5.0	11.4	2.62	ul
J1809–2004	X	0152832901	2003-10-12	PN/FF	Medium	6.3	4.4	7.2	4.78	ul
	X	0152832901	2003-10-12	MOS1	Medium	7.7	6.2	7.2	1.82	ul
	X	0152832901	2003-10-12	MOS2	Medium	8.0	5.6	7.2	1.51	ul
J1810–1820	C	13775	2012-04-22	ACIS-S	-	5.1	5.0	0.2	0.97	ul
J1811–1049	C	9005	2009-02-15	HRC-I	-	1.2	1.0	9.4	7.83	ul
J1811–1835	C	8167	2007-10-26	ACIS-S	-	3.0	1.8	12.7	1.69	ul
	C	8162	2007-05-04	ACIS-S	-	2.8	1.8	8.4	5.49	ul
J1812–1910	X	0152835501	2003-09-12	MOS2	Medium	2.9	1.0	11.6	3.00	ul
J1814–1744	X	0207010101	2004-09-14	PN/FF	Medium	0.9	0.7	1.5	38.36	ul
	X	0207010101	2004-09-14	MOS1	Medium	6.0	5.7	1.5	3.60	ul
	X	0207010101	2004-09-14	MOS2	Medium	5.9	5.7	1.5	6.61	ul
J1815–1738	X	0207010101	2004-09-14	PN/FF	Medium	0.9	0.1	10.3	25.56	ul
	X	0207010101	2004-09-14	MOS1	Medium	6.0	2.6	10.3	10.08	ul
	X	0207010101	2004-09-14	MOS2	Medium	5.9	2.5	10.3	6.16	ul

Continued on next page

Table B.2 – continued from previous page

PSR	satellite <sup>(<math>\alpha</math>)</sup>	obsID	date	instrument <sup>(<math>\beta</math>)</sup>	filter	$t_{\text{on-axis}}$	$t(\theta)$	$\theta$ <sup>(<math>\gamma</math>)</sup>	count rate <sup>(<math>\delta</math>)</sup>	flag <sup>(<math>\delta</math>)</sup>
J1816–5643	C	13804	2012-04-24	ACIS-S	-	3.5	3.4	0.2	0.91	ul
J1817–3618	C	2011	2001-10-24	ACIS-S	-	29.0	28.6	0.6	0.24	ul
J1818–1448	C	5530	2005-05-23	ACIS-S	-	9.2	6.9	11.9	0.87	ul
	C	6288	2005-05-25	ACIS-S	-	5.0	3.7	11.9	0.82	ul
	C	6289	2005-05-28	ACIS-S	-	15.1	11.4	11.9	1.29	ul
J1818–1519	X	0152834901	2003-04-04	PN/FF	Medium	5.6	2.1	10.2	19.92	ul
	X	0152834901	2003-04-04	MOS1	Medium	7.6	2.8	10.2	4.31	ul
	X	0152834901	2003-04-04	MOS2	Medium	7.2	2.9	10.2	1.06	ul
J1818–1541	X	0152834801	2003-04-06	PN/FF	Medium	5.8	1.7	12.8	13.53	ul
	X	0152834801	2003-04-06	MOS1	Medium	6.8	1.9	12.8	7.97	ul
	X	0152834801	2003-04-06	MOS2	Medium	7.0	1.4	12.8	8.46	ul
J1818–1556	C	7617	2007-10-21	ACIS-S	-	5.1	4.6	6.5	0.67	ul
	C	9609	2008-02-19	ACIS-S	-	1.7	1.2	3.1	2.38	ul
J1819–1008	X	0403410101	2006-09-18	MOS1	Thin	2.6	1.4	12.2	10.90	ul
	X	0403410101	2006-09-18	MOS2	Medium	2.6	1.2	12.2	2.49	ul
	X	0403410101	2006-09-18	MOS1	Thin	44.6	23.2	12.2	1.89	ul
	X	0403410101	2006-09-18	MOS2	Medium	45.9	22.3	12.2	1.26	ul
J1819–1510	X	0505240101	2008-03-31	PN/FF	Medium	52.3	16.0	14.8	3.36	ul
	X	0505240101	2008-03-31	MOS1	Medium	65.7	24.7	14.8	2.23	ul
	X	0505240101	2008-03-31	MOS2	Medium	65.8	21.0	14.8	2.57	ul
J1821–1419	X	0004210201	2001-03-08	PN/FF	Medium	3.5	1.5	10.1	8.47	ul
	X	0004210201	2001-03-08	MOS1	Medium	6.4	3.7	10.1	0.83	ul
	X	0004210201	2001-03-08	MOS2	Medium	6.5	3.8	10.1	2.09	ul
J1821–1432	C	11835	2010-08-14	ACIS-I	-	10.0	9.0	3.5	0.34	ul
J1822–1606	C	13511	2011-07-28	HRC-I	-	1.2	1.1	1.9	2.73	ul
J1822–1617	C	13511	2011-07-28	HRC-I	-	1.2	0.8	13.7	25.76	ul
J1823–1347	X	0040140201	2002-03-23	PN/FF	Medium	11.8	8.1	6.6	4.87	ul
	X	0040140201	2002-03-23	MOS1	Medium	15.2	12.4	6.6	1.48	ul
	X	0040140201	2002-03-23	MOS2	Medium	15.4	11.7	6.6	1.85	ul
J1824–1159	X	0051940101	2001-03-08	PN/FF	Medium	4.7	1.0	10.1	12.07	ul
	X	0051940101	2001-03-08	MOS1	Medium	7.5	3.4	10.1	3.99	ul
	X	0051940101	2001-03-08	MOS2	Medium	7.6	3.5	10.1	2.57	ul
J1825–0935	X	0112201001	2002-04-08	PN/FF	Medium	1.5	1.3	1.6	36.21	d
	X	0112201001	2002-04-08	MOS1	Medium	3.8	3.8	1.6	8.08	d
	X	0112201001	2002-04-08	MOS2	Medium	4.7	4.3	1.6	4.06	d
J1825–1446	X	0505530101	2008-04-10	PN/FF	Medium	29.0	10.8	11.0	2.80	ul
	X	0505530101	2008-04-10	MOS1	Medium	33.6	13.9	11.0	1.77	ul
	X	0505530101	2008-04-10	MOS2	Medium	33.6	13.7	11.0	1.30	ul
	C	5341	2004-07-11	ACIS-I	-	18.2	15.4	5.9	0.91	ul
	C	4600	2004-07-09	ACIS-I	-	11.2	9.5	5.9	1.60	ul
J1826–1131	X	0051940301	2001-03-10	PN/FF	Medium	5.8	4.7	5.0	4.45	ul
	X	0051940301	2001-03-10	MOS1	Medium	8.5	7.3	5.0	0.42	ul
	X	0051940301	2001-03-10	MOS2	Medium	8.5	6.9	5.0	0.45	ul
J1828–1007	X	0135741201	2001-09-10	PN/FF	Medium	1.2	0.6	7.1	5.04	ul
	X	0135741201	2001-09-10	MOS1	Medium	3.1	2.3	7.1	2.74	ul
	X	0135741201	2001-09-10	MOS2	Medium	3.3	2.5	7.1	3.51	ul
	X	0135745701	2002-09-27	PN/FF	Medium	5.6	3.0	7.3	3.73	ul
	X	0135745701	2002-09-27	MOS1	Medium	7.4	4.6	7.3	0.67	ul
	X	0135745701	2002-09-27	MOS2	Medium	7.4	5.5	7.3	0.56	ul
J1828–1057	X	0104460401	2000-10-12	PN/FF	Medium	3.3	1.3	11.4	2.36	ul
	X	0104460401	2000-10-12	MOS1	Medium	6.6	2.9	11.4	1.06	ul
	X	0104460401	2000-10-12	MOS2	Medium	7.6	3.2	11.4	3.83	ul
	X	0135747001	2003-09-15	PN/FF	Medium	4.1	1.6	11.5	8.64	ul
	X	0135747001	2003-09-15	MOS1	Medium	6.4	2.9	11.5	1.07	ul
	X	0135747001	2003-09-15	MOS2	Medium	6.5	2.7	11.5	1.16	ul
J1828–1101	X	0104460401	2000-10-12	PN/FF	Medium	3.3	2.2	6.8	5.30	ul
	X	0104460401	2000-10-12	MOS1	Medium	6.6	4.2	6.8	2.02	ul
	X	0104460401	2000-10-12	MOS2	Medium	6.7	3.6	6.8	0.86	ul
	X	0135747001	2003-09-15	PN/FF	Medium	4.1	2.3	6.9	9.05	ul
	X	0135747001	2003-09-15	MOS1	Medium	6.4	4.0	6.9	2.11	ul
	X	0135747001	2003-09-15	MOS2	Medium	6.5	3.3	6.9	0.95	ul

Continued on next page

Table B.2 – continued from previous page

PSR	satellite <sup>(<math>\alpha</math>)</sup>	obsID	date	instrument <sup>(<math>\beta</math>)</sup>	filter	$t_{\text{on-axis}}$	$t(\theta)$	$\theta$ <sup>(<math>\gamma</math>)</sup>	count rate <sup>(<math>\delta</math>)</sup>	flag <sup>(<math>\delta</math>)</sup>
J1830–1059	X	0135745901	2002-10-03	MOS1	Medium	8.9	3.0	12.3	1.02	ul
	X	0135745901	2002-10-03	MOS2	Medium	7.6	2.9	12.3	8.33	ul
J1831–0952	X	0135741701	2002-03-29	PN/FF	Medium	3.3	1.5	11.5	14.95	ul
	X	0135741701	2002-03-29	MOS1	Medium	6.8	3.4	11.5	6.72	ul
	X	0135741701	2002-03-29	MOS2	Medium	6.9	3.3	11.5	3.98	ul
J1831–1223	X	0601270501	2010-03-11	PN/FF	Thin	20.7	9.5	9.9	3.24	ul
	X	0601270501	2010-03-11	MOS1	Thin	28.3	4.2	9.9	3.31	ul
	X	0601270501	2010-03-11	MOS2	Thin	28.8	16.2	9.9	2.33	ul
	C	9055	2008-04-27	ACIS-I	-	4.8	3.6	10.3	0.87	ul
J1832+0029	C	9145	2007-10-19	ACIS-S	-	20.1	19.8	0.3	0.20	ul
	C	12556	2011-03-28	ACIS-S	-	23.0	22.7	0.3	0.18	ul
J1832–0836	X	0511010801	2007-10-16	PN/FF	Medium	25.3	4.7	5.0	8.26	ul
	X	0511010801	2007-10-15	MOS1	Medium	28.3	20.7	5.0	0.96	ul
	X	0511010801	2007-10-15	MOS2	Medium	28.7	22.6	5.0	1.74	ul
J1832–1021	X	0122700401	2000-04-15	PN/FF	Medium	15.4	4.0	10.1	7.89	ul
	X	0122700401	2000-04-15	MOS1	Medium	15.4	5.9	10.1	2.79	ul
	X	0122700401	2000-04-15	MOS2	Medium	15.5	5.7	10.1	2.93	ul
J1833–1055	X	0122700201	2000-04-09	PN/FF	Medium	24.5	8.7	13.8	2.39	ul
J1835–1106	C	9082	2008-10-27	ACIS-I	-	10.1	9.0	0.8	0.34	ul
J1837–0559	C	1986	2001-07-02	ACIS-S	-	9.1	5.4	9.5	0.57	ul
J1837–0604	C	1986	2001-07-02	ACIS-S	-	9.1	8.5	5.1	1.48	ul
J1837–0653	X	0400910301	2006-10-18	MOS2	Medium	8.5	3.3	11.9	2.88	ul
	X	0400910401	2006-10-18	PN/FF	Medium	7.5	3.1	11.6	5.21	ul
	X	0400910401	2006-10-18	MOS1	Medium	8.8	4.1	11.6	0.75	ul
	X	0400910401	2006-10-18	MOS2	Medium	8.8	4.4	11.6	0.70	ul
	X	0552950101	2008-10-16	MOS1	Medium	56.6	26.4	13.7	1.13	ul
	X	0552950101	2008-10-16	MOS2	Medium	58.3	24.5	13.7	1.07	ul
	C	6719	2006-08-19	ACIS-I	-	20.2	16.0	7.1	0.18	ul
	C	7545	2007-05-28	HRC-I	-	1.2	0.9	11.7	13.97	ul
J1838–0537	X	0690010101	2012-09-13	PN/FF	Medium	12.8	5.2	13.1	4.52	ul
	X	0690010101	2012-09-13	MOS1	Medium	23.3	11.0	13.1	2.24	ul
	X	0690010101	2012-09-13	MOS2	Medium	23.8	10.3	13.1	2.36	ul
J1838–0549	C	7493	2008-03-09	ACIS-I	-	19.5	18.8	11.6	0.96	ul
J1840–1419	C	12463	2011-02-20	ACIS-S	-	29.4	10.1	0.3	0.31	ul
J1841–0345	C	9084	2008-08-22	ACIS-I	-	10.1	9.1	0.8	0.54	ul
J1841–0500	C	729	2000-07-23	ACIS-S	-	29.6	20.4	3.2	0.15	ul
	C	6732	2006-07-30	ACIS-S	-	25.2	18.6	3.1	0.17	ul
J1841–0524	C	7552	2008-03-03	ACIS-I	-	19.1	16.7	3.9	0.71	ul
J1842–0359	X	0302970301	2006-04-13	PN/FF	Medium	22.1	13.0	4.7	7.92	ul
	X	0302970301	2006-04-13	MOS1	Medium	26.1	12.0	4.7	4.46	ul
	X	0302970301	2006-04-13	MOS2	Medium	26.5	14.2	4.7	2.38	ul
J1843–0137	X	0301880501	2006-04-07	PN/FF	Medium	6.6	2.0	9.0	29.44	ul
	X	0301880501	2006-04-07	MOS1	Medium	12.7	5.8	9.0	7.80	ul
	X	0301880501	2006-04-07	MOS2	Medium	14.0	6.6	9.0	5.64	ul
J1843–0355	C	2298	2001-05-20	ACIS-I	-	99.9	74.7	6.5	0.04	ul
J1843–0408	C	949	2000-02-25	ACIS-I	-	41.8	37.7	5.2	0.21	ul
	C	1523	2000-02-24	ACIS-I	-	58.5	54.1	5.1	0.13	ul
	C	8169	2008-02-29	ACIS-S	-	3.2	1.8	13.5	3.78	ul
J1843–1113	C	9114	2008-10-31	HRC-S	-	20.1	19.9	0.3	1.45	d
J1844–0244	X	0602350101	2010-04-14	MOS2	Medium	50.4	16.8	10.8	2.35	ul
	X	0602350201	2010-04-16	MOS2	Medium	42.0	14.5	10.8	1.49	ul
	C	1964	2002-03-03	HRC-I	-	19.7	14.4	12.0	3.11	ul
	C	3897	2003-09-14	ACIS-S	-	11.9	7.2	13.0	0.43	ul
	C	7583	2007-11-05	ACIS-S	-	5.2	2.5	14.2	1.22	ul
	C	7582	2007-09-18	ACIS-S	-	5.1	2.8	14.1	1.10	ul
	C	7579	2007-04-22	ACIS-S	-	5.0	3.7	10.7	0.83	ul
J1844–0256	C	11801	2010-06-17	ACIS-I	-	30.0	20.4	9.0	0.46	ul
	C	1964	2002-03-03	HRC-I	-	19.7	19.4	0.5	0.16	ul
	C	6659	2006-07-27	ACIS-S	-	15.2	10.9	2.3	0.28	ul
	C	6658	2006-02-21	ACIS-S	-	15.1	13.7	1.1	0.23	ul
	C	3897	2003-09-14	ACIS-S	-	11.9	11.7	1.5	0.40	ul

Continued on next page

Table B.2 – continued from previous page

PSR	satellite <sup>(<math>\alpha</math>)</sup>	obsID	date	instrument <sup>(<math>\beta</math>)</sup>	filter	$t_{\text{on-axis}}$	$t(\theta)$	$\theta$ <sup>(<math>\gamma</math>)</sup>	count rate <sup>(<math>\delta</math>)</sup>	flag <sup>(<math>\delta</math>)</sup>
	C	7583	2007-11-05	ACIS-S	-	5.2	4.8	2.7	0.65	ul
	C	7581	2007-08-04	ACIS-S	-	5.1	5.0	2.4	0.98	ul
	C	7582	2007-09-18	ACIS-S	-	5.1	4.0	2.6	1.19	ul
	C	7579	2007-04-22	ACIS-S	-	5.0	5.0	0.9	0.62	ul
	C	7580	2007-06-08	ACIS-S	-	4.8	4.8	0.8	0.61	ul
	C	7578	2007-02-19	ACIS-S	-	4.7	4.6	1.2	0.66	ul
J1844–0310	C	11801	2010-06-17	ACIS-I	-	30.0	25.0	6.4	0.24	ul
	C	11232	2009-08-11	ACIS-I	-	29.9	25.5	4.4	0.25	ul
	C	3897	2003-09-14	ACIS-S	-	11.9	7.3	13.3	0.42	ul
	C	7582	2007-09-18	ACIS-S	-	5.1	3.7	12.2	0.85	ul
	C	8163	2007-05-24	ACIS-S	-	2.8	2.5	5.6	1.16	ul
J1844–0433	X	0306170401	2006-04-03	PN/FF	Medium	17.2	6.9	5.5	4.16	ul
	X	0306170401	2006-04-03	MOS1	Medium	18.5	11.6	5.5	1.85	ul
	X	0306170401	2006-04-03	MOS2	Medium	19.0	12.4	5.5	1.30	ul
J1845–0256	C	11801	2010-06-17	ACIS-I	-	30.0	25.6	6.1	0.18	ul
	C	11232	2009-08-11	ACIS-I	-	29.9	24.5	7.8	0.16	ul
	C	1964	2002-03-03	HRC-I	-	19.7	18.9	3.6	0.16	ul
	C	3897	2003-09-14	ACIS-S	-	11.9	8.9	2.7	0.55	ul
	C	7581	2007-08-04	ACIS-S	-	5.1	4.9	2.2	0.62	ul
	C	7583	2007-11-05	ACIS-S	-	5.2	5.0	1.4	0.62	ul
	C	7582	2007-09-18	ACIS-S	-	5.1	4.9	1.5	0.91	ul
	C	7579	2007-04-22	ACIS-S	-	5.0	4.7	4.9	0.84	ul
	C	7580	2007-06-08	ACIS-S	-	4.8	4.5	4.8	0.97	ul
	C	7578	2007-02-19	ACIS-S	-	4.7	4.3	4.8	0.72	ul
J1845–0434	X	0306170401	2006-04-03	PN/FF	Medium	17.2	8.8	9.8	3.78	ul
	X	0306170401	2006-04-03	MOS1	Medium	18.5	11.3	9.8	1.68	ul
	X	0306170401	2006-04-03	MOS2	Medium	19.0	9.3	9.8	2.14	ul
	C	7505	2008-02-27	ACIS-S	-	5.0	1.7	8.3	2.75	ul
J1846+0919	C	13793	2012-06-12	ACIS-S	-	15.1	14.9	0.1	0.21	ul
J1846–0257	C	748	2000-10-15	ACIS-S	-	37.8	30.4	3.1	0.17	ul
	C	6686	2006-06-07	ACIS-S	-	55.3	52.9	1.7	0.09	ul
	C	7337	2006-06-05	ACIS-S	-	17.8	17.0	1.7	0.25	ul
	C	7338	2006-06-09	ACIS-S	-	40.1	38.4	1.7	0.08	ul
	C	7339	2006-06-12	ACIS-S	-	45.1	43.1	1.7	0.07	ul
J1847–0130	X	0207010201	2004-10-22	PN/FF	Medium	16.9	14.8	1.7	1.47	ul
J1848–0055	C	2786	2002-08-03	ACIS-S	-	61.6	39.0	9.7	0.23	ul
J1848–0123	C	6587	2006-08-15	ACIS-S	-	46.5	29.9	9.1	0.26	ul
J1848–1952	X	0653300101	2011-03-16	PN/LW	Thin	18.2	16.6	1.8	2.56	ul
	X	0653300101	2011-03-16	MOS1	Thin	36.2	35.6	1.8	1.23	ul
	X	0653300101	2011-03-16	MOS2	Thin	37.5	35.5	1.8	0.77	ul
	X	0554140401	2009-03-15	PN/LW	Thin	11.3	10.2	1.8	12.77	ul
	X	0554140401	2009-03-15	MOS1	Thin	9.7	9.2	1.8	2.96	ul
	X	0554140401	2009-03-15	MOS2	Thin	10.8	9.7	1.8	2.78	ul
J1850–0026	X	0136030101	2003-09-25	MOS1	Medium	17.1	15.5	1.3	1.81	ul
	X	0136030101	2003-09-25	MOS2	Medium	17.2	16.2	1.3	1.19	ul
J1850–0031	X	0136030101	2003-09-25	MOS1	Medium	17.2	9.2	7.0	1.51	ul
	X	0136030101	2003-09-25	MOS2	Medium	17.1	7.5	7.0	1.00	ul
J1852+0008	X	0017740401	2003-10-05	PN/FF	Medium	23.3	6.3	13.5	8.25	ul
	X	0017740501	2003-10-21	PN/FF	Medium	17.9	4.9	13.3	4.26	ul
J1852+0031	X	0204970201	2004-10-18	MOS1	Medium	30.8	17.5	8.2	1.06	ul
	X	0204970201	2004-10-18	MOS2	Medium	30.4	19.8	8.2	0.95	ul
	X	0204970301	2004-10-23	MOS1	Medium	30.6	18.4	8.2	1.40	ul
	X	0204970301	2004-10-23	MOS2	Medium	30.6	18.8	8.2	1.43	ul
	X	0400390201	2006-10-08	MOS2	Medium	28.1	18.5	8.0	1.01	ul
	X	0400390301	2007-03-20	MOS1	Medium	33.1	16.3	9.9	1.23	ul
	X	0400390301	2007-03-20	MOS2	Medium	33.8	15.2	9.9	1.36	ul
	X	0550670201	2008-09-19	MOS2	Medium	21.8	14.3	7.8	1.26	ul
	X	0550670301	2008-09-21	MOS2	Medium	30.7	20.2	7.8	1.03	ul
	X	0550670401	2008-09-23	MOS2	Medium	36.0	23.6	7.8	2.00	ul
	X	0550670501	2008-09-29	MOS2	Medium	33.3	21.9	7.8	1.01	ul
	X	0550670601	2008-10-11	MOS2	Medium	36.0	23.5	8.0	1.51	ul

Continued on next page

Table B.2 – continued from previous page

PSR	satellite <sup>(<math>\alpha</math>)</sup>	obsID	date	instrument <sup>(<math>\beta</math>)</sup>	filter	$t_{\text{on-axis}}$	$t(\theta)$	$\theta$ <sup>(<math>\gamma</math>)</sup>	count rate <sup>(<math>\delta</math>)</sup>	flag <sup>(<math>\delta</math>)</sup>
	X	0550671001	2009-03-16	MOS1	Medium	22.5	10.3	9.9	1.74	ul
	X	0550671001	2009-03-16	MOS2	Medium	24.8	11.3	9.9	1.44	ul
	X	0550670901	2009-03-17	MOS1	Medium	25.5	12.0	9.9	1.52	ul
	X	0550670901	2009-03-17	MOS2	Medium	25.3	11.4	9.9	2.39	ul
	X	0550671201	2009-03-23	MOS1	Medium	17.8	9.0	9.9	2.98	ul
	X	0550671201	2009-03-23	MOS2	Medium	22.4	10.0	9.9	1.88	ul
	X	0550671101	2009-03-25	MOS1	Medium	7.5	3.8	9.8	0.81	ul
	X	0550671101	2009-03-25	MOS2	Medium	8.7	3.9	9.8	0.80	ul
	X	0550671301	2009-04-04	MOS1	Medium	22.2	11.4	9.8	2.47	ul
	X	0550671301	2009-04-04	MOS2	Medium	22.9	10.6	9.8	3.24	ul
	X	0550671901	2009-04-10	MOS1	Medium	16.7	8.6	9.7	1.94	ul
	X	0550671901	2009-04-10	MOS2	Medium	17.5	8.2	9.7	1.75	ul
	X	0550671801	2009-04-22	MOS1	Medium	28.5	14.5	9.6	1.27	ul
	X	0550671801	2009-04-22	MOS2	Medium	28.3	14.0	9.6	1.78	ul
	C	1982	2001-07-31	ACIS-I	-	29.9	23.8	8.3	0.46	ul
J1852-0118	X	0652760201	2010-09-20	PN/FF	Medium	25.0	9.2	12.1	4.37	ul
	X	0652760201	2010-09-20	MOS1	Medium	26.4	11.1	12.1	1.74	ul
	X	0652760201	2010-09-20	MOS2	Medium	26.3	9.4	12.1	1.85	ul
J1852-0127	X	0652760201	2010-09-20	PN/FF	Medium	25.0	17.8	2.8	2.47	ul
	X	0652760201	2010-09-20	MOS1	Medium	26.3	23.5	2.8	1.64	ul
	X	0652760201	2010-09-20	MOS2	Medium	26.4	24.5	2.8	1.03	ul
J1853+1303	X	0503190301	2008-04-20	MOS1	Medium	14.8	14.6	1.7	2.00	ul
	X	0503190301	2008-04-20	MOS2	Medium	18.5	17.7	1.7	1.44	ul
J1856+0102	X	0112201101	2003-03-27	PN/FF	Medium	2.4	0.9	13.7	3.59	ul
	X	0112201101	2003-03-27	MOS1	Medium	3.3	1.4	13.7	2.20	ul
	X	0112201101	2003-03-27	MOS2	Medium	3.9	1.5	13.7	2.08	ul
	X	0551060101	2009-04-24	PN/FF	Medium	47.0	15.7	13.7	3.37	ul
	X	0551060101	2009-04-24	MOS1	Medium	67.0	25.3	13.7	1.78	ul
	X	0551060101	2009-04-24	MOS2	Medium	67.3	22.6	13.7	1.16	ul
J1901+0124	C	12500	2011-03-07	HRC-I	-	1.1	1.1	3.5	3.83	ul
J1901+0510	X	0136030201	2003-09-21	MOS1	Medium	13.8	5.6	12.5	2.26	ul
	X	0136030201	2003-09-21	MOS2	Medium	15.3	5.9	12.5	3.45	ul
J1905+0709	C	8147	2007-07-12	ACIS-S	-	2.2	1.3	11.6	1.85	ul
J1905+0902	C	3793	2003-05-26	ACIS-I	-	13.5	12.1	0.2	0.25	ul
J1906+0746	C	7618	2007-08-10	ACIS-I	-	32.0	28.2	0.8	0.11	ul
J1906+0912	C	1954	2001-06-17	ACIS-I	-	30.1	20.8	13.0	1.23	ul
	C	6731	2006-06-04	ACIS-I	-	25.0	18.1	13.0	0.17	ul
J1907+0534	C	7049	2006-06-28	ACIS-I	-	10.1	9.0	15.3	0.34	ul
J1907+0918	C	1954	2001-06-17	ACIS-I	-	30.1	27.1	2.4	0.11	ul
	C	3449	2002-03-11	ACIS-S	-	2.7	2.6	2.3	1.11	ul
	C	6731	2006-06-04	ACIS-I	-	25.0	14.4	2.4	0.22	ul
J1908+0734	C	9614	2008-02-28	ACIS-S	-	1.5	0.5	11.5	7.74	ul
J1908+0839	C	8223	2007-06-26	ACIS-S	-	3.5	2.2	7.7	1.43	ul
J1908+0916	C	3481	2002-04-15	ACIS-S	-	1.1	0.7	9.2	4.17	ul
J1911-1114	X	0406620201	2007-04-27	MOS1	Medium	52.5	51.5	1.8	3.35	d
	X	0406620201	2007-04-27	MOS2	Medium	51.7	48.7	1.8	3.59	d
J1913+0446	X	0075140401	2004-09-30	PN/FF	Medium	29.7	13.2	10.4	3.10	ul
	X	0075140401	2004-09-30	MOS1	Medium	31.8	13.5	10.4	1.79	ul
	X	0075140401	2004-09-30	MOS2	Medium	31.6	17.0	10.4	2.20	ul
J1913+1011	C	3854	2003-07-15	ACIS-S	-	19.8	18.1	0.6	0.33	ul
J1921+2153	X	0670940101	2012-03-20	PN/FF	Thin	4.1	3.6	1.7	7.03	ul
	X	0670940101	2012-03-20	MOS1	Thin	8.2	7.5	1.7	2.10	ul
	X	0670940101	2012-03-20	MOS2	Thin	8.6	8.3	1.7	1.50	ul
J1928+1746	C	9081	2008-03-01	ACIS-I	-	10.0	9.0	0.8	0.34	ul
J1933+2421	C	7335	2006-07-20	ACIS-S	-	9.4	9.2	0.1	0.53	ul
J1933-6211	C	9115	2007-12-09	HRC-S	-	20.2	19.9	0.3	1.68	d
J1954+2836	C	12148	2011-12-26	ACIS-I	-	10.0	0.6	0.9	5.32	ul
J1954+2923	C	12684	2010-12-22	ACIS-S	-	5.1	5.0	0.3	0.62	ul
J2005+3547	X	0556260301	2009-04-16	PN/FF	Medium	43.5	21.2	7.1	2.05	ul
	X	0556260301	2009-04-16	MOS1	Medium	50.0	25.3	7.1	1.03	ul
	X	0556260301	2009-04-16	MOS2	Medium	51.0	28.2	7.1	1.56	ul

Continued on next page

Table B.2 – continued from previous page

PSR	satellite <sup>(α)</sup>	obsID	date	instrument <sup>(β)</sup>	filter	$t_{\text{on-axis}}$	$t(\theta)$	$\theta$ <sup>(γ)</sup>	count rate <sup>(δ)</sup>	flag <sup>(δ)</sup>
J2007+2722	C	6438	2006-12-10	ACIS-I	-	22.9	17.8	5.8	0.17	ul
	C	7254	2006-01-07	ACIS-I	-	21.1	17.9	5.9	0.17	ul
	C	8492	2007-01-29	ACIS-I	-	51.1	47.6	6.0	0.06	ul
J2017+0603	C	12537	2011-07-30	ACIS-S	-	10.0	9.9	0.3	2.94	d
J2129-5721	X	0406620401	2007-04-19	MOS1	Medium	55.4	54.4	1.7	1.60	ul
	X	0406620401	2007-04-19	MOS2	Medium	55.6	53.6	1.7	0.72	ul
J2144-3933	X	0604550101	2009-10-24	PN/FF	Thin	18.0	15.4	1.7	3.22	ul
	X	0604550101	2009-10-23	MOS1	Thin	28.1	27.6	1.7	0.89	ul
	X	0604550101	2009-10-23	MOS2	Thin	28.0	27.0	1.7	0.91	ul
J2222-0137	C	12237	2010-09-26	ACIS-S	-	30.0	27.2	0.3	1.43	d
J2235+1506	C	13798	2011-12-30	ACIS-S	-	3.5	3.4	0.2	0.91	ul
J2238+5903	C	13286	2012-04-21	ACIS-I	-	10.0	8.8	4.1	5.32	ul

**Notes.** <sup>(α)</sup> C:Chandra X:XMM-Newton; <sup>(β)</sup> in the case of XMM-Newton EPIC-PN observations the used observation mode is added (EFF: Extended Full Frame; FF: Full Frame; LW: Large Window; SW: Small Window) <sup>(γ)</sup> off-axis angle; <sup>(δ)</sup> If flagged with *ul* than  $2\sigma$  upper limit on count rate, otherwise see text.

### B.3 Upper limits

Table B.3

PSR	DM pc cm <sup>-3</sup>	P ms	log(Age) yrs	log( $\dot{E}$ ) erg s <sup>-1</sup>	$N_{\text{H}}/N_{\text{H}}^{\text{AB}}$ 10 <sup>21</sup> cm <sup>-2</sup>	d kpc	$f_{0.1-2 \text{ keV}}^{\text{PL}}$ erg s <sup>-1</sup> cm <sup>-2</sup>	log( $L_{0.1-2 \text{ keV}}^{\text{PL}}$ ) erg s <sup>-1</sup>	$\mu_{0.1-2 \text{ keV}}^{\text{PL}}$	log( $T_{\infty}$ ) K
J0134-2937	21.806	136	7.4	33.1	0.7/0.2	0.6 [2]	$4.0 \times 10^{-15}$	29.5	$< 2.5 \times 10^{-4}$	5.51
J0139+5814	73.779	272	5.6	34.3	2.3/4.0	2.6 [1]	$7.8 \times 10^{-15}$	30.9	$< 3.8 \times 10^{-4}$	5.85
J0157+6212	30.21	2351	5.3	32.8	0.9/8.1	1.7 [2]	$5.3 \times 10^{-15}$	30.6	$< 6.4 \times 10^{-3}$	5.74
J0248+6021	370	217	4.8	35.3	11.4/8.2	23.2 [3]	$2.0 \times 10^{-14}$	33.5	$< 1.4 \times 10^{-2}$	6.29
J0609+2130	38.73	55	9.6	31.7	1.2/3.8	1.2 [2]	$4.1 \times 10^{-15}$	30.3	$< 3.4 \times 10^{-2}$	5.79
J0622+3749	-	333	5.3	34.4	-/0.5	-	$1.4 \times 10^{-14}$	-	-	-
J0742-2822	73.782	166	5.2	35.2	2.3/6.2	2.0 [1]	$1.7 \times 10^{-14}$	31.3	$< 1.2 \times 10^{-4}$	5.89
J0828-3417	52.2	1848	7.5	30.8	1.6/6.7	0.5 [2]	$2.3 \times 10^{-15}$	29.1	$< 1.9 \times 10^{-2}$	5.63
J0847-4316	292.5	5977	5.9	31.3	9.0/1.3	5.1 [2]	$5.3 \times 10^{-15}$	31.4	$< 1.1$	5.97
J0940-5428	134.5	87	4.6	36.3	4.2/0.2	3.0 [2]	$2.9 \times 10^{-15}$	30.6	$< 2.2 \times 10^{-6}$	5.86
J0943+1631	20.32	1087	8.3	30.4	0.6/5.9	0.8 [2]	$8.2 \times 10^{-15}$	30.1	$< 4.5 \times 10^{-1}$	5.68
J1001-5939	113	7733	6.3	30.7	3.5/4.7	2.8 [2]	$2.2 \times 10^{-15}$	30.5	$< 5.7 \times 10^{-1}$	5.87
J1038+0032	26.59	28	9.8	32.0	0.8/9.8	1.2 [2]	$5.5 \times 10^{-15}$	30.3	$< 1.6 \times 10^{-2}$	5.77
J1055-6022	590	947	5.2	33.6	18.2/6.5	12.5 [2]	$1.3 \times 10^{-14}$	32.5	$< 7.9 \times 10^{-2}$	6.15
J1055-6028	635.9	99	4.7	36.1	19.6/1.9	15.5 [2]	$6.9 \times 10^{-15}$	32.5	$< 2.4 \times 10^{-4}$	6.04
J1103-5403	103.915	3	10.2	33.6	3.2/11.7	2.5 [2]	$7.2 \times 10^{-15}$	30.9	$< 2.2 \times 10^{-3}$	5.91
J1104-6103	78.506	280	6.4	33.5	2.4/1.4	1.9 [2]	$5.5 \times 10^{-15}$	30.5	$< 1.0 \times 10^{-3}$	5.81
J1107-5907	40.2	252	8.6	31.3	1.2/1.0	1.3 [2]	$1.1 \times 10^{-14}$	30.5	$< 1.4 \times 10^{-1}$	5.79
J1157-6224	325.2	400	6.2	33.4	10.0/3.7	4.0 [1]	$1.3 \times 10^{-14}$	31.8	$< 2.4 \times 10^{-2}$	6.01
J1159-7910	59.24	525	6.5	32.9	1.8/13.3	1.9 [2]	$3.2 \times 10^{-14}$	31.3	$< 2.6 \times 10^{-2}$	5.88
J1225-6408	415.1	419	6.8	32.7	12.8/10.9	10.4 [2]	$1.7 \times 10^{-14}$	32.5	$< 6.2 \times 10^{-1}$	6.19
J1302-6313	500	967	6.4	32.4	15.4/0.9	8.9 [2]	$3.7 \times 10^{-15}$	31.7	$< 1.8 \times 10^{-1}$	5.90
J1303-6305	343	2306	7.2	30.8	10.6/11.5	6.2 [2]	$1.3 \times 10^{-14}$	31.9	$< 1.2 \times 10^{+1}$	6.12
J1305-6256	967	478	6.6	32.9	29.8/0.3	11.9 [2]	$7.6 \times 10^{-14}$	33.3	$< 2.4$	6.08
J1306-6242	480	981	6.4	32.4	14.8/0.2	8.2 [2]	$7.2 \times 10^{-15}$	31.9	$< 3.4 \times 10^{-1}$	5.85
J1309-6526	340	398	8.5	31.1	10.5/2.9	7.6 [2]	$3.2 \times 10^{-15}$	31.5	$< 2.7$	5.95
J1317-5759	145.3	2642	6.5	31.4	4.5/9.8	3.1 [2]	$8.6 \times 10^{-15}$	31.2	$< 5.3 \times 10^{-1}$	5.95
J1317-6302	678.1	261	7.6	32.4	20.9/12.1	12.1 [2]	$1.5 \times 10^{-14}$	32.6	$< 1.7$	6.19
J1320-3512	16.42	458	9.6	29.9	0.5/4.7	0.7 [2]	$5.2 \times 10^{-15}$	29.6	$< 5.4 \times 10^{-1}$	5.64
J1324-6302	497	2483	7.6	30.4	15.3/1.8	8.2 [2]	$1.5 \times 10^{-14}$	32.2	$< 7.0 \times 10^{+1}$	6.04
J1333-4449	44.3	345	10.0	29.7	1.4/0.12	1.4 [2]	$4.3 \times 10^{-15}$	30.1	$< 2.7$	5.59
J1339-4712	39.9	137	9.6	30.9	1.2/0.9	1.2 [2]	$5.4 \times 10^{-15}$	30.1	$< 1.7 \times 10^{-1}$	5.75

Continued on next page

Table B.3 – continued from previous page

PSR	DM	P	log(Age)	log( $\dot{E}$ )	$N_H/N_H^{LAB}$	d	$f_{0.1-2\text{ keV}}^{PL}$	$\log(L_{0.1-2\text{ keV}}^{PL})$	$\mu_{0.1-2\text{ keV}}^{PL}$	$\log(T_\infty)$
J1355–5925	354.8	1213	6.5	32.1	10.9/1.0	7.3 [2]	$1.0 \times 10^{-14}$	32.0	$< 7.2 \times 10^{-1}$	5.93
J1355–6206	547	276	9.1	30.8	16.9/0.2	8.3 [2]	$4.4 \times 10^{-15}$	31.7	$< 8.9$	5.87
J1359–6038	293.71	127	5.5	35.1	9.1/19.3	5.0 [1]	$3.7 \times 10^{-14}$	32.3	$< 1.8 \times 10^{-3}$	6.16
J1412–6145	514.7	315	4.7	35.1	15.9/16.3	7.8 [2]	$9.5 \times 10^{-15}$	32.0	$< 8.0 \times 10^{-4}$	6.18
J1413–6141	677	285	4.1	35.8	20.9/3.6	10.1 [2]	$1.0 \times 10^{-14}$	32.3	$< 3.2 \times 10^{-4}$	6.10
J1425–5723	43.4	353	8.4	31.3	1.3/13.6	1.2 [2]	$4.3 \times 10^{-15}$	30.0	$< 5.1 \times 10^{-2}$	5.77
J1432–5032	113	2034	6.7	31.4	3.5/17.0	2.8 [2]	$7.3 \times 10^{-15}$	31.0	$< 3.4 \times 10^{-1}$	5.91
J1444–5941	177.1	2760	6.7	31.2	5.5/17.2	3.3 [2]	$3.8 \times 10^{-14}$	31.8	$< 4.5$	6.07
J1453–6413	71.07	179	6.0	34.3	2.2/7.8	2.8 [1]	$1.0 \times 10^{-14}$	31.3	$< 1.1 \times 10^{-3}$	5.90
J1457–5900	175	1498	6.8	31.6	5.4/1.9	3.2 [2]	$2.3 \times 10^{-15}$	30.6	$< 9.6 \times 10^{-2}$	5.86
J1457–5902	477.2	390	5.7	33.9	14.7/0.14	6.8 [2]	$1.6 \times 10^{-15}$	31.1	$< 1.5 \times 10^{-3}$	5.77
J1507–6640	129.8	355	6.7	33.0	4.0/2.1	3.6 [2]	$1.0 \times 10^{-14}$	31.3	$< 2.2 \times 10^{-2}$	5.90
J1511–5835	332	301	7.1	32.7	10.2/0.4	5.0 [2]	$2.6 \times 10^{-15}$	31.0	$< 2.2 \times 10^{-2}$	5.81
J1514–5925	194.1	148	5.9	34.5	6.0/5.6	3.5 [2]	$4.5 \times 10^{-14}$	32.0	$< 2.7 \times 10^{-3}$	6.06
J1517–4636	127.0	886	6.8	32.1	3.9/14.5	3.2 [2]	$4.0 \times 10^{-14}$	32.4	$< 1.9$	6.09
J1524–5706	833	1116	4.7	34.0	25.7/1.1	11.4 [2]	$1.4 \times 10^{-15}$	31.5	$< 3.1 \times 10^{-3}$	5.99
J1529–5611	149	822	6.5	32.5	4.6/14.6	2.7 [2]	$1.1 \times 10^{-14}$	31.2	$< 4.9 \times 10^{-2}$	6.00
J1535–4114	66.28	432	6.2	33.3	2.0/17.7	2.0 [2]	$3.5 \times 10^{-15}$	30.9	$< 4.0 \times 10^{-3}$	5.86
J1538–5551	603	104	5.7	35.0	18.6/0.9	7.5 [2]	$1.9 \times 10^{-14}$	32.8	$< 5.7 \times 10^{-3}$	6.08
J1542–5034	91.0	599	6.4	32.9	2.8/6.9	3.2 [2]	$1.7 \times 10^{-14}$	32.0	$< 1.4 \times 10^{-1}$	6.06
J1548–4821	126.0	145	9.5	31.0	3.9/13.7	4.4 [2]	$8.2 \times 10^{-15}$	32.0	$< 8.8$	6.05
J1549+2113	24.8	1262	7.4	31.2	0.8/1.0	2.1 [2]	$7.8 \times 10^{-15}$	30.9	$< 4.8 \times 10^{-1}$	5.76
J1553–5456	210	1081	6.0	32.7	6.5/12.0	3.8 [2]	$1.2 \times 10^{-15}$	31.0	$< 2.1 \times 10^{-2}$	6.02
J1554–5512	450	3418	6.2	31.5	13.9/19.7	6.4 [2]	$1.1 \times 10^{-15}$	31.4	$< 8.7 \times 10^{-1}$	6.10
J1555–2341	51.901	532	7.1	32.3	1.6/15.6	1.9 [2]	$4.6 \times 10^{-15}$	30.5	$< 1.7 \times 10^{-2}$	5.77
J1611–5847	79.9	354	9.4	30.3	2.5/1.2	1.7 [2]	$6.1 \times 10^{-15}$	31.0	$< 5.7$	5.88
J1613–5211	360.1	457	5.6	33.9	11.1/5.2	6.4 [2]	$8.5 \times 10^{-15}$	32.3	$< 2.6 \times 10^{-2}$	6.10
J1614–5144	748	1534	6.5	31.9	23.1/9.0	9.9 [2]	$1.3 \times 10^{-14}$	32.9	$< 8.8$	6.21
J1616–5109	1160	1219	6.0	32.6	35.8/17.3	15.2 [2]	$2.5 \times 10^{-14}$	33.5	$< 8.2$	6.35
J1616–5208	488	1025	5.7	33.0	15.1/17.3	7.8 [2]	$1.4 \times 10^{-14}$	32.7	$< 4.7 \times 10^{-1}$	6.23
J1620–4927	-	171	5.4	34.9	-4.2	-	$1.7 \times 10^{-14}$	-	-	-
J1622–4944	755	1072	6.0	32.7	23.3/14.6	8.2 [2]	$4.0 \times 10^{-15}$	32.2	$< 2.9 \times 10^{-1}$	6.19
J1623–4949	183.3	725	5.4	33.6	5.7/1.5	3.6 [2]	$1.6 \times 10^{-14}$	32.1	$< 2.7 \times 10^{-2}$	5.97
J1625–4904	684.8	460	5.6	33.8	21.1/0.12	7.4 [2]	$2.9 \times 10^{-14}$	33.0	$< 1.3 \times 10^{-1}$	6.05
J1625–4913	720	355	5.9	33.8	22.2/13.2	7.7 [2]	$4.4 \times 10^{-14}$	33.2	$< 2.6 \times 10^{-1}$	6.28
J1632–4757	578	228	5.4	34.7	17.8/16.8	6.3 [2]	$8.0 \times 10^{-15}$	31.7	$< 1.1 \times 10^{-3}$	6.14
J1633–4805	1120	710	5.2	33.9	34.6/13.6	10.7 [2]	$4.7 \times 10^{-15}$	32.0	$< 1.1 \times 10^{-2}$	6.15
J1636–4803	503	1204	6.0	32.7	15.5/4.2	5.8 [2]	$1.3 \times 10^{-13}$	32.9	$< 1.6$	6.15
J1637–4553	193.23	118	5.8	34.9	6.0/18.3	3.2 [2]	$3.5 \times 10^{-14}$	31.8	$< 8.1 \times 10^{-4}$	6.05
J1637–4642	417.0	154	4.6	35.8	12.9/6.8	5.1 [2]	$1.5 \times 10^{-14}$	31.8	$< 1.0 \times 10^{-4}$	6.08
J1637–4721	448	1165	6.6	32.0	13.8/1.2	5.3 [2]	$2.8 \times 10^{-15}$	31.1	$< 1.2 \times 10^{-1}$	5.84
J1638–4725	552.1	763	6.4	32.6	17.0/16.1	6.1 [2]	$2.9 \times 10^{-15}$	31.3	$< 4.4 \times 10^{-2}$	6.11
J1640–4648	474	178	6.5	33.7	14.6/15.3	5.5 [2]	$1.1 \times 10^{-14}$	31.8	$< 1.0 \times 10^{-2}$	6.14
J1646–4346	490.4	231	4.5	35.6	15.1/7.2	5.8 [2]	$1.3 \times 10^{-13}$	32.9	$< 2.1 \times 10^{-3}$	6.19
J1648–4458	925	629	6.7	32.5	28.5/15.6	9.3 [2]	$4.6 \times 10^{-14}$	32.8	$< 2.3$	6.26
J1648–4611	392.9	164	5.0	35.3	12.1/2.5	5.0 [2]	$4.0 \times 10^{-15}$	31.2	$< 8.1 \times 10^{-5}$	5.99
J1649–4349	398.6	870	8.5	30.4	12.3/1.6	5.0 [2]	$1.6 \times 10^{-14}$	31.8	$< 2.7 \times 10^{+1}$	5.95
J1650–4341	673	309	8.5	31.3	20.8/14.2	7.5 [2]	$7.6 \times 10^{-15}$	31.9	$< 3.3$	6.15
J1652–4406	786	7707	7.1	29.9	24.3/15.3	8.4 [2]	$6.4 \times 10^{-14}$	32.9	$< 9.5 \times 10^{+2}$	6.27
J1653–4315	337	419	8.6	30.9	10.4/11.2	4.6 [2]	$1.0 \times 10^{-14}$	31.6	$< 4.5$	6.09
J1654–4140	307	1273	8.2	30.4	9.5/11.2	4.3 [2]	$4.6 \times 10^{-15}$	31.2	$< 5.9$	6.04
J1702–4217	629	227	8.5	31.6	19.4/2.1	7.1 [2]	$4.4 \times 10^{-15}$	31.6	$< 9.9 \times 10^{-1}$	5.97
J1702–4306	537	215	5.5	34.6	16.6/1.1	6.7 [2]	$3.2 \times 10^{-15}$	31.4	$< 6.2 \times 10^{-4}$	5.98
J1702–4310	377	240	4.2	35.8	11.6/9.7	5.2 [2]	$6.3 \times 10^{-15}$	31.5	$< 4.5 \times 10^{-5}$	6.09
J1703–4851	150.29	1396	6.6	31.9	4.6/4.2	3.0 [2]	$5.7 \times 10^{-15}$	30.9	$< 1.2 \times 10^{-1}$	5.93
J1705–1906	22.907	298	6.1	33.8	0.7/4.4	0.9 [2]	$1.4 \times 10^{-14}$	30.3	$< 3.1 \times 10^{-4}$	5.69
J1705–4108	1077	861	5.6	33.3	33.2/0.7	11.4 [2]	$4.0 \times 10^{-15}$	32.0	$< 4.2 \times 10^{-2}$	5.91
J1706–4310	656.1	616	6.2	33.0	20.2/6.8	10.0 [2]	$1.8 \times 10^{-13}$	33.5	$< 2.9$	6.27
J1707–4053	360.0	581	6.7	32.6	11.1/6.0	4.0 [1]	$6.9 \times 10^{-15}$	31.5	$< 7.7 \times 10^{-2}$	6.02

Continued on next page

Table B.3 – continued from previous page

PSR	DM	P	log(Age)	log( $\dot{E}$ )	$N_{\text{H}}/N_{\text{H}}^{\text{LAB}}$	d	$f_{0.1-2 \text{ keV}}^{\text{PL}}$	$\log(L_{0.1-2 \text{ keV}}^{\text{PL}})$	$\mu_{0.1-2 \text{ keV}}^{\text{PL}}$	$\log(T_{\infty})$
J1709–3626	393.6	447	6.5	33.0	12.1/13.4	5.9 [2]	$5.1 \times 10^{-13}$	33.5	< 3.1	6.29
J1709–4401	225.8	865	6.3	32.7	7.0/4.3	4.4 [2]	$4.8 \times 10^{-14}$	32.2	< $3.5 \times 10^{-1}$	6.08
J1711–3826	376	465	6.0	33.5	11.6/5.8	4.7 [2]	$4.8 \times 10^{-15}$	31.2	< $6.1 \times 10^{-3}$	6.01
J1712–2715	92.64	255	6.5	33.5	2.9/8.2	2.1 [2]	$7.1 \times 10^{-15}$	30.7	< $1.7 \times 10^{-3}$	5.85
J1715–3859	817	928	6.5	32.3	25.2/12.9	9.5 [2]	$8.0 \times 10^{-14}$	33.1	< 5.7	6.29
J1716–3720	682.7	630	5.7	33.5	21.1/1.8	7.9 [2]	$3.0 \times 10^{-14}$	32.5	< $1.1 \times 10^{-1}$	6.09
J1717–3737	525.8	682	6.3	32.8	16.2/1.6	5.7 [2]	$8.1 \times 10^{-15}$	31.7	< $7.0 \times 10^{-2}$	5.96
J1717–4043	452.6	397	5.7	33.9	14.0/3.5	6.3 [2]	$1.3 \times 10^{-13}$	33.0	< $1.2 \times 10^{-1}$	6.13
J1717–40433	539	349	6.5	33.2	16.6/13.4	7.6 [2]	$3.2 \times 10^{-13}$	33.5	< 2.0	6.29
J1718–3714	833	1289	5.9	32.7	25.7/2.6	9.9 [2]	$2.0 \times 10^{-15}$	31.5	< $7.1 \times 10^{-2}$	5.97
J1718–4539	254	590	6.1	33.2	7.8/14.1	6.4 [2]	$2.5 \times 10^{-14}$	32.2	< $1.2 \times 10^{-1}$	6.14
J1719–1438	36.766	5	10.1	33.2	1.1/13.1	1.2 [2]	$7.5 \times 10^{-15}$	30.3	< $1.3 \times 10^{-3}$	5.72
J1720–3659	381.6	351	8.2	31.5	11.8/1.6	4.6 [2]	$4.7 \times 10^{-15}$	31.2	< $5.7 \times 10^{-1}$	5.92
J1721–1936	75.7	1004	7.0	31.8	2.3/3.8	1.9 [2]	$3.7 \times 10^{-15}$	30.4	< $3.7 \times 10^{-2}$	5.85
J1723–3659	254.2	202	5.6	34.6	7.8/3.5	3.5 [2]	$4.9 \times 10^{-14}$	32.0	< $2.8 \times 10^{-3}$	6.04
J1725–3546	744	1032	6.0	32.7	23.0/12.7	8.7 [2]	$6.6 \times 10^{-14}$	32.9	< 1.6	6.24
J1726–3530	727	1110	4.2	34.5	22.4/10.8	8.4 [2]	$9.3 \times 10^{-15}$	32.1	< $3.3 \times 10^{-3}$	6.15
J1730–3350	259	139	4.4	36.1	8.0/12.2	3.5 [2]	$5.5 \times 10^{-15}$	31.1	< $9.7 \times 10^{-6}$	6.04
J1730–3353	256	3270	6.4	31.4	7.9/6.5	3.5 [2]	$1.3 \times 10^{-14}$	31.4	< 1.1	6.05
J1731–1847	106.56	2	9.2	34.9	3.3/4.0	2.6 [2]	$1.5 \times 10^{-14}$	31.2	< $2.2 \times 10^{-4}$	5.91
J1732–3426	513.5	332	7.1	32.6	15.8/1.4	5.8 [2]	$4.9 \times 10^{-14}$	32.4	< $6.5 \times 10^{-1}$	6.03
J1733–3030	636	362	6.5	33.1	19.6/1.8	9.5 [2]	$6.8 \times 10^{-14}$	33.0	< $7.8 \times 10^{-1}$	6.17
J1733–3322	524.0	1245	6.7	31.9	16.2/11.5	5.8 [2]	$2.8 \times 10^{-14}$	32.2	< 1.9	6.16
J1733–3716	153.5	337	5.6	34.2	4.7/12.1	2.8 [2]	$2.5 \times 10^{-14}$	31.5	< $2.1 \times 10^{-3}$	6.02
J1735–3258	754	350	5.3	34.4	23.3/11.3	9.6 [2]	$1.3 \times 10^{-14}$	32.3	< $8.5 \times 10^{-3}$	6.17
J1736–2843	331	6445	6.5	30.6	10.2/9.3	4.9 [2]	$3.0 \times 10^{-14}$	32.1	< $2.7 \times 10^{-1}$	6.15
J1739–2903	138.56	322	5.8	34.0	4.3/2.8	2.5 [2]	$1.4 \times 10^{-14}$	31.2	< $1.5 \times 10^{-3}$	5.93
J1739–3023	170.0	114	5.2	35.5	5.2/6.0	2.9 [2]	$1.2 \times 10^{-14}$	31.2	< $5.7 \times 10^{-5}$	5.97
J1739–3049	573.2	239	6.2	33.8	17.7/5.9	6.4 [2]	$3.3 \times 10^{-15}$	31.4	< $3.7 \times 10^{-3}$	6.05
J1739–3951	24.6	341	8.4	31.3	0.8/12.3	0.8 [2]	$3.8 \times 10^{-15}$	29.6	< $2.0 \times 10^{-2}$	5.68
J1740–3052	738.78	570	5.5	33.7	22.8/2.2	9.5 [2]	$3.9 \times 10^{-15}$	31.8	< $1.1 \times 10^{-2}$	5.97
J1741–2719	361.9	346	7.8	31.9	11.2/3.1	5.2 [2]	$2.2 \times 10^{-14}$	32.0	< 1.3	6.08
J1741–2733	149.2	892	8.0	30.9	4.6/9.3	2.7 [2]	$4.8 \times 10^{-14}$	31.8	< 7.3	6.07
J1743–3150	193.05	2414	5.5	32.5	6.0/2.8	3.3 [2]	$1.6 \times 10^{-14}$	31.5	< $8.8 \times 10^{-2}$	6.01
J1743–3153	505.7	193	5.5	34.8	15.6/0.8	6.6 [2]	$1.4 \times 10^{-14}$	32.0	< $1.8 \times 10^{-3}$	6.04
J1744–3130	192.9	1066	5.9	32.8	6.0/5.5	3.3 [2]	$2.2 \times 10^{-14}$	31.6	< $6.1 \times 10^{-2}$	6.06
J1744–3922	148.1	172	9.2	31.1	4.6/2.2	3.1 [2]	$2.5 \times 10^{-14}$	31.6	< 3.4	5.93
J1745–3040	88.373	367	5.7	33.9	2.7/3.3	1.9 [2]	$8.6 \times 10^{-15}$	30.7	< $6.4 \times 10^{-4}$	5.85
J1747–2802	835	2780	7.3	30.6	25.8/6.2	11.1 [2]	$5.5 \times 10^{-15}$	32.1	< $2.7 \times 10^{-1}$	6.10
J1748–3009	420.2	9	-	-	13.0/9.1	5.1 [2]	$2.2 \times 10^{-14}$	32.0	-	6.12
J1749–3002	509.4	609	6.1	33.1	15.7/0.7	5.8 [2]	$1.4 \times 10^{-14}$	31.9	< $6.0 \times 10^{-2}$	6.02
J1751–2857	42.808	3	9.7	33.9	1.3/2.7	1.1 [2]	$1.9 \times 10^{-14}$	30.6	< $5.4 \times 10^{-4}$	5.79
J1753–1914	105.3	62	8.7	32.5	3.2/0.7	2.2 [2]	$5.1 \times 10^{-15}$	30.6	< $1.3 \times 10^{-2}$	5.79
J1754–3443	187.7	361	7.0	32.7	5.8/8.9	4.1 [2]	$9.4 \times 10^{-15}$	31.4	< $5.9 \times 10^{-2}$	6.02
J1755–2725	115	261	8.5	31.5	3.5/3.1	2.4 [2]	$1.1 \times 10^{-14}$	31.0	< $3.6 \times 10^{-1}$	5.98
J1757–2421	179.454	234	5.5	34.6	5.5/3.1	4.4 [2]	$1.4 \times 10^{-14}$	31.7	< $1.2 \times 10^{-3}$	5.98
J1759–2205	177.157	460	5.8	33.6	5.5/9.8	3.6 [2]	$6.5 \times 10^{-14}$	32.2	< $3.3 \times 10^{-2}$	6.07
J1759–2302	889	810	6.1	32.9	27.4/10.3	11.6 [2]	$2.6 \times 10^{-14}$	32.8	< $7.4 \times 10^{-1}$	6.22
J1759–2307	812.6	558	6.4	32.9	25.1/11.2	10.9 [2]	$3.1 \times 10^{-14}$	32.8	< $7.3 \times 10^{-1}$	6.22
J1759–3107	128.6	1078	6.7	32.1	4.0/3.0	2.8 [2]	$9.5 \times 10^{-13}$	33.1	< $1.1 \times 10^{-1}$	6.14
J1801–2304	1073.9	415	4.8	34.8	33.1/2.9	4.0 [1]	$2.2 \times 10^{-14}$	31.8	< $1.0 \times 10^{-3}$	5.98
J1804–0735	186.316	23	8.9	33.2	5.7/3.1	5.0 [2]	$3.3 \times 10^{-15}$	31.2	< $9.6 \times 10^{-3}$	5.94
J1805–1504	225	1181	7.8	30.8	6.9/3.0	4.4 [2]	$2.5 \times 10^{-14}$	31.9	< $1.3 \times 10^{-1}$	6.01
J1806–2125	750.4	481	4.8	34.6	23.2/3.2	9.9 [2]	$1.3 \times 10^{-14}$	32.3	< $5.2 \times 10^{-3}$	6.07
J1808–2701	95	2457	5.8	32.2	2.9/2.6	1.8 [2]	$1.0 \times 10^{-14}$	30.7	< $3.2 \times 10^{-2}$	5.85
J1809–1850	598	1124	6.2	32.5	18.5/12.0	7.2 [2]	$5.4 \times 10^{-14}$	32.7	< 1.6	6.21
J1809–2004	867.1	434	6.0	33.5	26.8/0.7	10.9 [2]	$6.4 \times 10^{-15}$	32.1	< $3.7 \times 10^{-2}$	5.94
J1810–1820	452.2	153	7.7	32.8	14.0/2.8	5.6 [2]	$8.2 \times 10^{-15}$	31.7	< $7.9 \times 10^{-2}$	6.00
J1811–1049	253.3	2623	7.7	30.3	7.8/1.1	5.5 [2]	$1.5 \times 10^{-13}$	32.9	< $4.2 \times 10^{-2}$	6.06

Continued on next page

Table B.3 – continued from previous page

PSR	DM	P	log(Age)	log( $\dot{E}$ )	$N_{\text{H}}/N_{\text{H}}^{\text{LAB}}$	d	$f_{0.1-2 \text{ keV}}^{\text{PL}}$	$\log(L_{0.1-2 \text{ keV}}^{\text{PL}})$	$\mu_{0.1-2 \text{ keV}}^{\text{PL}}$	$\log(T_{\infty})$
J1811–1835	761	557	6.1	33.2	23.5/4.5	9.3 [2]	$2.1 \times 10^{-14}$	32.5	$< 2.2 \times 10^{-1}$	6.11
J1812–1910	892	430	5.3	34.3	27.5/12.4	11.2 [2]	$6.2 \times 10^{-14}$	33.1	$< 7.3 \times 10^{-2}$	6.29
J1814–1744	792	3975	4.9	32.7	24.4/11.6	9.6 [2]	$9.0 \times 10^{-14}$	33.2	$< 3.0$	6.26
J1815–1738	728	198	4.6	35.6	22.5/11.2	8.8 [2]	$9.4 \times 10^{-14}$	33.1	$< 3.2 \times 10^{-3}$	6.26
J1816–5643	52.4	217	9.3	30.9	1.6/1.1	1.5 [2]	$5.9 \times 10^{-15}$	30.4	$< 3.3 \times 10^{-1}$	5.80
J1817–3618	94.3	387	6.5	33.1	2.9/10.5	2.4 [2]	$2.1 \times 10^{-15}$	30.3	$< 1.5 \times 10^{-3}$	5.84
J1818–1448	644	281	5.9	34.0	19.9/6.9	7.4 [2]	$1.1 \times 10^{-14}$	32.0	$< 9.8 \times 10^{-3}$	6.10
J1818–1519	845	939	6.6	32.3	26.1/2.8	9.6 [2]	$3.3 \times 10^{-14}$	32.7	$< 2.6$	6.10
J1818–1541	690	551	6.0	33.4	21.3/3.0	7.8 [2]	$4.4 \times 10^{-14}$	32.7	$< 2.1 \times 10^{-1}$	6.10
J1818–1556	230	952	7.3	31.5	7.1/3.2	3.9 [2]	$4.7 \times 10^{-15}$	31.1	$< 3.8 \times 10^{-1}$	5.95
J1819–1008	404	301	6.6	33.3	12.5/12.8	7.2 [2]	$2.8 \times 10^{-14}$	32.4	$< 1.3 \times 10^{-1}$	6.18
J1819–1510	421.7	226	8.7	31.4	13.0/13.5	5.3 [2]	$1.7 \times 10^{-14}$	31.9	$< 3.1$	6.14
J1821–1419	1123	1656	4.5	33.9	34.7/10.4	11.3 [2]	$3.2 \times 10^{-14}$	32.8	$< 9.0 \times 10^{-2}$	6.22
J1821–1432	570	1915	6.8	31.5	17.6/5.3	6.5 [2]	$5.0 \times 10^{-15}$	31.6	$< 1.2$	6.06
J1822–1606	-	8437	5.6	31.3	-/3.9	-	$2.4 \times 10^{-14}$	-	-	-
J1822–1617	647	831	6.8	32.1	20.0/12.2	9.4 [2]	$2.1 \times 10^{-12}$	34.5	$< 2.5 \times 10^{+2}$	6.43
J1823–1347	1044	617	6.0	33.2	32.2/1.7	10.5 [2]	$8.5 \times 10^{-15}$	32.2	$< 1.0 \times 10^{-1}$	6.00
J1824–1159	463.4	362	6.0	33.6	14.3/1.5	5.6 [2]	$2.4 \times 10^{-14}$	32.1	$< 2.9 \times 10^{-2}$	5.97
J1825–1446	357	279	5.3	34.6	11.0/3.8	5.1 [2]	$5.7 \times 10^{-15}$	31.4	$< 6.1 \times 10^{-4}$	5.97
J1826–1131	320.58	2093	6.8	31.3	9.9/0.9	4.6 [2]	$6.3 \times 10^{-15}$	31.4	$< 1.1$	5.84
J1828–1007	302.6	153	6.6	33.8	9.3/6.3	4.4 [2]	$1.2 \times 10^{-14}$	31.6	$< 6.1 \times 10^{-3}$	6.04
J1828–1057	245	246	5.3	34.7	7.6/5.0	4.0 [2]	$1.6 \times 10^{-14}$	31.6	$< 8.0 \times 10^{-4}$	6.02
J1828–1101	607.4	72	4.9	36.2	18.7/4.4	6.6 [2]	$1.3 \times 10^{-14}$	32.0	$< 6.3 \times 10^{-5}$	6.05
J1830–1059	161.50	405	5.0	34.6	5.0/11.6	3.2 [2]	$5.0 \times 10^{-14}$	31.9	$< 2.4 \times 10^{-3}$	6.06
J1831–0952	247	67	5.1	36.0	7.6/8.3	4.1 [2]	$5.9 \times 10^{-14}$	32.2	$< 1.5 \times 10^{-4}$	6.12
J1831–1223	342	2857	6.9	31.0	10.6/12.2	5.0 [2]	$1.7 \times 10^{-14}$	31.9	$< 8.2$	6.12
J1832+0029	28.3	533	6.7	32.6	0.9/15.9	1.3 [2]	$6.8 \times 10^{-16}$	29.5	$< 7.2 \times 10^{-4}$	5.66
J1832–0836	28.18	2	9.7	34.2	0.9/1.8	1.1 [2]	$8.8 \times 10^{-15}$	30.3	$< 1.1 \times 10^{-4}$	5.70
J1832–1021	475.7	330	6.1	33.7	14.7/7.9	5.8 [2]	$2.8 \times 10^{-14}$	32.2	$< 3.5 \times 10^{-2}$	6.13
J1833–1055	543	633	7.3	31.9	16.8/12.0	7.1 [2]	$1.8 \times 10^{-14}$	32.2	$< 1.9$	6.16
J1835–1106	132.679	165	5.1	35.3	4.1/14.2	2.8 [2]	$4.5 \times 10^{-15}$	30.8	$< 3.5 \times 10^{-5}$	5.97
J1837–0559	317.8	201	6.0	34.2	9.8/14.8	5.4 [2]	$8.8 \times 10^{-15}$	31.7	$< 8.0 \times 10^{-3}$	6.10
J1837–0604	462	96	4.5	36.3	14.3/15.4	6.4 [2]	$2.9 \times 10^{-14}$	32.3	$< 1.0 \times 10^{-4}$	6.18
J1837–0653	316.1	1905	7.6	30.6	9.8/15.4	5.3 [2]	$1.0 \times 10^{-14}$	31.7	$< 1.1 \times 10^{+1}$	6.09
J1838–0537	-	145	3.7	36.8	-/14.7	-	$5.4 \times 10^{-15}$	-	-	-
J1838–0549	274	235	5.0	35.0	8.5/15.3	5.1 [2]	$1.7 \times 10^{-14}$	31.9	$< 7.9 \times 10^{-4}$	6.11
J1840–1419	19.4	6597	7.2	29.9	0.6/3.7	0.8 [2]	$1.8 \times 10^{-15}$	29.3	$< 2.5 \times 10^{-1}$	5.63
J1841–0345	194.32	204	4.7	35.4	6.0/15.7	4.8 [2]	$8.2 \times 10^{-15}$	31.5	$< 1.2 \times 10^{-4}$	6.05
J1841–0500	532	912	5.6	33.3	16.4/14.4	7.0 [2]	$1.6 \times 10^{-15}$	31.1	$< 7.4 \times 10^{-3}$	6.08
J1841–0524	289	445	4.5	35.0	8.9/13.6	5.3 [2]	$1.3 \times 10^{-14}$	31.8	$< 6.4 \times 10^{-4}$	6.11
J1842–0359	195.98	1839	7.8	30.5	6.0/10.7	4.7 [2]	$3.7 \times 10^{-14}$	32.1	$< 4.3 \times 10^{+1}$	6.08
J1843–0137	486	669	6.6	32.5	15.0/10.9	7.9 [2]	$8.9 \times 10^{-14}$	33.1	$< 4.0$	6.26
J1843–0355	797.6	132	6.3	34.2	24.6/1.8	8.8 [2]	$4.3 \times 10^{-16}$	30.8	$< 3.2 \times 10^{-4}$	5.92
J1843–0408	246	781	6.7	32.3	7.6/16.9	5.2 [2]	$2.5 \times 10^{-15}$	31.1	$< 5.9 \times 10^{-2}$	6.02
J1844–0244	429	507	5.7	33.7	13.2/15.8	6.6 [2]	$2.7 \times 10^{-14}$	32.3	$< 4.0 \times 10^{-2}$	6.17
J1844–0256	820.2	272	-	-	25.3/4.1	9.2 [2]	$1.4 \times 10^{-15}$	31.3	-	5.97
J1844–0310	836.1	525	5.9	33.4	25.8/4.8	9.2 [2]	$6.2 \times 10^{-16}$	31.0	$< 3.3 \times 10^{-3}$	5.98
J1844–0433	123.158	991	6.6	32.2	3.8/3.3	2.9 [2]	$8.3 \times 10^{-15}$	31.1	$< 7.7 \times 10^{-2}$	5.91
J1845–0256	-	6971	-	-	-/9.1	-	$4.6 \times 10^{-16}$	-	-	-
J1845–0434	230.8	486	5.8	33.6	7.1/16.2	5.1 [2]	$1.6 \times 10^{-14}$	31.8	$< 1.8 \times 10^{-2}$	6.07
J1846+0919	-	225	5.6	34.5	-/15.7	-	$9.5 \times 10^{-16}$	-	-	-
J1846–0257	237	4476	5.6	31.8	7.3/2.1	5.2 [2]	$1.3 \times 10^{-16}$	29.8	$< 8.8 \times 10^{-3}$	5.78
J1847–0130	667	6707	4.9	32.2	20.6/13.2	8.4 [2]	$1.2 \times 10^{-14}$	32.3	$< 1.1$	6.18
J1848–0055	1166	274	6.5	33.4	36.0/15.3	14.9 [2]	$4.7 \times 10^{-15}$	32.4	$< 9.4 \times 10^{-2}$	6.19
J1848–0123	159.531	659	6.3	32.9	4.9/16.7	4.4 [1]	$2.8 \times 10^{-15}$	30.9	$< 1.1 \times 10^{-2}$	5.94
J1848–1952	18.23	4308	6.5	31.1	0.6/8.8	0.8 [2]	$4.5 \times 10^{-15}$	29.6	$< 3.8 \times 10^{-2}$	5.58
J1850–0026	947	166	4.8	35.5	29.2/1.2	11.1 [2]	$9.0 \times 10^{-15}$	32.4	$< 7.8 \times 10^{-4}$	6.02
J1850–0031	895	734	7.0	32.1	27.6/12.9	10.5 [2]	$2.2 \times 10^{-14}$	32.8	$< 4.6$	6.23
J1852+0008	254.9	467	6.1	33.3	7.9/14.2	5.7 [2]	$2.8 \times 10^{-14}$	32.3	$< 9.7 \times 10^{-2}$	6.13

Continued on next page

Table B.3 – continued from previous page

PSR	DM	P	log(Age)	log( $\dot{E}$ )	$N_{\text{H}}/N_{\text{H}}^{\text{LAB}}$	d	$f_{0.1-2 \text{ keV}}^{\text{PL}}$	$\log(L_{0.1-2 \text{ keV}}^{\text{PL}})$	$\mu_{0.1-2 \text{ keV}}^{\text{PL}}$	$\log(T_{\infty})$
J1852+0031	787	2180	5.6	32.6	24.3/11.3	8.0 [1]	$4.9 \times 10^{-15}$	31.8	$< 1.6 \times 10^{-1}$	6.12
J1852-0118	286	451	6.6	32.9	8.8/2.0	5.9 [2]	$8.8 \times 10^{-15}$	31.9	$< 9.6 \times 10^{-2}$	5.96
J1852-0127	431	428	6.1	33.4	13.3/11.9	7.2 [2]	$1.3 \times 10^{-14}$	32.2	$< 5.9 \times 10^{-2}$	6.16
J1853+1303	30.5701	4	9.9	33.7	0.9/8.4	2.1 [2]	$1.0 \times 10^{-14}$	31.0	$< 2.1 \times 10^{-3}$	5.81
J1856+0102	554	620	6.9	32.3	17.1/13.4	8.5 [2]	$1.6 \times 10^{-14}$	32.4	$< 1.3$	6.20
J1901+0124	314.4	318	6.2	33.6	9.7/7.4	5.2 [2]	$2.1 \times 10^{-13}$	33.1	$< 3.4 \times 10^{-1}$	6.20
J1901+0510	429	614	5.5	33.7	13.2/12.5	7.3 [2]	$4.7 \times 10^{-14}$	32.8	$< 1.1 \times 10^{-1}$	6.23
J1905+0709	245.34	648	6.3	32.9	7.6/2.5	5.7 [2]	$1.5 \times 10^{-14}$	32.1	$< 1.6 \times 10^{-1}$	6.02
J1905+0902	433.4	218	6.0	34.1	13.4/3.0	9.1 [2]	$3.0 \times 10^{-15}$	31.8	$< 4.4 \times 10^{-3}$	6.06
J1906+0746	217.780	144	5.1	35.4	6.7/13.6	5.4 [2]	$1.8 \times 10^{-15}$	31.1	$< 4.5 \times 10^{-5}$	6.03
J1906+0912	265	775	8.0	31.0	8.2/5.7	6.4 [2]	$7.6 \times 10^{-15}$	31.9	$< 6.6$	6.09
J1907+0534	524	1138	6.8	31.9	16.2/4.2	9.6 [2]	$4.5 \times 10^{-15}$	32.0	$< 1.1$	6.09
J1907+0918	357.9	226	4.6	35.5	11.0/11.3	7.8 [2]	$1.4 \times 10^{-15}$	31.3	$< 6.4 \times 10^{-5}$	6.08
J1908+0734	11.104	212	6.6	33.5	0.3/0.5	1.0 [2]	$4.3 \times 10^{-14}$	31.0	$< 2.9 \times 10^{-3}$	5.77
J1908+0839	512.1	185	6.1	34.2	15.8/2.8	9.3 [2]	$1.2 \times 10^{-14}$	32.4	$< 1.6 \times 10^{-2}$	6.10
J1908+0916	249.8	830	8.1	30.8	7.7/3.3	5.9 [2]	$3.7 \times 10^{-14}$	32.5	$< 4.7 \times 10^{-1}$	6.12
J1913+0446	109.1	1616	5.0	33.4	3.4/13.5	3.8 [2]	$1.2 \times 10^{-14}$	31.6	$< 1.6 \times 10^{-2}$	5.96
J1913+1011	178.8	35	5.2	36.5	5.5/12.0	4.8 [2]	$3.8 \times 10^{-15}$	31.3	$< 6.9 \times 10^{-6}$	6.00
J1921+2153	12.455	1337	7.2	31.3	0.4/9.3	1.1 [2]	$5.6 \times 10^{-15}$	30.2	$< 7.1 \times 10^{-2}$	5.63
J1928+1746	176.68	68	4.9	36.2	5.5/3.5	5.8 [2]	$4.3 \times 10^{-15}$	31.5	$< 2.1 \times 10^{-5}$	6.04
J1933+2421	106.03	813	6.2	32.8	3.3/9.9	4.6 [2]	$4.7 \times 10^{-15}$	31.4	$< 3.9 \times 10^{-2}$	5.97
J1954+2836	-	92	4.8	36.0	-/11.2	-	$4.4 \times 10^{-14}$	-	-	-
J1954+2923	7.932	426	9.6	29.9	0.2/0.6	0.7 [2]	$3.3 \times 10^{-15}$	29.6	$< 4.3 \times 10^{-1}$	5.57
J2005+3547	401.6	615	7.5	31.7	12.4/0.6	30.0 [3]	$3.1 \times 10^{-15}$	32.9	$< 1.6 \times 10^{-1}$	6.06
J2007+2722	127.0	24	8.6	33.4	3.9/1.0	5.4 [2]	$3.5 \times 10^{-16}$	30.4	$< 9.3 \times 10^{-4}$	5.87
J2129-5721	31.853	3	9.5	34.2	1.0/7.2	0.4 [1]	$7.7 \times 10^{-15}$	29.5	$< 2.1 \times 10^{-5}$	5.64
J2144-3933	3.35	8509	8.4	28.5	0.10/6.4	0.2 [1]	$3.3 \times 10^{-15}$	28.1	$< 4.0 \times 10^{-1}$	5.34
J2235+1506	18.09	59	9.8	31.5	0.6/6.4	1.1 [2]	$5.3 \times 10^{-15}$	30.2	$< 4.9 \times 10^{-2}$	5.72
J2238+5903	-	162	4.4	35.9	-/6.4	-	$4.4 \times 10^{-14}$	-	-	-

**References.** [1] Verbiest et al. (2012); [2] Cordes and Lazio (2002); [3] Taylor and Cordes (1993).

# Bibliography

- Abdo, A. A., Ackermann, M., Ajello, M., Allafort, A., Baldini, L., Ballet, J., Barbiellini, G., Baring, M. G., Bastieri, D., and et al. (2011). Observations of the Young Supernova Remnant RX J1713.7-3946 with the Fermi Large Area Telescope. *ApJ*, 734:28.
- Abdo, A. A., Ackermann, M., Ajello, M., Atwood, W. B., Axelsson, M., Baldini, L., Ballet, J., Barbiellini, G., Baring, M. G., and et al. (2010a). Fermi Large Area Telescope Observations of the Crab Pulsar And Nebula. *ApJ*, 708:1254–1267.
- Abdo, A. A., Ackermann, M., Ajello, M., Baldini, L., Ballet, J., Barbiellini, G., Bastieri, D., Baughman, B. M., Bechtol, K., and et al. (2010b). PSR J1907+0602: A Radio-Faint Gamma-Ray Pulsar Powering a Bright TeV Pulsar Wind Nebula. *ApJ*, 711:64–74.
- Abdo, A. A., Ackermann, M., Atwood, W. B., Baldini, L., Ballet, J., Barbiellini, G., Baring, M. G., Bastieri, D., Baughman, B. M., and et al. (2009). Discovery of Pulsed  $\gamma$ -Rays from the Young Radio Pulsar PSR J1028-5819 with the Fermi Large Area Telescope. *ApJ*, 695:L72–L77.
- Abdo, A. A., Ajello, M., Allafort, A., Baldini, L., Ballet, J., Barbiellini, G., Baring, M. G., Bastieri, D., Belfiore, A., Bellazzini, R., and et al. et al. (2013). The Second Fermi Large Area Telescope Catalog of Gamma-Ray Pulsars. *ApJS*, 208:17.
- Acero, F., Gallant, Y., Ballet, J., Renaud, M., and Terrier, R. (2013). A new nearby pulsar wind nebula overlapping the RX J0852.0-4622 supernova remnant. *A&A*, 551:A7.
- Agüeros, M. A., Anderson, S. F., Covey, K. R., Hawley, S. L., Margon, B., Newsom, E. R., Posselt, B., Silvestri, N. M., Szkody, P., and Voges, W. (2009). X-Ray-Emitting Stars Identified from the ROSAT All-Sky Survey and the Sloan Digital Sky Survey. *ApJS*, 181:444–465.
- Aguilera, D. N., Pons, J. A., and Miralles, J. A. (2008). 2D Cooling of magnetized neutron stars. *A&A*, 486:255–271.
- Akmal, A., Pandharipande, V. R., and Ravenhall, D. G. (1998). Equation of state of nucleon matter and neutron star structure. *Phys. Rev. C*, 58:1804–1828.
- Alford, M. G., Han, S., and Prakash, M. (2013). Generic conditions for stable hybrid stars. *Phys. Rev. D*, 88(8):083013.

- Alford, M. G., Schmitt, A., Rajagopal, K., and Schäfer, T. (2008). Color superconductivity in dense quark matter. *Reviews of Modern Physics*, 80:1455–1515.
- An, H., Kaspi, V. M., Archibald, R., and Cumming, A. (2013). Spectral and Timing Properties of the Magnetar CXOU J164710.2-455216. *ApJ*, 763:82.
- Antoniadis, J., Freire, P. C. C., Wex, N., Tauris, T. M., Lynch, R. S., van Kerkwijk, M. H., Kramer, M., Bassa, C., Dhillon, V. S., and et al. (2013). A Massive Pulsar in a Compact Relativistic Binary. *Science*, 340:448.
- Arendt, J. P. N. and Eilek, J. A. (2002). Pair Creation in the Pulsar Magnetosphere. *ApJ*, 581:451–469.
- Arzoumanian, Z., Gotthelf, E. V., Ransom, S. M., Safi-Harb, S., Kothes, R., and Landecker, T. L. (2011). Discovery of an Energetic Pulsar Associated with SNR G76.9+1.0. *ApJ*, 739:39.
- Asaoka, I. and Aschenbach, B. (1994). An X-ray study of IC443 and the discovery of a new supernova remnant by ROSAT. *A&A*, 284:573–582.
- Asaoka, I., Egger, R., and Aschenbach, B. (1996). X-ray emission from a bright arc in the Cygnus region. In H. U. Zimmermann, J. Trümper, & H. Yorke, editor, *Röntgenstrahlung from the Universe*, pages 233–234.
- Aschenbach, B., Egger, R., and Trümper, J. (1995). Discovery of explosion fragments outside the Vela supernova remnant shock-wave boundary. *Nature*, 373:587–590.
- Atwood, W. B., Abdo, A. A., Ackermann, M., Althouse, W., Anderson, B., Axelsson, M., Baldini, L., Ballet, J., Band, D. L., and et al. (2009). The Large Area Telescope on the Fermi Gamma-Ray Space Telescope Mission. *ApJ*, 697:1071–1102.
- Baade, W. and Minkowski, R. (1954). On the Identification of Radio Sources. *ApJ*, 119:215.
- Baade, W. and Zwicky, F. (1934). On Super-novae. *Proceedings of the National Academy of Science*, 20:254–259.
- Badenes, C., Hughes, J. P., Bravo, E., and Langer, N. (2007). Are the Models for Type Ia Supernova Progenitors Consistent with the Properties of Supernova Remnants? *ApJ*, 662:472–486.
- Baier, V. N. and Katkov, V. M. (2007). Pair creation by a photon in a strong magnetic field. *Phys. Rev. D*, 75(7):073009.
- Barr, E. D., Guillemot, L., Champion, D. J., Kramer, M., Eatough, R. P., Lee, K. J., Verbiest, J. P. W., Bassa, C. G., Camilo, F., and et al. (2013). Pulsar searches of Fermi unassociated sources with the Effelsberg telescope. *MNRAS*, 429:1633–1642.
- Becker, W. (1995). *Untersuchung rotationsgetriebener Pulsare mit ROSAT. Auf der Suche nach kühlenden Neutronensternen (German)*. PhD thesis, LMU, Germany.

- Becker, W. (2009). X-Ray Emission from Pulsars and Neutron Stars. In Becker, W., editor, *Astrophysics and Space Science Library*, volume 357 of *Astrophysics and Space Science Library*, page 91.
- Becker, W. and Aschenbach, B. (2002). X-ray Observations of Neutron Stars and Pulsars: First Results from XMM-Newton. In Becker, W., Lesch, H., and Trümper, J., editors, *Neutron Stars, Pulsars, and Supernova Remnants*, page 64.
- Becker, W., Huang, H. H., and Prinz, T. (2010). X-ray Counterparts of Millisecond Pulsars in Globular Clusters. *ArXiv e-prints*.
- Becker, W., Jessner, A., Kramer, M., Testa, V., and Howaldt, C. (2005). A Multiwavelength Study of PSR B0628-28: The First Overluminous Rotation-powered Pulsar? *ApJ*, 633:367–376.
- Becker, W., Kramer, M., Jessner, A., Taam, R. E., Jia, J. J., Cheng, K. S., Mignani, R., Pellizzoni, A., de Luca, A., Słowikowska, A., and Caraveo, P. A. (2006). A Multiwavelength Study of the Pulsar PSR B1929+10 and Its X-Ray Trail. *ApJ*, 645:1421–1435.
- Becker, W., Prinz, T., Winkler, P. F., and Petre, R. (2012). The Proper Motion of the Central Compact Object RX J0822-4300 in the Supernova Remnant Puppis A. *ApJ*, 755:141.
- Becker, W. and Trümper, J. (1997). The X-ray luminosity of rotation-powered neutron stars. *A&A*, 326:682–691.
- Becker, W. and Trümper, J. (1999). The X-ray emission properties of millisecond pulsars. *A&A*, 341:803–817.
- Becker, W., Trümper, J., Brazier, K. T. S., and Belloni, T. (1993a). PSR J0437-4715. *IAU Circ.*, 5701:2.
- Becker, W., Trümper, J., and Ögelman, H. (1993b). Search for Cooling Neutron Stars in the ROSAT Survey. In van Riper, K. A., Epstein, R. I., and Ho, C., editors, *Isolated Pulsars*, page 104.
- Becker, W., Weisskopf, M. C., Tennant, A. F., Jessner, A., Dyks, J., Harding, A. K., and Zhang, S. N. (2004). Revealing the X-Ray Emission Processes of Old Rotation-powered Pulsars: XMM-Newton Observations of PSR B0950+08, PSR B0823+26, and PSR J2043+2740. *ApJ*, 615:908–920.
- Bell, A. R. (1978). The acceleration of cosmic rays in shock fronts. I. *MNRAS*, 182:147–156.
- Bionta, R. M., Blewitt, G., Bratton, C. B., Casper, D., and Ciocio, A. (1987). Observation of a neutrino burst in coincidence with supernova 1987A in the Large Magellanic Cloud. *Physical Review Letters*, 58:1494–1496.

- Blair, W. P., Ghavamian, P., Sankrit, R., and Danforth, C. W. (2006). Far Ultraviolet Spectroscopic Explorer Survey of Magellanic Cloud Supernova Remnants. *ApJS*, 165:480–511.
- Blandford, R. D. and Ostriker, J. P. (1978). Particle acceleration by astrophysical shocks. *ApJ*, 221:L29–L32.
- Blaschke, D., Grigorian, H., Voskresensky, D. N., and Weber, F. (2012). Cooling of the neutron star in Cassiopeia A. *Phys. Rev. C*, 85(2):022802.
- Blondin, J. M., Mezzacappa, A., and DeMarino, C. (2003). Stability of Standing Accretion Shocks, with an Eye toward Core-Collapse Supernovae. *ApJ*, 584:971–980.
- Blondin, J. M., Wright, E. B., Borkowski, K. J., and Reynolds, S. P. (1998). Transition to the Radiative Phase in Supernova Remnants. *ApJ*, 500:342.
- Bock, D. C.-J., Large, M. I., and Sadler, E. M. (1999). SUMSS: A Wide-Field Radio Imaging Survey of the Southern Sky. I. Science Goals, Survey Design, and Instrumentation. *AJ*, 117:1578–1593.
- Boese, F. G. (2000). The ROSAT point spread functions and associates. *A&AS*, 141:507–521.
- Bogdanov, S., Archibald, A. M., Hessels, J. W. T., Kaspi, V. M., Lorimer, D., McLaughlin, M. A., Ransom, S. M., and Stairs, I. H. (2011). A Chandra X-Ray Observation of the Binary Millisecond Pulsar PSR J1023+0038. *ApJ*, 742:97.
- Bogdanov, S. and Grindlay, J. E. (2009). Deep XMM-Newton Spectroscopic and Timing Observations of the Isolated Radio Millisecond Pulsar PSR J0030+0451. *ApJ*, 703:1557–1564.
- Bogdanov, S., van den Berg, M., Heinke, C. O., Cohn, H. N., Lugger, P. M., and Grindlay, J. E. (2010). A Chandra X-ray Observatory Study of PSR J1740-5340 and Candidate Millisecond Pulsars in the Globular Cluster NGC 6397. *ApJ*, 709:241–250.
- Böhringer, H., Voges, W., Huchra, J. P., McLean, B., Giacconi, R., Rosati, P., Burg, R., Mader, J., Schuecker, P., and et al. (2000). The Northern ROSAT All-Sky (NORAS) Galaxy Cluster Survey. I. X-Ray Properties of Clusters Detected as Extended X-Ray Sources. *ApJS*, 129:435–474.
- Böhringer, H. and Werner, N. (2010). X-ray spectroscopy of galaxy clusters: studying astrophysical processes in the largest celestial laboratories. *A&A Rev.*, 18:127–196.
- Borkowski, K. J., Hendrick, S. P., and Reynolds, S. P. (2006). Dense, Fe-rich Ejecta in Supernova Remnants DEM L238 and DEM L249: A New Class of Type Ia Supernova? *ApJ*, 652:1259–1267.
- Borkowski, K. J., Lyerly, W. J., and Reynolds, S. P. (2001). Supernova Remnants in the Sedov Expansion Phase: Thermal X-Ray Emission. *ApJ*, 548:820–835.

- Boyles, J., Lorimer, D. R., McLaughlin, M. A., Ransom, S. M., Lynch, R., Kaspi, V. M., Archibald, A. M., Stairs, I. H., McPhee, C. A., and et al. (2011). New Discoveries from the GBT 350-MHz Drift-Scan Survey. In Burgay, M., D'Amico, N., Esposito, P., Pellizzoni, A., and Possenti, A., editors, *American Institute of Physics Conference Series*, volume 1357 of *American Institute of Physics Conference Series*, pages 32–35.
- Boyles, J., Lynch, R. S., Ransom, S. M., Stairs, I. H., Lorimer, D. R., McLaughlin, M. A., Hessels, J. W. T., Kaspi, V. M., Kondratiev, V. I., and et al. (2013). The Green Bank Telescope 350 MHz Drift-scan survey. I. Survey Observations and the Discovery of 13 Pulsars. *ApJ*, 763:80.
- Briel, U. G. and Pfeffermann, E. (1986). The position sensitive proportional counter (PSPC) of the Rosat telescope. *Nuclear Instruments and Methods in Physics Research A*, 242:376–381.
- Brisken, W. F., Benson, J. M., Goss, W. M., and Thorsett, S. E. (2002). Very Long Baseline Array Measurement of Nine Pulsar Parallaxes. *ApJ*, 571:906–917.
- Brisken, W. F., Thorsett, S. E., Golden, A., and Goss, W. M. (2003). The Distance and Radius of the Neutron Star PSR B0656+14. *ApJ*, 593:L89–L92.
- Broadbent, A., Osborne, J. L., and Haslam, C. G. T. (1989). A technique for separating the galactic thermal radio emission from the non-thermal component by means of the associated infrared emission. *MNRAS*, 237:381–410.
- Brogan, C. L., Gelfand, J. D., Gaensler, B. M., Kassim, N. E., and Lazio, T. J. W. (2006). Discovery of 35 New Supernova Remnants in the Inner Galaxy. *ApJ*, 639:L25–L29.
- Burkey, M. T., Reynolds, S. P., Borkowski, K. J., and Blondin, J. M. (2013). X-Ray Emission from Strongly Asymmetric Circumstellar Material in the Remnant of Kepler's Supernova. *ApJ*, 764:63.
- Burrows, A., Hayes, J., and Fryxell, B. A. (1995). On the Nature of Core-Collapse Supernova Explosions. *ApJ*, 450:830.
- Burrows, A., Livne, E., Dessart, L., Ott, C. D., and Murphy, J. (2006). A New Mechanism for Core-Collapse Supernova Explosions. *ApJ*, 640:878–890.
- Burrows, A., Livne, E., Dessart, L., Ott, C. D., and Murphy, J. (2007). Features of the Acoustic Mechanism of Core-Collapse Supernova Explosions. *ApJ*, 655:416–433.
- Burwitz, V., Haberl, F., Neuhäuser, R., Predehl, P., Trümper, J., and Zavlin, V. E. (2003). The thermal radiation of the isolated neutron star RX J1856.5-3754 observed with Chandra and XMM-Newton. *A&A*, 399:1109–1114.
- Bußer, J.-U. (1998). *Galaktische Supernova-Überreste in der ROSAT-Himmelsdurchmusterung (German)*. PhD thesis, LMU, Germany.

- Busser, J.-U., Egger, R., and Aschenbach, B. (1996). G 299.2-2.9: a new galactic supernova remnant discovered by ROSAT. In H. U. Zimmermann, J. Trümper, & H. Yorke, editor, *Röntgenstrahlung from the Universe*, pages 239–240.
- Cameron, P. B., Rutledge, R. E., Camilo, F., Bildsten, L., Ransom, S. M., and Kulkarni, S. R. (2007). Variability of 19 Millisecond Pulsars in 47 Tucanae with Chandra HRC-S. *ApJ*, 660:587–594.
- Camilo, F., Bell, J. F., Manchester, R. N., Lyne, A. G., Possenti, A., Kramer, M., Kaspi, V. M., Stairs, I. H., D’Amico, N., Hobbs, G., Gotthelf, E. V., and Gaensler, B. M. (2001). PSR J1016-5857: A Young Radio Pulsar with Possible Supernova Remnant, X-Ray, and Gamma-Ray Associations. *ApJ*, 557:L51–L55.
- Camilo, F., Lorimer, D. R., Bhat, N. D. R., Gotthelf, E. V., Halpern, J. P., Wang, Q. D., Lu, F. J., and Mirabal, N. (2002a). Discovery of a 136 Millisecond Radio and X-Ray Pulsar in Supernova Remnant G54.1+0.3. *ApJ*, 574:L71–L74.
- Camilo, F., Manchester, R. N., Gaensler, B. M., Lorimer, D. R., and Sarkissian, J. (2002b). PSR J1124-5916: Discovery of a Young Energetic Pulsar in the Supernova Remnant G292.0+1.8. *ApJ*, 567:L71–L75.
- Camilo, F., Ransom, S. M., Chatterjee, S., Johnston, S., and Demorest, P. (2012). PSR J1841-0500: A Radio Pulsar That Mostly is Not There. *ApJ*, 746:63.
- Camilo, F., Ransom, S. M., Gaensler, B. M., and Lorimer, D. R. (2009a). Discovery of the Energetic Pulsar J1747-2809 in the Supernova Remnant G0.9+0.1. *ApJ*, 700:L34–L38.
- Camilo, F., Ray, P. S., Ransom, S. M., Burgay, M., Johnson, T. J., Kerr, M., Gotthelf, E. V., Halpern, J. P., Reynolds, J., and et al. (2009b). Radio Detection of LAT PSRs J1741-2054 and J2032+4127: No Longer Just Gamma-ray Pulsars. *ApJ*, 705:1–13.
- Caraveo, P. A. (1993). Associating Young Pulsars and Supernova Remnants: PSR 1610-50 and the Case for High-Velocity Pulsars. *ApJ*, 415:L111.
- Caraveo, P. A., De Luca, A., Marelli, M., Bignami, G. F., Ray, P. S., Saz Parkinson, P. M., and Kanbach, G. (2010). X-ray Pulsations from the Radio-quiet Gamma-ray Pulsar in CTA 1. *ApJ*, 725:L6–L10.
- Caraveo, P. A., De Luca, A., Mignani, R. P., and Bignami, G. F. (2001). The Distance to the Vela Pulsar Gauged with Hubble Space Telescope Parallax Observations. *ApJ*, 561:930–937.
- Carey, S. J., Noriega-Crespo, A., Mizuno, D. R., Shenoy, S., Paladini, R., Kraemer, K. E., Price, S. D., Flagey, N., Ryan, E., and et al. (2009). MIPS GAL: A Survey of the Inner Galactic Plane at 24 and 70  $\mu\text{m}$ . *PASP*, 121:76–97.
- Castro, D., Slane, P. O., Gaensler, B. M., Hughes, J. P., and Patnaude, D. J. (2011). An XMM-Newton Study of the Bright, Nearby Supernova Remnant G296.1-0.5. *ApJ*, 734:86.

- Caswell, J. L. and Haynes, R. F. (1987). Southern H II regions - an extensive study of radio recombination line emission. *A&A*, 171:261–276.
- Chadwick, J. (1932). The Existence of a Neutron. *Royal Society of London Proceedings Series A*, 136:692–708.
- Chakrabarty, D., Pivovarov, M. J., Hernquist, L. E., Heyl, J. S., and Narayan, R. (2001). The Central X-Ray Point Source in Cassiopeia A. *ApJ*, 548:800–810.
- Chang, C., Konopelko, A., and Cui, W. (2008). Search for Pulsar Wind Nebula Associations with Unidentified TeV  $\gamma$ -Ray Sources. *ApJ*, 682:1177–1184.
- Chang, H.-K., King, S.-K., Liang, J.-S., Wu, P.-S., Lin, L. C.-C., and Chiu, J.-L. (2006). Occultation of X-rays from Scorpius X-1 by small trans-neptunian objects. *Nature*, 442:660–663.
- Chang, H.-K., Liu, C.-Y., and Chen, K.-T. (2013). Search for serendipitous trans-Neptunian object occultation in X-rays. *MNRAS*, 429:1626–1632.
- Chatterjee, S., Cordes, J. M., Vlemmings, W. H. T., Arzoumanian, Z., Goss, W. M., and Lazio, T. J. W. (2004). Pulsar Parallaxes at 5 GHz with the Very Long Baseline Array. *ApJ*, 604:339–345.
- Chen, Y., Wang, Q. D., Gotthelf, E. V., Jiang, B., Chu, Y.-H., and Gruendl, R. (2006). Chandra ACIS Spectroscopy of N157B: A Young Composite Supernova Remnant in a Superbubble. *ApJ*, 651:237–249.
- Chernyakova, M., Neronov, A., Lutovinov, A., Rodriguez, J., and Johnston, S. (2006). XMM-Newton observations of PSR B1259-63 near the 2004 periastron passage. *MNRAS*, 367:1201–1208.
- Chevalier, R. A. (1982). Self-similar solutions for the interaction of stellar ejecta with an external medium. *ApJ*, 258:790–797.
- Chiotellis, A., Schure, K. M., and Vink, J. (2012). The imprint of a symbiotic binary progenitor on the properties of Kepler’s supernova remnant. *A&A*, 537:A139.
- Chodos, A., Jaffe, R. L., Johnson, K., and Thorn, C. B. (1974). Baryon structure in the bag theory. *Phys. Rev. D*, 10:2599–2604.
- Clark, B. G. (1980). An efficient implementation of the algorithm ‘CLEAN’. *A&A*, 89:377.
- Clifton, T. R., Frail, D. A., Kulkarni, S. R., and Weisberg, J. M. (1988). Neutral hydrogen absorption observations toward high-dispersion measure pulsars. *ApJ*, 333:332–340.
- Cognard, I., Guillemot, L., Johnson, T. J., Smith, D. A., Venter, C., Harding, A. K., Wolff, M. T., Cheung, C. C., Donato, D., and et al. (2011). Discovery of Two Millisecond Pulsars in Fermi Sources with the Nançay Radio Telescope. *ApJ*, 732:47.

- Condon, J. J., Broderick, J. J., and Seielstad, G. A. (1989). A 4.85 GHz sky survey. I - Maps covering delta between 0 and + 75 deg. *AJ*, 97:1064–1073.
- Condon, J. J., Cotton, W. D., Greisen, E. W., Yin, Q. F., Perley, R. A., Taylor, G. B., and Broderick, J. J. (1998). The NRAO VLA Sky Survey. *AJ*, 115:1693–1716.
- Cordes, J. M. and Lazio, T. J. W. (2002). NE2001.I. A New Model for the Galactic Distribution of Free Electrons and its Fluctuations. *ArXiv Astrophysics e-prints*.
- Culhane, J. L. (1977). X-Rays from Supernova Remnants. In D. N. Schramm, editor, *Supernovae*, volume 66 of *Astrophysics and Space Science Library*, page 29.
- Cusumano, G., Mineo, T., Massaro, E., Nicastro, L., Trussoni, E., Massaglia, S., Hermsen, W., and Kuiper, L. (2001). The curved X-ray spectrum of PSR B1509-58 observed with BeppoSAX. *A&A*, 375:397–404.
- Cutri, R. M., Skrutskie, M. F., van Dyk, S., Beichman, C. A., Carpenter, J. M., Chester, T., Cambresy, L., Evans, T., Fowler, J., and et al. (2003). *2MASS All Sky Catalog of point sources*.
- Danner, R., Kulkarni, S. R., and Trumper, J. (1998). The X-ray Counterpart to SGR 0526-66: Results from a monitoring campaign of N49 with ROSAT. In *American Astronomical Society Meeting Abstracts #192*, volume 30 of *Bulletin of the American Astronomical Society*, page 875.
- Daugherty, J. K. and Harding, A. K. (1986). Compton scattering in strong magnetic fields. *ApJ*, 309:362–371.
- Davies, J. G., Lyne, A. G., and Seiradakis, J. H. (1972). Pulsar Associated with the Supernova Remnant IC 443. *Nature*, 240:229–230.
- de Jager, O. C., Raubenheimer, B. C., and Swanepoel, J. W. H. (1989). A powerful test for weak periodic signals with unknown light curve shape in sparse data. *A&A*, 221:180–190.
- de Luca, A. (2008). Central Compact Objects in Supernova Remnants. In C. Bassa, Z. Wang, A. Cumming, & V. M. Kaspi, editor, *40 Years of Pulsars: Millisecond Pulsars, Magnetars and More*, volume 983 of *American Institute of Physics Conference Series*, pages 311–319.
- De Luca, A., Caraveo, P. A., Mereghetti, S., Negroni, M., and Bignami, G. F. (2005). On the Polar Caps of the Three Musketeers. *ApJ*, 623:1051–1069.
- De Luca, A., Marelli, M., Mignani, R. P., Caraveo, P. A., Hummel, W., Collins, S., Shearer, A., Saz Parkinson, P. M., Belfiore, A., and Bignami, G. F. (2011). Discovery of a Faint X-Ray Counterpart and a Parsec-long X-Ray Tail for the Middle-aged,  $\gamma$ -Ray-only Pulsar PSR J0357+3205. *ApJ*, 733:104.
- de Rosa, A., Bassani, L., Ubertini, P., Panessa, F., Malizia, A., Dean, A. J., and Walter, R. (2008). An X-ray view of absorbed INTEGRAL AGN. *A&A*, 483:749–758.

- Demorest, P. B., Pennucci, T., Ransom, S. M., Roberts, M. S. E., and Hessels, J. W. T. (2010). A two-solar-mass neutron star measured using Shapiro delay. *Nature*, 467:1081–1083.
- den Hartog, P. R., Kuiper, L., and Hermsen, W. (2008). Detailed high-energy characteristics of AXP 1RXS J170849-400910. Probing the magnetosphere using INTEGRAL, RXTE, and XMM-Newton. *A&A*, 489:263–279.
- Dickel, J. (1991). The Radio Spectra of Supernova Remnants. In S. E. Woosley, editor, *Supernovae*, page 675.
- Dickey, J. M. and Lockman, F. J. (1990). H I in the Galaxy. *ARA&A*, 28:215–261.
- Diehl, R., Halloin, H., Kretschmer, K., Lichti, G. G., Schönfelder, V., Strong, A. W., von Kienlin, A., Wang, W., Jean, P., and et al. (2006). Radioactive  $^{26}\text{Al}$  from massive stars in the Galaxy. *Nature*, 439:45–47.
- Dubner, G., Loiseau, N., Rodríguez-Pascual, P., Smith, M. J. S., Giacani, E., and Castelletti, G. (2013). The most complete and detailed X-ray view of the SNR Puppis A. *A&A*, 555:A9.
- Duncan, A. R., Stewart, R. T., Haynes, R. F., and Jones, K. L. (1997). Supernova remnant candidates from the Parkes 2.4-GHz survey. *MNRAS*, 287:722–738.
- Dyks, J. and Rudak, B. (2003). Two-Pole Caustic Model for High-Energy Light Curves of Pulsars. *ApJ*, 598:1201–1206.
- Ebeling, H., Mullis, C. R., and Tully, R. B. (2002). A Systematic X-Ray Search for Clusters of Galaxies behind the Milky Way. *ApJ*, 580:774–788.
- Egger, R., Greiner, J., and Aschenbach, B. (1996). G 272.2-3.2 - a young and centrally filled supernova remnant discovered by ROSAT. In H. U. Zimmermann, J. Trümper, & H. Yorke, editor, *Röntgenstrahlung from the Universe*, pages 247–248.
- Elshamouty, K. G., Heinke, C. O., Sivakoff, G. R., Ho, W. C. G., Shternin, P. S., Yakovlev, D. G., Patnaude, D. J., and David, L. (2013). Measuring the Cooling of the Neutron Star in Cassiopeia A with all Chandra X-Ray Observatory Detectors. *ApJ*, 777:22.
- Erben, T., Schirmer, M., Dietrich, J. P., Cordes, O., Habertzettl, L., Hetterscheidt, M., Hildebrandt, H., Schmithuesen, O., Schneider, P., and et al. (2005). GaBoDS: The Garching-Bonn Deep Survey. IV. Methods for the image reduction of multi-chip cameras demonstrated on data from the ESO Wide-Field Imager. *Astronomische Nachrichten*, 326:432–464.
- Esposito, P., Tiengo, A., Rea, N., Turolla, R., Fenzi, A., Giuliani, A., Israel, G. L., Zane, S., Mereghetti, S., and et al. (2013). X-ray and radio observations of the magnetar Swift J1834.9-0846 and its dust-scattering halo. *MNRAS*, 429:3123–3132.
- Evans, I. N., Primini, F. A., Glotfelty, K. J., Anderson, C. S., Bonaventura, N. R., Chen, J. C., Davis, J. E., Doe, S. M., Evans, J. D., and et al. (2010). The Chandra Source Catalog. *ApJS*, 189:37–82.

- Fesen, R., Rudie, G., Hurford, A., and Soto, A. (2008). Optical Imaging and Spectroscopy of the Galactic Supernova Remnant 3C 58 (G130.7+3.1). *ApJS*, 174:379–395.
- Fesen, R. A., Blair, W. P., and Kirshner, R. P. (1985). Optical emission-line properties of evolved galactic supernova remnants. *ApJ*, 292:29–48.
- Fesen, R. A., Hammell, M. C., Morse, J., Chevalier, R. A., Borkowski, K. J., Dopita, M. A., Gerardy, C. L., Lawrence, S. S., Raymond, J. C., and van den Bergh, S. (2006). The Expansion Asymmetry and Age of the Cassiopeia A Supernova Remnant. *ApJ*, 645:283–292.
- Fich, M., Blitz, L., and Stark, A. A. (1989). The rotation curve of the Milky Way to  $2 R(0)$ . *ApJ*, 342:272–284.
- Finkbeiner, D. P. (2003). A Full-Sky  $H\alpha$  Template for Microwave Foreground Prediction. *ApJS*, 146:407–415.
- Flesch, E. (2010). An All-Sky Atlas of Radio/X-ray Associations. *PASA*, 27:283–289.
- Folgheraiter, E. L., Watson, M. G., and Warwick, R. S. (1996). The supernova remnant G 32.1-0.9: ROSAT and ASCA results. In H. U. Zimmermann, J. Trümper, & H. Yorke, editor, *Röntgenstrahlung from the Universe*, pages 253–254.
- Frail, D. A., Goss, W. M., and Whiteoak, J. B. Z. (1994). The radio lifetime of supernova remnants and the distribution of pulsar velocities at birth. *ApJ*, 437:781–793.
- Friese, V. (2006). The CBM experiment at GSI/FAIR. *Nuclear Physics A*, 774:377–386.
- Fuhrmeister, B. and Schmitt, J. H. M. M. (2003). A systematic study of X-ray variability in the ROSAT all-sky survey. *A&A*, 403:247–260.
- Fürst, E., Reich, W., and Sofue, Y. (1987). The identification of galactic radio sources based on a comparison of radio-continuum and infrared emission. *A&AS*, 71:63–67.
- Gaensler, B. M., Schulz, N. S., Kaspi, V. M., Pivovarov, M. J., and Becker, W. E. (2003). XMM-Newton Observations of PSR B1823-13: An Asymmetric Synchrotron Nebula around a Vela-like Pulsar. *ApJ*, 588:441–451.
- Gaensler, B. M. and Slane, P. O. (2006). The Evolution and Structure of Pulsar Wind Nebulae. *ARA&A*, 44:17–47.
- Gaensler, B. M., van der Swaluw, E., Camilo, F., Kaspi, V. M., Baganoff, F. K., Yusef-Zadeh, F., and Manchester, R. N. (2004). The Mouse that Soared: High-Resolution X-Ray Imaging of the Pulsar-powered Bow Shock G359.23-0.82. *ApJ*, 616:383–402.
- Gaustad, J. E., McCullough, P. R., Rosing, W., and Van Buren, D. (2001). A Robotic Wide-Angle  $H\alpha$  Survey of the Southern Sky. *PASP*, 113:1326–1348.

- Gelfand, J. D. and Gaensler, B. M. (2007). The Compact X-Ray Source 1E 1547.0-5408 and the Radio Shell G327.24-0.13: A New Proposed Association between a Candidate Magnetar and a Candidate Supernova Remnant. *ApJ*, 667:1111–1118.
- Gentile, P., Roberts, M., McLaughlin, M., Camilo, F., Hessels, J., Kerr, M., Ransom, S., Ray, P., and Stairs, I. (2013). X-Ray Observations of Black Widow Pulsars. *ArXiv e-prints*.
- Giacconi, R., Branduardi, G., Briel, U., Epstein, A., Fabricant, D., Feigelson, E., Forman, W., Gorenstein, P., Grindlay, J., and et al. (1979). The Einstein /HEAO 2/ X-ray Observatory. *ApJ*, 230:540–550.
- Giacconi, R., Gursky, H., Paolini, F. R., and Rossi, B. B. (1962). Evidence for x Rays From Sources Outside the Solar System. *Physical Review Letters*, 9:439–443.
- Gil, J., Haberl, F., Melikidze, G., Geppert, U., Zhang, B., and Melikidze, J. G. (2008). XMM-Newton Observations of Radio Pulsars B0834+06 and B0826-34 and Implications for the Pulsar Inner Accelerator. *ApJ*, 686:497–507.
- Ginzburg, V. L. and Syrovatskii, S. I. (1965). Cosmic Magnetobremstrahlung (synchrotron Radiation). *ARA&A*, 3:297.
- Ginzburg, V. L. and Syrovatskij, S. I. (1967). Cosmic rays in the Galaxy (Introductory Report). In van Woerden, H., editor, *Radio Astronomy and the Galactic System*, volume 31 of *IAU Symposium*, page 411.
- Gold, T. (1968). Rotating Neutron Stars as the Origin of the Pulsating Radio Sources. *Nature*, 218:731–732.
- Goldreich, P. and Julian, W. H. (1969). Pulsar Electrodynamics. *ApJ*, 157:869.
- Gonzalez, M. and Safi-Harb, S. (2003). Chandra Detection of the High Magnetic Field Radio Pulsar J1119-6127 in the Supernova Remnant G292.2-0.5. *ApJ*, 591:L143–L146.
- Gonzalez, M. E., Kaspi, V. M., Camilo, F., Gaensler, B. M., and Pivovarov, M. J. (2005). Unusual Pulsed X-Ray Emission from the Young, High Magnetic Field Pulsar PSR J1119-6127. *ApJ*, 630:489–494.
- Gonzalez, M. E., Kaspi, V. M., Lyne, A. G., and Pivovarov, M. J. (2004). An XMM-Newton Observation of the High Magnetic Field Radio Pulsar PSR B0154+61. *ApJ*, 610:L37–L40.
- Gonzalez, M. E., Kaspi, V. M., Pivovarov, M. J., and Gaensler, B. M. (2006). Chandra and XMM-Newton Observations of the Vela-like Pulsar B1046-58. *ApJ*, 652:569–575.
- Gotthelf, E. V. (2004). A Spin-down Power Threshold for Pulsar Wind Nebula Generation? In F. Camilo & B. M. Gaensler, editor, *Young Neutron Stars and Their Environments*, volume 218 of *IAU Symposium*, page 225.

- Gotthelf, E. V., Gavriil, F. P., Kaspi, V. M., Vasisht, G., and Chakrabarty, D. (2002). A Phase-connected Timing Solution for the Magnetar Candidate 1E 1841-045. *ApJ*, 564:L31–L34.
- Gotthelf, E. V. and Halpern, J. P. (2007). Precise Timing of the X-ray Pulsar 1E 1207.4-5209: A Steady Neutron Star Weakly Magnetized at Birth. *ApJ*, 664:L35–L38.
- Gotthelf, E. V. and Halpern, J. P. (2008a). CCO Pulsars as Anti-Magnetars: Evidence of Neutron Stars Weakly Magnetized at Birth. In C. Bassa, Z. Wang, A. Cumming, & V. M. Kaspi, editor, *40 Years of Pulsars: Millisecond Pulsars, Magnetars and More*, volume 983 of *American Institute of Physics Conference Series*, pages 320–324.
- Gotthelf, E. V. and Halpern, J. P. (2008b). Discovery of a Young, Energetic 70.5 ms Pulsar Associated with the TeV Gamma-Ray Source HESS J1837-069. *ApJ*, 681:515–521.
- Gotthelf, E. V. and Halpern, J. P. (2009a). Discovery of a 112 ms X-Ray Pulsar in Puppis A: Further Evidence of Neutron Stars Weakly Magnetized at Birth. *ApJ*, 695:L35–L39.
- Gotthelf, E. V. and Halpern, J. P. (2009b). Discovery of a Highly Energetic X-Ray Pulsar Powering HESS J1813-178 in the Young Supernova Remnant G12.82-0.02. *ApJ*, 700:L158–L161.
- Gotthelf, E. V., Halpern, J. P., Terrier, R., and Mattana, F. (2010a). Discovery of PSR J1849-0001, a 38.5 ms Pulsar Powering IGR J18490-0000/HESS J1849-000. *The Astronomer's Telegram*, 3057:1.
- Gotthelf, E. V. and Kaspi, V. M. (1998). X-Ray Emission from the Radio Pulsar PSR J1105-6107. *ApJ*, 497:L29.
- Gotthelf, E. V. and Kaspi, V. M. (1999). X-ray emission from the 63ms radio pulsar PSR J1105-6107. *Nuclear Physics B Proceedings Supplements*, 69:261–264.
- Gotthelf, E. V., Perna, R., and Halpern, J. P. (2010b). Modeling the Surface X-ray Emission and Viewing Geometry of PSR J0821-4300 in Puppis A. *ApJ*, 724:1316–1324.
- Göğüş, E., Cusumano, G., Levan, A. J., Kouveliotou, C., Sakamoto, T., Barthelmy, S. D., Campana, S., Kaneko, Y., Stappers, B. W., and et al. (2010a). Discovery of a New Soft Gamma Repeater, SGR J1833-0832. *ApJ*, 718:331–339.
- Göğüş, E., Güver, T., Özel, F., Eichler, D., and Kouveliotou, C. (2011). Long-term Radiative Behavior Of SGR 1900+14. *ApJ*, 728:160.
- Göğüş, E., Woods, P. M., Kouveliotou, C., Kaneko, Y., Gaensler, B. M., and Chatterjee, S. (2010b). Spatial, Temporal, and Spectral Properties of X-ray Emission from the Magnetar SGR 0501+4516. *ApJ*, 722:899–908.
- Green, D. A. (2004). Galactic supernova remnants: an updated catalogue and some statistics. *Bulletin of the Astronomical Society of India*, 32:335–370.

- Green, D. A. (2009). A revised Galactic supernova remnant catalogue. *Bulletin of the Astronomical Society of India*, 37:45–61.
- Green, D. A. and Stephenson, F. R. (2003). Historical Supernovae. In K. Weiler, editor, *Supernovae and Gamma-Ray Bursters*, volume 598 of *Lecture Notes in Physics*, Berlin Springer Verlag, pages 7–19.
- Griffith, M. R. and Wright, A. E. (1993). The Parkes-MIT-NRAO (PMN) surveys. I - The 4850 MHz surveys and data reduction. *AJ*, 105:1666–1679.
- Gritschneder, M., Lin, D. N. C., Murray, S. D., Yin, Q.-Z., and Gong, M.-N. (2012). The Supernova Triggered Formation and Enrichment of Our Solar System. *ApJ*, 745:22.
- Gudmundsson, E. H., Pethick, C. J., and Epstein, R. I. (1982). Neutron star envelopes. *ApJ*, 259:L19–L23.
- Guerrero, M. A., Chu, Y.-H., and Gruendl, R. A. (2000). ROSAT Observations of X-Ray Emission from Planetary Nebulae. *ApJS*, 129:295–313.
- Guerrero, M. A., Chu, Y.-H., and Gruendl, R. A. (2006). The X-ray Planetary Nebulae Database. In A. Wilson, editor, *The X-ray Universe 2005*, volume 604 of *ESA Special Publication*, page 85.
- Guillemot, L., Kramer, M., Johnson, T. J., Craig, H. A., Romani, R. W., Venter, C., Harding, A. K., Ferdman, R. D., Stairs, I. H., and Kerr, M. (2013). Fermi LAT Pulsed Detection of PSR J0737-3039A in the Double Pulsar System. *ApJ*, 768:169.
- Haberl, F., Pietsch, W., and Motch, C. (1999). RX J0420.0-5022: an isolated neutron star candidate with evidence for 22.7 s X-ray pulsations. *A&A*, 351:L53–L57.
- Haberl, F. and Zavlin, V. E. (2002). XMM-Newton observations of the isolated neutron star RX J0806.4-4123. *A&A*, 391:571–576.
- Hachisu, I., Kato, M., and Nomoto, K. (1999). A Wide Symbiotic Channel to Type IA Supernovae. *ApJ*, 522:487–503.
- Haensel, P., Potekhin, A. Y., and Yakovlev, D. G., editors (2007). *Neutron Stars 1 : Equation of State and Structure*, volume 326 of *Astrophysics and Space Science Library*.
- Hakobyan, A. A., Petrosian, A. R., Mamon, G. A., McLean, B., Kunth, D., Turatto, M., Cappellaro, E., Mannucci, F., Allen, R. J., Panagia, N., and Della Valle, M. (2011). Five supernova survey galaxies in the southern hemisphere. II. The supernova rates. *Astrophysics*, 54:301–314.
- Halpern, J. P., Camilo, F., and Gotthelf, E. V. (2007a). The Next Geminga: Search for Radio and X-Ray Pulsations from the Neutron Star Identified with 3EG J1835+5918. *ApJ*, 668:1154–1157.

- Halpern, J. P., Camilo, F., Gotthelf, E. V., Helfand, D. J., Kramer, M., Lyne, A. G., Leighly, K. M., and Eracleous, M. (2001). PSR J2229+6114: Discovery of an Energetic Young Pulsar in the Error Box of the EGRET Source 3EG J2227+6122. *ApJ*, 552:L125–L128.
- Halpern, J. P., Gotthelf, E. V., Camilo, F., Helfand, D. J., and Ransom, S. M. (2004). X-Ray, Radio, and Optical Observations of the Putative Pulsar in the Supernova Remnant CTA 1. *ApJ*, 612:398–407.
- Halpern, J. P., Gotthelf, E. V., Camilo, F., and Seward, F. D. (2007b). X-Ray Timing of PSR J1852+0040 in Kesteven 79: Evidence of Neutron Stars Weakly Magnetized at Birth. *ApJ*, 665:1304–1310.
- Halpern, J. P. and Wang, F. Y.-H. (1997). A Broadband X-Ray Study of the Geminga Pulsar. *ApJ*, 477:905.
- Hammer, N. J., Janka, H.-T., and Müller, E. (2010). Three-dimensional Simulations of Mixing Instabilities in Supernova Explosions. *ApJ*, 714:1371–1385.
- Hands, S. (2001). The phase diagram of QCD. *Contemporary Physics*, 42:209–225.
- Harding, A. K. (2009). High-energy Emission from the Polar Cap and Slot Gap. In Becker, W., editor, *Astrophysics and Space Science Library*, volume 357 of *Astrophysics and Space Science Library*, page 521.
- Harrison, F. A., Craig, W. W., Christensen, F. E., Hailey, C. J., Zhang, W. W., Boggs, S. E., Stern, D., Cook, W. R., Forster, K., and et al. (2013). The Nuclear Spectroscopic Telescope Array (NuSTAR) High-energy X-Ray Mission. *ApJ*, 770:103.
- Harry, G. M. and LIGO Scientific Collaboration (2010). Advanced LIGO: the next generation of gravitational wave detectors. *Classical and Quantum Gravity*, 27(8):084006.
- Hartmann, D. H., Predehl, P., Greiner, J., Egger, R., Trumper, J., Aschenbach, B., Iyudin, A. F., Diehl, R. D., Oberlack, U., and et al. (1997). On Flamsteed’s supernova Cas A. *Nuclear Physics A*, 621:83–91.
- Helfand, D. J., Becker, R. H., White, R. L., Fallon, A., and Tuttle, S. (2006). MAGPIS: A Multi-Array Galactic Plane Imaging Survey. *AJ*, 131:2525–2537.
- Hellier, C. (1994). 4U 0142+614 and RX J0146.9+6121. *IAU Circ.*, 5994:2.
- Heng, K. (2010). Balmer-Dominated Shocks: A Concise Review. *PASA*, 27:23–44.
- H.E.S.S. Collaboration, Abramowski, A., Acero, F., Aharonian, F., Akhperjanian, A. G., Anton, G., Balenderan, S., Balzer, A., Barnacka, A., and et al. (2012). Identification of HESS J1303-631 as a pulsar wind nebula through  $\gamma$ -ray, X-ray, and radio observations. *A&A*, 548:A46.

- Hessels, J. W. T., Roberts, M. S. E., Ransom, S. M., Kaspi, V. M., Romani, R. W., Ng, C.-Y., Freire, P. C. C., and Gaensler, B. M. (2004). Observations of PSR J2021+3651 and its X-Ray Pulsar Wind Nebula G75.2+0.1. *ApJ*, 612:389–397.
- Hewish, A., Bell, S. J., Pilkington, J. D. H., Scott, P. F., and Collins, R. A. (1968). Observation of a Rapidly Pulsating Radio Source. *Nature*, 217:709–713.
- Hewitt, J. W., Grondin, M.-H., Lemoine-Goumard, M., Reposeur, T., Ballet, J., and Tanaka, T. (2012). Fermi-LAT and WMAP Observations of the Puppis A Supernova Remnant. *ApJ*, 759:89.
- Hillebrandt, W. and Niemeyer, J. C. (2000). Type IA Supernova Explosion Models. *ARA&A*, 38:191–230.
- Hinton, J. A., Funk, S., Carrigan, S., Gallant, Y. A., de Jager, O. C., Kosack, K., Lemièrre, A., and Pühlhofer, G. (2007). Discovery of an X-ray nebula around PSR J1718-3825 and implications for the nature of the  $\gamma$ -ray source HESS J1718-385. *A&A*, 476:L25–L28.
- Hinton, J. A. and Hofmann, W. (2009). Teraelectronvolt Astronomy. *ARA&A*, 47:523–565.
- Hirata, K., Kajita, T., Koshiba, M., Nakahata, M., and Oyama, Y. (1987). Observation of a neutrino burst from the supernova SN1987A. *Physical Review Letters*, 58:1490–1493.
- Ho, W. C. G. and Heinke, C. O. (2009). A neutron star with a carbon atmosphere in the Cassiopeia A supernova remnant. *Nature*, 462:71–73.
- Hobbs, G., Faulkner, A., Stairs, I. H., Camilo, F., Manchester, R. N., Lyne, A. G., Kramer, M., D’Amico, N., Kaspi, V. M., and et al. (2004). The Parkes multibeam pulsar survey - IV. Discovery of 180 pulsars and parameters for 281 previously known pulsars. *MNRAS*, 352:1439–1472.
- Hobbs, G., Lorimer, D. R., Lyne, A. G., and Kramer, M. (2005). A statistical study of 233 pulsar proper motions. *MNRAS*, 360:974–992.
- Høg, E., Fabricius, C., Makarov, V. V., Urban, S., Corbin, T., Wycoff, G., Bastian, U., Schwekendiek, P., and Wicenec, A. (2000). The Tycho-2 catalogue of the 2.5 million brightest stars. *A&A*, 355:L27–L30.
- Hollow, N. J. (1973). P-N Junctions in Pulsar Magnetospheres ? *Nature Physical Science*, 246:6–9.
- Huang, H. H. and Becker, W. (2007). XMM-Newton observations of PSR B1957+20. *A&A*, 463:L5–L8.
- Hughes, J. P., Slane, P. O., Burrows, D. N., Garmire, G., Nousek, J. A., Olbert, C. M., and Keohane, J. W. (2001). A Pulsar Wind Nebula in the Oxygen-rich Supernova Remnant G292.0+1.8. *ApJ*, 559:L153–L156.

- Hughes, J. P., Slane, P. O., Park, S., Roming, P. W. A., and Burrows, D. N. (2003). An X-Ray Pulsar in the Oxygen-rich Supernova Remnant G292.0+1.8. *ApJ*, 591:L139–L142.
- Hui, C. Y. and Becker, W. (2006). Probing the proper motion of the central compact object in Puppis-A with the Chandra high resolution camera. *A&A*, 457:L33–L36.
- Hui, C. Y. and Becker, W. (2007a). Radio and X-ray nebulae associated with PSR J1509-5850. *A&A*, 470:965–968.
- Hui, C. Y. and Becker, W. (2007b). X-ray emission properties of the old pulsar PSR B2224+65. *A&A*, 467:1209–1214.
- Hurley, K. (2009). Soft Gamma-Ray Repeaters and Magnetars. In Becker, W., editor, *Astrophysics and Space Science Library*, volume 357 of *Astrophysics and Space Science Library*, page 575.
- Hwang, U., Holt, S. S., and Petre, R. (2000). Mapping the X-Ray-emitting Ejecta in Cassiopeia A with Chandra. *ApJ*, 537:L119–L122.
- İçdem, B., Baykal, A., and Ç. Inam, S. (2012). RXTE timing analysis of the anomalous X-ray pulsar 1E 2259+586. *MNRAS*, 419:3109–3114.
- Jackson, M. S., Safi-Harb, S., Kothes, R., and Foster, T. (2008). XMM-Newton, Chandra, and CGPS observations of the Supernova Remnants G85.4+0.7 and G85.9-0.6. *ApJ*, 674:936–953.
- Jacoby, B. A., Bailes, M., Ord, S. M., Knight, H. S., and Hotan, A. W. (2007). Discovery of Five Recycled Pulsars in a High Galactic Latitude Survey. *ApJ*, 656:408–413.
- Janka, H.-T. (2012). Explosion Mechanisms of Core-Collapse Supernovae. *Annual Review of Nuclear and Particle Science*, 62:407–451.
- Janka, H.-T. and Mueller, E. (1994). Neutron star recoils from anisotropic supernovae. *A&A*, 290:496–502.
- Kaaret, P., Marshall, H. L., Aldcroft, T. L., Graessle, D. E., Karovska, M., Murray, S. S., Rots, A. H., Schulz, N. S., and Seward, F. D. (2001). Chandra Observations of the Young Pulsar PSR B0540-69. *ApJ*, 546:1159–1167.
- Kaastra, J. S., Paerels, F. B. S., Durret, F., Schindler, S., and Richter, P. (2008). Thermal Radiation Processes. *Space Sci. Rev.*, 134:155–190.
- Kahabka, P. and van den Heuvel, E. P. J. (1997). Luminous Supersoft X-Ray Sources. *ARA&A*, 35:69–100.
- Kalberla, P. M. W., Burton, W. B., Hartmann, D., Arnal, E. M., Bajaja, E., Morras, R., and Pöppel, W. G. L. (2005). The Leiden/Argentine/Bonn (LAB) Survey of Galactic HI. Final data release of the combined LDS and IAR surveys with improved stray-radiation corrections. *A&A*, 440:775–782.

- Kaplan, D. L., Esposito, P., Chatterjee, S., Possenti, A., McLaughlin, M. A., Camilo, F., Chakrabarty, D., and Slane, P. O. (2009). Upper limits on X-ray emission from two rotating radio transients. *MNRAS*, 400:1445–1450.
- Kaplan, D. L., Frail, D. A., Gaensler, B. M., Gotthelf, E. V., Kulkarni, S. R., Slane, P. O., and Nechita, A. (2004). An X-Ray Search for Compact Central Sources in Supernova Remnants. I. SNRS G093.3+6.9, G315.4-2.3, G084.2+0.8, and G127.1+0.5. *ApJS*, 153:269–315.
- Kaplan, D. L., Gaensler, B. M., Kulkarni, S. R., and Slane, P. O. (2006). An X-Ray Search for Compact Central Sources in Supernova Remnants. II. Six Large-Diameter SNRs. *ApJS*, 163:344–371.
- Kaplan, D. L., Stovall, K., Ransom, S. M., Roberts, M. S. E., Kotulla, R., Archibald, A. M., Biwer, C. M., Boyles, J., Dartez, L., and et al. (2012). Discovery of the Optical/Ultraviolet/Gamma-Ray Counterpart to the Eclipsing Millisecond Pulsar J1816+4510. *ApJ*, 753:174.
- Kaplan, D. L. and van Kerkwijk, M. H. (2005). A Coherent Timing Solution for the Nearby Isolated Neutron Star RX J1308.6+2127/RBS 1223. *ApJ*, 635:L65–L68.
- Kaplan, D. L., van Kerkwijk, M. H., Marshall, H. L., Jacoby, B. A., Kulkarni, S. R., and Frail, D. A. (2003). The Nearby Neutron Star RX J0720.4-3125 from Radio to X-Rays. *ApJ*, 590:1008–1019.
- Kargaltsev, O., Durant, M., Pavlov, G. G., and Garmire, G. (2012). Chandra Pulsar Survey (ChaPS). *ApJS*, 201:37.
- Kargaltsev, O., Misanovic, Z., Pavlov, G. G., Wong, J. A., and Garmire, G. P. (2008). X-Ray Observations of Parsec-scale Tails behind Two Middle-Aged Pulsars. *ApJ*, 684:542–557.
- Kargaltsev, O. and Pavlov, G. G. (2007). X-Ray Emission from PSR J1809-1917 and Its Pulsar Wind Nebula, Possibly Associated with the TeV Gamma-Ray Source HESS J1809-193. *ApJ*, 670:655–667.
- Kargaltsev, O. and Pavlov, G. G. (2010). Pulsar-wind nebulae in X-rays and TeV  $\gamma$ -rays. *X-ray Astronomy 2009; Present Status, Multi-Wavelength Approach and Future Perspectives*, 1248:25–28.
- Kargaltsev, O., Pavlov, G. G., and Garmire, G. P. (2006a). X-Ray Emission from the Double Neutron Star Binary B1534+12: Powered by the Pulsar Wind? *ApJ*, 646:1139–1148.
- Kargaltsev, O., Pavlov, G. G., and Garmire, G. P. (2006b). X-Ray Emission from the Nearby PSR B1133+16 and Other Old Pulsars. *ApJ*, 636:406–410.
- Kargaltsev, O., Pavlov, G. G., and Garmire, G. P. (2007). X-Ray Emission from PSR B1800-21, Its Wind Nebula, and Similar Systems. *ApJ*, 660:1413–1423.

- Kargaltsev, O., Pavlov, G. G., Sanwal, D., and Garmire, G. P. (2002). The Compact Central Object in the Supernova Remnant G266.2-1.2. *ApJ*, 580:1060–1064.
- Kargaltsev, O., Rangelov, B., and Pavlov, G. G. (2013). Gamma-ray and X-ray Properties of Pulsar Wind Nebulae and Unidentified Galactic TeV Sources. *ArXiv e-prints*.
- Kaspi, V. M., Bailes, M., Manchester, R. N., Stappers, B. W., Sandhu, J. S., Navarro, J., and D’Amico, N. (1997). Discovery of the Young, Energetic Radio Pulsar PSR J1105-6107. *ApJ*, 485:820.
- Kaspi, V. M., Gotthelf, E. V., Gaensler, B. M., and Lyutikov, M. (2001). X-Ray Detection of Pulsar PSR B1757-24 and Its Nebular Tail. *ApJ*, 562:L163–L166.
- Kaspi, V. M., Manchester, R. N., Johnston, S., Lyne, A. G., and D’Amico, N. (1992). PSR J1341-6220 - A young pulsar in a supernova remnant. *ApJ*, 399:L155–L157.
- Kaspi, V. M. and McLaughlin, M. A. (2005). Chandra X-Ray Detection of the High Magnetic Field Radio Pulsar PSR J1718-3718. *ApJ*, 618:L41–L44.
- Kato, M. (1997). Optically Thick Winds from Degenerate Dwarfs. I. Classical Novae of Populations I and II. *ApJS*, 113:121.
- Katsuda, S. (2003). *X-Ray Studies of Evolved Supernova Remnants*. PhD thesis, Osaka University, Japan.
- Keane, E. F. and Kramer, M. (2008). On the birthrates of Galactic neutron stars. *MNRAS*, 391:2009–2016.
- Keane, E. F., McLaughlin, M. A., Kramer, M., Stappers, B. W., Bassa, C. G., Purver, M. B., and Weltevrede, P. (2013). PSR J1840–1419: A Very Cool Neutron Star. *ApJ*, 764:180.
- Keith, M. J., Johnston, S., Ray, P. S., Ferrara, E. C., Saz Parkinson, P. M., Çelik, Ö., Belfiore, A., Donato, D., Cheung, C. C., and et al. (2011). Discovery of millisecond pulsars in radio searches of southern Fermi Large Area Telescope sources. *MNRAS*, 414:1292–1300.
- Kerr, F. J. and Lynden-Bell, D. (1986). Review of galactic constants. *MNRAS*, 221:1023–1038.
- Kerr, M., Camilo, F., Johnson, T. J., Ferrara, E. C., Guillemot, L., Harding, A. K., Hessels, J., Johnston, S., Keith, M., and et al. (2012). Five New Millisecond Pulsars from a Radio Survey of 14 Unidentified Fermi-LAT Gamma-Ray Sources. *ApJ*, 748:L2.
- Kocevski, D. D., Ebeling, H., Mullis, C. R., and Tully, R. B. (2007). A Systematic X-Ray Search for Clusters of Galaxies behind the Milky Way. II. The Second CIZA Subsample. *ApJ*, 662:224–235.
- Komesaroff, M. M., Ables, J. G., Cooke, D. J., Hamilton, P. A., and McCulloch, P. M. (1973). Results and Implications of a Recent Search for High-Dispersion Pulsars. *Astrophys. Lett.*, 15:169.

- Koribalski, B., Johnston, S., Weisberg, J. M., and Wilson, W. (1995). H I line measurements of eight southern pulsars. *ApJ*, 441:756–764.
- Kraft, R. P., Burrows, D. N., and Nousek, J. A. (1991). Determination of confidence limits for experiments with low numbers of counts. *ApJ*, 374:344–355.
- Kramer, M., Bell, J. F., Manchester, R. N., Lyne, A. G., Camilo, F., Stairs, I. H., D’Amico, N., Kaspi, V. M., Hobbs, G., and et al. (2003a). The Parkes Multibeam Pulsar Survey - III. Young pulsars and the discovery and timing of 200 pulsars. *MNRAS*, 342:1299–1324.
- Kramer, M., Lyne, A. G., Hobbs, G., Löhmer, O., Carr, P., Jordan, C., and Wolszczan, A. (2003b). The Proper Motion, Age, and Initial Spin Period of PSR J0538+2817 in S147. *ApJ*, 593:L31–L34.
- Kramer, M., Lyne, A. G., O’Brien, J. T., Jordan, C. A., and Lorimer, D. R. (2006). A Periodically Active Pulsar Giving Insight into Magnetospheric Physics. *Science*, 312:549–551.
- Krause, O., Tanaka, M., Usuda, T., Hattori, T., Goto, M., Birkmann, S., and Nomoto, K. (2008). Tycho Brahe’s 1572 supernova as a standard type Ia as revealed by its light-echo spectrum. *Nature*, 456:617–619.
- Krautter, J., Wichmann, R., Schmitt, J. H. M. M., Alcalá, J. M., Neuhauser, R., and Terranegra, L. (1997). New “weak-line”-T Tauri stars in Lupus. *A&AS*, 123:329–352.
- Krautter, J., Zickgraf, F.-J., Appenzeller, I., Thiering, I., Voges, W., Chavarria, C., Kneer, R., Mujica, R., Pakull, M. W., Serrano, A., and Ziegler, B. (1999). Identification of a complete sample of northern ROSAT All-Sky Survey X-ray sources. IV. Statistical analysis. *A&A*, 350:743–752.
- Kuiper, L., Hermsen, W., Verbunt, F., Ord, S., Stairs, I., and Lyne, A. (2002). High-Resolution Spatial and Timing Observations of Millisecond Pulsar PSR J0218+4232 with Chandra. *ApJ*, 577:917–922.
- Kumar, H. S. and Safi-Harb, S. (2008). Variability of the High Magnetic Field X-Ray Pulsar PSR J1846-0258 Associated with the Supernova Remnant Kes 75 as Revealed by the Chandra X-Ray Observatory. *ApJ*, 678:L43–L46.
- Kumar, H. S., Safi-Harb, S., and Gonzalez, M. E. (2012). Chandra and XMM-Newton Studies of the Supernova Remnant G292.2-0.5 Associated with the Pulsar J1119-6127. *ApJ*, 754:96.
- Kuntz, K. D. and Snowden, S. L. (2008). The EPIC-MOS particle-induced background spectra. *A&A*, 478:575–596.
- Lai, D. (2001). Neutron Star Kicks and Asymmetric Supernovae. In Blaschke, D., Glendenning, N. K., and Sedrakian, A., editors, *Physics of Neutron Star Interiors*, volume 578 of *Lecture Notes in Physics*, Berlin Springer Verlag, page 424.

- Lai, D., Chernoff, D. F., and Cordes, J. M. (2001). Pulsar Jets: Implications for Neutron Star Kicks and Initial Spins. *ApJ*, 549:1111–1118.
- Lattimer, J. M. (2012). The Nuclear Equation of State and Neutron Star Masses. *Annual Review of Nuclear and Particle Science*, 62:485–515.
- Lattimer, J. M. and Prakash, M. (2001). Neutron Star Structure and the Equation of State. *ApJ*, 550:426–442.
- Lattimer, J. M. and Prakash, M. (2007). Neutron star observations: Prognosis for equation of state constraints. *Phys. Rep.*, 442:109–165.
- Lattimer, J. M., Prakash, M., Pethick, C. J., and Haensel, P. (1991). Direct URCA process in neutron stars. *Physical Review Letters*, 66:2701–2704.
- Lazendic, J. S., Slane, P. O., Gaensler, B. M., Plucinsky, P. P., Hughes, J. P., Galloway, D. K., and Crawford, F. (2003). X-Ray Observations of the Compact Central Object in Supernova Remnant G347.3-0.5. *ApJ*, 593:L27–L30.
- Leahy, D. A., Xizhen, Z., Xinji, W., and Jiale, L. (1998). A multi-frequency radio study of the supernova remnant HB9. *A&A*, 339:601–609.
- Lemoine-Goumard, M., Zavlin, V. E., Grondin, M.-H., Shannon, R., Smith, D. A., Burgay, M., Camilo, F., Cohen-Tanugi, J., Freire, P. C. C., and et al. (2011). Discovery of gamma- and X-ray pulsations from the young and energetic PSR J1357-6429 with Fermi and XMM-Newton. *A&A*, 533:A102.
- Levin, L., Bailes, M., Bates, S., Bhat, N. D. R., Burgay, M., Burke-Spolaor, S., D’Amico, N., Johnston, S., Keith, M., and et al. (2010). A Radio-loud Magnetar in X-ray Quiescence. *ApJ*, 721:L33–L37.
- Li, W., Chornock, R., Leaman, J., Filippenko, A. V., Poznanski, D., Wang, X., Ganeshalingam, M., and Mannucci, F. (2011). Nearby supernova rates from the Lick Observatory Supernova Search - III. The rate-size relation, and the rates as a function of galaxy Hubble type and colour. *MNRAS*, 412:1473–1507.
- Li, X. H., Lu, F. J., and Li, T. P. (2005). X-Ray Spectroscopy of PSR B1951+32 and Its Pulsar Wind Nebula. *ApJ*, 628:931–937.
- Li, X.-H., Lu, F.-J., and Li, Z. (2008). Nonthermal X-Ray Properties of Rotation-powered Pulsars and Their Wind Nebulae. *ApJ*, 682:1166–1176.
- Lin, L. C. C., Hui, C. Y., Hu, C. P., Wu, J. H. K., Huang, R. H. H., Trepl, L., Takata, J., Seo, K. A., Wang, Y., Chou, Y., and Cheng, K. S. (2013). Discovery of X-Ray Pulsation from the Geminga-like Pulsar PSR J2021+4026. *ApJ*, 770:L9.

- Lopez, L. A., Ramirez-Ruiz, E., Badenes, C., Huppenkothen, D., Jeltema, T. E., and Pooley, D. A. (2009). Typing Supernova Remnants Using X-Ray Line Emission Morphologies. *ApJ*, 706:L106–L109.
- Lorimer, D. R. and Kramer, M. (2004). *Handbook of Pulsar Astronomy*.
- Lorimer, D. R., Lyne, A. G., Bailes, M., Manchester, R. N., D’Amico, N., Stappers, B. W., Johnston, S., and Camilo, F. (1996). Discovery of Four Binary Millisecond Pulsars. *MNRAS*, 283:1383–1387.
- Lorimer, D. R., Lyne, A. G., McLaughlin, M. A., Kramer, M., Pavlov, G. G., and Chang, C. (2012). Radio and X-Ray Observations of the Intermittent Pulsar J1832+0029. *ApJ*, 758:141.
- Lorimer, D. R., Nicastro, L., Lyne, A. G., Bailes, M., Manchester, R. N., Johnston, S., Bell, J. F., D’Amico, N., and Harrison, P. A. (1995). Four new millisecond pulsars in the galactic disk. *ApJ*, 439:933–938.
- Lucke, P. B. (1978). The distribution of color excesses and interstellar reddening material in the solar neighborhood. *A&A*, 64:367–377.
- Lyne, A. G. (2009). Intermittent Pulsars. In Becker, W., editor, *Astrophysics and Space Science Library*, volume 357 of *Astrophysics and Space Science Library*, page 67.
- Lyne, A. G. and Graham-Smith, F. (2005). *Pulsar Astronomy*.
- Maccacaro, T., Gioia, I. M., Wolter, A., Zamorani, G., and Stocke, J. T. (1988). The X-ray spectra of the extragalactic sources in the Einstein extended medium sensitivity survey. *ApJ*, 326:680–690.
- Manchester, R. N. (2007). Searching for a Pulsar in SN1987A. In Immler, S., Weiler, K., and McCray, R., editors, *Supernova 1987A: 20 Years After: Supernovae and Gamma-Ray Bursters*, volume 937 of *American Institute of Physics Conference Series*, pages 134–143.
- Manchester, R. N., Damico, N., and Tuohy, I. R. (1985). A search for short-period pulsars. *MNRAS*, 212:975–986.
- Manchester, R. N., Hobbs, G. B., Teoh, A., and Hobbs, M. (2005). The Australia Telescope National Facility Pulsar Catalogue. *AJ*, 129:1993–2006.
- Manchester, R. N., Lyne, A. G., Camilo, F., Bell, J. F., Kaspi, V. M., D’Amico, N., McKay, N. P. F., Crawford, F., Stairs, I. H., and et al. (2001). The Parkes multi-beam pulsar survey - I. Observing and data analysis systems, discovery and timing of 100 pulsars. *MNRAS*, 328:17–35.
- Manchester, R. N., Lyne, A. G., Taylor, J. H., Durdin, J. M., Large, M. I., and Little, A. G. (1978). The second Molonglo pulsar survey - discovery of 155 pulsars. *MNRAS*, 185:409–421.

- Manzali, A., De Luca, A., and Caraveo, P. A. (2007). Phase-resolved Spectroscopy of the Vela Pulsar with XMM-Newton. *ApJ*, 669:570–578.
- Marcaide, J. M., Martí-Vidal, I., Alberdi, A., Pérez-Torres, M. A., Ros, E., Diamond, P. J., Guirado, J. C., Lara, L., Shapiro, I. I., and et al. (2009). A decade of SN 1993J: discovery of radio wavelength effects in the expansion rate. *A&A*, 505:927–945.
- Marelli, M., De Luca, A., and Caraveo, P. A. (2011). A Multiwavelength Study on the High-energy Behavior of the Fermi/LAT Pulsars. *ApJ*, 733:82.
- Markwardt, C. B., Swank, J. H., Klein-Wolt, M., and Smith, D. M. (2007). RXTE and Swift Discovery of the Intermittent Source XTE J1704-445. *The Astronomer's Telegram*, 1164:1.
- Marshall, H. L. and Schulz, N. S. (2002). Using the High-Resolution X-Ray Spectrum of PSR B0656+14 to Constrain the Chemical Composition of the Neutron Star Atmosphere. *ApJ*, 574:377–381.
- Massaro, E., Cusumano, G., Litterio, M., and Mineo, T. (2000). Fine phase resolved spectroscopy of the X-ray emission of the Crab pulsar (PSR B0531+21) observed with BeppoSAX. *A&A*, 361:695–703.
- Matheson, H. and Safi-Harb, S. (2010). The Plerionic Supernova Remnant G21.5-0.9 Powered by PSR J1833-1034: New Spectroscopic and Imaging Results Revealed with the Chandra X-ray Observatory. *ApJ*, 724:572–587.
- Mazure, A. and Basa, S. (2009). *Exploding Superstars Understanding Supernovae and Gamma-Ray Bursts*.
- McClure-Griffiths, N. M., Dickey, J. M., Gaensler, B. M., Green, A. J., Haverkorn, M., and Strasser, S. (2005). The Southern Galactic Plane Survey: H I Observations and Analysis. *ApJS*, 158:178–187.
- McGarry, M. B., Gaensler, B. M., Ransom, S. M., Kaspi, V. M., and Veljkovic, S. (2005). X-Ray Timing, Spectroscopy, and Photometry of the Anomalous X-Ray Pulsar Candidate CXOU J010043.1-721134. *ApJ*, 627:L137–L140.
- McGowan, K. E., Kennea, J. A., Zane, S., Córdova, F. A., Cropper, M., Ho, C., Sasseen, T., and Vestrand, W. T. (2003). Detection of Pulsed X-Ray Emission from XMM-Newton Observations of PSR J0538+2817. *ApJ*, 591:380–387.
- McGowan, K. E., Vestrand, W. T., Kennea, J. A., Zane, S., Cropper, M., and Córdova, F. A. (2007). X-ray observations of PSR B0355+54 and its pulsar wind nebula. *Ap&SS*, 308:309–316.
- McGowan, K. E., Zane, S., Cropper, M., Kennea, J. A., Córdova, F. A., Ho, C., Sasseen, T., and Vestrand, W. T. (2004). XMM-Newton Observations of PSR B1706-44. *ApJ*, 600:343–350.

- McGowan, K. E., Zane, S., Cropper, M., Vestrand, W. T., and Ho, C. (2006). Evidence for Surface Cooling Emission in the XMM-Newton Spectrum of the X-Ray Pulsar PSR B2334+61. *ApJ*, 639:377–381.
- McKee, C. F. (1987). Astrophysical shocks in diffuse gas. In A. Dalgarno & D. Layzer, editor, *Spectroscopy of Astrophysical Plasmas*, pages 226–254.
- McLaughlin, M. (2009). Rotating Radio Transients. In Becker, W., editor, *Astrophysics and Space Science Library*, volume 357 of *Astrophysics and Space Science Library*, page 41.
- McLaughlin, M. A., Rea, N., Gaensler, B. M., Chatterjee, S., Camilo, F., Kramer, M., Lorimer, D. R., Lyne, A. G., Israel, G. L., and Possenti, A. (2007). Discovery of Pulsations and a Possible Spectral Feature in the X-Ray Emission from Rotating Radio Transient J1819-1458. *ApJ*, 670:1307–1313.
- Mereghetti, S., Sartore, N., Tiengo, A., De Luca, A., Turolla, R., and Haberl, F. (2012). A Study of the Long Term Variability of RX J1856.5-3754 with XMM-Newton. In Lewandowski, W., Maron, O., and Kijak, J., editors, *Electromagnetic Radiation from Pulsars and Magnetars*, volume 466 of *Astronomical Society of the Pacific Conference Series*, page 33.
- Mereghetti, S., Tiengo, A., Esposito, P., Götz, D., Stella, L., Israel, G. L., Rea, N., Feroci, M., Turolla, R., and Zane, S. (2005). An XMM-Newton View of the Soft Gamma Repeater SGR 1806-20: Long-Term Variability in the Pre-Giant Flare Epoch. *ApJ*, 628:938–945.
- Merloni, A., Predehl, P., Becker, W., Böhringer, H., Boller, T., Brunner, H., Brusa, M., Dennerl, K., Freyberg, M., and et al. (2012). eROSITA Science Book: Mapping the Structure of the Energetic Universe. *ArXiv e-prints*.
- Mestel, L. (1971). Pulsar Magnetosphere. *Nature Physical Science*, 233:149–152.
- Mewe, R. (1999). Atomic Physics of Hot Plasmas. In van Paradijs, J. and Bleeker, J. A. M., editors, *X-Ray Spectroscopy in Astrophysics*, volume 520 of *Lecture Notes in Physics*, Berlin Springer Verlag, page 109.
- Mewe, R., Lemen, J. R., and van den Oord, G. H. J. (1986). Calculated X-radiation from optically thin plasmas. VI - Improved calculations for continuum emission and approximation formulae for nonrelativistic average Gaunt factors. *A&AS*, 65:511–536.
- Mignani, R. P., Vande Putte, D., Cropper, M., Turolla, R., Zane, S., Pellizza, L. J., Bignone, L. A., Sartore, N., and Treves, A. (2013). The birthplace and age of the isolated neutron star RX J1856.5-3754. *MNRAS*, 429:3517–3521.
- Milne, D. K., Caswell, J. L., and Haynes, R. F. (1993). A Faint Polarized Arc Near the Supernova Remnant MSH:15-52 G:320.4-1.2. *MNRAS*, 264:853.
- Mirabel, I. F. and Rodríguez, L. F. (1999). Sources of Relativistic Jets in the Galaxy. *ARA&A*, 37:409–443.

- Monet, D. G., Levine, S. E., Canzian, B., Ables, H. D., Bird, A. R., Dahn, C. C., Guetter, H. H., Harris, H. C., Henden, A. A., and et al. (2003). The USNO-B Catalog. *AJ*, 125:984–993.
- Morrison, R. and McCammon, D. (1983). Interstellar photoelectric absorption cross sections, 0.03-10 keV. *ApJ*, 270:119–122.
- Morrissey, P., Conrow, T., Barlow, T. A., Small, T., Seibert, M., Wyder, T. K., Budavári, T., Arnouts, S., Friedman, P. G., and et al. (2007). The Calibration and Data Products of GALEX. *ApJS*, 173:682–697.
- Mukherjee, R., Gotthelf, E. V., Halpern, J., and Tavani, M. (2000). Multiwavelength Examination of the COS B Field 2CG 075+00 Yields a Blazar Identification for 3EG J2016+3657. *ApJ*, 542:740–749.
- Müller, G., Hartwig, E., and (Germany), A. G. (1922). *Geschichte und Literatur des Lichtwechsels der bis Ende 1915 als sicher veränderlich anerkannten Sterne: nebst einem Katalog der Elemente ihres Lichtwechsels*. Number Bd. 3 in *Geschichte und Literatur des Lichtwechsels der bis Ende 1915 als sicher veränderlich anerkannten Sterne: nebst einem Katalog der Elemente ihres Lichtwechsels*. In Kommission Bei Poeschel & Trepte.
- Mullis, C. R., Ebeling, H., Kocevski, D. D., and Tully, R. B. (2005). XMM-Newton Observations of CIZA J1324.6-5736 – A Massive, Newly Discovered Galaxy Cluster in the Great Attractor Region. In Fairall, A. P. and Woudt, P. A., editors, *Nearby Large-Scale Structures and the Zone of Avoidance*, volume 329 of *Astronomical Society of the Pacific Conference Series*, page 183.
- Muno, M. P., Gaensler, B. M., Nechita, A., Miller, J. M., and Slane, P. O. (2008). A Search for New Galactic Magnetars in Archival Chandra and XMM-Newton Observations. *ApJ*, 680:639–653.
- Murray, S. S., Slane, P. O., Seward, F. D., Ransom, S. M., and Gaensler, B. M. (2002). Discovery of X-Ray Pulsations from the Compact Central Source in the Supernova Remnant 3C 58. *ApJ*, 568:226–231.
- Muslimov, A. G. and Harding, A. K. (2003). Extended Acceleration in Slot Gaps and Pulsar High-Energy Emission. *ApJ*, 588:430–440.
- Nandra, K., Barret, D., Barcons, X., Fabian, A., den Herder, J.-W., Piro, L., Watson, M., Adami, C., Aird, J., Afonso, J. M., and et al. et al. (2013). The Hot and Energetic Universe: A White Paper presenting the science theme motivating the Athena+ mission. *ArXiv e-prints*.
- Naylor, T. and Fabian, A. C. (1999). ROSAT observations of Cepheus OB3: the discovery of low-mass stars. *MNRAS*, 302:714–722.
- Nicastro, L., Cusumano, G., Löhmer, O., Kramer, M., Kuiper, L., Hermsen, W., Mineo, T., and Becker, W. (2004). BeppoSAX observation of PSR B1937+21. *A&A*, 413:1065–1072.

- Nice, D. J., Altieri, E., Bogdanov, S., Cordes, J. M., Farrington, D., Hessels, J. W. T., Kaspi, V. M., Lyne, A. G., Popa, L., and et al. (2013). Timing and Interstellar Scattering of 35 Distant Pulsars Discovered in the PALFA Survey. *ApJ*, 772:50.
- Nolan, P. L., Abdo, A. A., Ackermann, M., Ajello, M., Allafort, A., Antolini, E., Atwood, W. B., Axelsson, M., Baldini, L., and et al. (2012). Fermi Large Area Telescope Second Source Catalog. *ApJS*, 199:31.
- Nordhaus, J., Brandt, T. D., Burrows, A., and Almgren, A. (2012). The hydrodynamic origin of neutron star kicks. *MNRAS*, 423:1805–1812.
- Olausen, S. A., Kaspi, V. M., Lyne, A. G., and Kramer, M. (2010). XMM-Newton X-ray Observation of the High-magnetic-field Radio Pulsar PSR J1734-3333. *ApJ*, 725:985–989.
- Olausen, S. A., Zhu, W. W., Vogel, J. K., Kaspi, V. M., Lyne, A. G., Espinoza, C. M., Stappers, B. W., Manchester, R. N., and McLaughlin, M. A. (2013). X-Ray Observations of High-B Radio Pulsars. *ApJ*, 764:1.
- Oosterbroek, T., Kennea, J., Much, R., and Córdova, F. A. (2004). XMM-Newton observations of a sample of radio pulsars. *Nuclear Physics B Proceedings Supplements*, 132:636–639.
- Oppenheimer, J. R. and Volkoff, G. M. (1939). On Massive Neutron Cores. *Physical Review*, 55:374–381.
- Osten, R. A., Hawley, S. L., Allred, J. C., Johns-Krull, C. M., and Roark, C. (2005). From Radio to X-Ray: Flares on the dMe Flare Star EV Lacertae. *ApJ*, 621:398–416.
- Ott, C. D., Burrows, A., Thompson, T. A., Livne, E., and Walder, R. (2006). The Spin Periods and Rotational Profiles of Neutron Stars at Birth. *ApJS*, 164:130–155.
- Özel, F. (2013). Surface emission from neutron stars and implications for the physics of their interiors. *Reports on Progress in Physics*, 76(1):016901.
- Pacini, F. (1967). Energy Emission from a Neutron Star. *Nature*, 216:567–568.
- Pacini, F. (1968). Rotating Neutron Stars, Pulsars and Supernova Remnants. *Nature*, 219:145–146.
- Page, D., Geppert, U., and Weber, F. (2006). The cooling of compact stars. *Nuclear Physics A*, 777:497–530.
- Page, D., Lattimer, J. M., Prakash, M., and Steiner, A. W. (2004). Minimal Cooling of Neutron Stars: A New Paradigm. *ApJS*, 155:623–650.
- Page, D., Lattimer, J. M., Prakash, M., and Steiner, A. W. (2009). Neutrino Emission from Cooper Pairs and Minimal Cooling of Neutron Stars. *ApJ*, 707:1131–1140.

- Page, D., Prakash, M., Lattimer, J. M., and Steiner, A. W. (2011). Rapid Cooling of the Neutron Star in Cassiopeia A Triggered by Neutron Superfluidity in Dense Matter. *Physical Review Letters*, 106(8):081101.
- Pancrazi, B., Webb, N. A., Becker, W., Cognard, I., Guillemot, L., Hill, A. B., Jackson, M., Mignani, R. P., and Rea, N. (2012). X-ray follow-up observations of the two  $\gamma$ -ray pulsars PSR J1459-6053 and PSR J1614-2230. *A&A*, 544:A108.
- Park, S., Kargaltsev, O., Pavlov, G. G., Mori, K., Slane, P. O., Hughes, J. P., Burrows, D. N., and Garmire, G. P. (2009). Nonthermal X-Rays from Supernova Remnant G330.2+1.0 and the Characteristics of its Central Compact Object. *ApJ*, 695:431–441.
- Park, S., Roming, P. W. A., Hughes, J. P., Slane, P. O., Burrows, D. N., Garmire, G. P., and Nousek, J. A. (2002). The Structure of the Oxygen-rich Supernova Remnant G292.0+1.8 from Chandra X-Ray Images: Shocked Ejecta and Circumstellar Medium. *ApJ*, 564:L39–L43.
- Parker, Q. A., Phillipps, S., Pierce, M. J., Hartley, M., Hambly, N. C., Read, M. A., MacGillivray, H. T., Tritton, S. B., Cass, C. P., and et al. (2005). The AAO/UKST SuperCOSMOS  $H\alpha$  survey. *MNRAS*, 362:689–710.
- Patnaude, D. J. and Fesen, R. A. (2009). Proper Motions and Brightness Variations of Nonthermal X-ray Filaments in the Cassiopeia A Supernova Remnant. *ApJ*, 697:535–543.
- Pavlov, G. G., Kargaltsev, O., Garmire, G. P., and Wolszczan, A. (2007). X-Ray Emission from the Planet Pulsar B1257+12. *ApJ*, 664:1072–1078.
- Pavlov, G. G., Kargaltsev, O., Wong, J. A., and Garmire, G. P. (2009). Detection of X-Ray Emission from the Very Old Pulsar J0108-1431. *ApJ*, 691:458–464.
- Pavlov, G. G., Zavlin, V. E., Sanwal, D., Burwitz, V., and Garmire, G. P. (2001). The X-Ray Spectrum of the Vela Pulsar Resolved with the Chandra X-Ray Observatory. *ApJ*, 552:L129–L133.
- Pellizzoni, A., Tiengo, A., De Luca, A., Esposito, P., and Mereghetti, S. (2008). PSR J0737-3039: Interacting Pulsars in X-Rays. *ApJ*, 679:664–674.
- Perlmutter, S., Aldering, G., Goldhaber, G., Knop, R. A., Nugent, P., Castro, P. G., Deustua, S., Fabbro, S., and A. Goobar, e. (1999). Measurements of Omega and Lambda from 42 High-Redshift Supernovae. *ApJ*, 517:565–586.
- Petre, R., Becker, C. M., and Winkler, P. F. (1996). A Central Stellar Remnant in Puppis A. *ApJ*, 465:L43.
- Petre, R., Kuntz, K. D., and Shelton, R. L. (2002). The X-Ray Structure and Spectrum of the Pulsar Wind Nebula Surrounding PSR B1853+01 in W44. *ApJ*, 579:404–410.

- Pfeffermann, E. and Aschenbach, B. (1996). ROSAT observation of a new supernova remnant in the constellation Scorpius. In H. U. Zimmermann, J. Trümper, & H. Yorke, editor, *Röntgenstrahlung from the Universe*, pages 267–268.
- Pfeffermann, E., Aschenbach, B., and Predehl, P. (1991). Discovery of a galactic supernova remnant with ROSAT. *A&A*, 246:L28–L31.
- Phillips, J. P. (2006). The Problem with Reddening Distances to Planetary Nebulae. *Rev. Mexicana Astron. Astrofis.*, 42:229–239.
- Phillips, M. M. (1993). The absolute magnitudes of Type IA supernovae. *ApJ*, 413:L105–L108.
- Piekarewicz, J., Agrawal, B. K., Colò, G., Nazarewicz, W., Paar, N., Reinhard, P.-G., Roca-Maza, X., and Vretenar, D. (2012). Electric dipole polarizability and the neutron skin. *Phys. Rev. C*, 85(4):041302.
- Pierbattista, M., Grenier, I. A., Harding, A. K., and Gonthier, P. L. (2012). Constraining  $\gamma$ -ray pulsar gap models with a simulated pulsar population. *A&A*, 545:A42.
- Pinheiro Gonçalves, D., Noriega-Crespo, A., Paladini, R., Martin, P. G., and Carey, S. J. (2011). The MIPS GAL View of Supernova Remnants in the Galactic Plane. *AJ*, 142:47.
- Pivovarov, M. J., Kaspi, V. M., and Gotthelf, E. V. (2000). ASCA Observations of the Young Rotation-powered Pulsars PSR B1046-58 and PSR B1610-50. *ApJ*, 528:436–444.
- Pletsch, H. J., Guillemot, L., Fehrmann, H., Allen, B., Kramer, M., Aulbert, C., Ackermann, M., Ajello, M., de Angelis, A., and et al. (2012). Binary Millisecond Pulsar Discovery via Gamma-Ray Pulsations. *Science*, 338:1314–1317.
- Plucinsky, P. P., Snowden, S. L., Aschenbach, B., Egger, R., Edgar, R. J., and McCammon, D. (1996). ROSAT Survey Observations of the Monogem Ring. *ApJ*, 463:224.
- Posselt, B., Pavlov, G. G., and Garmire, G. P. (2011). Chandra observations of PSR B1451-68. In *American Astronomical Society Meeting Abstracts #218*, page #232.02.
- Possenti, A., Cerutti, R., Colpi, M., and Mereghetti, S. (2002). Re-examining the X-ray versus spin-down luminosity correlation of rotation powered pulsars. *A&A*, 387:993–1002.
- Potekhin, A. Y., Chabrier, G., and Yakovlev, D. G. (1997). Internal temperatures and cooling of neutron stars with accreted envelopes. *A&A*, 323:415–428.
- Prakash, M. (2013). Neutron Stars and the EOS. *ArXiv e-prints*.
- Predehl, P., Andritschke, R., Böhringer, H., Bornemann, W., Bräuninger, H., Brunner, H., Brusa, M., Burkert, W., Burwitz, V., and et al. (2010). eROSITA on SRG. In *Society of Photo-Optical Instrumentation Engineers (SPIE) Conference Series*, volume 7732 of *Society of Photo-Optical Instrumentation Engineers (SPIE) Conference Series*.

- Predehl, P. and Schmitt, J. H. M. M. (1995). X-raying the interstellar medium: ROSAT observations of dust scattering halos. *A&A*, 293:889–905.
- Prinz, T. and Becker, W. (2012). Exploring the supernova remnant G308.4-1.4. *A&A*, 544:A7.
- Prinz, T. and Becker, W. (2013). Supernova remnant G296.7-0.9 in X-rays. *A&A*, 550:A33.
- Ransom, S. M., Ray, P. S., Camilo, F., Roberts, M. S. E., Çelik, Ö., Wolff, M. T., Cheung, C. C., Kerr, M., Pennucci, T., and et al. (2011). Three Millisecond Pulsars in Fermi LAT Unassociated Bright Sources. *ApJ*, 727:L16.
- Ray, P. S., Abdo, A. A., Parent, D., Bhattacharya, D., Bhattacharyya, B., Camilo, F., Cognard, I., Theureau, G., Ferrara, E. C., and et al. (2012). Radio Searches of Fermi LAT Sources and Blind Search Pulsars: The Fermi Pulsar Search Consortium. *ArXiv e-prints*.
- Ray, P. S., Kerr, M., Parent, D., Abdo, A. A., Guillemot, L., Ransom, S. M., Rea, N., Wolff, M. T., Makeev, A., and et al. (2011). Precise  $\gamma$ -ray Timing and Radio Observations of 17 Fermi  $\gamma$ -ray Pulsars. *ApJS*, 194:17.
- Ray, P. S., Ransom, S. M., Cheung, C. C., Giroletti, M., Cognard, I., Camilo, F., Bhattacharyya, B., Roy, J., Romani, R. W., and et al. (2013). Radio Detection of the Fermi-LAT Blind Search Millisecond Pulsar J1311-3430. *ApJ*, 763:L13.
- Rea, N. and Esposito, P. (2011). Magnetar outbursts: an observational review. In Torres, D. F. and Rea, N., editors, *High-Energy Emission from Pulsars and their Systems*, page 247.
- Reich, W., Fuerst, E., Haslam, C. G. T., Steffen, P., and Reif, K. (1984). A radio continuum survey of the Galactic Plane at 11 CM wavelength. I - The area  $L = 357.4$  to  $76$  deg,  $B = -1.5$  to  $+1.5$  deg. *A&AS*, 58:197–199.
- Renaud, M., Marandon, V., Gotthelf, E. V., Rodriguez, J., Terrier, R., Mattana, F., Lebrun, F., Tomsick, J. A., and Manchester, R. N. (2010). Discovery of a Highly Energetic Pulsar Associated with IGR J14003-6326 in the Young Uncataloged Galactic Supernova Remnant G310.6-1.6. *ApJ*, 716:663–670.
- Rest, A., Suntzeff, N. B., Olsen, K., Prieto, J. L., Smith, R. C., Welch, D. L., Becker, A., Bergmann, M., Clocchiatti, A., and et al. (2005). Light echoes from ancient supernovae in the Large Magellanic Cloud. *Nature*, 438:1132–1134.
- Rest, A., Welch, D. L., Suntzeff, N. B., Ooster, L., Lanning, H., Olsen, K., Smith, R. C., Becker, A. C., Bergmann, M., and et al. (2008). Scattered-Light Echoes from the Historical Galactic Supernovae Cassiopeia A and Tycho (SN 1572). *ApJ*, 681:L81–L84.
- Reynolds, S. P. (2008). Supernova Remnants at High Energy. *ARA&A*, 46:89–126.
- Reynolds, S. P., Borkowski, K. J., Green, D. A., Hwang, U., Harrus, I., and Petre, R. (2008). The Youngest Galactic Supernova Remnant: G1.9+0.3. *ApJ*, 680:L41–L44.

- Reynoso, E. M., Green, A. J., Johnston, S., Dubner, G. M., Giacani, E. B., and Goss, W. M. (2003). Observations of the neutral hydrogen surrounding the radio-quiet neutron star RX J0822-4300 in Puppis A. *MNRAS*, 345:671–677.
- Rho, J. and Borkowski, K. J. (2002). ROSAT/ASCA Observations of the Mixed-Morphology Supernova Remnant W28. *ApJ*, 575:201–216.
- Robbins, W. J., Gaensler, B. M., Murphy, T., Reeves, S., and Green, A. J. (2012). A multiwavelength study of the radio source G296.7-0.9: confirmation as a Galactic supernova remnant. *MNRAS*, 419:2623–2632.
- Roberts, M. S. E. and Brogan, C. L. (2008). Discovery of a New X-Ray Filled Radio Supernova Remnant around the Pulsar Wind Nebula in 3EG J1809-2328. *ApJ*, 681:320–324.
- Roberts, M. S. E., Romani, R. W., and Johnston, S. (2001). Multiwavelength Studies of PSR J1420-6048, a Young Pulsar in the Kookaburra. *ApJ*, 561:L187–L190.
- Roberts, M. S. E., Tam, C. R., Kaspi, V. M., Lyutikov, M., Vasisht, G., Pivovarov, M., Gotthelf, E. V., and Kawai, N. (2003). The Pulsar Wind Nebula in G11.2-0.3. *ApJ*, 588:992–1002.
- Rodney, S. A., Riess, A. G., Strolger, L., Ferguson, H. C., Casertano, S., Koekemoer, A., Dahlen, T., Grogin, N. A., Hjorth, J., and et al. (2011). Type Ia Supernovae at  $z \geq 1.5$  from the HST Multi-Cycle Treasury Surveys. In *American Astronomical Society Meeting Abstracts #218*, page #219.01.
- Roger, R. S., Milne, D. K., Kesteven, M. J., Wellington, K. J., and Haynes, R. F. (1988). Symmetry of the radio emission from two high-latitude supernova remnants, G296.5 + 10.0 and G327.6 + 14.6 (SN 1006). *ApJ*, 332:940–953.
- Romani, R. W. and Ng, C.-Y. (2003). The Pulsar Wind Nebula Torus of PSR J0538+2817 and the Origin of Pulsar Velocities. *ApJ*, 585:L41–L44.
- Roques, F. and Moncuquet, M. (2000). A Detection Method for Small Kuiper Belt Objects: The Search for Stellar Occultations. *Icarus*, 147:530–544.
- Roques, F., Moncuquet, M., and Sicardy, B. (1987). Stellar occultations by small bodies - Diffraction effects. *AJ*, 93:1549–1558.
- Ruderman, M. A. and Sutherland, P. G. (1975). Theory of pulsars - Polar caps, sparks, and coherent microwave radiation. *ApJ*, 196:51–72.
- Sabin, L., Parker, Q. A., Contreras, M. E., Olguín, L., Frew, D. J., Stupar, M., Vázquez, R., Wright, N. J., Corradi, R. L. M., and Morris, R. A. H. (2013). New Galactic supernova remnants discovered with IPHAS. *MNRAS*, 431:279–291.
- Safi-Harb, S., Harrus, I. M., Petre, R., Pavlov, G. G., Koptsevich, A. B., and Sanwal, D. (2001). X-Ray Observations of the Supernova Remnant G21.5-0.9. *ApJ*, 561:308–320.

- Safi-Harb, S. and Kumar, H. S. (2008). Using Chandra to Unveil the High-Energy Properties of the High Magnetic Field Radio Pulsar J1119-6127. *ApJ*, 684:532–541.
- Sako, M., Bassett, B., Becker, A., Cinabro, D., DeJongh, F., Depoy, D. L., Dilday, B., Doi, M., Frieman, J. A., and et al. (2008). The Sloan Digital Sky Survey-II Supernova Survey: Search Algorithm and Follow-Up Observations. *AJ*, 135:348–373.
- Sato, T., Bamba, A., Nakamura, R., and Ishida, M. (2010). Identification of CXOU J171405.7-381031 as a New Magnetar with XMM-Newton. *PASJ*, 62:L33–L36.
- Sault, R. J., Teuben, P. J., and Wright, M. C. H. (1995). A Retrospective View of MIRIAD. In R. A. Shaw, H. E. Payne, & J. J. E. Hayes, editor, *Astronomical Data Analysis Software and Systems IV*, volume 77 of *Astronomical Society of the Pacific Conference Series*, page 433.
- Schaudel, D. (2003). *X-ray Properties of Galactic Supernova Remnants*. PhD thesis, LMU, Germany.
- Schaudel, D., Becker, W., Voges, W., Aschenbach, B., Reich, W., and Weisskopf, M. (2002). Galactic SNR Candidates in the ROSAT All-Sky Survey. In P. O. Slane & B. M. Gaensler, editor, *Neutron Stars in Supernova Remnants*, volume 271 of *Astronomical Society of the Pacific Conference Series*, page 391.
- Scheck, L., Kifonidis, K., Janka, H.-T., and Müller, E. (2006). Multidimensional supernova simulations with approximative neutrino transport. I. Neutron star kicks and the anisotropy of neutrino-driven explosions in two spatial dimensions. *A&A*, 457:963–986.
- Scheck, L., Plewa, T., Janka, H.-T., Kifonidis, K., and Müller, E. (2004). Pulsar Recoil by Large-Scale Anisotropies in Supernova Explosions. *Physical Review Letters*, 92(1):011103.
- Schwentker, O. (1994). Evidence for a low-luminosity X-ray pulsar associated with a supernova remnant. *A&A*, 286:L47–L50.
- Sedov, L. I. (1959). *Similarity and Dimensional Methods in Mechanics*.
- Seok, J. Y., Koo, B.-C., Onaka, T., Ita, Y., Lee, H.-G., Lee, J.-J., Moon, D.-S., Sakon, I., Kaneda, H., Lee, H. M., Lee, M. G., and Kim, S. E. (2008). Supernova Remnants in the AKARI IRC Survey of the Large Magellanic Cloud. *PASJ*, 60:453.
- Seward, F. D., Dame, T. M., Fesen, R. A., and Aschenbach, B. (1995). A ROSAT-detected, New Galactic Supernova Remnant in Sagittarius, G13.3-1.3. *ApJ*, 449:681.
- Seward, F. D., Forman, W. R., Giacconi, R., Griffiths, R. E., Harnden, J. F. R., Jones, C., and Pye, J. P. (1979). X-rays from Eta Carinae and the surrounding nebula. *ApJ*, 234:L55–L58.
- Seward, F. D. and Wang, Z.-R. (1988). Pulsars, X-ray synchrotron nebulae, and guest stars. *ApJ*, 332:199–205.

- Shapiro, S. L. and Teukolsky, S. A. (1983). *Black holes, white dwarfs, and neutron stars: The physics of compact objects*.
- Shternin, P. S., Yakovlev, D. G., Heinke, C. O., Ho, W. C. G., and Patnaude, D. J. (2011). Cooling neutron star in the Cassiopeia A supernova remnant: evidence for superfluidity in the core. *MNRAS*, 412:L108–L112.
- Slane, P., Chen, Y., Lazendic, J. S., and Hughes, J. P. (2002). An ASCA Study of the High-Luminosity Supernova Remnant G349.7+0.2. *ApJ*, 580:904–908.
- Slane, P., Helfand, D. J., van der Swaluw, E., and Murray, S. S. (2004a). New Constraints on the Structure and Evolution of the Pulsar Wind Nebula 3C 58. *ApJ*, 616:403–413.
- Slane, P., Zimmerman, E. R., Hughes, J. P., Seward, F. D., Gaensler, B. M., and Clarke, M. J. (2004b). X-Ray Observations of the Compact Source in CTA 1. *ApJ*, 601:1045–1049.
- Smith, D. A., Guillemot, L., Camilo, F., Cognard, I., Dumora, D., Espinoza, C., Freire, P. C. C., Gotthelf, E. V., Harding, A. K., and et al. (2008). Pulsar timing for the Fermi gamma-ray space telescope. *A&A*, 492:923–931.
- Smith, R. K., Brickhouse, N. S., Liedahl, D. A., and Raymond, J. C. (2001). Collisional Plasma Models with APEC/APED: Emission-Line Diagnostics of Hydrogen-like and Helium-like Ions. *ApJ*, 556:L91–L95.
- Smits, R., Kramer, M., Stappers, B., Lorimer, D. R., Cordes, J., and Faulkner, A. (2009). Pulsar searches and timing with the square kilometre array. *A&A*, 493:1161–1170.
- Snowden, S. L., Mushotzky, R. F., Kuntz, K. D., and Davis, D. S. (2008). A catalog of galaxy clusters observed by XMM-Newton. *A&A*, 478:615–658.
- Speagle, J. S., Kaplan, D. L., and van Kerkwijk, M. H. (2011). The X-Ray Counterpart of the High-B Pulsar PSR J0726-2612. *ApJ*, 743:183.
- Staelin, D. H. and Reifenstein, I. E. C. (1968). Pulsating Radio Sources near the Crab Nebula. *Science*, 162:1481–1483.
- Stelzer, B., Robrade, J., Schmitt, J. H. M. M., and Bouvier, J. (2009). New X-ray detections of Herbig stars. *A&A*, 493:1109–1119.
- Stokes, G. H., Taylor, J. H., Welsberg, J. M., and Dewey, R. J. (1985). A survey for short-period pulsars. *Nature*, 317:787.
- Strüder, L., Briel, U., Dennerl, K., Hartmann, R., Kendziorra, E., Meidinger, N., Pfeiffermann, E., Reppin, C., Aschenbach, B., and et al. (2001). The European Photon Imaging Camera on XMM-Newton: The pn-CCD camera. *A&A*, 365:L18–L26.
- Stupar, M., Parker, Q. A., Filipović, M. D., Frew, D. J., Bojičić, I., and Aschenbach, B. (2007). Multiwavelength study of a new Galactic SNR G332.5-5.6. *MNRAS*, 381:377–388.

- Sturrock, P. A. (1971). A Model of Pulsars. *ApJ*, 164:529.
- Sun, M., Wang, Z.-R., and Chen, Y. (1999). X-Ray Observation and Analysis of the Composite Supernova Remnant G327.1-1.1. *ApJ*, 511:274–281.
- Tananbaum, H. (1999). Cassiopeia A. *IAU Circ.*, 7246:1.
- Taylor, J. H. and Cordes, J. M. (1993). Pulsar distances and the galactic distribution of free electrons. *ApJ*, 411:674–684.
- Tetzlaff, N., Eisenbeiss, T., Neuhäuser, R., and Hohle, M. M. (2011). The origin of RX J1856.5-3754 and RX J0720.4-3125 - updated using new parallax measurements. *MNRAS*, 417:617–626.
- Thielemann, F.-K., Brachwitz, F., Höflich, P., Martinez-Pinedo, G., and Nomoto, K. (2004). The physics of type Ia supernovae. *New A Rev.*, 48:605–610.
- Tian, W. W., Li, Z., Leahy, D. A., Yang, J., Yang, X. J., Yamazaki, R., and Lu, D. (2010). X-Ray Emission from HESS J1731-347/SNR G353.6-0.7 and Central Compact Source XMMS J173203-344518. *ApJ*, 712:790–796.
- Tiengo, A., Göhler, E., Staubert, R., and Mereghetti, S. (2002). The anomalous X-ray pulsar 1E 1048.1-5937: Phase resolved spectroscopy with the XMM-Newton satellite. *A&A*, 383:182–187.
- Tolman, R. C. (1939). Static Solutions of Einstein's Field Equations for Spheres of Fluid. *Physical Review*, 55:364–373.
- Torii, K., Saito, Y., Nagase, F., Yamagami, T., Kamae, T., Hirayama, M., Kawai, N., Sakurai, I., Namiki, M., Shibata, S., Gunji, S., and Finley, J. P. (2001). ASCA Detection of Pulsed X-Ray Emission from PSR J0631+1036. *ApJ*, 551:L151–L154.
- Townsley, L. K., Broos, P. S., Chu, Y.-H., Gruendl, R. A., Oey, M. S., and Pittard, J. M. (2011). The Integrated Diffuse X-ray Emission of the Carina Nebula Compared to Other Massive Star-forming Regions. *ApJS*, 194:16.
- Truelove, J. K. and McKee, C. F. (1999). Evolution of Nonradiative Supernova Remnants. *ApJS*, 120:299–326.
- Tsang, M. B., Zhang, Y., Danielewicz, P., Famiano, M., Li, Z., Lynch, W. G., and Steiner, A. W. (2009). Constraints on the Density Dependence of the Symmetry Energy. *Physical Review Letters*, 102(12):122701.
- Tsuruta, S. (1998). Thermal properties and detectability of neutron stars. II. Thermal evolution of rotation-powered neutron stars. *Phys. Rep.*, 292:1–130.
- Tsuruta, S. (2009). Neutron Star Cooling: II. In Becker, W., editor, *Astrophysics and Space Science Library*, volume 357 of *Astrophysics and Space Science Library*, page 289.

- Turolla, R. (2009). Isolated Neutron Stars: The Challenge of Simplicity. In Becker, W., editor, *Astrophysics and Space Science Library*, volume 357 of *Astrophysics and Space Science Library*, page 141.
- Turtle, A. J., Pugh, J. F., Kenderdine, S., and Pauliny-Toth, I. I. K. (1962). The spectrum of the galactic radio emission, I. Observations of low resolving power. *MNRAS*, 124:297.
- van der Horst, A. J., Connaughton, V., Kouveliotou, C., Briggs, M. S., Paciesas, W. S., Pal'Shin, V., Golenetskii, S., Aptekar, R., Frederiks, D., and et al. (2009). Discovery of a new soft gamma repeater source, SGR 0418+5729. *The Astronomer's Telegram*, 2077:1.
- van der Klis, M., Swank, J. H., Zhang, W., Jahoda, K., Morgan, E. H., Lewin, W. H. G., Vaughan, B., and van Paradijs, J. (1996). Discovery of Submillisecond Quasi-periodic Oscillations in the X-Ray Flux of Scorpius X-1. *ApJ*, 469:L1.
- Van Etten, A., Romani, R. W., and Ng, C.-Y. (2012). A Chandra Proper Motion for PSR J1809-2332. *ApJ*, 755:151.
- van Kerkwijk, M. H., Kaplan, D. L., Durant, M., Kulkarni, S. R., and Paerels, F. (2004). A Strong, Broad Absorption Feature in the X-Ray Spectrum of the Nearby Neutron Star RX J1605.3+3249. *ApJ*, 608:432–443.
- van Loon, J. T., Cioni, M.-R. L., Zijlstra, A. A., and Loup, C. (2005). An empirical formula for the mass-loss rates of dust-enshrouded red supergiants and oxygen-rich Asymptotic Giant Branch stars. *A&A*, 438:273–289.
- Verbiest, J. P. W., Weisberg, J. M., Chael, A. A., Lee, K. J., and Lorimer, D. R. (2012). On Pulsar Distance Measurements and Their Uncertainties. *ApJ*, 755:39.
- Vink, J. (2006). High Energy Emission from Supernova Remnants. In Meurs, E. J. A. and Fabbiano, G., editors, *Populations of High Energy Sources in Galaxies*, volume 230 of *IAU Symposium*, pages 16–23.
- Vink, J. (2012). Supernova remnants: the X-ray perspective. *A&A Rev.*, 20:49.
- Voges, W., Aschenbach, B., Boller, T., Bräuninger, H., Briel, U., Burkert, W., Dennerl, K., Englhauser, J., Gruber, R., and et al., F. (1999). The ROSAT all-sky survey bright source catalogue. *A&A*, 349:389–405.
- Wachter, S., Patel, S. K., Kouveliotou, C., Bouchet, P., Özel, F., Tennant, A. F., Woods, P. M., Hurley, K., Becker, W., and Slane, P. (2004). Precise Localization of the Soft Gamma Repeater SGR 1627-41 and the Anomalous X-Ray Pulsar AXP 1E1841-045 with Chandra. *ApJ*, 615:887–896.
- Waller, W. H. (1990). Emission-line and continuum fluxes from narrow- and broad-band imagery. *PASP*, 102:1217–1223.

- Wang, B. and Han, Z. (2012). Progenitors of type Ia supernovae. *New A Rev.*, 56:122–141.
- Wang, C., Lai, D., and Han, J. L. (2007a). Spin-Kick Correlation in Neutron Stars: Alignment Conditions and Implications. *ApJ*, 656:399–407.
- Wang, J., Townsley, L. K., Feigelson, E. D., Getman, K. V., Broos, P. S., Garmire, G. P., and Tsujimoto, M. (2007b). An X-Ray Census of Young Stars in the Massive Southern Star-forming Complex NGC 6357. *ApJS*, 168:100–127.
- Wang, N., Manchester, R. N., Pace, R. T., Bailes, M., Kaspi, V. M., Stappers, B. W., and Lyne, A. G. (2000). Glitches in southern pulsars. *MNRAS*, 317:843–860.
- Watson, M. G., Schröder, A. C., Fyfe, D., Page, C. G., Lamer, G., Mateos, S., Pye, J., Sakano, M., Rosen, S., and et al. (2009). The XMM-Newton serendipitous survey. V. The Second XMM-Newton serendipitous source catalogue. *A&A*, 493:339–373.
- Webb, N. A., Olive, J.-F., Barret, D., Kramer, M., Cognard, I., and Löhmer, O. (2004). XMM-Newton spectral and timing analysis of the faint millisecond pulsars PSR J0751+1807 and PSR J1012+5307. *A&A*, 419:269–276.
- Webber, W. R. (1998). A New Estimate of the Local Interstellar Energy Density and Ionization Rate of Galactic Cosmic Cosmic Rays. *ApJ*, 506:329–334.
- Weber, F., Negreiros, R., and Rosenfield, P. (2009). Neutron Star Interiors and the Equation of State of Superdense Matter. In Becker, W., editor, *Astrophysics and Space Science Library*, volume 357 of *Astrophysics and Space Science Library*, page 213.
- Weber, F., Orsaria, M., and Negreiros, R. (2013a). Impact of Rotation on the Structure and Composition of Neutron Stars. *ArXiv e-prints*.
- Weber, F., Orsaria, M., Rodrigues, H., and Yang, S.-H. (2013b). Structure of Quark Stars. In *IAU Symposium*, volume 291 of *IAU Symposium*, pages 61–66.
- Weisberg, J. M., Nice, D. J., and Taylor, J. H. (2010). Timing Measurements of the Relativistic Binary Pulsar PSR B1913+16. *ApJ*, 722:1030–1034.
- Weisskopf, M. C., Tennant, A. F., Yakovlev, D. G., Harding, A., Zavlin, V. E., O’Dell, S. L., Elsner, R. F., and Becker, W. (2011). Chandra Phase-resolved X-Ray Spectroscopy of the Crab Pulsar. *ApJ*, 743:139.
- Wheeler, J. C., Meier, D. L., and Wilson, J. R. (2002). Asymmetric Supernovae from Magneto-centrifugal Jets. *ApJ*, 568:807–819.
- Whiteoak, J. B. Z. and Green, A. J. (1996). The MOST supernova remnant catalogue (MSC). *A&AS*, 118:329–380.

- Williams, B. J., Blair, W. P., Blondin, J. M., Borkowski, K. J., Ghavamian, P., Long, K. S., Raymond, J. C., Reynolds, S. P., Rho, J., and Winkler, P. F. (2011). RCW 86: A Type Ia Supernova in a Wind-blown Bubble. *ApJ*, 741:96.
- Winkler, P. F. and Petre, R. (2007). Direct Measurement of Neutron Star Recoil in the Oxygen-rich Supernova Remnant Puppis A. *ApJ*, 670:635–642.
- Winkler, P. F., Tuttle, J. H., Kirshner, R. P., and Irwin, M. J. (1988). Kinematics of Oxygen-Rich Filaments in Puppis a. In Roger, R. S. and Landecker, T. L., editors, *IAU Colloq. 101: Supernova Remnants and the Interstellar Medium*, page 65.
- Woltjer, L. (1972). Supernova Remnants. *ARA&A*, 10:129.
- Wongwathanarat, A., Janka, H.-T., and Müller, E. (2010). Hydrodynamical Neutron Star Kicks in Three Dimensions. *ApJ*, 725:L106–L110.
- Wongwathanarat, A., Janka, H.-T., and Müller, E. (2013). Three-dimensional neutrino-driven supernovae: Neutron star kicks, spins, and asymmetric ejection of nucleosynthesis products. *A&A*, 552:A126.
- Woosley, S. E., Heger, A., and Weaver, T. A. (2002). The evolution and explosion of massive stars. *Reviews of Modern Physics*, 74:1015–1071.
- Wright, E. L., Eisenhardt, P. R. M., Mainzer, A. K., Ressler, M. E., Cutri, R. M., Jarrett, T., Kirkpatrick, J. D., Padgett, D., McMillan, R. S., and et al. (2010). The Wide-field Infrared Survey Explorer (WISE): Mission Description and Initial On-orbit Performance. *AJ*, 140:1868–1881.
- Wu, J. H. K., Kong, A. K. H., Huang, R. H. H., Takata, J., Tam, P. H. T., Wu, E. M. H., and Cheng, K. S. (2012). Discovery of  $\gamma$ -Ray Pulsation and X-Ray Emission from the Black Widow Pulsar PSR J2051-0827. *ApJ*, 748:141.
- Yakovlev, D. G. and Pethick, C. J. (2004). Neutron Star Cooling. *ARA&A*, 42:169–210.
- Yar-Uyaniker, A., Uyaniker, B., and Kothes, R. (2004). Distance of Three Supernova Remnants from H I Line Observations in a Complex Region: G114.3+0.3, G116.5+1.1, and CTB 1 (G116.9+0.2). *ApJ*, 616:247–256.
- Yoshita, K., Miyata, E., and Tsunemi, H. (2000). Discovery of a New Supernova Remnant in the Direction of G69.7+1.0. *PASJ*, 52:867–873.
- Zacharias, N., Finch, C., Girard, T., Hambly, N., Wycoff, G., Zacharias, M. I., Castillo, D., Corbin, T., Divittorio, M., and et al. (2009). Third U.S. Naval Observatory CCD Astrograph Catalog (UCAC3). *VizieR Online Data Catalog*, 1315:0.
- Zane, S., Haberl, F., Israel, G. L., Pellizzoni, A., Burgay, M., Mignani, R. P., Turolla, R., Possenti, A., Esposito, P., and et al. (2011). Discovery of 59 ms pulsations from 1RXS J141256.0+792204 (Calvera). *MNRAS*, 410:2428–2445.

- Zavlin, V. E. (2006). XMM-Newton Observations of Four Millisecond Pulsars. *ApJ*, 638:951–962.
- Zavlin, V. E. (2007). First X-Ray Observations of the Young Pulsar J1357-6429. *ApJ*, 665:L143–L146.
- Zavlin, V. E. and Pavlov, G. G. (2004a). X-Ray Emission from the Old Pulsar B0950+08. *ApJ*, 616:452–462.
- Zavlin, V. E. and Pavlov, G. G. (2004b). XMM observations of three middle-aged pulsars. *Mem. Soc. Astron. Italiana*, 75:458.
- Zavlin, V. E., Pavlov, G. G., and Trümper, J. (1998). The neutron star in the supernova remnant PKS 1209-52. *A&A*, 331:821–828.
- Zavlin, V. E., Trümper, J., and Pavlov, G. G. (1999). X-Ray Emission from the Radio-quiet Neutron Star in Puppis A. *ApJ*, 525:959–967.
- Zhang, B., Sanwal, D., and Pavlov, G. G. (2005). An XMM-Newton Observation of the Drifting Pulsar B0943+10. *ApJ*, 624:L109–L112.
- Zhu, W., Kaspi, V. M., Gonzalez, M. E., and Lyne, A. G. (2009). Xmm-Newton X-Ray Detection of the High-Magnetic-Field Radio Pulsar PSR B1916+14. *ApJ*, 704:1321–1326.
- Zhu, W. W., Kaspi, V. M., McLaughlin, M. A., Pavlov, G. G., Ng, C.-Y., Manchester, R. N., Gaensler, B. M., and Woods, P. M. (2011). Chandra Observations of the High-magnetic-field Radio Pulsar J1718-3718. *ApJ*, 734:44.
- Zirakashvili, V. N. and Aharonian, F. (2007). Analytical solutions for energy spectra of electrons accelerated by nonrelativistic shock-waves in shell type supernova remnants. *A&A*, 465:695–702.
- Zombeck, M. (2007). *Handbook of Space Astronomy and Astrophysics: Third Edition*. Cambridge University Press.

# Danksagung

Diese Doktorarbeit entstand am Max-Planck Institut für extraterrestrische Physik (MPE) unter der Leitung von Herrn Prof. Dr. Werner Becker.

Ich möchte Werner Becker für die sehr gute, kompetente und immer freundliche Betreuung danken. Es hat Spaß gemacht vier Jahre mit ihm zusammenzuarbeiten. Besonders möchte ich ihm dafür danken, dass er es mir ermöglicht hat am MPE meine Doktorarbeit zu schreiben.

Außerdem danke ich Mike Bernhardt für die gute Zusammenarbeit in den letzten vier Jahren, für die vielen hilfreichen Diskussionen und für das Korrekturlesen. Ein Dank geht auch an Hanno Kaupp und Florian Hofmann für viele gefundene und korrigierte Rechtschreib-, Grammatikfehler- und Ausdrucksfehler. Many thanks to Jeremy Sanders for checking parts of the work.

Ein besonderes Dankeschön geht an meine Freundin Mirjam Appel, die es immer wieder geschafft hat mich zu motivieren und mich mit viele wertvolle Tipps unterstützt hat. Ohne sie wäre ich nicht so weit gekommen.

Ein Dank geht auch an die Teilnehmer meines Thesis Komitees, Herr Prof. Dr. Ulrich Walter von der TU München und Gottfried Kanbach vom MPE, die mich die letzten drei Jahre bei der Doktorarbeit begleitet haben und mir immer das Gefühl gaben, dass ich auf den richtigen Weg bin. Zudem bedanke ich mich für die finanzielle Unterstützung durch die *International Max Planck Research School on Astrophysics (IMPRS)* bedanken.

Außerdem danke ich allen vom MPE, die direkt oder indirekt an meiner Arbeit beteiligt waren. Insbesondere Veronika Schubert, Christa Ingram und Birgit Boller für die Unterstützung mit allem was nicht die Wissenschaft betraf, sowie Harald Baumgartner für seine Hilfe bei allen Installationen und Computerproblemen. Ein Dank geht auch an Hans Böhringer, der es mir ermöglicht hat 10 Tage für optische Beobachtungen nach Chile fahren zu können, was eine unvergessliche Zeit war.

Zu guter Letzt möchte ich meinen Eltern und meiner leider vor zwei Jahren verstorbenen Großmutter für deren Unterstützung danken, ohne die ich nach meiner Ausbildung nie den Weg in die Wissenschaft einschlagen hätte können.